Supermanoeuvrability in a biomimetic morphing-wing aircraft

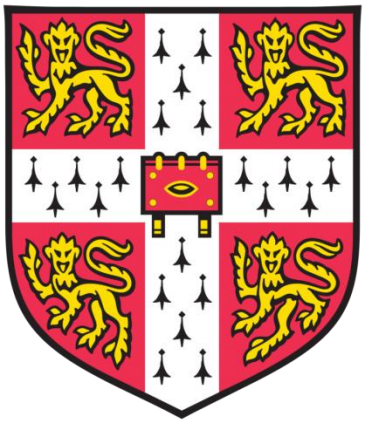

Arion Douglas Pons

Trinity Hall

University of Cambridge

February 2019

This dissertation is submitted for the degree of Doctor of Philosophy.

DECLARATION

This dissertation is an account of research carried out by the author at the Department of Engineering, University of Cambridge between October 2015 and February 2019. The work described herein is the author's own and includes nothing which is the outcome of work done in collaboration. Other publications of the results presented here are listed. Neither this work, nor any substantial part, nor any substantially similar work have been submitted or are being concurrently submitted for any qualification at any other university or similar institution. Prior to examination, it contains 146 figures and 62,500 words, conforming to prescribed limits.

Arion Pons

February 2019

SUMMARY

Name: Arion Pons

Title: Supermanoeuvrability in a biomimetic morphing-wing aircraft

In this work we study the supermanoeuvrability of a biomimetic morphing-wing case study aircraft system. Analytical and computational models of biomimetic flight dynamics are developed, utilising multibody dynamics, computational fluid dynamics, and reduced-order aerodynamic models; and validated with respect to experimentally-derived flight dynamics of a Pioneer RQ-2 UAV. These models are used to explore the capability of this system for a wide range of biological and other supermanoeuvres: multi-axis quasistatic nose-pointing-and-shooting (NPAS) / direct force capability; multi-axis rapid-nose-pointing-and-shooting (RaNPAS) including Pugachev's cobra; ballistic transition; and anchor turning. Novel contributions include the development of transient aerodynamic models for a three-dimensional flight-simulation context; the development of novel methods for assessing transient model validity; the development of improved methods of quaternion variational integration; the development of quasi-trim and continuation-based methods for the design, exploration, analysis and control of manoeuvres in biomimetic morphing-wing systems; an assessment of the complex spiral mode stability effects present in asymmetrically-morphed system trim states; and a demonstration of the wide-ranging potential for advanced supermanoeuvrability in biomimetic morphing-wing systems. Industrial applications include the design of high-precision guided missiles for use in complex, e.g. urban, environments.

ACKNOWLEDGMENTS

To the Southern Alps: for always being there when I needed you.

To the Church of England; the chapels of Trinity Hall and Christ's College;
and to Christchurch Cathedral, New Zealand: my lifeblood.

To the Cambridge Trust: for the generosity of their scholarship.

To my supervisor, Dr. Fehmi Cirak: for freedom.

To my parents and to Angela: for love.

To the reader: with my apologies.

PUBLICATIONS

1. A Pons and F Cirak, Three-dimensional flight simulation with transient moving-aerofoil models, in Proc. IUTAM Symposium on Recent Advances on Moving Boundary Problems in Mechanics, Springer Nature, Cham, Switzerland, 2019.

Table of contents

Chapter 1: Introduction

1.1. INTRODUCTION

Readers who are familiar with any of the numerous wildlife documentaries filmed over the last decade will recognise the extraordinary flight capabilities of biological creatures. These films frequently show birds, bats and other flying creatures performing complex aerial manoeuvres – for display, combat, or other motivations – which far outpace the capability of conventional fixed-wing aircraft. Such manoeuvres include complex perching [1], stall turning [2–5], zero-airspeed rolling [6], and parachute braking [7,8]. Many of these creatures could indeed be accurately characterised as *supermanoeuvrable* [9–11]: a descriptor originating from the study of highly manoeuvrable aircraft, and denoting their capability for controlled flight beyond conventional stall boundaries.

Biologically-inspired approaches to achieving analogous levels of manoeuvrability in aircraft thus become apparent. However, the first supermanoeuvrable aircraft owed their capability not to biomimicry but to advances in the study of unstable airframes. In the late 1970s, a Sukhoi Su-27 carried out the *Pugachev Cobra* – a high-amplitude post-stall pitching manoeuvre [12] – utilising only static structural and aerodynamic design: large wing strake, nose chines, and an unstable airframe [12–15]. Within a decade supermanoeuvrable aircraft were rapidly acquiring greater capability through the introduction of thrust vectoring / vectored propulsion [12]. Supermanoeuvrability has now become synonymous with thrust vectoring; and as such is a feature of many recent high-performance jet aircraft, including the Sukhoi PAK FA [16], and Mitsubishi X-2 Shinshin [17] and Lockheed Martin F-22 Raptor [13].

However, the problem and potential of biologically-inspired supermanoeuvrability remains. Much research has gone into designing biomimetic aircraft, e.g. [18–20], with an emphasis on wing flapping as a propulsive mechanism. The scope for biomimicry is vast: among vertebrate-inspired systems alone, there are mimetic seagulls [18], pigeons [21], bats [22,23], pterosaurs [24,25] and hummingbirds [26]. Interestingly, biological research indicates that the mechanisms of propulsion and supermanoeuvrability in flying creatures are partially distinct – for instance, flying squirrels, not capable of powered-flight, show supermanoeuvrability when gliding [27–30]. Evolutionary studies suggest that, in the lineage

of birds, flight manoeuvrability evolved before a strong power stroke [31]; and today birds and bats can carry out stall turns in under the timescale of a single wingbeat [32,33].

A pertinent open question, therefore, is whether supermanoeuvrability is attainable in a biomimetic UAV / MAV, independent of flapping-wing propulsion. A hybrid aircraft with a conventional propulsion system and basic wing morphing might attain a degree of biomimetic supermanoeuvrability, while retaining the advantages in airspeed, range, endurance and actuator requirements offered by a conventional propulsion system. UAV development is a highly competitive environment, with fixed-wing, rotorcraft, fully-biomimetic, and other morphing UAV systems to contend against; but potential niches for this form of hybrid aircraft can be identified, e.g. in the design of highly-manoeuvrable loitering munitions. Target applications are discussed in more detail in Section 1.4.2.

Existing studies into supermanoeuvrable biomimetic systems have focused strongly on perching manoeuvres: indeed, it has been demonstrated that, given sufficient elevator authority, perching manoeuvres may be successfully performed by fixed-wing glider MAVs solely under elevator control [34–37]. Improvements in perching performance can be attained using wing morphing [37]: changes in wing dihedral [38,39] or incidence [40,41], sometimes combined with tail displacement motion [42,43] have all shown potential, and some impressive flight tests have been carried out. However, more complex forms of biomimetic supermanoeuvrability are only rarely recognised (e.g. [44]) and not well understood. This work will investigate the mechanisms behind a range of forms of biological and biomimetic supermanoeuvrability, and will explore the potential for such capability in a hybrid aircraft. To start this exploration, a review of existing research into biological supermanoeuvrability and morphing-wing systems is required.

1.2. BIOLOGICAL SUPERMANOEUVRABILITY: A REVIEW

1.2.1. Terminology

For readers unfamiliar with biological and/or engineering studies of morphing-wing flight, Figure 1.2.1 gives a brief overview of the terminology describing the forms of wing motion that are relevant to our study. In general, biological terms (e.g. pronation) refer to motion,

whereas engineering terms (e.g. incidence) refer to a state: for consistency in Figure 1.2.1 appropriate motion descriptors are used (e.g. increasing incidence). Biologically, not all degrees of freedom may be active, and some may be coupled – for example, pigeon (*Columba livia*) wing extension has been noted to also change the forward / aft location of the wing centre of area, functioning as a form of sweep variation [45].

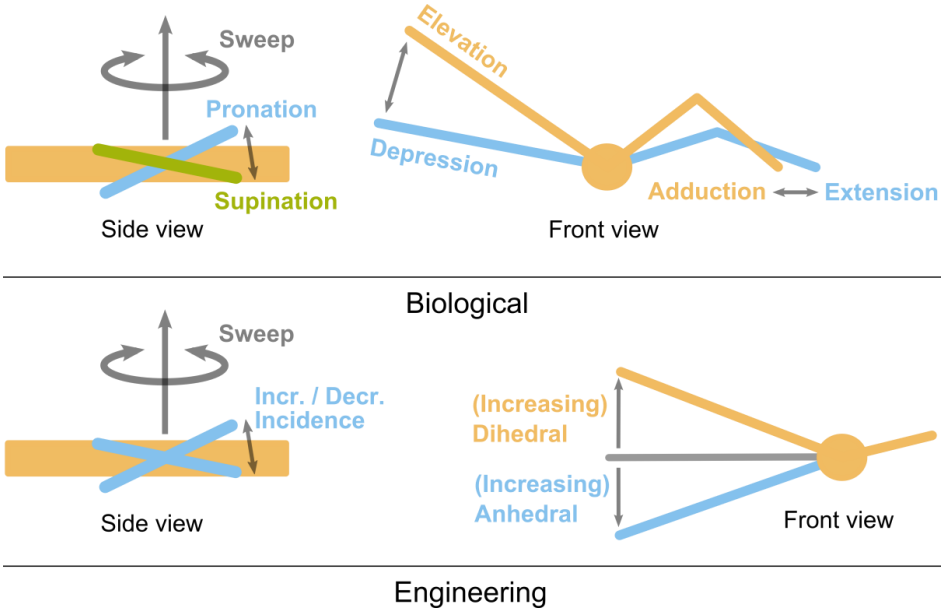

Figure 1.2.1: Terminology for avian wing motion commonly used in biological and engineering literature.

1.2.2. Avian turning flight

A wide variety of bird and bat species are known to carry out sharp stall or anchor turns by supinating (pitching upwards) the inboard wing, stalling it and generating a large drag force and yaw moment [2–4]. In bats turns of 180° in a space of less than half a wingspan and a time of two to three wingbeats have been observed [5,33,46]. The mechanism of these turns is surprisingly similar to that of the Herbst manoeuvre in supermanoeuvrable aircraft, involving an altitude increase to bleed off airspeed, rapid braking using the airframe drag and a low-airspeed roll into the new orientation [5,12,33,46,47]. The use of altitude to store kinetic energy enables both a tighter turn radius and a more rapid reacceleration after the manoeuvre. Figure 1.2.2 shows 180° turning flight paths for two bat species, *Myotis mystacinus* and *Cynopterus brachyotis*, recorded by Aldridge [33] and Tian et al. [5]; compare the schematic of the Herbst manoeuvre carried out by an X-31 aircraft shown in Figure 1.2.3.

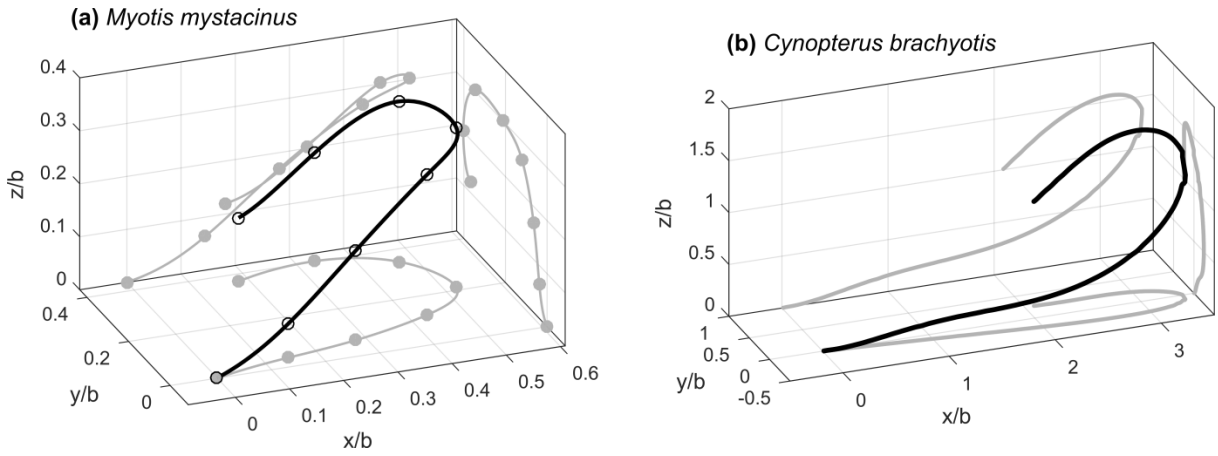

Figure 1.2.2: 180° turning flight paths for two bat species, in dimensionless wingspan (*b*) coordinates: **(a)** *M. mystacinus*, from Aldridge [33] with eight data points and taking 0.28 s, and **(b)** *C. brachyotis*, from Tian et al. [5] and with fine measured data over five wingbeats.

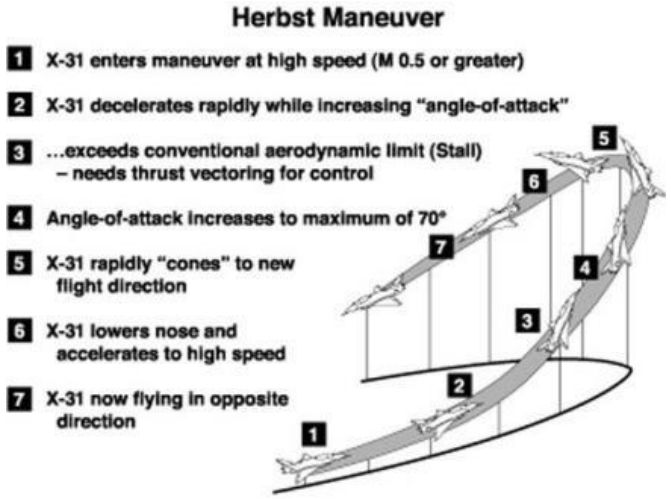

Figure 1.2.3: A diagram and description of the Herbst manoeuvre in an X-31 aircraft, reproduced from NASA [48], maximum resolution, public domain.

More relaxed banked turns are also widespread. At low speeds these manoeuvres place greater reliance on continuous propulsive flapping: short banked turns of radius two to three wingspans and about three wingbeats are common in pigeons [6]; cockatoos have been observed to perform 90° banked turns in about 1.2 wingspans and three wingbeats [49]. The minimum instantaneous radii of such turns are tiny – in bats, banked turns have been observed to occur in 0.8 of a wingspan (at a bearing rate of over 400°/s) [50]; and Figure 1.2.4 shows traced images of a c. 140° turn performed by a long-eared bat (*Plecotus auritus*) at a radius of c. half a wingspan, observed by Rayer and Aldridge [46]. In the most extreme case, instantaneous turning radii of below 0.03 of a wingspan were observed [33] –

effectively indicating on-the-spot turning, which may be regarded as a form of direct force capability as described by Herbst [10]. Centripetal accelerations of up to nearly 8*g* have been observed in such high-speed turns [51], and they involve complex wing motion [4,6,52].

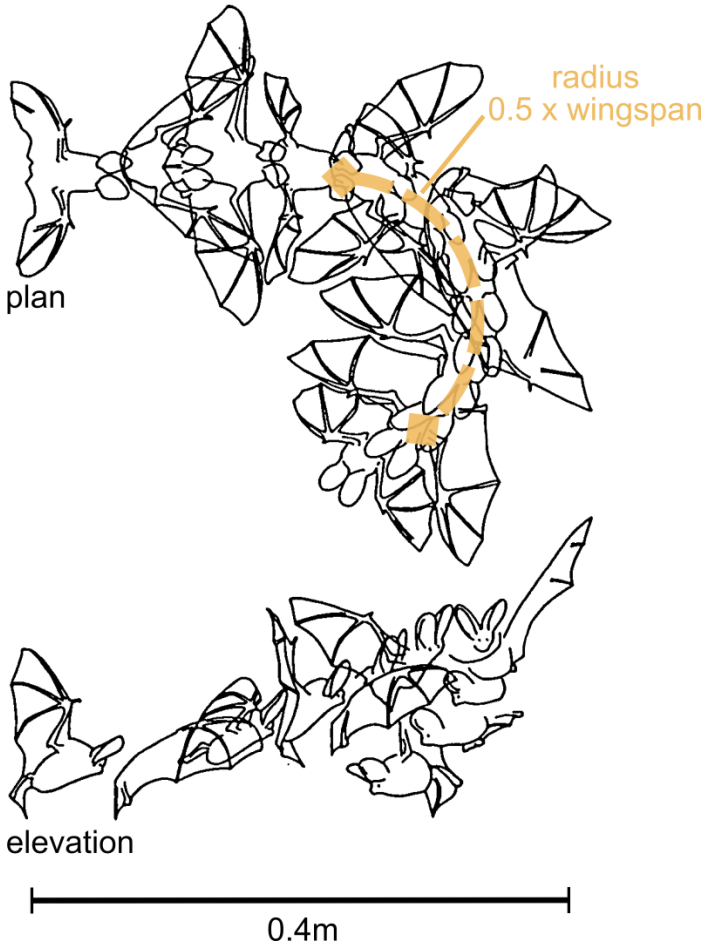

Figure 1.2.4: Traced images from high-speed film, plan and elevation views, 50 ms apart, of a long-eared bat (*P. auritus*) undergoing a shallow powered turn through c. 140°. Adapted from Rayner and Aldridge [46] with permission.

1.2.3. Avian complex manoeuvres

Other than turning flight, a variety of more complex rotational and direct-force manoeuvres have also been observed in avian flyers. In pigeons a remarkable zero-airspeed rolling manoeuvre has been observed which allows the bird to right itself after free fall in an inverted position [6]: this is achieved through an asymmetric flapping stroke, wherein each wing is alternately elevated or depressed (for the appropriate direction of roll) while the opposite wing is held closer to the body to avoid generating a counteracting drag moment.

Degrees of both post-stall aerodynamic control and inertial manoeuvring, c.f. [53], are likely to be involved, though the relative significance of each is uncertain. Figure 1.2.5 shows traced images of a pigeon (*Columba livia*) performing this manoeuvre, which may again be regarded as a biological example of direct force capability, as defined by Herbst [10].

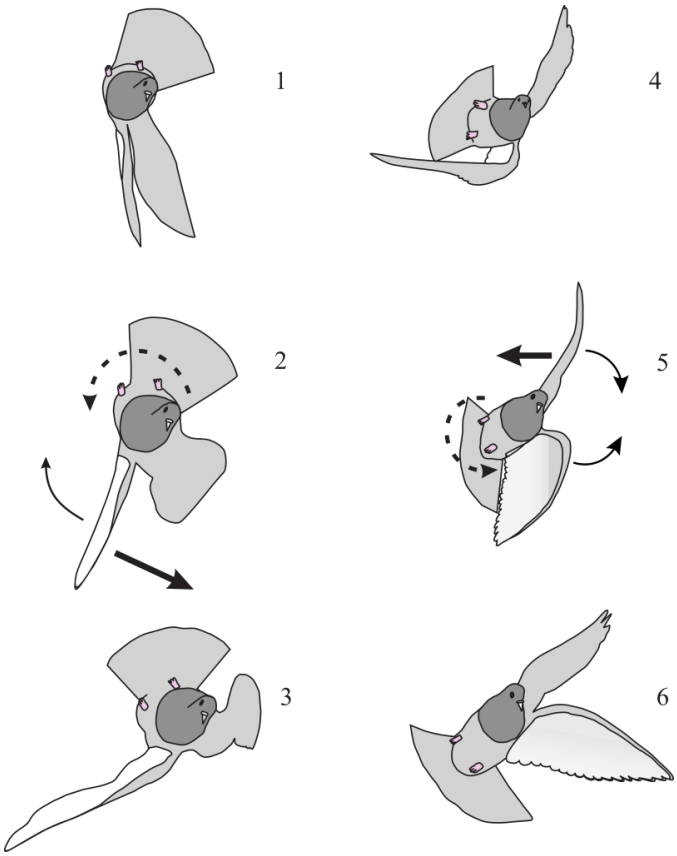

Figure 1.2.5: Traced images from high-speed film, 12 ms apart, of a pigeon (*C. livia*) undergoing a near-zero-airspeed rolling manoeuvre. Thin arrows denote wing movement, dashed arrows the direction of body roll, and thick arrows are inferred lift (frame 2) and drag (frame 5) forces. The pigeon rolls 135° in approximately 50 ms. Reproduced from Warrick and Dial [6] with permission.

A similar manoeuvre has been observed by Bergou et al. [54] in Seba's short-tailed bat (*Carollia perspicillata*). This consists of an abortive upwards landing operation (*C. perspicillata* and other bats perch upside-down) followed by a righting operation to return to normal flight. This sequence of operations is induced in captivity by removing a landing pad habitually used by the bat; in the wild it might be observed in other abortive landing scenarios, e.g. defence or aggression from a perched bat in the landing zone. The combination produces a complex rotational manoeuvre involving all three degrees of

freedom. Figure 1.2.6 shows images of the full manoeuvre, captured on high-speed film by Bergou et al. [54]. As may be seen, the initial high-angle upwards flight leads to an apex point of minimal airspeed, coinciding with strong leftwards yaw. Alongside some finer roll and pitch control this reorientates the bat into a dive position, leading to a short dive before full recovery. The altitude gain and sharp turning motion show parallels with the anchor turns of Section 1.2.2, and it is possible this manoeuvre is a simple variant of such turns.

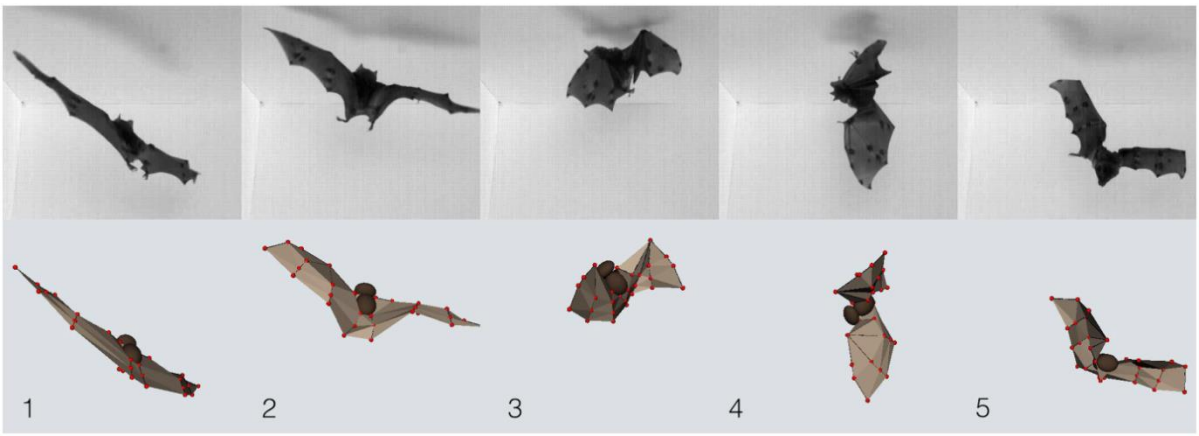

Figure 1.2.6: (**Top**): Images from high-speed film, 75 ms apart, of a Seba's short-tailed bat (*C. perspicillata*) performing an upwards landing manoeuvre, and upon failing to find a landing site, performing a righting manoeuvre. As a scale, the bat wingspan is c. 30 cm. (**Bottom**): Reconstruction of the wing and body kinematics with a discrete element model. Reproduced from Bergou et al. [54] under CC BY 4.0.

Notably, an analysis by Bergou et al. [54] of this abortive landing manoeuvre concluded that inertial manoeuvring was a dominant factor in the control of the main reorientation sequence (from frame 2 in Figure 1.2.6). However this conclusion does not distinguish between the use of active inertial control during the reorientation, and passive reorientation via the generation of a suitable initial momentum. Indeed, given the relatively minimal wing motion observed during reorientation, it seems probable that only fine-level inertial and/or aerodynamic control is carried out then, with the manoeuvre being strongly dependent on the generation of a suitable torque and angular momentum by aerodynamic forces prior to reorientation. This is consistent with the observation that the bat's wings remain tucked relatively close to the body during reorientation (see Figure 1.2.6, Frame 3): this would decrease its capability for inertial or aerodynamic control, but increase its angular velocity with reference to an initial momentum. However, an additional

complication in this manoeuvre is the confined space in which it takes place: this is likely to pressure the bat into taking a more compact shape during reorientation, and may eliminate some wing operations which might otherwise be more effective or efficient.

Successful upwards landing manoeuvres in bats sometimes also involve complex rotational motion. A study by Riskin et al. [55] of several species distinguished two key landing modes, with clear inter-species differences. Four-point landings involved pitch motion with minimal yaw and roll, followed by landing contact in an inverted position (angle of attack c. 180°) with all four limbs. A similarity with pitch-dominant perching and ballistic transition manoeuvres in other species may be noted – see Section 1.2.4. Two-point landings involved an initial pitch-up motion, followed concurrently by left or right yaw motion (distinguishing left-handed or right-handed two point landings respectively) and a small corresponding roll, until the bat's feet were above its head. This leads to landing contact with two hindlimbs in an inverted position, concurrent with a strong pitch-backwards momentum that rotates the bat into the nose-down roost position – with the wing plane orientated 90° relative to the roost position after a four-point landing. The abortive landing and reorientation manoeuvre observed by Bergou et al. [54] represents a two-point landing; thus the affinity between two-point landing and the anchor turn manoeuvres of Section 1.2.2 may be noted. It may be possible to conceptualise the two-point landing as a form of anchor turn which involves landing contact at the turn apex. However insufficient data is available to explore this more fully.

Figure 1.2.7 shows a schematic of these two landing modes from Riskin et al. [55], representing the mean orientation histories from four-point landings observed in *Cynopterus brachyotis* and right-handed two-point landings in *Carollia perspicillata*. Figure 1.2.8 (**A-G**) shows the orientation histories for three bat species performing one or more of these landing manoeuvres. *C. brachyotis* only performed four-point landings (**A**), whereas *C. perspicillata* performed both left-hand (**B**) and right-hand (**C**) two-point landings, as well as variants of these (**D** and **E** respectively) with more pitch and less yaw motion, showing some affinity with the four-point mode of landing. *Glossophaga soricina*, the third species, performed only conventional left- (**F**) and right-handed (**G**) two-point landings.

The strong association of particular species with particular landing modes is thought to be related to the bone stress associated with each manoeuvre; four-point landings being significantly gentler than two-point landings. A distinction may then be considered on the grounds of roosting habits (cave-roosting bats landing more gently than foliage-roosting bats due to the rigidity of the landing surface) and at least partly the bat mass (heavier bats tending to show a preference for four-point landing, though counterexamples are known) [55]. Phylogenetic differences in forelimb usage could also be a significant factor.

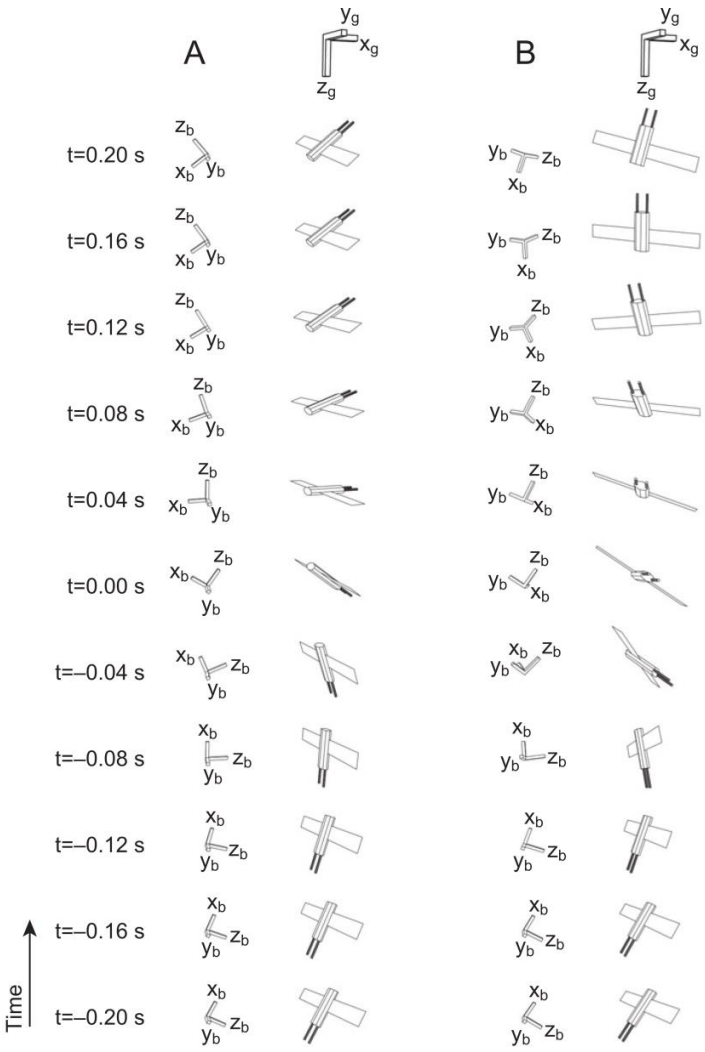

Figure 1.2.7: Schematic of a four-point (**A**) and right-hand two-point landing (**B**), representing the mean orientation histories from Figure 1.2.7.**A-B** respectively. Time = 0 is the time of peak impact force into the ceiling. Reproduced from Riskin et al. [55] with permission.

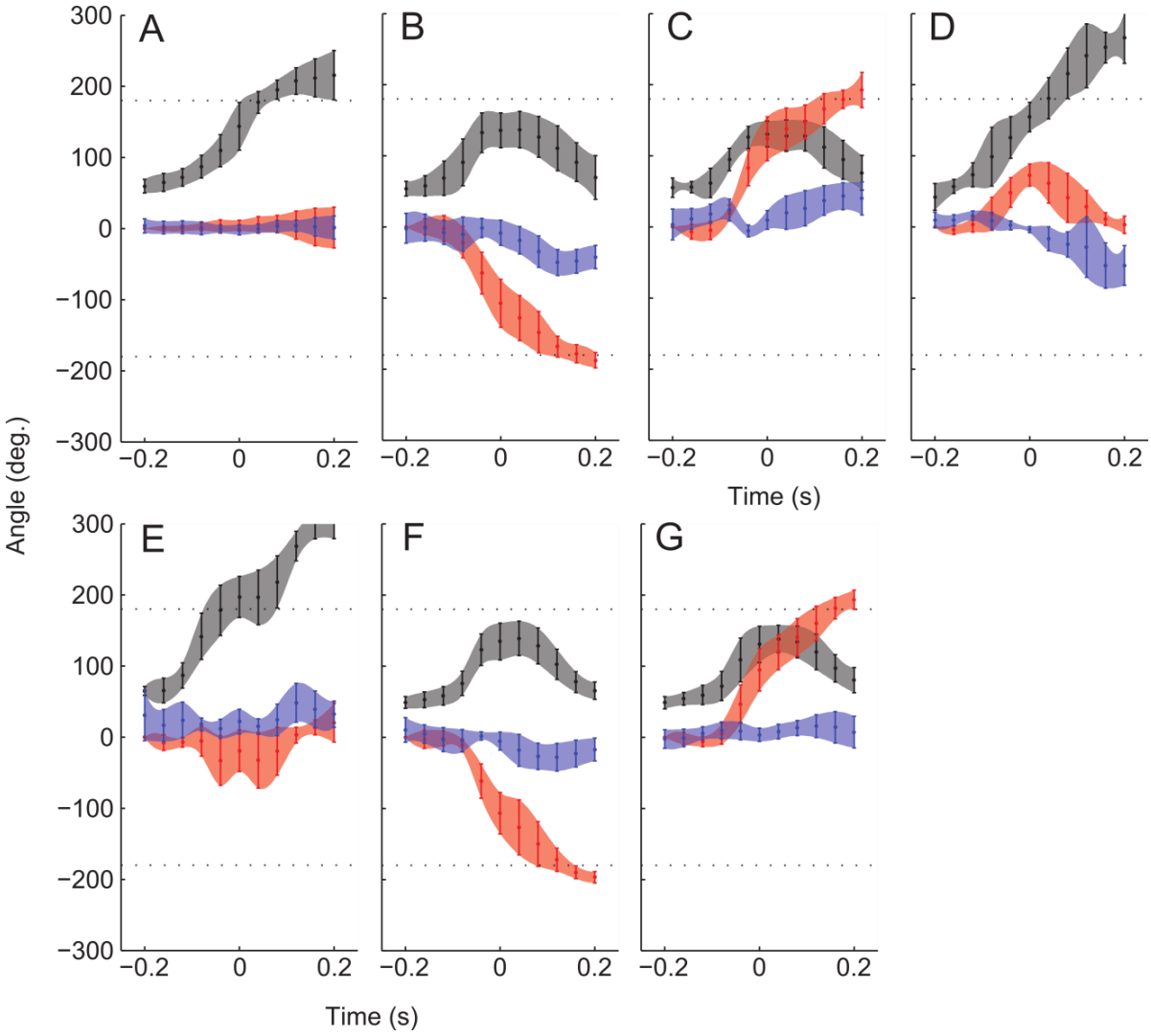

Figure 1.2.8: Statistical orientation histories (pitch: grey, yaw: red, roll: blue) of several bat species performing vertical perching manoeuvres. Species: (**A**) *Cynopterus brachyotis*, (**B–E**) *Carollia perspicillata*, (**F,G**) *Glossophaga soricina*. Sample sizes are: **A** 29, **B** 22, **C** 13, **D** 4, **E** 6, **F** 15 and **G** 32. Error bars extend one standard deviation above and below the mean. Broken lines are at ±180 deg, and time = 0 is the time of peak impact force into the ceiling. Adapted from Riskin et al. [55] with permission.

Several other high-performance roll and yaw manoeuvres are seen in other avian and pteropine species. Whiffling is a high-airspeed roll manoeuvre in geese and waterfowl that is associated with landing operations [56–58], courtship [59], and predator evasion [60]. Similar behaviour in steppe eagles (*A. nipalensis*) is associated with aerial defence using talons [4]. Fast dive-rolls, probably for the purpose of insect capture, have been observed in the common noctule bat (*Nyctalus noctula*) by Norberg [61]. Roll rates of c. 2000°/s are generated via pronation/supination on opposite wings, combined with mild wing adduction leading to a decrease in the bat's rotational inertia. Deceleration immediately prior reaching

an inverted flight state is achieved via extension of the wings to maximum, leading to stabilising drag and an increase in the bat's rotational inertia. The dive component of the manoeuvre is achieved via symmetric pronation at the end of the manoeuvre (during inverted flight) [61]. While none of these operations necessarily involve post-stall capability, the manoeuvre is notable as an example of conventional manoeuvrability enhancements achieved via biomimetic wing motion – both in the generation of extreme roll moments via wing pronation, and the use of adduction and extension (comparable to a sweep degree of freedom) to increase and decrease bat rotational inertia. Overall, the range of different roll and yaw reorientation manoeuvres observed in avian and pteropine species suggests that there are multiple avenues for biological and biomimetic supermanoeuvrable orientation control in these degrees of freedom.

1.2.4. Turning manoeuvres in non-avian gliders

Demonstrable supermanoeuvrability is not even restricted to creatures with well-articulated wings. Flying squirrels and other mammals (*Glaucomys* spp., *Petaurus* spp., *Petauroides volans*, etc.) have been observed to undertake sharp 90°-180° turns [27,28], and detailed research has indicated that these turns are largely drag-based and occur at wing-membrane angles of attack up to 60° [29,30]. Angles of attack above 40° are common in straight glides, and though these creatures have a number of adaptions to delay stall, several experimental studies suggest that partial or full flow separation is involved [62,63]. Gliding frogs (*Polypedates dennysi*) show similar manoeuvrability, performing drag-based (crabbed) turns of over 80° at bearing rates of 400°/s, at angles of attack up to 60° [64]. Based on several basic manoeuvrability metrics, McCay [64] went so far as to conclude that "the manoeuvrability of tree frogs was approximately one-third of the manoeuvrability of a falcon (*Falcon jugger*)" – remarkable given the complete lack of significant lifting surfaces on the frog airframe, though the comparison does not do justice to the much wider range of manoeuvres available in birds.

1.2.5. Perching manoeuvres

Of all the post-stall manoeuvres observed in biological creatures, perching has seen the most study from an industrial aerospace perspective. Perching-type manoeuvres are widespread in many species, including non-avian gliders: flying squirrels and other mammals

use stall-perching manoeuvres for landing. A large number of species [30] have been observed to undergo a 'ballistic transition' near to landing, pitching up to a vertical angle-of-attack and completing the flight manoeuvre in the manner of a parachute [7,8]. Figure 1.2.9 shows an experimentally-observed ballistic transition trajectory of a northern flying squirrel (*Glaucomys sabrinus*), alongside the estimated aerodynamic forces, from Bahlmann et al. [63] undergoing such a manoeuvre. Note the significant increase in drag in the final stages of the manoeuvre (f-g), attained via high pitch-up, and required in order to bleed off airspeed before the impact landing. The presence of a significant lift force in Figure 1.2.9, even in the late stages of the manoeuvre, implies that the squirrel does not reach vertical angle-of-attack (for which there is zero or minimal lift) until immediately before or upon impact. Other trajectories observed experimentally by Bahlmann et al. [63] almost universally show upwards vertical acceleration through the end phase of the manoeuvre, supporting this general inference. Frustratingly, no direct orientation imagery is available to confirm this.

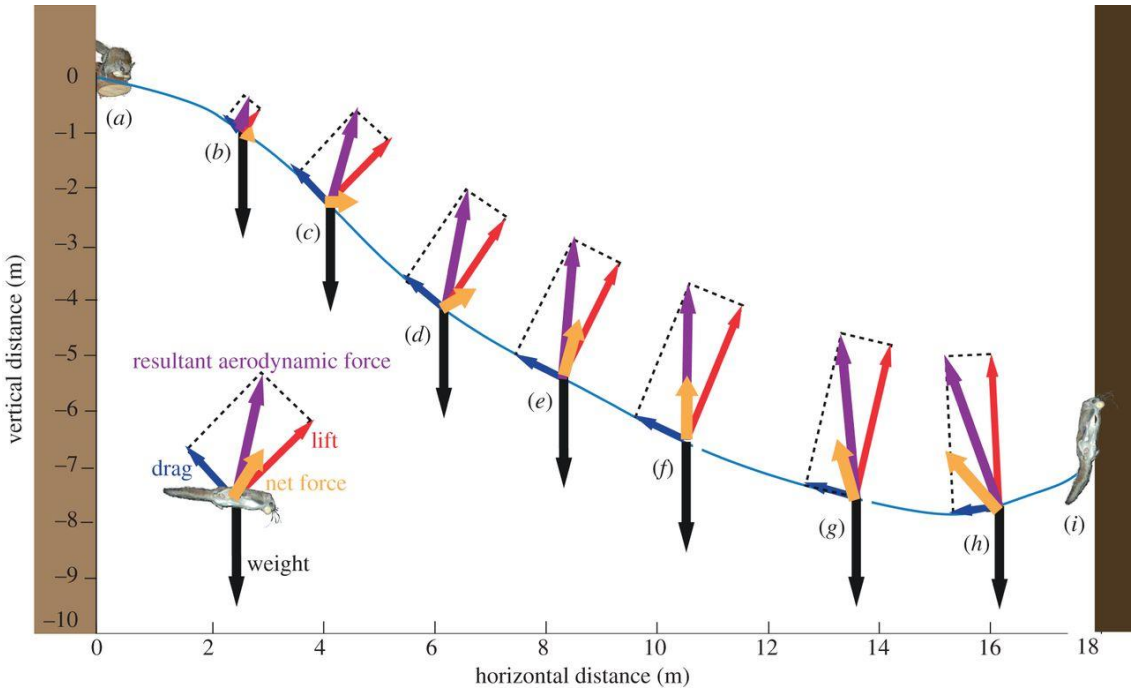

Figure 1.2.9: Schematic of ballistic transition manoeuvre in a northern flying squirrel (*G. sabrinus*). Reproduced from Bahlmann et al. [63] with permission.

In more complex fliers, perching or stall diving may be combined with other conventional or post-stall manoeuvres; or may be disassociated with ground landing. Kereru (*Hemiphaga novaeseelandiae*) utilise stall diving in breeding rituals [65]. Bildstein [66] and later surveys

[67,68] characterised several different types of pouncing manoeuvres used by harriers in hunting. One of these, the hook pounce, involves a perching landing manoeuvre immediately preceded by an extremely sharp turn – over 270° in a radius of slightly over one wingspan [66]; well equal to the anchor turn performance of other species noted in Section 1.2.2. The aerodynamic aspects of such manoeuvres are not well understood, though in the case of stall dives by steppe eagles (*A. nipalensis*) wing sweep changes and pulsed stall braking are involved [4].

1.3. ENGINEERING APPLICATIONS OF WING MORPHING

1.3.1. Overview

The study of morphing-wing systems (cf. Figure 1.3.1) is a vast topic, extending from insectoid flight vehicles smaller than a penny [69], to swept-wing aeroplanes that are among the largest aircraft ever built [70]. There are many morphing systems and technologies, in varying stages of development; and a large number of existing reviews, of varying completeness, are available [71–79]. Several key themes may be identified in the literature.

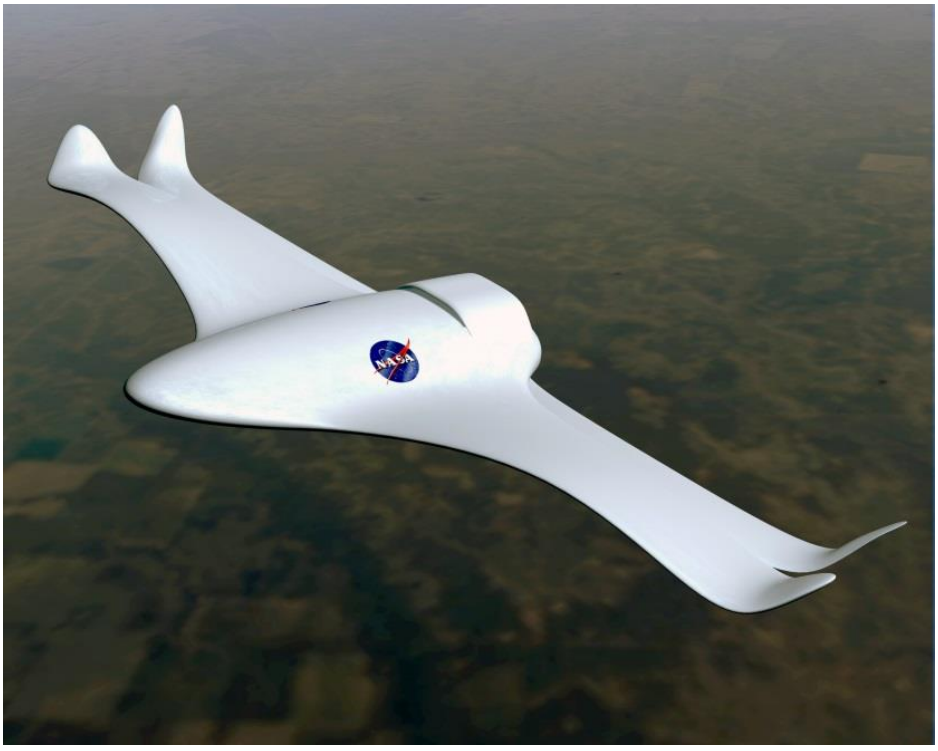

Figure 1.3.1: A NASA Artist's rendering of a futuristic air vehicle with mission-morphing wings; a widespread poster picture for morphing aircraft. NASA Photo ED01-0348-1, public domain.

1.3.2. Mission morphing

Mission morphing denotes the use of wing or airframe morphing to specialise a multipurpose aircraft to particular discrete manoeuvres, tasks, or missions [75,80,81]. Such systems are intended to switch between two or more discrete airframe states, typically during flight, avoiding the need for separate aircraft to perform the associated discrete missions, and increasing the efficiency with which a sequence of missions can be carried out. For example, loiter-dash / loiter-attack systems are intended to switch between a slow, high-endurance loiter state (e.g. with dihedral and no sweep) to a fast, high-performance dash or attack state (e.g. with backwards sweep and anhedral) [82,83].

A wide variety of mission morphing operations have been considered. Symmetrical span variation has seen frequent study as an avenue to loiter-and-dash capability [84–86], and sweep motion has been considered for the same purpose [87] – historical uses of sweep motion for the purpose of reducing wave drag in supersonic aircraft are early variants of this idea. Recent developments include the study of loiter-dash systems with multiple degrees of freedom in sweep [25,88,89], and of camber morphing for adaptive changes in take-off and landing performance and cruise efficiency [81]. The NextGen MFX-1 and MFX-2 [90–93] represent functional loiter-dash aircraft utilising combined span and sweep variation, and are under continued development.

Wing deployment may also be regarded as a form of mission morphing; the two mission states typically being an undeployed launch state and a deployed flight state. Key applications include sweep-deployable wings for cruise missiles [94] and other rapid-launch MAV craft [95]. Complex wing deployment operations have been considered for the ARES Mars Mission [96–99], US Navy Flying Radar Target (FLYRT) [100,101], and conceptual MAVs [102]. A notable feature of the study of wing deployment, compared to other mission morphing, is the relative importance of the transition states and transient aerodynamics, associated with the greater speed of lifting surface motion.

1.3.3. Pre-stall control morphing

Control morphing is a second key theme in engineering literature on wing morphing. The term refers to morphing which is carried out dynamically as a flight control mechanism

[75,103]. In the trivial case, conventional aircraft control surfaces (aileron, elevator, etc.) represent a basic example of control morphing. More recently, in normal pre-stall flight regimes, articulated winglets have been shown the ability to perform turning manoeuvres at lower speeds than would be possible with conventional ailerons [104–106]. Asymmetric span morphing has been studied as an avenue to high-authority roll control, but results are preliminary [84,107–109]. Asymmetric sweep morphing has been considered in connection with crosswind rejection [89]. A few micro-scale technologies have also been studied: deployable strakes have been studied for side-force and yaw control [110,111], and small adaptive bumps could also be used for yaw control [112].

1.3.4. Post-stall control morphing

Relatively few studies have been made into morphing for post-stall control, and these focus primarily on perching manoeuvres. In mimicry of the tail motions used by birds [113], it has been shown that perching can be successfully performed by fixed-wing glider MAVs using only the control of oversized elevators [34–37]. Changes in wing dihedral [38,39] or incidence [40,41], sometimes combined with larger tail displacement motion [42,43], have all shown to improve perching performance, and some impressive flight tests have been carried out. Large-angle incidence control has been shown to allow not only perching, but also hover-to-cruise transition [114], and asymmetric post-stall manoeuvres [115]. This is entirely consistent with the importance of pronation and supination (incidence control) in avian stall turns [2–4]. The possibility of more general supermanoeuvrability in biomimetic morphing-wing systems has only rarely been recognized, e.g. by Evers [44], and no detailed studies have been carried out.

1.3.5. Stall delay and control

As an alternative to direct post-stall control, wing morphing may be used to delay stall onset, thus increasing the flight envelope over which normal control effectiveness can be expected. Morphing-based stall delay systems have been largely studied in the context of passive or active aerofoil shape deformation. On the macro scale some control morphing technologies, including leading-edge droops [116,117] and compliant ailerons [118,119], have the potential to delay wing stall onset and thus increase the range of aileron authority. This capability is particularly relevant to perching manoeuvres [120], and has biological

precedent, in the camber morphing operations shown in bats and flying squirrels during landing and/or ballistic transition manoeuvres [62,121]. Preliminary research has also gone into oscillatory compliant camber and thickness morphing for separation control [122]. On the largest scale, positive gull-wing folding, as in a biological gull, has been found to delay stall entry, reduce stall intensity and improve recovery [123].

On the micro scale, deployable or passively-morphing micro shape changes for stall delay have seen significant interest. Fields of passively-morphing micro-flaps or micro-tabs [124–126] have seen much study as a mechanism for stall delay: this is in direct mimicry of bird feathers, which serve the same purpose in the natural environment [124,127]. Deployable vortex generators can allow a fixed-wing aircraft to both delay stall and avoid a parasitic drag penalty in normal flight [128–130]. Interestingly, while many micro-morphing stall delay systems are biologically inspired, the extent to which these stall delay mechanisms are an enabling factor in biological supermanoeuvrability is an open problem. On the one hand, the presence of such adaptions implies an evolutionary advantage is conferred in terms of flight performance, and it is clear that stall delay mechanisms will improve the performance and controllability of otherwise post-stall manoeuvres. However, on the other, a variety of biological supermanoeuvres are observed in demonstrably post-stall conditions, including zero-airspeed rolling in pigeons [6] (Figure 1.2.4), and ballistic transition manoeuvres in flying squirrels [62,63] (Figure 1.2.8). Capability approaching supermanoeuvrability is also observed in gliding frogs (*P. dennysi*) [64] which have no known stall delay mechanisms – and highly ineffective lifting surfaces.

These observations indicate that post-stall control via large-scale wing motion is present in some flying creatures, and is capable of enabling at least a degree of supermanoeuvrability without micro-scale stall-delay adaptions. However, the details remain unclear, particularly regarding system capability in the limit case of maximal micro-morphing stall delay and minimal wing motion. These considerations also call into question the close association between supermanoeuvrability and post-stall control found in studies of thrust vectoring aircraft [9,10]: in both macro- and micro-morphing systems, supermanoeuvrability may instead be attainable by transforming a conventionally post-stall state into a pre-stall one; either by stall delay or by large-scale lifting surface motion; rendering the specific post-stall

control less significant. This work will help to elucidate some of these effects by exploring the capability of a biomimetic macro-morphing system for supermanoeuvrability, independent of any micro-morphing enhancements. This will allow us to assess the extent to which macro-morphing alone enables biomimetic supermanoeuvrability; and to which post-stall / pre-stall transformation is a factor within this.

1.4. MORPHING-WING SUPERMANOEUVREABILITY

1.4.1. Case study system

We approach the many aspects of biomimetic supermanoeuvrability through the lens of a hypothetical case-study system: a hybrid biomimetic UAV / MAV, of fixed properties, with 6DOF wing rotation (independent sweep / incidence / dihedral motion) and a conventional propulsion system (propeller / jet / rocket). We will study the capability of this system for a wide range of biomimetic manoeuvres. This case-study or feasibility-study approach will allow us to provide a broad assessment of the potential applications of biomimetic morphing in UAV supermanoeuvrability, and identify promising avenues for further research and development. A key limitation of this approach is, however, that only one case-study system can be analysed; and so the choice of this system must be justified.

This work focuses on the larger scales, $\mathcal{O}(1\,\mathrm{m})$, of biological wing morphing and supermanoeuvrability; with particular reference to the greylag goose (*Anser anser*) and the steppe eagle (*Aquila nipalensis*). This lengthscale overlaps with several existing morphing-wing aircraft, such as the NextGen MFX-1 [90]. Relative to these similarly-scaled biological creatures, the system mass is increased by a factor of c. 2x to account for the inefficiencies of non-biological design. 6DOF morphing represents a simple mimicry of a bird, and accounts for the key features of biological wing morphing with minimal actuator complexity. It should be noted that the use of 6DOF morphing represents a hypothetical state for the purposes of analysis: it is part of the scope of this study to determine which of these morphing DOFs are effective or necessary for particular manoeuvres. Potential industrial applications, particularly in the first instance, would be expected to show a more restricted control space, e.g. 2-3DOF morphing. Figure 1.4.1 presents a scale rendering of our case

study system with the active morphing degrees of freedom; a complete parameter and system description is given in Appendix 1.

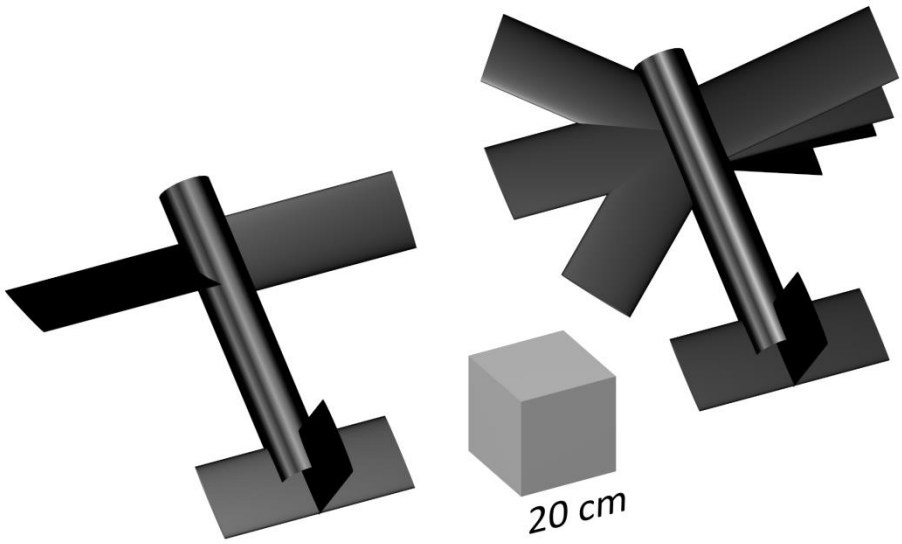

Figure 1.4.1: Rendering of the case study system, showing the morphing degrees of freedom: incidence (left) and sweep and dihedral (right).

The larger scales of this case study system may restrict its capability for post-stall manoeuvrability relative to smaller biological creatures (e.g. pigeons, *C. livia,* $\mathcal{O}(0.3\text{ m})$), due to the increased structural stresses and actuator requirements. However, the possibility of attaining or retaining an industrially-relevant flight time – a deficiency of existing biomimetic aircraft – is of greater importance. The scope of this study does not extend to a consideration of the aircraft structural stresses or projected range and endurance; the specification of our case study system will not extend to materials, avionics, approaches to MDOF control, or dedicated application feasibility studies. It is instead our purpose to determine the capability of our case study system for supermanoeuvrability across a wide range of manoeuvres; the methods by which such manoeuvres can be designed and performed; and the associated actuator DOF requirements and choices. Producing robust results in these areas will also entail methodological developments in biomimetic flight dynamics which are a prerequisite for further dedicated studies.

1.4.2. Target applications

The motivation of this study thus far has been general and abstract: an understanding of biological or biomimetic supermanoeuvrability, and the potential for the design of supermanoeuvrable UAVs based on this understanding. However, more specific motivations are also present. Supermanoeuvrability in general is relevant solely to combat aircraft, and is motivated by associated improvements in combat-relevant metrics, e.g. dogfight performance and short-takeoff capability. This remains the case for supermanoeuvrable MAVs / UAVs, though the prospective applications for such aircraft are very different to those of full-scale supermanoeuvrable aircraft. In a hypothetical future environment of UAV-to-UAV or UAV-to-manned air-to-air combat, UAV supermanoeuvrability could be utilised in an immediately analogous way; but such an environment is currently a distant prospect.

A more immediate application revolves around complex combat environments – most pertinently, cities; but also mountainous and forested terrain. Equipping a biomimetic UAV with a warhead could lead to a supermanoeuvrable 'urban missile' capable of precision operations in confined spaces. This includes both surface-to-surface or surface-to-air combat (enabling ground forces to engage surface or aerial targets around corners or from behind cover); and air-to-surface combat (enabling aircraft to engage hidden urban targets precisely, with minimal collateral damage). In this context, key supermanoeuvres include stall turns (to manoeuvre laterally around obstacles) and their longitudinal analogy, 'stall pitching' (to clear vertical obstacles).

Such a system has additional potential utility in an air-to-air context – apart from the distant potential for a highly-manoeuvrable combat UAV, there is the prospect of a 'persistent missile', capable of multiple reorientations and reengagements in the event of a target evasion. Finally, a further motivation to this study concerns existing biomimetic aircraft. While our case study system is conceived as a hybrid aircraft with conventional propulsion, and on a slightly larger scale, the manoeuvres studied in this work may directly applicable to such systems in the glide state; and may be generalisable to, or superimposable on, a state of continuous flapping-wing propulsion. With these factors in mind, we move to a detailed specification of the system parameters.

CHAPTER REFERENCES

[1] Carruthers, A. C., Thomas, A. L. R., Walker, S. M., and Taylor, G. K., "Mechanics and aerodynamics of perching manoeuvres in a large bird of prey," *The Aeronautical Journal*, Vol. 114, No. 1161, 2010, pp. 673–680.

[2] Warrick, D. R., "Bird Maneuvering Flight: Blurred Bodies, Clear Heads," *Integrative and Comparative Biology*, Vol. 42, No. 1, 2002, pp. 141–148. DOI:10.1093/icb/42.1.141.

[3] Altenbach, J. S., "Locomotor morphology of the vampire bat, Desmodus rotundus," *Special Publications of the American Society of Mammalogists*, Vol. 6, 1979, pp. 1–135.

[4] Gillies, J. A., Thomas, A. L. R., and Taylor, G. K., "Soaring and manoeuvring flight of a steppe eagle Aquila nipalensis," *Journal of Avian Biology*, Vol. 42, No. 5, 2011, pp. 377–386. DOI:10.1111/j.1600-048X.2011.05105.x.

[5] Tian, X., Iriarte-Diaz, J., Middleton, K., Galvao, R., Israeli, E., Roemer, A., Sullivan, A., Song, A., Swartz, S., and Breuer, K., "Direct measurements of the kinematics and dynamics of bat flight," *Bioinspiration & Biomimetics*, Vol. 1, No. 4, 2006, pp. S10–S18. DOI:10.1088/1748-3182/1/4/S02.

[6] Warrick, D. R., and Dial, K. P., "Kinematic, aerodynamic and anatomical mechanisms in the slow, maneuvering flight of pigeons," *Journal of Experimental Biology*, Vol. 201, No. 12, 1998, pp. 655–672.

[7] Ando, M., and Shiraishi, S., "Gliding flight in the Japanese giant flying squirrel Petaurista leucogenys," *Journal of the Mammalogical Society of Japan*, Vol. 18, No. 1, 1993, pp. 19–32.

[8] Stafford, B. J., Thorington, R. W., and Kawamichi, T., "Gliding behaviour of Japanese giant flying squirrels (Petaurista Leucogenys)," *Journal of Mammalogy*, Vol. 83, No. 2, 2002, pp. 553–562.

[9] Gal-Or, B., *Vectored propulsion, supermaneuverability, and robot aircraft*, Springer-Verlag, New York, 1990.

[10] Herbst, W. B., "Future fighter technologies," *Journal of Aircraft*, Vol. 17, No. 8, 1980, pp. 561–566. DOI:10.2514/3.44674.

[11] Sibilski, K., "Numerical Investigation into flight dynamics of an agile aircraft," *Journal of Theoretical and Applied Mechanics*, Vol. 38, No. 1, 2000, pp. 167–187.

[12] Joyce, D. A., *Flying beyond the stall: the X-31 and the advent of supermaneuverability*, NASA, Washington, DC, 2014.

[13] Erickson, G. E., "High Angle-of-Attack Aerodynamics," *Annual Review of Fluid Mechanics*, Vol. 27, No. 1, 1995, pp. 45–88. DOI:10.1146/annurev.fl.27.010195.000401.

[14] Ericsson, L. E., "Cobra maneuver unsteady aerodynamic considerations," *Journal of Aircraft*, Vol. 32, No. 1, 1995, pp. 214–216. DOI:10.2514/3.46706.

[15] Huenecke, K., *Modern Combat Aircraft Design*, Airlife, Shrewsbury, UK, 1994.

[16] Anonymous, "Russia flies PAK FA for Indian visit," *Flight International*, Vol. 178, No. 5257, 2010, p. 19.

[17] Simpson, J., "Japan keeps F-3 options open," *Flight International*, Vol. 187, No. 5473, 2015, pp. 18–19.

[18] MacKenzie, D., "A Flapping of Wings," *Science*, Vol. 335, No. 6075, 2012, pp. 1430–1433.

[19] Gerdes, J. W., Gupta, S. K., and Wilkerson, S. A., "A Review of Bird-Inspired Flapping Wing Miniature Air Vehicle Designs," *Journal of Mechanisms and Robotics*, Vol. 4, No. 2, 2012, p. 021003. DOI:10.1115/1.4005525.

[20] Ward, T. A., Rezadad, M., Fearday, C. J., and Viyapuri, R., "A Review of Biomimetic Air Vehicle Research: 1984-2014," *International Journal of Micro Air Vehicles*, Vol. 7, No. 3, 2015, pp. 375–394. DOI:10.1260/1756-8293.7.3.375.

[21] Mahardika, N., Nguyen, Q. V., and Park, H. C., "A pigeon-inspired design for a biomimetic flapping wing," M.N. Ghasemi-Nejhad, ed., Active and Passive Smart Structures and Integrated Systems, San Diego, CA, pp. 76431Q-76431Q–11.

[22] Furst, S. J., Bunget, G., and Seelecke, S., "Design and fabrication of a bat-inspired flapping-flight platform using shape memory alloy muscles and joints," *Smart Materials and Structures*, Vol. 22, No. 1, 2013, p. 014011. DOI:10.1088/0964-1726/22/1/014011.

[23] Recchiuto, C. T., Molfino, R., Hedenströem, A., Peremans, H., Cipolla, V., Frediani, A., Rizzo, E., and Muscolo, G. G., "Bioinspired Mechanisms and Sensorimotor Schemes for Flying: A Preliminary Study for a Robotic Bat," *Advances in Autonomous Robotics Systems*, M. Mistry, A. Leonardis, M. Witkowski, and C. Melhuish, eds., Springer, Cham, Switzerland, 2014, pp. 37–47.

[24] Zakaria, M. Y., Taha, H. E., and Hajj, M. R., "Design Optimization of Flapping Ornithopters: The Pterosaur Replica in Forward Flight," *Journal of Aircraft*, Vol. 53, No. 1, 2016, pp. 48–59. DOI:10.2514/1.C033154.

[25] Chatterjee, S., Lind, R., and Roberts, B., "The novel characteristics of pterosaurs: biological inspiration for robotic vehicles," *International Journal of Design & Nature and Ecodynamics*, Vol. 8, No. 2, 2013, pp. 113–143. DOI:10.2495/DNE-V8-N2-113-143.

[26] Keennon, M., Klingebiel, K., and Won, H., "Development of the Nano Hummingbird: A Tailless Flapping Wing Micro Air Vehicle."

[27] Harris, J. M., and Maloney, K. S., "Petauroides volans (Diprotodontia: Pseudocheiridae)," *Mammalian Species*, Vol. 42, 2010, pp. 207–219. DOI:10.1644/866.1.

[28] Dolan, P. G., and Carter, D. C., "Glaucomys volans," *Mammalian Species*, No. 78, 1977, p. 1. DOI:10.2307/3504026.

[29] Bishop, K. L., and Brim-Deforest, W., "Kinematics of turning maneuvers in the southern flying squirrel, Glaucomys volans," *Journal of Experimental Zoology. Part A, Ecological Genetics and Physiology*, Vol. 309, No. 5, 2008, pp. 225–242. DOI:10.1002/jez.447.

[30] Jackson, S. M., "Glide angle in the genus Petaurus and a review of gliding in mammals," *Mammal Review*, Vol. 30, No. 1, 2000, pp. 9–30. DOI:10.1046/j.1365-2907.2000.00056.x.

[31] Evangelista, D., Cam, S., Huynh, T., Kwong, A., Mehrabani, H., Tse, K., and Dudley, R., "Shifts in stability and control effectiveness during evolution of Paraves support aerial maneuvering hypotheses for flight origins," *PeerJ*, Vol. 2, 2014, p. e632. DOI:10.7717/peerj.632.

[32] Kane, S. A., Fulton, A. H., and Rosenthal, L. J., "When hawks attack: animal-borne video studies of goshawk pursuit and prey-evasion strategies," *Journal of Experimental Biology*, Vol. 218, No. 2, 2015, pp. 212–222. DOI:10.1242/jeb.108597.

[33] Aldridge, H. D. J. N., "Turning flight of bats," *Journal of Experimental Biology*, Vol. 128, 1987, pp. 419–425.

[34] Moore, J., Cory, R., and Tedrake, R., "Robust post-stall perching with a simple fixed-wing glider using LQR-Trees," *Bioinspiration & Biomimetics*, Vol. 9, No. 2, 2014, p. 025013. DOI:10.1088/1748-3182/9/2/025013.

[35] Moore, J. L., "Powerline Perching with a Fixed-Wing UAV," Master's Thesis, Massachusetts Institute of Technology, 2011.

[36] Cory, R., and Tedrake, R., "Experiments in Fixed-Wing UAV Perching," AIAA Guidance, Navigation and Control Conference and Exhibit, Honolulu, HI.

[37] Cory, R., "Supermaneuverable Perching," Doctoral Dissertation, Massachusetts Institute of Technology, 2010.

[38] Lukens, J., Reich, G., and Sanders, B., "Wing Mechanization Design and Analysis for a Perching Micro Air Vehicle," 49th AIAA/ASME/ASCE/AHS/ASC Structures, Structural Dynamics, and Materials Conference, Schaumburg, IL.

[39] Paranjape, A., Kim, J., Gandhi, N., and Chung, S.-J., "Experimental Demonstration of Perching by an Articulated Wing MAV," AIAA Guidance, Navigation, and Control Conference, Portland, OR.

[40] Seigler, T., Lubbers, J., and Reich, G., "Perch Landing Manuevers (sic) for a Rotating Wing MAV," 51st AIAA/ASME/ASCE/AHS/ASC Structures, Structural Dynamics, and Materials Conference, Orlando, FL.

[41] Lubbers, J. L., "Perching landing maneuvres and control for a rotating-wing MAV," Master's Thesis, University of Kentucky, 2011.

[42] Wickenheiser, A. M., and Garcia, E., "Optimization of Perching Maneuvers Through Vehicle Morphing," *Journal of Guidance, Control, and Dynamics*, Vol. 31, No. 4, 2008, pp. 815–823. DOI:10.2514/1.33819.

[43] Wickenheiser, A. M., and Garcia, E., "Longitudinal Dynamics of a Perching Aircraft," *Journal of Aircraft*, Vol. 43, No. 5, 2006, pp. 1386–1392. DOI:10.2514/1.20197.

[44] Evers, J. H., "Biological Inspiration for Agile Autonomous Air Vehicles," Platform Innovations and System Integration for Unmanned Air, Land and Sea Vehicles (AVT-SCI Joint Symposium), Neuilly-sur-Seine, France.

[45] Tucker, V. A., "Pitching Equilibrium, Wing Span and Tail Span in a Gliding Harris' Hawk, Parabuteo Unicinctus," *Journal of Experimental Biology*, Vol. 165, 1992, pp. 21–41.

[46] Rayner, J. M. V., and Aldridge, H. D. J. N., "Three-Dimensional Reconstruction of Animal Flight Paths and the Turning Flight of Microchiropteran Bats," *Journal of Experimental Biology*, Vol. 118, 1985, pp. 247–265.

[47] Lyons, T. J., *Human Consequences of Agile Aircraft*, NATO RTO HFM, Neuilly-sur-Seine, France, 2001.

[48] NASA, *X-31 Enhanced Fighter Maneuverability Demonstrator*, 2007.

[49] Hedrick, T. L., and Biewener, A. A., "Low speed maneuvering flight of the rose-breasted cockatoo (Eolophus roseicapillus). I. Kinematic and neuromuscular control of turning," *Journal of Experimental Biology*, Vol. 210, No. 11, 2007, pp. 1897–1911. DOI:10.1242/jeb.002055.

[50] Iriarte-Diaz, J., and Swartz, S. M., "Kinematics of slow turn maneuvering in the fruit bat Cynopterus brachyotis," *Journal of Experimental Biology*, Vol. 211, No. 21, 2008, pp. 3478–3489. DOI:10.1242/jeb.017590.

[51] Shelton, R. M., Jackson, B. E., and Hedrick, T. L., "The mechanics and behavior of cliff swallows during tandem flights," *Journal of Experimental Biology*, Vol. 217, No. 15, 2014, pp. 2717–2725. DOI:10.1242/jeb.101329.

[52] Ros, I. G., Badger, M. A., Pierson, A. N., Bassman, L. C., and Biewener, A. A., "Pigeons produce aerodynamic torques through changes in wing trajectory during low speed aerial turns," *Journal of Experimental Biology*, Vol. 218, No. 3, 2015, pp. 480–490. DOI:10.1242/jeb.104141.

[53] Jusufi, A., Kawano, D. T., Libby, T., and Full, R. J., "Righting and turning in mid-air using appendage inertia: reptile tails, analytical models and bio-inspired robots," *Bioinspiration & Biomimetics*, Vol. 5, No. 4, 2010, p. 045001. DOI:10.1088/1748-3182/5/4/045001.

[54] Bergou, A. J., Swartz, S. M., Vejdani, H., Riskin, D. K., Reimnitz, L., Taubin, G., and Breuer, K. S., "Falling with Style: Bats Perform Complex Aerial Rotations by Adjusting Wing Inertia," *PLOS Biology*, Vol. 13, No. 11, 2015, p. e1002297. DOI:10.1371/journal.pbio.1002297.

[55] Riskin, D. K., Bahlman, J. W., Hubel, T. Y., Ratcliffe, J. M., Kunz, T. H., and Swartz, S. M., "Bats go head-under-heels: the biomechanics of landing on a ceiling," *Journal of Experimental Biology*, Vol. 212, No. 7, 2009, pp. 945–953. DOI:10.1242/jeb.026161.

[56] Ogilvie, M. A., and Wallace, D. I. M., "Field identification of grey geese," *British Birds*, Vol. 68, 1975, pp. 57–67.

[57] Pete, A. E., Kress, D., Dimitrov, M. A., and Lentink, D., "The role of passive avian head stabilization in flapping flight," *Journal of The Royal Society Interface*, Vol. 12, No. 110, 2015, p. 20150508. DOI:10.1098/rsif.2015.0508.

[58] Marchant, S., and Higgins, P. J., *Handbook of Australian, New Zealand & Antarctic Birds. Volume 1, Ratites to ducks; Part B, Australian pelican to ducks*, Oxford University Press, Melbourne, Australia, 1990.

[59] Sackl, P., "Form and function of aerial courtship displays in Black Storks Ciconia nigra," *Acrocephalus*, Vol. 21, 2000, pp. 223–229.

[60] Driver, P. M., and Humphries, D. A., "Defence by Prey Animals," *Oecologia*, Vol. 5, No. 4, 1970, pp. 285–302.

[61] Norberg, U. M., "Some Advanced Flight Manoeuvres of Bats," *Journal of Experimental Biology*, Vol. 64, 1976, pp. 489–495.

[62] Bishop, K. L., "The relationship between 3-D kinematics and gliding performance in the southern flying squirrel, Glaucomys volans," *Journal of Experimental Biology*, Vol. 209, No. 4, 2006, pp. 689–701. DOI:10.1242/jeb.02062.

[63] Bahlman, J. W., Swartz, S. M., Riskin, D. K., and Breuer, K. S., "Glide performance and aerodynamics of non-equilibrium glides in northern flying squirrels (Glaucomys sabrinus)," *Journal of The Royal Society Interface*, Vol. 10, No. 80, 2012, pp. 20120794–20120794. DOI:10.1098/rsif.2012.0794.

[64] McCay, M. G., "Aerodynamic stability and maneuverability of the gliding frog Polypedates dennysi," *The Journal of Experimental Biology*, Vol. 204, No. 16, 2001, pp. 2817–2826.

[65] Hallett, D., *Native birds of New Zealand*, Sandfly Publishing, Christchurch, New Zealand, 2014.

[66] Bildstein, K. L., "Behavioral ecology of red-tailed hawks (Buteo jamaicensis), rough-legged hawks (Buteo lagopus), northern harriers (Circus cyaneus), and American kestrels (Falco sparverius) in south central Ohio," Doctoral Dissertation, Ohio State University, 1978.

[67] Collopy, M. W., and Bildstein, K. L., "Foraging Behavior of Northern Harriers Wintering in Southeastern Salt and Freshwater Marshes," *The Auk*, Vol. 104, No. 1, 1987, pp. 11–16. DOI:10.2307/4087227.

[68] Vukovich, M., and Ritchison, G., "Foraging Behavior of Short-Eared Owls and Northern Harriers on a Reclaimed Surface Mine in Kentucky," *Southeastern Naturalist*, Vol. 7, No. 1, 2008, pp. 1–10.

[69] Ma, K. Y., Chirarattananon, P., Fuller, S. B., and Wood, R. J., "Controlled Flight of a Biologically Inspired, Insect-Scale Robot," *Science*, Vol. 340, No. 6132, 2013, pp. 603–607. DOI:10.1126/science.1231806.

[70] Taylor, M., ed., *Brassey's World Aircraft & Systems Directory*, Brassey's, Herndon, VA, 1999.

[71] Barbarino, S., Bilgen, O., Ajaj, R. M., Friswell, M. I., and Inman, D. J., "A Review of Morphing Aircraft," *Journal of Intelligent Material Systems and Structures*, Vol. 22, No. 9, 2011, pp. 823–877. DOI:10.1177/1045389X11414084.

[72] Sofla, A. Y. N., Meguid, S. A., Tan, K. T., and Yeo, W. K., "Shape morphing of aircraft wing: Status and challenges," *Materials & Design*, Vol. 31, No. 3, 2010, pp. 1284–1292. DOI:10.1016/j.matdes.2009.09.011.

[73] Weisshaar, T. A., "Morphing Aircraft Systems: Historical Perspectives and Future Challenges," *Journal of Aircraft*, Vol. 50, No. 2, 2013, pp. 337–353. DOI:10.2514/1.C031456.

[74] Thill, C., Etches, J., Bond, I., Potter, K., and Weaver, P., "Morphing skins," *The Aeronautical Journal*, Vol. 112, No. 1129, 2008.

[75] Min, Z., Kien, V. K., and Richard, L. J. Y., "Aircraft morphing wing concepts with radical geometry change," *The IES Journal Part A: Civil & Structural Engineering*, Vol. 3, No. 3, 2010, pp. 188–195. DOI:10.1080/19373261003607972.

[76] Weisshaar, T. A., "Morphing Aircraft Technology - New Shapes for Aircraft Design," NATO RTO-MP-AVT-141: Multifunctional Structures / Integration of Sensors and Antennas, Neuilly-sur-Seine, France.

[77] Inman, D. J., Gern, F. H., Robertshaw, H. H., Kapania, R. K., Pettit, G., Natarajan, A., and Sulaeman, E., "Comments on prospects of fully adaptive aircraft wings," A.-M.R. McGowan, ed., Smart Structures and Materials 2001: Industrial and Commercial Applications of Smart Structures Technologies, Newport Beach, CA, pp. 1–9.

[78] Kang, H., Saberi, H., and Gandhi, F., "Dynamic Blade Shape for Improved Helicopter Rotor Performance," *Journal of the American Helicopter Society*, Vol. 55, No. 3, 2010, p. 032008. DOI:10.4050/JAHS.55.032008.

[79] Yeo, H., "Assessment of Active Controls for Rotor Performance Enhancement," *Journal of the American Helicopter Society*, Vol. 53, No. 2, 2008, p. 152. DOI:10.4050/JAHS.53.152.

[80] Butt, J. R., "A Study of Morphing Wing Effectiveness in Fighter Aircraft using Exergy Analysis and Global Optimization Techniques," Master's Thesis, Virginia Polytechnic Institute and State University, 2005.

[81] Jha, A. K., and Kudva, J. N., "Morphing aircraft concepts, classifications, and challenges," E.H. Anderson, ed., Smart Structures and Materials 2004: Industrial and Commercial Applications of Smart Structures Technologies, San Diego, CA, pp. 213–224.

[82] Neal III, D. A., "Design, Development, and Analysis of a Morphing Aircraft Model for Wind Tunnel Experimentation," Master's Thesis, Virginia Polytechnic Institute and State University, 2006.

[83] Valasek, J., ed., *Morphing Aerospace Vehicles and Structures*, John Wiley & Sons, Ltd, Chichester, UK, 2012.

[84] Felício, J. M. I., "Development and Testing of a Variable-Span Morphing Wing," Master's Thesis, University of Beira Interior, 2010.

[85] Ajaj, R. M., Friswell, M. I., I Saavedra Flores, E., Keane, A., Isikveren, A. T., Allegri, G., and Adhikari, S., "An integrated conceptual design study using span morphing technology," *Journal of Intelligent Material Systems and Structures*, Vol. 25, No. 8, 2014, pp. 989–1008. DOI:10.1177/1045389X13502869.

[86] Mestrinho, J., Gamboa, P., and Santos, P., "Design Optimization of a Variable-Span Morphing Wing for a Small UAV," 52nd AIAA/ASME/ASCE/AHS/ASC Structures, Structural Dynamics and Materials Conference, Denver, CO.

[87] de Marmier, P., and Wereley, N., "Control of Sweep Using Pneumatic Actuators to Morph Wings of Small Scale UAVs," 44th AIAA/ASME/ASCE/AHS/ASC Structures, Structural Dynamics, and Materials Conference, Norfolk, VA.

[88] Chakravarthy, A., Grant, D., and Lind, R., "Time-Varying Dynamics of a Micro Air Vehicle with Variable-Sweep Morphing," *Journal of Guidance, Control, and Dynamics*, Vol. 35, No. 3, 2012, pp. 890–903. DOI:10.2514/1.55078.

[89] Grant, D., Abdulrahim, M., and Lind, R., "Flight Dynamics of a Morphing Aircraft Utilizing Independent Multiple-Joint Wing Sweep," *International Journal of Micro Air Vehicles*, Vol. 2, No. 2, 2010, pp. 91–106. DOI:10.1260/1756-8293.2.2.91.

[90] Flanagan, J., Strutzenberg, R., Myers, R., and Rodrian, J., "Development and Flight Testing of a Morphing Aircraft, the NextGen MFX-1," 48th AIAA/ASME/ASCE/AHS/ASC Structures, Structural Dynamics, and Materials Conference, Honolulu, HI.

[91] Bowman, J., Sanders, B., Cannon, B., Kudva, J., Joshi, S., and Weisshaar, T., "Development of Next Generation Morphing Aircraft Structures," 48th AIAA/ASME/ASCE/AHS/ASC Structures, Structural Dynamics, and Materials Conference, Honolulu, HI.

[92] Gandhi, N., Jha, A., Monaco, J., Seigler, T., Ward, D., and Inman, D., "Intelligent Control of a Morphing Aircraft," 48th AIAA/ASME/ASCE/AHS/ASC Structures, Structural Dynamics, and Materials Conference, Honolulu, HI.

[93] Popov, A. V., Grigorie, L. T., Botez, R. M., Mamou, M., and Mébarki, Y., "Real Time Morphing Wing Optimization Validation Using Wind-Tunnel Tests," *Journal of Aircraft*, Vol. 47, No. 4, 2010, pp. 1346–1355. DOI:10.2514/1.47431.

[94] Shmoldas, J. D., Hutchings, M. B., and Barlow, C. W., "Extendable wing for guided missiles and munitions," US 5615846 A, April 1, 1997.

[95] Hall, J., Mohseni, K., Lawrence, D., and Geuzaine, P., "Investigation of Variable Wing-Sweep for Applications in Micro Air Vehicles," Infotech@Aerospace Conference, Arlington, VA.

[96] Braun, R. D., Wright, H. S., Croom, M. A., Levine, J. S., and Spencer, D. A., "Design of the ARES Mars Airplane and Mission Architecture," *Journal of Spacecraft and Rockets*, Vol. 43, No. 5, 2006, pp. 1026–1034. DOI:10.2514/1.17956.

[97] Ledé, J.-C., Parks, R., and Croom, M., "High Altitude Drop Testing in Mars Relevant Conditions for the ARES Mars Scout Mission," 2nd AIAA "Unmanned Unlimited" Conf. and Workshop & Exhibit, San Diego, CA.

[98] Wright, H., Croom, M., Braun, R., Qualls, G., Cosgrove, P., and Levine, J., "ARES Mission Overview - Capabilities and Requirements of the Robotic Aerial Platform," 2nd AIAA "Unmanned Unlimited" Conf. and Workshop & Exhibit, San Diego, CA.

[99] Kenney, P. S., and Croom, M., "Simulating The ARES Aircraft In The Mars Environment," 2nd AIAA "Unmanned Unlimited" Conf. and Workshop & Exhibit, San Diego, CA.

[100] Bovais, C., and Davidson, P., "Flight testing the Flying Radar Target (FLYRT)," Biennial Flight Test Conference, Hilton Head, SC.

[101] Munson, K., *Jane's Unmanned Aerial Vehicles and Targets*, Jane's Information Group, Surrey, UK, 2000.

[102] Jacob, J., and Smith, S., "Design Limitations of Deployable Wings for Small Low Altitude UAVs," 47th AIAA Aerospace Sciences Meeting, Orlando, FL.

[103] Seigler, T. M., "Dynamics and Control of Morphing Aircraft," Doctoral Dissertation, Virginia Polytechnic Institute and State University, 2005.

[104] Bourdin, P., Gatto, A., and Friswell, M. I., "Aircraft Control via Variable Cant-Angle Winglets," *Journal of Aircraft*, Vol. 45, No. 2, 2008, pp. 414–423. DOI:10.2514/1.27720.

[105] Gatto, A., Bourdin, P., and Friswell, M. I., "Experimental Investigation into Articulated Winglet Effects on Flying Wing Surface Pressure Aerodynamics," *Journal of Aircraft*, Vol. 47, No. 5, 2010, pp. 1811–1815. DOI:10.2514/1.C000251.

[106] Gatto, A., Bourdin, P., and Friswell, M. I., "Experimental Investigation into the Control and Load Alleviation Capabilities of Articulated Winglets," *International Journal of Aerospace Engineering*, Vol. 2012, 2012, pp. 1–15. DOI:10.1155/2012/789501.

[107] Tavares, F. M. T., "Roll Motion Control of a Dissymmetrical Wingspan Aircraft," Master's Thesis, University of Beira Interior, 2011.

[108] Sanches, T. N., "Longitudinal Flight Control with a Variable Span Morphing Wing," Master's Thesis, University of Beira Interior, 2012.

[109] Henry, J. J., "Roll control for UAVs by use of a variable span morphing wing," Master's Thesis, University of Maryland, 2005.

[110] Rao, D. M., and Sharma, G., "Side-force control on a diamond forebody at high angles of attack," *Journal of Aircraft*, Vol. 31, No. 4, 1994, pp. 915–921. DOI:10.2514/3.46579.

[111] Stucke, R. A., "High angle-of-attack yaw control using strakes on blunt-nose bodies," Master's Thesis, The University of Toledo, 2006.

[112] Natarajan, A., Kapania, R. K., and Inman, D. J., "Aeroelastic Optimization of Adaptive Bumps for Yaw Control," *Journal of Aircraft*, Vol. 41, No. 1, 2004, pp. 175–185. DOI:10.2514/1.477.

[113] Green, P. R., and Cheng, P., "Variation in kinematics and dynamics of the landing flights of pigeons on a novel perch," *The Journal of Experimental Biology*, Vol. 201, No. 24, 1998, pp. 3309–3316.

[114] Maqsood, A., and Go, T. H., "Optimization of Hover-to-Cruise Transition Maneuver Using Variable-Incidence Wing," *Journal of Aircraft*, Vol. 47, No. 3, 2010, pp. 1060–1064. DOI:10.2514/1.44453.

[115] Dwivedi, V., and Damodaran, M., "Computational Aeromechanics of a Manuevering Unmanned Aerial Vehicle with Variable-Incidence Wings," *Journal of Aircraft*, Vol. 52, No. 6, 2015, pp. 1914–1926. DOI:10.2514/1.C033102.

[116] Ross, H. M., Offerman, H. A. J. M., Perkins, J. N., Vess, R. J., and Owens, D. B., "Wing leading-edge droop/slot modification for stall departure resistance," *Journal of Aircraft*, Vol. 28, No. 7, 1991, pp. 436–442. DOI:10.2514/3.46046.

[117] Ross, H. M., and Perkins, J. N., "Tailoring stall characteristics using leading edge droop modification," *Journal of Aircraft*, Vol. 31, No. 4, 1994, pp. 767–772. DOI:10.2514/3.46559.

[118] Pankonien, A., Faria, C. T., and Inman, D., "Synergistic Smart Morphing Aileron," AIAA/ASME/ASCE/AHS/ASC Structures, Structural Dynamics, and Materials Conference, Boston, MA.

[119] Gern, F. H., Inman, D. J., and Kapania, R. K., "Structural and Aeroelastic Modeling of General Planform Wings with Morphing Airfoils," *AIAA Journal*, Vol. 40, No. 4, 2002, pp. 628–637. DOI:10.2514/2.1719.

[120] Lego, Z. M., and Altman, A., "Analysis of a Variable Camber Wing during Highly Unsteady Maneuvers," 31st AIAA Applied Aerodynamics Conference, San Diego, CA.

[121] von Busse, R., Hedenstrom, A., Winter, Y., and Johansson, L. C., "Kinematics and wing shape across flight speed in the bat, Leptonycteris yerbabuenae," *Biology Open*, Vol. 1, No. 12, 2012, pp. 1226–1238. DOI:10.1242/bio.20122964.

[122] Munday, D., and Jacob, J., "Active Control of Separation on a Wing with Oscillating Camber," *Journal of Aircraft*, Vol. 39, No. 1, 2002, pp. 187–189. DOI:10.2514/2.2915.

[123] Abdulrahim, M., and Lind, R., "Flight Testing and Response Characteristics of a Variable Gull-Wing Morphing Aircraft," AIAA Guidance, Navigation, and Control Conference and Exhibit, Providence, RI.

[124] Bechert, D. W., Hage, W., and Meyer, R., "Self-actuating flaps on bird and aircraft wings," *Flow Phenomena in Nature*, R. Liebe, ed., WIT Press, 2006.

[125] Sarigul-Klijn, N., Kuo, B. C., and Karnopp, D. C., "Deployable Micro-Tabs in Aircraft Noise Control Near Airports: Scaled Experimental Apparatus and Computational Results," pp. 29–36.

[126] Kernstine, K., Moore, C., Cutler, A., and Mittal, R., "Initial Characterization of Self-Activated Movable Flaps, 'Pop-Up Feathers,'" 46th AIAA Aerospace Sciences Meeting and Exhibit, Reno, NV.

[127] Bechert, D. W., Bruse, M., Hage, W., and Meyer, R., "Fluid Mechanics of Biological Surfaces and their Technological Application," *Naturwissenschaften*, Vol. 87, No. 4, 2000, pp. 157–171. DOI:10.1007/s001140050696.

[128] Storms, B. L., and Jang, C. S., "Lift enhancement of an airfoil using a Gurney flap and vortex generators," *Journal of Aircraft*, Vol. 31, No. 3, 1994, pp. 542–547. DOI:10.2514/3.46528.

[129] Quackenbush, T., McKillip, R., and Whitehouse, G., "Development and Testing of Deployable Vortex Generators Using SMA Actuation," 28th AIAA Applied Aerodynamics Conference, Chicago, IL.

[130] Lin, J. C., Robinson, S. K., McGhee, R. J., and Valarezo, W. O., "Separation control on high-lift airfoils via micro-vortex generators," *Journal of Aircraft*, Vol. 31, No. 6, 1994, pp. 1317–1323. DOI:10.2514/3.46653.

Chapter 2:
Quaternion and Euler angle kinematics

2.1. INTRODUCTION

A variety of approaches are available for the parameterisation of the system orientation and airframe component configuration – Euler angles, quaternions, rotation matrices, and others [1]. Euler angles are a common approach for rotation within a fixed sector: they are an unconstrained orientation parameterization – yielding unconstrained integrators for rotational motion – and have immediate physical interpretation. Their key disadvantage is gimbal lock – the unavoidable presence of singularity at some orientation within the system (the pole), typically leading to integration and interpolation failure in the near vicinity [1]. If the system rotation is constrained to or unlikely to leave a fixed sector, then the system pole can be oriented outside this by the choice of Euler angle definition; but for a fully three-dimensional flight simulation this will not always be the case.

Quaternions are a system of hypercomplex numbers that extend the conventional complex number system ($\mathbb{C}$) to three imaginary units and a real part. They may be used to parameterise orientation and rotation [1]. Unlike Euler angles they are singularity-free and thus do not suffer from gimbal lock; but are subject to a normalisation constraint over their four scalar components. The absence of singularity makes them particularly suitable for the analysis of complex manoeuvres, but their constrainedness will complicate the integration of the system equations of motion. They have seen significant previous use in multibody dynamics, for general [2,3] and specific systems [4,5], and in the flight simulation of satellites [6–8]. In comparison with rotation matrices, which show significant similarity, both being singularity-free and endowed with a Lie Algebra [9,10] – quaternions are more computationally efficient, requiring the integration of four scalar variables (with one normalisation constraint), whereas rotation matrices involve the integration of six scalar variables (with three skew-symmetry constraints) [11].

This chapter presents a generalised framework for the analysis of the case study system kinematics, formulated in quaternion and Euler angle frameworks. The former will be utilised as the optimal choice of orientation parameterisation for the system, and will lead to the development of a quaternion variational integrator for the system. The latter will lead to an adaptive pole-switching Runge-Kutta 4(5) (RK45) integrator for validation and time-efficient simulation, and will be utilised to post-processing quaternion orientation results.

2.2. ORIENTATION PARAMETERISATION WITH QUATERNIONS

2.2.1. Properties of quaternions

In the quaternion algebra ($\mathbb{H}$), three imaginary units (i, j, k) are postulated, all of them roots of -1, and with the unique multiplicative property [12]:

$$ijk = i^2 = j^2 = k^2 = -1. \tag{2.2.1}$$

A quaternion is a linear combination of these units and a real component ($\in \mathbb{R}$). Formally, quaternions constitute a Lie algebra: a vector space with a non-associative operator, in this case, quaternion multiplication (Eq. 2.2.4) [10,13]. In notation, they may also be denoted by a 4-vector, or a concatenation of a scalar (the real component) and a 3-vector (the imaginary components) [12]:

$$q = q_0 + ai + bj + ck = \begin{bmatrix} q_0 \\ a \\ b \\ c \end{bmatrix} = \begin{bmatrix} q_0 \\ \mathbf{q}_v \end{bmatrix}, \qquad \mathbf{q}_v = \begin{bmatrix} a \\ b \\ c \end{bmatrix}. \tag{2.2.2}$$

A quaternion with no real part ($a = 0$, $q = ai + bj + ck$) is a pure or imaginary quaternion. Under appropriate conditions quaternions degenerate naturally to the real numbers ($q = q_0$ implies $q \in \mathbb{R}$) and the complex numbers ($q = q_0 + ai$ implies $q \in \mathbb{C}$, but not $q = q_0 + bj$). In the context of rotation operations, imaginary quaternions also correspond to vectors in 3-space in via the q_0-$\mathbf{q}_v$ formulation, though notably these vectors are in fact pseudovectors [14]. Correspondingly, vectors or pseudovectors in 3-space correspond to imaginary quaternions , e.g. $\mathbf{x} = [a\ b\ c]^T$ corresponds to quaternion $[0\ a\ b\ c] = ai + bj + ck$. For simplicity of notation, bold face quantities ($\mathbf{x}$, etc.) are taken to be both imaginary quaternions (endowed e.g. with quaternion multiplication $\otimes$) and vectors (endowed e.g. with the cross product $\times$). More formally, this equivalence represents the fact that the set of pure quaternions, $\mathrm{Im}\,\mathbb{H}$, are isomorphic to $\mathbb{R}^3$ endowed with the cross product: they are equivalent Lie algebras [13].

The operators with which all quaternions are endowed include:

- **Addition and subtraction**, $\pm$, which is commutative and associative:

$$\begin{bmatrix} q_0 \\ \mathbf{q}_v \end{bmatrix} \pm \begin{bmatrix} p_0 \\ \mathbf{p}_v \end{bmatrix} = \begin{bmatrix} q_0 + p_0 \\ \mathbf{q}_v + \mathbf{p}_v \end{bmatrix}.$$
$$q + p = p + q,$$
$$(q + p) + r = p + (q + r). \tag{2.2.3}$$

- **Multiplication**, $\otimes$, which is defined uniquely. It is associative, but notably not generally commutative:

$$\begin{bmatrix} q_0 \\ \mathbf{q}_v \end{bmatrix} \otimes \begin{bmatrix} p_0 \\ \mathbf{p}_v \end{bmatrix} = \begin{bmatrix} q_0 p_0 - \mathbf{p}_v^T \mathbf{q}_v \\ p_0 \mathbf{q}_v + q_0 \mathbf{p}_v + \mathbf{p}_v \times \mathbf{q}_v \end{bmatrix}.$$
$$(p \otimes q) \otimes r = p \otimes (q \otimes r),$$
$$q \otimes p \neq p \otimes q. \tag{2.2.4}$$

- **Conjugation**, $(\cdot)^\dagger$, which is analogous to the complex equivalent:

$$\begin{bmatrix} q_0 \\ \mathbf{q}_v \end{bmatrix}^\dagger = \begin{bmatrix} q_0 \\ -\mathbf{q}_v \end{bmatrix}. \tag{2.2.5}$$

- **The norm**, $\|\cdot\|$, defined e.g. in a Euclidean sense as:

$$\|q\| = \sqrt{q \otimes q^\dagger} = \sqrt{q^\dagger \otimes q},$$
$$\|a + bi + cj + dk\| = \sqrt{a^2 + b^2 + c^2 + d^2}, \tag{2.2.6}$$

  which takes value 1 for quaternions parameterising rotations.

- **Inversion**, $(\cdot)^{-1}$, which may be computed via the conjugate and the norm, and relates to the identity, scalar 1 (i.e., $1 + 0i + 0j + 0k$):

$$q^{-1} = \frac{q^\dagger}{\|q\|}, \qquad (q \otimes q^{-1}) = (q^{-1} \otimes q) = 1. \tag{2.2.7}$$

  Notably, for unit quaternions, $\|q\| = 1$, inversion and conjugation are equivalent.

- **Exponentiation**, $\exp(\cdot)$, may be computed via scalar exponential and trigonometric functions:

$$\exp\left(\begin{bmatrix} q_0 \\ \mathbf{q}_v \end{bmatrix}\right) = \exp(q_0) \begin{bmatrix} \cos\|\mathbf{q}_v\| \\ \frac{\mathbf{q}_v}{\|\mathbf{q}_v\|} \sin\|\mathbf{q}_v\| \end{bmatrix}. \tag{2.2.8}$$

  Though some properties of scalar exponentiation do not generally hold, e.g.

$$\exp(q + p) \neq \exp(q) \otimes \exp(p). \tag{2.2.9}$$

Finally, one other notable relation is the degeneration of the commutator of the quaternion product to the cross product in the case of imaginary quaternions:

$$\mathbf{p}_v \otimes \mathbf{q}_v - \mathbf{q}_v \otimes \mathbf{p}_v = 2\mathbf{p}_v \times \mathbf{q}_v. \tag{2.2.10}$$

These are the relations that will be of relevance to this analysis. Further algebraic properties of quaternions are detailed in many reference works and papers; e.g. [15,16].

2.2.2. Parameterisation of reference frames

Quaternions can be utilised for several forms of orientation parameterisation: the form utilised in this study is that of reference frame parameterisation. This involves the use of quaternions to parameterisation the rotations between reference frames in a kinematic chain. Beginning with a globally-fixed reference frame – the earth frame – the orientation of an aircraft reference frame, fixed to the airframe, with respect to the earth frame can be represented as a unit quaternion q ($\|q\| = 1$). This representation is uniquely constrained by, and necessarily implies, the definition of the frame transformation of any vector $\mathbf{x}$ between the earth and aircraft reference frames [16]:

$$\begin{aligned} \mathbf{x}^{(e)} &= q \otimes \mathbf{x}^{(b)} \otimes q^{\dagger}, \\ \mathbf{x}^{(b)} &= q^{\dagger} \otimes \mathbf{x}^{(e)} \otimes q, \end{aligned} \tag{2.2.11}$$

where (e) denotes resolution in earth reference frame, and (b) in the body-fixed aircraft reference frame. Note the notational equivalence of $\mathbf{x}$ as 3-vector and imaginary quaternion, as per Section 2.2.1 and note also that the earth frame is Cartesian: the scale of manoeuvres studied here, $\mathcal{O}(100\,\mathrm{m})$, is sufficiently small that the earth's curvature is negligible.

It follows that that quaternion derivative $\dot{q}$ and the angular velocity $\boldsymbol{\omega}$ (resolved in any frame) are proxies for each other, via the relations [16]:

$$\begin{aligned} \boldsymbol{\omega}^{(e)} &= 2\dot{q} \otimes q^{\dagger}, \qquad \dot{q} = \frac{1}{2}\boldsymbol{\omega}^{(e)} \otimes q, \\ \boldsymbol{\omega}^{(b)} &= 2q^{\dagger} \otimes \dot{q}, \qquad \dot{q} = \frac{1}{2} q \otimes \boldsymbol{\omega}^{(b)}, \end{aligned} \tag{2.2.12}$$

where the relation between $\boldsymbol{\omega}^{(e)}$ and $\boldsymbol{\omega}^{(b)}$ is consistent with Eq. 2.2.11. However, $\boldsymbol{\omega}$ is of significantly greater utility, as the quaternion derivative $\dot{q}$ represents a tangent to the space of admissible orientation quaternions, the surface of a hypersphere with $\|q\| = 1$. Numerical integration using the quaternion derivative becomes more complex, as a simple finite-difference approximation of $\dot{q}$ (e.g. $q(t+h) = q(t) + h\dot{q}(t)$) will produce

quaternions outside the admissible space: forms of spherical integration are required. The motivates the use of $\boldsymbol{\omega}$ as a proxy derivative for q; an aspect which will become relevant in Chapter 4.

Finally, in terms of implementation into an analysis framework based on rotation matrices, the rotation matrix $\mathrm{R}_{E/B}$ associated with the earth-body frame quaternion q $(= [q_0 \ \mathbf{q}_v])$ can be computed as [16]:

$$\mathrm{R}_{E/B} = (q_0^2 - \mathbf{q}_v^T\mathbf{q}_v)\mathrm{E}_3 + 2\mathbf{q}_v\mathbf{q}_v^T + 2q_0[\mathbf{q}_v]_\times. \tag{2.2.13}$$

The operator $[\cdot]_\times$ is the skew-symmetric operator, which maps $\mathbb{R}^3 \to \mathbb{R}^{3\times3}$ [17–19]. It has several applications in the kinematics of rotation and is defined as

$$[\mathbf{x}]_\times = \left[\begin{bmatrix}\mathrm{x}_1\\ \mathrm{x}_2\\ \mathrm{x}_3\end{bmatrix}\right]_\times = \begin{bmatrix}0 & -\mathrm{x}_3 & \mathrm{x}_2\\ \mathrm{x}_3 & 0 & -\mathrm{x}_1\\ -\mathrm{x}_2 & \mathrm{x}_1 & 0\end{bmatrix}. \tag{2.2.14}$$

A corresponding inverse operator may be defined for matrices of the appropriate format. Reference frame transformation via $\mathrm{R}_{E/B}$ is easy; for vectors $\mathbf{x}$ and matrices/tensors M:

$$\begin{aligned}\mathbf{x}^{(e)} &= \mathrm{R}_{E/B}\mathbf{x}^{(b)}, & \mathrm{M}^{(e)} &= \mathrm{R}_{E/B}\mathrm{M}^{(b)}\mathrm{R}_{E/B}^T,\\ \mathbf{x}^{(b)} &= \mathrm{R}_{E/B}^T\mathbf{x}^{(e)}, & \mathrm{M}^{(b)} &= \mathrm{R}_{E/B}^T\mathrm{M}^{(e)}\mathrm{R}_{E/B}.\end{aligned} \tag{2.3.12}$$

The use of rotation matrices for numerical computation is more efficient that the construction of a local numerical quaternion algebra, and synthesises directly with any nearby Euler angle orientation parameterisations. However, the efficiencies of the base quaternion parameterisation are retained: this too becomes relevant in Chapter 4.

2.2.3. Choices of convention

The quaternion parameterisation of orientation presented in Sections 2.3.1-2.3.2, known as the Hamilton convention, is only one of many such conventions. The set of orientation quaternion relations and properties is dependent on the choice of several aspects of the quaternion definition:

- The ordering of the quaternion q_0-$\mathbf{q}_v$ form: $[q_0 \ \mathbf{q}_v]^T$ or $[\mathbf{q}_v \ q_0]^T$, a convention which affect relations defined using this form, and the numerical implementation of quaternion algebra.

- The handedness of the quaternion, governed by the fundamental definition of the quaternion algebra. While all quaternions obey Eq. 2.3.1, this admits two solutions: $ij = -ji = k$ or $ji = -ij = k$, also representing pre- and post- multiplication of the quaternion coefficients (bi vs. ib). These solutions correspond to right- and left-handed quaternions respectively, denoting the handedness of the rotation the quaternion represents.

- The nature of the orientation parameterisation: whether the quaternion represents the rotation of the reference frame in which a fixed vector is resolved (*passive* function), or the physical rotation of a vector in one reference frame (*active* function). These conceptual distinctions have an impact on the effect of Eq. 2.2.11 on the system kinematics.

- In the case of passive function, whether the $q^{\dagger} \otimes \mathbf{x} \otimes q$ represents transformation from an global (earth) frame to a local frame, or vice versa. The former convention, for example, is represented in Eq. 2.3.11.

The Hamilton convention, applied in this study, uses $[q_0 \ \mathbf{q}_v]^T$ ordering and is right-handed, passive and global-to-local [16,20]. Alternatives include the Caltech Jet Propulsion Lab (JPL) convention, which uses $[\mathbf{q}_v \ q_0]^T$ ordering and is left-handed, passive and local-to-global [21,22]; as well as the European Space Agency (ESA), International Space Station (ISS), Space Transportation System (STS) and other conventions [16].

2.3. ORIENTATION PARAMETERISATION WITH EULER ANGLES

2.3.1. Definition

In format, an Euler angle parameterisation consists of three angles (e.g. $\boldsymbol{\theta} \in \mathbb{R}^3$), association with three defined axes that are constrained with respect to the earth and/or body-fixed reference frames. The orientation represented by these angles is constructed via sequential rotations of the parameterisation object (e.g. a reference frame) by each angle around its associated axis. These axes are the key defining and generating features of the parameterisation, and particular choices lead to angles recognisable to different industrial communities: for example, in aerospace, the pitch, yaw and roll angles. Here again, the

Euler angle framework is used to parameterise the orientation of the aircraft reference or body-fixed frame with respect to the earth frame.

2.3.2. General properties

The definition of the Euler angle parameterisation as a set of sequential rotations, alongside the addition theorem [2], imply directly that any 3-vector of Euler angle rates may be transformed into a corresponding angular velocity pseudovector [23] via a matrix of the parameterisation's defining axes. For $\Theta = [\theta, \psi, \phi]^T$ with associated vectors $\left[\widehat{\boldsymbol{\alpha}}, \widehat{\boldsymbol{\beta}}, \widehat{\boldsymbol{\gamma}}\right]$, taking note of the order of rotations, this linear transformation is given by:

$$\begin{aligned} \boldsymbol{\omega}^{(e)} &= \widehat{\boldsymbol{\alpha}}^{(e)}\dot{\theta} + \widehat{\boldsymbol{\beta}}^{(e)}\dot{\psi} + \widehat{\boldsymbol{\gamma}}^{(e)}\dot{\phi} = \Omega^{(e)}\dot{\Theta}, \\ \Omega^{(e)} &= \left[\widehat{\boldsymbol{\alpha}}^{(e)}, \widehat{\boldsymbol{\beta}}^{(e)}, \widehat{\boldsymbol{\gamma}}^{(e)}\right]. \end{aligned} \tag{2.3.1}$$

Note that, given the invariance of $\dot{\Theta}$ with respect to coordinate system, $\Omega^{(e)}$ is transforms under rotation matrix premultiplication, as it were a vector, e.g.

$$\boldsymbol{\omega}^{(b)} = \Omega^{(b)}\dot{\Theta} = \mathrm{R}_{E/B}\Omega^{(e)}\dot{\Theta}. \tag{2.3.2}$$

It is of little utility to transform the Euler angle 3-vector itself via Ω, as this yields only an axis-angle product – time-integral of the angular velocity pseudovector – which is only physically relevant in the case of uniaxial rotation. However, the rotated reference frame unit vectors can be constructed via the solution of a system of vector relations, leading to a definition of the rotation matrix associated with a given rotation. This process is complex and strongly dependent of the definition of the parameterisation axes, and the location of the zero values in the angles; but a full outline for the case study system is offered in Section 2.5. Here it suffices to define the resulting rotation matrix, a nonlinear and trigonometric function, as $\mathrm{R}(\Theta)$.

2.3.3. Singularity

The Euler angle framework, while intuitive, has a key deficiency: a singularity or pole must be present in the orientation space, at which point the representation loses a degree of freedom. In the vicinity of this pole, numerical integration will fail (a facet of the gimbal lock phenomenon), and the Euler angle values will be discontinuous and thus non-interpolable [1,24]. The quaternion orientation parameterisation avoids this singularity, but an Euler angle parameterisation is also required, for three reasons: to provide a framework for

intuitive post-processing and visualisation; for verification of the quaternion variational integrator that will be devised via an alternate Euler angle RK45 integrator; and because this Euler angle RK45 integrator may prove to be more efficient or effective that the quaternion variational integrator in some contexts.

2.4. KINEMATIC CHAINS

2.4.1 Generalised formulation

The kinematics of any aircraft with airframe components undergoing rigid motions or rotations can be modelled under a generalised kinematic chain framework [25,26]. Taking at first a system reference point (S) that is fixed with respect to at least one airframe component; and assigning a local reference frame to each airframe component, we may compute the position ($\mathbf{x}_i$) of any airframe component centre of mass with respect to S via a kinematic chain connecting these points. Such a process may be expressed as:

$$\mathbf{x}_i^{(e)} = \mathbf{x}_S^{(e)} + \sum_{c=1}^{l_{c,i}} \mathrm{P}_{i,c}\mathbf{L}_{i,c}, \quad \text{with } i \in \mathcal{S}\text{, the set of all components,} \tag{2.4.1}$$

where $l_{c,i}$ represents the length of the kinematic chain for each component, and at each point on the chain (c), $\mathrm{P}_{i,c}$ represents a local reference frame rotation matrix relative to the earth frame, and $\mathbf{L}_{i,c}$ the local translation vector to the next chain point in this local reference frame. Note that the kinematic chains for each component will vary in length, from a necessary $l_{c,i} = 1$ for the body on which S is fixed up to a maximum value of the total number of bodies in the system. The angular velocity pseudovector [23] of each body relative to the earth frame may be expressed using the same kinematic chain used to compute the body centre of mass positions:

$$\boldsymbol{\omega}_i^{(e)} = \sum_{c=1}^{l_{c,i}} \mathrm{P}_{i,c}\boldsymbol{\omega}_{i,c}, \quad \text{with } i \in \mathcal{S}, \tag{2.4.2}$$

where $\boldsymbol{\omega}_{i,c}$ represent the angular velocity pseudovectors of the local reference frame (of index c), relative to the previous reference frame ($c-1$) or the earth frame for $c = 1$, and resolved in the local reference frame (c).

The velocities of the system bodies, whether at their centres of mass or at other points, are affected by the both rotational and positional kinematics. Using Eq. 2.4.1 and Eq. 2.4.2 we may compute the body centre of mass velocities in the earth frame as [27,28]:

$$\begin{aligned}\dot{\mathbf{x}}_i^{(e)} &= \dot{\mathbf{x}}_S^{(e)} + \boldsymbol{\omega}_i^{(e)} \times \left(\mathbf{x}_i^{(e)} - \mathbf{x}_S^{(e)}\right) \\ &= \dot{\mathbf{x}}_S^{(e)} + \left(\sum_{c=1}^{l_{c,i}} \mathrm{P}_{i,c}\boldsymbol{\omega}_{i,c}\right) \times \sum_{c=1}^{l_{c,i}} \mathrm{P}_{i,c}\mathbf{L}_{i,c}\,, \qquad i \in \mathcal{S}.\end{aligned} \tag{2.4.3}$$

Via the skew operator $[\cdot]_\times$ this may be reframed as:

$$\dot{\mathbf{x}}_i^{(e)} = \dot{\mathbf{x}}_S^{(e)} + \left[\sum_{c=1}^{l_{c,i}} \mathrm{P}_{i,c}\mathbf{L}_{i,c}\right]_\times^T \sum_{c=1}^{l_{c,i}} \mathrm{P}_{i,c}\boldsymbol{\omega}_{i,c}\,, \qquad i \in \mathcal{S}. \tag{2.4.4}$$

The complete set of centre-of-mass kinematic chains for a system can be represented in a tabular format. For example, for the three-body system of Figure 2.4.1, Table 2.4.1 shows the kinematic chain parameters from reference point S to the centres of mass of each body.

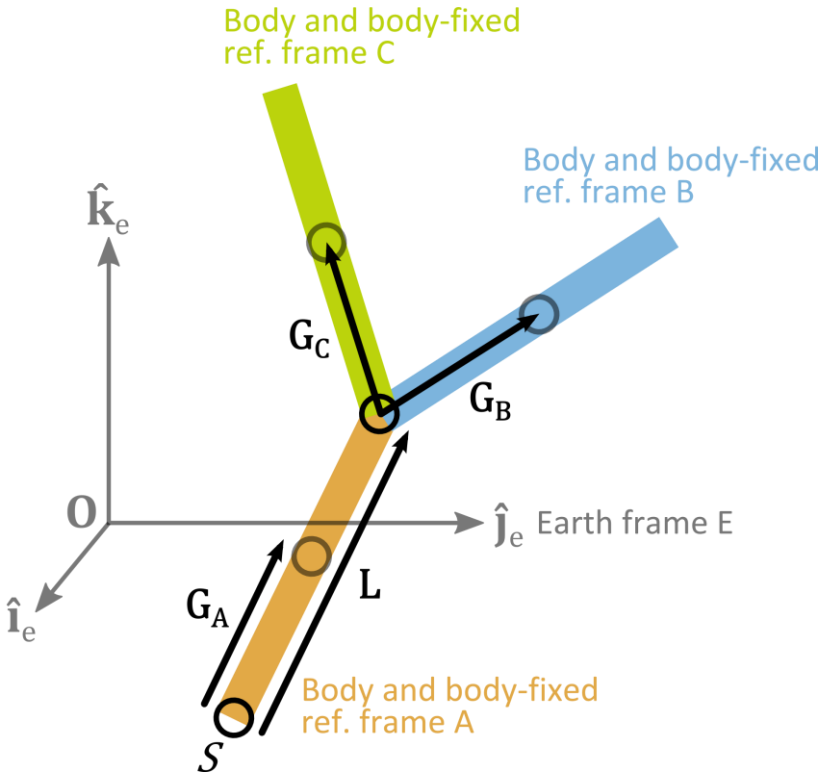

Figure 2.4.1: Three-body system with example kinematic chain

Table 2.4.1: Tabulated kinematic chain for a three-body example system

Body Name	Index	l_c	$c=1$		$c=2$		[…]
			$\mathbf{L}_{i,1}$	$\mathrm{P}_{i,1}$	$\mathbf{L}_{i,2}$	$\mathrm{P}_{i,2}$	
component A	a	1	$\mathbf{G}_\mathrm{A}$	$\mathrm{P}_{E/A}$			
component B	b	2	$\mathbf{L}$	$\mathrm{P}_{E/A}$	$\mathbf{G}_\mathrm{B}$	$\mathrm{P}_{E/A}\mathrm{P}_{A/B}$	
component C	c	2	$\mathbf{L}$	$\mathrm{P}_{E/A}$	$\mathbf{G}_\mathrm{C}$	$\mathrm{P}_{E/A}\mathrm{P}_{A/C}$	

2.4.2. Application to case study system

The reference point for the body-fixed frame, and thus the entire morphing-wing system, is a point S: the rearmost point on the fuselage body and the centre of the empennage. Any fixed point may be chosen as a reference; the choice of S simplifies the analysis of the empennage bodies. It is alternately possible to utilise the instantaneous centre of mass (in motion relative to the fuselage) as a reference point; this reduces the level of coupling but complicates the kinematics. The fixed-point approach utilised here is more standard in multibody dynamics [29], but differences are largely of convenience. The instantaneous centre of mass can be computed during post-processing.

From the reference point S, kinematic chains are constructed to the centre of mass of each of the airframe components: the fuselage (on which S is fixed); the individual horizontal stabilisers and vertical stabiliser (which are fixed with respect to the fuselage); and the two wings, which rotate about their root, a point R on the fuselage. Table 2.4.2 represents the complete set of kinematic chains for the case study system, and for reference, Figure 2.4.3 defines the geometric parameters used to compute $\mathbf{L}_{i,c}$. Figure 2.4.2 renders an example kinematic chain to the left wing centre of mass. Parameter values are given in Appendix 1.

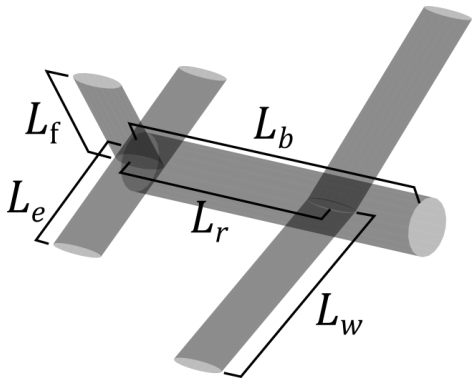

Figure 2.4.3: Geometric parameter definitions for the kinematic chains

Table 2.4.2: Tabulated kinematic chain for the case study system

Component Name	Index	l_c	$c=1$		$c=2$		[...]
			$\mathbf{L}_{i,1}$	$\mathrm{P}_{i,1}$	$\mathbf{L}_{i,2}$	$\mathrm{P}_{i,2}$	
fuselage	b	1	$[G_b\ 0\ 0]^T$	$\mathrm{P}_{E/B}$			
right wing	wr	2	$[L_r\ 0\ 0]^T$	$\mathrm{P}_{E/B}$	$\left[\frac{1}{2}L_{wr}\ 0\ 0\right]^T$	$\mathrm{P}_{E/B}\mathrm{P}_{B/WR}$	
left wing	wl	2	$[L_r\ 0\ 0]^T$	$\mathrm{P}_{E/B}$	$\left[\frac{1}{2}L_{wl}\ 0\ 0\right]^T$	$\mathrm{P}_{E/B}\mathrm{P}_{B/WL}$	
right elevator / horz. stabiliser	er	1	$\left[\frac{1}{2}L_e\ 0\ 0\right]^T$	$\mathrm{P}_{E/B}\mathrm{P}_{B/ER}$			
left elevator / horz. stabiliser	el	1	$\left[\frac{1}{2}L_e\ 0\ 0\right]^T$	$\mathrm{P}_{E/B}\mathrm{P}_{B/EL}$			
fin / vert stabiliser	f	1	$\left[\frac{1}{2}L_\mathrm{f}\ 0\ 0\right]^T$	$\mathrm{P}_{E/B}\mathrm{P}_{B/F}$			
point mass	pm	1	$\left[L_\mathrm{pm}\ 0\ 0\right]^T$	$\mathrm{P}_{E/B}$			

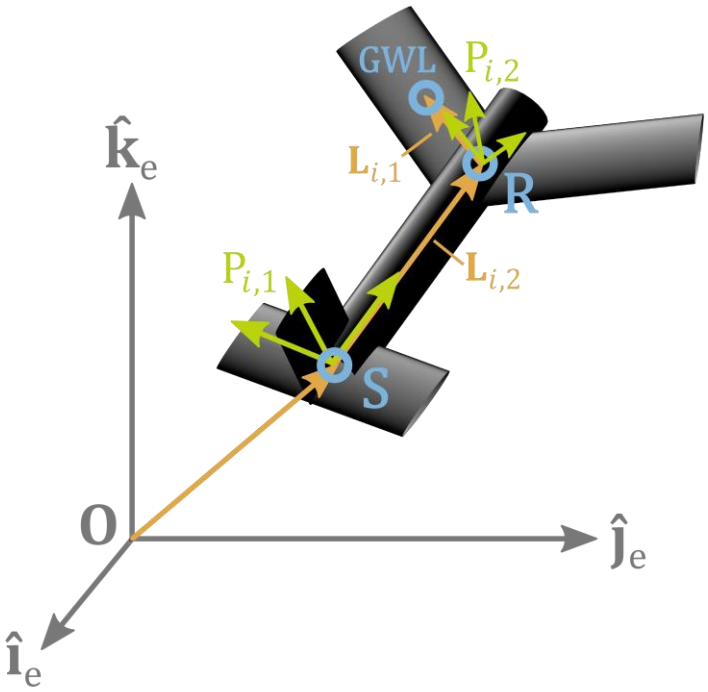

Figure 2.4.2: Example kinematic chain between the origin and the left wing centre of mass (GWL)

The matrices $\mathrm{P}_{i,c}$ are given by the orientation parameterisations of the individual bodies. To implement this framework, it remains to define the orientation parameterisations of each component in the case study airframe.

2.5. CASE STUDY SYSTEM PARAMETERISATION

2.5.1. Quaternion parameterisation of the body-fixed reference frame

From the reference point S, the orientation of the aircraft's body-fixed reference frame is parameterised with a unit quaternion, $\|q\| = 1$, with right-handedness and under the Hamilton convention (see Section 2.2.3). Fundamentally, this quaternion is constrained with reference to $\hat{\boldsymbol{\imath}}_b$, the fuselage axis and primary axis of the body-fixed reference frame:

$$\hat{\boldsymbol{\imath}}_b^{(e)} = q \otimes \hat{\boldsymbol{\imath}}_b^{(b)} \otimes q^{\dagger}, \quad \hat{\boldsymbol{\imath}}_b^{(b)} = [1\ 0\ 0]^T = 1i. \tag{2.5.1}$$

The values of the orientation quaternion corresponding to several example orientations are shown in Figure 2.5.1. Note, for instance, the case $q = 1$; $\hat{\boldsymbol{\imath}}_b^{(e)} = 1 \otimes 1i \otimes 1 = 1i = \hat{\boldsymbol{\imath}}_b^{(b)}$. This parameterisation is simple and easily defined.

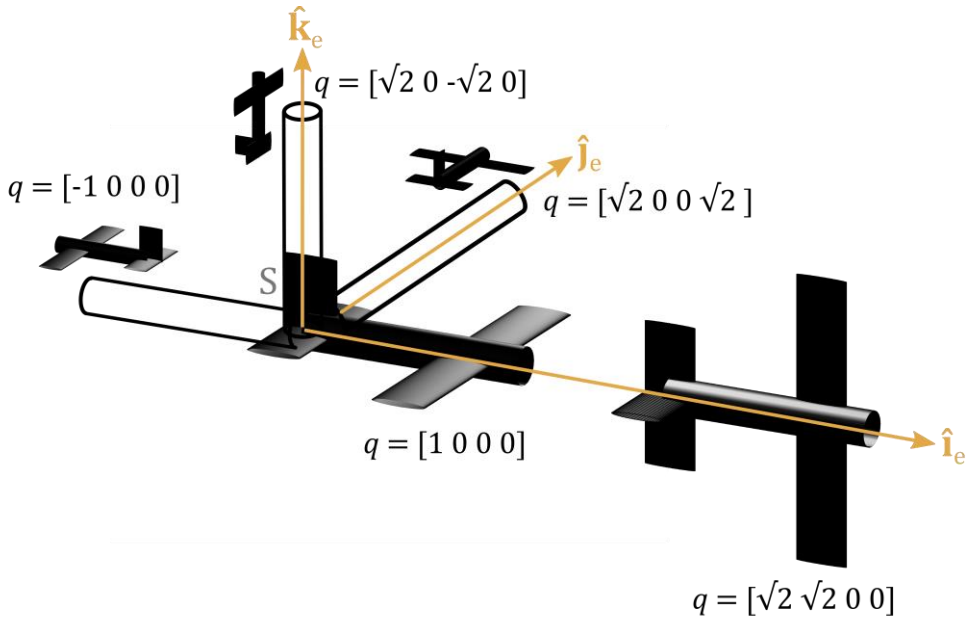

Figure 2.5.1: Values of the orientation quaternion q corresponding to several example aircraft orientations.

2.5.2. Euler angle parameterisation of the body-fixed reference frame

Defining the Euler angle parameterisation of the aircraft's body-fixed reference frame is more complex, and a multiplicity of angle definitions are possible. A pitch-yaw-roll (θ, ψ, ϕ) definition of the Euler angles is utilised, with axes defined as per Figure 2.5.2. The axes arrangement of Figure 2.5.2 corresponds to an intrinsic 3-2-1 (z-y-x) parameterisation, denoting the order of axis rotations [1]; or more strictly, a (-3)-(-2)-(-1) parameterisation, denoting also the sign of the direction of rotation according to the right hand rule.

Concatenating $\boldsymbol{\theta} = [\theta, \psi, \phi]^T$, it follows from Section 2.3.2 that the transformation between the Euler angle rate vector and its associated angular velocity pseudovector is:

$$\begin{aligned} \boldsymbol{\omega}^{(e)} &= -\hat{\mathbf{r}}_b^{(e)}\dot{\theta} - \hat{\mathbf{k}}_e^{(e)}\dot{\psi} - \hat{\boldsymbol{\imath}}_b^{(e)}\dot{\phi} = \Omega_0^{(e)}\dot{\boldsymbol{\theta}}, \\ \Omega_0^{(e)} &= \left[-\hat{\mathbf{r}}_b, -\hat{\mathbf{k}}_e, -\hat{\boldsymbol{\imath}}_b\right]. \end{aligned} \tag{2.5.2}$$

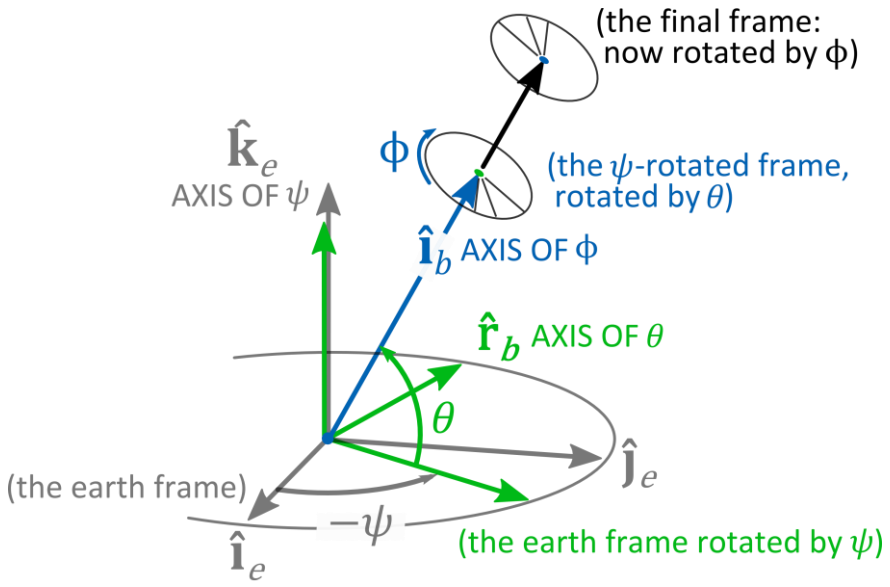

Figure 2.5.2: diagram of Euler angle ordering

To utilise this definition, the rotated reference frame (including partial rotations such as $\hat{\mathbf{r}}_b$) must be constructed: this is derived thoroughly, as there are many possible frame definitions, yielding many differing forumulations. The body axis, or first axis of the body-fixed reference frame, unit vector $\hat{\boldsymbol{\imath}}_b$, can be constructed trigonometrically from Figure 2.5.2. In the earth reference frame, $\hat{\boldsymbol{\imath}}_b$ is given as:

$$\hat{\boldsymbol{\imath}}_b^{(e)} = \begin{bmatrix} \cos\theta\cos\psi \\ -\cos\theta\sin\psi \\ \sin\theta \end{bmatrix}. \tag{2.5.3}$$

To construct the rest of the body-fixed reference frame the effect of the body roll (ϕ), defined as per Figure 2.5.3, must be included. Two unit disks, $\mathcal{D}_1$ and $\mathcal{D}_2$, are defined, with unit normals $\hat{\mathbf{k}}_e$ and $\hat{\boldsymbol{\imath}}_b$ respectively. On $\mathcal{D}_2$ three unit vectors are defined:

(1) $\hat{\mathbf{r}}_b$, which is the body-fixed reference axis for ϕ

(2) $\hat{\mathbf{j}}_b$, which is the body-fixed y-axis

(3) $\hat{\mathbf{k}}_b$, which is the body-fixed z-axis

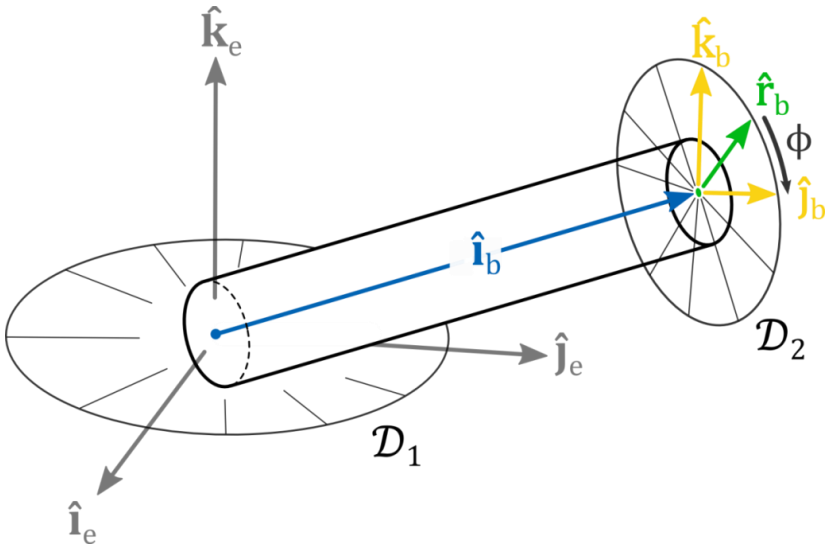

Figure 2.5.3: Diagram of body-fixed coordinate system. Note that disk $\mathcal{D}_1$ is shown at the origin: its spatial location is irrelevant as it serves only to constrain the directions of unit vectors.

The reference vector $\hat{\mathbf{r}}_b$ is additionally constrained to lie in $\mathcal{D}_1$. This defines its magnitude and axis of direction completely. However, the direction itself is still not defined completely, as there will two solutions in opposite directions to each other. As a final constraint, the continuous solution is selected in which $\hat{\mathbf{r}}_b$ degenerates into $\hat{\mathbf{j}}_e$ when the angles (θ,ψ,ϕ) are zero. This ensures that the coordinate system is right-hand. The equations governing $\hat{\mathbf{r}}_b$ are thus:

$$\begin{aligned} &\hat{\boldsymbol{\imath}}_b \cdot \hat{\mathbf{r}}_b = 0 && \text{(lies in } \mathcal{D}_2\text{)}, \\ &\hat{\mathbf{k}}_e \cdot \hat{\mathbf{r}}_b = 0 && \text{(lies in } \mathcal{D}_1\text{)}, \\ &\hat{\mathbf{r}}_b|_{\phi=0,\,\psi=0,\,\theta=0} = \hat{\mathbf{j}}_e && \text{(direction)}, \\ &\|\hat{\mathbf{r}}_b\|_2 = 1 && \text{(unit)}, \end{aligned} \tag{2.5.4}$$

with solution:

$$\hat{\mathbf{r}}_b^{(e)} = \begin{bmatrix} \sin\psi \\ \cos\psi \\ 0 \end{bmatrix}. \tag{2.5.5}$$

The unit vector $\hat{\mathbf{j}}_b$ is then defined: this lies in $\mathcal{D}_2$ at an angle of ϕ clockwise from $\hat{\mathbf{r}}_b$. To constrain the rotation angle (irrespective of direction) the dot product angle formula is used, and to ensure clockwise rotation an additional constraint is defined:

$$\hat{\mathbf{j}}_b \times \hat{\mathbf{r}}_b = \begin{cases} |k(\phi)|\hat{\boldsymbol{\imath}}_b & 0 \le \phi \le \pi \\ -|k(\phi)|\hat{\boldsymbol{\imath}}_b & \pi \le \phi \le 2\pi, \end{cases} \tag{2.5.6}$$

for some nonnegative constant $|k(\phi)|$ that may vary with ϕ. The sine function $\sin\phi$ will perform the function of this constant, and hence this constraint becomes:

$$\hat{\mathbf{j}}_b \times \hat{\mathbf{r}}_b = \hat{\boldsymbol{\imath}}_b \sin\phi. \tag{2.5.7}$$

The equality in Eq. 2.5.7 (in the absence of any arbitrary scaling constants) arises from the definition of the cross product that $\mathbf{a} \times \mathbf{b} = \|\mathbf{a}\|\|\mathbf{b}\| \sin\phi\, \hat{\mathbf{n}}$ (see [30]), with right-hand unit normal vector $\hat{\mathbf{n}}$. . Note, however, that the Eq. 2.5.7 is not by definition satisfied by all vectors satisfying the other constraints: these may satisfy $\hat{\mathbf{j}}_b \times \hat{\mathbf{r}}_b = -\hat{\boldsymbol{\imath}}_b \sin\phi$, or may oscillate in sign. The full set of constraints for $\hat{\mathbf{j}}_b$ is:

$$\begin{aligned}
&\hat{\boldsymbol{\imath}}_b \cdot \hat{\mathbf{j}}_b = 0 && \text{(lies in } \mathcal{D}_2\text{)},\\
&\hat{\mathbf{r}}_b \cdot \hat{\mathbf{j}}_b = \cos\phi && \text{(lies at } \phi \text{ from } \hat{r}_b\text{)},\\
&\hat{\mathbf{j}}_b \times \hat{\mathbf{r}}_b = \hat{\boldsymbol{\imath}}_b \sin\phi && \text{(clockwise)},\\
&\|\hat{\mathbf{j}}_b\|_2 = 1 && \text{(unit)},
\end{aligned} \tag{2.5.8}$$

with solution:

$$\hat{\mathbf{j}}_b^{(e)} = \begin{bmatrix} \sin\psi\cos\phi + \sin\theta\cos\psi\sin\phi \\ \cos\psi\cos\phi + \sin\theta\sin\psi\sin\phi \\ -\cos\theta\sin\phi \end{bmatrix}. \tag{2.5.9}$$

Finally, $\hat{\mathbf{k}}_b$ is the unit vector that is right-hand orthogonal to $\hat{\boldsymbol{\imath}}_b$ and $\hat{\mathbf{j}}_b$, given simply as:

$$\hat{\mathbf{k}}_b^{(e)} = \hat{\boldsymbol{\imath}}_b^{(e)} \times \hat{\mathbf{j}}_b^{(e)} = \begin{bmatrix} \sin\psi\sin\phi - \sin\theta\cos\psi\cos\phi \\ \cos\psi\sin\phi + \sin\theta\sin\psi\cos\phi \\ \cos\theta\cos\phi \end{bmatrix}. \tag{2.5.10}$$

This completes the body-fixed reference frame. The transformation between the body-fixed and earth reference frames can be expressed as a concatenation of the body-fixed unit vectors:

$$\mathrm{P}_{E/B} = \left[\hat{\boldsymbol{\imath}}_b^{(e)},\ \hat{\mathbf{j}}_b^{(e)},\ \hat{\mathbf{k}}_b^{(e)}\right]. \tag{2.5.11}$$

$\mathrm{P}_{E/B}$ is orthogonal and so the inverse transform is given by the matrix transpose. The derivatives of the rotation matrix $\mathrm{P}_{E/B}$ can be related to $\boldsymbol{\omega}^{(e)}$ via [31]:

$$\dot{\mathrm{P}}_{E/B} = \left[\boldsymbol{\omega}^{(e)}\right]_\times \mathrm{P}_{E/B}, \tag{2.5.12}$$

2.5.3. Euler angle parameterisation of the wing reference frames

Each wing has three degrees of freedom relative to the body-fixed reference system; representing full three-dimensional rotation control. A number of assumptions are made about the nature of this rotation: that it occurs about a single root, located on the axis $\hat{\boldsymbol{\imath}}_b$, and that actuator freeplay and wing deformation are negligible. These assumptions are embedded in the kinematic chains of Section 2.4.2. The wing orientations will be parameterised via Euler angles, rather than quaternions, for both of the body-fixed frame parameterisations. This parameterisation is more useful for describing the wing orientation, as the Euler angle parameters are more intuitive from a control perspective; corresponding to actual hypothetical actuator degrees of freedom, and allowing these degrees of freedom to be restricted easily. Given the controlled nature of the wing motion, gimbal lock will never be unexpected, and the angle definitions can be chosen to orientate their poles conveniently. Poles at the $\pm 90^{\circ}$ dihedral state are chosen; a state which is aerodynamically ineffectual and thus unlikely to be of relevance to the analysis.

Two reference systems for each wing are defined: one of which is incidence-invariant (e.g. $\hat{\boldsymbol{\imath}}_{wl}$, $\hat{\mathbf{r}}_{wl}$, $\widehat{\mathbf{q}}_{wl}$) and the other of which is incidence-variant (e.g. $\hat{\boldsymbol{\imath}}_{wl}$, $\hat{\mathbf{j}}_{wl}$, $\hat{\mathbf{k}}_{wl}$). These will be useful in the aerodynamic analysis of the wings. Figure 2.5.1 shows an overview of all four wing reference systems (incidence-invariant and variant systems for the two different wings), with the definitions of all the wing orientation angles. $\widehat{\mathbf{q}}_{wi}$, which is perpendicular to $\hat{\mathbf{r}}_{wi}$ and $\hat{\boldsymbol{\imath}}_{wi}$ in the upwards orientation, has been omitted for clarity. The Euler angles are defined as dihedral (θ), sweep (ψ) and incidence (ϕ), in a 3-2-1 ordering with some sign changes between the wings. Note that the incidence angles ϕ_w are always defined nose-up and hence are of opposite hands for the two wings. The sweep angles, ψ_w, on the other hand, are defined in the same direction and so the natural state of the aircraft is $\psi_{wl} = -\psi_{wr}$. The wing sweep and dihedral angles are also restricted to certain ranges:

$$\begin{aligned} -\pi \leq \psi_{wl} \leq 0, \qquad & 0 \leq \psi_{wr} \leq \pi, \\ -\tfrac{1}{2}\pi \leq \theta_{wl} \leq \tfrac{1}{2}\pi, \qquad & -\tfrac{1}{2}\pi \leq \theta_{wr} \leq \tfrac{1}{2}\pi, \end{aligned} \tag{2.5.13}$$

but the incidence angles ϕ_w are unconstrained in $\mathbb{R}$. In the case of symmetric sweep there is the parameterisation via the more traditional sweep angle Λ, cf. [32]:

$$\psi_{wl} = -\frac{\pi}{2} - \Lambda, \qquad \psi_{wr} = \frac{\pi}{2} + \Lambda, \tag{2.5.14}$$

representing the backwards angle from the natural aircraft state ($\psi_{wl} = -\psi_{wr} = \pi/2$, $\Lambda = 0$). $0 < \Lambda < \pi/2$ thus represents backwards sweep and $-\pi/2 < \Lambda < 0$ forwards sweep.

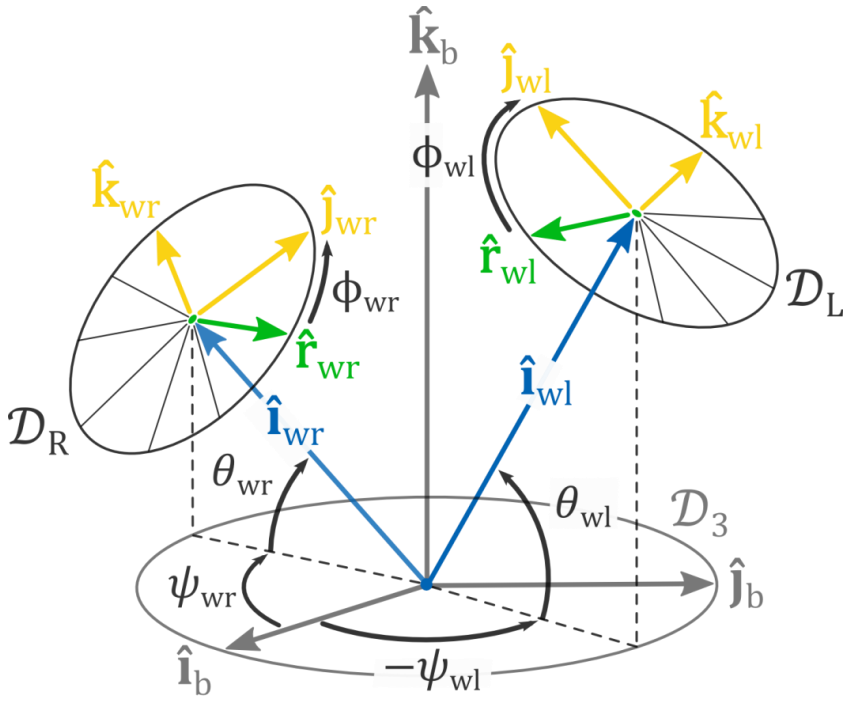

Figure 2.5.4: Diagram of the wing-fixed coordinate systems.

The unit vectors referenced in Figure 2.5.4 must now be defined. The wing span unit vectors $\hat{\boldsymbol{\imath}}_w$ are identical for the invariant and variant systems. They are defined identically to $\hat{\boldsymbol{\imath}}_b$, *mutatis mutandis*, as the definitions of the pitch (dihedral), yaw (sweep) and roll (incidence) angles, relative to the base unit vectors, have not changed between the earth and body-fixed coordinate systems. Hence:

$$\hat{\boldsymbol{\imath}}_{wl}^{(b)} = \begin{bmatrix} \cos\theta_{wl}\cos\psi_{wl} \\ -\cos\theta_{wl}\cos\psi_{wl} \\ \sin\theta_{wl} \end{bmatrix}, \qquad \hat{\boldsymbol{\imath}}_{wr}^{(b)} = \begin{bmatrix} \cos\theta_{wr}\cos\psi_{wr} \\ -\cos\theta_{wr}\cos\psi_{wr} \\ \sin\theta_{wr} \end{bmatrix}. \tag{2.5.15}$$

These are written with reference to the body-fixed reference frame. As unit normal vectors $\hat{\boldsymbol{\imath}}_{wl}$ and $\hat{\boldsymbol{\imath}}_{wr}$ define two unit disks, $\mathcal{D}_L$ and $\mathcal{D}_R$, on which other unit vectors are defined in order to complete the wing reference frames. As have noted earlier, two orthogonal reference frames are defined on each disk: one of which is invariant with respect to changes in local wing incidence (ϕ_{wl} or ϕ_{wr}) and the other of which is variant (the true wing-fixed reference frame).

As a basis for the incidence-invariant frames, vectors $\hat{\mathbf{r}}_{wl}$ and $\widehat{\mathbf{q}}_{wl}$ for the left wing and $\hat{\mathbf{r}}_{wr}$ and $\widehat{\mathbf{q}}_{wr}$ for the right wing are defined. The $\hat{\mathbf{r}}_{wi}$ are defined in a manner analogous to $\hat{\mathbf{r}}_b$: that is, $\hat{\mathbf{r}}_{wl}$ lies in $\mathcal{D}_L$ and $\mathcal{D}_3$, and $\hat{\mathbf{r}}_{wr}$ in $\mathcal{D}_R$ and $\mathcal{D}_3$. However, the handedness of these vectors relative to $\hat{\mathbf{k}}_e$ and their respective $\hat{\boldsymbol{\imath}}_w$ is different, because the wing coordinate systems are intended to be symmetric. $\hat{\mathbf{r}}_{wl}$ is defined to degenerate to $-\hat{\mathbf{j}}_b$ when all the left-wing angles are zero. The complete set of constraints for this vector is thus:

$$\begin{aligned}
&\hat{\boldsymbol{\imath}}_{wl} \cdot \hat{\mathbf{r}}_{wl} = 0 && \text{(lies in } \mathcal{D}_L\text{)},\\
&\hat{\mathbf{k}}_b \cdot \hat{\mathbf{r}}_{wl} = 0 && \text{(lies in } \mathcal{D}_3\text{)},\\
&\hat{\mathbf{r}}_{wl}|_{\phi_{wl}=0,\,\psi_{wl}=0,\,\theta_{wl}=0} = -\hat{\mathbf{j}}_b && \text{(left-hand)},\\
&\|\hat{\mathbf{r}}_{wl}\|_2 = 1 && \text{(unit)},
\end{aligned} \tag{2.5.16}$$

with solution:

$$\hat{\mathbf{r}}_{wl}^{(b)} = \begin{bmatrix} -\sin\psi_{wl} \\ -\cos\psi_{wl} \\ 0 \end{bmatrix}. \tag{2.5.17}$$

However, $\hat{\mathbf{r}}_{wr}$ is defined to degenerate to $\hat{\mathbf{j}}_b$ when the right-wing angles are zero. $\hat{\mathbf{r}}_{wr}$ thus has constraints:

$$\begin{aligned}
&\hat{\boldsymbol{\imath}}_{wr} \cdot \hat{\mathbf{r}}_{wr} = 0 && \text{(lies in } \mathcal{D}_R\text{)},\\
&\hat{\mathbf{k}}_b \cdot \hat{\mathbf{r}}_{wr} = 0 && \text{(lies in } \mathcal{D}_3\text{)},\\
&\hat{\mathbf{r}}_{wr}|_{\phi_{wr}=0,\,\psi_{wr}=0,\,\theta_{wr}=0} = \hat{\mathbf{j}}_b && \text{(right-hand)},\\
&\|\hat{\mathbf{r}}_{wr}\|_2 = 1 && \text{(unit)},
\end{aligned} \tag{2.5.18}$$

with solution:

$$\hat{\mathbf{r}}_{wr}^{(b)} = \begin{bmatrix} \sin\psi_{wr} \\ \cos\psi_{wr} \\ 0 \end{bmatrix}. \tag{2.5.19}$$

In both cases of $\hat{\mathbf{r}}_w$, the change in sign of the angle relative to $\hat{\mathbf{j}}_b$ ensures that $\hat{\mathbf{r}}_b$ always points forwards when both wings are in their natural positions ($-\pi < \psi_{wl} < 0$ and $0 < \psi_{wr} < \pi$).

The two $\widehat{\mathbf{q}}_w$ vectors then complete the orthonormal basis involving $\hat{\boldsymbol{\imath}}_{wr}$ and $\hat{\mathbf{r}}_{wr}$. The left-wing system is left-handed and the right-wing system is right-handed: as with $\hat{\mathbf{r}}_w$, this ensures that $\widehat{\mathbf{q}}_w$ points in the body-fixed upwards direction when the wings are in their natural positions. Hence:

$$\widehat{\mathbf{q}}_{wl}^{(b)} = -\hat{\boldsymbol{\imath}}_{wl}^{(b)} \times \hat{\mathbf{j}}_{wl}^{(b)} = \begin{bmatrix} \sin\psi_{wl} \sin\phi_{wl} - \sin\theta_{wl} \cos\psi_{wl} \cos\phi_{wl} \\ \cos\psi_{wl} \sin\phi_{wl} + \sin\theta_{wl} \sin\psi_{wl} \cos\phi_{wl} \\ \cos\theta_{wl} \cos\phi_{wl} \end{bmatrix}, \tag{2.5.20}$$

and

$$\widehat{\mathbf{q}}_{wr}^{(b)} = \hat{\boldsymbol{\imath}}_{wr}^{(b)} \times \hat{\mathbf{j}}_{wr}^{(b)} = \begin{bmatrix} \sin\psi_{wr} \sin\phi_{wr} - \sin\theta_{wr} \cos\psi_{wr} \cos\phi_{wr} \\ \cos\psi_{wr} \sin\phi_{wr} + \sin\theta_{wr} \sin\psi_{wr} \cos\phi_{wr} \\ \cos\theta_{wr} \cos\phi_{wr} \end{bmatrix}. \tag{2.5.21}$$

where × denotes the right-handed cross produce in all cases. This completes the definition of the two incidence-invariant bases. Again, the orthogonal transformation matrices are:

$$\mathrm{P}_{B/WLD} = \left[\hat{\boldsymbol{\imath}}_{wl}^{(b)},\ \hat{\mathbf{r}}_{wl}^{(b)},\ \widehat{\mathbf{q}}_{wl}^{(b)}\right] = \mathrm{P}_{WLD/B}^{T}, \tag{2.5.22}$$

and

$$\mathrm{P}_{B/WRD} = \left[\hat{\boldsymbol{\imath}}_{wr}^{(b)},\ \hat{\mathbf{r}}_{wr}^{(b)},\ \widehat{\mathbf{q}}_{wr}^{(b)}\right] = \mathrm{P}_{WRD/B}^{T}. \tag{2.5.23}$$

where WLD and WRD denote the left/right wing datum (i.e. incidence-invariant) coordinate systems.

The incidence-variant or true wing coordinate systems must then be defined. As with $\hat{\mathbf{j}}_b$, the true wing y-axes $\hat{\mathbf{j}}_w$ are defined with reference to the corresponding reference vectors, $\hat{\mathbf{r}}_w$. The constraints on $\hat{\mathbf{j}}_w$ are identical to those of Eq. 2.5.8, *mutatis mutandis*, except for the direction of rotation (clockwise or anticlockwise); i.e. the sign of the cross product $\hat{\mathbf{j}}_w \times \hat{\mathbf{r}}_w$ relative to $\hat{\boldsymbol{\imath}}_w$. In the case of $\hat{\mathbf{j}}_{wl}$ the sign is positive ($\hat{\mathbf{j}}_{wl} \times \hat{\mathbf{r}}_{wl} = \hat{\boldsymbol{\imath}}_{wl} \sin\phi_{wl}$) and the following constraints are obtained:

$$\begin{aligned} &\hat{\boldsymbol{\imath}}_{wl} \cdot \hat{\mathbf{j}}_{wl} = 0 && \text{(lies in } \mathcal{D}_L\text{)}, \\ &\hat{\mathbf{r}}_{wl} \cdot \hat{\mathbf{j}}_{wl} = \cos\phi_{wl} && \text{(lies at } \phi \text{ from } \hat{r}_{wl}\text{)}, \\ &\hat{\mathbf{j}}_{wl} \times \hat{\mathbf{r}}_{wl} = \hat{\boldsymbol{\imath}}_{wl} \sin\phi_{wl} && \text{(clockwise)}, \\ &\|\hat{\mathbf{j}}_{wl}\|_2 = 1 && \text{(unit)}; \end{aligned} \tag{2.5.24}$$

and in the case of $\hat{\mathbf{j}}_{wr}$ the sign is negative ($\hat{\mathbf{j}}_{wr} \times \hat{\mathbf{r}}_{wr} = -\hat{\boldsymbol{\imath}}_{wr} \sin\phi_{wr}$) and the set of constraints is:

$$\begin{aligned} &\hat{\boldsymbol{\imath}}_{wr} \cdot \hat{\mathbf{j}}_{wr} = 0 && \text{(lies in } \mathcal{D}_R\text{)}, \\ &\hat{\mathbf{r}}_{wr} \cdot \hat{\mathbf{j}}_{wr} = \cos\phi_{wr} && \text{(lies at } \phi \text{ from } \hat{r}_{wl}\text{)}, \\ &\hat{\mathbf{j}}_{wr} \times \hat{\mathbf{r}}_{wr} = -\hat{\boldsymbol{\imath}}_{wr} \sin\phi_{wr} && \text{(clockwise)}, \\ &\|\hat{\mathbf{j}}_{wr}\|_2 = 1 && \text{(unit)}. \end{aligned} \tag{2.5.25}$$

The solutions to these two sets of constraints are:

$$\hat{\mathbf{j}}_{wl}^{(b)} = \begin{bmatrix} -\sin\psi_{wl}\cos\phi_{wl} - \sin\theta_{wl}\cos\psi_{wl}\sin\phi_{wl} \\ -\cos\psi_{wl}\cos\phi_{wl} + \sin\theta_{wl}\sin\psi_{wl}\sin\phi_{wl} \\ \cos\theta_{wl}\sin\phi_{wl} \end{bmatrix}, \tag{2.5.26}$$

and

$$\hat{\mathbf{j}}_{wr}^{(b)} = \begin{bmatrix} \sin\psi_{wr}\cos\phi_{wr} - \sin\theta_{wr}\cos\psi_{wr}\sin\phi_{wr} \\ \cos\psi_{wr}\cos\phi_{wr} + \sin\theta_{wr}\sin\psi_{wr}\sin\phi_{wr} \\ \cos\theta_{wr}\sin\phi_{wr} \end{bmatrix}. \tag{2.5.27}$$

Finally, $\hat{\mathbf{k}}_w$ are the unit vectors that are orthogonal to $\hat{\boldsymbol{\imath}}_w$ and $\hat{\mathbf{j}}_w$ – left-hand orthogonal for the left wing system, and right-hand orthogonal for the right wing system. Hence:

$$\hat{\mathbf{k}}_{wl}^{(b)} = -\hat{\boldsymbol{\imath}}_{wl}^{(b)} \times \hat{\mathbf{j}}_{wl}^{(b)} = \begin{bmatrix} \sin\psi_{wl}\sin\phi_{wl} - \sin\theta_{wl}\cos\psi_{wl}\cos\phi_{wl} \\ \cos\psi_{wl}\sin\phi_{wl} + \sin\theta_{wl}\sin\psi_{wl}\cos\phi_{wl} \\ \cos\theta_{wl}\cos\phi_{wl} \end{bmatrix}, \tag{2.5.28}$$

and

$$\hat{\mathbf{k}}_{wr}^{(b)} = \hat{\boldsymbol{\imath}}_{wr}^{(b)} \times \hat{\mathbf{j}}_{wr}^{(b)} = \begin{bmatrix} -\sin\psi_{wr}\sin\phi_{wr} - \sin\theta_{wr}\cos\psi_{wr}\cos\phi_{wr} \\ -\cos\psi_{wr}\sin\phi_{wr} + \sin\theta_{wr}\sin\psi_{wr}\cos\phi_{wr} \\ \cos\theta_{wr}\cos\phi_{wr} \end{bmatrix}. \tag{2.5.29}$$

This completes the definition of the wing-fixed reference frames. Their transformation matrices to the body-fixed reference system are:

$$\begin{aligned} \mathrm{P}_{B/WL} &= \left[\hat{\boldsymbol{\imath}}_{wl}^{(b)},\ \hat{\mathbf{j}}_{wl}^{(b)},\ \hat{\mathbf{k}}_{wl}^{(b)}\right] = \mathrm{P}_{WL/B}^{T}, \\ \mathrm{P}_{B/WR} &= \left[\hat{\boldsymbol{\imath}}_{wr}^{(b)},\ \hat{\mathbf{j}}_{wr}^{(b)},\ \hat{\mathbf{k}}_{wr}^{(b)}\right] = \mathrm{P}_{WR/B}^{T}. \end{aligned} \tag{2.5.30}$$

The transformation of $\dot{\boldsymbol{\Theta}}_{wi}$ to the angular velocity associated with wing rotation relative to the body frame, $\boldsymbol{\omega}_{i,2}$, is given as:

$$\begin{aligned} \boldsymbol{\omega}_{wl,2}^{(b)} &= \hat{\mathbf{r}}_{wl}^{(b)}\dot{\theta}_{wl} - \hat{\mathbf{k}}_{b}^{(b)}\dot{\psi}_{wl} - \hat{\boldsymbol{\imath}}_{wl}^{(b)}\dot{\phi}_{wl} = \Omega_{wl}^{(b)}\dot{\boldsymbol{\Theta}}_{wl}, \\ \boldsymbol{\omega}_{wr,2}^{(b)} &= -\hat{\mathbf{r}}_{wr}^{(b)}\dot{\theta}_{wr} - \hat{\mathbf{k}}_{b}^{(b)}\dot{\psi}_{wr} + \hat{\boldsymbol{\imath}}_{wr}^{(b)}\dot{\phi}_{wr} = \Omega_{wr}^{(b)}\dot{\boldsymbol{\Theta}}_{wr}, \\ \Omega_{wl}^{(b)} &= \left[\hat{\mathbf{r}}_{wl}^{(b)}, -\hat{\mathbf{k}}_{b}^{(b)}, -\hat{\boldsymbol{\imath}}_{wl}^{(b)}\right], \\ \Omega_{wr}^{(b)} &= \left[-\hat{\mathbf{r}}_{wr}^{(b)}, -\hat{\mathbf{k}}_{b}^{(b)}, \hat{\boldsymbol{\imath}}_{wr}^{(b)}\right]. \end{aligned} \tag{2.5.31}$$

which may be utilised in the kinematic chains (Section 2.4). Given the uniformity of the angular velocity pseudovector throughout all of the $c = 1$ chain points in the case study system, the total angular velocity pseudovector of each wing can be constructed simply as:

$$\boldsymbol{\omega}_{i}^{(e)} = \boldsymbol{\omega}^{(e)} + \mathrm{P}_{i,2}\boldsymbol{\omega}_{i,2}, \qquad i \in [WL, WR], \tag{2.5.32}$$

2.5.4. The orthogonal stabiliser reference frames

The horizontal and vertical stabilisers (tailplanes, containing the elevators, and tailfin, containing the rudder) will be modelled as separate bodies in the multibody analysis: this both simplifies the aerodynamic analysis (see Chapter 3) and allows the model to be easily generalised to study tail surface motion in future studies: defining a consistent set of aerofoil-fixed unit vectors for each aerofoil will enable us to perform one aerodynamic analysis in this aerofoil-fixed reference frame, which will then generalise to each specific lifting surface. It is thus helpful to define independent reference frames for each stabiliser. Figure 2.5.5 shows these reference frames. All of these are 90° rotations and/or hand changes of the body-fixed reference frame, and thus can be sufficiently defined by their rotation matrices with respect to this frame, in lieu of any more detailed orientation parameterisation.

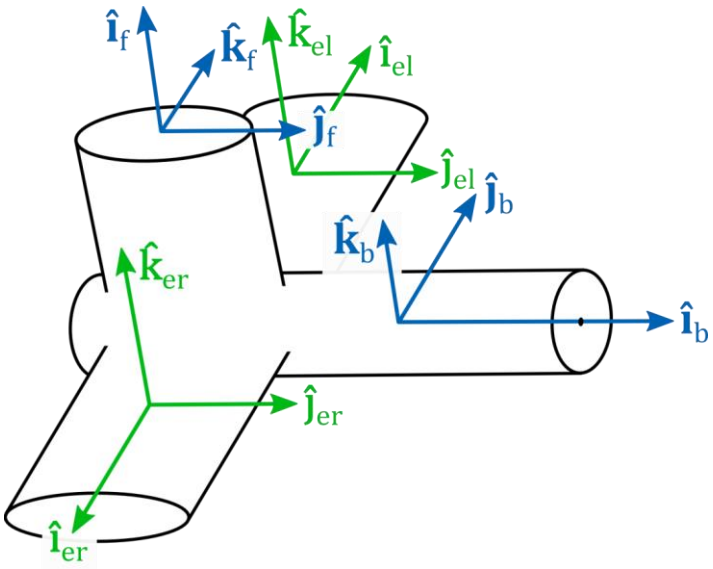

Figure 2.5.5: Diagram of the stabiliser coordinate systems.

For the left tailplane / elevator:

$$\begin{aligned} \hat{\boldsymbol{\imath}}_{el} &= \hat{\mathbf{j}}_b = [0,1,0]^{(b),T}, \\ \hat{\mathbf{j}}_{el} &= \hat{\boldsymbol{\imath}}_b = [1,0,0]^{(b),T}, \\ \hat{\mathbf{k}}_{el} &= \hat{\mathbf{k}}_b = [0,0,1]^{(b),T}, \end{aligned} \tag{2.5.33}$$

and hence:

$$\mathrm{P}_{B/EL} = \left[\hat{\boldsymbol{\imath}}_{el},\ \hat{\mathbf{j}}_{el},\ \hat{\mathbf{k}}_{el}\right] = \begin{bmatrix} 0 & 1 & 0 \\ 1 & 0 & 0 \\ 0 & 0 & 1 \end{bmatrix}. \tag{2.5.34}$$

This coordinate system is left-handed. For the right tailplane / elevator:

$$\begin{aligned}\hat{\boldsymbol{\imath}}_{er} &= -\hat{\mathbf{j}}_b = [0,-1,0]^{(b),T},\\ \hat{\mathbf{j}}_{er} &= \hat{\boldsymbol{\imath}}_b = [1,0,0]^{(b),T},\\ \hat{\mathbf{k}}_{er} &= \hat{\mathbf{k}}_b = [0,0,1]^{(b),T},\end{aligned} \tag{2.5.35}$$

and hence:

$$\mathrm{P}_{B/ER} = \left[\hat{\boldsymbol{\imath}}_{er},\ \hat{\mathbf{j}}_{er},\ \hat{\mathbf{k}}_{er}\right] = \begin{bmatrix} 0 & 1 & 0\\ -1 & 0 & 0\\ 0 & 0 & 1\end{bmatrix}. \tag{2.5.36}$$

This coordinate system is right-handed. And for the fin / rudder:

$$\begin{aligned}\hat{\boldsymbol{\imath}}_f &= \hat{\mathbf{k}}_b = [0,0,1]^{(b),T},\\ \hat{\mathbf{j}}_f &= \hat{\boldsymbol{\imath}}_b = [1,0,0]^{(b),T},\\ \hat{\mathbf{k}}_f &= \hat{\mathbf{j}}_b = [0,1,0]^{(b),T},\end{aligned} \tag{2.5.37}$$

and hence:

$$\mathrm{P}_{B/F} = \left[\hat{\boldsymbol{\imath}}_f,\ \hat{\mathbf{j}}_f,\ \hat{\mathbf{k}}_f\right] = \begin{bmatrix} 0 & 1 & 0\\ 0 & 0 & 1\\ 1 & 0 & 0\end{bmatrix}. \tag{2.5.38}$$

2.6. VERIFICATION AND VISUALISATION

2.6.1. Kinematic verification

To verify that the kinematic expressions for linear and angular velocity are correct, these expressions are compared to finite-difference estimates that are dependent only on the kinematics of position. These estimates are computed via incrementing the aircraft orientation, position, and wing control parameters proportional to their input derivatives, and computing appropriate forward differences:

$$\begin{aligned}&\mathbf{s}(t_0+\Delta t) = \mathbf{s}(t_0) + \dot{\mathbf{s}}(t_0)\Delta t,\\ &q(t_0+\Delta t) = q(t_0)\otimes \exp\left(\frac{1}{2}\Delta t\boldsymbol{\omega}^{(b)}(t_0)\right),\\ &\dot{\mathbf{x}}_{i,\mathrm{est}}(t_0) = \frac{1}{\Delta t}\Big(\mathbf{x}_i\big(\mathbf{s}(t_0+\Delta t)\big) - \mathbf{x}_i\big(\mathbf{s}(t_0)\big)\Big),\end{aligned} \tag{2.6.1}$$

where $\mathbf{s}$ denotes the 12-DOF aircraft state: in Euler angles $\mathbf{s} = [\theta, \theta_{wl}, \theta_{wr}, \mathbf{x}_S]$; in quaternions $\mathbf{s} = [q, \theta_{wl}, \theta_{wr}, \mathbf{x}_S]$**,** with the particular norm-preserving increment on the quaternion as noted [16]. Sets of states ($\mathbf{s}$) and state derivatives ($\dot{\mathbf{s}}$) are generated randomly, and numerical estimates of all the body centre of mass velocities (linear and angular) are

compared to the kinematic relations. The finite-different time increment is $\Delta t = 10^{-10}$, and over 10^4 trials for both orientation parameterisations (quaternion and Euler angle), no error for any velocity or angular velocity at any location exceeded 10^{-6}. This verifies the kinematic velocity relationships.

2.6.2. Visualisation

The preceding verification is dependent on the accuracy of the positional kinematics: the very definition of the aircraft. To ensure this definition is correct, a system visualization routine is developed in MATLAB that will animate a model of the aircraft given all of the aircraft geometric, control and orientation parameter values. This animated model may then be checked visually to ensure that all of these parameter values are having an appropriate effect, validating the positional kinematic model. Among examples of this are Figures 2.4.3, 2.4.4 and 1.4.1, already presented, which demonstrate variation in the orientation quaternion and individual wing degrees of freedom. As an additional example, Figure 2.6.1 shows an example specified motion and morphing path, actuating multiple system degrees of freedom simultaneously. The accuracy of the specified motion path may be confirmed. This animated model has additional value as a method of visualising the flight simulation results that will proceed from this analysis.

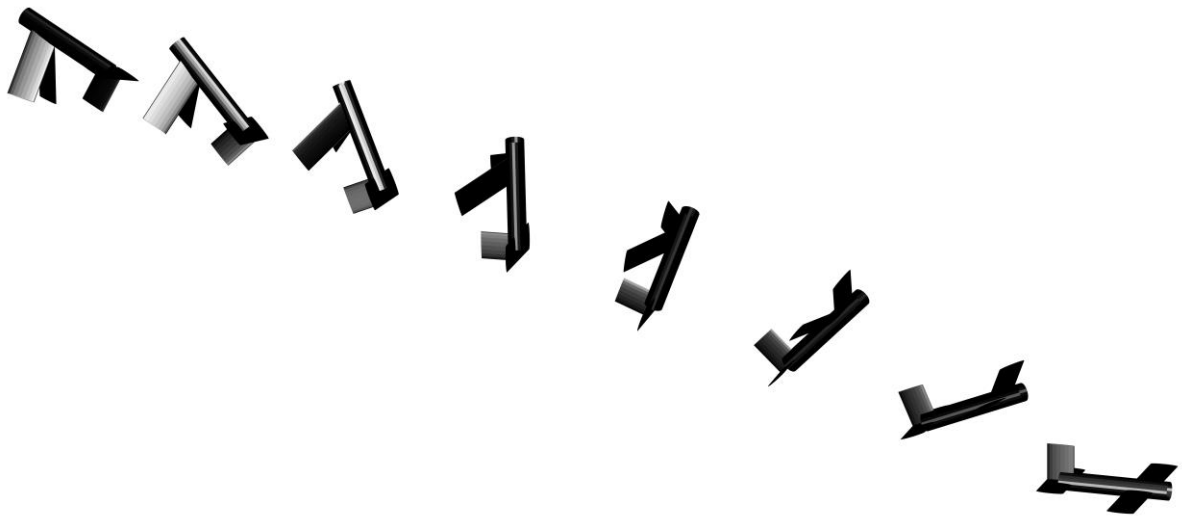

Figure 2.6.1: Visualisation in MATLAB of the case study system, under example specified motion and morphing path.

CHAPTER REFERENCES

[1] Diebel, J., *Representing Attitude: Euler Angles, Unit Quaternions, and Rotation Vectors*, Stanford University, Stanford, CA, 2006.

[2] Bauchau, O. A., *Flexible multibody dynamics*, Springer, Dordrecht, The Netherlands, 2011.

[3] Wittenburg, J., *Dynamics of multibody systems*, Springer, Berlin, 2008.

[4] Yu, M., Zhao, J., Zhang, L., and Wang, Y., "Study on the dynamic characteristics of a virtual-axis hybrid polishing machine tool by flexible multibody dynamics," *Proceedings of the Institution of Mechanical Engineers, Part B: Journal of Engineering Manufacture*, Vol. 218, No. 9, 2004, pp. 1067–1076. DOI:10.1243/0954405041897167.

[5] Geradin, M., and Cardona, A., "Kinematics and dynamics of rigid and flexible mechanisms using finite elements and quaternion algebra," *Computational Mechanics*, Vol. 4, No. 2, 1988, pp. 115–135. DOI:10.1007/BF00282414.

[6] Manchester, Z. R., and Peck, M. A., "Quaternion Variational Integrators for Spacecraft Dynamics," *Journal of Guidance, Control, and Dynamics*, Vol. 39, No. 1, 2016, pp. 69–76. DOI:10.2514/1.G001176.

[7] Kristiansen, R., Nicklasson, P. J., and Gravdahl, J. T., "Satellite Attitude Control by Quaternion-Based Backstepping," *IEEE Transactions on Control Systems Technology*, Vol. 17, No. 1, 2009, pp. 227–232. DOI:10.1109/TCST.2008.924576.

[8] Wie, B., and Barba, P. M., "Quaternion feedback for spacecraft large angle maneuvers," *Journal of Guidance, Control, and Dynamics*, Vol. 8, No. 3, 1985, pp. 360–365. DOI:10.2514/3.19988.

[9] Hall, B. C., *Lie groups, Lie algebras, and representations: an elementary introduction*, Springer, New York, 2015.

[10] Farnsteiner, R., "Quaternionic lie algebras," *Linear Algebra and its Applications*, Vol. 61, 1984, pp. 225–231. DOI:10.1016/0024-3795(84)90033-8.

[11] Lee, T., Leok, M., and McClamroch, N. H., "Lie group variational integrators for the full body problem," *Computer Methods in Applied Mechanics and Engineering*, Vol. 196, No. 29–30, 2007, pp. 2907–2924. DOI:10.1016/j.cma.2007.01.017.

[12] Kuipers, J. B., *Quaternions and rotation sequences*, Princeton University Press, Princeton, NJ, 2002.

[13] Naber, G. L., *Topology, geometry, and gauge fields: interactions*, Springer, New York, 2011.

[14] Altmann, S. L., *Rotations, quaternions, and double groups*, Dover Publications, Mineola, NY, 2005.

[15] Xu, J., and Halse, K. H., "Dual Quaternion Variational Integrator for Rigid Body Dynamic Simulation," *arXiv*, No. 1611.00616, 2016.

[16] Sola, J., *Quaternion kinematics for the error-state KF*, Universitat Politecnica de Catalunya, Barcelona, Spain, 2016.

[17] Mohd Harithuddin, A. S., "Derivative Kinematics in Relatively Rotating Coordinate Frames: Investigation on the Razi Acceleration," Doctoral Dissertation, RMIT University, 2014.

[18] Liu, S., and Trenkler, G., "Hadamard, Khatri-Rao, Kronecker and other matrix products," *International Journal of Information and Systems Sciences*, Vol. 4, No. 1, 2008, pp. 160–177.

[19] Valasek, J., ed., *Morphing Aerospace Vehicles and Structures: Valasek/Morphing Aerospace Vehicles and Structures*, John Wiley & Sons, Ltd, Chichester, UK, 2012.

[20] Santamaria-Navarro, A., Loianno, G., Solà, J., Kumar, V., and Andrade-Cetto, J., "Autonomous navigation of micro aerial vehicles using high-rate and low-cost sensors," *Autonomous Robots*, 2017. DOI:10.1007/s10514-017-9690-5.

[21] Breckenridge, W. G., *Quaternions - Proposed Standard Conventions*, NASA Jet Propulsion Laboratory, Pasadena, CA, 1979.

[22] de Morais Alves Rondão, D. O., "Modeling and Simulation of the ECOSat-III Attitude Determination and Control System," Master's Thesis, Técnico Lisboa, 2016.

[23] Marshall, J. S., Pounder, E. R., and Stewart, R. W., *Physics*, Macmillan, London, 2016.

[24] Okasha, M., and Newman, B., "Switching Principles to Circumvent Euler Angle Singularity."

[25] Shabana, A. A., *Dynamics of Multibody Systems*, Cambridge University Press, Cambridge, UK, 2005.

[26] Xie, M., *Fundamentals of robotics*, World Scientific, River Edge, NJ, 2003.

[27] Strauch, D., *Classical Mechanics*, Springer Berlin Heidelberg, Berlin, Heidelberg, 2009.

[28] Lanczos, C., *The variational principles of mechanics*, Dover Publications, New York, 1986.

[29] Jain, A., *Robot and multibody dynamics: analysis and algorithms*, Springer, New York, NY, 2011.

[30] Polyanin, A. D., and Manzhirov, A. V., *Handbook of mathematics for engineers and scientists*, Chapman & Hall/CRC, Boca Raton, FL, 2007.

[31] Sciavicco, L., and Siciliano, B., *Modelling and control of robot manipulators*, Springer, London, 2000.

[32] Huenecke, K., *Modern Combat Aircraft Design*, Airlife, Shrewsbury, UK, 1994.

THIS PAGE LEFT BLANK

Chapter 3:
Flight dynamic model with quasisteady aerodynamics

3.1. STRUCTURAL DYNAMICS: LITERATURE REVIEW

3.1.1. Structural dynamic modelling

To analyse the flight dynamics of the case study system, and thereby explore its capability for supermanoeuvrability, models of the structural behaviour of the system and the aerodynamic effects it induces are required. In this section the structural (rigid-body) modelling of the system is considered. Several existing structural modelling strategies for morphing-wing aircraft are attested in the literature.

At the simplest level, Newtonian rigid-body dynamics (RBD) can be used to derived a simple 6-DOF model with a time-varying inertia – computed with respect to a centre of mass which is fixed relative to the fuselage – representing the effects of wing morphing [1]. This approach neglects centre-of-mass motion and momentum changes arising from wing morphing, and as such is accurate when the wing mass is small and the wing motion is slow and low-amplitude. As such it has seen common use in the study of control morphing [2,3] – see Grant et al. [4] for a short review. In some cases, e.g. incidence control morphing, the time-varying inertial effects are neglected altogether, so that the structural model is entirely time-invariant [5]. This latter approximation is common in the study of biomimetic flapping-wing systems, cf. the review by Orlowski and Girard [6], with a wing-body mass ratio of less than 6% usually taken as its zone of validity. Nevertheless several studies have indicated that, even with such low wing mass, the effects of wing inertia may have a significant influence on the system flight dynamics [7,8].

The time-varying inertia approach is also appropriate when the effect of transition morphing states are of little significance to the analysis, e.g. if any complex effects arising from transition are assumed to be constrained via appropriate avionics control further down the analysis change. This suits it also to the analysis of mission morphing, cf. [9–11]. Its key advantages over higher-fidelity models are a low computational cost for time-domain simulation and amenability to piecewise state-state representation, allowing conventional linear time-invariant control and flight stability analyses to be carried out, cf. [10–12]. It is possible to extend this approach to account for the effect of centre-of-mass motion by computing the time-varying inertia relative to the instantaneous exact centre of mass, which is not fixed relative to the fuselage. This would improve its modelling fidelity for

systems with large wing masses and (slow) large-amplitude wing motion – an improvement which is particularly relevant to mission morphing systems. However no studies utilising solely this extension are attested. The 'extended rigid-body dynamics' (ERBD) of Obradovic and Subbarao [1,17] goes a step further. Their approach postulates a time-varying inertia, and then adds to it virtual forces corresponding to the dynamic effects of wing morphing, including morphing-induced centre-of-mass motion. If all virtual forces are included this yields an exact model of the system's rigid body dynamics.

However, a more widespread method of modelling morphing-wing dynamic effects exactly is through multibody dynamics: this is the dominant approach in high-fidelity biomimetic flight simulation, seeing application on a variety of scales [13–15]. The multibody approach is a default for flexible or compliant morphing-wing systems, as these cannot easily be treated by any of the previous Newtonian approaches: non-biomimetic applications include flexible high-altitude long-endurance (HALE) aircraft [16–18], and smart projectiles [19]. For rigid multibody morphing-wing systems, the key advantages of multibody dynamics over ERBD are generality (being simpler to apply to systems with many morphing degrees of freedom) and availability in a variational formulation (allowing the use of variational integration, a recently developed approach showing excellent momentum and energy conservation properties [20–22]). Applications in this area have included sweep morphing [23], folding-wing [24,25], morphing tandem-wing [26], and avian flapping-wing aircraft [27].

3.1.2. Actuator modelling

One further aspect of the system dynamic model is its actuator model – the choice of which is largely independent with respect to the structural dynamic model used. Several approaches have been used in the study of morphing-wing systems. Full actuator models may be utilised, which specify the output parameters as a function of the actuator properties, control parameters, and input signal [28,29]. These can represent the mechatronic behaviour of the system accurately, though they do require a high degree of specificity regarding the actuator arrangement. Alternatively servoconstraints – constraints enforced via penalty methods – provide a simpler method of modelling a degree of actuator

lag [10,30,31]. Finally, a direct specification of the controlled parameters corresponds to the assumption of an perfect actuator [31].

3.1.3. Application to the case study system

Given the significance of wing inertial effects in biomimetic supermanoeuvrability – something which is at least the case in several manoeuvres [32], and at most may often be a dominant effect [33,34] (cf. Chapter 1, Section 1.2.3) – the study of biomimetic supermanoeuvrability through the case study system will thus require accurate structural dynamic modelling. The importance of inertia effects even in systems with low wing mass has been noted [7,8]. For this reason a multibody dynamic approach is utilised in this study, formulated variationally to allow for variational integration. The broad scope of this work largely precludes the use of a precise actuator model, or a detailed actuator specification, at this early stage. Morphing degrees of freedom may be sometimes disabled in the case study model, representing a variety of hypothetical actuator arrangements. Moreover, detailed specifications for these actuator arrangements – such as the required control ranges, velocities and forces – are dependent on the results of the flight dynamic study. Hence simple passive constraints are utilised to model the case study system actuators.

This chapter is concerned with the multibody dynamics of the case study aircraft, and the development of simple aerodynamic model for flight simulation. It covers the formulation of the system kinetic energy and generalised forces preliminary to a variational analysis, and the derivation of variational and adaptive integrators, in Chapter 4.

3.2. AIRCRAFT STRUCTURAL DYNAMICS

3.2.1. Objective

To analyse the system via the principle of least action [35], expressions for the system Lagrangian and the generalise forces corresponding to the system coordinates (q or θ and $\mathbf{x}_S$) are requires. The Lagrangian is given by the difference of the system total kinetic energy and any potential energies that may be assigned to it: in this study the gravitational potential is the only candidate for the latter. However as a framework of generalised forces will be required regardless – to account for the dissipative aerodynamic forces – it is more

convenient to treat the gravitational effects as such a force. The system Lagrangian is thus given identically by its total kinetic energy. In this section we formulate this kinetic energy and the associated generalised forces.

3.2.2. Total kinetic energy

The kinetic energy, T_i, of any body in our system may be defined generally as:

$$2T_i = \dot{\mathbf{x}}_i^T m_i \dot{\mathbf{x}}_i + \boldsymbol{\omega}_i^T \mathrm{I}_i \boldsymbol{\omega}_i, \qquad i \in \mathcal{S}, \tag{3.2.1}$$

which via the body's kinematic chain becomes, in the earth frame:

$$\begin{aligned} 2T_i = {} & \dot{\mathbf{x}}_S^{(e),T} m_i \dot{\mathbf{x}}_S^{(e)} + 2\dot{\mathbf{x}}_S^{(e),T} m_i \left[\sum_{c=1}^{l_{c,i}} \mathrm{P}_{i,c}\mathbf{L}_{i,c}\right]_\times^T \boldsymbol{\omega}^{(e)} + 2\dot{\mathbf{x}}_S^{(e),T} m_i \left[\sum_{c=1}^{l_{c,i}} \mathrm{P}_{i,c}\mathbf{L}_{i,c}\right]_\times^T \left(\mathrm{P}_{i,2}\boldsymbol{\omega}_{i,2}\right) \\ & + \boldsymbol{\omega}^{(e),T} \left[\sum_{c=1}^{l_{c,i}} \mathrm{P}_{i,c}\mathbf{L}_{i,c}\right]_\times m_i \left[\sum_{c=1}^{l_{c,i}} \mathrm{P}_{i,c}\mathbf{L}_{i,c}\right]_\times^T \boldsymbol{\omega}^{(e)} \\ & + 2\left(\mathrm{P}_{i,2}\boldsymbol{\omega}_{i,2}\right)^T \left[\sum_{c=1}^{l_{c,i}} \mathrm{P}_{i,c}\mathbf{L}_{i,c}\right]_\times m_i \left[\sum_{c=1}^{l_{c,i}} \mathrm{P}_{i,c}\mathbf{L}_{i,c}\right]_\times^T \boldsymbol{\omega}^{(e)} \\ & + \left(\mathrm{P}_{i,2}\boldsymbol{\omega}_{i,2}\right)^T \left[\sum_{c=1}^{l_{c,i}} \mathrm{P}_{i,c}\mathbf{L}_{i,c}\right]_\times m_i \left[\sum_{c=1}^{l_{c,i}} \mathrm{P}_{i,c}\mathbf{L}_{i,c}\right]_\times^T \left(\mathrm{P}_{i,2}\boldsymbol{\omega}_{i,2}\right) \\ & + \boldsymbol{\omega}^{(e),T} \mathrm{I}_i^{(e)} \boldsymbol{\omega}^{(e)} + 2\left(\mathrm{P}_{i,2}\boldsymbol{\omega}_{i,2}\right)^T \mathrm{I}_i^{(e)} \boldsymbol{\omega}^{(e)} + \left(\mathrm{P}_{i,2}\boldsymbol{\omega}_{i,2}\right)^T \mathrm{I}_i^{(e)} \left(\mathrm{P}_{i,2}\boldsymbol{\omega}_{i,2}\right). \end{aligned} \tag{3.2.2}$$

The total system kinetic energy may then be expressed as:

$$\begin{aligned} T = \sum_{i\in\mathcal{S}} T_i = {} & \dot{\mathbf{x}}_S^{(e),T} \mathrm{a}_{xx} \dot{\mathbf{x}}_S^{(e)} + \dot{\mathbf{x}}_S^{(e),T} \mathrm{A}_{x\omega}^{(e)} \boldsymbol{\omega}^{(e)} + \boldsymbol{\omega}^{(e),T} \mathrm{A}_{\omega\omega}^{(e)} \boldsymbol{\omega}^{(e)} + \dot{\mathbf{x}}_S^{(e),T} \mathbf{a}_x^{(e)} \\ & + \boldsymbol{\omega}^{(e),T} \mathbf{a}_\omega^{(e)} + \mathrm{a}_0, \end{aligned} \tag{3.2.3}$$

with coefficients:

$$\begin{aligned} \mathrm{a}_{xx} &= \frac{1}{2}\sum_{i\in\mathcal{S}} m_i, \\ \mathrm{A}_{x\omega}^{(e)} &= \frac{1}{2}\sum_{i\in\mathcal{S}} 2m_i \left[\sum_{c=1}^{l_{c,i}} \mathrm{P}_{i,c}\mathbf{L}_{i,c}\right]_\times^T, \\ \mathrm{A}_{\omega\omega}^{(e)} &= \frac{1}{2}\sum_{i\in\mathcal{S}} \left[\sum_{c=1}^{l_{c,i}} \mathrm{P}_{i,c}\mathbf{L}_{i,c}\right]_\times m_i \left[\sum_{c=1}^{l_{c,i}} \mathrm{P}_{i,c}\mathbf{L}_{i,c}\right]_\times^T + \mathrm{I}_i^{(e)}, \end{aligned} \tag{3.2.4}$$

$$\mathbf{a}_{\omega}^{(e)} = \frac{1}{2}\sum_{i\in\mathcal{S}} 2\left[\sum_{c=1}^{l_{c,i}} \mathrm{P}_{i,c}\mathbf{L}_{i,c}\right]_{\times}^{T} m_i \left[\sum_{c=1}^{l_{c,i}} \mathrm{P}_{i,c}\mathbf{L}_{i,c}\right]_{\times} \mathrm{P}_{i,2}\boldsymbol{\omega}_{i,2} + 2\mathrm{I}_i^{(e)}\,\mathrm{P}_{i,2}\boldsymbol{\omega}_{i,2},$$

$$\mathbf{a}_{x}^{(e)} = \frac{1}{2}2m_i\left[\sum_{c=1}^{l_{c,i}} \mathrm{P}_{i,c}\mathbf{L}_{i,c}\right]_{\times}^{T}\left(\mathrm{P}_{i,2}\boldsymbol{\omega}_{i,2}\right),$$

$$\mathrm{a}_0 = \frac{1}{2}\sum_{i\in\mathcal{S}}\left(\mathrm{P}_{i,2}\boldsymbol{\omega}_{i,2}\right)^T \mathrm{I}_i^{(e)}\left(\mathrm{P}_{i,2}\boldsymbol{\omega}_{i,2}\right) + \left(\mathrm{P}_{i,2}\boldsymbol{\omega}_{i,2}\right)^T\left[\sum_{c=1}^{l_{c,i}} \mathrm{P}_{i,c}\mathbf{L}_{i,c}\right]_{\times} m_i \left[\sum_{c=1}^{l_{c,i}} \mathrm{P}_{i,c}\mathbf{L}_{i,c}\right]_{\times}^{T}\left(\mathrm{P}_{i,2}\boldsymbol{\omega}_{i,2}\right).$$

This completes the definition of the aircraft total kinetic energy. Note that the wing angular velocities $\boldsymbol{\omega}_{i,2}$ may be computed from their Euler angle rates $\dot{\boldsymbol{\theta}}_i$, see Chapter 2, Section 2.6.3. Note the distinction between the wing Euler angles ($\boldsymbol{\theta}_i, i \in [wl, wr]$) and the body Euler angle ($\boldsymbol{\theta}$). The terms in the expression for the total kinetic energy may be interpreted physically as follows:

$$T = \underbrace{\tfrac{1}{2}\dot{\mathbf{x}}_S^T m \dot{\mathbf{x}}_S}_{\substack{\text{kinetic energy of}\\ \text{translational motion}}} + \underbrace{\dot{\mathbf{x}}_S^T \mathrm{A}_{x\omega}\boldsymbol{\omega}}_{\substack{\text{interaction between}\\ \text{translation and body}\\ \text{rotation}}} + \underbrace{\dot{\mathbf{x}}_S^T \mathbf{a}_x}_{\substack{\text{translational motion}\\ \text{induced by wing motion}}} + \underbrace{\boldsymbol{\omega}^T \mathrm{A}_{\omega\omega}\boldsymbol{\omega}}_{\substack{\text{kinetic energy of}\\ \text{rotational motion}}} + \underbrace{\boldsymbol{\omega}^T \mathbf{a}_{\omega}}_{\substack{\text{rotational motion}\\ \text{induced by wing}\\ \text{motion}}} + \underbrace{\mathrm{a}_0}_{\substack{\text{kinetic energy}\\ \text{of wing motion}}}. \tag{3.2.5}$$

3.2.3. Moment of inertia tensors

The moment of inertia tensors, I_i, of the bodies in the system have been referenced. In this work, without loss of generality, all bodies are modelled as having uniform density. The fuselage is taken as cylindrical; the body moment of inertia tensor about its centre of mass in the body-fixed frame is thus:

$$\mathrm{I}_b^{(b)} = \begin{bmatrix} \frac{1}{2}m_b r_b^2 & & \\ & \frac{1}{12}m_b(3r_b^2 + L_b) & \\ & & \frac{1}{12}m_b(3r_b^2 + L_b) \end{bmatrix}. \tag{3.2.6}$$

Solely in the context of inertia computation, all aerodynamic surfaces as having a rectangular cross-section at their mean thicknesses: this assumption is expected to be negligible with the thin aerofoils utilised in this work. Denoting $h_{i,\mathrm{av}}$ the mean thickness of the aerofoil ($h_{\mathrm{W,av}}$ or $h_{\mathrm{H,av}}$), the lifting surface moments of inertia, about their centres of mass and in their respective local fixed reference frames, are given by:

$$\mathrm{I}_i^{(i)} = \begin{bmatrix} \frac{1}{12}m_i\left(c_i^2 + h_{i,\mathrm{av}}^2\right) & & \\ & \frac{1}{12}m_i\left(L_i^2 + h_{i,\mathrm{av}}^2\right) & \\ & & \frac{1}{12}m_i(L_i^2 + c_i^2) \end{bmatrix}, \qquad (3.2.7)$$

$$i \in [wl, wr, el, er, \mathrm{f}].$$

All these tensors are then resolved in the earth reference frame via their local frame transformation matrices. Note of course that the point mass ($i = \mathrm{pm}$) has a zero moment of inertia tensor about its centre of mass in any reference frame.

3.2.4. Forces and generalised forces

The effect of several forces and moments acting on the aircraft must be considered. Gravity generates a force and a moment about S. These may be expressed as:

$$\begin{aligned} \mathbf{F}_{\mathrm{grav}}^{(e)} &= [0 \quad 0 \quad -m_{\mathcal{S}}g]^{T}, \\ \boldsymbol{\tau}_{\mathrm{grav}}^{(e)} &= \sum_{i\in\mathcal{S}}\left(\mathbf{x}_i^{(e)} - \mathbf{x}_S^{(e)}\right) \times [0 \quad 0 \quad -m_i g]^{T}, \end{aligned} \qquad (3.2.8)$$

where $m_{\mathcal{S}}$ denotes the total system mass. As a conservative force, gravity's effect could alternately be expressed in terms of potential energy. However, mature simulations in this work will always be non-conservative due to the dissipative aerodynamic forces.

The system is hypothetically fitted with a propulsion device, about which no further assumptions are made at this point. The propulsive force is supposed to act in the direction of the body axis ($\hat{\boldsymbol{\imath}}_b$), passing through an arbitrary point V, defined in the body-fixed reference frame by the relative position vector $\Delta\mathbf{x}_V^{(b)}$. Unless otherwise noted, $\mathbf{x}_V^{(b)} = \mathbf{0}$ and thus $V = S$. The forces and moments on S exerted by the propulsion device are:

$$\begin{aligned} \mathbf{F}_{\mathrm{prop}}^{(e)} &= F_{\mathrm{prop}}\hat{\boldsymbol{\imath}}_b^{(e)}, \\ \boldsymbol{\tau}_{\mathrm{prop}}^{(e)} &= \Delta\mathbf{x}_V^{(e)} \times F_{\mathrm{prop}}\hat{\boldsymbol{\imath}}_b^{(e)}. \end{aligned} \qquad (3.2.9)$$

The details of the aerodynamic forces will be studied in further chapters; here it suffices to introduce a total aerodynamic force and total aerodynamic moment about S, resolved in the earth reference frame: $\mathbf{F}_{\mathrm{aero,tot}}^{(e)}$ and $\boldsymbol{\tau}_{\mathrm{aero,tot}}^{(e)}$ respectively. The total force and moment are then:

$$\begin{aligned}\mathbf{F}_{\text{tot}}^{(e)} &= \mathbf{F}_{\text{grav}}^{(e)} + \mathbf{F}_{\text{prop}}^{(e)} + \mathbf{F}_{\text{aero,tot}}^{(e)},\\ \boldsymbol{\tau}_{\text{tot}}^{(e)} &= \boldsymbol{\tau}_{\text{grav}}^{(e)} + \boldsymbol{\tau}_{\text{prop}}^{(e)} + \boldsymbol{\tau}_{\text{aero,tot}}^{(e)}.\end{aligned} \tag{3.2.10}$$

For use in a variational analysis – either via the Euler-Lagrange equation or the principle of least action (see Chapter 4) – generalised forces corresponding to the generalised coordinate of the orientation parameterisation are required. The generalised translational force ($\mathcal{Q}_x$) associated with both orientation parameterisations is identically $\mathbf{F}_{\text{tot}}^{(e)}$; whereas the generalised rotational forces are transformations of $\boldsymbol{\tau}_{\text{tot}}^{(e)}$. The generalised rotational force in the quaternion parameterisation ($\mathcal{Q}_q$) is given by [20]:

$$\mathcal{Q}_q = 2q \otimes \boldsymbol{\tau}_{\text{tot}}^{(b)} = 2\boldsymbol{\tau}_{\text{tot}}^{(e)} \otimes q. \tag{3.2.11}$$

The generalised rotational force in the 3-2-1 Euler angle parameterisation involves a transformation equivalent to that of $\boldsymbol{\omega}^{(e)}$ (see Chapter 2, Section 2.5.2), that is:

$$\mathcal{Q}_\theta = \Omega_0^{-1}\boldsymbol{\tau}_{\text{tot}}^{(e)}. \tag{3.2.12}$$

Physically, these generalised rotational forces correspond to the force effect of $\boldsymbol{\tau}_{\text{tot}}^{(e)}$ when resolved in the orientation parameterisations themselves ($\mathcal{Q}_\theta$ e.g. representing the pitch/yaw/roll rate forces, and $\mathcal{Q}_q$ the corresponding for abstract effect for an orientation quaternion). They will be required in the variational analysis of the system.

3.2.5. Verification of aircraft dynamics

To validate our aircraft kinetic energy formulation (Eq. 3.2.3-3.2.4), we compare it to the classical results for the kinetic energy of a rigid body about its centre of mass. Generating random aircraft Euler angles and positions, centre of mass translational and angular velocities ($\boldsymbol{\omega}^{(e)}$ and $\dot{\mathbf{x}}_{\text{c.o.m.}}^{(e)}$), and wing morphing angles (with zero wing morphing rates), the centre-of-mass kinetic energy is computed as:

$$T = \frac{1}{2}\boldsymbol{\omega}^{(e),T}\mathrm{I}_{\text{c.o.m.}}^{(e)}\boldsymbol{\omega}^{(e)} + \frac{1}{2}\dot{\mathbf{x}}_{\text{c.o.m.}}^{(e),T} m_{\text{tot}} \dot{\mathbf{x}}_{\text{c.o.m.}}^{(e)}, \tag{3.2.13}$$

with inertia tensor about the centre of mass via the parallel axis theorem [36]:

$$\begin{aligned}\mathrm{I}_{\text{c.o.m.}}^{(e)} &= \sum_{i\in\mathcal{S}} \mathrm{I}_i^{(i)} + m_i\left(\left(\mathbf{r}_i^{(e)} \cdot \mathbf{r}_i^{(e)}\right)\mathrm{E}_3 - \mathbf{r}_i^{(e),T} \otimes_{\text{kr}} \mathbf{r}_i^{(e)}\right),\\ \mathbf{r}_i^{(e)} &= \mathbf{x}_{\text{c.o.m.}}^{(e)} - \mathbf{x}_i^{(e)}, \qquad \mathbf{x}_{\text{c.o.m.}}^{(e)} = \frac{1}{m_{\text{tot}}}\sum_{i\in\mathcal{S}} m_i \mathbf{x}_i^{(e)}.\end{aligned} \tag{3.2.14}$$

where $\otimes_{\mathrm{kr}}$ denotes the Kronecker (Outer) product, not the quaternion product [37]. The aircraft orientation, position and morphing parameters are then passed to the multibody model. By rigid-body kinematics, $\boldsymbol{\omega}^{(e)}$ remains unchanged, and $\dot{\mathbf{x}}_S^{(e)}$ is given by:

$$\dot{\mathbf{x}}_S^{(e)} = \boldsymbol{\omega}^{(e)} \times \left(\mathbf{x}_S^{(e)} - \mathbf{x}_{\mathrm{c.o.m.}}^{(e)}\right) + \dot{\mathbf{x}}_{\mathrm{c.o.m.}}^{(e)}. \tag{3.2.15}$$

The results for 10^3 random trails indicate no discrepancies above the level of machine precision ($> 3 \times 10^{-13}$).

3.3. AERODYNAMICS: LITERATURE REVIEW

In the context of the flight dynamic analysis of morphing-wing systems – biomimetic or otherwise – a very wide range of model fidelities are observed. At the highest level, 3D turbulent computational fluid dynamics (CFD) simulations via direct numerical simulation (DNS), large-eddy simulation (LES) or Reynolds-averaging are expensive but are capable of capturing complex aerodynamic effects [38,39]. Typical larger-scale application utilise Reynolds-averaging with the Spalart-Allmaras turbulence model [5,40–42]; LES approaches are feasible only for low Reynolds number applications, e.g. biomimetic insect systems [25].

In situations where computational models are too computationally intensive, some form of lower-order dynamic stall and lift hysteresis model is required. Phenomenological models of this form include the ONERA [12] and Goman-Khrabrov (GK) [13] models, among others [14]. Non-phenomenological model-reduction and machine learning techniques such as eigensystem realisation [43], Volterra theory [44] and support vector machines [45] are also available – though these still require higher-fidelity (e.g. CFD) data to work on. At a slightly simpler level, Theodorsen's aerodynamic theory provides a method by which the dynamic effects of low-amplitude pitching and dihedral motion may be modelled [46,47]; though the method does not extend to large amplitudes [48] and is more common in the study of aeroelasticity. Similar alternatives to Theodorsen's theory include the use of Wagner's indicial response function [48] and the finite-state theory of Peters et al. [49].

These low-order models of specific transient aerodynamic effects have the key advantage of accounting for such effects – e.g. those with known relevance to the application – without

the computational burden of obtaining a full flow field solution. Their key disadvantage, however, is that the uniqueness of their formulation typically excludes a synthesis with models of other aerodynamic effects. In particular, this includes extensions beyond their current application to two-dimensional section models: implementations e.g. in an aerodynamic panel method framework cannot currently be countenanced. Furthermore, these models focus largely on the dynamic effects of aerofoil pitching, and to a lesser extent, dihedral motion. The effects of dynamic sweep motion, apart from the obvious induced flow, are only rarely studied [50] – though results from the study of unsteady freestream flows indicate that they may have more significance than previously thought [51–53]. However, modelling approaches for such effects have not yet been proposed in the literature; and indeed few of all these low-order transient models have been applied to morphing-wing systems.

Finally, quasisteady or steady section models or panel methods are available, based on an analysis of the local static airframe state, with or without a morphing-induced flow model respectively. These approaches still consider to some extent the dynamic effect of wing morphing if they include a morphing-induced flow model – that is, a model of the instantaneous flow induced by the lifting-surface morphing / relative motion itself. If not; then no dynamic effects are being considered at all. The vast majority of morphing-wing aerodynamic modules are of this latter type, typically in the form of vortex-lattice [54,55], doublet-source [2] or lifting-line methods [56,57]. Second-order extensions to quasisteady section models are also available [27]. The panel method formulation of these models have the advantage of including some 3D (e.g. finite-span) effects; however they suffer also from the significant disadvantage of being unable to be generalised to model dynamic stall or other unsteady effects. Most implementations are indeed constrained to linear pre-stall aerodynamic models, and a generalization to even static stall behaviour requires additional techniques such as nonlinear lifting-line theory [58] or iterative decambering [59,60].

In this work we utilise a discrete framework of local section models, in the manner of strip theory or blade element momentum theory [61,62]. This will allow us to apply low-order models of transient effects (such as the GK-type models) to the whole airframe. However, in the first instance, for validation testing purposes, a quasisteady aerodynamic model

formulated in this section model framework is utilised. In this chapter we construct this aerodynamic framework and describe the local quasisteady model, leading to a full (if, simplistic) flight dynamic model. This model will be used for integrator testing, flight dynamics validation, and as a reference point for the more complex models of transient aerodynamic effects studied in Chapter 8. This study begins with a quasisteady model for three reasons: (1) the novel guidance procedures that we will devise require a quasisteady model; (2) with the quasisteady model, flight dynamic validation can to some degree be separated from novel aerodynamic model validation; and (3) the novel aerodynamic models that we will devise are subject to significant limitations and areas of model breakdown; they are not suitable as a broadly-applied base model for this system. Note also that this model is both quasisteady (in terms of flow modelling) and quasistatic (in terms of with morphing motion); these two characteristics have an impact of differing aspects of model validity and contextual use.

3.4. QUASISTEADY AERODYNAMIC MODELLING

3.4.1. Aerodynamic mesh

To model the aerodynamics of the entire airframe, a mesh of local section models is generated, as per strip theory or blade element momentum theory [61,62]. Each body in the multibody system is discretised into N_i aerodynamic stations ($i \in \mathcal{S}$) along the body reference axes – for the aerofoils, the quarter-chord points, and for the fuselage, the centroid. The aerodynamic forces on each section model will then be computed from only from the dynamic state and properties of the local station. This approach may be regarded as a generalised form of blade-element model [63,64], a form of strip theory [62], has been previously used before by Ananda and Selig [65,66], among others.

The location of the stations within each body is described by a variable x_{stat}, the distance along the reference axis from the body origin. An example mesh for the case study system, showing the locations of these origins, is given in Figure 3.4.1. The station locations for the different aircraft components are thus given by:

wings ($i \in [WL, WR]$):

$$\mathbf{x}_{\text{stat}}^{(e)}(x_{\text{stat}}) = x_{\text{stat}}\mathrm{P}_{E/B}\hat{\imath}_i^{(b)} + \dot{\mathrm{P}}_{E/B}\mathbf{L}_{i,1} + \mathbf{x}_S;$$

stabilisers ($i \in [EL, ER]$):

$$\mathbf{x}_{\text{stat}}^{(e)}(x_{\text{stat}}) = x_{\text{stat}}\mathrm{P}_{E/B}\hat{\imath}_i^{(b)} + \mathbf{x}_S;$$

fuselage: ($i = F$):

$$\mathbf{x}_{\text{stat}}^{(e)}(x_{\text{stat}}) = x_{\text{stat}}\hat{\imath}_b^{(e)} + \mathbf{x}_S. \tag{3.4.1}$$

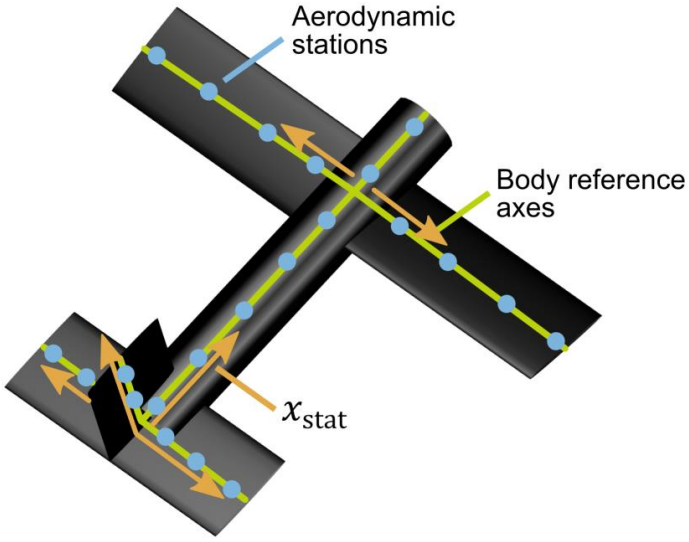

Figure 3.4.1: An example aerodynamic mesh.

The local induced flow at each station is related to the time derivative of these quantities, but strictly references the aerofoil quarter-chord point. For this reason, the velocity of the quarter-chord point is taken:

quarter-chord location ($\forall i$):

$$\mathbf{r}_{\text{stat},\, c/4,i} = \left[x_{\text{stat}}, \frac{1}{4}c_i, 0\right]^T;$$

wings ($i \in [WL, WR]$):

$$\dot{\mathbf{x}}_{\text{stat}}^{(e)}(x_{\text{stat}}) = \left(\dot{\mathrm{P}}_{E/B}\mathrm{P}_{B/i} + \mathrm{P}_{E/B}\dot{\mathrm{P}}_{B/i}\right)\mathbf{r}_{\text{stat},\, c/4,i} + \dot{\mathrm{P}}_{E/B}\mathbf{L}_{i,1} + \dot{\mathbf{x}}_S;$$

stabilisers ($i \in [EL, ER]$):

$$\dot{\mathbf{x}}_{\text{stat}}^{(e)}(x_{\text{stat}}) = \dot{\mathrm{P}}_{E/B}\mathrm{P}_{B/i}\mathbf{r}_{\text{stat},\, c/4,i} + \mathbf{x}_S; \tag{3.4.2}$$

fuselage: ($i = F$):

$$\dot{\mathbf{x}}_{\text{stat}}^{(e)}(x_{\text{stat}}) = x_{\text{stat}}\dot{\hat{\imath}}_b^{(e)} + \mathbf{x}_S.$$

The local induced flow velocity at any station is then given by $\mathbf{u}_{\text{stat}}^{(e)} = -\dot{\mathbf{x}}_{\text{stat}}^{(e)} + \mathbf{u}_{\text{global}}^{(e)}$. This analysis neglects the effects of any global flow field, $\mathbf{u}_{\text{global}}^{(e)}$, including wind fields, the effect of flow shadowing from other parts of the airframe, and a propulsion-induced flow field. The inclusion of a global wind flow field, if this is relevant to the analysis, is trivial. The inclusion of flow shadowing effects is made more difficult than is the case for more restrictive flight simulators, as flow shadowing is possible between any two lifting surfaces, in any direction and with wakes from translating and rotating airframe components. Devising a flow shadowing model for this system would be a significant undertaking as is beyond the scope of this work. Including a propulsion-induced flow field is simple, when the propulsion system is defined; but here we treat a more general aircraft.

We then resolve the local flow velocity in the local section model-fixed fame (denoted b_i); $\mathbf{u}_{\text{stat}}^{(b_i)} = \mathrm{P}_{E/b_i}^{T}\mathbf{u}_{\text{stat}}^{(e)}$. This velocity can then be decomposed into polar coordinates, representing the local effective angle-of-attack and flow magnitude. The spanwise component $\mathrm{u}_{\text{stat},1}^{(b_i)}$, is neglected. The polar decomposition may be computed as:

$$\phi_{\text{eff}} = -\tan_2^{-1}\frac{-\mathrm{u}_{\text{stat},3}^{(b_i)}}{-\mathrm{u}_{\text{stat},2}^{(b_i)}}, \qquad U = \left\|\mathbf{u}_{\text{stat}}^{(b_i)}\right\|_2, \tag{3.4.3}$$

where $\mathrm{u}_{\text{stat},i}^{(b_i)}$ denotes the i-th element of $\mathbf{u}_{\text{stat}}^{(b_i)}$. The function $\tan_2^{-1}$ denotes the two-argument (four-quadrant) arctangent [67].

3.4.2. Limitations to the aerodynamic mesh

We will use this aerodynamic mesh framework for all both the quasisteady aerodynamic analysis contained in this chapter and the more complex transient models considered in Chapter 8, and so here its limitations are noted. Key assumptions contained in this approach are the neglect of flow shadowing with the airframe, and the spanwise component of flow at each station. The latter leads to a modelling deficiency in the modelling of vortex shedding at the lifting surface tips, and the formation of other structures along the lifting surface spans; for example at high roll rates. This deficiency is a feature of the section model approach in general, which does not account for coupling between any of the aerodynamic station parameters. While the aerodynamic mesh framework does not preclude the

modelling of inter-station coupling effects via a lifting-line theory, this approach is incompatible with the modelling of strong transient effects.

The former will result in a degradation of accuracy in the case of deep stall [68], involving flow shadowing between the wings and the horizontal stabilisers – for example, in forward flight when the wing incidence is high. Other potentially significant cases of flow shadowing include that between the horizontal and vertical stabilisers in manoeuvres at low airspeed and fast roll rate, and that between the wings and fuselage when the wings are swept back at a high angle. One previous flight simulator, that of Selig [66], considered the effect of intra-tailplane flow shadowing in conventional flight regimes, and implemented a simple correctors to account for this. However, as more complex and more diverse forms of shadowing are likely to be dominant in supermanoeuvres, and to preserve a uniform modelling approach across the system, this individual corrector is not implemented. The creation of a more general wake-tracking and flow-shadowing in the modelling context of this work is certainly within the realms of possibility, particularly as the aerodynamic mesh framework provides convenient wake generation points which can then be appropriately decayed (or indeed, transported or diffused), and which can be modelled to influence the local flow field. This is an area for future research which shows significant potential.

3.4.3. Lifting surface quasisteady aerodynamic model

In the simplest case, at each section model on the lifting surfaces the local aerodynamic forces are computed via a quasisteady aerodynamic model. In such a model, these forces are dependent only on ϕ_{eff}, U and the section model state (including e.g. control surface commands). For the aircraft lifting surfaces, aerodynamic coefficient data is taken from Selig [66] for wing (ST50W) and stabiliser (ST50H) airfoils; generated via data fusion techniques from experimental data, potential flow models and semi-empirical techniques. This data covers the full α range and includes the effect of wing aileron and stabiliser control surface deflection. The section model lift, drag and moment coefficients can then be interpolated from ϕ_{eff} and the relevant control surface deflection β_i. The foil sections are approximately equivalent to NACA0015 and NACA007 airfoils, for the ST50W and ST50H respectively. The effect of varying Reynolds number is not accounted for: the Reynolds for aerodynamic data is unspecified, but for a ShowTime 50 aircraft in flight Re $\approx 3 \times 10^5$ is expected (cf. [66]).

The aerodynamic forces on each section model may then be computed as:

$$\begin{aligned}\mathbf{L}_i^{(e)} &= \frac{1}{2}\rho U_i^2 c_i C_{\mathrm{L}}\left(\phi_{\mathrm{eff},i}\right)\hat{\mathbf{L}}_i^{(e)},\\ \mathbf{D}_i^{(e)} &= \frac{1}{2}\rho U_i^2 c_i C_{\mathrm{D}}\left(\phi_{\mathrm{eff},i}\right)\hat{\mathbf{D}}_i^{(e)},\\ \mathbf{M}_i^{(e)} &= \frac{1}{2}\rho U_i^2 c_i^2 C_{\mathrm{M}}\left(\phi_{\mathrm{eff},i}\right)\hat{\mathbf{M}}_i^{(e)},\end{aligned} \tag{3.4.4}$$

where c_i is the local chord, ρ the constant air density, and $\hat{\mathbf{L}}_i^{(e)}$ (etc.) the force unit vectors in the earth frame. They may be computed by:

$$\begin{aligned}\hat{\mathbf{D}}^{(e)} &= \mathrm{P}_{E/B}\mathrm{P}_{B/W}\frac{\mathbf{u}_{\mathrm{stat}}^{(b_i)}}{U},\\ \hat{\mathbf{L}}^{(e)} &= \hat{\mathbf{D}}^{(e)} \times [1 \quad 0 \quad 0]^T,\\ \hat{\mathbf{M}}^{(e)} &= \mathrm{sgn}_{b_i}\hat{\imath}_{b_i}^{(e)},\end{aligned} \tag{3.4.5}$$

where sgn_w denotes the handedness sign of the local body-fixed coordinate system.

3.4.4. Fuselage quasisteady aerodynamic model

The same approach, with a few modifications, is applied to the fuselage section models. As they are assumed to be cylindrical, $\phi_{\mathrm{eff},i}$ is irrelevant and the drag coefficient is taken to be uniformly $C_{\mathrm{D}} = 1.0$ [69]. Lift and moment forces are neglected. Additionally, a frontal drag force is also modelled, based on the airspeed in the fuselage frontal direction and a frontal drag coefficient, and assumed to act about along the fuselage axis ($\hat{\imath}_b$) and about the centre of mass. This force is given by:

$$\begin{aligned}\mathbf{D}_{\mathrm{front}}^{(e)} &= \frac{1}{2}\rho U_{\mathrm{front}}^2 C_{\mathrm{D,front}} A_{\mathrm{front}}\hat{\imath}_b^{(e)},\\ U_{\mathrm{front}} &= \left|\mathrm{u}_{\mathrm{stat},1}^{(b)}\right|, \qquad A_{\mathrm{front}} = \pi r_b^2,\end{aligned} \tag{3.4.6}$$

and corresponds to the effect of spanwise flow over the fuselage. In the absence of further detail regarding the fuselage geometry, the case study system is taken to have $C_{\mathrm{D,front}} = 0$. However a nonzero identified value will be used for validation flight simulations. Given the general nature of this aircraft, this is taken to be at least sufficiently representative that manoeuvre simulations are not qualitatively affected. More complex assymetric forebody separation effects will be considered in Chapter 7.

3.4.5. Integration of aerodynamic forces

Finally, lift, drag and moment distributions are integrated over the N stations on a single airframe component to obtain its contribution to the total lift, drag and moment about S. The total moment consists of both the moment-coefficient moment ($\mathbf{M}$) and the moment induced by the lift and drag forces ($\mathbf{N}$). The lift and drag forces act through the approximate aerodynamic centre at the quarter-chord location (i.e. a quarter of the chord from the leading edge): the aerodynamic coefficients in Selig [66] are defined for an aerodynamic centre at this location. For details about the aerodynamic centre see e.g. [70]. The pertinent aspect of this is that the induced moment integration must be carried out using the quarter-chord location as the force position ($\mathbf{r}_{\text{stat},\, c/4}$; see Eq. 3.4.1-3.4.2). The integration is carried out numerically with the trapezium rule:

$$\begin{aligned}
\mathbf{L}_{i,\,\text{tot}}^{(e)} &= \int_{\text{trapezium}} \mathbf{L}_i^{(e)} dx_{\text{stat}}, \\
\mathbf{D}_{i,\,\text{tot}}^{(e)} &= \int_{\text{trapezium}} \mathbf{D}_i^{(e)} dx_{\text{stat}}, \\
\mathbf{M}_{i,\,\text{tot}}^{(e)} &= \int_{\text{trapezium}} \mathbf{M}_i^{(e)} dx_{\text{stat}}, \\
\mathbf{N}_{i,\,\text{tot}}^{(e)} &= \int_{\text{trapezium}} \left(\mathbf{L}_i^{(e)} + \mathbf{D}_i^{(e)}\right) \times \mathbf{r}_{\text{stat},\, c/4} dx_{\text{stat}},
\end{aligned} \tag{3.4.7}$$

$$\mathbf{r}_{\text{stat},\, c/4} = \begin{cases} \dfrac{1}{4} c_i \mathrm{P}_{E/B} \hat{\mathbf{j}}_i^{(b)} + x_{\text{stat}} \mathrm{P}_{E/B} \hat{\mathbf{i}}_i^{(b)} & i \in \mathcal{F}/\{b\} \\ \dfrac{1}{4} c_i \mathrm{P}_{E/B} \hat{\mathbf{j}}_i^{(b)} + x_{\text{stat}} \mathrm{P}_{E/B} \hat{\mathbf{i}}_i^{(b)} + L_r \hat{\mathbf{i}}_b^{(e)} & i \in \mathcal{W}. \end{cases}$$

This yields the lift, drag and total aerodynamic moment acting about S that arises from the given lifting surface. This computation is repeated for each of the lifting surfaces. The total aerodynamic force on the fuselage is computed identically, with the force positions taken as the fuselage centroid ($x_{\text{stat}} \hat{\mathbf{i}}_b^{(e)}$); or the system centre of mass ($\mathbf{L}_{\text{c.o.g.}}^{(e)}$) for the frontal drag force. The results from all surfaces are summed into the total aerodynamic force $\mathbf{F}_{\text{aero,tot}}$ and moment $\boldsymbol{\tau}_{\text{aero,tot}}$ about S, in the earth reference frame, acting on the aircraft:

$$\mathbf{F}_{\text{aero,tot}}^{(e)} = \sum_{i \in \mathcal{S}} \mathbf{L}_{i,\text{tot}}^{(e)} + \mathbf{D}_{i,\text{tot}}^{(e)},$$
$$\boldsymbol{\tau}_{\text{aero,tot}}^{(e)} = \sum_{i \in \mathcal{S}} \mathbf{M}_{i,\text{tot}}^{(e)} + \mathbf{N}_{i,\text{tot}}^{(e)}. \tag{3.4.8}$$

with appropriate transformation in the case of the moments ($\boldsymbol{\tau}_{\text{aero,tot}}^{(b)} = P_{E/B}^{T} \boldsymbol{\tau}_{\text{aero,tot}}^{(e)}$) these terms may be used directly in the variational integrator of Chapter 4.

3.5. CONCLUDING REMARKS

This chapter has presented a full dynamics framework and low-order aerodynamic model for the case study system. A dynamical analysis of the system, leading to the system weak formulation (in quaternion kinematics) and equations of motion (in Euler angle kinematics) is presented in Chapter 4. The aerodynamic model presented in this chapter is intentionally simple: to allow an assessment of the numerical properties of our integrators in the presence of dissipative forces; to enable validation simulations against other fixed-wing flight path data, and to enable initial studies into biomimetic supermanoeuvrability to be made. Further aerodynamic extensions are presented in Chapter 8.

CHAPTER REFERENCES

[1] Obradovic, B., and Subbarao, K., “Modeling and Simulation of Morphing Wing Aircraft,” *Morphing Aerospace Vehicles and Structures*, J. Valasek, ed., John Wiley & Sons, Chichester, UK, 2012, pp. 87–125.

[2] Niksch, A., Valasek, J., Strganac, T., and Carlson, L., “Six Degree-of-Freedom Dynamical Model of a Morphing Aircraft,” AIAA Atmospheric Flight Mechanics Conference, Chicago, IL.

[3] Valasek, J., Lampton, A., and Marwaha, M., “Morphing Unmanned Air Vehicle Intelligent Shape and Flight Control,” AIAA Infotech@Aerospace Conference, Seattle, WA.

[4] Grant, D. T., Sorley, S., Chakravarthy, A., and Lind, R., "Flight Dynamics of Morphing Aircraft with Time-Varying Inertias," *Morphing Aerospace Vehicles and Structures*, J. Valasek, ed., John Wiley & Sons, Chichester, UK, 2012, pp. 151–175.

[5] Dwivedi, V., and Damodaran, M., "Computational Aeromechanics of a Manuevering Unmanned Aerial Vehicle with Variable-Incidence Wings," *Journal of Aircraft*, Vol. 52, No. 6, 2015, pp. 1914–1926. DOI:10.2514/1.C033102.

[6] Orlowski, C. T., and Girard, A. R., "Dynamics, stability, and control analyses of flapping wing micro-air vehicles," *Progress in Aerospace Sciences*, Vol. 51, 2012, pp. 18–30. DOI:10.1016/j.paerosci.2012.01.001.

[7] Bolender, M., "Rigid Multi-Body Equations-of-Motion for Flapping Wing MAVs Using Kane's Equations," AIAA Guidance, Navigation, and Control Conference, Chicago, IL.

[8] Orlowski, C. T., and Girard, A. R., "Modeling and Simulation of Nonlinear Dynamics of Flapping Wing Micro Air Vehicles," *AIAA Journal*, Vol. 49, No. 5, 2011, pp. 969–981. DOI:10.2514/1.J050649.

[9] Shi, R., and Wan, W., "Analysis of flight dynamics for large-scale morphing aircraft," *Aircraft Engineering and Aerospace Technology*, Vol. 87, No. 1, 2015, pp. 38–44. DOI:10.1108/AEAT-01-2013-0004.

[10] Seigler, T. M., Neal, D. A., Bae, J.-S., and Inman, D. J., "Modeling and Flight Control of Large-Scale Morphing Aircraft," *Journal of Aircraft*, Vol. 44, No. 4, 2007, pp. 1077–1087. DOI:10.2514/1.21439.

[11] Baldelli, D. H., Lee, D.-H., Sánchez Peña, R. S., and Cannon, B., "Modeling and Control of an Aeroelastic Morphing Vehicle," *Journal of Guidance, Control, and Dynamics*, Vol. 31, No. 6, 2008, pp. 1687–1699. DOI:10.2514/1.35445.

[12] Seigler, T. M., and Neal, D. A., "Analysis of Transition Stability for Morphing Aircraft," *Journal of Guidance, Control, and Dynamics*, Vol. 32, No. 6, 2009, pp. 1947–1954. DOI:10.2514/1.44108.

[13] Kim, J.-K., and Han, J.-H., "A multibody approach for 6-DOF flight dynamics and stability analysis of the hawkmoth *Manduca sexta*," *Bioinspiration & Biomimetics*, Vol. 9, No. 1, 2014, p. 016011. DOI:10.1088/1748-3182/9/1/016011.

[14] Mahjoubi, H., and Byl, K., "Dynamics of insect-inspired flapping-wing MAVs: Multibody modeling and flight control simulations," pp. 3089–3095.

[15] Bin Abas, M. F., Bin Mohd Rafie, A. S., Bin Yusoff, H., and Bin Ahmad, K. A., "Flapping wing micro-aerial-vehicle: Kinematics, membranes, and flapping mechanisms of ornithopter and insect flight," *Chinese Journal of Aeronautics*, Vol. 29, No. 5, 2016, pp. 1159–1177. DOI:10.1016/j.cja.2016.08.003.

[16] Köthe, A., and Luckner, R., "Flight Path Control for a Multi-body HALE Aircraft," *Advances in Aerospace Guidance, Navigation and Control*, B. Dołęga, R. Głębocki, D. Kordos, and M. Żugaj, eds., Springer International Publishing, Cham, 2018, pp. 421–442.

[17] Nitardi, L. M., Roccia, B. A., Preidikman, S., and Flores, F. G., "Multibody Dynamic Analysis of a High-Altitude Long-Endurance Aircraft Concept," *Multibody Mechatronic Systems*, J.C.M. Carvalho, D. Martins, R. Simoni, and H. Simas, eds., Springer, Cham, Switzerland, 2018, pp. 223–232.

[18] Patil, M. J., and Hodges, D. H., "Flight Dynamics of Highly Flexible Flying Wings," *Journal of Aircraft*, Vol. 43, No. 6, 2006, pp. 1790–1799. DOI:10.2514/1.17640.

[19] Leylek, E., Ward, M., and Costello, M., "Flight Dynamic Simulation for Multibody Aircraft Configurations," *Journal of Guidance, Control, and Dynamics*, Vol. 35, No. 6, 2012, pp. 1828–1842. DOI:10.2514/1.55858.

[20] Manchester, Z. R., and Peck, M. A., "Quaternion Variational Integrators for Spacecraft Dynamics," *Journal of Guidance, Control, and Dynamics*, Vol. 39, No. 1, 2016, pp. 69–76. DOI:10.2514/1.G001176.

[21] Lee, T., and Leve, F., "Lagrangian mechanics and Lie group variational integrators for spacecraft with imbalanced reaction wheels," pp. 3122–3127.

[22] Lee, D., Springmann, J., Spangelo, S., and Cutler, J., "Satellite Dynamics Simulator Development Using Lie Group Variational Integrator," AIAA Modeling and Simulation Technologies Conference, Portland, OR.

[23] Tong, L., and Ji, H., "Multi-body dynamic modelling and roll control of asymmetric variable sweep morphing aircrafts," *2013 10th IEEE International Conference on Control and Automation (ICCA)*, 2013 10th IEEE International Conference on Control and Automation (ICCA), Hangzhou, China, pp. 1567–1572.

[24] Yue, T., Wang, L., and Ai, J., "Multibody Dynamic Modeling and Simulation of a Tailless Folding Wing Morphing Aircraft," AIAA Atmospheric Flight Mechanics Conference, Chicago, IL.

[25] Scarlett, J., Canfield, R., and Sanders, B., "Multibody Dynamic Aeroelastic Simulation of a Folding Wing Aircraft," 47th AIAA/ASME/ASCE/AHS/ASC Structures, Structural Dynamics, and Materials Conference, Newport, Rhode Island.

[26] Gao, L., Jin, H., Zhao, J., Cai, H., and Zhu, Y., "Flight Dynamics Modeling and Control of a Novel Catapult Launched Tandem-wing Micro Aerial Vehicle with Variable Sweep," *IEEE Access*, 2018, pp. 1–1. DOI:10.1109/ACCESS.2018.2858293.

[27] Grauer, J., and Hubbard, J., "Flight Dynamics Modeling of Avian-Inspired Aircraft," *Morphing Aerospace Vehicles and Structures*, J. Valasek, ed., John Wiley & Sons, Chichester, UK, 2012, pp. 127–149.

[28] Vos, R., Breuker, R. D., Barrett, R. M., and Tiso, P., "Morphing Wing Flight Control Via Postbuckled Precompressed Piezoelectric Actuators," *Journal of Aircraft*, Vol. 44, No. 4, 2007, pp. 1060–1068. DOI:10.2514/1.21292.

[29] Grigorie, T. L., Popov, A. V., Botez, R. M., Mamou, M., and Mebarki, Y., "On-off and proportional-integral controller for a morphing wing. Part 1: Actuation mechanism and control design," *Proceedings of the Institution of Mechanical Engineers, Part G: Journal of Aerospace Engineering*, Vol. 226, No. 2, 2012, pp. 131–145. DOI:10.1177/0954410011408226.

[30] Golubev, Yu. F., "Mechanical systems with servoconstraints," *Journal of Applied Mathematics and Mechanics*, Vol. 65, No. 2, 2001, pp. 205–217. DOI:10.1016/S0021-8928(01)00024-7.

[31] Arczewski, K., Blajer, W., Fraczek, J., and Wojtyra, M., eds., *Multibody Dynamics*, Springer, Dordrecht, The Netherlands, 2011.

[32] Riskin, D. K., Bahlman, J. W., Hubel, T. Y., Ratcliffe, J. M., Kunz, T. H., and Swartz, S. M., "Bats go head-under-heels: the biomechanics of landing on a ceiling," *Journal of Experimental Biology*, Vol. 212, No. 7, 2009, pp. 945–953. DOI:10.1242/jeb.026161.

[33] Bergou, A. J., Swartz, S. M., Vejdani, H., Riskin, D. K., Reimnitz, L., Taubin, G., and Breuer, K. S., "Falling with Style: Bats Perform Complex Aerial Rotations by Adjusting Wing Inertia," *PLOS Biology*, Vol. 13, No. 11, 2015, p. e1002297. DOI:10.1371/journal.pbio.1002297.

[34] Jusufi, A., Kawano, D. T., Libby, T., and Full, R. J., "Righting and turning in mid-air using appendage inertia: reptile tails, analytical models and bio-inspired robots,"

Bioinspiration & Biomimetics, Vol. 5, No. 4, 2010, p. 045001. DOI:10.1088/1748-3182/5/4/045001.

[35] De Sapio, V., Khatib, O., and Delp, S., "Least action principles and their application to constrained and task-level problems in robotics and biomechanics," *Multibody System Dynamics*, Vol. 19, No. 3, 2008, pp. 303–322. DOI:10.1007/s11044-007-9097-8.

[36] Papastavridis, J. G., *Analytical Mechanics*, World Scientific, Singapore, 2014.

[37] Liu, S., and Trenkler, G., "Hadamard, Khatri-Rao, Kronecker and other matrix products," *International Journal of Information and Systems Sciences*, Vol. 4, No. 1, 2008, pp. 160–177.

[38] Culbreth, M., Allaneau, Y., and Jameson, A., "High-Fidelity Optimization of Flapping Airfoils and Wings," 29th AIAA Applied Aerodynamics Conference.

[39] De Gaspari, A., and Ricci, S., "Knowledge-Based Shape Optimization of Morphing Wing for More Efficient Aircraft," *International Journal of Aerospace Engineering*, Vol. 2015, 2015, pp. 1–19. DOI:10.1155/2015/325724.

[40] Lankford, J., Mayo, D., and Chopra, I., "Computational investigation of insect-based flapping wings for micro air vehicle applications," *International Journal of Micro Air Vehicles*, Vol. 8, No. 2, 2016, pp. 64–78. DOI:10.1177/1756829316646640.

[41] Fincham, J. H., Ajaj, R. M., and Friswell, M. I., "Aerodynamic Performance of Corrugated Skins for Spanwise Wing Morphing," 14th AIAA Aviation Technology, Integration, and Operations Conference, Atlanta, GA.

[42] Jones, M. A., "CFD Analysis and Design Optimization of Flapping Wing Flows," Doctoral Thesis, North Carolina Agricultural and Technical State University, 2013.

[43] Brunton, S., and Rowley, C., "Unsteady Aerodynamic Models for Agile Flight at Low Reynolds Number," 48th AIAA Aerospace Sciences Meeting, Orlando, FL.

[44] Balajewicz, M., Nitzsche, F., and Feszty, D., "Application of Multi-Input Volterra Theory to Nonlinear Multi-Degree-of-Freedom Aerodynamic Systems," *AIAA Journal*, Vol. 48, No. 1, 2010, pp. 56–62. DOI:10.2514/1.38964.

[45] Wang, Q., Qian, W., and He, K., "Unsteady aerodynamic modeling at high angles of attack using support vector machines," *Chinese Journal of Aeronautics*, Vol. 28, No. 3, 2015, pp. 659–668. DOI:10.1016/j.cja.2015.03.010.

[46] Liska, S., and Dowell, E. H., "Continuum Aeroelastic Model for a Folding-Wing Configuration," *AIAA Journal*, Vol. 47, No. 10, 2009, pp. 2350–2358. DOI:10.2514/1.40475.

[47] Wang, I., "Aeroelastic and Flight Dynamics Analysis of Folding Wing Systems," Doctoral Dissertation, Duke University, 2013.

[48] Brunton, S., and Rowley, C., "Modeling the Unsteady Aerodynamic Forces on Small-Scale Wings," 47th AIAA Aerospace Sciences Meeting, Orlando, FL.

[49] Peters, D. A., Karunamoorthy, S., and Cao, W.-M., "Finite state induced flow models. I - Two-dimensional thin airfoil," *Journal of Aircraft*, Vol. 32, No. 2, 1995, pp. 313–322. DOI:10.2514/3.46718.

[50] An, J., Yan, M., Zhou, W., Sun, X., and Yan, Z., "Aircraft dynamic response to variable wing sweep geometry," *Journal of Aircraft*, Vol. 25, No. 3, 1988, pp. 216–221. DOI:10.2514/3.45580.

[51] Karbasian, H. R., Esfahani, J. A., and Barati, E., "Effect of acceleration on dynamic stall of airfoil in unsteady operating conditions: Effect of acceleration on dynamic stall of airfoil," *Wind Energy*, Vol. 19, No. 1, 2016, pp. 17–33. DOI:10.1002/we.1818.

[52] Gharali, K., and Johnson, D. A., "Dynamic stall simulation of a pitching airfoil under unsteady freestream velocity," *Journal of Fluids and Structures*, Vol. 42, 2013, pp. 228–244. DOI:10.1016/j.jfluidstructs.2013.05.005.

[53] Shi, Z.-W., and Ming, X., "Effects of Unsteady Freestream on Aerodynamic Characteristics of a Pitching Delta Wing," *Journal of Aircraft*, Vol. 45, No. 6, 2008, pp. 2182–2185. DOI:10.2514/1.38925.

[54] Chakravarthy, A., Grant, D., and Lind, R., "Time-Varying Dynamics of a Micro Air Vehicle with Variable-Sweep Morphing," *Journal of Guidance, Control, and Dynamics*, Vol. 35, No. 3, 2012, pp. 890–903. DOI:10.2514/1.55078.

[55] Stanford, B., Abdulrahim, M., Lind, R., and Ifju, P., "Investigation of Membrane Actuation for Roll Control of a Micro Air Vehicle," *Journal of Aircraft*, Vol. 44, No. 3, 2007, pp. 741–749. DOI:10.2514/1.25356.

[56] Cuji, E., and Garcia, E., "Prediction of aircraft dynamics with shape changing wings," Active and Passive Smart Structures and Integrated Systems 2008, San Diego, CA.

[57] Wickenheiser, A., and Garcia, E., "Aerodynamic Modeling of Morphing Wings Using an Extended Lifting-Line Analysis," *Journal of Aircraft*, Vol. 44, No. 1, 2007, pp. 10–16. DOI:10.2514/1.18323.

[58] Gallay, S., and Laurendeau, E., "Nonlinear Generalized Lifting-Line Coupling Algorithms for Pre/Poststall Flows," *AIAA Journal*, Vol. 53, No. 7, 2015, pp. 1784–1792. DOI:10.2514/1.J053530.

[59] Mukherjee, R., and Gopalarathnam, A., "Poststall Prediction of Multiple-Lifting-Surface Configurations Using a Decambering Approach," *Journal of Aircraft*, Vol. 43, No. 3, 2006, pp. 660–668. DOI:10.2514/1.15149.

[60] Cho, J., and Cho, J., "Calculation of nonlinear aerodynamic characteristics of a wing using a 3-D panel method," *International Journal for Numerical Methods in Fluids*, Vol. 56, No. 1, 2008, pp. 23–35. DOI:10.1002/fld.1521.

[61] Sørensen, J. N., *General Momentum Theory for Horizontal Axis Wind Turbines*, Springer-Verlag, Cham, Switzerland, 2016.

[62] Dowell, E. H., and Clark, R., eds., *A modern course in aeroelasticity*, Kluwer Academic Publishers, Dordrecht ; Boston, 2004.

[63] Mueller, T. J., ed., *Fixed and Flapping Wing Aerodynamics for Micro Air Vehicle Applications*, AIAA, Reston, VA, 2001.

[64] Osborne, M. F. M., "Aerodynamics of flapping flight with application to insects," *The Journal of Experimental Biology*, Vol. 28, No. 2, 1951, pp. 221–245.

[65] Ananda, G. K., and Selig, M. S., "Stall/Post-Stall Modeling of the Longitudinal Characteristics of a General Aviation Aircraft," AIAA Atmospheric Flight Mechanics Conference, Washington, DC.

[66] Selig, M., "Modeling Full-Envelope Aerodynamics of Small UAVs in Realtime," AIAA Atmospheric Flight Mechanics Conference, Toronto, ON.

[67] Corless, R. M., and Fillion, N., *A Graduate Introduction to Numerical Methods*, Springer, Dordrecht, The Netherlands, 2013.

[68] Montgomery, R. C., and Moul, M. T., "Analysis of deep-stall characteristics of T- tailed aircraft configurations and some recovery procedures.," *Journal of Aircraft*, Vol. 3, No. 6, 1966, pp. 562–566. DOI:10.2514/3.43777.

[69] White, F. M., *Fluid mechanics*, McGraw-Hill, New York, 2016.

[70] Chattot, J.-J., and Hafez, M., *Theoretical and Applied Aerodynamics*, Springer, New York, 2015.

Chapter 4:
Variational integration

4.1. INTRODUCTION

4.1.1. Variational integration

Variational integrators represent a recent development in the study of computational mechanics [1,2]. They have several advantages over non-variational forms of time integration; most particularly, favourable energy and momentum conservation properties. The application of variational integration to the dynamics of three-dimensional rotation commonly leads to the study of Lie group variational integrators (LGVIs) [3,4], referring to the fact that pole-free rotation parameterizations such as rotation matrices or quaternions are endowed with a Lie algebra. A key aspect of LGVIs is their treatment of the rotation matrix or quaternion constraints (special orthogonality, $\mathrm{R} \in \mathrm{SO}(3)$ [5] or normalization, $\|q\| = 1$ [6]) via appropriate definition of the variational perturbations invoked in the integrator derivation.

Previous aerospace applications of LGVIs in aeronautics have been confined to systems of relatively low complexity – spacecraft uncoupled rotational dynamics, with reaction wheels or a variety of generalised forces [3,4]. The more specific class of quaternion variational integrators (QVIs) have seen even more restricted study [7]. However, in addition to their favourable conservation properties, variational integrators present an attractive prospect for flight dynamic models based on quaternions, as traditional ordinary-differential approaches are complicated by the special nature of the orientation quaternion derivative as a result of the quaternion normalisation constraint. Solutions to this either involve an additional complexity in the analysis (e.g. via analysis as a differential-algebraic equation [8,9]) or a degradation in integrator accuracy through the use of the quaternion pseudo-derivative [10] (integrating via conventional finite-difference, and periodically normalising the result [11]).

This chapter concerns the development of a quaternion variational integrator for the case study biomimetic aircraft model. This system is significantly more complex than those previously considered for quaternion variational integration, and we identify several key deficiencies in existing QVIs that limit their effectiveness when applied to the case study system. As a solution, an improved QVI is devised, based on a change of integration variables and an increase in integration order. This new approach shows particular

advantages over existing QVIs in long-timescale energy and momentum conservation, stable step size, and applicability to systems with non-conservative canonical momenta.

4.1.2. Adaptive integration

For unconstrained orientation parameterizations such as Euler angles, integration via a wide range of integrators is available, without any special considerations. Variational integrators may be devised for such systems too, after [1,2], but of particular prominence in the literature are adaptive Runge-Kutta (RK) integrators. These explicit integrators are well-established, computationally efficient, and are available at high orders of accuracy (beyond 4th order). However of particular note is the potential for many of these integrators to be used with adaptive time-stepping, either through step doubling [12], or via embedded estimates of the integrator local truncation errors [12,13]. The availability of the latter – embedded RK methods – at high integration order is perhaps the most significant of their advantages. Adaptive time-stepping reduces the requirements for system-specific oversight, maintains accuracy and stability, and maximises the integrator computational efficiency. As such, despite the difficulties associated with Euler angle orientation parameterisation, adaptive RK45 integrators in Euler angles are highly competitive with quaternion variational integrators, as will be demonstrated. Hence the additional need for an Euler angle integrator.

4.2. ADAPTIVE RK45 INTEGRATOR IN EULER ANGLES

4.2.1. System formulation in Euler angle rates

To the end of obtaining an integrator for the system Euler angles, the system dynamics are expressed in terms of the Euler angle rates. This involves a simple substitution of the relation $\boldsymbol{\omega}^{(e)} = \Omega_0 \dot{\boldsymbol{\theta}}$ (with $\dot{\boldsymbol{\theta}}$ the aircraft Euler angle rates, see Chapter 2, Section 2.5.3) into the expression for the system kinetic energy (Eq. 3.2.3-3.2.4), yielding:

$$\begin{aligned} T &= \dot{\mathbf{x}}_S^{(e),T} \mathrm{a}_{xx} \dot{\mathbf{x}}_S^{(e)} + \dot{\mathbf{x}}_S^{(e),T} \mathrm{A}_{x\theta}^{(e)} \dot{\boldsymbol{\theta}} + \dot{\boldsymbol{\theta}}^T \mathrm{A}_{\theta\theta}^{(e)} \dot{\boldsymbol{\theta}} + \dot{\mathbf{x}}_S^{(e),T} \mathbf{a}_x^{(e)} + \dot{\boldsymbol{\theta}}^T \mathbf{a}_\theta^{(e)} + \mathrm{a}_0 \,, \\ \mathrm{A}_{x\theta}^{(e)} &= \Omega_0^{(e),T} \mathrm{A}_{x\omega}^{(e)}, \qquad \mathrm{A}_{\theta\theta}^{(e)} = \Omega_0^{(e),T} \mathrm{A}_{\omega\omega}^{(e)} \Omega_0^{(e)}, \qquad \mathbf{a}_\theta^{(e)} = \Omega_0^{(e),T} \mathbf{a}_\omega^{(e)}. \end{aligned} \tag{4.2.1}$$

4.2.2. Equations of motion in Euler angles

To implement an adaptive RK45 integrator, we ultimately require a description of the system dynamics in the form of a first-order ordinary differential equation (ODE), typically nonlinear. To obtain this, the system equations of motion must be derived in the strong form; here, via the Euler-Lagrange equation [14]. Under this approach, the translational component of system equations of motion is given by:

$$\frac{d}{dt}\left(\frac{\partial T}{\partial \dot{\mathbf{x}}_S}\right) - \frac{\partial T}{\partial \mathbf{x}_S} = \mathcal{Q}_{\mathbf{x}}. \tag{4.2.2}$$

The reader may confirm that T (Eq. 4.2.1) is independent of $\mathbf{x}_S$ and thus $\partial T/\partial \mathbf{x}_S^{(e)} = 0$. To compute $\partial T/\partial \dot{\mathbf{x}}_S^{(e)}$, note the following results from matrix calculus [15]:

$$\begin{aligned} &\frac{d}{d\mathbf{x}}(\mathbf{x}^T \mathrm{M}\mathbf{x}) = (\mathrm{M} + \mathrm{M}^T)\mathbf{x}, \\ &\frac{d}{d\mathbf{x}}(\mathbf{x}^T \mathbf{v}) = \frac{d}{d\mathbf{x}}(\mathbf{v}^T \mathbf{x}) = \mathbf{v}. \end{aligned} \tag{4.3.3}$$

Here we follow denominator layout, a layout convention in which the derivatives with respect to a vector are order (in a row or column) in the manner of the denominator of the derivative. This is in apposition to numerator layout, in which the layout is derived from the numerator. Hence for $\partial T/\partial \dot{\mathbf{x}}_S^{(e)}$:

$$\frac{\partial T}{\partial \dot{\mathbf{x}}_S^{(e)}} = m\dot{\mathbf{x}}_S^{(e)} + \mathrm{A}_{x\theta}^{(e)}\dot{\boldsymbol{\theta}} + \mathbf{a}_x^{(e)}. \tag{4.2.4}$$

Computing the derivative of this expression by time we obtain:

$$\frac{d}{dt}\left(\frac{\partial T}{\partial \dot{\mathbf{x}}_S^{(e)}}\right) = m\ddot{\mathbf{x}}_S^{(e)} + \mathrm{A}_{x\theta}^{(e)}\ddot{\boldsymbol{\theta}} + \dot{\mathrm{A}}_{x\theta}^{(e)}\dot{\boldsymbol{\theta}} + \dot{\mathbf{a}}_x^{(e)}. \tag{4.2.5}$$

Here a choice exists as to how to deal with the time-derivatives of the matrix coefficients. It is most convenient to compute the time-derivatives of the coefficients via finite-difference methods (either at each point in the iteration using an increment separate from the iteration timestep, or by using data from previous timesteps). As an alternative, it is possible to differentiate them with respect to $\boldsymbol{\theta}$ (and also, θ_i) the chain rule and thus relate them to $\boldsymbol{\theta}$ and $\dot{\boldsymbol{\theta}}_i$. However, this alternative is expensive in terms of the other derivatives in $\boldsymbol{\theta}$ and θ_i that are required, and so the former approach is taken. The computation of these quantities

is discussed later in this section. In the meantime, the translational equation of motion is thus:

$$m\ddot{\mathbf{x}}_S^{(e)} + \mathrm{A}_{x\theta}^{(e)}\ddot{\boldsymbol{\theta}} + \dot{\mathrm{A}}_{x\theta}^{(e)}\dot{\boldsymbol{\theta}} + \dot{\mathbf{a}}_x^{(e)} = \mathcal{Q}_{\mathbf{x}}. \tag{4.2.6}$$

The rotation component of the Euler-Lagrange equation applied to this system is:

$$\frac{d}{dt}\left(\frac{\partial T}{\partial \dot{\boldsymbol{\theta}}}\right) - \frac{\partial T}{\partial \boldsymbol{\theta}} = \mathcal{Q}_{\boldsymbol{\theta}}. \tag{4.2.7}$$

In the first instance the total kinetic energy is differentiated by two terms, $\boldsymbol{\theta}$ and $\dot{\boldsymbol{\theta}}$. For $\partial T/\partial\dot{\boldsymbol{\theta}}$ this yields:

$$\frac{\partial T}{\partial \dot{\boldsymbol{\theta}}} = \mathrm{A}_{x\theta}^{(e),T}\dot{\mathbf{x}}_S^{(e)} + \left(\mathrm{A}_{\theta\theta}^{(e)} + \mathrm{A}_{\theta\theta}^{(e),T}\right)\dot{\boldsymbol{\theta}} + \mathbf{a}_\theta^{(e)}. \tag{4.2.8}$$

Computing $\partial T/\partial\boldsymbol{\theta}$ is more difficult, as all the matrix coefficients bar a_{xx} are strongly nonlinear function of $\boldsymbol{\theta}$:

$$\begin{aligned}\frac{\partial T}{\partial \boldsymbol{\theta}} = \frac{\partial}{\partial \boldsymbol{\theta}}\left(\dot{\mathbf{x}}_S^{(e),T}\mathrm{A}_{x\theta}^{(e)}\dot{\boldsymbol{\theta}}\right) + \frac{\partial}{\partial \boldsymbol{\theta}}\left(\dot{\mathbf{x}}_S^{(e),T}\mathbf{a}_x^{(e)}\right) + \frac{\partial}{\partial \boldsymbol{\theta}}\left(\dot{\boldsymbol{\theta}}^T\mathrm{A}_{\theta\theta}^{(e)}\dot{\boldsymbol{\theta}}\right) + \frac{\partial}{\partial \boldsymbol{\theta}}\left(\dot{\boldsymbol{\theta}}^T\mathbf{a}_\theta^{(e)}\right) \\ + \frac{\partial}{\partial \boldsymbol{\theta}}(\mathrm{a}_0).\end{aligned} \tag{4.2.9}$$

Three of these derivatives can be expressed via simple matrix-operator expressions [15]:

$$\begin{aligned}\frac{\partial}{\partial \boldsymbol{\theta}}\left(\dot{\mathbf{x}}_S^{(e),T}\mathbf{a}_x^{(e)}\right) &= \frac{\partial \mathbf{a}_x^{(e)}}{\partial \boldsymbol{\theta}}\dot{\mathbf{x}}_S = \mathrm{B}_x^{(e)}\dot{\mathbf{x}}_S^{(e)}, \\ \frac{\partial}{\partial \boldsymbol{\theta}}\left(\dot{\boldsymbol{\theta}}^T\mathbf{a}_\theta^{(e)}\right) &= \frac{\partial \mathbf{a}_\theta^{(e)}}{\partial \boldsymbol{\theta}}\dot{\boldsymbol{\theta}} = \mathrm{B}_\theta^{(e)}\dot{\boldsymbol{\theta}}, \\ \frac{\partial}{\partial \boldsymbol{\theta}}(\mathrm{a}_0) &= \nabla_\theta \mathrm{a}_0 = \mathbf{b}_0,\end{aligned} \tag{4.2.10}$$

where the derivatives $\partial\mathbf{a}_x^{(e)}/\partial\boldsymbol{\theta}$ and $\partial\mathbf{a}_\theta^{(e)}/\partial\boldsymbol{\theta}$ are laid out according to denominator layout conventions, that is [15]:

$$\left(\frac{\partial \mathbf{x}}{\partial \mathbf{y}}\right)_{ij} = \frac{\partial x_j}{\partial y_i} = \mathrm{J}_{\mathbf{xy}}^T, \tag{4.2.11}$$

where $\mathrm{J}_{\mathbf{xy}}$ is the Jacobian matrix of $\mathbf{x}$ with respect to $\mathbf{y}$. The two other derivatives are more difficult, as they require the derivative of a matrix with respect to a vector; a quantity that is in general only expressible as a higher-order tensor. Lacking the framework for expressing

the multiplication of higher-order tensors with vectors, these tensor derivative terms are defined explicitly as:

$$\mathbf{v}_{x\theta}^{(e)} = \frac{\partial}{\partial \boldsymbol{\theta}}\left(\dot{\mathbf{x}}_S^{(e),T} \mathrm{A}_{x\theta}^{(e)} \dot{\boldsymbol{\theta}}\right) = \begin{bmatrix} \dot{\mathbf{x}}_S^T \dfrac{\partial \mathrm{A}_{x\theta}^{(e)}}{\partial \theta} \dot{\boldsymbol{\theta}} \\ \dot{\mathbf{x}}_S^T \dfrac{\partial \mathrm{A}_{x\theta}^{(e)}}{\partial \psi} \dot{\boldsymbol{\theta}} \\ \dot{\mathbf{x}}_S^T \dfrac{\partial \mathrm{A}_{x\theta}^{(e)}}{\partial \phi} \dot{\boldsymbol{\theta}} \end{bmatrix},$$

$$\mathbf{v}_{\theta\theta}^{(e)} = \frac{\partial}{\partial \boldsymbol{\theta}}\left(\dot{\boldsymbol{\theta}}^T \mathrm{A}_{\theta\theta}^{(e)} \dot{\boldsymbol{\theta}}\right) = \begin{bmatrix} \dot{\boldsymbol{\theta}}^T \dfrac{\partial \mathrm{A}_{\theta\theta}^{(e)}}{\partial \theta} \dot{\boldsymbol{\theta}} \\ \dot{\boldsymbol{\theta}}^T \dfrac{\partial \mathrm{A}_{\theta\theta}^{(e)}}{\partial \psi} \dot{\boldsymbol{\theta}} \\ \dot{\boldsymbol{\theta}}^T \dfrac{\partial \mathrm{A}_{\theta\theta}^{(e)}}{\partial \phi} \dot{\boldsymbol{\theta}} \end{bmatrix}. \tag{4.2.12}$$

Thus:

$$\frac{\partial T}{\partial \boldsymbol{\theta}} = \mathbf{v}_{x\theta}^{(e)} + \mathrm{B}_x^{(e)} \dot{\mathbf{x}}_S^{(e)} + \mathbf{v}_{\theta\theta}^{(e)} + \mathrm{B}_\theta^{(e)} \dot{\boldsymbol{\theta}} + \mathbf{b}_0. \tag{4.2.13}$$

Finally, differentiating $\partial T / \partial \dot{\boldsymbol{\theta}}$ with respect to time, we obtain:

$$\frac{d}{dt}\left(\frac{\partial T}{\partial \dot{\boldsymbol{\theta}}}\right) = \mathrm{A}_{x\theta}^{(e),T} \ddot{\mathbf{x}}_S + \dot{\mathrm{A}}_{x\theta}^{(e),T} \dot{\mathbf{x}}_S + \left(\mathrm{A}_{\theta\theta}^{(e)} + \mathrm{A}_{\theta\theta}^{(e),T}\right)\ddot{\boldsymbol{\theta}} + \left(\dot{\mathrm{A}}_{\theta\theta}^{(e)} + \dot{\mathrm{A}}_{\theta\theta}^{(e),T}\right)\dot{\boldsymbol{\theta}} + \dot{\mathbf{a}}_\theta^{(e)}, \tag{4.2.14}$$

and the rotational equation of motion is:

$$\begin{aligned} \mathrm{A}_{x\theta}^{(e)} \ddot{\mathbf{x}}_S^{(e)} + \left(\dot{\mathrm{A}}_{x\theta}^{(e)} - \mathrm{B}_x^{(e)}\right)\dot{\mathbf{x}}_S^{(e)} + \left(\mathrm{A}_{\theta\theta}^{(e)} + \mathrm{A}_{\theta\theta}^{(e),T}\right)\ddot{\boldsymbol{\theta}} + \left(\dot{\mathrm{A}}_{\theta\theta}^{(e)} + \dot{\mathrm{A}}_{\theta\theta}^{(e),T} - \mathrm{B}_\theta^{(e)}\right)\dot{\boldsymbol{\theta}} \\ - \mathbf{v}_{x\theta}^{(e)} - \mathbf{v}_{\theta\theta}^{(e)} + \dot{\mathbf{a}}_\theta^{(e)} - \mathbf{b}_0 = \mathcal{Q}_{\boldsymbol{\theta}}. \end{aligned} \tag{4.2.15}$$

The two equations of motion are defined, but the coefficient time-derivative terms remain undefined: $\dot{\mathrm{A}}_{\theta\theta}^{(e)}$, $\dot{\mathrm{A}}_{x\theta}^{(e)}$, $\dot{\mathbf{a}}_\theta^{(e)}$ and $\dot{\mathbf{a}}_x^{(e)}$. Computing these is not trivial, as contributions arise both from the aircraft's total motion ($\boldsymbol{\theta}$) and the wing motion ($\dot{\boldsymbol{\theta}}_i$), and therefore the use of the chain rule introduces many subsidiary derivatives. It is simpler to estimate these derivatives directly via a finite-difference in time. For all the relevant coefficients, $\mathbf{p} \in \left\{\mathrm{A}_{\theta\theta}^{(e)}, \mathrm{A}_{x\theta}^{(e)}, \mathbf{a}_\theta^{(e)}, \mathbf{a}_x^{(e)}\right\}$, and some small time increment, Δt, $\dot{\mathbf{p}}(t)$ is given as:

$$\dot{\mathbf{p}}(t) = \frac{\mathbf{p}(t+\Delta t) - \mathbf{p}(t)}{\Delta t}, \tag{4.2.16}$$

with:

$$\mathbf{p}(t+\Delta t) = \mathbf{p}(\theta + \Delta\theta, \theta_{wl} + \Delta\theta_{wl}, \theta_{wr} + \Delta\theta_{wr}), \tag{4.2.17}$$

and

$$\begin{aligned} \Delta\theta &= \Delta t\dot{\theta}, \\ \Delta\theta_{wl} &= \Delta t\dot{\theta}_{wr} + \frac{1}{2}\Delta t\ddot{\theta}_{wr}, \\ \Delta\theta_{wr} &= \Delta t\dot{\theta}_{wl} + \frac{1}{2}\Delta t\ddot{\theta}_{wl}. \end{aligned} \tag{4.2.18}$$

For these relations, the increment $\Delta t = 10^{-10}$ is taken universally in this work.

The equations of motion for the case study system are thus fully defined. They may be represented together as a single second-order nonlinear ODE:

$$\mathrm{A}_{qq}\ddot{\mathbf{q}} + \mathrm{A}_q\dot{\mathbf{q}} + \mathbf{k} = \mathbf{f}, \tag{4.2.19}$$

with:

$$\begin{aligned} \mathrm{A}_{qq} &= \begin{bmatrix} m\mathrm{E}_3 & \mathrm{A}_{x\theta} \\ \mathrm{A}_{x\theta} & \mathrm{A}_{\theta\theta} + \mathrm{A}_{\theta\theta}^T \end{bmatrix}, \\ \mathrm{A}_q &= \begin{bmatrix} 0 & \dot{\mathrm{A}}_{\mathcal{S},x\theta} \\ \dot{\mathrm{A}}_{x\theta} + \mathrm{B}_x & \dot{\mathrm{A}}_{\mathcal{S},\theta\theta} + \dot{\mathrm{A}}_{\mathcal{S},\theta\theta}^T + \mathrm{B}_{\mathcal{S},\theta} \end{bmatrix}, \\ \mathbf{k} &= \begin{bmatrix} \dot{\mathbf{a}}_{\mathcal{S},x} \\ \mathbf{v}_{\mathcal{S},x\theta} + \mathbf{v}_{\mathcal{S},\theta\theta} + \dot{\mathbf{a}}_{\mathcal{S},\theta} + \mathbf{b}_{\mathcal{S},0} \end{bmatrix}, \\ \mathbf{f} &= \begin{bmatrix} \mathcal{Q}_{\mathbf{x}} \\ \mathcal{Q}_{\theta} \end{bmatrix}, \qquad \mathbf{q} = \begin{bmatrix} \mathbf{x}_S \\ \theta \end{bmatrix}. \end{aligned} \tag{4.2.20}$$

To enable integration by standard solvers, the system is transformed into a first-order nonlinear ODE – a process which is without approximation:

$$\dot{\mathbf{z}} = \mathbf{F}_{\mathrm{z}}(t, \mathbf{z}) = \mathrm{B}_1^{-1}(\mathbf{F} - \mathrm{B}_0\mathbf{z}), \tag{4.2.21}$$

with

$$\begin{aligned} \mathrm{B}_1 &= \begin{bmatrix} \mathrm{A}_{qq} & 0_{6\times6} \\ 0_{6\times6} & \mathrm{E}_6 \end{bmatrix}, \quad \mathbf{F} = \begin{bmatrix} \mathbf{f} - \mathbf{k} \\ 0_{6\times1} \end{bmatrix}, \\ \mathrm{B}_0 &= \begin{bmatrix} \mathrm{A}_q & 0_{6\times6} \\ -\mathrm{E}_6 & 0_{6\times6} \end{bmatrix}, \quad \mathbf{z} = \begin{bmatrix} \dot{\mathbf{q}} \\ \mathbf{q} \end{bmatrix}, \end{aligned} \tag{4.2.22}$$

This completes the dynamic analysis of the case study system. These equations will now be discretised in readiness for simulation.

4.2.3. Adaptive Runge-Kutta 4(5) integration

Eq. 4.2.21 may be integrated directly via standard first-order ODE solvers. We utilise an Adaptive Runge-Kutta 4(5) (RK45) method, the Dormand-Prince method [13,16]. This integrator is fourth-order accurate, with an embedded fifth-order method providing a first-order estimation of the local truncation error. By constraining the local truncation error with a tolerance, the integrator step size can be adapted to fulfil the local truncation error constraint with the maximum possible step size.

A single step of Runge-Kutta-type integration may be expressed in general terms as:

$$\mathbf{z}_{i+1} = \mathbf{z}_i + h\sum_{n=1}^{N} b_n \mathbf{k}_n$$

$$\begin{aligned}
\mathbf{k}_1 &= \mathbf{F}_{\mathrm{z}}(t_n, \mathbf{z}_n) \\
\mathbf{k}_2 &= \mathbf{F}_{\mathrm{z}}\left(t_n + hc_2, \mathbf{z}_n + ha_{2,1}\mathbf{k}_1\right) \\
\mathbf{k}_3 &= \mathbf{F}_{\mathrm{z}}\left(t_n + hc_3, \mathbf{z}_n + h\left(a_{3,1}\mathbf{k}_1 + a_{3,2}\mathbf{k}_2\right)\right)
\end{aligned} \tag{4.2.23}$$

and in general:

$$\mathbf{k}_n = \mathbf{F}_{\mathrm{z}}\left(t_n + hc_n, \mathbf{z}_n + h\sum_{m=1}^{n-1} a_{n,m}\mathbf{k}_m\right)$$

where h is the current integrator step size, N the number of internal steps, and with sets of coefficients $\{a_{i,j}\}$, $\{b_{i,j}\}$, $\{c_i\}$. These coefficients may be presented and understood in the form of a Butcher tableau [17]. For the Dormand-Prince method [13]:

c_1	**0**	$a_{1,j}$:	0						
c_2	**1/5**	$a_{2,j}$:	1/5	0					
⋮	**3/10**	⋮	3/40	9/40	0				
	4/5		44/45	−56/15	32/9	0			
	8/9		19372/6561	−25360/2187	64448/6561	−212/729	0		
⋮	**1**	⋮	9017/3168	−355/33	46732/5247	49/176	−5103/18656	0	
c_n	**1**	$a_{n,j}$:	35/384	0	500/1113	125/192	−2187/6784	11/84	0
			$a_{i,1}$	$a_{i,2}$	⋯			⋯	$a_{i,n}$
(4th-order)		b_i:	35/384	0	500/1113	125/192	−2187/6784	11/84	0
(5th-order)		b_i:	5179/57600	0	7571/16695	393/640	−92097/339200	187/2100	1/40
			b_1	b_2	⋯			⋯	b_n

(4.2.24)

The local truncation error (LTE) may then be estimated as the norm of the difference between the 4th- and 5th-order estimates of $\mathbf{z}_{i+1}$:

$$e_{i+1} = \left\| \mathbf{z}_{i+1}^{(4\text{th})} - \mathbf{z}_{i+1}^{(5\text{th})} \right\|. \tag{4.2.25}$$

This error can be constrained in a variety of ways; we use the built-in implementation of this method in MATLAB, which uses the criterion [16]:

$$e_{i+1} \leq r \left\| \mathbf{z}_{i+1}^{(4\text{th})} \right\| + a_i \tag{4.2.26}$$

where r is a relative tolerance and a_i a set of absolute tolerances. The method of adapting step based on the error value and this criterion is relatively complex [12] and is not detailed here.

4.2.4. Pole-switching

The integrator so far presented suffers from gimbal lock at aircraft pitch values of $\theta = \pm 90°$, as a result of the singularities in the Euler angle representation at these orientations. This terminates the simulation. A practical solution to this difficulty may be found in changing the location of these singularities when the simulation nears them, by switching to an alternate Euler angle representation [18–20]. We choose a representation with singularities at the original $\psi = \pm 90°$. Rather than defining another kinematic framework and switching between the two, the existing framework is utilised, with the direction of gravitational force modified from $[0,0,-1]^T$ to $[0,-1,0]^T$ and with a change of the system location in the Euler angle space.

Denoting the existing Euler angle representation (poles $\theta = \pm 90°$) as E, and the switched basis (poles $\psi = \pm 90°$) as E', the transformation between these bases may be defined as per Eq. 4.2.27-4.2.28. Note that the identification formulae for ψ / ψ' etc. are common to both transformation directions – they are simply one of many approaches to identify the Euler angles from their unit vectors $\hat{\boldsymbol{\imath}}_b^{(e)}$ etc. as given in Chapter 2, Sections 2.4-2.5. The other component of the basis transformation procedure involves simply transforming all variables in E to E' or vice versa via the transformation matrix $P_{E'/E}$.

$E \to E'$:

$$P_{E'/E} = \begin{bmatrix} 1 & 0 & 0 \\ 0 & 0 & 1 \\ 0 & -1 & 0 \end{bmatrix},$$

$$\begin{aligned}
&\mathbf{x}_S^{(e')} = P_{E'/E}\mathbf{x}_S^{(e)}, \qquad \dot{\mathbf{x}}_S^{(e')} = P_{E'/E}\dot{\mathbf{x}}_S^{(e)}, \\
&\hat{\boldsymbol{\imath}}_b^{(e')} = P_{E'/E}\hat{\boldsymbol{\imath}}_b^{(e)}, \qquad \hat{\mathbf{j}}_b^{(e')} = P_{E'/E}\hat{\mathbf{j}}_b^{(e)}, \\
&\boldsymbol{\omega}^{(e')} = P_{E'/E}\boldsymbol{\omega}^{(e)}, \\
&\psi' = -\tan_2^{-1}\left(\hat{\imath}_{b,2}^{(e')}, \hat{\imath}_{b,1}^{(e')}\right), \\
&\theta' = \tan_2^{-1}\left(\hat{\imath}_{b,3}^{(e')}\cos\psi', \hat{\imath}_{b,1}^{(e')}\right), \\
&\phi' = \cos^{-1}\left(\hat{\mathbf{r}}_b^{(e')} \cdot \hat{\mathbf{j}}_b^{(e')}\right), \\
&\qquad\qquad \text{with } \hat{\mathbf{r}}_b^{(e')} = [\sin\psi', \cos\psi', 0]^T, \\
&\dot{\theta}' = \Omega_0^{(e'),-1}\boldsymbol{\omega}^{(e')}, \\
&\qquad\qquad \text{with } \Omega_0^{(e')} = -\left[\hat{\mathbf{r}}_b^{(e')}, \hat{\mathbf{k}}_{e'}^{(e')}, \hat{\boldsymbol{\imath}}_b^{(e')}\right];
\end{aligned} \tag{4.2.27}$$

and;

$E' \to E$:

$$\begin{aligned}
&\mathbf{x}_S^{(e)} = P_{E'/E}^T\mathbf{x}_S^{(e')}, \qquad \dot{\mathbf{x}}_S^{(e)} = P_{E'/E}^T\dot{\mathbf{x}}_S^{(e')}, \\
&\hat{\boldsymbol{\imath}}_b^{(e)} = P_{E'/E}^T\hat{\boldsymbol{\imath}}_b^{(e')}, \qquad \hat{\mathbf{j}}_b^{(e)} = P_{E'/E}^T\hat{\mathbf{j}}_b^{(e')}, \\
&\boldsymbol{\omega}^{(e)} = P_{E'/E}^T\boldsymbol{\omega}^{(e')}, \\
&\psi = -\tan_2^{-1}\left(\hat{\imath}_{b,2}^{(e)}, \hat{\imath}_{b,1}^{(e)}\right), \\
&\theta = \tan_2^{-1}\left(\hat{\imath}_{b,3}^{(e)}\cos\psi, \hat{\imath}_{b,1}^{(e)}\right), \\
&\phi = \cos^{-1}\left(\hat{\mathbf{r}}_b^{(e)} \cdot \hat{\mathbf{j}}_b^{(e)}\right), \\
&\qquad\qquad \text{with } \hat{\mathbf{r}}_b^{(e)} = [\sin\psi, \cos\psi, 0]^T, \\
&\dot{\theta} = \Omega_0^{(e),-1}\boldsymbol{\omega}^{(e)}, \\
&\qquad\qquad \text{with } \Omega_0^{(e)} = -\left[\hat{\mathbf{r}}_b^{(e)}, \hat{\mathbf{k}}_{e'}^{(e)}, \hat{\boldsymbol{\imath}}_b^{(e)}\right].
\end{aligned} \tag{4.2.28}$$

Within the adaptive RK45 integrator, a basis transformation test occurs at the end of each integrator step. Wrapping the pitch angle to the interval $[-\pi, \pi]$,

$$\hat{\theta} = \theta - 2\pi \left\lfloor \frac{\theta + \pi}{2\pi} \right\rfloor \text{ rad}, \tag{4.2.29}$$

its proximity to $\pm\pi/2$ is tested:

$$\left| \hat{\theta} - \frac{\pi}{2} \right| \leq \theta_{\text{crit}}. \tag{4.2.30}$$

Note that this applies identically to θ'. θ_{crit} is measures the angular proximity of the system to the pole; a standard tolerance of $\theta_{\text{crit}} = 0.4$ rad is set. Upon failure of the criterion, the system is transformed to the alternate basis ($E \to E'$, $E' \to E$) and integration resumes. The only possibility of the integrator reaching gimbal lock is if the step starts outside θ_{crit} and then progresses to the pole ($\pm$ 90°) within the space of a single integrator step. With proper exception handling, however, this should trigger a failure of the local truncation error criterion – leading to a smaller step size, successful step integration, and then a transformation of basis before gimbal lock occurs in the following steps.

The location of basis transformation events is stored through the integration process, and in post-processing the system orientation results can be transformed to a consistent basis (typically E) via the transformations of Eq. 4.2.27-4.2.28. This leads to an integrator in Euler angles, with an output in a consistent frame of reference, which does not suffer from gimbal lock. We will use this integrator both to validate the quaternion integrators presented next, and, based on its advantages and disadvantages relative to these integrators, for simulation of the case study biomimetic aircraft.

4.3. LEFT-RECTANGLE QVI FOR UNCOUPLED ROTATION

4.3.1. Proxy generalised derivatives

As an initial test system, following Manchester and Peck [7], the free rotation of a rigid body in the absence of any translation-rotation coupling is considered. The Lagrangian L and kinetic energy T of such a system are equivalent, and are given by:

$$L\left(\boldsymbol{\omega}^{(b)}\right) = T\left(\boldsymbol{\omega}^{(b)}\right) = \frac{1}{2}\boldsymbol{\omega}^{(b),T}\mathrm{I}^{(b)}\boldsymbol{\omega}^{(b)}, \tag{4.3.1}$$

where $\boldsymbol{\omega}^{(b)}$ is the system angular velocity and $\mathrm{I}^{(b)}$ the system rotational inertia, both in the body-fixed reference frame. As in [7], the system dynamics are formulated using the principle of least action, asserting that the system action functional is stationary w.r.t to first-order perturbations. For a general system this may be expressed:

$$\delta S + \delta W = \int_{t_0}^{t_N} \delta L + \mathbf{F} \cdot \delta \mathbf{r}\, dt = 0, \tag{4.3.2}$$

for generalised forces $\mathbf{F}$ and generalised coordinates $\mathbf{r}$.

To undertake a variational analysis of this system, a set of generalised coordinates and associated time-derivative variables are required. In a conventional variational analysis, e.g. with translational dynamics, these would be related directly via the time differentiation operator [1,2]. However, in the case of a quaternion generalised coordinate q (defined under the Hamilton convention [6]), direct time differentiation is unsuitable: $\dot{q}$ is an underconstrained parameterisation of the orientation rate, requiring an additional constraint in the integrator inter-step equations derived from $\|q\| = 1$. Moreover the q-$\dot{q}$ pairing introduces a dependency of the kinetic energy on q via $\boldsymbol{\omega}^{(b)}$:

$$\boldsymbol{\omega}^{(b)} = 2q^{\dagger} \otimes \dot{q}, \tag{4.3.3}$$

complicating the variational analysis by introducing further terms in the chain rule expansion of δL.

Manchester and Peck [7] overcame this difficulty by formulating the Lagrangian in a discrete proxy derivative variable (or, quasi-velocity [21]) f_k, representing the rotation quaternion between adjacent discrete timesteps:

$$q_{k+1} = q_k \otimes \mathrm{f}_k. \tag{4.3.4}$$

Under a finite difference approximation for $\dot{q}$, f_k may be related to the discrete angular velocity $\boldsymbol{\omega}_k^{(b)}$:

$$\boldsymbol{\omega}_k^{(b)} = 2q_k^{\dagger} \otimes \dot{q}_k = \frac{2}{h} q_k^{\dagger} \otimes (q_{k+1} - q_k) = \frac{2}{h}(\mathrm{f}_k - 1), \tag{4.3.5}$$

leading to a Lagrangian of similar form, but accounting for the fact that f_k is full quaternion ($\mathrm{f}_k = 1 + ai + bj + ck$), whereas $\boldsymbol{\omega}^{(b)}$ is imaginary (i.e. a 3-vector):

$$L(\mathrm{f}_k) = \frac{1}{2}\mathrm{f}_k^T \begin{bmatrix} 0 & 0 \\ 0 & \mathrm{I}_k^{(b)} \end{bmatrix} \mathrm{f}_k. \tag{4.3.6}$$

While this approach solves the immediate problems associated with $\dot{q}$, it introduces a few others. The fact that f_k is full quaternion means that it also generates an overconstrainted inter-step equation, which must be parameterised further with a nonphysical variable ϕ_k, introducing additional complexity into the inter-step equations and the analysis process. This parameterization also restricts the maximum step size [7].

As a novel alternative to the approach of Manchester and Peck [7], we derive an integrator using $\boldsymbol{\omega}^{(b)}$ directly as a proxy generalised derivative. While $\boldsymbol{\omega}^{(b)}$ has a slightly more complex relation with the q (Eq. 4.3.3), the system Lagrangian assumes a convenient form (Eq. 4.3.1) and the parameterisation has direct physical relevance. We will show that this leads to leads to computational savings and increased integrator stability.

4.3.2. Integrator derivation

In the discrete mechanics framework of [1,2] Eq. 4.3.6 may be approximated with left-rectangle integration:

$$\delta S + \delta W = h\sum_{k=1}^{N-1} \delta L_k + \mathbf{F}_k \cdot \delta \mathbf{r}_k = 0. \tag{4.3.7}$$

The variational derivative of L_k, δL_k, is defined with reference to first-order perturbations in the orientation (q_k). Following [7], q_k is subjected to a continuous norm-preserving perturbation defined via the quaternion exponential [6];

$$q_k^{\epsilon} = q_k \otimes \exp\left(\epsilon \boldsymbol{\eta}_k^{(b)}\right) \cong q_k + \delta q_k + \mathcal{O}(\epsilon^2) = q_k + \epsilon q_k \otimes \boldsymbol{\eta}_k^{(b)} + \mathcal{O}(\epsilon^2), \tag{4.3.8}$$

where $\boldsymbol{\eta}_k^{(b)}$ represents a perturbative angular velocity axis in the body-fixed frame; that is, the axis around which the system will be perturbed by a small angle. Under a first-order (two step) approximation, the discrete analogue of Eq. 4.3.3 and its corresponding variational derivative may be expressed:

$$\begin{aligned} \boldsymbol{\omega}_k^{(b)} &= \frac{2}{h} q_k^{\dagger} \otimes (q_{k+1} - q_k), \\ \delta\boldsymbol{\omega}_k^{(b)} &= \boldsymbol{\omega}_k^{(b)} \otimes \boldsymbol{\eta}_{k+1}^{(b)} - \boldsymbol{\eta}_k^{(b)} \otimes \boldsymbol{\omega}_k^{(b)} + \frac{2}{h}\left(\boldsymbol{\eta}_{k+1}^{(b)} - \boldsymbol{\eta}_k^{(b)}\right). \end{aligned} \tag{4.3.9}$$

Using the results for the expansion of the quaternion product into dot and scalar products [6], and the mixed product property, δL_k is obtained:

$$\begin{aligned}\delta L_k &= \frac{\partial L_k}{\partial \boldsymbol{\omega}_k^{(b)}} \cdot \delta \boldsymbol{\omega}_k^{(b)} = \mathrm{I}_k^{(b)} \cdot \delta \boldsymbol{\omega}_k^{(b)} \\ &= \left(\frac{2}{h}\mathrm{I}\boldsymbol{\omega}_k^{(b)} - \boldsymbol{\omega}_k^{(b)} \times \mathrm{I}\boldsymbol{\omega}_k^{(b)}\right) \cdot \boldsymbol{\eta}_{k+1}^{(b)} - \left(\frac{2}{h}\mathrm{I}\boldsymbol{\omega}_k^{(b)} + \boldsymbol{\omega}_k^{(b)} \times \mathrm{I}\boldsymbol{\omega}_k^{(b)}\right) \cdot \boldsymbol{\eta}_k^{(b)},\end{aligned} \tag{4.3.10}$$

Utilizing the expression for quaternion generalised force and virtual work in [7]:

$$\mathbf{F}_k \cdot \delta \mathbf{r}_k = \boldsymbol{\mathcal{Q}}_{q,k} \cdot \delta q_k = \boldsymbol{\tau}_k^{(b)} \cdot \boldsymbol{\eta}_k^{(b)}, \tag{4.3.11}$$

the inter-step integrator relation is obtained:

$$\mathrm{I}\boldsymbol{\omega}_k^{(b)} + \frac{1}{2}h\boldsymbol{\omega}_k^{(b)} \times \mathrm{I}\boldsymbol{\omega}_k^{(b)} = \mathrm{I}\boldsymbol{\omega}_{k-1}^{(b)} - \frac{1}{2}h\boldsymbol{\omega}_{k-1}^{(b)} \times \mathrm{I}\boldsymbol{\omega}_{k-1}^{(b)} + h\boldsymbol{\tau}_k^{(b)}. \tag{4.3.12}$$

This inter-step relation can be interpreted as a momentum balance, via the application of the two discrete Legendre transforms to L_k, as per Marsden and West [1]:

$$\begin{gathered}\mathbf{p}_k^+ = \mathbf{p}_k^- + h\boldsymbol{\tau}_k^{(b)}, \\ \mathbf{p}_k^+ = \mathrm{I}\boldsymbol{\omega}_k^{(b)} + \frac{1}{2}h\boldsymbol{\omega}_k^{(b)} \times \mathrm{I}\boldsymbol{\omega}_k^{(b)}, \qquad \mathbf{p}_k^- = \mathrm{I}\boldsymbol{\omega}_{k-1}^{(b)} - \frac{1}{2}h\boldsymbol{\omega}_{k-1}^{(b)} \times \mathrm{I}\boldsymbol{\omega}_{k-1}^{(b)},\end{gathered} \tag{4.3.13}$$

where $\mathbf{p}_k^+$ and $\mathbf{p}_k^-$ represent the momentum at step k computed in the bracket $[k, k+1]$ or $[k-1, k]$ respectively. It follows that a momentum-conserving estimate of the local angular velocity, $\boldsymbol{\omega}_{\mathrm{cons.},k}^{(b)}$, can be obtained from the definition of momentum in continuous time, $\mathbf{p} = \mathrm{I}\boldsymbol{\omega}^{(b)}$:

$$\boldsymbol{\omega}_{\mathrm{cons.},k}^{(b)} = \mathrm{I}^{-1}\mathbf{p}_k^+ = \mathrm{I}^{-1}\mathbf{p}_k^-. \tag{4.3.14}$$

This estimate is a key factor in the excellent conservation properties of the integrator; note however that it is a post-processing result and does not overwrite $\boldsymbol{\omega}_k^{(b)}$. Finally, Eq. 4.3.13 can be solved at each step via Newton's method with an analytical Jacobian:

$$\begin{gathered}\boldsymbol{\omega}_{k,i+1}^{(b)} = \boldsymbol{\omega}_{k,i}^{(b)} + \mathrm{J}_{k,i}^{-1}\left(\mathbf{p}_{k,i}^+ - \mathbf{p}_k^- - h\boldsymbol{\tau}_k^{(b)}\right), \\ \mathbf{p}_{k,i}^+ = \mathrm{I}\boldsymbol{\omega}_{k,i}^{(b)} + \frac{1}{2}h\boldsymbol{\omega}_{k,i}^{(b)} \times \mathrm{I}\boldsymbol{\omega}_{k,i}^{(b)}, \qquad \mathrm{J}_{k,i} = \mathrm{I} + \frac{1}{2}h\left(\left[\boldsymbol{\omega}_{k,i}^{(b)}\right]_\times \mathrm{I} + \left[\mathrm{I}\boldsymbol{\omega}_{k,i}^{(b)}\right]_\times\right),\end{gathered} \tag{4.3.15}$$

This inter-step equation is formulated directly in the angular velocity variable ($\boldsymbol{\omega}_k^{(b)}$), in contrast to previous integrators [7,22] which have used the discrete quaternion rotation

$\mathrm{f}_k = q_k^{\dagger} q_{k+1}$ as the proxy generalised velocity – this generates a constrained integrator equation, requiring further parameterization by the nonphysical variable ϕ_k [7,22]. The use of $\boldsymbol{\omega}_k^{(b)}$ simplifies both the analysis process and the integrator inter-step equation, yielding a more computational efficient integrator. The orientation quaternion can be integrated directly from $\boldsymbol{\omega}_k^{(b)}$; under the assumption of a constant $\boldsymbol{\omega}^{(b)}$ across the step interval (k, $k+1$), $q_{k+1}$is given by [6]:

$$q_{k+1} = q_k \otimes \exp\left(\frac{1}{2} h \boldsymbol{\omega}_k^{(b)}\right). \tag{4.3.16}$$

4.3.3. Numerical experiments

Figure 4.3.1 demonstrates this integrator applied to the freely-rotating system considered by Manchester and Peck [7] ($\mathrm{I} = \mathrm{diag}[1,2,3]$, $\boldsymbol{\omega}_{t=0}^{(b)} = [\pi/10\,, \pi/6\,, \pi/8]^T$, $q_{t=0} = [1,0,0,0]$), with $h = 0.05\,\mathrm{s}$. The results are compared to the QVI in ϕ_k and benchmark adaptive RK45 integrator of Manchester and Peck [7]. The latter is formulated quaternions, and utilised the quaternion pseudo-derivative with periodic normalisation – it is not equivalent to the RK45 integrator presented in Section 4.2. Key aspects of the integrator performance are the energy conservation error $e_{L,k} = \max_{i \le k}(|L_k - L_1|/L_1)$, $L_k = \boldsymbol{\omega}_{\mathrm{cons.},k}^{(b),T} \mathbf{p}_k$, and the momentum conservation error $e_{p,k} = \max_{i \le k}(\|\mathbf{p}_k - \mathbf{p}_1\|/\|\mathbf{p}_1\|)$. Also included are a representative section of $\boldsymbol{\omega}^{(b)}(t)$ (the results from all solvers are visually identical), the wall-clock computation times (using identical implementations in code), and values of $e_{L,k}$ and $e_{p,k}$ computed with only the step data (and not $\mathbf{p}_k$ or $\boldsymbol{\omega}_{\mathrm{cons.},k}^{(b)}$):

$$\begin{aligned} \mathbf{p}_{\mathrm{non-cons.},k} &= \mathrm{I}\boldsymbol{\omega}_k^{(b)}, \\ L_{\mathrm{non-cons.},k} &= \boldsymbol{\omega}_k^{(b),T} \mathrm{I} \boldsymbol{\omega}_k^{(b)}. \end{aligned} \tag{4.3.17}$$

These e-values simulate the effect of applying these integrators to symmetry-breaking systems in which the canonical momenta are not conserved, and Eq. 4.3.12 ceases to represent a symmetric momentum balance, due to a dependency of the kinetic energy on the generalised coordinates. The case study biomimetic aircraft is one such system; it is considered in Sections 4.4-4.5.

Several points may be noted. The long-timescale conservation properties of both integrators are excellent, significantly outperforming the RK45 integrator; and this has an effect on the accuracy of the solution in $\boldsymbol{\omega}^{(b)}$. The QVI in $\boldsymbol{\omega}_k^{(b)}$ is c. 30% more efficient than the form in $\boldsymbol{\phi}_k$ in terms of wall-clock computation time, however, it does show a small oscillatory momentum error, here of relative amplitude c. 10^{-4}. This oscillation is stable over very long timescales, hence the constant value of $e_{p,k}$, and has only a slight effect on the solution in $\boldsymbol{\omega}^{(b)}$. This effect of the $\boldsymbol{\omega}_k^{(b)}$ form, while a slight deficiency at small timesteps, is associated with significantly improved integrator stability at larger timesteps. Figure 4.3.2 demonstrates the effect of timestep (h) on the integrator solution.

As can be seen, the QVI in $\boldsymbol{\phi}_k$ becomes unstable at $h > 1.2$ s, whereas the QVI in $\boldsymbol{\omega}_k^{(b)}$ remains stable for significantly larger timesteps. However, even before the conservation errors for the QVI in $\boldsymbol{\phi}_k$ are observed to diverge, a significant degradation in its performance is observed. At $h = 1$ s, despite the negligible momentum and kinetic energy errors this integrator, its solution in $\boldsymbol{\omega}^{(b)}$ matches poorly with the benchmark solution. The solution from the QVI in $\boldsymbol{\omega}_k^{(b)}$ is significantly more accurate, despite oscillatory momentum conservation error in this integrator: indeed, the effect of this error at large step sizes is to increase the frequency of the periodic solution in $\boldsymbol{\omega}^{(b)}$; its amplitude remains constant. These results are indicative of the fact that excellent integrator conservation properties do not guarantee accurate integration. The key advantages of the QVI in $\boldsymbol{\omega}_k^{(b)}$ are its lower computational cost and greater stability, enabling the use of larger timesteps. Both of these factors make it particularly well suited to systems in which computational cost of integration is a major factor; for example, large multibody systems, discretised models (e.g. discretised beam models [23,24]) and long-timescale simulations.

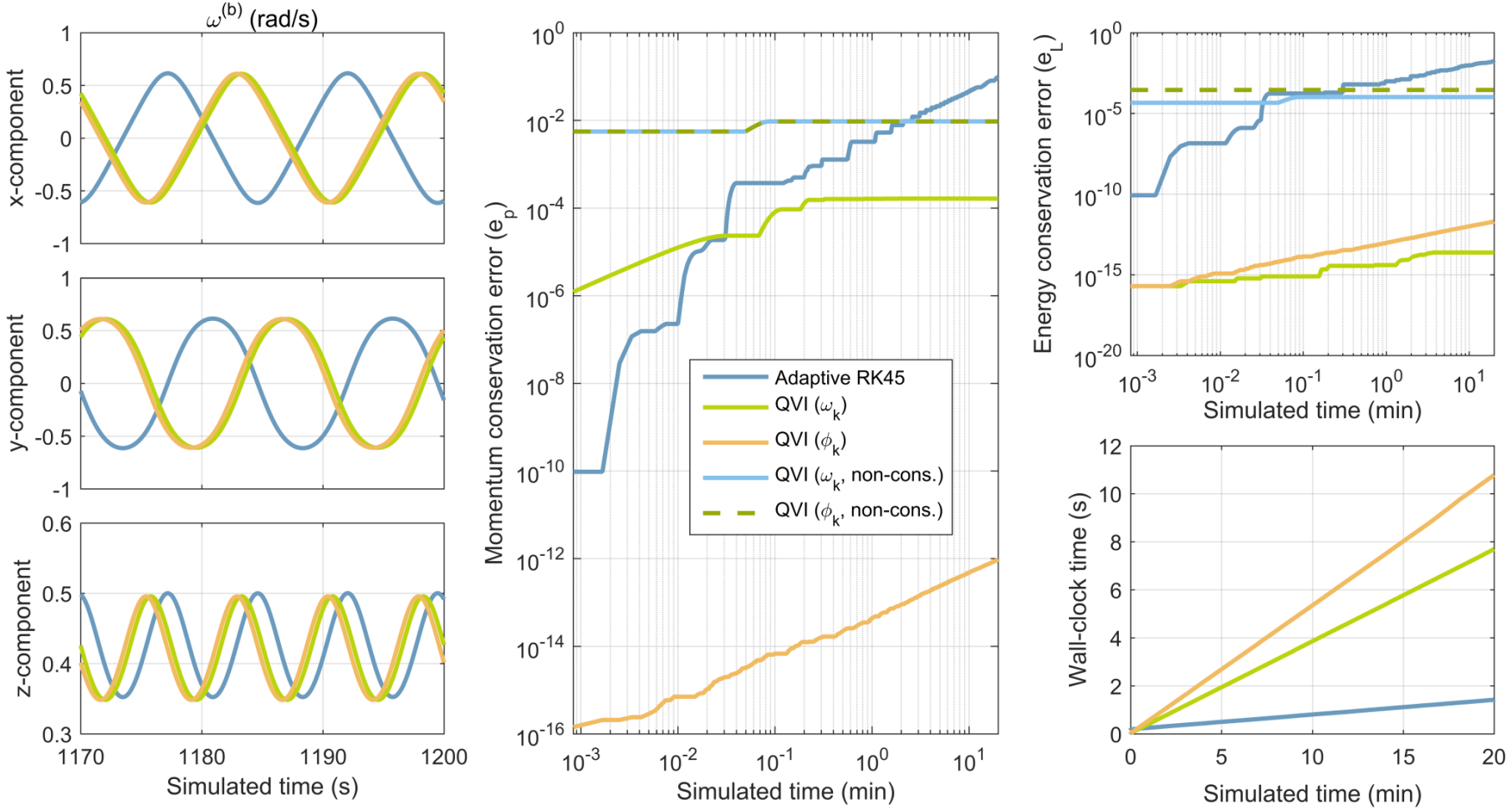

Figure 4.3.1: Integration results for the free rotation of a rigid body.

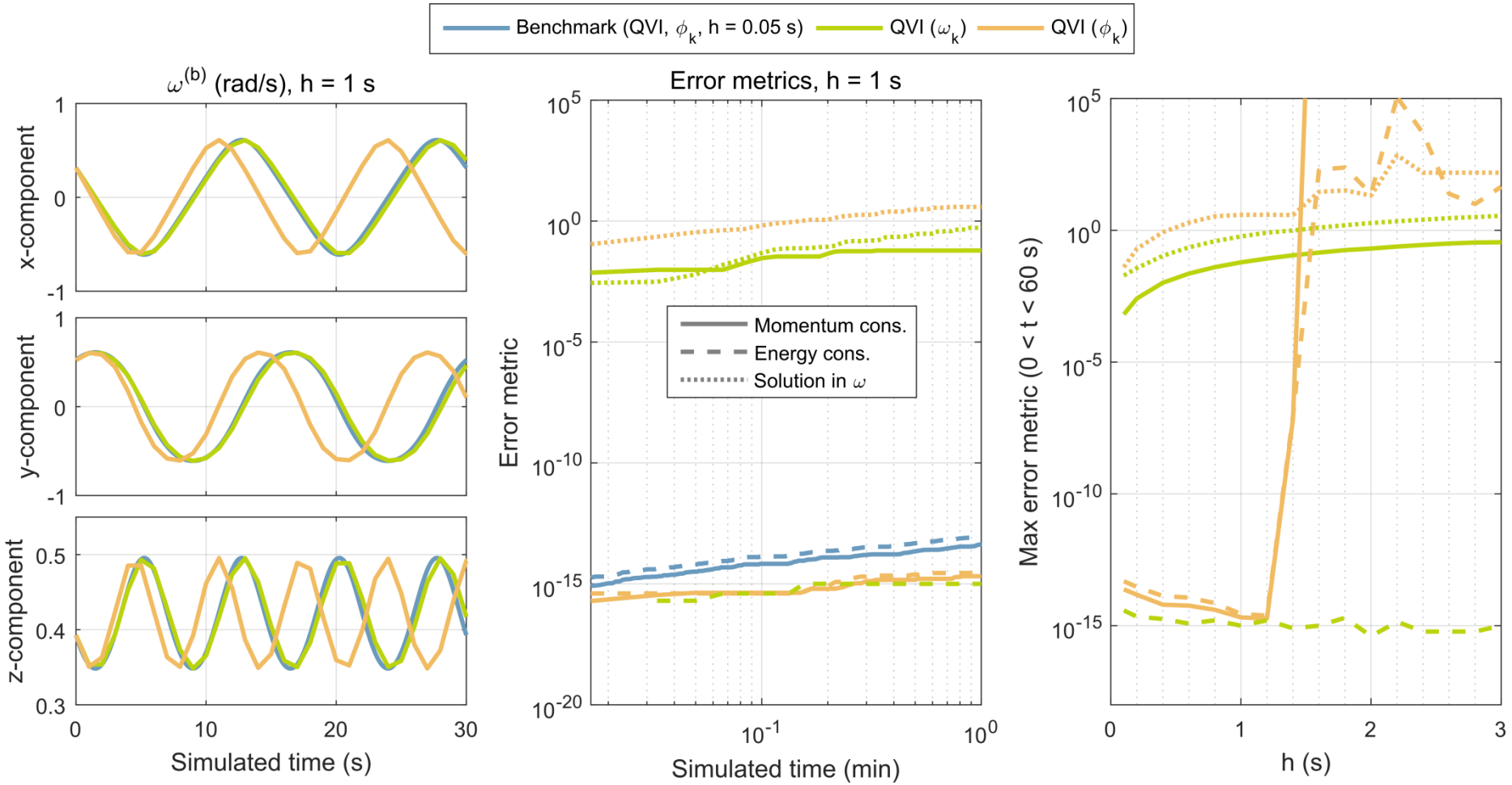

Figure 4.3.2: The effect of step size on integration results for the free rotation of a rigid body: results for large step size ($h = 1$ s), and the maximum error metrics as a function of step size.

4.4. LEFT-RECTANGLE QVI FOR COUPLED ROTATIONAL DYNAMICS

4.4.1. Kinetic energy in a rotating frame of reference

In Chapter 3 the total system kinetic energy was expressed as a function of variables and coefficients resolved in the earth frame, in the form:

$$T\left(\dot{\mathbf{x}}^{(e)},\boldsymbol{\omega}^{(e)},t\right)=\dot{\mathbf{x}}_S^{(e),T}\mathrm{a}_{xx}\dot{\mathbf{x}}_S^{(e)}+\dot{\mathbf{x}}_S^{(e),T}\mathrm{A}_{x\omega}^{(e)}(q,t)\boldsymbol{\omega}^{(e)}+\boldsymbol{\omega}^{(e),T}\mathrm{A}_{\omega\omega}^{(e)}(q,t)\boldsymbol{\omega}^{(e)}+\dot{\mathbf{x}}_S^{(e),T}\mathbf{a}_x^{(e)}(q,t)+\boldsymbol{\omega}^{(e),T}\mathbf{a}_\omega^{(e)}(q,t)+\mathrm{a}_0, \tag{4.4.1}$$

with coefficients as per Eq. 3.2.4. The resolution of these coefficients in the earth frame endows them with a dependence on the orientation (q) which is undesired as it will complicate the chain derivatives involved in variational analysis.

To isolate the coefficient dependency on orientation, $\mathrm{P}_{E/B}$ (the only q-dependent function in the system) is factorised out of the kinematic chain. This requires the definition of modified kinematic chain matrices $\widehat{\mathrm{P}}_{i,c}=\mathrm{P}_{E/B}^T\mathrm{P}_{i,c}$, according to Table 3.1. This yields a modification of the system velocity kinematics:

$$\dot{\mathbf{x}}_i^{(e)}=\dot{\mathbf{x}}_S^{(e)}+\left(\boldsymbol{\omega}^{(e)}+\mathrm{P}_{E/B}\mathrm{P}_{i,2}\boldsymbol{\omega}_{i,2}\right)\times\sum_{c=1}^{l_{c,i}}\mathrm{P}_{E/B}\widehat{\mathrm{P}}_{i,c}\mathbf{L}_{i,c}\,,\qquad i\in\mathcal{S}, \tag{4.4.2}$$

Table 4.1: Modified kinematic chain parameters for case study system

Body Name	Index	l_c	$c=1$		$c=2$		[…]
			$\mathbf{L}_{i,1}$	$\widehat{\mathrm{P}}_{i,1}$	$\mathbf{L}_{i,2}$	$\widehat{\mathrm{P}}_{i,2}$	
body	b	1	$[G_b\ 0\ 0]^T$	$\mathrm{E}_{3\times3}$			
right wing	wr	2	$[L_r\ 0\ 0]^T$	$\mathrm{E}_{3\times3}$	$[G_{wr}\ 0\ 0]^T$	$\mathrm{P}_{B/WR}$	
left wing	wl	2	$[L_r\ 0\ 0]^T$	$\mathrm{E}_{3\times3}$	$[G_{wl}\ 0\ 0]^T$	$\mathrm{P}_{B/WL}$	
right horz. stabiliser	er	1	$[G_e\ 0\ 0]^T$	$\mathrm{P}_{B/ER}$			
left horz. stabiliser	el	1	$[G_e\ 0\ 0]^T$	$\mathrm{P}_{B/EL}$			
fin / vert. stabiliser	f	1	$[G_\mathrm{f}\ 0\ 0]^T$	$\mathrm{P}_{B/F}$			
point mass	pm	1	$\left[L_\mathrm{pm}\ 0\ 0\right]^T$	$\mathrm{E}_{3\times3}$			

which, via the skew operator, may be expressed as:

$$\begin{aligned}\dot{\mathbf{x}}_i^{(e)} &= \dot{\mathbf{x}}_S^{(e)} + \mathrm{P}_{E/B}\left(\left(\mathrm{P}_{E/B}^T\boldsymbol{\omega}^{(e)} + \mathrm{P}_{i,2}\boldsymbol{\omega}_{i,2}\right) \times \sum_{c=1}^{l_{c,i}} \widehat{\mathrm{P}}_{i,c}\mathbf{L}_{i,c}\right) \\ &= \dot{\mathbf{x}}_S^{(e)} + \mathrm{P}_{E/B}\left[\sum_{c=1}^{l_{c,i}} \widehat{\mathrm{P}}_{i,c}\mathbf{L}_{i,c}\right]_\times^T \left(\mathrm{P}_{E/B}^T\boldsymbol{\omega}^{(e)} + \mathrm{P}_{i,2}\boldsymbol{\omega}_{i,2}\right), \qquad i \in \mathcal{S}.\end{aligned} \tag{4.4.3}$$

Propagating these modifications of the kinematics chain through the kinetic energy, an alternative representation of the individual body kinetic energy is obtained in which the q-dependent terms ($\mathrm{P}_{E/B}$) consistently premultiply the state variables ($\dot{\mathbf{x}}_S^{(e)}$ and $\boldsymbol{\omega}^{(e)}$):

$$\begin{aligned}2T_i = \dot{\mathbf{x}}_S^{(e),T} m_i \dot{\mathbf{x}}_S^{(e)} &+ 2\left(\mathrm{P}_{E/B}^T\dot{\mathbf{x}}_S^{(e)}\right)^T m_i \left[\sum_{c=1}^{l_{c,i}} \widehat{\mathrm{P}}_{i,c}\mathbf{L}_{i,c}\right]_\times^T \left(\mathrm{P}_{E/B}^T\boldsymbol{\omega}^{(e)}\right) \\ &+ 2\left(\mathrm{P}_{E/B}^T\dot{\mathbf{x}}_S^{(e)}\right)^T m_i \left[\sum_{c=1}^{l_{c,i}} \widehat{\mathrm{P}}_{i,c}\mathbf{L}_{i,c}\right]_\times^T \left(\widehat{\mathrm{P}}_{i,2}\boldsymbol{\omega}_{i,2}\right) \\ &+ \left(\mathrm{P}_{E/B}^T\boldsymbol{\omega}^{(e)}\right)^T \left(\left[\sum_{c=1}^{l_{c,i}} \widehat{\mathrm{P}}_{i,c}\mathbf{L}_{i,c}\right]_\times m_i \left[\sum_{c=1}^{l_{c,i}} \widehat{\mathrm{P}}_{i,c}\mathbf{L}_{i,c}\right]_\times^T + \mathrm{I}_i^{(b)}\right)\left(\mathrm{P}_{E/B}^T\boldsymbol{\omega}^{(e)}\right) \\ &+ \left(\mathrm{P}_{E/B}^T\boldsymbol{\omega}^{(e)}\right)^T \left(\left[\sum_{c=1}^{l_{c,i}} \widehat{\mathrm{P}}_{i,c}\mathbf{L}_{i,c}\right]_\times m_i \left[\sum_{c=1}^{l_{c,i}} \widehat{\mathrm{P}}_{i,c}\mathbf{L}_{i,c}\right]_\times^T + \mathrm{I}_i^{(b)}\right)\left(\widehat{\mathrm{P}}_{i,2}\boldsymbol{\omega}_{i,2}\right) \\ &+ \left(\widehat{\mathrm{P}}_{i,2}\boldsymbol{\omega}_{i,2}\right)^T \left(\left[\sum_{c=1}^{l_{c,i}} \widehat{\mathrm{P}}_{i,c}\mathbf{L}_{i,c}\right]_\times m_i \left[\sum_{c=1}^{l_{c,i}} \widehat{\mathrm{P}}_{i,c}\mathbf{L}_{i,c}\right]_\times^T + \mathrm{I}_i^{(b)}\right)\left(\widehat{\mathrm{P}}_{i,2}\boldsymbol{\omega}_{i,2}\right), \\ &i \in \mathcal{S}.\end{aligned} \tag{4.4.4}$$

To eliminate the kinetic energy dependency on orientation entirely, $\dot{\mathbf{x}}_S^{(e)}$ and $\boldsymbol{\omega}^{(e)}$ are resolved in the body-fixed reference frame. However there are two ways to conceptualise the resolution of e.g. the body velocity in the body-fixed frame, which is a rotating frame of reference: (a) the velocity of the aircraft (S) resolved in the instantaneously motionless body-fixed frame; or (b) this velocity relative to the velocity of the origin (O) viewed in the body-fixed frame (arising from the rotation of the frame). Mathematically, the former arises from a direct application of the rotational transformation matrix:

$$\dot{\mathbf{x}}_S^{(b)} = \mathrm{P}_{E/B}^T\dot{\mathbf{x}}_S^{(e)}, \tag{4.4.5}$$

and the latter from chain rule differentiation of the definition of $\mathbf{x}_S^{(b)}$, the position of S resolved in the body-fixed frame:

$$\dot{\mathbf{x}}_S^{(b)} = \frac{d}{dt}\left(\mathrm{P}_{E/B}^T \mathbf{x}_S^{(e)}\right) = \mathrm{P}_{E/B}^T \dot{\mathbf{x}}_S^{(e)} + \dot{\mathrm{P}}_{E/B}^T \mathbf{x}_S^{(e)}. \tag{4.4.6}$$

A similar distinction arises generally in angular velocity: between a given angular velocity ($\boldsymbol{\omega}$) resolved in an instantaneously motionless frame ($\mathrm{P}_{\mathrm{frame}}\boldsymbol{\omega}$), and the same angular velocity as viewed in the frame i.e. relative to the angular velocity of the rotating frame ($\mathrm{P}_{\mathrm{frame}}(\boldsymbol{\omega} - \boldsymbol{\omega}_{\mathrm{frame}})$). Here, when this given angular velocity is the angular velocity of the frame itself ($\boldsymbol{\omega} = \boldsymbol{\omega}_{\mathrm{frame}}$) the latter choice yields a resolved angular velocity of zero and may be discarded. Making an analogous choice with regard to the definition of $\dot{\mathbf{x}}_S^{(b)}$ yields a resolution based on instantaneously motionless body-fixed frame, i.e. via direct application of the rotational transformation matrix. This is also the more mathematically convenient choice, and the one which is immediately motivated by the form of Eq. 4.4.4. Hence:

$$\boldsymbol{\omega}^{(b)} = \mathrm{P}_{E/B}^T \boldsymbol{\omega}^{(e)}, \qquad \dot{\mathbf{x}}_S^{(b)} = \mathrm{P}_{E/B}^T \dot{\mathbf{x}}_S^{(e)}. \tag{4.4.7}$$

These transformations yield a total system kinetic energy of the form:

$$\begin{aligned} T\left(\dot{\mathbf{x}}^{(b)}, \boldsymbol{\omega}^{(b)}, t\right) = {} & \dot{\mathbf{x}}^{(b),T} \mathrm{a}_{xx} \dot{\mathbf{x}}^{(b)} + \dot{\mathbf{x}}^{(b),T} \mathrm{A}_{x\omega}(t) \boldsymbol{\omega}^{(b)} + \dot{\mathbf{x}}^{(b),T} \mathbf{a}_x(t) \\ & + \boldsymbol{\omega}^{(b),T} \mathrm{A}_{\omega\omega}(t) \boldsymbol{\omega}^{(b)} + \boldsymbol{\omega}^{(b),T} \mathbf{a}_\omega(t) + \mathrm{a}_0(t), \end{aligned} \tag{4.4.8}$$

with coefficients:

$$\begin{aligned} \mathrm{a}_{xx}(q,t) &= \frac{1}{2}\sum_{i\in\mathcal{S}} m_i, \\ \mathrm{A}_{x\omega}^{(e)}(q,t) &= \frac{1}{2}\sum_{i\in\mathcal{S}} 2m_i \left[\sum_{c=1}^{l_{c,i}} \mathrm{P}_{i,c}\mathbf{L}_{i,c}\right]_\times^T, \\ \mathrm{A}_{\omega\omega}^{(e)}(q,t) &= \frac{1}{2}\sum_{i\in\mathcal{S}} \left[\sum_{c=1}^{l_{c,i}} \mathrm{P}_{i,c}\mathbf{L}_{i,c}\right]_\times m_i \left[\sum_{c=1}^{l_{c,i}} \mathrm{P}_{i,c}\mathbf{L}_{i,c}\right]_\times^T + \mathrm{I}_i^{(e)}, \\ \mathbf{a}_\omega^{(e)}(q,t) &= \frac{1}{2}\sum_{i\in\mathcal{S}} 2\left[\sum_{c=1}^{l_{c,i}} \mathrm{P}_{i,c}\mathbf{L}_{i,c}\right]_\times^T m_i \left[\sum_{c=1}^{l_{c,i}} \mathrm{P}_{i,c}\mathbf{L}_{i,c}\right]_\times \mathrm{P}_{i,2}\boldsymbol{\omega}_{i,2} + 2\mathrm{I}_i^{(e)}\,\mathrm{P}_{i,2}\boldsymbol{\omega}_{i,2}, \end{aligned} \tag{4.4.9}$$

$$\mathbf{a}_x^{(e)}(q,t) = \frac{1}{2} 2 m_i \left[\sum_{c=1}^{l_{c,i}} \mathrm{P}_{i,c} \mathbf{L}_{i,c} \right]_{\times}^{T} \left(\mathrm{P}_{i,2} \boldsymbol{\omega}_{i,2} \right),$$

$$\mathrm{a}_0 = \frac{1}{2} \sum_{i \in \mathcal{S}} \left(\mathrm{P}_{i,2} \boldsymbol{\omega}_{i,2} \right)^T \mathrm{I}_i^{(e)} \left(\mathrm{P}_{i,2} \boldsymbol{\omega}_{i,2} \right) + \left(\mathrm{P}_{i,2} \boldsymbol{\omega}_{i,2} \right)^T \left[\sum_{c=1}^{l_{c,i}} \mathrm{P}_{i,c} \mathbf{L}_{i,c} \right]_{\times} m_i \left[\sum_{c=1}^{l_{c,i}} \mathrm{P}_{i,c} \mathbf{L}_{i,c} \right]_{\times}^{T} \left(\mathrm{P}_{i,2} \boldsymbol{\omega}_{i,2} \right).$$

For clarity, from henceforth the notation $\mathbf{x}^{(b)} = \mathbf{x}_S^{(b)}$, $\dot{\mathbf{x}}^{(b)} = \dot{\mathbf{x}}_S^{(b)}$ (etc.) is used.

4.4.2. Variational analysis

From a variational perspective, this system represents a significant departure from the uncoupled analysis, as the indirect dependency of the system kinetic energy on generalised coordinates – contained in the proxy derivative relation, Eq. 4.3.3 – means that at least one of the system's canonical momenta will not be conserved, as the associated generalised coordinate will not be ignorable [25]. That is, there is no set of generalised coordinates and (non-proxy) velocities in which the system kinetic energy is independent of all the generalised coordinates and thus all canonical momenta are conserved.

In the case of Eq. 4.3.1, a particle-based axis-angle representation ($\mathbf{n}$-$\delta\theta$, the generalised coordinate(s) corresponding to $\boldsymbol{\omega}^{(b)}$) leads to conservation of angular momentum ($\mathrm{I}^{(b)}\boldsymbol{\omega}^{(b)}$) [26]. Notably, the quaternion canonical momentum is not conserved in any case [27]. However, in Eq. 4.4.8 a suitable choice of translational coordinate is not available: a formulation in $\dot{\mathbf{x}}^{(e)}$-$\mathbf{x}^{(e)}$ leads to a dependency of the kinetic energy coefficients (A_i) on orientation; and a formulation in $d/dt\left(\mathbf{x}^{(b)}\right)$-$\mathbf{x}^{(b)}$ leads to a dependency of these coefficients on $\mathbf{x}^{(b)}$. In the $\dot{\mathbf{x}}^{(b)}$-$\mathbf{x}^{(b)}$ formulation the orientation-dependence of the proxy derivative-coordinate relation (Eq. 4.4.7) breaks the conservation of the rotational canonical momentum. The corresponding discrete rotational momentum (cf. Eq. 4.3.13) will also not be conserved; and so, crucially, a momentum-conservative estimate for the $\boldsymbol{\omega}_k^{(b)}$ analogous to Eq. 4.3.17 will not be available. The integrator conservation and momentum performance will suffer as a result. Note that this is not a result of any changes in the integrator; but a property of the system itself.

Applying the techniques of Section 4.3 to this system nonetheless, we utilise the left-rectangle rule discretization (Eq. 4.3.7) and apply a translation perturbation, yielding the variational derivative of $\dot{\mathbf{x}}_k^{(b)}$:

$$\begin{aligned} \mathbf{x}_k^{(e),\epsilon} &= \mathbf{x}_k^{(e)} + \epsilon\delta\mathbf{x}_k^{(e)} + \mathcal{O}(\epsilon^2), \\ \delta\dot{\mathbf{x}}_k^{(b)} &= 2\dot{\mathbf{x}}_k^{(b)} \times \boldsymbol{\eta}_k^{(b)} + \frac{1}{h} q_k^{\dagger}\left(\delta\mathbf{x}_{k+1}^{(e)} - \delta\mathbf{x}_k^{(e)}\right) q_k. \end{aligned} \tag{4.4.10}$$

The variational derivative of kinetic energy may be expressed:

$$\begin{aligned} \delta T_k &= \mathbf{D}_{1,k} \cdot \delta\dot{\mathbf{x}}_k^{(b)} + \mathbf{D}_{2,k} \cdot \delta\boldsymbol{\omega}_k^{(b)}, \\ \mathbf{D}_{1,k}\left(\dot{\mathbf{x}}_k^{(b)}, \boldsymbol{\omega}_k^{(b)}, t_k\right) &= \partial T_k / \partial\dot{\mathbf{x}}_k^{(b)} = 2\mathrm{a}_{xx}\dot{\mathbf{x}}_k^{(b)} + \mathrm{A}_{x\omega}(t_k)\boldsymbol{\omega}_k^{(b)} + \mathbf{a}_x(t_k), \\ \mathbf{D}_{2,k}\left(\dot{\mathbf{x}}_k^{(b)}, \boldsymbol{\omega}_k^{(b)}, t_k\right) &= \partial T_k / \partial\boldsymbol{\omega}_k^{(b)} = 2\mathrm{A}_{\omega\omega}(t_k)\boldsymbol{\omega}_k^{(b)} + \mathrm{A}_{x\omega}(t_k)^T\dot{\mathbf{x}}_k^{(b)} + \mathbf{a}_{\omega}(t_k), \end{aligned} \tag{4.4.11}$$

yielding the two coupled inter-step equations; in translation and rotation respectively:

$$\begin{aligned} q_k\mathbf{D}_{1,k}q_k^{\dagger} &= q_{k-1}\mathbf{D}_{1,k-1}q_{k-1}^{\dagger} + h\mathbf{F}_{\mathrm{tot},k}^{(e)}, \\ \mathbf{D}_{2,k} + \frac{1}{2}h\boldsymbol{\omega}_k^{(b)} \times \mathbf{D}_{2,k} + h\dot{\mathbf{x}}_k^{(b)} \times \mathbf{D}_{1,k} &= \mathbf{D}_{2,k-1} - \frac{1}{2}h\boldsymbol{\omega}_{k-1}^{(b)} \times \mathbf{D}_{2,k-1} + \boldsymbol{\tau}_{\mathrm{tot},k}^{(b)}. \end{aligned} \tag{4.4.12}$$

Note that, as anticipated from the continuous analysis, the rotational equation contains a symmetry-breaking term, $h\dot{\mathbf{x}}_k^{(b)} \times \mathbf{D}_{1,k}$, in addition to the momentum-balance terms analogous to Eq. 4.3.13. The translation equation is symmetric with $\mathbf{p}_{x,k} = q_k\mathbf{D}_{1,k}q_k^{\dagger}$, and although dependence of $\mathbf{D}_{1,k}$ on $\boldsymbol{\omega}_k^{(b)}$ precludes a direct solution for the conservative $\dot{\mathbf{x}}_k^{(b)}$. The Newton iteration for the inter-step relation may be expressed in an asymmetric momentum-balance form:

$$\begin{aligned} \begin{bmatrix} \boldsymbol{\omega}_{k,i+1}^{(b)} \\ \dot{\mathbf{x}}_{k,i+1}^{(b)} \end{bmatrix} &= \begin{bmatrix} \boldsymbol{\omega}_{k,i}^{(b)} \\ \dot{\mathbf{x}}_{k,i}^{(b)} \end{bmatrix} + \mathrm{J}_{k,i}^{-1}\left(\mathbf{p}_{k,i}^{+} + \mathbf{a}_{k,\boldsymbol{i}} - \mathbf{p}_k^{-} - h\begin{bmatrix} \mathbf{F}_{\mathrm{tot},k}^{(e)} \\ \boldsymbol{\tau}_k^{(b)} \end{bmatrix}\right), \\ \mathbf{p}_{k,i}^{+} &= \begin{bmatrix} q_k\mathbf{D}_{1,k,i}q_k^{\dagger} \\ \mathbf{D}_{2,k,i} + \frac{1}{2}h\boldsymbol{\omega}_k^{(b)} \times \mathbf{D}_{2,k,i} \end{bmatrix}, \qquad \mathbf{a}_{k,\boldsymbol{i}} = \begin{bmatrix} \mathbf{0} \\ h\dot{\mathbf{x}}_{k,i}^{(b)} \times \mathbf{D}_{1,k,i} \end{bmatrix}, \\ \mathbf{p}_k^{-} &= \begin{bmatrix} q_{k-1}\mathbf{D}_{1,k-1}q_{k-1}^{\dagger} \\ \mathbf{D}_{2,k-1} - \frac{1}{2}h\boldsymbol{\omega}_{k-1}^{(b)} \times \mathbf{D}_{2,k-1} \end{bmatrix}. \end{aligned} \tag{4.4.13}$$

An analytical expression is available for the Jacobian matrix $\mathrm{J}_{k,i}$. This matrix is of the form:

$$\mathrm{J}_{k,i} = \begin{bmatrix} \mathrm{J}_{k,i,1,1} & \mathrm{J}_{k,i,1,2} \\ \mathrm{J}_{k,i,2,1} & \mathrm{J}_{k,i,2,2} \end{bmatrix}, \tag{4.4.14}$$

with:

$$\begin{aligned} \mathrm{J}_{k,i,1,1} &= 2q_k \mathrm{E}_{3\times3} \mathrm{a}_{xx} q_k^{\dagger}, \\ \mathrm{J}_{k,i,1,2} &= q_k \mathrm{A}_{x\omega,k} q_k^{\dagger}, \\ \mathrm{J}_{k,i,2,1} &= \left(1 + \tfrac{1}{2}h\left[\boldsymbol{\omega}_{k,i}^{(b)}\right]_{\times}\right) \mathrm{A}_{x\omega,k}^{T} - h\left[\mathrm{A}_{x\omega}\boldsymbol{\omega}_{k,i}^{(b)} + \mathbf{a}_{x}\right]_{\times}, \\ \mathrm{J}_{k,i,2,2} &= \left(2 + h\left[\boldsymbol{\omega}_{k,i}^{(b)}\right]_{\times}\right) \mathrm{A}_{\omega\omega,k} + h\left[\dot{\mathbf{x}}_{k,i}^{(b)}\right]_{\times} \mathrm{A}_{x\omega} \\ &\quad - h\left[\mathrm{A}_{\omega\omega,k}\boldsymbol{\omega}_{k,i}^{(b)} + \tfrac{1}{2}\mathrm{A}_{x\omega,k}^{T}\dot{\mathbf{x}}_{k,i}^{(b)} + \tfrac{1}{2}\mathbf{a}_{\omega,k}\right]_{\times}. \end{aligned} \tag{4.4.15}$$

4.4.3. Numerical experiments

Figure 4.4.1 shows the results of this integrator applied to the coupled free rotation and translation of the biomimetic case study system, as specified in Chapter 2, Section 2.2. Aerodynamic and gravitational forces are excluded, and the aircraft wings remain fixed. In the fixed-wing case, all the system kinetic energy coefficients (as per Eq. 4.4.9) are constant:

$$\begin{aligned} \mathrm{a}_{xx} &= 4 \text{ kg}, \qquad \mathbf{a}_x = \mathbf{a}_\omega = [0\ 0\ 0]^T, \\ \mathrm{A}_{x\omega}^{(b)} &= \begin{bmatrix} 0.0400 & & \\ -0.0400 & & 6.350 \\ & -6.350 & \end{bmatrix} \text{ kg m}, \\ \mathrm{A}_{\omega\omega}^{(b)} &= \begin{bmatrix} 0.2342 & & -6.4761 \times 10^{-5} \\ & 3.0539 & \\ -6.4761 \times 10^{-5} & & 3.2699 \end{bmatrix} \text{ kg m}^2. \end{aligned} \tag{4.4.16}$$

The results from the left-rectangle QVI are compared to those from the adaptive RK45 integrator in Euler angles with pole-switching, as described in Section 4.2, using a default absolute local truncation error (LTE) tolerance of 10^{-6} and relative tolerance of 10^{-3}. This test case is analogous to that of Section 4.3, except that the system translational and rotational degrees of freedom are coupled and so the system canonical momenta are not all conserved. However, the conventional rigid-body momenta and energy are still conserved. These momenta may be computed as:

$$\begin{aligned} \mathbf{p}_{x,k} &= m_{\mathrm{tot}}\dot{\mathbf{x}}_{\mathrm{c.o.m.},k}^{(e)}, \\ \mathbf{p}_{\omega,k} &= q_k \mathrm{I}_{\mathrm{c.o.m.},k}^{(b)} \boldsymbol{\omega}_k^{(b)} q_k^{\dagger}, \end{aligned} \tag{4.4.17}$$

where m_{tot} is the total system mass, $\dot{\mathbf{x}}^{(e)}_{\text{c.o.m.}}$ the velocity of the system center of mass in the earth frame, and $\mathrm{I}^{(b)}_{\text{c.o.m.}}$ the total system rotational inertia about the center of mass, resolved in the body-fixed frame. The translational and angular momentum conservation errors are thus given again by $e_{p,i,k} = \max_{i \leq k}(\|\mathbf{p}_{i,k} - \mathbf{p}_{i,1}\| / \|\mathbf{p}_{i,1}\|)$, and the energy error by $e_{L,k} = \max_{i \leq k}(|L_k - L_1| / L_1)$.

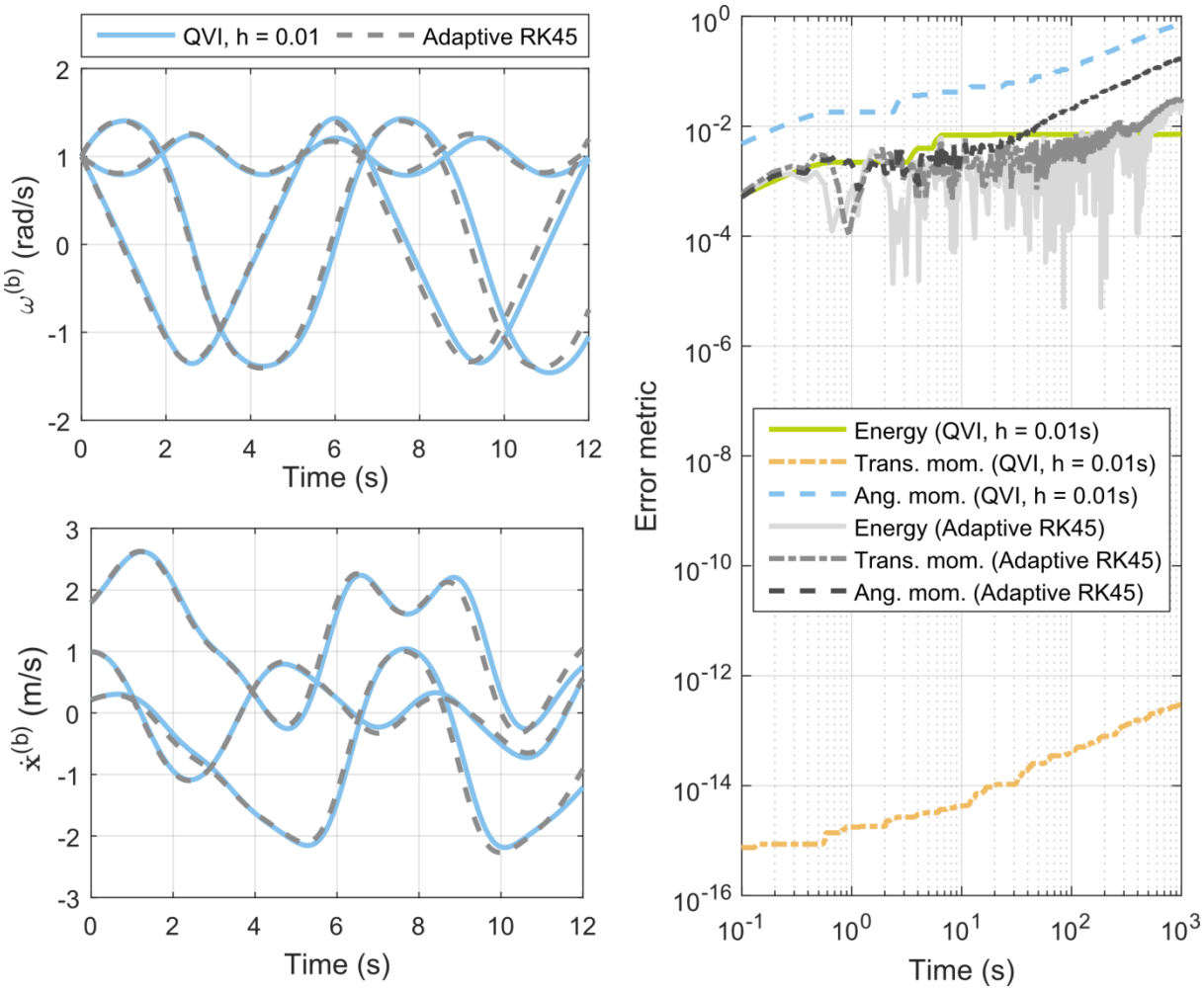

Figure 4.4.1: Integration results for the left-rectangle QVI applied to the free rotation and translation of the case study system.

In Figure 4.4.1 it may be seen that the Adaptive RK45 integrator allows significantly larger step size, with a mean step size $\bar{h} = 0.0947$ s over the simulation, in comparison to the specified $h = 0.01$ s for the QVI. This QVI step size is such that the system angular momentum error reaches c. 100% by the simulation end time, $T = 1000$ s: significantly higher step sizes do not destabilise the integrator, but promote a more rapid growth of angular momentum error. Despite this, the integrator does show excellent conservation

properties in translational momentum and energy. The system translational momentum is conserved almost exactly (to within 10^{-12}). The energy conservation error, while reaching a maximum magnitude of c. 10^{-2}, follows an extremely stable oscillation: the energy conservation integral error;

$$\int_{t=0}^{T} \big(L(\tau) - L(0)\big)/L(0)\, d\tau \cong \sum_{k=1}^{N} (L_k - L_1)/(NhL_1), \tag{4.4.18}$$

shows magnitude less than 2×10^{-4} at the simulation end time $T = 1000$ s.

Both these results are significantly superior to those of the RK45 integrator. However, the QVI integrator performs poorly in its conservation of angular momentum. As noted, by the end of the simulation its angular momentum conservation error is significantly larger than that of the RK45 integrator, for a smaller mean step size. However, at the specified current step size and RK45 LTE tolerances, the left-rectangle QVI is about 7% faster in real time. While the left-rectangle QVI shows a wide domain of stability, larger step sizes lead to more rapid angular momentum error growth and greater (stable) kinetic energy oscillations. These effects manifest themselves in the solution in $\boldsymbol{\omega}^{(b)}$ as a shift in the period of the periodic solution, and a consistent error in the periodic solution. The slight increase in period may be observed in Figure 4.4.1. The solution remains strongly periodic over long timescales: the effect of integrator error is seen primarily in the nature of this periodic solution. This is in contrast to the RK4 integrator, for which integrator error is expressed as a breakdown in the solution periodicity.

In overview, the QVI may be interpreted as trading local or short-timescale accuracy for long-term stability and energy/momentum conservation. In the context of biomimetic flight simulation, this makes it useful for long-timescale simulations and/or those in which the dissipation or gain of energy is of significance, including perching and take-off manoeuvres. However, to achieve a reasonably precise solution on the short timescale, a smaller step size is required – or, an increase in integrator order.

4.5. MIDPOINT QVI FOR COUPLED ROTATIONAL DYNAMICS

4.5.1. Motivation

The deficiency in the angular momentum conservation of the coupled left-rectangle QVI may be connected directly with the non-conservative behaviour of the system's angular canonical momentum. This in turn significantly degrades the accuracy of the left-rectangle integration: when the system canonical momenta are conserved (i.e. constant), a left rectangle discretization is an exact representation of the system conservation properties. When however the system canonical momenta are not conserved and may vary, left rectangle integration becomes simply a low-order approximation of the system canonical momenta behaviour. A more accurate form of integration is thus one key avenue to re-attaining good conservation properties in this situation. Here we apply midpoint integration, representing only a relatively small increase in integration accuracy – but one not utilised before in quaternion variational integration.

4.5.2. Variational analysis

Applying discrete midpoint integration to the continuous formulation of the principle of least action, we obtain:

$$\delta S + \delta W = h \sum_{k=1}^{N-1} \delta \tilde{T}_k + \tilde{\mathbf{F}}_k \cdot \delta \tilde{\mathbf{r}}_k = 0, \tag{4.5.1}$$

where the tilde ($\tilde{x}$) denotes evaluation at the inter-step midpoint. The midpoint location in all the non-quaternion system variables (t, $\mathbf{x}^{(e)}$, etc.) can be computed via linear interpolation, but to compute the midpoint quaternion ($\tilde{q}_k$) a different scheme is appropriate, as linear interpolation does not preserve the orientation quaternion normalization [28]. Other schemes available include normalised linear interpolation (NLERP), spherical linear interpolation (SLERP), spherical spline interpolation (SQUAD) [28] and eigenvector quaternion averaging [29]. For any choice of interpolation, the variational derivative of $\tilde{T}_k$ is thus:

$$\begin{gathered}
\delta \tilde{T}_k = \widetilde{\mathbf{D}}_{1,k} \cdot \delta \tilde{\tilde{\mathbf{x}}}_k^{(b)} + \widetilde{\mathbf{D}}_{2,k} \cdot \delta \tilde{\omega}_k^{(b)}, \\
\mathbf{D}_{1,k}\left(\tilde{\tilde{\mathbf{x}}}_k^{(b)}, \tilde{\omega}_k^{(b)}, \tilde{t}_k\right) = \partial \tilde{T}_k / \partial \tilde{\tilde{\mathbf{x}}}_k^{(b)} = 2\mathrm{a}_{xx} \tilde{\tilde{\mathbf{x}}}_k^{(b)} + \mathrm{A}_{x\omega}(\tilde{t}_k) \boldsymbol{\omega}_k^{(b)} + \mathbf{a}_x(\tilde{t}_k), \\
\mathbf{D}_{2,k}\left(\tilde{\tilde{\mathbf{x}}}_k^{(b)}, \tilde{\omega}_k^{(b)}, \tilde{t}_k\right) = \partial \tilde{T}_k / \partial \tilde{\omega}_k^{(b)} = 2\mathrm{A}_{\omega\omega}(\tilde{t}_k) \boldsymbol{\omega}_k^{(b)} + \mathrm{A}_{x\omega}(\tilde{t}_k)^T \tilde{\tilde{\mathbf{x}}}_k^{(b)} + \mathbf{a}_\omega(\tilde{t}_k).
\end{gathered} \tag{4.5.2}$$

The variational derivatives of the proxy derivatives at the midpoint, $\delta\tilde{\mathbf{x}}_k^{(b)}$ and $\delta\widetilde{\boldsymbol{\omega}}_k^{(b)}$, must then be related to the perturbations at the step points (k and $k+1$). The midpoint proxy derivatives and their perturbations are defined as:

$$\begin{aligned} \widetilde{\boldsymbol{\omega}}_k^{(b)} &= 2\tilde{q}_k^{\dagger}\,\tilde{q}_k, & \widetilde{\boldsymbol{\omega}}_k^{(b),\epsilon} &= 2\tilde{q}_k^{\epsilon,\dagger}\,\tilde{q}_k^{\epsilon}, \\ \tilde{\mathbf{x}}_k^{(b)} &= \tilde{q}_k^{\dagger}\tilde{\mathbf{x}}^{(e)}\,\tilde{q}_k, & \tilde{\mathbf{x}}_k^{(b),\epsilon} &= \tilde{q}_k^{\epsilon,\dagger}\tilde{\mathbf{x}}^{(e),\epsilon}\,\tilde{q}_k^{\epsilon}. \end{aligned} \tag{4.5.3}$$

Here the central difficulty of the midpoint integrator arises, which is the definition of the perturbed midpoint, $\tilde{q}_k^{\epsilon}$. The unperturbed midpoint can be computed via any of the interpolation methods noted earlier. Notably, the midpoint estimates under SLERP and NLERP are given by:

$$\begin{aligned} &\text{SLERP} && \tilde{q}_k = \left(q_{k+1}q_k^{\dagger}\right)^{1/2} q_k, \\ &\text{NLERP} && \tilde{q}_k = \frac{q_{k+1}+q_k}{\|q_{k+1}+q_k\|}. \end{aligned} \tag{4.5.4}$$

However the perturbed midpoint cannot be computed similarly, as the limitations on quaternion algebra and calculus prohibit a closed-form identification of variational derivative $\delta\widetilde{\boldsymbol{\omega}}_k^{(b)}$ (via $\widetilde{\boldsymbol{\omega}}_k^{(b),\epsilon}$). In particular, the quaternion power and norm terms, $\left(q_{k+1}^{\epsilon}q_k^{\epsilon,\dagger}\right)^{1/2}$ and $1/\|q_{k+1}^{\epsilon}+q_k^{\epsilon}\|$, do not permit first order expansion in ϵ under current techniques. Note that quaternion power and exponential operators fail to fulfil a range of identities associated with their real scalar counterparts.

Instead, diverging from the derivation of Section 4.4, the quaternion perturbations are defined with reference to a perturbation direction resolved in the earth frame:

$$q_k^{\epsilon} = \exp\left(\epsilon\boldsymbol{\eta}_k^{(e)}\right) q_k \cong q_k + \epsilon\boldsymbol{\eta}_k^{(e)}q_k + \mathcal{O}(\epsilon^2). \tag{4.5.5}$$

This change simplifies the manipulation, and is not fundamental – it may be verified that the equivalence between the earth and body perturbations is exact:

$$q_k^{\epsilon} = \exp\left(\epsilon\boldsymbol{\eta}_k^{(e)}\right) q_k = \exp\left(\epsilon q_k\boldsymbol{\eta}_k^{(b)}q_k^{\dagger}\right) q_k = q_k \exp\left(\epsilon\boldsymbol{\eta}_k^{(b)}\right). \tag{4.5.6}$$

By parameterizing the perturbed midpoint a local perturbative direction $\tilde{\boldsymbol{\eta}}_k^{(e)}$;

$$\begin{aligned}\tilde{q}_k^{\epsilon} &= \exp\left(\epsilon\widetilde{\boldsymbol{\eta}}_k^{(e)}\right)\tilde{q}_k \cong \tilde{q}_k + \epsilon\widetilde{\boldsymbol{\eta}}_k^{(e)}\tilde{q}_k + \mathcal{O}(\epsilon^2),\\ \tilde{\dot{q}}_k^{\epsilon} &\cong \tilde{\dot{q}}_k + \epsilon\widetilde{\dot{\boldsymbol{\eta}}}_k^{(e)}\tilde{q}_k + \widetilde{\boldsymbol{\eta}}_k^{(e)}\tilde{\dot{q}}_k + \mathcal{O}(\epsilon^2),\end{aligned} \tag{4.5.7}$$

results are obtained for the generalised derivatives $\delta\widetilde{\boldsymbol{\omega}}_k^{(b)}$ and $\delta\tilde{\dot{\mathbf{x}}}_k^{(b)}$:

$$\begin{aligned}\delta\widetilde{\boldsymbol{\omega}}_k^{(b)} &= 2\tilde{q}_k^{\dagger}\widetilde{\dot{\boldsymbol{\eta}}}_k^{(e)}\tilde{q}_k,\\ \delta\tilde{\dot{\mathbf{x}}}_k^{(b)} &= 2\tilde{\dot{\mathbf{x}}}_k^{(b)} \times \tilde{q}_k^{\dagger}\widetilde{\boldsymbol{\eta}}_k^{(b)}\tilde{q}_k + \frac{1}{h}\tilde{q}_k^{\dagger}\left(\delta\mathbf{x}_{k+1}^{(e)} - \delta\mathbf{x}_k^{(e)}\right)\tilde{q}_k.\end{aligned} \tag{4.5.8}$$

This has transformed the problem of computing $\tilde{q}_k^{\epsilon}$ into one of computing $\widetilde{\boldsymbol{\eta}}_k^{(b)}$ and $\widetilde{\dot{\boldsymbol{\eta}}}_k^{(e)}$, as a function of $\boldsymbol{\eta}_k^{(e)}$ $\boldsymbol{\eta}_{k+1}^{(e)}$. For the same reasons, this cannot be done exactly, but discrete approximations are significantly easier to obtain:

$$\begin{aligned}\widetilde{\boldsymbol{\eta}}_k^{(e)} &= \frac{1}{2}\left(\boldsymbol{\eta}_{k+1}^{(e)} + \boldsymbol{\eta}_k^{(e)}\right),\\ \widetilde{\dot{\boldsymbol{\eta}}}_k^{(e)} &= \frac{1}{h}\left(\boldsymbol{\eta}_{k+1}^{(e)} - \boldsymbol{\eta}_k^{(e)}\right).\end{aligned} \tag{4.5.9}$$

Both these estimates are accurate to first order in h. Essentially, this approach has approximated the quaternion interpolation problem by an interpolation of the quaternion generators (cf. [30]). This leads to results for the variational derivatives of the proxy derivatives:

$$\begin{aligned}\delta\widetilde{\boldsymbol{\omega}}_k^{(b)} &= \frac{2}{h}\tilde{q}_k^{\dagger}\left(\boldsymbol{\eta}_{k+1}^{(e)} - \boldsymbol{\eta}_k^{(e)}\right)\tilde{q}_k,\\ \delta\tilde{\dot{\mathbf{x}}}_k^{(b)} &= \tilde{\dot{\mathbf{x}}}_k^{(b)} \times \tilde{q}_k^{\dagger}\left(\boldsymbol{\eta}_{k+1}^{(e)} + \boldsymbol{\eta}_k^{(e)}\right)\tilde{q}_k + \frac{1}{h}\tilde{q}_k^{\dagger}\left(\delta\mathbf{x}_{k+1}^{(e)} - \delta\mathbf{x}_k^{(e)}\right)\tilde{q}_k,\end{aligned} \tag{4.5.10}$$

and thus, with some manipulation, the integrator inter-step equations, in translation and rotation respectively:

$$\begin{aligned}\tilde{q}_k\widetilde{\mathbf{D}}_{1,k}\tilde{q}_k^{\dagger} &= \tilde{q}_{k-1}\widetilde{\mathbf{D}}_{1,k-1}\tilde{q}_{k-1}^{\dagger} + h\tilde{\mathbf{F}}_{\mathrm{tot},k}^{(e)},\\ \tilde{q}_k\left(\widetilde{\mathbf{D}}_{2,k} + h\tilde{\dot{\mathbf{x}}}_k^{(b)} \times \widetilde{\mathbf{D}}_{1,k}\right)\tilde{q}_k^{\dagger} &= \tilde{q}_{k-1}\left(\widetilde{\mathbf{D}}_{2,k-1} - h\tilde{\dot{\mathbf{x}}}_{k-1}^{(b)} \times \widetilde{\mathbf{D}}_{1,k-1}\right)\tilde{q}_{k-1}^{\dagger} + \tilde{\boldsymbol{\tau}}_{\mathrm{tot},k}^{(b)}.\end{aligned} \tag{4.5.11}$$

Notably, the rotational equation shows a symmetry after the manner of Eq. 4.3.12, though with cross products in $\tilde{\dot{\mathbf{x}}}_k^{(b)}$. The midpoint quaternion $\tilde{q}_k$ contains a dependency on $\widetilde{\boldsymbol{\omega}}_k^{(b)}$ via SLERP interpolation (Eq. 4.5.4) and q_{k+1}, integrated under the assumption of a constant angular velocity of $\boldsymbol{\omega}^{(b)} = \widetilde{\boldsymbol{\omega}}_k^{(b)}$ over the step interval $(k,k+1)$, corresponding again to midpoint integration:

$$q_{k+1} = q_k \exp\left(\frac{1}{2}\tilde{\omega}_k^{(b)}\right). \tag{4.5.12}$$

These inter-step equations are solved via Newton's method; though the dependency of $\tilde{q}_k$ on $\tilde{\omega}_k^{(b)}$ precludes the computation of an analytical Jacobian due to the breakdown of the chain rule in quaternions. A numerical Jacobian is implemented instead. This completes the derivation of the integrator.

4.5.3. Numerical experiments

Figures 4.5.1-4.5.2 show the results of this midpoint QVI applied to the freely-rotating biomimetic case study system. Figure 4.5.1 shows the integrator solution and conservation errors compared to results from the adaptive RK45 integrator in Euler angles at an equivalent step size: $h = \bar{h}_{RK} = 0.0947$ s; 1.4% of the $\omega^{(b)}$ solution period, the mean step size for the RK45 integration.

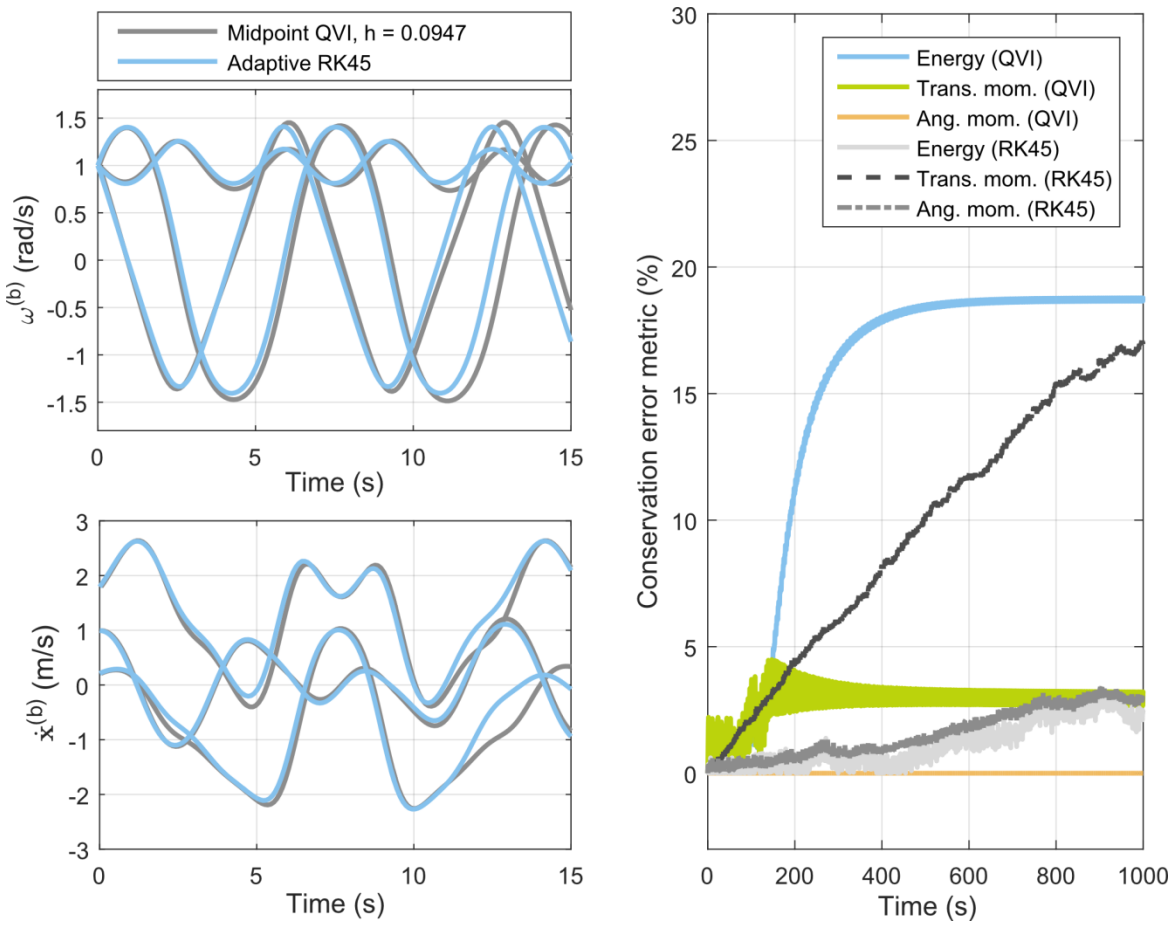

Figure 4.5.1: Integration results for the midpoint QVI applied to the free rotation and translation of the case study system, $h = h_{RK} = 0.0947$ s, compared to the adaptive RK45 integrator in Euler angles.

A qualitative breakdown in solution accuracy occurs at $t = 130$ s: an event reflected in the conservation error histories. The breakdown occurs when $\boldsymbol{\omega}_3^{(b)}$ (the z-component of $\boldsymbol{\omega}^{(b)}$, ordinarily oscillating between c. 0.8-1.2) drifts eventually to $\boldsymbol{\omega}_3^{(b)} < 0$. This triggers a sudden switch in solution behaviour, eventually settling at a near-constant state of $\boldsymbol{\omega}^{(b)} \cong [-4.2, 0, 0.1]^T$. The effect is notable in that it affirms that this QVI is still prone to instability or qualitative breakdown at high step sizes and long timescales. As per the left-rectangle integrator, short-timescale solution inaccuracy also manifests itself as a shift in the period of the oscillatory solution in $\boldsymbol{\omega}^{(b)}$, and in associated changes in $\dot{\mathbf{x}}^{(b)}$. The latter grow rapidly, as the shift in $\boldsymbol{\omega}^{(b)}$ changes the system orientation and thus the resolution of $\dot{\mathbf{x}}^{(b)}$; compounding the divergence between the QVI and RK45 solutions in this variable. Figure 4.5.2 shows the midpoint QVI integration results at a step size that is more suitable for long-timescale simulation, $h = 1/3\, h_{RK} = 0.0316$ s.

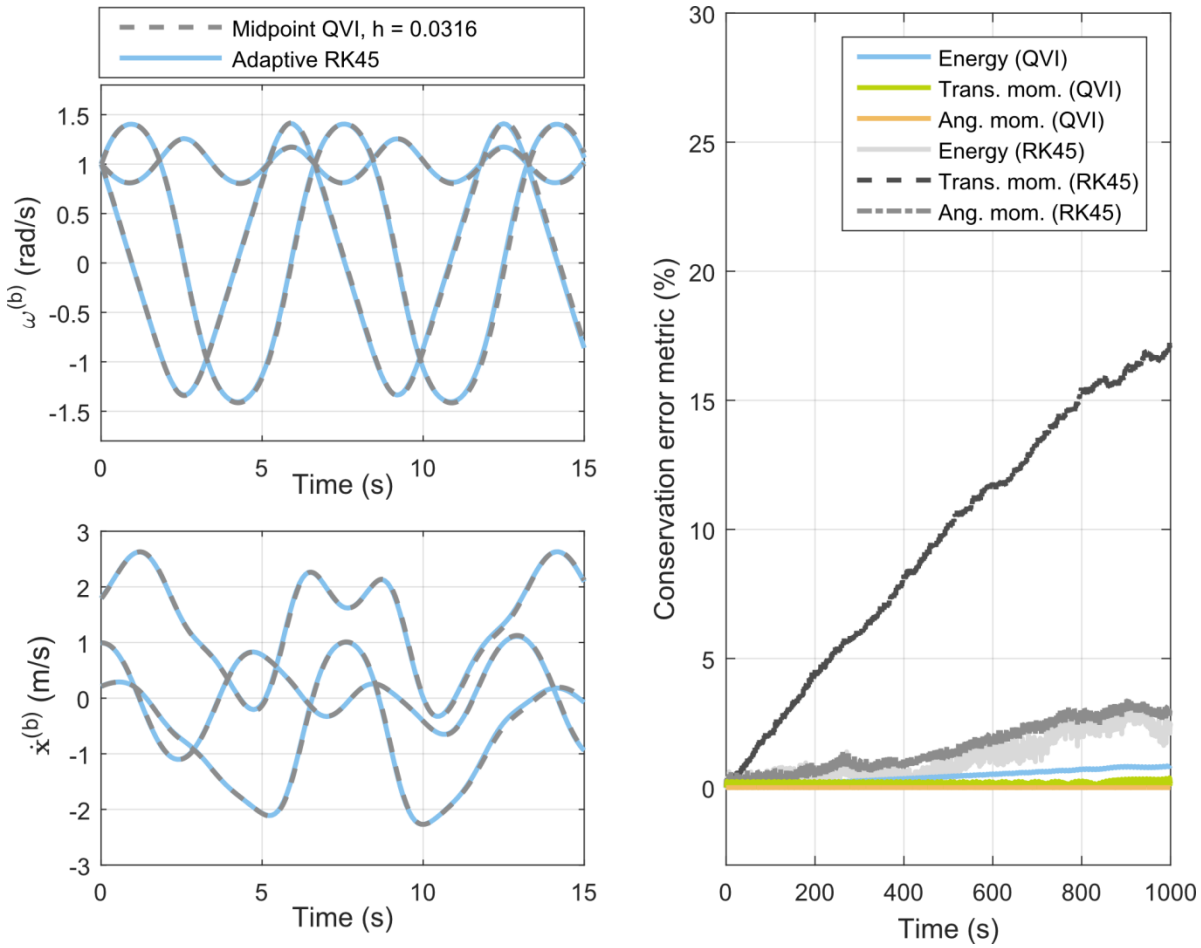

Figure 4.5.2: Integration results for the midpoint QVI applied to the free rotation and translation of the case study system, $h = 1/3\, h_{RK} = 0.0316$ s, compared to the adaptive RK45 integrator in Euler angles.

At this step size the QVI remains completely qualitatively accurate over the simulated time range, and by the conservation errors is probably more quantitatively accuracy than the RK45 integrator. A breakdown like that in Figure 4.5.1 is observed only at $t = 1700$ s. While the system conservation errors significantly outperform that of the RK45 integrator, but the wall-clock computation time is several factors higher. Figure 4.5.3 shows the midpoint QVI results for the case study system, compared to the left-rectangle QVI at a step size which is suitable for the latter ($h = 0.01$ s). The midpoint method generates an accurate local solution, with energy and angular momentum conservation errors over two orders of magnitude smaller that the left-rectangle method, verifying the performance benefits associated with the increase in integration order, and confirming it as a preferable choice for systems with translation-rotation coupling.

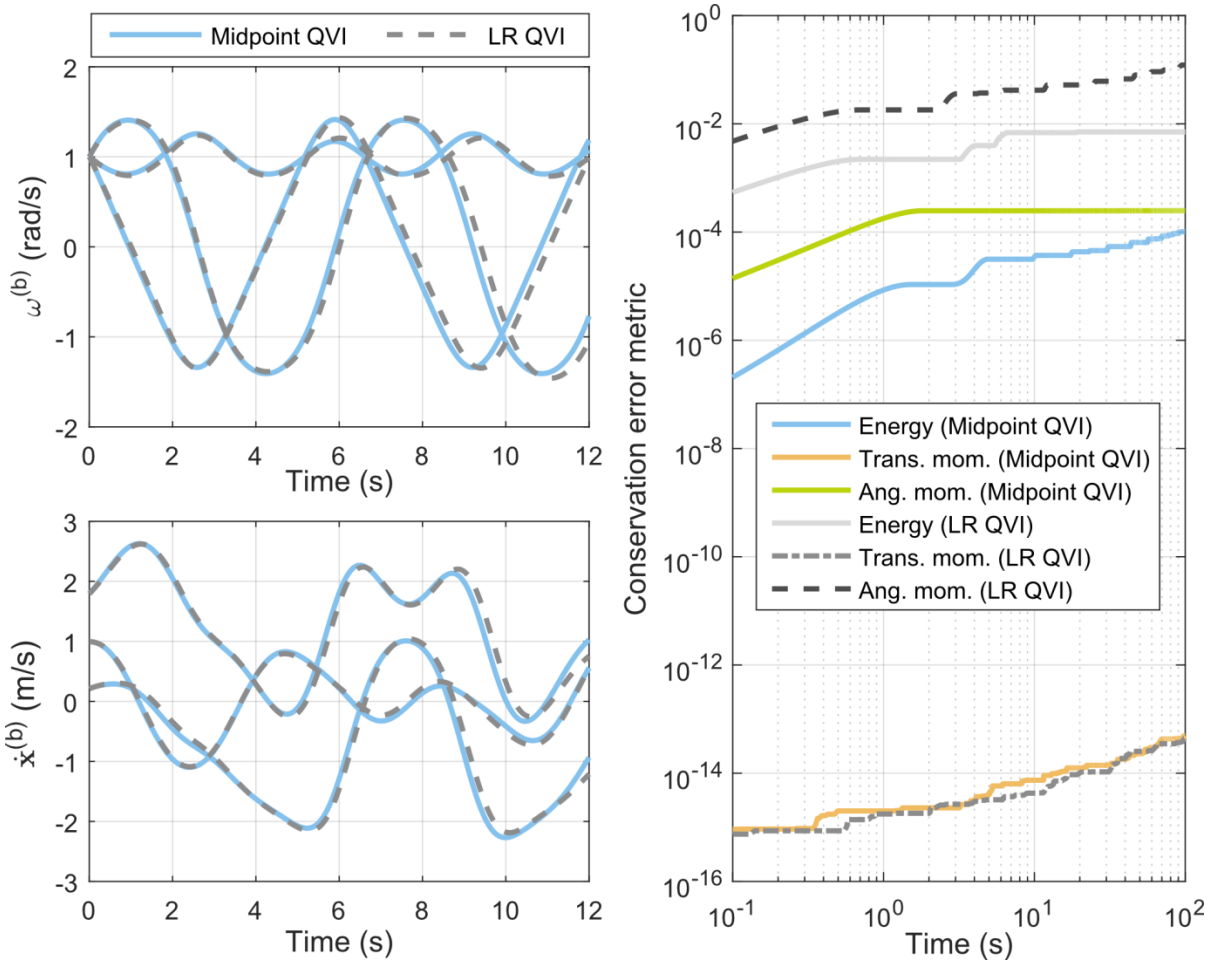

Figure 4.5.3: Integration results for the midpoint QVI applied to the free rotation and translation of the case study system, compared to the left-rectangle QVI for $h = 0.01$ s.

Finally, Figures 4.5.4-4.5.5 shows the midpoint QVI results for a flapping-wing simulation involving the generation of a pitch-up moment via wing biomimetic flapping motion, similar to that presented in Bergou et al. [31], and again using the biomimetic case study system. For simplicity, following [31], propulsive and gravitational forces are omitted. Dissipative aerodynamic forces are included via the quasisteady strip theory model formulated in Chapter 3, Section 3.4. The symmetric wing control inputs are dihedral $\theta_w(t) = \sin(t)$ rad and incidence $\phi_w(t) = -0.5\cos(t)$ rad: Figure 4.5.6 shows a rendering of these control inputs. Note that, as a result of wing motion, the system coefficients are now time-varying.

Figure 4.5.4 presents the solutions for three different timesteps, $h = 2.0h_{\mathrm{RK}}$, $1.0h_{\mathrm{RK}}$ and $0.5h_{\mathrm{RK}}$, where the mean stepsize of the adaptive RK45 integrator is $h_{\mathrm{RK}} = 0.1923$ s (over a 100 s simulation). The QVI performs excellently – significantly better than in the free rotation and translation test case. Accurate solutions are obtained even for step sizes greater than h_{RK}: the pitch angle solution at $2.0h_{\mathrm{RK}}$ shows only 8% error relative to the adaptive RK45 solution at the simulation end point ($T = 30$ s, c. 5 periods of flapping). Figure 4.5.5 presents a rendering of the flapping-wing simulation for the QVI at $h = 2.0h_{\mathrm{RK}}$ and the adaptive RK45 integrator: the 8% pitch error may be noted. The solutions at $1.0h_{\mathrm{RK}}$ and $0.5h_{\mathrm{RK}}$ show only 3% and 1% end-point error respectively – sufficiently low that the accuracy of the RK45 integrator itself may have an influence. This demonstrates the effectiveness of the QVI for the simulation of some forms of flapping-wing flight. It additionally demonstrates the differences between the QVI and the RK45 integrator in terms of the suitable step size for a given system. In this flapping-wing flight simulation, the QVI is capable of matching and exceeding the adaptive RK45 step size; whereas attempting this in the free rotation and translation test case leads to unacceptably large errors and qualitative solution breakdown. The mean adaptive RK45 step size is thus not necessary a good metric for comparing the QVI performance against. Numerical analysis techniques may be able to shed light on these effects, but given the complexity of the integrators system-specific testing is likely to be a more practical approach for assessing integrator suitability.

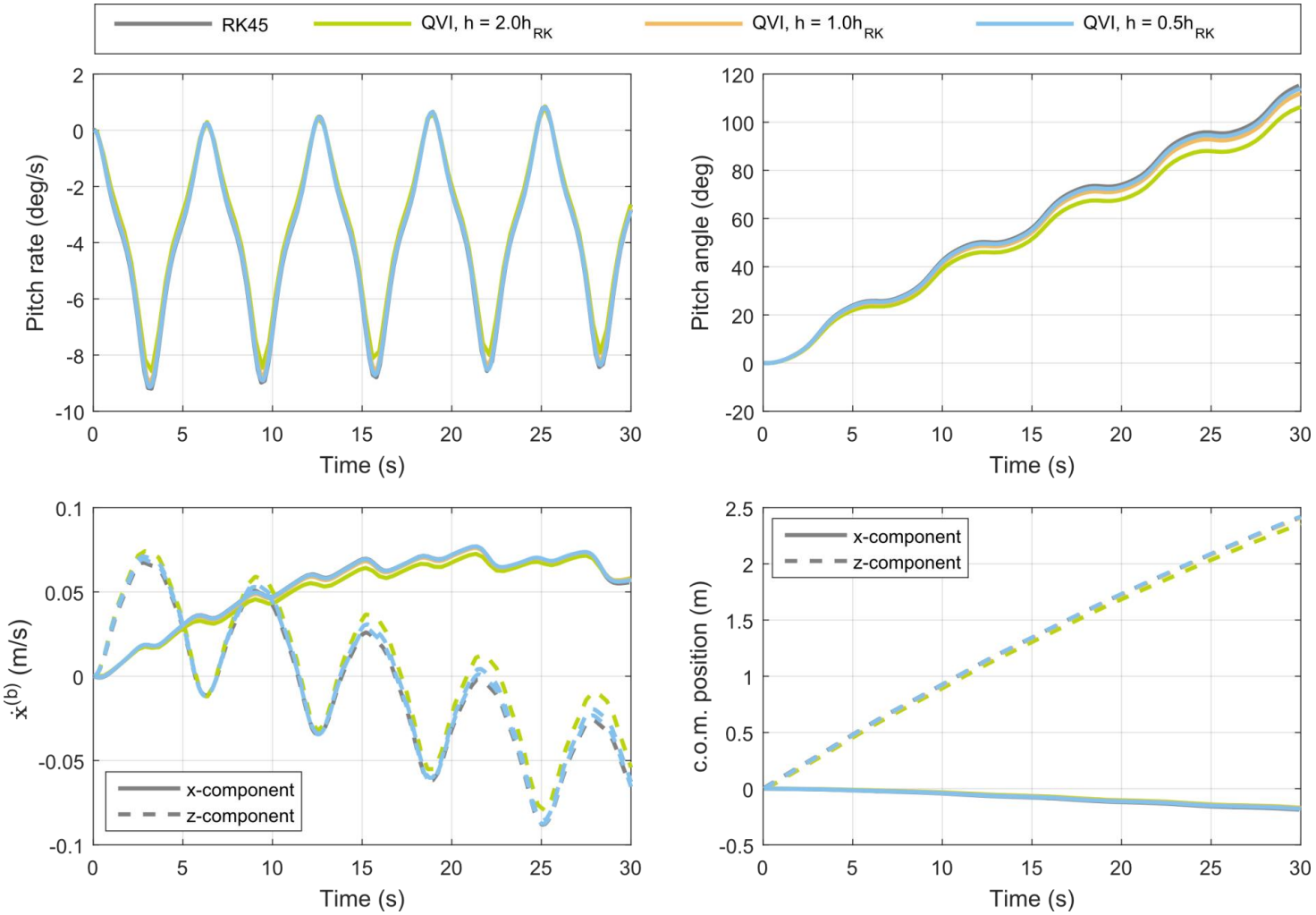

Figure 4.5.4: Integration results for the midpoint QVI applied to a biomimetic wing-flapping simulation, including aerodynamic forcing.

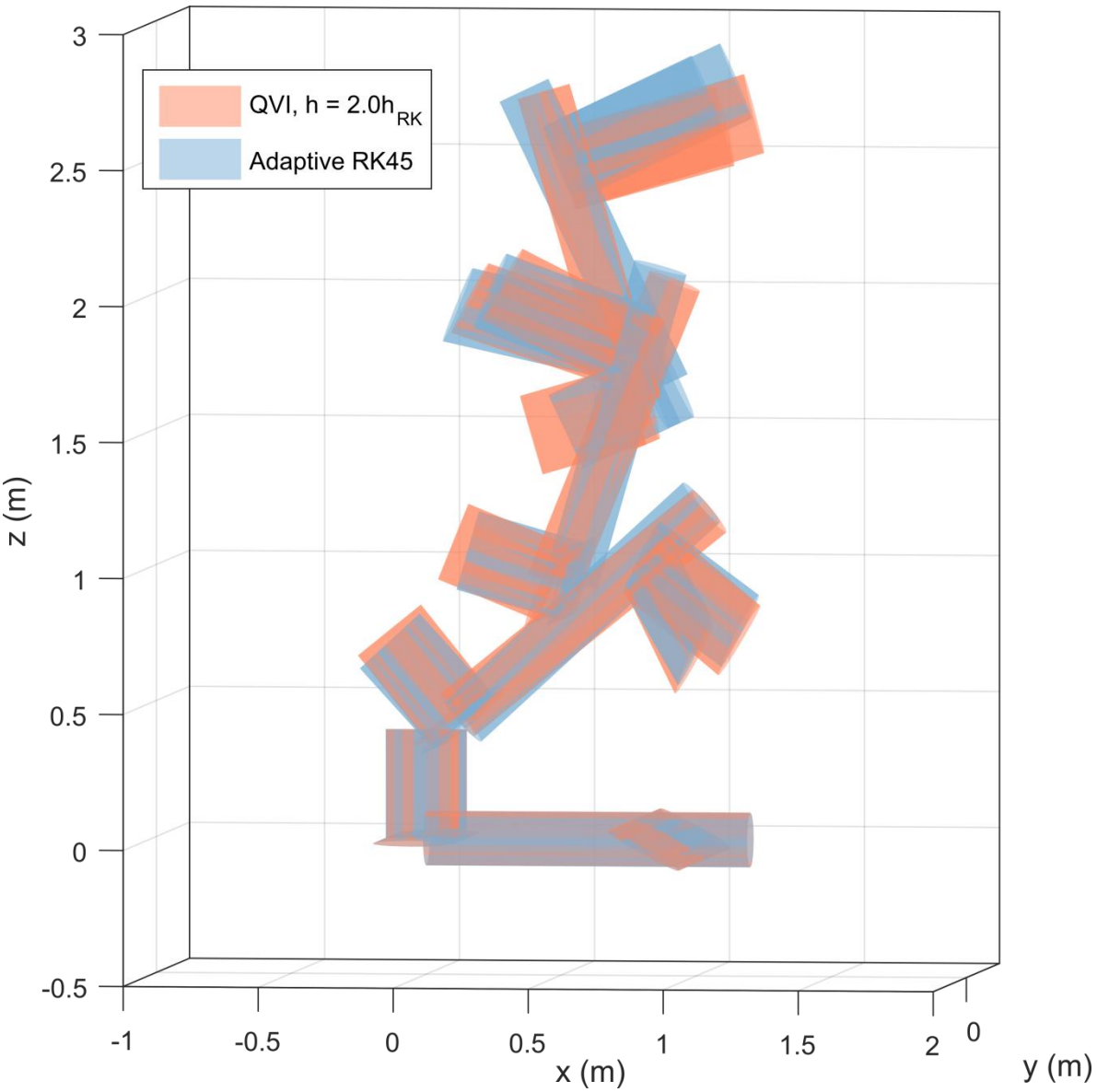

Figure 4.5.5: Flapping-wing simulation rendering for the midpoint QVI ($h = 2.0h_{RK}$) and the adaptive RK45 integrator, at $t \in [0, 7.5, 15, 22.5, 30]$ s.

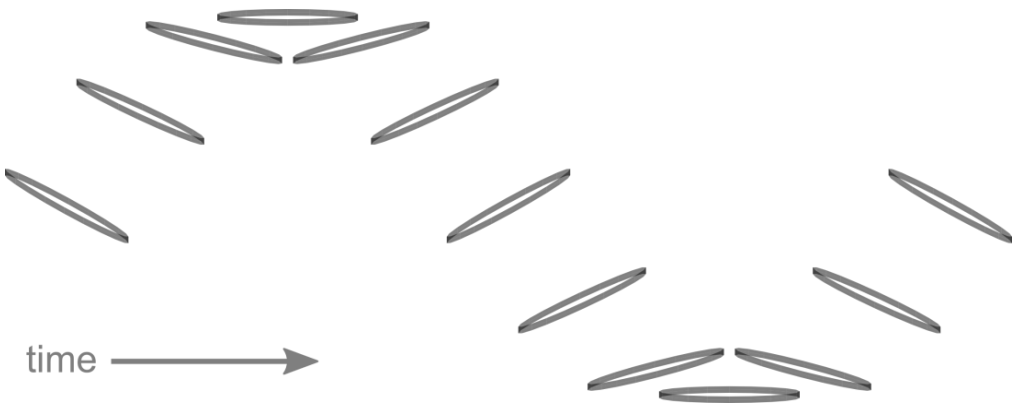

Figure 4.5.6: Rendering of wing control inputs for the flapping wing simulation.

CHAPTER REFERENCES

[1] Marsden, J. E., and West, M., "Discrete mechanics and variational integrators," *Acta Numerica 2001*, Vol. 10, 2001, pp. 357–514. DOI:10.1017/S096249290100006X.

[2] Lew, A., Marsden, J. E., Ortiz, M., and West, M., "Variational time integrators," *International Journal for Numerical Methods in Engineering*, Vol. 60, No. 1, 2004, pp. 153–212. DOI:10.1002/nme.958.

[3] Taeyoung Lee, N. H. M., "A Lie Group Variational Integrator for the Attitude Dynamics of a Rigid Body with Applications to the 3D Pendulum," pp. 962–967.

[4] Lee, D., Springmann, J., Spangelo, S., and Cutler, J., "Satellite Dynamics Simulator Development Using Lie Group Variational Integrator," AIAA Modeling and Simulation Technologies Conference, Portland, OR.

[5] Lee, T., and Leve, F., "Lagrangian mechanics and Lie group variational integrators for spacecraft with imbalanced reaction wheels," pp. 3122–3127.

[6] Sola, J., *Quaternion kinematics for the error-state KF*, Universitat Politecnica de Catalunya, Barcelona, Spain, 2016.

[7] Manchester, Z. R., and Peck, M. A., "Quaternion Variational Integrators for Spacecraft Dynamics," *Journal of Guidance, Control, and Dynamics*, Vol. 39, No. 1, 2016, pp. 69–76. DOI:10.2514/1.G001176.

[8] Müller, A., and Terze, Z., "Geometric methods and formulations in computational multibody system dynamics," *Acta Mechanica*, Vol. 227, No. 12, 2016, pp. 3327–3350. DOI:10.1007/s00707-016-1760-9.

[9] Müller, A., Terze, Z., and Pandza, V., "A Non-Redundant Formulation for the Dynamics Simulation of Multibody Systems in Terms of Unit Dual Quaternions," p. V006T09A011.

[10] Xu, D., Jahanchahi, C., Took, C. C., and Mandic, D. P., "Enabling quaternion derivatives: the generalized HR calculus," *Royal Society Open Science*, Vol. 2, No. 8, 2015, p. 150255. DOI:10.1098/rsos.150255.

[11] Cooke, J. M., Zyda, M. J., Pratt, D. R., and McGhee, R. B., "NPSNET: Flight Simulation Dynamic Modeling Using Quaternions," *Prescence*, Vol. 1, No. 4, 1992, pp. 404–420.

[12] Press, W. H., ed., *Numerical recipes*, Cambridge University Press, Cambridge, UK, 2007.

[13] Dormand, J. R., and Prince, P. J., "A family of embedded Runge-Kutta formulae," *Journal of Computational and Applied Mathematics*, Vol. 6, No. 1, 1980, pp. 19–26. DOI:10.1016/0771-050X(80)90013-3.

[14] Terze, Z., ed., *Multibody dynamics: computational methods and applications*, Springer, Cham, Switzerland, 2014.

[15] Magnus, J. R., and Neudecker, H., *Matrix differential calculus with applications in statistics and econometrics*, John Wiley, New York, 1999.

[16] Shampine, L. F., and Reichelt, M. W., "The MATLAB ODE Suite," *SIAM Journal on Scientific Computing*, Vol. 18, No. 1, 1997, pp. 1–22. DOI:10.1137/S1064827594276424.

[17] Atkinson, K. E., Han, W., and Stewart, D., *Numerical Solution of Ordinary Differential Equations*, John Wiley & Sons, Hoboken, NJ, 2009.

[18] Sussman, G. J., Wisdom, J., and Mayer, M. E., *Structure and interpretation of classical mechanics*, MIT Press, Cambridge, MA, 2001.

[19] Okasha, M., and Newman, B., "Switching Principles to Circumvent Euler Angle Singularity."

[20] Shah, S. V., Saha, S. K., and Dutt, J. K., *Dynamics of tree-type robotic systems*, Springer, Dordrecht, 2013.

[21] Jain, A., *Robot and multibody dynamics: analysis and algorithms*, Springer, New York, NY, 2011.

[22] Xu, J., and Halse, K. H., "Dual Quaternion Variational Integrator for Rigid Body Dynamic Simulation," *arXiv*, No. 1611.00616, 2016.

[23] Leitz, T., Ober-Blöbaum, S., and Leyendecker, S., "Variational integrators for dynamical systems with rotational degrees of freedom," 11th World Congress on Computational Mechanics, Barcelona, Spain.

[24] Demoures, F., Gay-Balmaz, F., Kobilarov, M., and Ratiu, T. S., "Multisymplectic Lie group variational integrator for a geometrically exact beam in," *Communications in Nonlinear Science and Numerical Simulation*, Vol. 19, No. 10, 2014, pp. 3492–3512. DOI:10.1016/j.cnsns.2014.02.032.

[25] Kibble, T. W. B., and Berkshire, F. H., *Classical mechanics*, Imperial College Press, London, 2004.

[26] Calkin, M. G., *Lagrangian and Hamiltonian mechanics*, World Scientific, Singapore, 1996.

[27] Nielsen, M. B., and Krenk, S., “Conservative integration of rigid body motion by quaternion parameters with implicit constraints,” *International Journal for Numerical Methods in Engineering*, Vol. 92, No. 8, 2012, pp. 734–752. DOI:10.1002/nme.4363.

[28] Dam, E. B., Koch, M., and Lillholm, M., *Quaternions, Interpolation and Animation*, University of Copenhagen, Copenhagen, Denmark, 1998.

[29] Markley, F. L., Cheng, Y., Crassidis, J. L., and Oshman, Y., “Averaging Quaternions,” *Journal of Guidance, Control, and Dynamics*, Vol. 30, No. 4, 2007, pp. 1193–1197. DOI:10.2514/1.28949.

[30] Boyle, M., “The Integration of Angular Velocity,” *Advances in Applied Clifford Algebras*, Vol. 27, No. 3, 2017, pp. 2345–2374. DOI:10.1007/s00006-017-0793-z.

[31] Bergou, A. J., Swartz, S. M., Vejdani, H., Riskin, D. K., Reimnitz, L., Taubin, G., and Breuer, K. S., “Falling with Style: Bats Perform Complex Aerial Rotations by Adjusting Wing Inertia,” *PLOS Biology*, Vol. 13, No. 11, 2015, p. e1002297. DOI:10.1371/journal.pbio.1002297.

Chapter 5:
Flight dynamics validation

5.1. INTRODUCTION: APPROACHES TO VALIDATION AND VERIFICATION

Flight simulator validation is a topic in which the literature is somewhat deficient – especially as pertaining to simulators of morphing-wing systems and/or those with fully three-dimensional aerodynamics. In broad terms, three modes of validation may be considered: validation in flight path data directly; validation in derivative flight dynamic metrics (e.g. trim states, flight dynamic modes); some form of piece-wise validation in which individual model components are validated separately. An independent distinction may be made between the sources of the validation dataset: physical experiments; higher-fidelity computational models; or alternative flight simulators of similar or lower fidelity.

These distinctions may be elucidated through a number of case studies. For example, the NATASHA simulator has seen significant use in low angle-of-attack flight path simulation for flexible HALE aircraft [1–3]. Its structural model is validated against existing beam dynamics results, and its combined flight dynamic / aeroelastic model is validated against an analogous flexible-dynamics simulator, RCAS [4], in basic flight dynamic metrics (trim states and wing loadings). In this case of low angle-of-attack flight simulation, a validation in terms of these flight dynamic metrics is sufficient. However, such an approach does not validate post-stall behaviour, as the authors note [1].

In contrast, the EBRD flight dynamic models of Obradovic and Subbaro [5–7] have been utilised for low angle-of-attack flight path simulation of morphing gull wing systems. However, despite further applications of analogous EBRB gull wing models by other authors [8] these models have no published validation in any aspect, aerodynamic or structural dynamic. Other morphing-wing flight dynamic models in the literature, including those of Seigler et al. [8,9], Wickenheiser and Garcia [10–12] and Mir Alikhan Bin [13] show the same lack of validation – despite, in some cases, the use of novel GK-type aerodynamic models. Two notable exceptions are the morphing-wing simulator of Niksch et al. [14] (subject to extensive aerodynamic model validation at quasistatic low angle-of-attack conditions) and the flapping-wing flight dynamic model of Orlowski and Girard [15] (subject to qualitative aerodynamic validation via comparison with a bespoke semi-empirical aerodynamic model). Orlowski and Girard [16] note the lack of validation in many similar studies of flapping-wing aircraft. At a component level, higher-fidelity aerodynamic models (e.g. GK or ONERA) have

seen extensive validation via experimentation [17,18] or computational fluid dynamics [19]; but implementations of these models in a flight dynamics context have seen little further validation.

This chapter concerns the validation of the case study morphing-wing flight dynamic model. Previous aspects of the analysis have provided a significant degree of verification – in confirming the accurate solution of the specified system. They have also provided a degree of validation, in that the parallel model derivation (in orientation parameterisation, weak/strong formulation and integrator derivation) provides some cross-validation of both modelling approaches. Indeed, the case study model has seen already a form of piece-wise validation: with the rigid-body dynamics validated w.r.t. alternate modelling approaches, and the aerodynamic data with control surface effects obtained directly from the literature.

However, further validation is required. In this chapter the completed case study flight dynamic model is validated against an experimentally-derived nonlinear stability derivative model of a 0.4-scale RQ-2 Pioneer UAV. Wind-tunnel data for this aircraft, from Bray [8], has been implemented by Selig and Scott [20] into the architecture of the open-source flight simulator *FlightGear* [21], utilising the flight dynamic model JSBSim, which has itself seen extensive verification and validation [22–25]. This yields a nonlinear flight dynamic model, valid for an angle-of-attack from -7° to 17°, based entirely on experimental aerodynamic data. *FlightGear* is then used to generate a variety of flight paths for different initial conditions, which are logged and compared to the results from the case study model. This validation has its limitations: it is restricted to pre-stall conditions (angle-of-attack from -7° to 17°) and does not account for wing morphing, but it does capture some attached-flow transient effects – via the nonlinear stability derivative terms in the validation model. It is thus useful for validating the aerodynamic mesh approach, and the complete flight dynamic model at least in a general sense. Computational fluid dynamics will be utilised for validating post-stall and strongly transient aerodynamic effects in Chapter 8.

5.2. RQ-2 PIONEER UAV MODEL

5.2.1. Parameter identification

The primary source of model-relevant data for the 0.4-scale RQ-2 Pioneer UAV is the work of Bray [26]; the source of the aerodynamic data used in the *FlightGear* flight dynamic model. This provides a variety of geometric and mass parameters: however, not all required parameters are specified. Additional data is taken from drawings in an available US Department of Defence (DoD) report [27] (reproduced in Figure 5.2.1). In the absence of a scale indicator the known wingspan is used to infer system measurements. It should be noted that these sources are slightly inconsistent: Bray [26] studies a RQ-2A, an early-model variant deployed in the Persian Gulf (1990-1991); whereas the DoD [27] depicts a RQ-2B, a systematic modification of several existing RQ-2A airframes made midway through the Gulf War (late 1990), and utilised in later operations [28]. A fully consistent dataset is unavailable due to the relative sparsity of information on this aircraft – nor is a fully-consistent dataset available for any other aircraft suitable for use in validation –but discrepancies between the two models are relatively minor. Table 5.2.1 gives the complete set of identified parameters for the RQ-2 Pioneer UAV model.

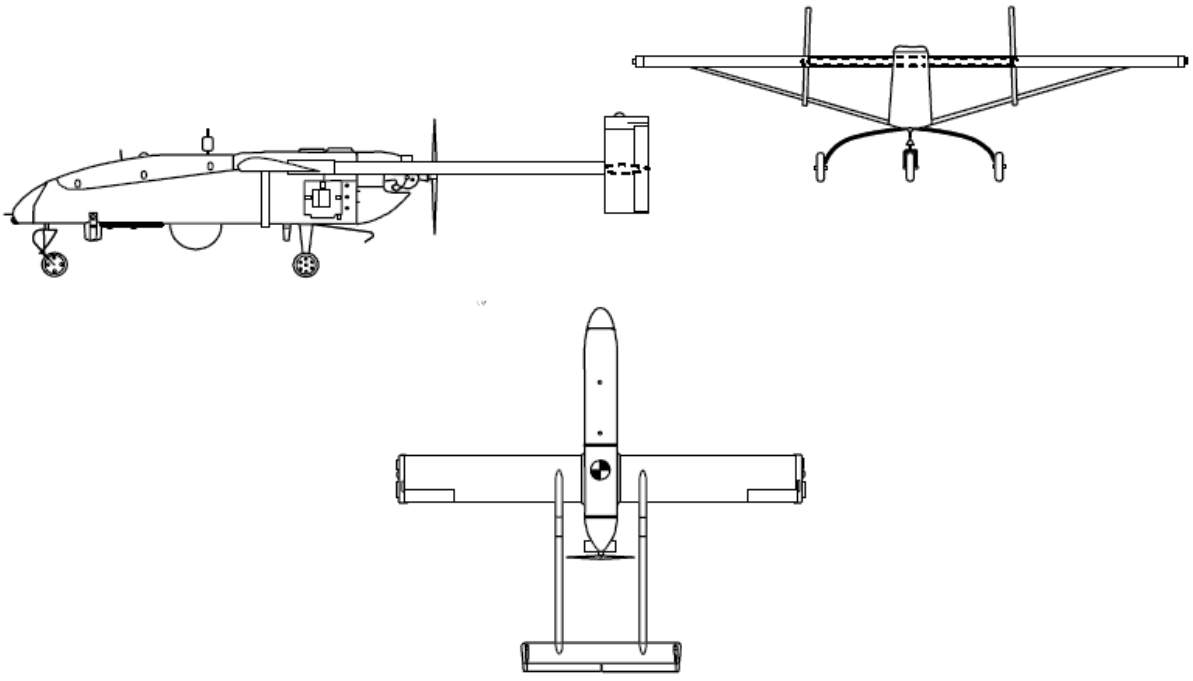

Figure 5.2.1: Drawing of a RQ-2 Pioneer UAV, reproduced from the US DoD [27], public domain. No scale is provided: measurements are inferred from the known wingspan.

Table 5.2.1: Parameters for the RQ-2 Pioneer UAV model

Property:	**Value**	**Source**
Airframe geometry:		
Body length – L_b	4.249 m	DoD [27]
Wing root location – $L_{r,x}$	2.150 m	DoD [27]
Wing and tailplane shoulder – $L_{r,z}$	0.371 m	Optimisation
Wing semispan – L_w	2.57 m	Bray [26]
Wing incidence – α_w	2°	Bray [26]
Wing chord – c_w	0.549 m	Bray [26]
Horizontal stabiliser semispan – L_e	0.925 m	Bray [26]
Horizontal stabiliser chord – c_e	0.305 m	Bray [26]
Vertical stabiliser height – L_f	0.661 m	Bray [26]
Vertical stabiliser chord – c_f	0.305 m	Bray [26]
Fuselage effective radius – r_b	0.194 m	DoD [27] (v. approx)
Point mass location – $L_{pm,x}$	2.19 m	Optimisation
Point mass location – $L_{pm,z}$	-0.387 m	Optimisation
Centre of mass location – $L_{\mathrm{c.o.m.},x}$	2.14 m	Flight data match
Centre of mass location – $L_{\mathrm{c.o.m.},z}$	0.60 m	Flight data match
Mass properties:		
Total mass – m_S	190.5 kg	Bray [26]
Fuselage mass – m_b	42.1 kg	Optimisation
Single wing mass – m_w	7.06 kg	Optimisation
Single elevator mass – m_e	0.250 kg	Optimisation
Fin mass – m_f	1.23 kg	Optimisation
Point mass – m_{pm}	131.3 kg	Optimisation
Inertia tensor – $I^{(b)}_{\mathrm{c.o.m.}}$	$\begin{bmatrix} 47.23 & & 6.647 \\ & 90.96 & \\ 6.647 & & 111.5 \end{bmatrix}$ kg m^2	Bray [26]
Aerofoil properties:		
Aerofoils	NACA4415/NACA0012	Bray [26]
NACA4415 max. thickness – $h_{\mathrm{W,max}}$	15% of chord	NACA [29]
NACA4415 mean thickness – $h_{\mathrm{W,av}}$	10% of chord	NACA [29]
NACA0012 max. thickness – $h_{\mathrm{H,max}}$	12% of chord	NACA [29]
NACA0012 mean thickness – $h_{\mathrm{H,av}}$	8.1% of chord	NACA [29]
Aerodynamic properties:		
Fuselage frontal drag – $C_{\mathrm{D,front}}A_{\mathrm{front}}$	0.0889 m^2	Bray [26] (derived)
Fuselage cross-section drag – $C_{\mathrm{D},b}$	0.465	Bray [26] (derived)

The case study multibody formulation requires a detailed description of the airframe mass distribution: something which is currently available. However, the total system mass and inertia tensor about the centre of mass are known from Bray [26], and this allows the a fully-constrained system mass distribution to be identified via a least-squares optimisation. Note that this optimisation does not entail a weakening of validation: it simply represents a translation between differing methods of encoding inertia information. The only remaining parameters to constrain this identification are the location of the system centre of mass, in x and z, for which a reliable source is unavailable – the depicted centre of mass location in [27] is of low precision, and of dubious reliability given the non-technical nature of the source document. The centre of mass location is instead identified with reference to the validation flight data. This process in presented in Section 5.2.2: while it weakens the validation somewhat, these two parameters are not enough to generate a false positive match on their own, given the twenty-six other parameters identified directly from data.

Aerofoil coordinate data for the system aerofoils (NACA4415 for the wings, and NACA0012 for the stabilisers) is defined by NACA [29]. Their maximum thicknesses are given in their 4-digit designations (15% and 12% of chord, respectively); mean thicknesses can be computed. Taking the experimental estimate of the total airframe frontal drag at zero angle-of-attack in Bray [26] and subtracting the contributions from the lifting surfaces, an estimate of the fuselage frontal drag coefficient is obtained: $C_{\mathrm{D,front}}A_{\mathrm{front}} = 0.0889$ m^2. The fuselage cross section is complex, with a tapered rectangular main fuselage, two boons extending to the tailplane, and landing gear and camera geometry. For inertial modelling this is taken as a cylindrical cross-section with approximate effective fuselage radius $r_b = 0.194$ m: as the system inertia tensor is matched to the result from Bray [26], the highly approximation nature of this model is of no significance. The cross-section drag coefficient is then identified from the airframe drag data at angle-of-attack 0.6 rad (c. 78°) [26]. Based on $r_b = 0.194$ m and $C_{\mathrm{D,front}}A_{\mathrm{front}} = 0.0889$ m^2, $C_{\mathrm{D},b} = 0.465$. The system kinematic chain then needs modifications to account for the new geometry, including the H-tail. Table 5.2.2 specifies the new kinematic chain for the system. Figure 5.2.2 shows a rendering of the model in MATLAB, with the shoulder parameters ($L_{r,x}$, $L_{r,z}$) defined. Alongside the addition of an extra vertical stabiliser in the computation of the aerodynamic forces, this completes the definition of the RQ-2 Pioneer UAV in the case study modelling framework.

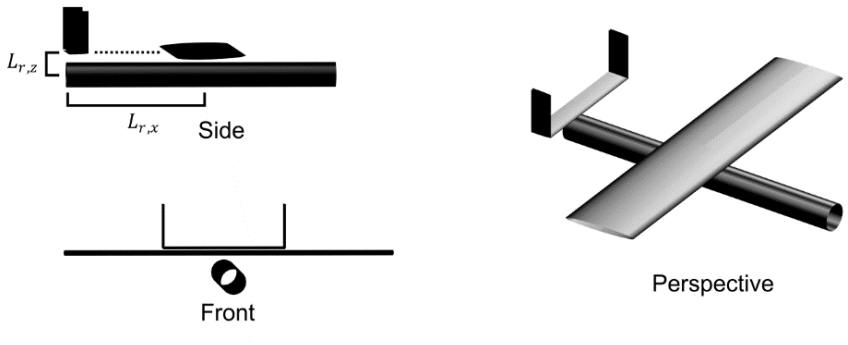

Figure 5.2.2: Rendering of the RQ-2 Pioneer UAV model in MATLAB, not to scale, with the H-tail visible and the shoulder parameters defined.

Table 5.2.2: Kinematic chain parameters for the RQ-2 Pioneer UAV model

Body Name	Index	l_c	$c=1$		$c=2$		[…]
			$\mathbf{L}_{i,1}$	$\mathrm{P}_{i,1}$	$\mathbf{L}_{i,2}$	$\mathrm{P}_{i,2}$	
body	b	1	$\left[\frac{1}{2}L_b\ 0\ 0\right]^T$	$\mathrm{P}_{E/B}$			
right wing	wr	2	$\left[L_{r,x}\ 0\ L_{r,z}\right]^T$	$\mathrm{P}_{E/B}$	$[G_{wr}\ 0\ 0]^T$	$\mathrm{P}_{E/B}\mathrm{P}_{B/WR}$	
left wing	wl	2	$\left[L_{r,x}\ 0\ L_{r,z}\right]^T$	$\mathrm{P}_{E/B}$	$[G_{wl}\ 0\ 0]^T$	$\mathrm{P}_{E/B}\mathrm{P}_{B/WL}$	
right elevator / horz. stabiliser	er	1	$\left[\frac{1}{2}L_e\ 0\ L_{r,z}\right]^T$	$\mathrm{P}_{E/B}\mathrm{P}_{B/ER}$			
left elevator / horz. stabiliser	el	1	$\left[\frac{1}{2}L_e\ 0\ L_{r,z}\right]^T$	$\mathrm{P}_{E/B}\mathrm{P}_{B/EL}$			
left fin / vert stabiliser	fl	2	$[L_e\ 0\ 0]^T$	$\mathrm{P}_{E/B}\mathrm{P}_{B/ER}$	$\left[\frac{1}{2}L_\mathrm{f}\ 0\ 0\right]^T$	$\mathrm{P}_{E/B}\mathrm{P}_{B/FL}$	
right fin / vert stabiliser	fl	2	$[L_e\ 0\ 0]$	$\mathrm{P}_{E/B}\mathrm{P}_{B/EL}$	$\left[\frac{1}{2}L_\mathrm{f}\ 0\ 0\right]^T$	$\mathrm{P}_{E/B}\mathrm{P}_{B/FL}$	
point mass	pm	1	$\left[L_{\mathrm{pm},x}\ 0\ L_{\mathrm{pm},z}\right]^T$	$\mathrm{P}_{E/B}$			

5.2.2. Identification of inertial properties

As noted, the RQ-2 UAV moment of inertia tensor about the system centre of mass is specified, as per Bray [26]. In the case study body-fixed coordinate system this tensor is:

$$I^{(b)}_{\mathrm{c.o.m.,\,spec}} = \begin{bmatrix} 47.23 & & 6.647 \\ & 90.96 & \\ 6.647 & & 111.5 \end{bmatrix} \mathrm{kg\,m^2}. \tag{5.2.1}$$

In the case study modelling framework it may be computed as:

$$I^{(b)}_{\mathrm{c.o.m.}} = \sum_{i\in\mathcal{S}} I^{(b)}_i + m_i\left(\mathbf{r}^{(b)}_i \cdot \mathbf{r}^{(b)}_i \mathrm{E}_{3\times3} - \mathbf{r}^{(b),T}_i \otimes \mathbf{r}^{(b)}_i\right), \tag{5.2.2}$$

where $\otimes$ denotes the vector Kronecker product, and $\mathbf{r}_i^{(b)} = \mathbf{x}_{\text{c.o.m.}}^{(b)} - \mathbf{x}_i^{(b)}$. The centre of mass location in the body-fixed reference frame, $\mathbf{x}_{\text{c.o.m.}}^{(b)}$, may be computed as:

$$\mathbf{x}_{\text{c.o.m.}}^{(b)} = \frac{1}{m_{\mathcal{S}}} \sum_{i \in \mathcal{S}} m_i \mathbf{x}_i^{(b)} = \left[L_{\text{c.o.m.},x}, 0, L_{r,z} - L_{\text{c.o.m.},z} \right] = \mathbf{x}_{\text{c.o.m., spec}}^{(b)}. \tag{5.2.3}$$

Note here the definition of $L_{\text{c.o.m.},x}$ and $L_{\text{c.o.m.},z}$: this formulation allows us to easily constrain the centre of mass location to be below the wing shoulder. Specified values of $I_{\text{c.o.m.}}^{(b)}$ and $\left[L_{\text{c.o.m.},x}, L_{\text{c.o.m.},z} \right]$ are then used to constrain the system mass parameters ($m_w, m_e, m_{\text{f}}, m_{pm}$, with $m_b = m_{\mathcal{S}} - 2m_w - 2m_e - 2m_{\text{f}} - m_{pm}$, constrained by $m_{\mathcal{S}} =$ 190.5 kg) as well as the point mass locations $L_{\text{pm},x}$, $L_{\text{pm},z}$ and the wing and tailplane shoulder $L_{r,z}$. These seven variables are only slightly underconstrained exactly by the six inertial variables – four in $I_{\text{c.o.m., spec}}^{(b)}$ and two in $\mathbf{x}_{\text{c.o.m., spec}}^{(b)}$. However, the addition of physically-derived inequality constraints $m_i > 0$ (positive masses), $L_{r,z} > 0$ (upwards shoulder), $L_{\text{c.o.m.},z} > 0$ (c.o.m. below shoulder) reduces the solution space. Suitable system parameter sets are computed via an interior point optimisation algorithm [30,31] applied to the error $\left\| I_{\text{c.o.m., spec}}^{(b)} - I_{\text{c.o.m.}}^{(b)} \right\|$ subject to the nonlinear constraints $\mathbf{x}_{\text{c.o.m., spec}}^{(b)} = \mathbf{x}_{\text{c.o.m.}}^{(b)}$ and the inequality constraints noted. The identified parameters, for $\left[L_{\text{c.o.m.},x}, L_{\text{c.o.m.},z} \right] =$ [2.14, 0.60] m are shown in Table 5.2.1. These values are predicated on the results of flight simulation tests presented in Section 5.5.

5.3. RQ-2 UAV INTEGRATOR TESTING

5.3.1. Overview

It is pertinent to perform a brief set of integrator tests on the RQ-2 Pioneer UAV system, particularly for the purpose of validating the application of these integrators to this system – both in terms of validation between integrators, and with relevant comparison to the analogous results in Chapter 4, Sections 4.4-4.5. Additionally, these integrator tests provide further data for the understanding of integrator behaviour – the differences in mass distribution between the systems has the potential to elucidate the effect of translation-rotation coupling on integrator performance. The kinetic energy coefficients for the RQ-2 UAV system, resolved in the body-fixed frame, are:

$$\begin{gathered} \mathrm{a}_{xx} = 95.25 \text{ kg}, \qquad \mathbf{a}_x = \mathbf{a}_\omega = [0\ 0\ 0]^T \\ \mathrm{A}_{x\omega}^{(b)} = \begin{bmatrix} & -43.6509 & \\ 43.6509 & & 407.670 \\ & -407.670 & \end{bmatrix} \text{ kg m} \\ \mathrm{A}_{\omega\omega}^{(b)} = \begin{bmatrix} 28.6188 & & 50.0316 \\ & 486.6903 & \\ 50.0316 & & 491.9502 \end{bmatrix} \text{ kg m}^2 \end{gathered} \tag{5.3.1}$$

In the absence of morphing-wing motion, these coefficients are time-invariant. They show a few notable differences to those of the case study system under similar conditions (cf. Eq. 4.4.16), which may affect integrator performance. Nondimensionalising $\mathrm{A}_{x\omega}^{(b)}$ and $\mathrm{A}_{\omega\omega}^{(b)}$ for each system by a_{xx} (= half the system total mass), and the wingspan $2L_w$, allows for a basic comparison. The case study system values are indicated in parentheses:

$$\begin{gathered} \frac{\mathrm{A}_{x\omega}^{(b)}}{2L_w \mathrm{a}_{xx}} = \begin{bmatrix} & -9\%\ (\mathbf{0.5\%}) & \\ 9\%\ (-\mathbf{0.5\%}) & & 83\%\ (\mathbf{87\%}) \\ & -83\%\ (-\mathbf{87\%}) & \end{bmatrix}, \\ \frac{\mathrm{A}_{\omega\omega}^{(b)}}{4L_w^2 \mathrm{a}_{xx}} = \begin{bmatrix} 1\%\ (\mathbf{2\%}) & & 2\%\ (\mathbf{0\%}) \\ & 19\%\ (\mathbf{25\%}) & \\ 2\%\ (\mathbf{0\%}) & & 19\%\ (\mathbf{26\%}) \end{bmatrix}. \end{gathered} \tag{5.3.2}$$

The RQ-2 UAV system is farther from its principal axes (as indicated by the non-diagonal term in $\mathrm{A}_{\omega\omega}^{(b)}$, which is significant with respect to the principal axes terms) and shows a greater degree of translation-rotation coupling, especially in the x-y axes, which additionally show a reversed direction of coupling.

5.3.2. Left-rectangle integration

Figure 5.3.1 shows the results of the quaternion left-rectangle variational integrator and the Euler angle adaptive RK4 integrator applied to the free rotation of the RQ-2 Pioneer UAV system (coefficients defined in Eq. 5.3.1); analogous to Chapter 4, Section 4.4.3. Definitions of the conventional system momenta, and the momenta and energy conservation errors, remain unchanged; and the RK4 integrator again takes a local truncation error (LTE) tolerance of 10^{-6} and relative tolerance of 10^{-3}. The adaptive RK45 integrator again allows a significantly larger step size, with a mean step size $\bar{h} = 0.088$ s over the simulation, in comparison to the specified $h = 0.01$ s for the QVI. This QVI step size is such that the integrator reaches a rotational momentum error equivalent to that of the RK45 integrator (c. 30%) by the simulation end time, $T = 1000$ s.

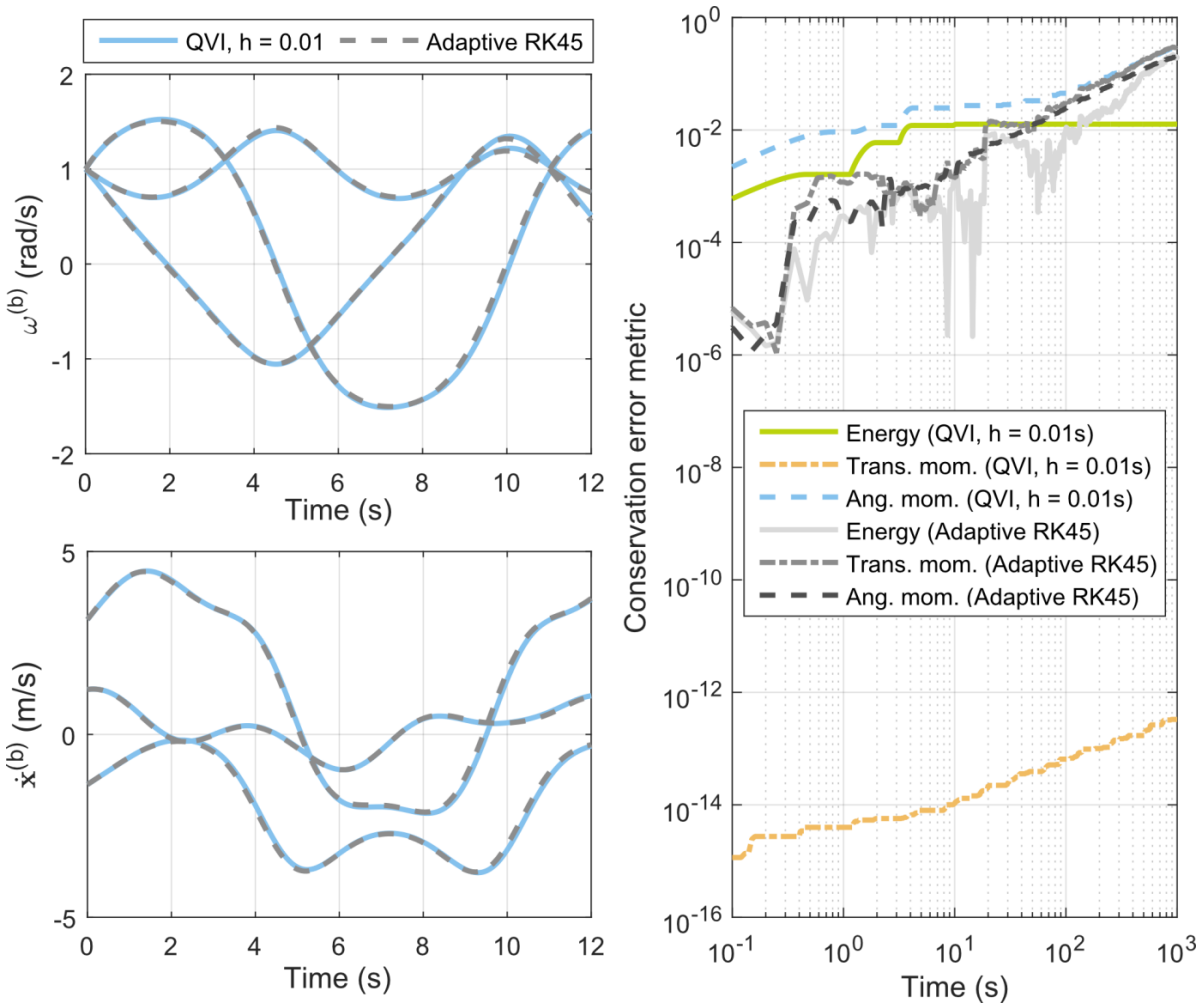

Figure 5.3.1: Integration results for the left-rectangle QVI applied to the free rotation of the RQ-2 Pioneer UAV system, compared to those of the adaptive RK45 integrator.

Again, the QVI shows excellent conservation properties in translational momentum and energy, with near-exact conservation of translational momentum, and a strongly stable oscillation in energy error – maximum magnitude c. 10^{-2}, and integral error 3×10^{-4} at $T = 1000$ s. However, again the conservation of angular momentum is poor: at the simulation end time the angular momentum conservation error is equivalent to that of the RK45 integrator, for a smaller mean step size and a slightly (5%) larger wall-clock computation time. The integrator does not show a hard stability threshold, but step sizes greater than $h \cong 0.01$ s result in rapid angular momentum error growth (at $h = 0.03$ s, reaching 30% by $T = 100$ s). As in the case study system application, this restriction on step size is a significant limitation on integrator application.

5.3.3. Midpoint integration

Figure 5.3.2 shows the midpoint QVI results for the RQ-2 Pioneer UAV system, compared to the left-rectangle QVI, at $h = 0.01$ s. The midpoint method energy and angular momentum conservation errors are approximately two orders of magnitude smaller that the left-rectangle method, again demonstrating the benefit of the increase in integration order, consistent with Chapter 4, Section 4.5.3. Figure 5.3.3 shows the results of the midpoint QVI applied to the freely-rotating RQ-2 Pioneer UAV, again in comparison to the Euler angle adaptive RK45 integrator. The QVI step size is taken as the mean step size for the RK45 integration ($h = h_{RK} = 0.088$ s). As can be seen, the midpoint QVI significantly outperforms the RK45 integrator in long-term energy and momentum conservation; but is associated with a degree of local solution error, particularly in terms of the timescale of the oscillations in $\boldsymbol{\omega}^{(b)}$. These effects are identical to those identified in Chapter 4, Section 4.5.3: local accuracy is traded for long-term stability and energy/momentum conservation. However, a notable difference for this test case is that the permissible step size for qualitative accuracy over the simulated time range is significantly larger relative to the RK45 integrator – the mean RK45 step size performs well at $h = h_{RK}$. Compare Chapter 4, Figure 4.5.1.

Figure 5.3.4 shows the midpoint QVI results for a pitch-up flapping wing simulation analogous to that of Chapter 4, Section 4.5.3. The aerodynamic and structural model of the RQ-2 UAV system is used (Section 5.2), while propulsive and gravitational forces are omitted. The symmetric wing control inputs are identical to those of Chapter 4, Section 4.5.3: dihedral $\theta_w(t) = \sin(t)$ rad and incidence $\phi_w(t) = -0.5\cos(t)$ rad. Note that the RQ-2 UAV system is not in reality fitted with morphing-capability: this is only a simulation test case. Figure 5.3.4 presents the solutions for three different timesteps, $h = h_{\mathrm{RK}}$, $0.5h_{\mathrm{RK}}$ and $0.25h_{\mathrm{RK}}$, where the mean stepsize of the adaptive RK45 integrator is $h_{\mathrm{RK}} = 0.0940$ s. The solution at $h = h_{\mathrm{RK}}$ shows notable inaccuracy, underestimating the aircraft pitch angle by c. 20% at the end of the simulation, c. 5 periods of flapping. The solutions at $0.5h_{\mathrm{RK}}$ and $0.25h_{\mathrm{RK}}$ are more accurate; to within 10% and 5% respectively. However the QVI performance for this test case, relative to the adaptive RK45 integrator, is significantly worse than the corresponding test in the case study system – see Chapter 4, Section 4.5.3.

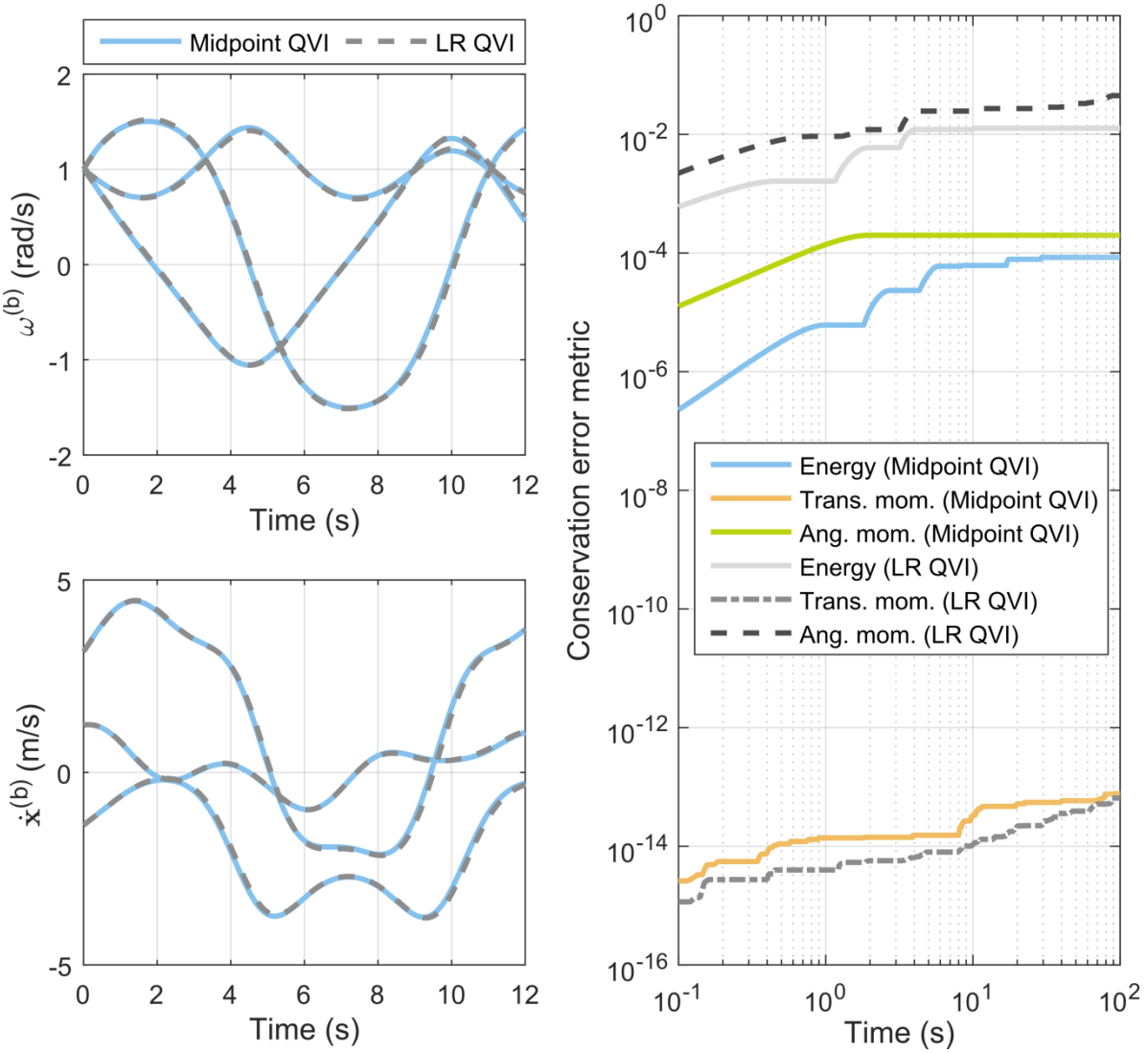

Figure 5.3.2: Integration results for the midpoint QVI applied to the free rotation and translation of the RQ-2 Pioneer UAV, compared to the left-rectangle QVI.

For further comparison, Figure 5.3.5 shows the simulation result for a different flapping-wing simulation; this time generating pitch-down motion, with dihedral $\theta_w(t) = \sin(t)$ rad and incidence $\phi_w(t) = 0.5\cos(t)$ rad. Note that the flapping-wing frequency is the same, and the adaptive RK45 mean step size is effectively identical ($h_{\mathrm{RK}} = 0.0940$ s). The QVI step sizes are $h = 2.0h_{\mathrm{RK}}$, $1.0h_{\mathrm{RK}}$ and $0.5h_{\mathrm{RK}}$, and these show pitch angle errors of 43%, 21%, 10% at $T = 30$ s. These results are consistent with those of the pitch-up simulation in Figure 5.3.4, and further demonstrate the poor performance of the QVI when applied to the RQ-2 UAV system. It is clear that the QVI performance is strongly system-dependent, and in particular suffers when applied to systems with canonical momenta that are not conserved.

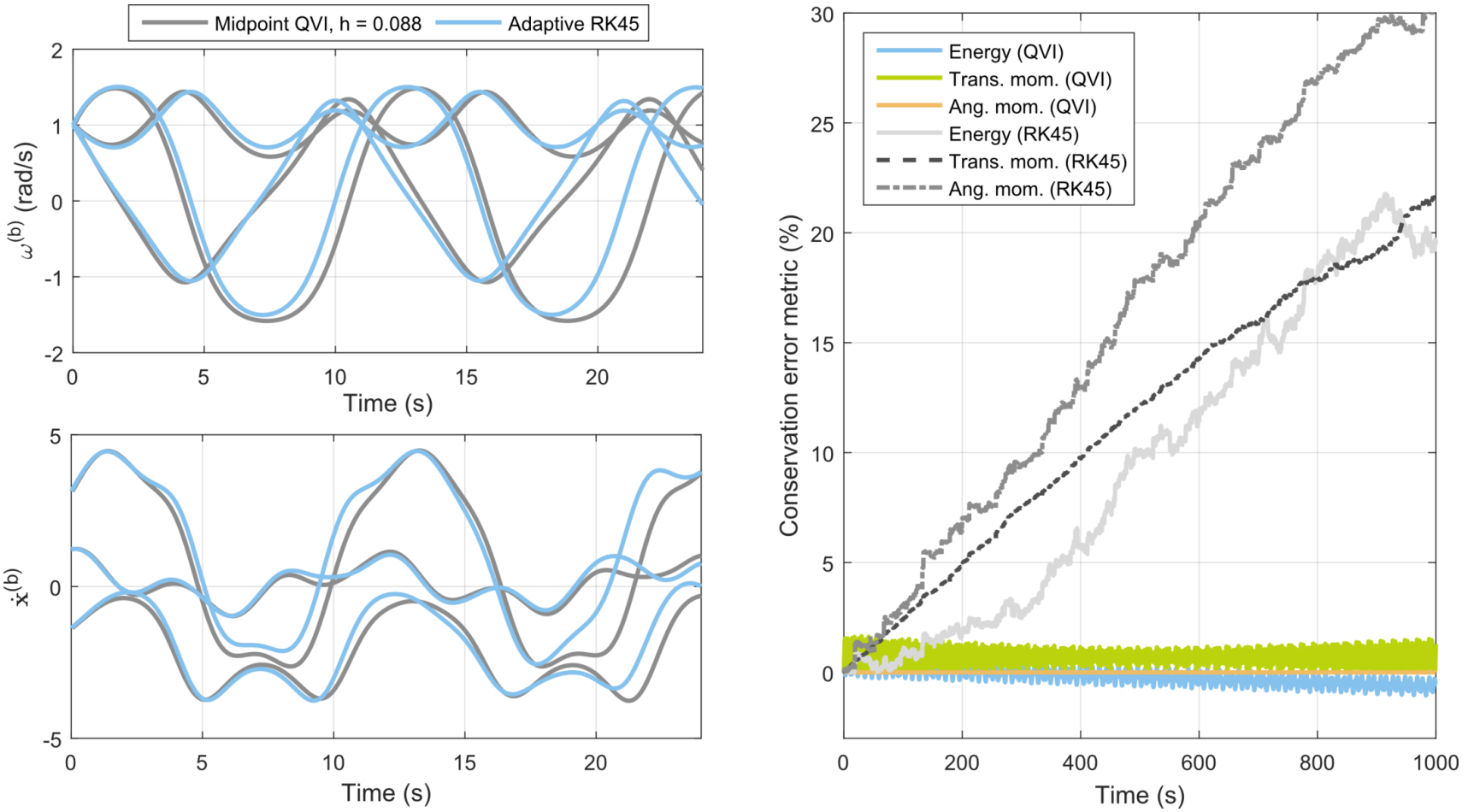

Figure 5.3.3: Integration results for the midpoint QVI applied to the free rotation and translation of the RQ-2 Pioneer UAV system, compared to the adaptive RK45 integrator.

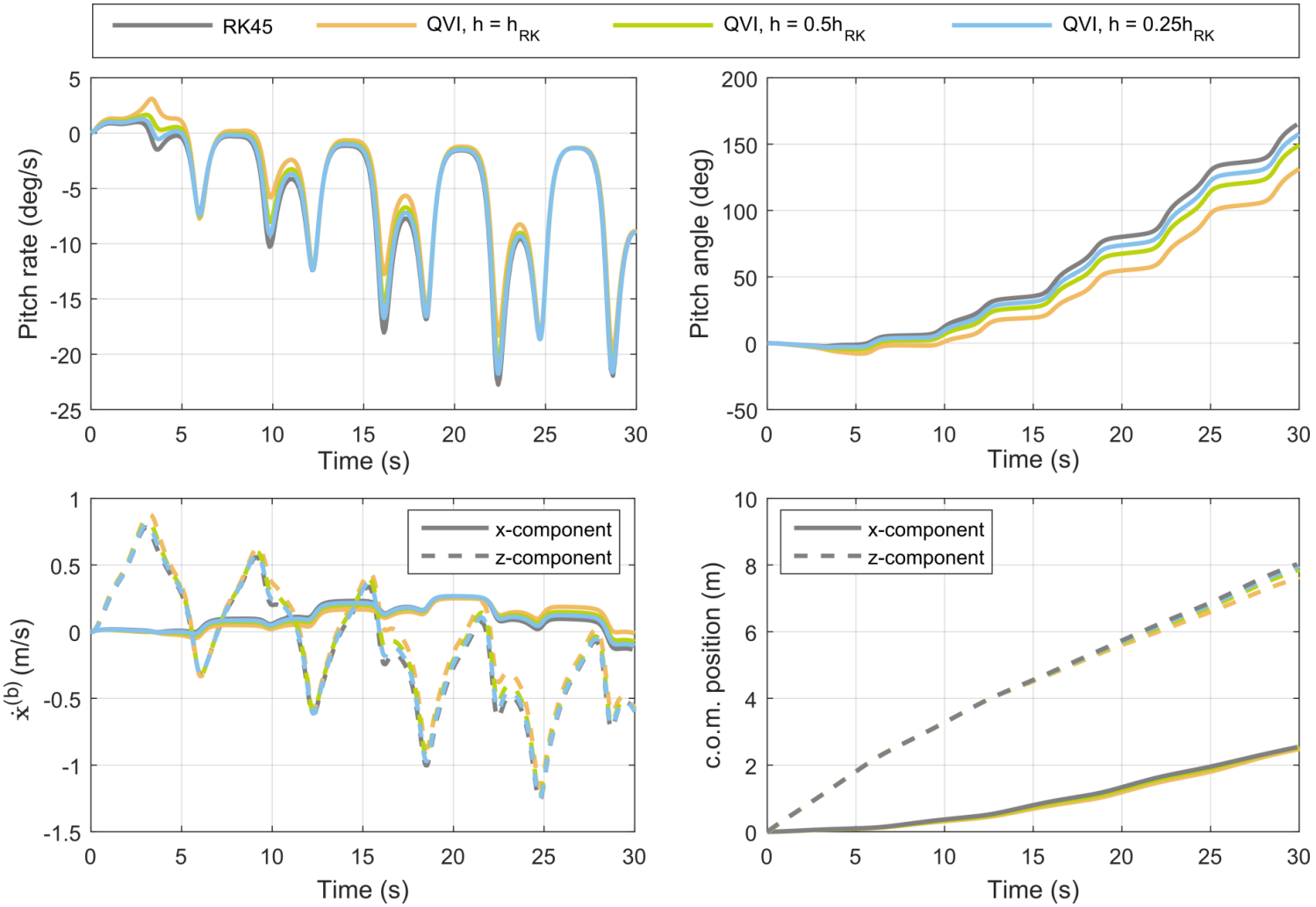

Figure 5.3.4: Integration results for the midpoint QVI applied to a pitch-up wing-flapping manoeuvre in the RQ-2 Pioneer UAV.

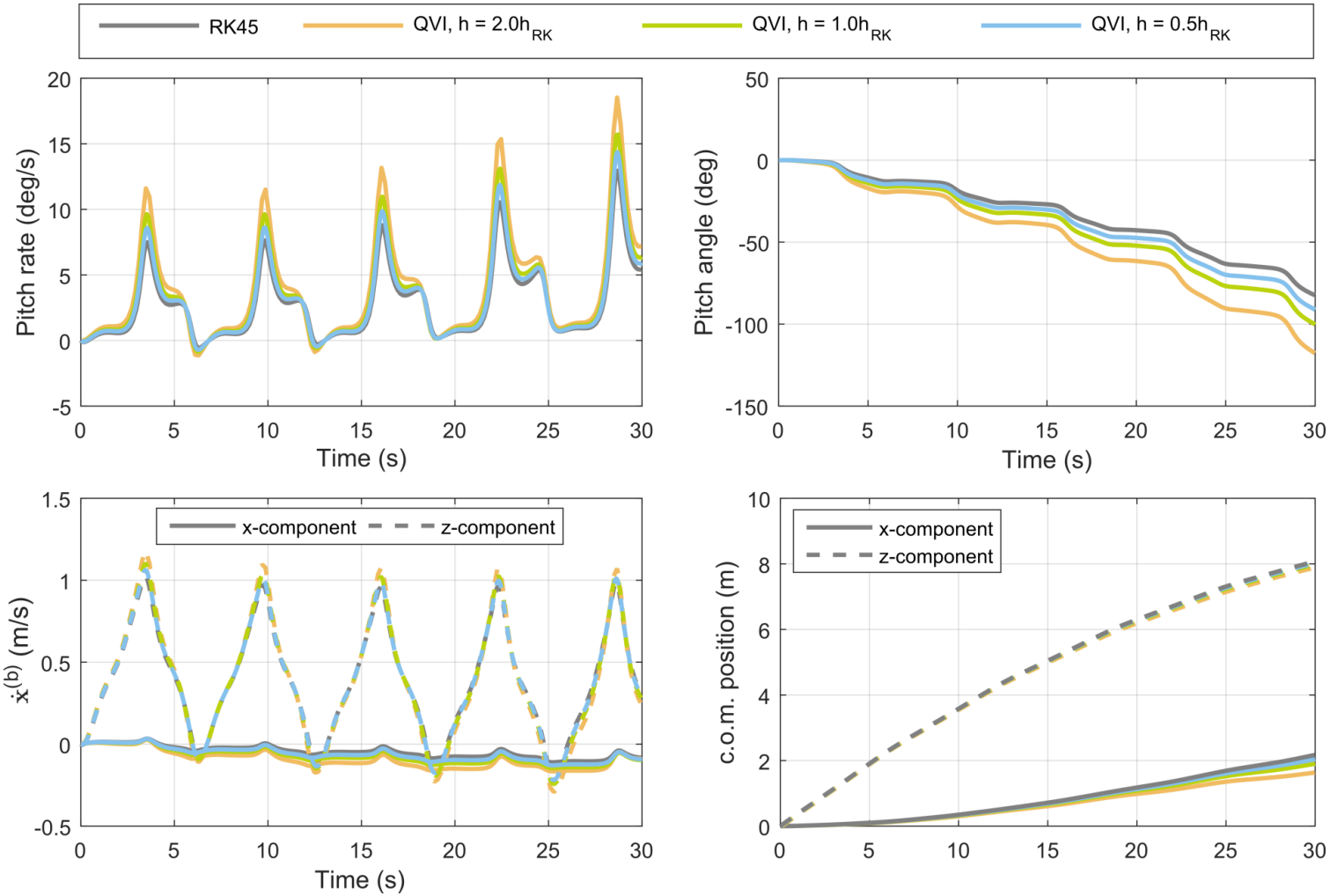

Figure 5.3.5: Integration results for the midpoint QVI applied to a pitch-down wing-flapping manoeuvre in the RQ-2 Pioneer UAV.

5.4. AERODYNAMIC COEFFICIENT VALIDATION

It is possible to compare aerodynamic forces and coefficients generated by the case study model of the Pioneer RQ-2 UAV to those utilised directly in the stability-derivative model of this UAV in *FlightGear* / JSBSim; which are taken directly from Bray [26]. This provides a first line of validation for the case study model. Bray [26] defines the 6DOF aerodynamic forces on the system with six coefficients; lift (C_L), drag (C_D), sideforce (C_Y), pitching moment (C_m), yawing moment (C_n), and rolling moment (C_l), defined in the stability reference frame. This reference frame tracks with the body reference frame in yaw, but not in pitch and roll. In the case study framework, this is analogous to a set of axes (denoted frame T) with unit vectors:

$$\begin{aligned} \hat{\boldsymbol{\imath}}_t &= \hat{\mathbf{r}}_b \times \hat{\mathbf{k}}_e, && \text{the appropriate frame completion;} \\ \hat{\mathbf{j}}_t &= \hat{\mathbf{r}}_b, && \text{an internal body-fixed frame unit vector;} \\ \hat{\mathbf{k}}_t &= \hat{\mathbf{k}}_e, && \text{the earth frame vertical unit vector;} \end{aligned} \tag{5.4.1}$$

and thus with frame transformation matrix:

$$\mathrm{P}_{E/T} = \left[\hat{\mathbf{r}}_b^{(e)} \times \hat{\mathbf{k}}_e^{(e)}, \hat{\mathbf{r}}_b^{(e)}, \ \hat{\mathbf{k}}_e^{(e)}\right]. \tag{5.4.2}$$

Note that the reference frame defined by Bray [26] shows several sign changes with respect to the case study analogue; these are easily accounted for when comparing coefficients. The data of Bray [26] decomposes these 6DOF stability axes coefficients into a number of key dependencies. Several of these concern the dependency of a coefficient on a control surface deflection: these dependencies are ignored, as the case study model of the RQ-2 UAV does not contain a control surface model due to the lack of information regarding the RQ-2 UAV control surface geometry.

The remaining coefficient dependencies are then distinguished as to their linearity: five coefficient dependencies are defined in a tabulated format, capturing nonlinear effects; whereas the rest (10+) are defined as linear relationships. The five tabular / nonlinear dependencies provide the most robust avenue to coefficient validation, as they cover a wider spectrum of flight states. These dependencies all relate to aircraft orientation angles (angle-of-attack α and sideslip angle β) and are as follows: the lift as a function of angle-of-attack, $C_L(\alpha)$; the drag as a function of angle-of-attack, $C_D(\alpha)$; the sideforce as a function of

sideslip angle, $C_Y(\beta)$; the pitching moment as a function of angle-of-attack, $C_m(\alpha)$; and the yawing moment as a function of sideslip angle, $C_n(\beta)$. Figure 5.4.1 shows a comparison of these coefficient dependencies with the coefficient predictions of the case study model; which are computed at the aerodynamic reference point: 33% MAC, i.e. 33% of the wing chord aft of the wing leading edge, and on the thrust line which lies approximately in the wing plane. As can be seen, the coefficients yield a good match. The case study model underestimates the aircraft drag somewhat; understandably, as it does not account for the complexity of the fuselage drag. The drag spike at low angles of attack is an artefact of extrapolation for the wing aerodynamic coefficients and does not affect the flight simulation comparison; the *FlightGear* / JSBSim model cannot simulate to these low angles of attack either.

Overall, our coefficients results tend to show a more extreme gradient than the empirical coefficients in the pre-stall regime, and a less extreme gradient in the post-stall regime. The results of Bray [26] show stronger linear trends bridging pre- and post-stall regimes, and a weaker stall transition. This difference could be attributable to differing aerodynamic data, and the corresponding strength of the stall transition; differing model properties with particular reference to the location of the aerodynamic reference point; and three-dimensional effects which are likely to decrease the strength of the coefficient gradients.

Comparisons between the linear coefficient dependencies are less easy to contextualise than with the nonlinear dependencies; and moreover, the majority concern isolated angle rate dependencies, which are defined via heuristic methods and not computed experimentally, making them a less robust target for validation. Only one linear dependency is important to compare: the rolling moment coefficient as a function of sideslip angle; physically, the dihedral effect. Figure 5.4.2 shows a comparison between the linear dihedral effect computed by Bray [26] and the predictions of the case study model.

Here a difficulty reference point definition in Bray [26] becomes apparent: in the wind-tunnel test model, the centre of mass / aerodynamic reference point is defined along the thrust line, which in Figure 5.2.1 lies in the wing plane, almost on the upper surface of the fuselage. This is a not a reasonable physical location: the mass distributed beneath the wing

plane will be many times larger than that that distributed in the thin strip of material above it. The fact that the fuselage shows upwards tapering adds further to this assertion. It is thus probable that the thrust line for the model used by Bray [26] is located at a lower waterline; but no further information is given. The height of the centre of mass / aerodynamic reference point has a minor effect on the coefficient profiles in Figure 5.4.1, but has a large effect on the dihedral effect. Figure 5.4.2 shows the effect of two reference point locations: on the thrust line / wing plane; and 100 mm beneath the wing plane into the fuselage. There is good agreement between the predictions in the linear regime at low sideslip angles: in particular, the 100 mm reference point shift leads unexpectedly to a near-exact agreement. This supports the hypothesis that the centre of mass / reference point should be located further in the fuselage.

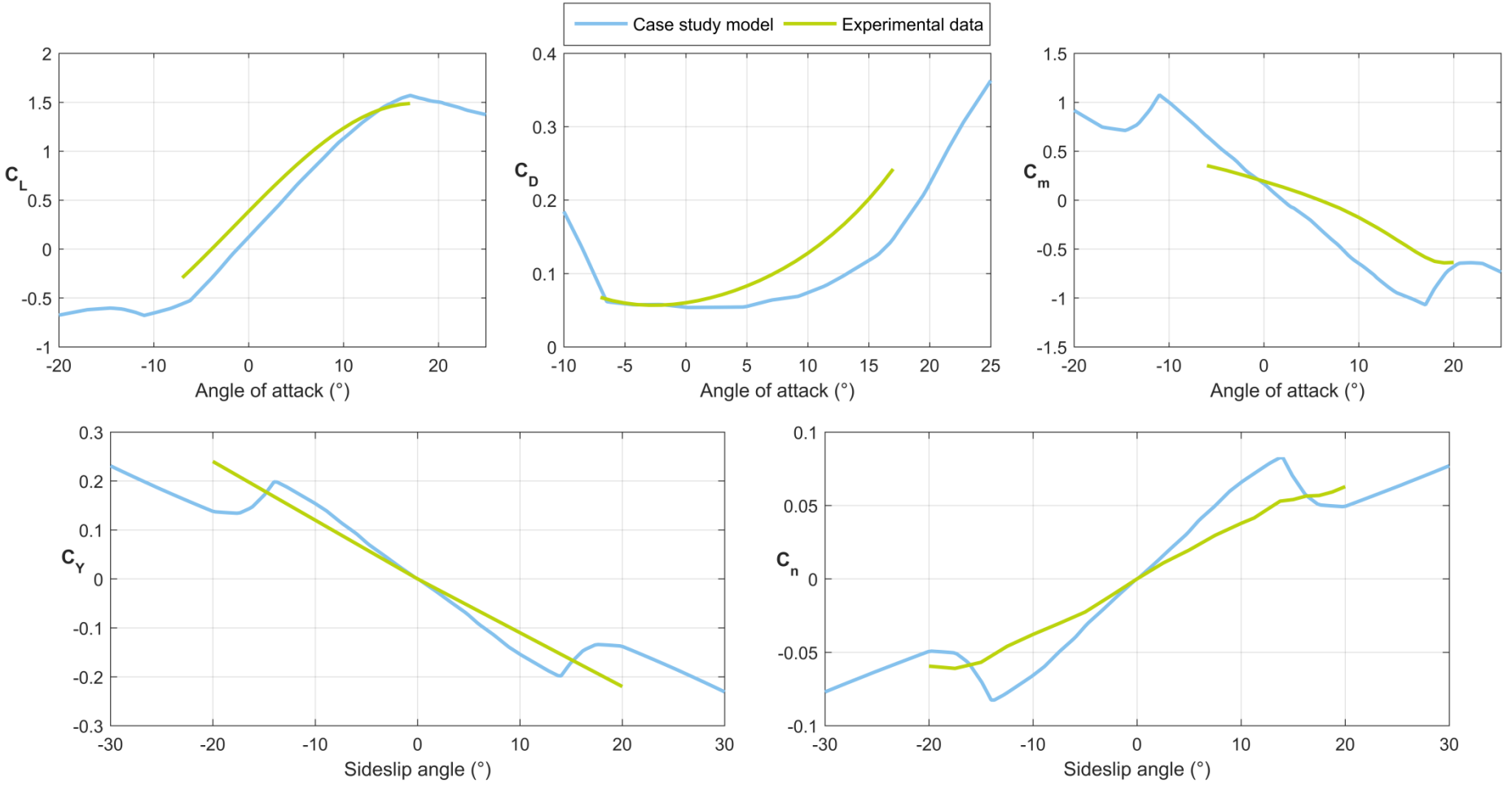

Figure 5.4.1: Lift, drag and pitching moment coefficients as a function of angle of attack; and sideforce and yaw moment coefficients as a function sideslip angle: compared between the case study model and the experimental data from Bray [26].

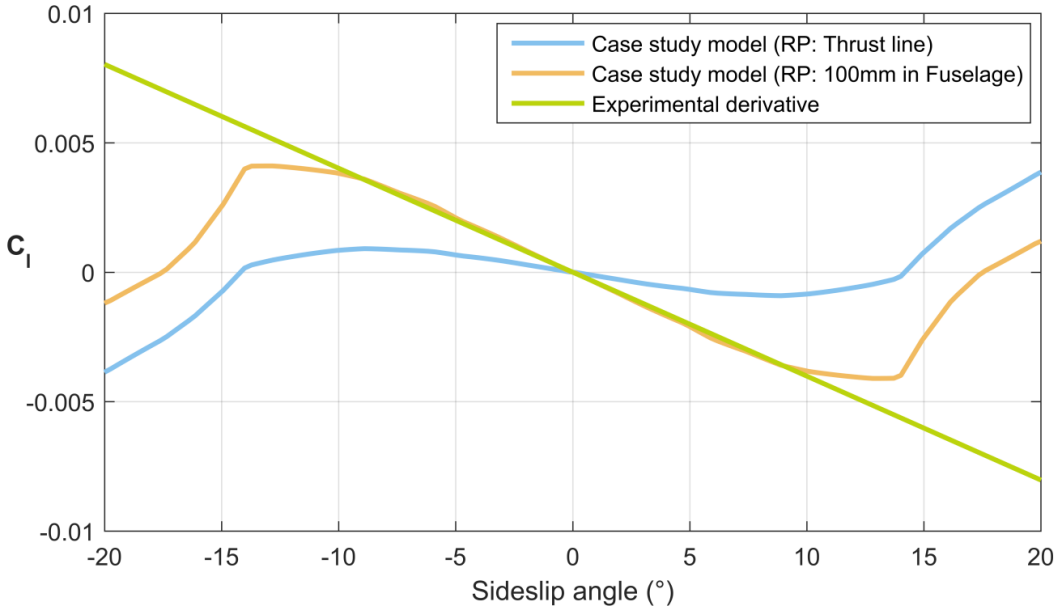

Figure 5.4.2: Roll coefficient as a function of sideslip angle (the dihedral effect) for the case study model (two reference point locations) and the experimental value from Bray [26].

5.5. FLIGHT SIMULATION VALIDATION

5.5.1. Validation simulations in *FlightGear*

The experimental aerodynamic and structural data of Bray [26] is implemented by Selig and Scott [20] in a nonlinear stability-derivative model in *FlightGear* / JSBSim. In addition to the traditional stability derivatives, the first-order effects of angular velocity (pitch, roll and yaw rate) on the aircraft aerodynamic coefficients are included as nonlinear functions of their respective angles. The strongly empirical nature of this model leads us to expect a high degree of realism from the simulation results – within the limits of model validity – making it a useful benchmark for the validation of the case study flight dynamic model. The use of manoeuvre flight simulation allows a broad-spectrum validation which accounts for all the complex empirically-derived coefficients of Bray [26] in a holistic manner. The simulation engine itself, JSBSim, has itself seen extensive verification and validation [22–25]. JSBSim uses traditional 6DOF equations of motion, following Stevens et al. [32] formulated in an aircraft body-fixed reference frame, operating within a spherical earth reference frame (latitude/longitude/altitude). The aircraft orientation is parameterized with a unit quaternion. Aerodynamic forces – the only forces, other than gravity, that are relevant to our analysis – are computed via their full-aircraft aerodynamic coefficients; and these are built up via the decoupled tabulated or linear contributions as per Section 5.4.

We are unable to consider the effects of control surface deflection or morphing-wing motion in this validation – the former due to a lack of control surface information and aerodynamic data to implement; the latter as a limitation of the aerodynamic data of Bray [26] and the functionality of FlightGear / JSBSim. Propulsive effects are also omitted, to the end of further model simplicity. As all these effects represent relatively simple additions to the overall multibody dynamic / aerodynamic mesh framework, the validation of the flight dynamic model in fixed-wing conditions should endow at least some validity to the overall model. The strongly transient effects that might arise from rapid wing or aircraft motion, and the limits to the validity of the quasisteady aerodynamic model, will be considered in more detail in Chapter 8. The purpose of the *FlightGear* model is to validate the case study flight dynamic model under more conventional flight conditions.

Flight simulations are carried out in completely still weather over the Canterbury Plains, New Zealand (without loss of generality). Figure 5.5.1 shows an image of the flight simulation interface in *FlightGear*: a generic low-poly glider model is used as a placeholder for the aircraft. The aircraft coordinate histories (latitude/longitude) are converted to Cartesian distances via a flat-earth model about the initial aircraft location. The aircraft orientation and Cartesian position histories are then used to provide initial conditions (orientation, angular and translational velocity) for simulations in the case study modelling framework. The adaptive RK45 integrator in Euler angles is used; it is confirmed that the midpoint QVI generates identical results at sufficiently small step sizes.

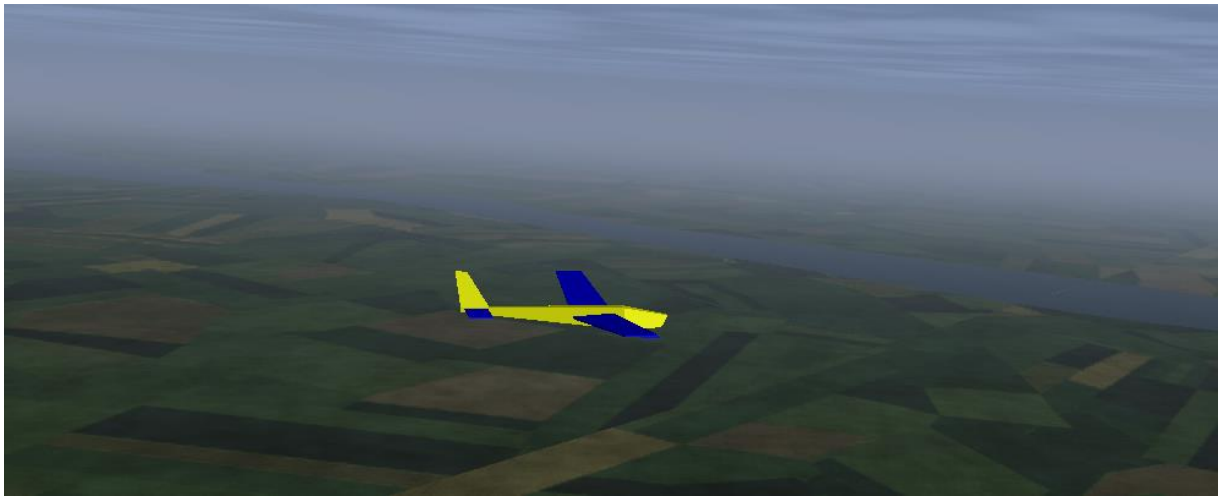

Figure 5.5.1: Flight simulation of the RQ-2 Pioneer UAV in *FlightGear*.

5.5.2. Validation results

Figures 5.5.2 and 5.5.3 show the orientation histories and flight paths (respectively) for eight validation simulations (A-H), covering a wide range of motion amplitudes, and corresponding to three forms of aircraft behaviour – phugoid oscillations (A-B), dives (C-D) and spiral dives (E-H), starting at large and small initial perturbations in bank (E 37° and F 23°, G 5° and H 9°). The centre of mass location is taken as $L_{\text{c.o.m.},x} = 2.14$ m , $L_{\text{c.o.m.},z} = 0.60$ m, as per Table 5.2.1, and corresponding to an overall good flight simulation match, with particular reference to the phugoid flight simulations (A-B). The details of the selection of this location, and possible alternatives, are discussed in Section 5.5.4.

The simulation affinities for the phugoid and dive simulations are all excellent: the case study model even captures the small roll and yaw drift associated with simulation (A). An excitation of the short period mode is observed in the phugoid simulations (A-B). However, this is not a significant phenomenological difference, and probably represents a slight perturbation away from the locally consistent state for the case study model at the start of the manoeuvre. That is, the specified initial translational velocity and orientation (derived from *FlightGear* simulations) are inconsistent with the specified initial angular velocity (also so derived) and so a corrective short-period response in angular velocity/orientation occurs.

The areas of greatest discrepancy are the spiral dives (E-H), which are sharper in the *FlightGear* model, and associated with greater altitude loss. The spiral dives with a large initial perturbation (E-F) show a reasonably good match, but those with small initial perturbations (G-H) show significant deviation. That these deviations show consistent characteristics at least supports the overall validation, and indicates simply a difference in spiral mode stability between the two models. This can probably be attributed to the inconsistency in the aircraft geometric properties due to the mismatch in aircraft model number noted earlier. Overall, the validation results are good, indicating that the case study model does not suffer any significant deficiencies in modelling conventional flight regimes, and supporting the modelling framework which is extended to include post-stall and strongly transient behaviour. Further validation of these more complex effects is carried out in Chapters 8-9.

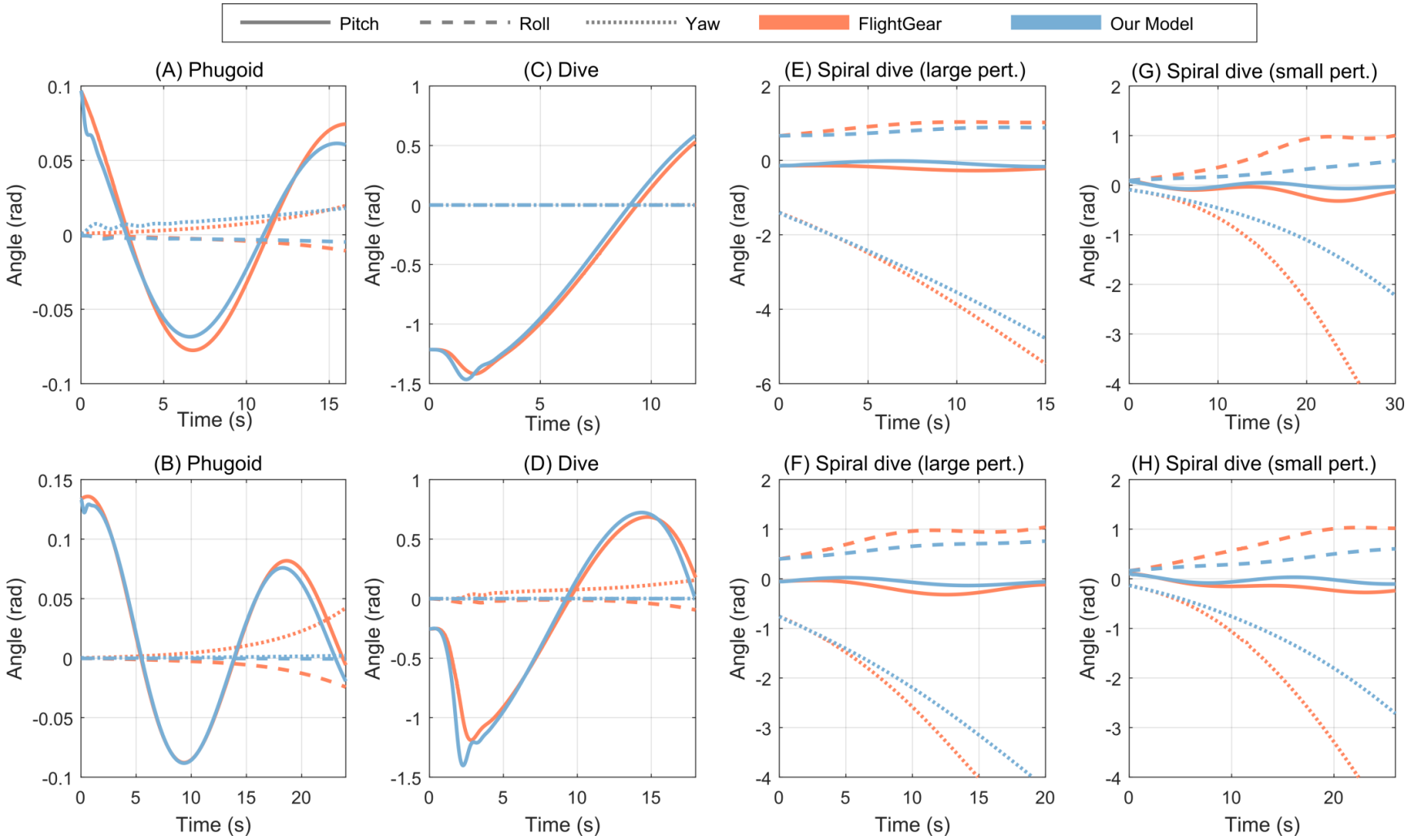

Figure 5.5.2: Orientation histories for the RQ-2 Pioneer UAV validation simulations.

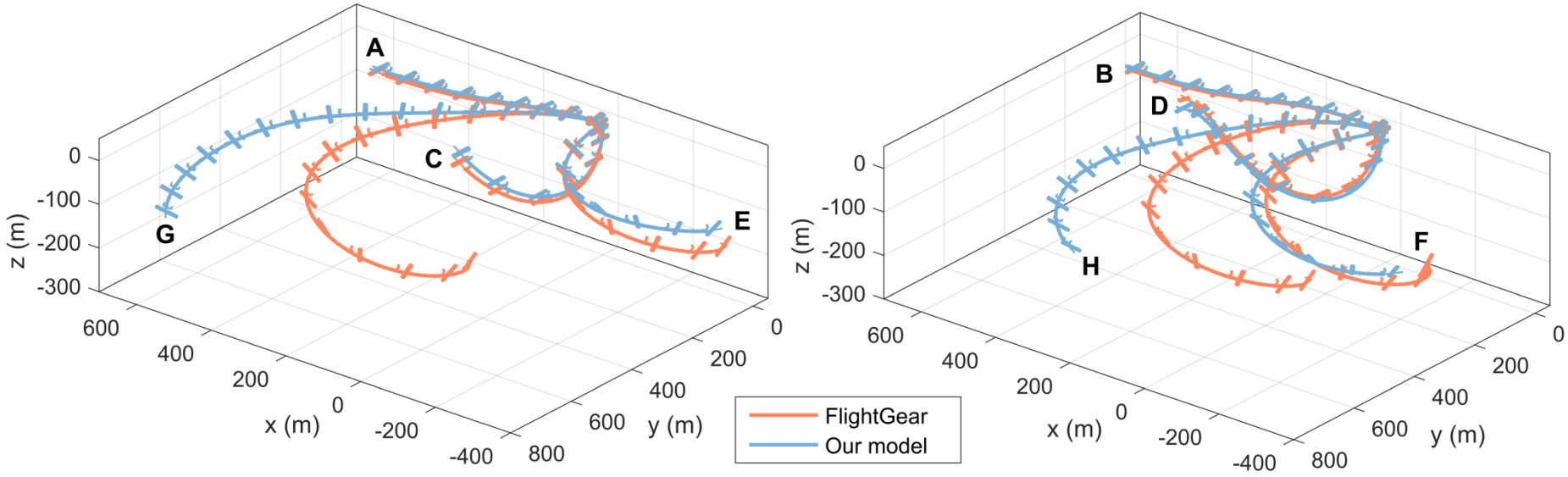

Figure 5.5.3: Flight paths for the RQ-2 Pioneer UAV validation simulations, with the aircraft rendered at 10:1 scale every 2 s.

5.5.3. Centre of mass location

The location of the centre of mass within the RQ-2 Pioneer system, governed by parameters $[L_{\text{c.o.m.},x}, L_{\text{c.o.m.},z}]$, cannot be adequately identified from system structural data, even given the approximate imagery in Figure 5.2.1. Instead these parameters are identified via the flight simulations in Figures 5.5.2-5.5.3, with particular reference to the phugoid flight simulations (A-B). To demonstrate the effect of $[L_{\text{c.o.m.},x}, L_{\text{c.o.m.},z}]$ on the flight simulation results, Figures 5.5.4-5.5.7 show the effect of univariate changes in the centre of mass location. Figure 5.5.4-5.5.5 show the effect of the centre of mass location in z ($L_{\text{c.o.m.},z}$) on the RQ-2 flight simulation results. A continuous parameter set corresponding to variation in $L_{\text{c.o.m.},z}$ in given: this parameter set is constrained by $m_{\text{f}} = 1.225$ kg (Table 5.2.1), leading to a smooth solution curve. Other such curves are possible. As may be seen, $L_{\text{c.o.m.},z}$ has relatively little effect on the validation accuracy, with its effects visible only in the smallest-amplitude phugoid flight simulation (A). Figures 5.5.6-5.5.7 show the effect of the centre of mass location in x ($L_{\text{c.o.m.},x}$) on the RQ-2 flight simulation results. The smooth parameter curve is this time generated with the constraint $m_e = 0.2504$ kg . $L_{\text{c.o.m.},x}$ has significant effects on the flight simulation results; modifying the amplitude and frequency of the phugoid oscillations, and the sharpness of the spiral dive.

It may be inferred from Figure 5.5.7 that a significantly better match for the spiral dive validation simulations can be obtained with a change in centre of mass location relative to the standard validation parameters (Table 5.2.1); but at the cost of a poorer match in the pitch histories across all simulations. This is unsurprising, as the standard parameters were based on matching the aircraft phugoid response. Figure 5.5.8 shows a comparison of the full set of validation simulations for the original parameter set (Table 5.2.1, $L_{\text{c.o.m.},x} = 2.14$ m, $L_{\text{c.o.m.},z} = 0.60$ m) and a spiral-dive roll/yaw-matched parameter set at $L_{\text{c.o.m.},x} = 2.10$ m, $L_{\text{c.o.m.},z} = 0.40$ m. Specifically, this set is $L_{pm,x} - L_{r,x} = 0.0155$ m, $L_{pm,z} = -0.549$ m, $L_{r,z} = 0.0156$ m, $m_{pm} = 135$ kg, $m_w = 6.96$ kg, $m_e = 1.34$ kg, $m_{\text{f}} = 1.16$ kg. This roll/yaw-matched set shows an excellent agreement in the spiral dive yaw histories, and a good agreement in the associated roll histories. However the pitch histories of all simulations show a notably poorer match with this parameter set – in particular, the phugoid simulations and the pitch component of the spiral dives.

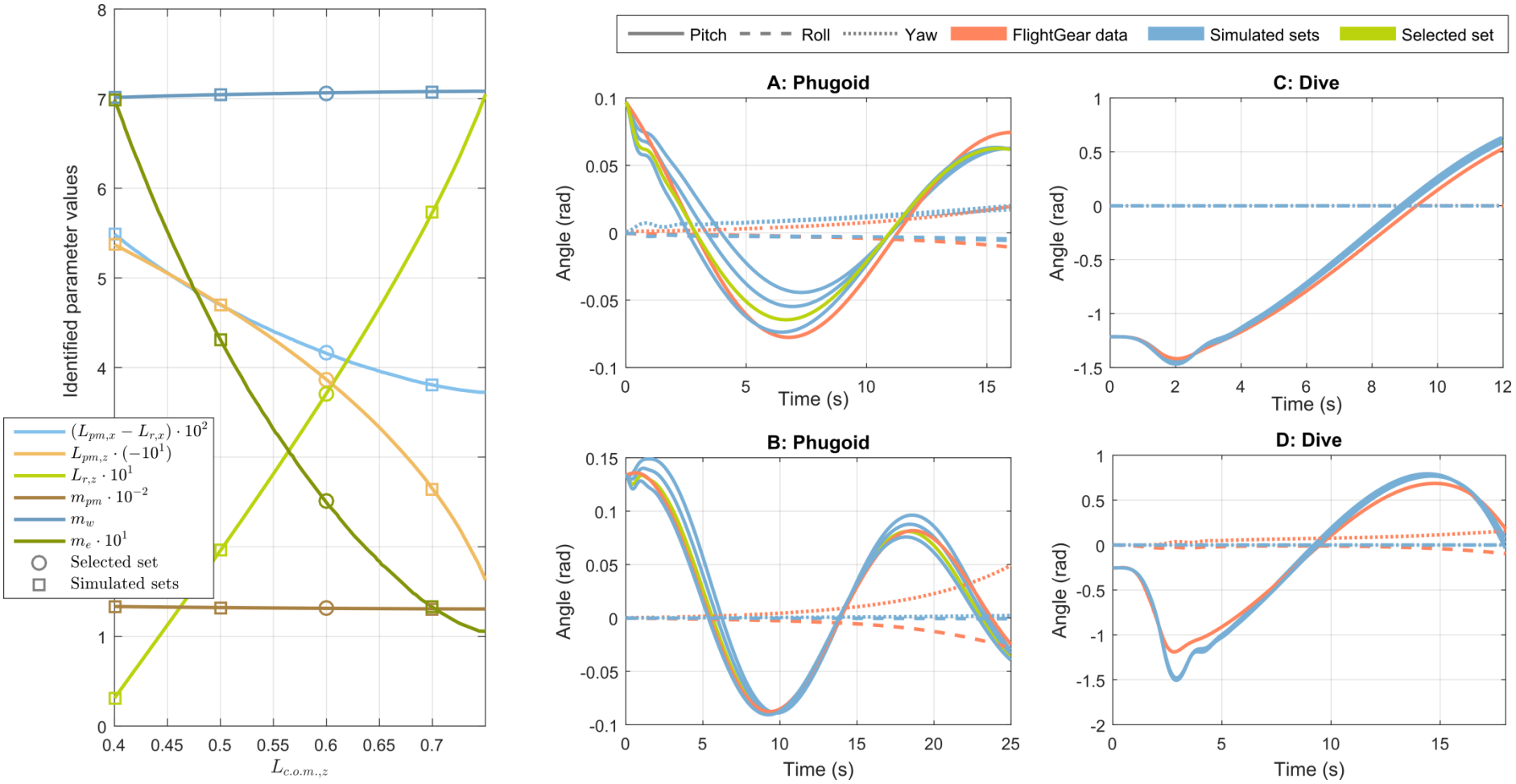

Figure 5.5.4: Effect of the system centre of mass location in z ($L_{\mathrm{c.o.m.},z}$) on the pitch-dominant RQ-2 UAV validation simulations.

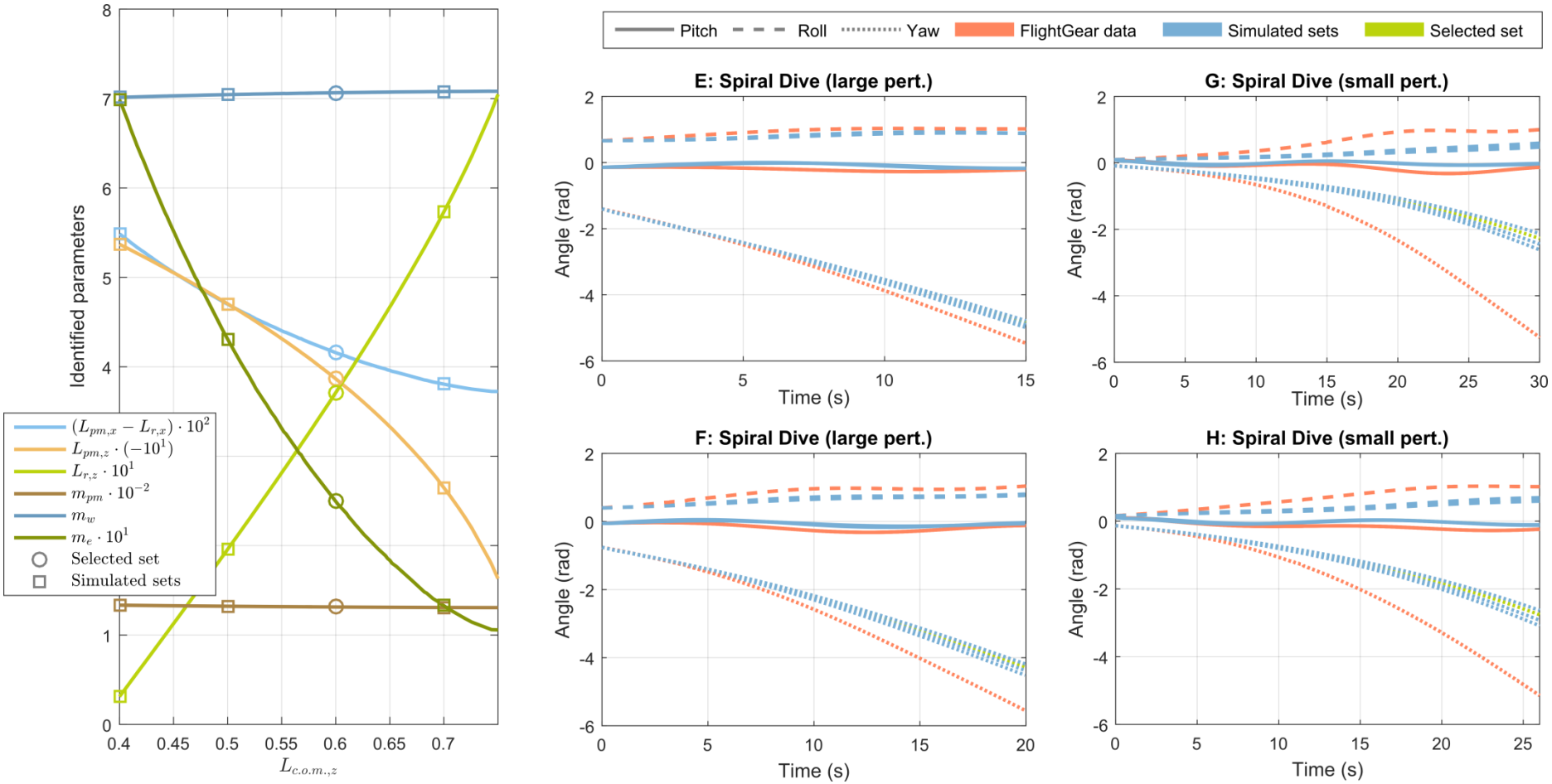

Figure 5.5.5: Effect of the system centre of mass location in z ($L_{\mathrm{c.o.m.},z}$) on the spiral dive RQ-2 UAV validation simulations.

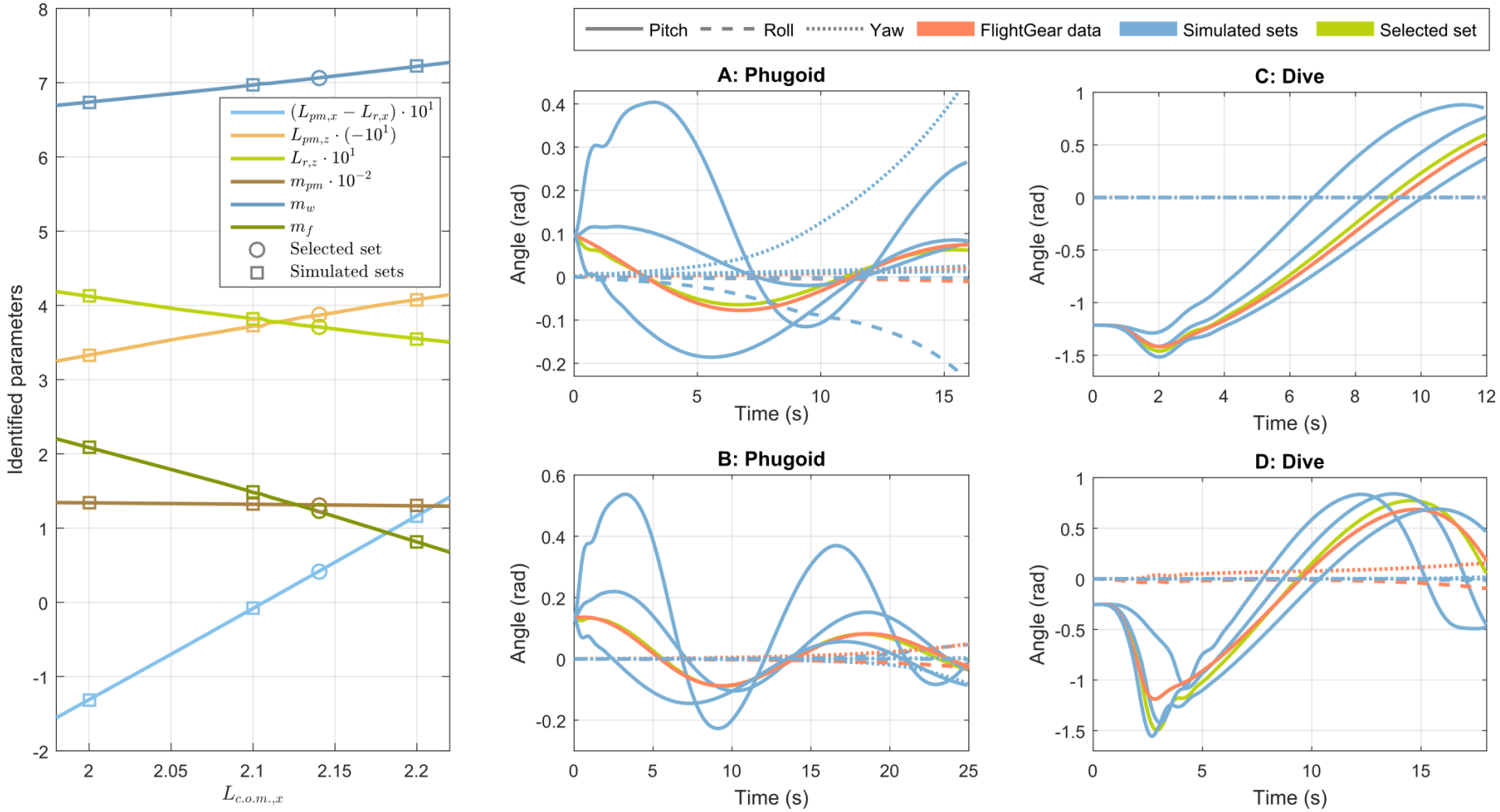

Figure 5.5.6: Effect of the system centre of mass location in x ($L_{\mathrm{c.o.m.},x}$) on the pitch-dominant RQ-2 UAV validation simulations.

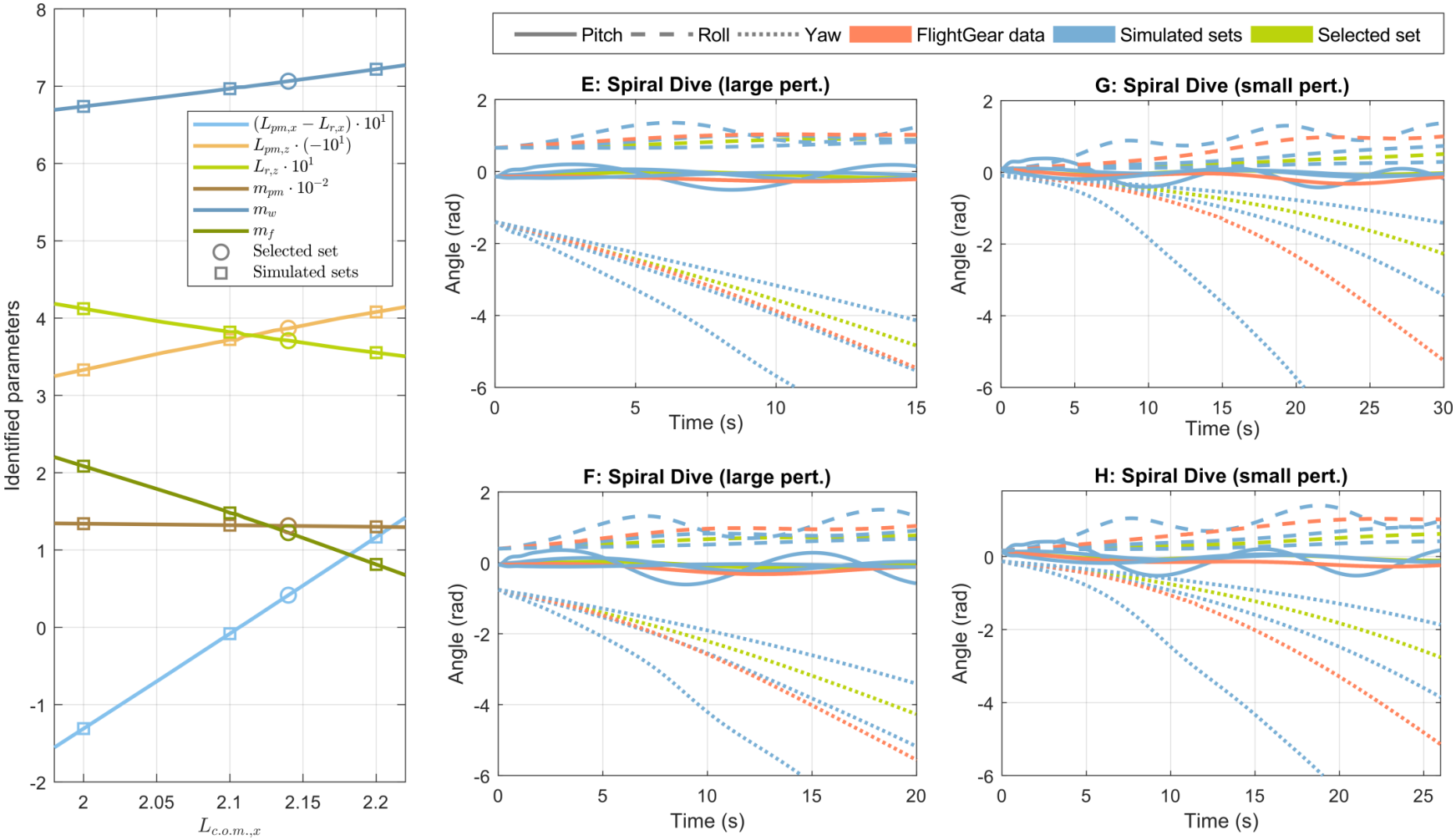

Figure 5.5.7: Effect of the system centre of mass location in x ($L_{\mathrm{c.o.m.},x}$) on the spiral dive RQ-2 UAV validation simulations.

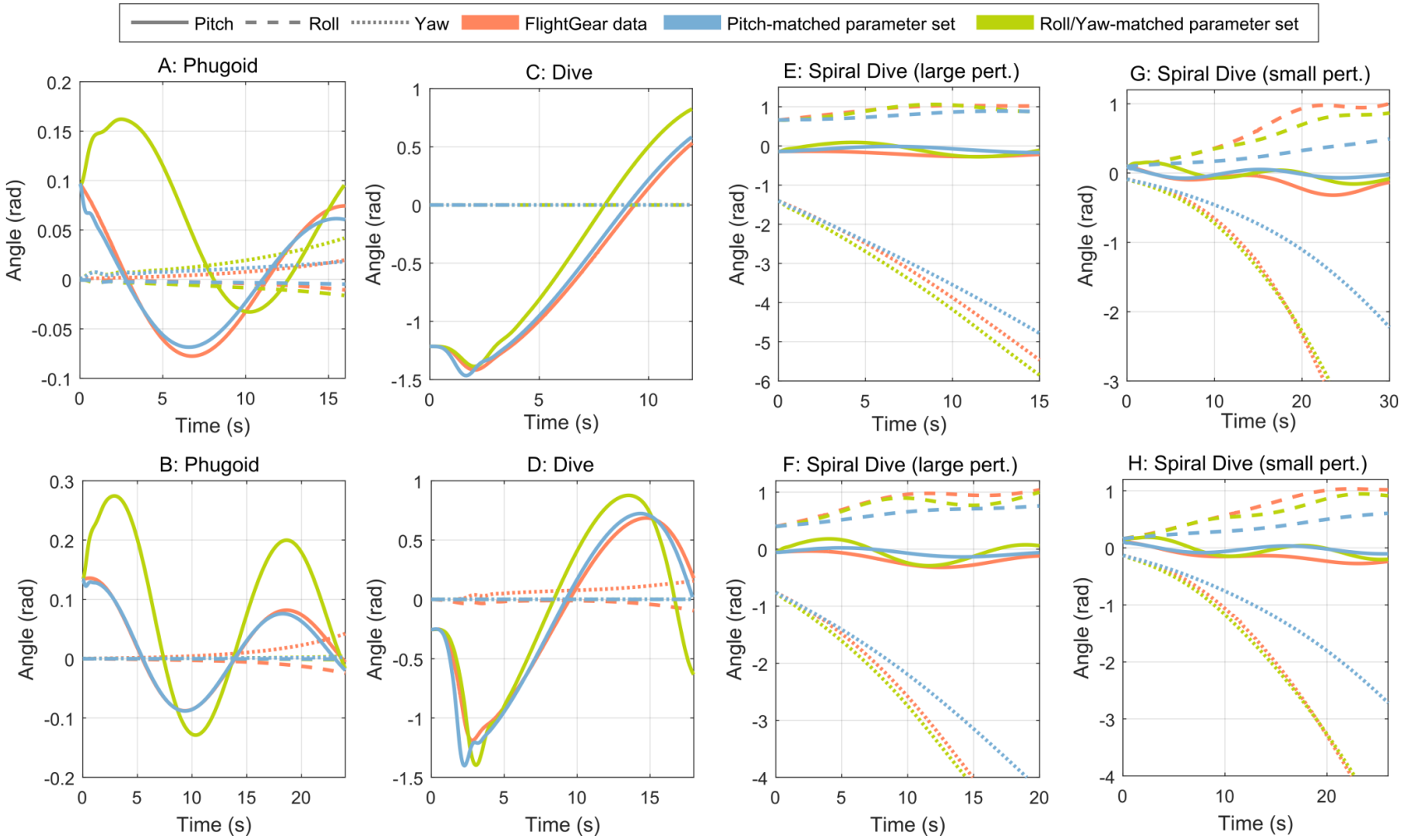

Figure 5.5.8: Orientation histories of the RQ-2 Pioneer UAV validation simulations for two parameter sets: pitch- and roll/yaw-matched.

The inconsistency between the pitch-matched and roll/yaw-matched parameter sets can be attributed to the physical model variation between the *FlightGear* simulated system (the RQ-2A) and the parameter source (the RQ-2B). Overall, the flight simulations results represent a good match between the case study model and the empirically-based *FlightGear* model, validating the former. Furthermore, the parametric study results in the case study model are consistent with the classical effects of centre of mass location on flight dynamic properties.

5.6. FURTHER CONSIDERATIONS FROM COMPUTATIONAL FLUID DYNAMICS

5.6.1. Motivation

The RQ-2 UAV flight simulation and aerodynamic coefficient validation presented over Sections 5.2-5.5 is valuable in that covers the complete and integrated system (rigid body dynamics / numerical integration / aerodynamics). However, correspondingly, this validation occurs only over a limited set of flight regimes: low angle of attack, and low transience. As noted, a suitable system for complete-system validation at all relevant flight regimes does not currently exist in the literature. Instead, a combination of piecewise quantitative and qualitative validation using existing studies of more limited scope can be used to provide more basis for the modelling processes and assumptions that have been utilised; this is the concern of this section.

5.6.2. Quantitative considerations

Sachs and Moelyadi [33] undertook a computational study into the effects of static dihedral angle on pigeon wing aerodynamics. Given the analogous flight conditions, and the defined nature of the wing in absence of the body aerodynamics, this constitutes a useful test case against the treatment of dihedral in the case study model. Figure 5.6.1 shows the force coefficients computed by Sachs and Moelyadi [33]; and Figure 5.6.2 the equivalent coefficients computed by the case study model. This comparison is quantitative in that we can directly observe trends in the coefficient; a comparison of exact values is not possible because Sachs and Moelyadi [33] define neither the dimensions of the wing, nor the reference lengths or point for the aerodynamic coefficients; and the aerofoil is of custom design. Nevertheless, in comparison, the case study model, under a simple uniform chord approximation, predicts all the key trends observed in the reported data.

Trends of decreased drag coefficient and decreased lift coefficient with increased dihedral, according to a scale factor, are unsurprising. The trends in sideforce are more instructive, with the approximately parabolic curve being replicated, and with appropriate scaling under dihedral changes. Overall, these force comparisons serve to further validate the case study model, and indicate that its model of quasistatic high-dihedral states is likely to be accurate. Sachs and Moelyadi [33] also provide two sets of moment coefficient data along with moment derivatives with respect to sideslip angle; but suspected sign and labelling errors have been identified in these datasets (involving inconsistency between the computed derivatives and the source dataset), and so they are not a secure source of validation.

Figure 5.6.1: Force coefficient data reproduced from Sachs and Moelyadi [33]: drag (C_D), lift (C_L) and sideforce (C_{FY}) coefficients as a function of angle-of-attack (α), for three dihedral (ν) values and two sideslip (β) values.

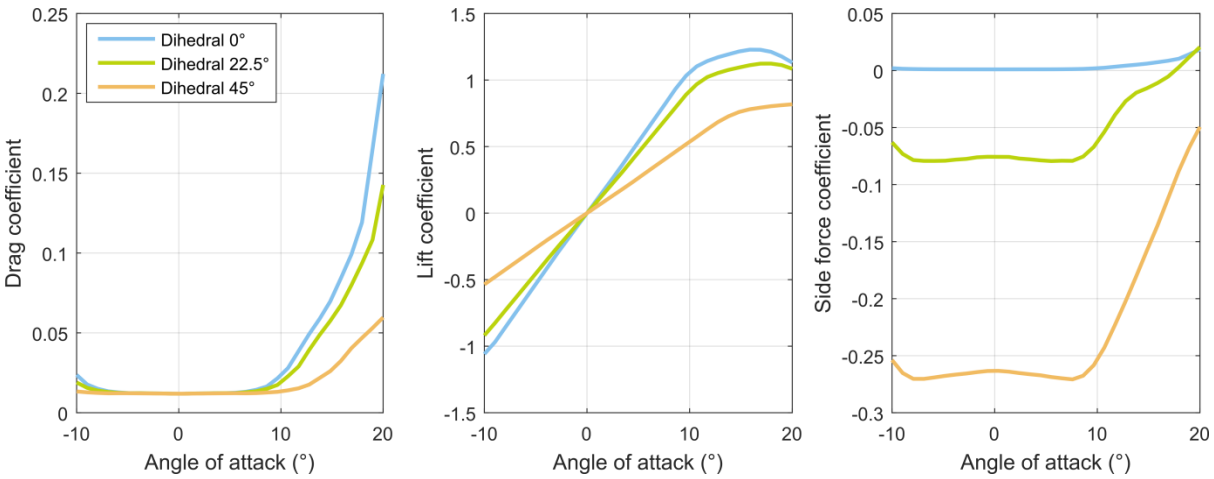

Figure 5.6.2: Force coefficient predictions from the case study model.

5.6.3. Qualitative considerations

The majority of UAV / morphing aircraft / biomimetic aircraft CFD studies are not sufficiently analogous to the case study system, and its modelling framework, to allow a direct comparison. However, qualitative observations made in these studies do shed light on more fundamental phenomena that may be relevant. For example, experimental studies of the X-31 [34] found that wing leading edge design strongly influences vortex generation and pitching behaviour of the aircraft at high angles of attack, leading to a range of aerodynamic force characteristics. Obliquely, this supports the generic modelling of the case study system that has been applied here: leading edge design can be tailored to a wide range of desired aerodynamic characteristics, and so, in the manner of an inverse problem, a physical system is likely to exist that replicates and/or compensates for the aerodynamic modelling used in this study (quasistatic and GK dynamic stall; see Chapters 8-9). Note that this does not imply that such a design would be optimal; only that the aerodynamic performance and characteristics taken for the case study system are at least attainable.

In addition, a RANS study by Soni et al. [35] indicated the presence of several wake stabilisation effects in a case study biomimetic morphing-wing aircraft at low to moderate Reynolds numbers. In a test model at low Reynolds numbers (c. 1000), an increase in wingspan led to decreased total drag via wake stabilisation, up to a critical aspect ratio value representing the maximum available stabilisation effect; and an increment or decrement of dihedral, even at very small angles (<6°), both led to increases in drag through wake destabilisation. Reynolds number changes led to the creation or suppression of stable structures in the wake, while increases in angle of attack generally supressed stable structures, leading to increases in drag. These effects are phenomenologically complex, but, as described, are expressible by empirically-based quasistatic modelling. A key absence of knowledge is in the effect of transient morphing or motion on these wake structures.

A 2D Discrete Vortex Method (DVM) and Particle Image Velocimetry (PIV) study by Lego [36] on the aerodynamics of morphing aircraft at high angles of attack indicated that:

(1) Reduced frequency effects are more significant than Reynolds number effects, justifying the use of a representative Reynolds number in this study; and motivating the development of a dynamic stall (high reduced-frequency) model in Chapter 8.

(2) Two-dimensional DVM can be capable of accurately modelling a three-dimensional wing undergoing a rapid pitching motion. In Lego [36], a 2D DVM accurately predicted all the key flow features seen in experiments, except for 3D instabilities arising from wing spanwise flow; and in addition, the DVM showed notably accurate results in more inertially-dominant regimes (higher transience). This demonstrates in principle that transient aerodynamic effects can be captured effectively by reduced-order modelling.

(3) Higher levels of transience led to greater lift peaks in post-stall pitching motions, consistent with the phenomenon of dynamic stall [37]: these peaks are likely to improve supermanoeuvre performance (e.g. by decreasing altitude loss), indicating that the quasistatic case study model is likely to be conservative in estimating supermanoeuvre performance.

5.7. SCOPE AND LIMITATIONS OF VALIDATION

The validation studies presented in this section are subject to several limitations. Notably, strongly transient manoeuvres cannot be accurately simulated with the *FlightGear* /JSBSim stability-derivatives simulator, due to its relatively limited unsteady aerodynamic modelling, and thus the case study model cannot be adequately tested in transient flow regimes. Simulations of dive manoeuvres come closest to validating this regime – starting from initial static state, the zero-airspeed pitch-down and recovery procedure at least includes strong induced-flow effects. The *FlightGear* /JSBSim model includes the effect of angular velocity on the system aerodynamics, and in the dive simulations this model shows excellent agreement to the case study model. More local transient effects – e.g. wingtip vortices or clap-and-fling mechanisms – remain unmodelled and unvalidated, and their effect on the system is uncertain. In Chapter 8 strongly transient and post-stall effects are investigated further through computational fluid dynamics. The limitation of the *FlightGear* model to the pre-stall regime is not, however, a key obstacle in itself – the transition to stall in the case

study model does not involve any change in modelling formulation, only a change in aerofoil coefficients, and thus a validation in pre-stall regimes should extend to post-stall. Strongly transient aerodynamic effects – in any flight regime – are the key limitation to validation.

In reference to the RQ-2 UAV system identification: while it may seem unreasonable that e.g. the fin and elevator mass are allowed to vary arbitrarily (and are allowed to differ), these are merely proxy parameters for a system model with non-elementary body shapes and non-uniform mass distribution – both the case for the RQ-2 UAV. The modelling framework presented in Chapters 2-4 is capable of modelling such effects directly, through the specification of appropriate non-elementary inertia tensors and centre of mass locations, but with the sparsity of mass and inertia data for the RQ-2 makes such a direct model infeasible. Moreover, in a non-morphing context, the details of the mass distribution have no effect; only the total inertia tensor and centre of mass location. Thus, a simple extension of the case study system is matched to the known inertia tensors, with a specified centre of mass location, as per Section 5.5.3.

Finally, Section 5.6 presented a broader and largely qualitative validation based on a variety of results from the literature. The qualitative nature of much of this validation is unfortunate; but overall, results from the literature support the modelling assumptions utilised. Transient effects, such as are the key limitation to the validation of the case study model, are observed to improve aircraft performance in our key metrics in several cases. These effects are also observed to show a strong dependency on the details of the airframe and its lifting surfaces (e.g. leading edge design); and this is a key factor behind the decision not to model these details and their possible effects. Only a more broad-spectrum transient aerodynamic model will be considered; in Chapter 8. Manoeuvre analyses utilising the case study model, as concerns Chapters 6-7, are intended to be firm qualitative demonstrations of the capability of this class of system for such manoeuvres. They may indeed approach good quantitative accuracy in a physical system that is tailored to match the aerodynamic characteristics that are assumed; but this is not the key aspect: rather, methods are identified to obtain these results in a variety of systems; and the fact that these manoeuvres are identified and demonstrated even with a relatively conservatively-defined system (in airframe and in aerodynamic model) indicates their applicability to physical UAVs.

CHAPTER REFERENCES

[1] Patil, M. J., and Hodges, D. H., "Flight Dynamics of Highly Flexible Flying Wings," *Journal of Aircraft*, Vol. 43, No. 6, 2006, pp. 1790–1799. DOI:10.2514/1.17640.

[2] Mardanpour, P., and Hodges, D. H., "On the Importance of Nonlinear Aeroelasticity and Energy Efficiency in Design of Flying Wing Aircraft," *Advances in Aerospace Engineering*, Vol. 2015, 2015, pp. 1–11. DOI:10.1155/2015/613962.

[3] Sotoudeh, Z., and Hodges, D. H., "Incremental Method for Structural Analysis of Joined-Wing Aircraft," *Journal of Aircraft*, Vol. 48, No. 5, 2011, pp. 1588–1601. DOI:10.2514/1.C031302.

[4] Saberi, H., Khoshlahjeh, M., Ormiston, M., and Rutkowski, M., "RCAS Overview and Application to Advanced Rotorcraft Problems," 4th Decennial Specialists' Conference on Aeromechanics, Alexandria, VA.

[5] Obradovic, B., and Subbarao, K., "Modeling and Simulation of Morphing Wing Aircraft," *Morphing Aerospace Vehicles and Structures*, J. Valasek, ed., John Wiley & Sons, Chichester, UK, 2012, pp. 87–125.

[6] Obradovic, B., and Subbarao, K., "Modeling of Flight Dynamics of Morphing Wing Aircraft," *Journal of Aircraft*, Vol. 48, No. 2, 2011, pp. 391–402. DOI:10.2514/1.C000269.

[7] Obradovic, B., and Subbarao, K., "Modeling of Dynamic Loading of Morphing-Wing Aircraft," *Journal of Aircraft*, Vol. 48, No. 2, 2011, pp. 424–435. DOI:10.2514/1.C000313.

[8] Seigler, T. M., Neal, D. A., Bae, J.-S., and Inman, D. J., "Modeling and Flight Control of Large-Scale Morphing Aircraft," *Journal of Aircraft*, Vol. 44, No. 4, 2007, pp. 1077–1087. DOI:10.2514/1.21439.

[9] Seigler, T. M., "Dynamics and Control of Morphing Aircraft," Doctoral Dissertation, Virginia Polytechnic Institute and State University, 2005.

[10] Wickenheiser, A., and Garcia, E., "Aerodynamic Modeling of Morphing Wings Using an Extended Lifting-Line Analysis," *Journal of Aircraft*, Vol. 44, No. 1, 2007, pp. 10–16. DOI:10.2514/1.18323.

[11] Wickenheiser, A. M., and Garcia, E., "Optimization of Perching Maneuvers Through Vehicle Morphing," *Journal of Guidance, Control, and Dynamics*, Vol. 31, No. 4, 2008, pp. 815–823. DOI:10.2514/1.33819.

[12] Wickenheiser, A. M., and Garcia, E., "Longitudinal Dynamics of a Perching Aircraft," *Journal of Aircraft*, Vol. 43, No. 5, 2006, pp. 1386–1392. DOI:10.2514/1.20197.

[13] Mir Alikhan Bin, M. F., "Dynamics and Control of Three-Dimensional Perching Maneuver under Dynamic Stall Influence," Florida Institute of Technology, 2016.

[14] Niksch, A., Valasek, J., Strganac, T., and Carlson, L., "Six Degree-of-Freedom Dynamical Model of a Morphing Aircraft," AIAA Atmospheric Flight Mechanics Conference, Chicago, IL.

[15] Orlowski, C. T., and Girard, A. R., "Modeling and Simulation of Nonlinear Dynamics of Flapping Wing Micro Air Vehicles," *AIAA Journal*, Vol. 49, No. 5, 2011, pp. 969–981. DOI:10.2514/1.J050649.

[16] Orlowski, C. T., and Girard, A. R., "Dynamics, stability, and control analyses of flapping wing micro-air vehicles," *Progress in Aerospace Sciences*, Vol. 51, 2012, pp. 18–30. DOI:10.1016/j.paerosci.2012.01.001.

[17] Reich, G. W., Eastep, F. E., Altman, A., and Albertani, R., "Transient Poststall Aerodynamic Modeling for Extreme Maneuvers in Micro Air Vehicles," *Journal of Aircraft*, Vol. 48, No. 2, 2011, pp. 403–411. DOI:10.2514/1.C000278.

[18] Reich, G., Wojnar, O., and Albertani, R., "Aerodynamic Performance of a Notional Perching MAV Design," 47th AIAA Aerospace Sciences Meeting, Orlando, FL.

[19] Luchtenburg, D. M., Rowley, C. W., Lohry, M. W., Martinelli, L., and Stengel, R. F., "Unsteady High-Angle-of-Attack Aerodynamic Models of a Generic Jet Transport," *Journal of Aircraft*, Vol. 52, No. 3, 2015, pp. 890–895. DOI:10.2514/1.C032976.

[20] Selig, M., and Scott, J., *IAI Pioneer Nonlinear Model*, 2002.

[21] Perry, A. R., "The FlightGear Flight Simulator," *Proc. USENIX 2004 Annual Technical Conference*, USENIX 2004 Annual Technical Conference, Boston, MA, pp. 171–182.

[22] Cantarelo, O. C., Rolland, L., and O'Young, S., "Validation discussion of an Unmanned Aerial Vehicle (UAV) using JSBSim Flight Dynamics Model compared to MATLAB/Simulink AeroSim Blockset," *2016 IEEE International Conference on Systems, Man, and Cybernetics (SMC)*, 2016 IEEE International Conference on Systems, Man, and Cybernetics (SMC), Budapest, Hungary, pp. 003989–003994.

[23] Coopmans, C., Podhradsky, M., and Hoffer, N. V., "Software- and hardware-in-the-loop verification of flight dynamics model and flight control simulation of a fixed-wing unmanned aerial vehicle," *2015 Workshop on Research, Education and Development of*

Unmanned Aerial Systems (RED-UAS), 2015 Workshop on Research, Education and Development of Unmanned Aerial Systems (RED-UAS), Cancun, pp. 115–122.

[24] Cantarelo, O. C., Rolland, L., and O'Young, S., "Giant Big Stik R/C UAV Computer Model Development in JSBSim for Sense and Avoid Applications," *Drones*, Vol. 3, No. 2, 2019, p. 48. DOI:10.3390/drones3020048.

[25] Chen, X. Q., Ou, Q., R., D., J., Y., Sinclair, M., and Marburg, A., "Flight Dynamics Modelling and Experimental Validation for Unmanned Aerial Vehicles," *Mobile Robots - State of the Art in Land, Sea, Air, and Collaborative Missions*, X. Chen, Y.Q. Chen, and J.G. Chase, eds., InTech, 2009.

[26] Bray, R. M., "A wind tunnel study of the Pioneer remotely piloted vehicle," Master's Thesis, Naval Postgraduate School, 1991.

[27] US Department of Defense, *Unmanned Aircraft Systems Roadmap 2005-2030*, Office of the Secretary of Defense, Washington, DC, 2005.

[28] US Department of Defense, *Unmanned Aerial Vehicle Reliability Study*, Office of the Secretary of Defense, Washington, DC, 2003.

[29] Jacobs, E. N., Ward, K. E., and Pinkerton, R. M., *The characteristics of 78 related airfoil sections from tests in the variable-density wind tunnel*, NACA, Washington, D.C., 1933.

[30] Byrd, R. H., Gilbert, J. C., and Nocedal, J., "A trust region method based on interior point techniques for nonlinear programming," *Mathematical Programming*, Vol. 89, No. 1, 2000, pp. 149–185. DOI:10.1007/PL00011391.

[31] Byrd, R. H., Hribar, M. E., and Nocedal, J., "An Interior Point Algorithm for Large-Scale Nonlinear Programming," *SIAM Journal on Optimization*, Vol. 9, No. 4, 1999, pp. 877–900. DOI:10.1137/S1052623497325107.

[32] Stevens, B. L., Lewis, F. L., and Johnson, E. N., *Aircraft control and simulation: dynamics, controls design, and autonomous systems*, John Wiley & Sons, Hoboken, NJ, 2016.

[33] Sachs, G., and Moelyadi, M. A., "CFD based determination of aerodynamic effects on birds with extremely large dihedral," *Journal of Bionic Engineering*, Vol. 7, No. 1, 2010, pp. 95–101. DOI:10.1016/S1672-6529(09)60191-8.

[34] Boelens, O. J., "CFD analysis of the flow around the X-31 aircraft at high angle of attack," *Aerospace Science and Technology*, Vol. 20, No. 1, 2012, pp. 38–51. DOI:10.1016/j.ast.2012.03.003.

[35] Soni, A., and Tiwari, S., "Three-dimensional numerical study on aerodynamics of non-flapping bird flight," *Sādhanā*, Vol. 44, No. 2, 2019. DOI:10.1007/s12046-018-1018-4.

[36] Lego, Z. M., "Analysis of High Angle of Attack Maneuvers to Enhance Understanding of the Aerodynamics of Perching," Master's Thesis, University of Dayton, 2012.

[37] Gharali, K., and Johnson, D. A., "Dynamic stall simulation of a pitching airfoil under unsteady freestream velocity," *Journal of Fluids and Structures*, Vol. 42, 2013, pp. 228–244. DOI:10.1016/j.jfluidstructs.2013.05.005.

THIS PAGE LEFT BLANK

Chapter 6:
Supermanoeuvrability:
NPAS and quasistatic manoeuvres

6.1. INTRODUCTION

The flight dynamic model developed over the past five chapters is now at a stage where it may be applied to the study of supermanoeuvrability. As noted in Chapter 5, Section 5.4.3, the aircraft aerodynamic submodel is expected to break down at some critical level of transience. The development of a transient aerodynamic submodel is detailed in further chapters; here, we analyse a key subspace of supermanoeuvres which show low levels of transience, at least some of which are phenomenologically and quantifiably subcritical in terms of aerodynamic model breakdown. This subspace of manoeuvres has been referred to as nose-pointing-and-shooting (NPAS) capability [1] or orientation direct force capability [2]; and involves aircraft orientation control independent of its flight path. In the case study system, such capability is available on arbitrarily long timescales, and thus for some subspace of NPAS capability, the quasistatic aerodynamic model will be sufficient. In this chapter we analyse this NPAS capability in the case study biomimetic system, and demonstrate the use of trim state analysis to design and possibly control NPAS manoeuvres. As part of this analysis the aircraft flight dynamic stability across its space of trim states is characterised.

6.2. TRIMMED FLIGHT

6.2.1. Context

The analysis of steady level flight in the biomimetic case study system provides an avenue through which forms of NPAS capability can be developed. To obtain steady level flight it is necessary to trim the aircraft, conventionally done via the elevators [3]. However, this system has a larger set of controlled degrees of freedom than a conventional aircraft, yielding a larger set of trimmed flight states. Even under the assumption of fixed wing sweep and dihedral, symmetrical control configuration and orientation (no roll or yaw relative to the airstream), and specified airspeed, the wing incidence is retained as an additional control degree of freedom relative to a conventional aircraft. Varying the wing incidence allows us to trim the aircraft at a varying angle-of-attack – including beyond stall – for the single specified airspeed. More generally, it is possible to devise trim states at asymmetric orientations (nonzero roll or yaw) and/or with asymmetric control configurations.

In the most general case, the trimmed aircraft must satisfy conditions of zero angular acceleration and zero translational acceleration at a given state of zero angular velocity and some fixed translational velocity. These accelerations are directly proportional to their corresponding moments and forces, and may be physically interpreted as such. In the case of symmetric forward flight with fixed wing sweep and dihedral, these conditions reduce to three conditions of zero pitching acceleration and zero vertical (z) and forward (x) translational acceleration – at given conditions of zero angular velocity, zero vertical and lateral translational velocity, and some specified forward velocity (the airspeed). The five free trim parameters are the body pitch (angle of attack), wing incidence, elevator deflection, airspeed and thrust force. This leaves two trim degrees of freedom unconstrained, and thus even if one is specified initially (e.g. the airspeed or angle of attack), then in general there will exist a continuous spectrum of trim states. As we have alluded to, this leads to the existence of trim states at a continuous range of angle-of-attack for a given airspeed.

6.2.2. Trim state solvers

To compute these continuous trim states a nonlinear solution / optimisation routine is devised. Given any initial complete state of the aircraft, with definitions both of the trim parameters (defined in some vector $\mathbf{p}$) and the other local state, structure and environmental parameters, the aircraft equations of motion in an Euler angle framework may be generated through the results in Chapters 2-4. The quaternion framework is not conducive to a trim state analysis, as the system is discretised before the variational analysis is carried out, and thus its strong form (à la Eq. 4.2.21) is never formulated, and thus the aircraft accelerations are never defined. A quaternion implementation would require the computational of finite-difference gradients of velocity as an approximation of local acceleration. Moreover, the Euler angle framework allows constraints on flight symmetry (e.g. the restriction to the x-z plane) to be defined simply. In this framework, the aircraft accelerations at a given state may be computed via Eq. 4.2.21:

$$\dot{\mathbf{z}} = \begin{bmatrix} \ddot{\mathbf{x}}_S^{(e)} \\ \ddot{\theta} \\ \dot{\mathbf{x}}_S^{(e)} \\ \dot{\theta} \end{bmatrix} = \mathbf{F}_z(t, \mathbf{z}, \mathbf{p}) = \mathrm{B}_1(\mathbf{p})^{-1}(\mathbf{F}(\mathbf{p}) - \mathrm{B}_0(\mathbf{p})\mathbf{z}), \qquad \mathbf{z} = \begin{bmatrix} \dot{\mathbf{x}}_S^{(e)} \\ \dot{\theta} \\ \mathbf{x}_S^{(e)} \\ \theta \end{bmatrix}, \tag{6.2.1}$$

where $\mathbf{p}$ represents the set of trim-relevant internal parameters. Generally this will represent the wing control parameters and other control surface deflections, but other parameters may be included (e.g. a payload mass). The variables $\mathbf{x}_S^{(e)}$ and $\boldsymbol{\theta}$ and their derivatives are relevant to the trim optimisation in different way. The spatial location ($\mathbf{x}_S^{(e)}$) is arbitrary and may be taken as zero with loss of generality. The orientation ($\boldsymbol{\theta}$) and translational velocity ($\dot{\mathbf{x}}_S^{(e)}$) comprise the trim state variables; in the most general case all their elements are unconstrained. The angular velocity (proxy $\boldsymbol{\theta}$) is specified to be zero; and the angular and translational acceleration ($\boldsymbol{\theta}$ and $\ddot{\mathbf{x}}_S^{(e)}$) comprise the trim optimisation objective function in vector form. Trim state variables ($\boldsymbol{\theta}$, $\dot{\mathbf{x}}_S^{(e)}$) such that the norm of this objective function ($\boldsymbol{\theta}$, $\ddot{\mathbf{x}}_S^{(e)}$) is zero are desired.

The aircraft equations of motion under trim conditions may thus be expressed:

$$\dot{\mathbf{z}} = \begin{bmatrix} \ddot{\mathbf{x}}_S^{(e)} \\ \ddot{\boldsymbol{\theta}} \\ \dot{\mathbf{x}}_S^{(e)} \\ \mathbf{0}_{3\times 1} \end{bmatrix} = \mathbf{F}_{\mathrm{z}}(0, \mathbf{z}), \quad \mathbf{z} = \begin{bmatrix} \dot{\mathbf{x}}_S^{(e)} \\ \mathbf{0}_{3\times 1} \\ \mathbf{0}_{3\times 1} \\ \boldsymbol{\theta} \end{bmatrix}, \tag{6.2.2}$$

or, as a relation between the trim state ($\mathbf{v}$) and the trim objective vector $\boldsymbol{\varepsilon}$:

$$\boldsymbol{\varepsilon} = \begin{bmatrix} \ddot{\mathbf{x}}_S^{(e)} \\ \ddot{\boldsymbol{\theta}} \end{bmatrix} = \mathbf{F}_{\boldsymbol{\varepsilon}}(\mathbf{v}), \qquad \mathbf{v} = \begin{bmatrix} \dot{\mathbf{x}}_S^{(e)} \\ \boldsymbol{\theta} \\ \mathbf{p} \end{bmatrix}. \tag{6.2.3}$$

If the $\boldsymbol{\varepsilon}$ and $\mathbf{v}$ is sufficiently constrained – via direct parameter specification – then trim states may be computed with nonlinear equation solvers. For example, a restriction to the x-z plane with symmetrical control inputs and an initially specified airspeed U and pitch angle θ, yields a 3DOF trim state composed of $\boldsymbol{\theta} = [\theta\ 0\ 0]^T$, $\dot{\mathbf{x}}_S^{(e)} = [U\ 0\ 0]^T$, $\mathbf{p} = \left[\phi_w, \beta_e, \mathrm{F}_{\mathrm{prop}}\right]^T$ for wing incidence ϕ_w, elevator deflection β_e and thrust force $\mathrm{F}_{\mathrm{prop}}$. The trim objective function is analogously reduced to 3DOF: $\ddot{\mathbf{x}}_S^{(e)} = [\ddot{x}\ 0\ \ddot{z}]^T$, $\boldsymbol{\theta} = \left[\theta\ 0\ 0\right]^T$. The trim equation $\boldsymbol{\varepsilon}^* = \mathbf{F}_{\boldsymbol{\varepsilon}}^*(\mathbf{v}^*) = 0$, with reduced states $(\cdot)^*$ omitting the zero terms, may then be solved via Newton's method:

$$\mathbf{v}_{i+1}^* = \mathbf{v}_i^* + \mathrm{J}_{\mathbf{v}^*}^{-1}(\mathbf{v}_i^*)\mathbf{F}_{\boldsymbol{\varepsilon}}^*(\mathbf{v}_i^*) = \mathbf{0}, \tag{6.2.4}$$

where $\mathrm{J}_{\mathbf{v}^*}$ is the Jacobian of $\mathbf{F}_{\boldsymbol{\varepsilon}}^*$ with respect to $\mathbf{v}^*$. This Jacobian is computed using simple first-order forward differences.

In situations for which the trim equation is underconstrained – for instance, when the entire space of control surface and morphing deflections are available; many more than the 6DOF constraints – optimisation techniques, applied to a scalar trim error $\varepsilon = \|\boldsymbol{\varepsilon}\|_2$, are required. We use MATLAB's inbuilt simplex algorithm, an implementation of the method described in Lagarias et al. [4]. Lagrange multipliers or other discontinuous penalties may be included in the error definition ($\varepsilon = \|\boldsymbol{\varepsilon}\|_2 + k$), to account for inequality constraints on the trim state, e.g. elevator deflection out of range. The optimisation approach is thus useful for probing the existence of trim states *in extremis*, and locating the boundary of their existence. This is augmented by its ability to reliably compute near-trim states – those with small but nonzero pitching and translational moment/acceleration. However, latter also degrades its performance in conventional circumstances where only true trim states are desired.

6.2.3. Trim states as a function of pitch angle

Figure 6.2.1 shows several trim states at different pitch angles, and zero yaw or roll angle, computed via Newton's method applied to the symmetric 3DOF x-z plane trim equation just noted, and confirmed with flight simulations (0.3 s excerpt shown). These demonstrate the range of trimmed angles-of-attack available to the aircraft, even at a fixed airspeed (25 m/s). Simulations indicate that the minimum stable speed on the aircraft is $U = 16$ m/s though lower speeds are possible if the lifting surfaces are stalled. A basic but natural method of understanding the complex trim behaviour of the aircraft is to define a grid over the set of possible trim states. Recall that in the symmetric 3DOF model, the trim state parameters are wing incidence (ϕ_w), elevator deflection (β_e), angle of attack (θ), airspeed (U) and propulsive force (F_{prop}). As grid parameters θ and U are taken, and at each grid point a solution attempt is made: yielding either a trim state, or information regarding the nonexistence of the trim state. However, attempting to compute each grid point solution independently is both inefficient and prone to generating false negatives due to nonconvergence of the iterative trim equation solver. This grid method can be improved significantly by introducing numerical continuation. In this modified method, the solver starts at a known solution (here, $\theta = 0$ rad and $U = 25$ m/s, cf. Figure 6.2.1), and increment out into the (θ, U) grid. The initial guesses for a Newton iteration at a given grid point (as per Eq. 6.2.4) are taken to be the trim solutions from the previous point, thus greatly increasing the speed of the solver convergence.

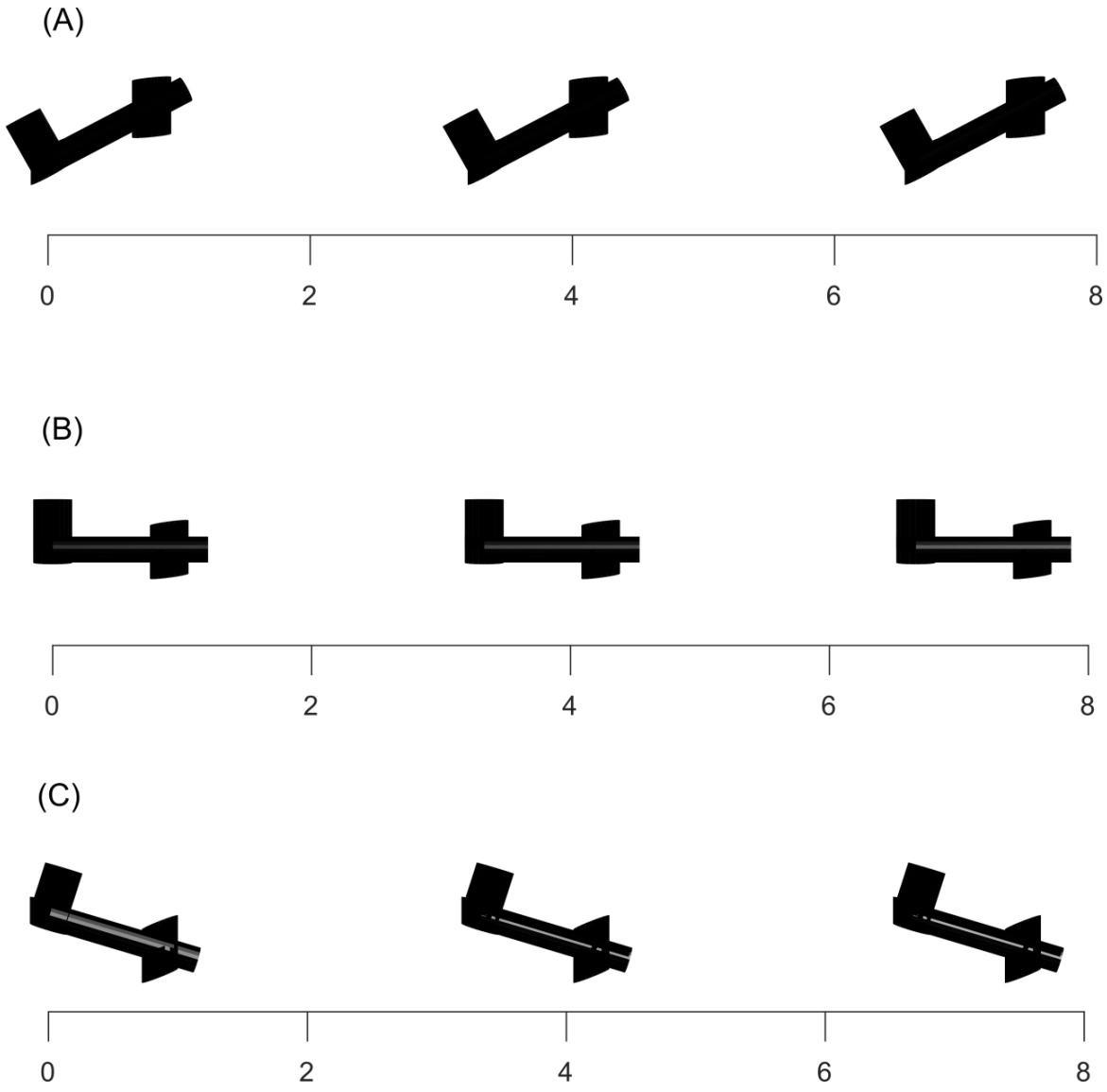

Figure 6.2.1: Flight simulations of three aircraft trim states for $U = 25$ m/s, scale in m.
(**A**) Angle of attack 0.500 rad, Elevator deflection -0.717 rad, Wing incidence -0.397 rad, Thrust 19.2 N forward.
(**B**) Angle of attack 0 rad, Elevator deflection 0.139 rad, Wing incidence 0.136 rad, Thrust 4.15 N forward.
(**C**) Angle of attack -0.300 rad, Elevator deflection 0.592 rad, Wing incidence 0.687 rad, Thrust 33.5 N forward.

When the solver fails to converge, we can reliably conclude that the the limits of trim stability have been reached – at least on the given solution branch. For intelligibility, a natural continuation method [5], i.e. over a pre-specified grid, is used, with θ incremented first until solution failure and then a return to the initial state and an increment in U. For each level of U, both positive ($+\theta$) and negative ($-\theta$) continuation branches are followed, leading to a complete bound on trim existence. A more efficient approach would be to use

pseudo-arclength / Riks' continuation in (θ, U) [6,7], but the resulting trim solution paths would be irregularly spaced, and thus difficult to understand visually or interpolate upon.

The Newton solution process precludes any direct specification of the elevator limits ($\pm$0.87 rad), and more generally any other control limits. However, these limits are key determiners of the bounds of trim state existence. To include their effect, the limiting values are substituted into any attempted evaluation on the elevator outside of them. The aerodynamic data of Selig [8] is defined only within these limits, and moreover this effect models accurately the response of a real aircraft to an out-of-range control command. It has the additional advantage of automatically triggering the termination of the Newton iteration, as the Jacobian becomes singular. Note that this may exclude some trim states just before the elevator cut-off, for which the iterations oscillate beyond the limits before converging. This problem could be circumvented by devising a Newton iteration using the pseudoinverse of the Jacobian, as is common in underconstrained problems, e.g. [9]. However the (potential) loss of these trim states is not significant, as they show no elevator control effectiveness in the direction of the limit and thus are likely to be useless for orientation control.

Figures 6.2.2-6.2.4 show the results of this continuation analysis, with the continuation starting from $\theta = 0$ rad and $U = 25$ m/s. Several points may be noted. Greater airspeeds are associated with slightly wider ranges of trim state, though this is a process of diminishing returns; by 50 m/s the extension is insignificant (<0.01 rad). The point of transition to trim state non-existence is, in this case, determined entirely by the elevator limits – prescribed to be 0.87 rad, slightly less than the exact elevator limit. In Figure 6.2.4 it is observed that the trim continuation terminates at a grid point immediately beyond this limit. The wing itself remains within a narrowly varying effective angle of attack for each given airspeed. A sum of the approximate linear relation between with incidence and angle of attack, $\phi_w(\theta, U) = -1.067\theta + \phi_{w,0}(U)$, with the angle of attack itself (θ) yields the effective wing angle of attack, $\phi_{\mathrm{eff},w}(\theta, U) = -0.067\theta + \phi_{\mathrm{eff},w,0}(U)$, which shows a tiny gradient.

Physically, the process of obtaining a trim state at extreme fuselage angles of attack may be interpreted as a process of obtaining lift forces on the wings and horizontal stabiliser that

are near-identical to their trimmed values in the zero angle-of attack of attack state – for the wing, by maintaining a near-constant effective angle of attack, and for the horizontal stabiliser, by using elevator deflection as a corrector. The small nonlinearities in this relation are to account for (1) the slight difference in moment arm between the wings and horizontal stabiliser, due both to trigonometric effects, and more notably, the vertical (z) position of the aircraft centre of mass; and (2) drag effects.

These indicate structural approaches which have the potential to widen the trim state range within the given elevator limits. Moving the aircraft centre of mass vertically downwards ($-z$) with generate a more favourable moment arm for the horizontal tailplane in the pitch-up state – creating further trim states at higher angles of attack – but will have an adverse effect on pitch-down trim states. Alternately, the wing can be mounted on a shoulder, above ($+z$) the centre of mass and tailplane, leading to the same result. The opposite combination of effects can be obtaining by upwards ($+z$) centre-of-mass motion or a downwards ($-z$) shoulder, though both these may have a destabilising effect on the aircraft's flight dynamic modes. Modification of the tailplane is also a possibility: larger horizontal stabilisers and / or elevators; leading to greater stabiliser lift and / or greater elevator control effectiveness, are an obvious approach, and tailplane incidence morphing is an extension of this. However, an intriguing alternative is simply the generation of additional tailplane drag (e.g. via tail-mounted airbrakes), which acts as an additional stabilising force and thus reduces the burden on the elevator controls.

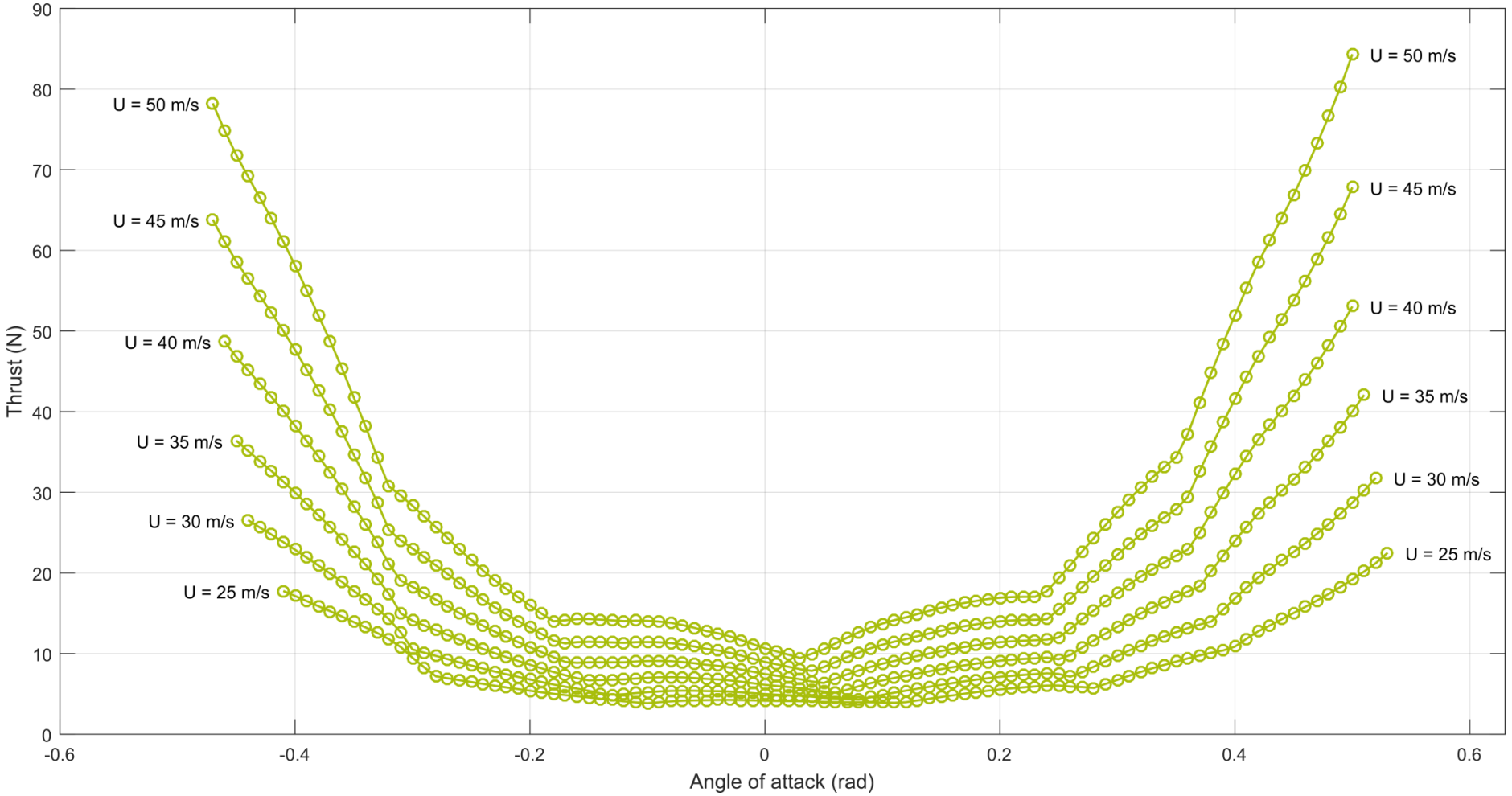

Figure 6.2.2: Trim state thrust as a function of airspeed and angle of attack (body pitch, θ), computed with numerical continuation starting from a solution at $\theta = 0$ rad, $U = 25$ m/s. The limits of the continuation paths in θ represent the limits of trim state existence in this locality.

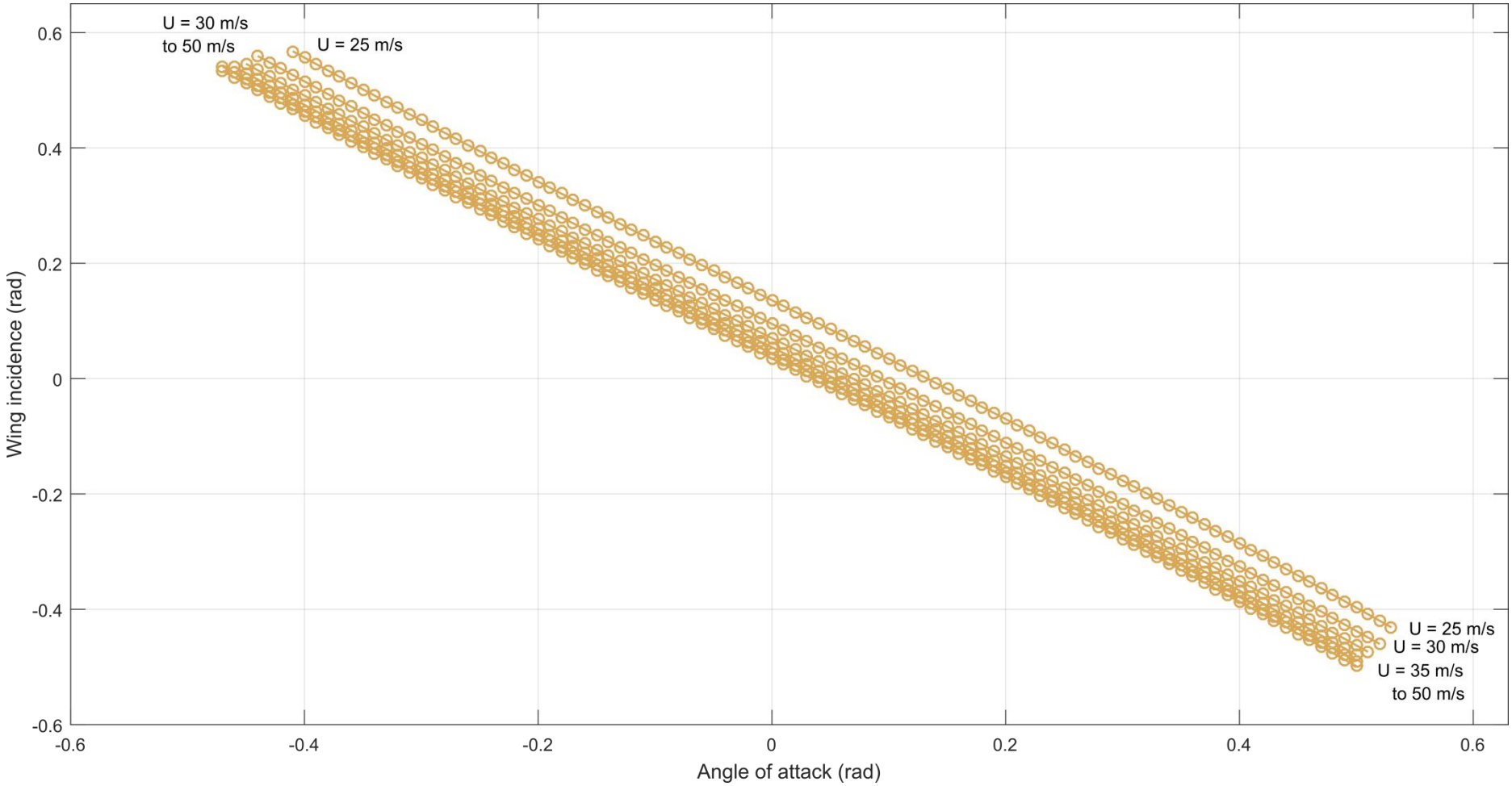

Figure 6.2.3: Trim state wing incidence as a function of airspeed and angle of attack, computed with numerical continuation starting from a solution at $\theta = 0$ rad, $U = 25$ m/s. The limits of the continuation paths in θ represent the limits of trim state existence in this locality.

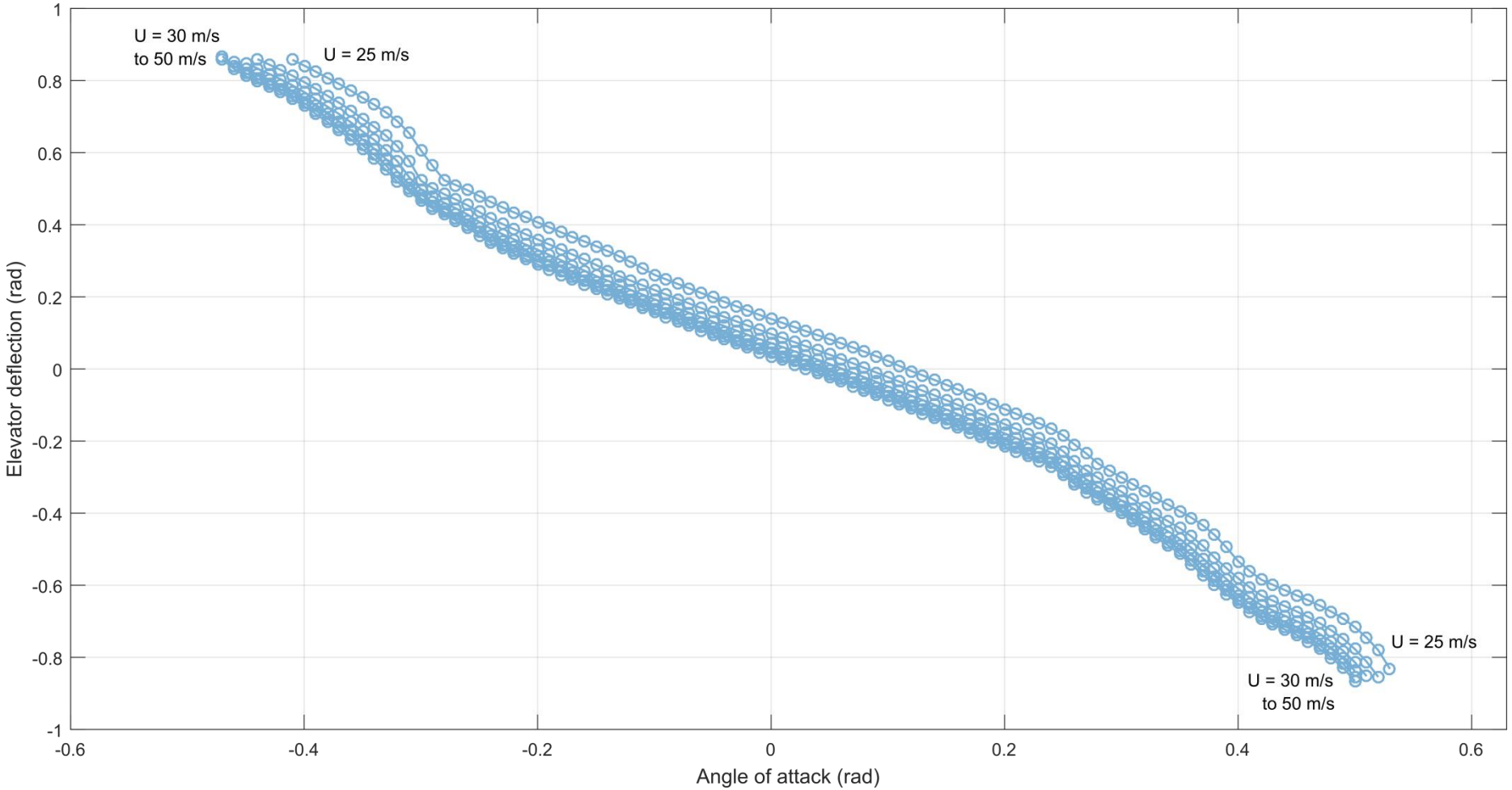

Figure 6.2.4: Trim state elevator deflection as a function of airspeed and angle of attack, computed with numerical continuation starting from a solution at $\theta = 0$ rad, $U = 25$ m/s. The limits of the continuation paths in θ represent the limits of trim state existence in this locality.

6.2.4. Trim states as a function of yaw angle

Figure 6.2.5 shows two trim states at different yaw angles, and zero pitch and roll angles, computed via Newton's method applied to the generalised trim equation (Eq. 6.2.4), and confirmed with flight simulations (0.4 s excerpt shown). The wing sweep is fixed, but asymmetric variation in the wing dihedral and incidence is permitted. The rudder and elevator deflection are additional trim parameters, but in this simulation differential elevator deflection (for roll/yaw control [10]) is not permitted. These trim results are highly significant in that they demonstrate that the wing morphing control – in the basic degrees of freedom studied here – leads to the existence of trim states at high yaw angles.

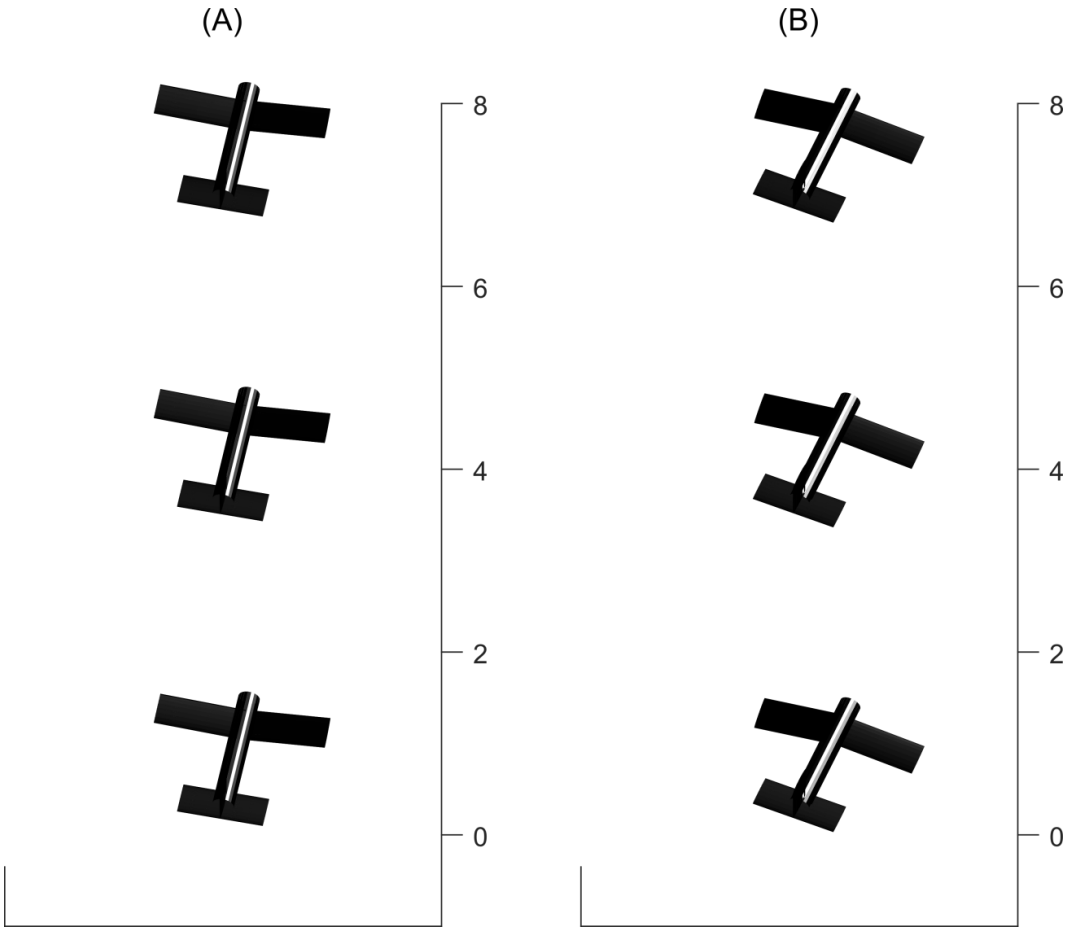

Figure 6.2.5: Flight simulations of two aircraft trim states for $U = 25$ m/s, scale in m, aircraft velocity exactly in the upwards direction:

(**A**) Yaw angle 0.400 rad, Left incidence 0.268 rad, Right incidence 0.131 rad, Left dihedral -0.2376 rad, Right dihedral −0.0436 rad, Elevator 0.182 rad, Rudder 0.809 rad, Thrust 14.1 N.

(**B**) Yaw angle 0.200 rad, Left incidence 0.135 rad, Right incidence 0.166 rad, Left dihedral 0.0373 rad, Right dihedral 0.128 rad, Elevator 0.147 rad, Rudder 0.254 rad, Thrust 5.30 N.

Figure 6.2.5 indicates that, with only small-amplitude dihedral and incidence motion alongside conventional control surfaces, trim states with at least 0.4 rad (c. 22°) yaw are attainable. In a real system, flow shadowing effects between the fuselage and the inboard horizontal stabiliser (i.e. the right-hand one, in the direction of the velocity axis) will lead to a loss of lift on this stabiliser, and thus a rightwards roll moment in the currently computed state. However these effects are not likely to prove a barrier to the existence of these high-yaw trim states, as any such moment can be corrected by incidence morphing or, if required, differential elevator control.

The question of the relation between the active morphing or control surface degrees of freedom, and the size and / or existence of the set of yawed trim states is complex. Yawed trim states to not exist for systems constrained to conventional control surfaces – consistent with the nonexistence of such states in conventional aircraft. Nor do they exist for those additionally utilising only incidence morphing, symmetric or asymmetric. While, for both the latter, near-trim states (e.g. $\|\boldsymbol{\varepsilon}\|_2 < 0.1$ at $\psi = 0.1$ rad) are available, these also may not be entirely reliable as flow shadowing effects may not be correctable within these morphing constraints.

In the case of asymmetric incidence and single-wing dihedral control, trim states do exist for systems exactly constrained with respect to the six acceleration degrees of freedom, though these all show slightly more restricted trim ranges relative to the general case of asymmetric dihedral and incidence. This shows a maximum yaw within $0.5 < \psi < 0.6$ rad. The system with asymmetric incidence and one of either dihedral constrained to zero ($\theta_{wl} = 0$ or $\theta_{wr} = 0$), shows a maximum within $0.4 < \psi < 0.5$ rad. Note that the trims solution for these two constrains are not symmetrically equivalent to each other. The system with asymmetric incidence and symmetric incidence ($\theta_{wl} = \theta_{wr}$) shows a maximum within $0.3 < \psi < 0.4$ rad. However, despite the degradation in trim ranges, the constrainedness of these systems permits the use of Newton-based continuation methods as in Section 6.2.3. Continuation can be carried out with underconstrained systems via the simplex algorithm, but the continuous paths that are generated will generally be non-smooth, and unreliable for tracing solution branches and their limits.

Figures 6.2.6-6.2.9 show an exploration of the trim state space via the continuation method as discussed in Section 6.2.3, using Newton's method applied to the fully-constrained system with $\theta_{wr} = \Gamma = 0$. This constraint is retained even at $\psi < 0$, corresponding to a switch between the constraining the outboard and inboard wings and thus generating a set of trim states that is asymmetric about $\psi = 0$. The solution e.g. with the inboard wing always constrained ($\psi > 0$, $\theta_{wr} = 0$ and $\psi < 0$, $\theta_{wl} = 0$) will self-evidently be symmetric, in the absence of any lateral asymmetries in the aircraft. The difference between the inboard and outboard constraints can be seen. The outboard constraints show a highly consistent limiting yaw angle of $\psi = 0.42$ rad. The inboard constraint allows this maximum yaw angle to be matched or exceeded at all airspeeds considered, reaching up to $\psi = 0.48$ rad. However, it requires also much greater (c. 2x) dihedral angles, representing a significant increase in the control effort required to reach this maximum state from a trimmed nose-forward condition. The slight increase (3°) in maximum stable yaw angle is thus unlikely to be worthwhile.

Analogous to the pitched trim states, the key limiting factor is the maximum rudder deflection – all the solution paths terminate at this limit. Physically, this is because the rudder provides the main avenue for counteracting the lateral component of the thrust force. Notably, while the asymmetric dihedral and incidence provide a partial proxy for rudder deflection, trim states are nevertheless not possible under the initial assumption of zero rudder deflection. This underlines the dual importance of conventional control surfaces and morphing controls in generating these trim states.

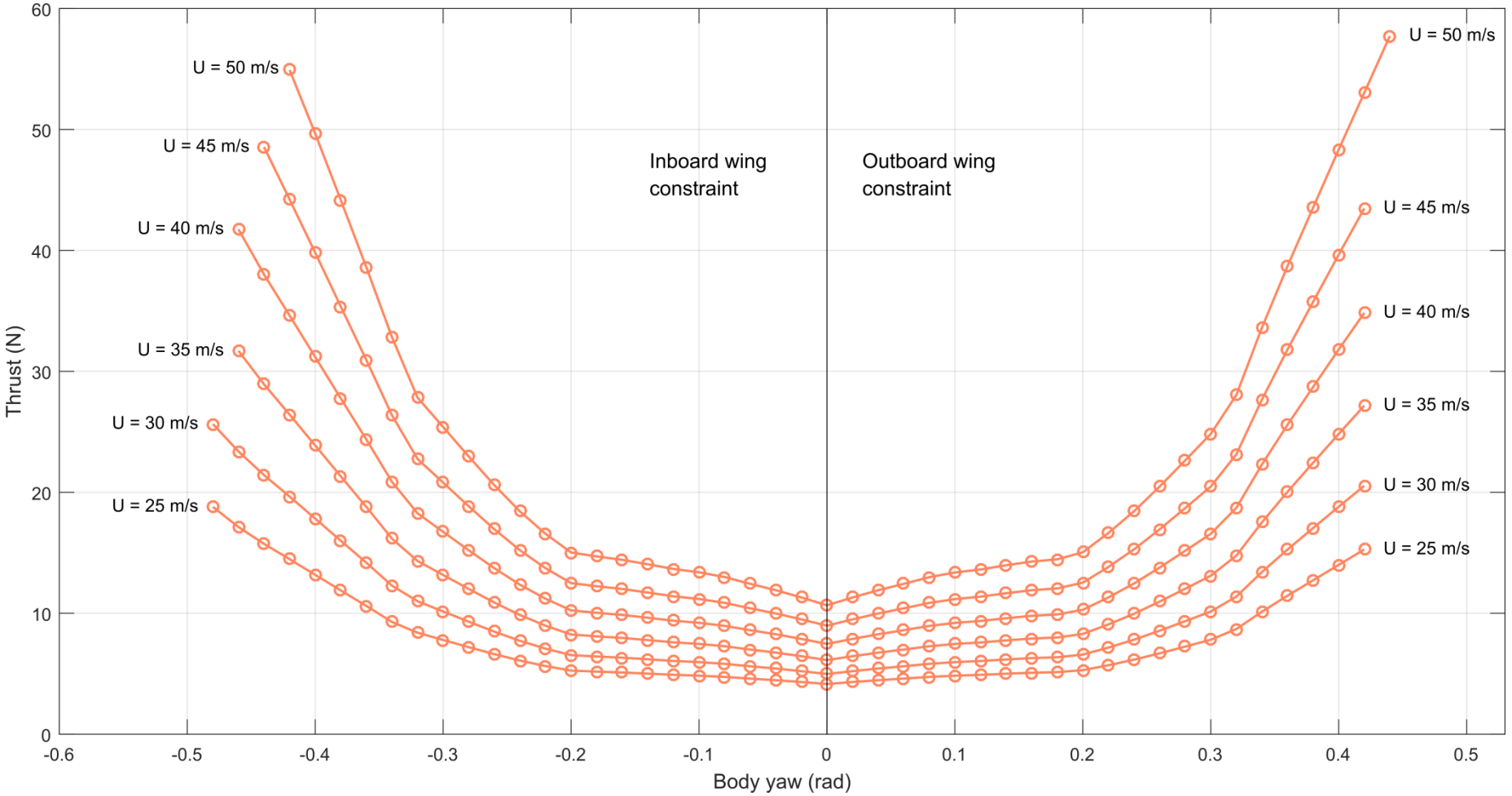

Figure 6.2.6: Trim state thrust as a function of airspeed and body yaw, computed with numerical continuation starting from a solution at $\psi = 0$ rad, $U = 25$ m/s. The limits of the continuation paths in θ represent the limits of trim state existence in this locality.

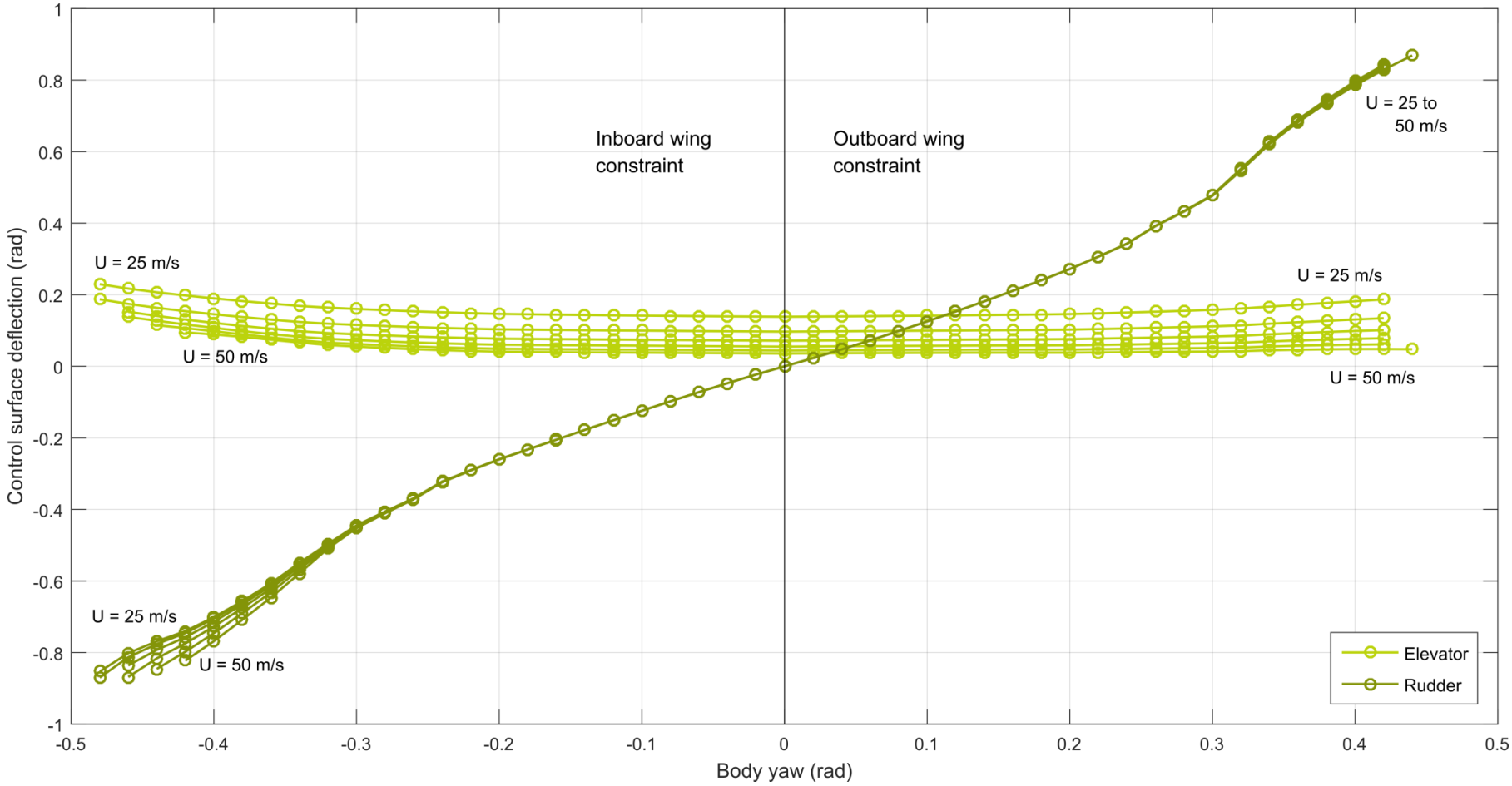

Figure 6.2.7: Trim state control surface deflections (elevator and rudder) as a function of airspeed and body yaw, computed with numerical continuation starting from a solution at $\psi = 0$ rad, $U = 25$ m/s. The limits of the continuation paths in θ represent the limits of trim state existence in this locality.

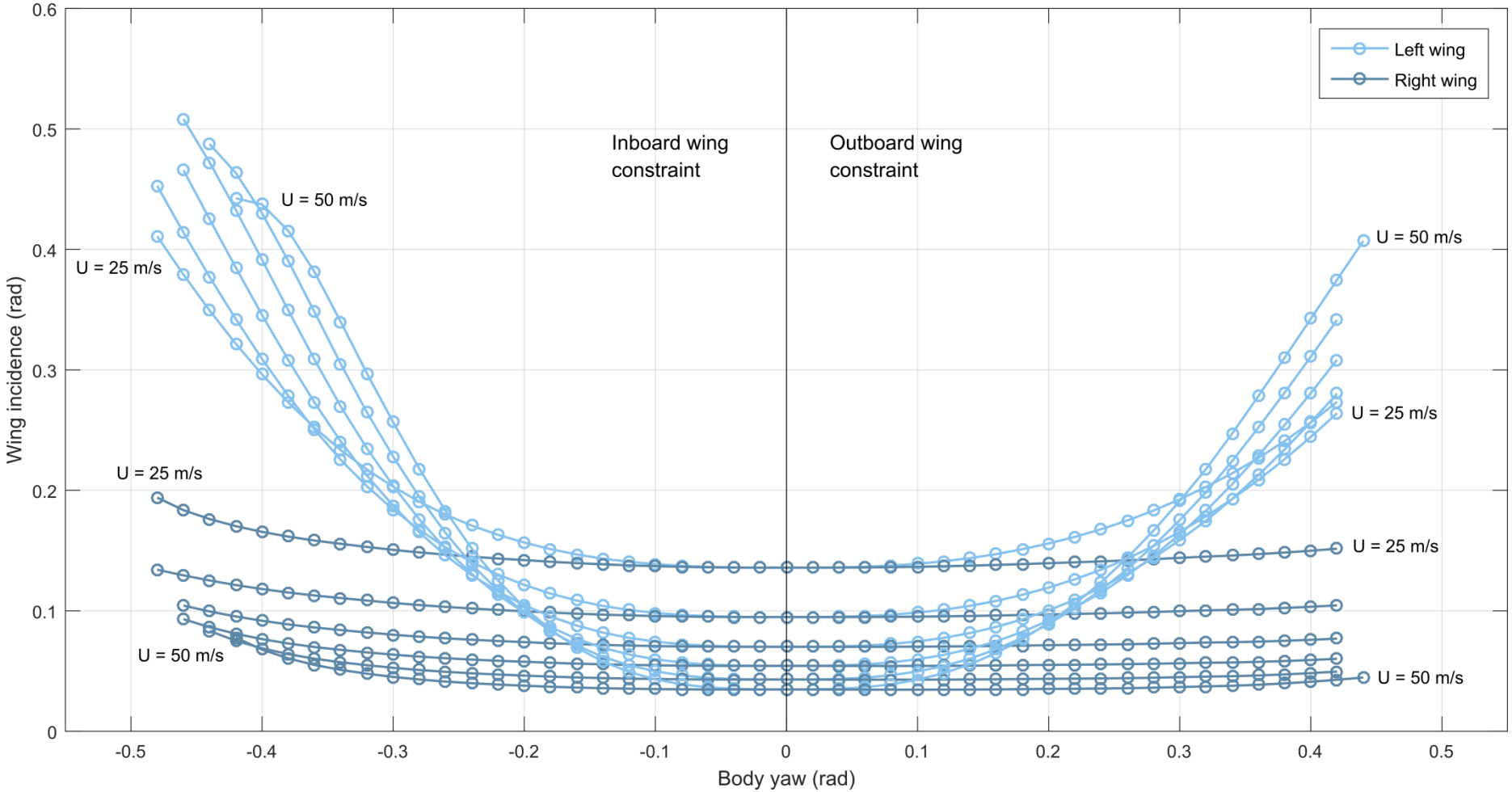

Figure 6.2.8: Trim state wing incidences (left and right) as a function of airspeed and body yaw, computed with numerical continuation starting from a solution at $\psi = 0$ rad, $U = 25$ m/s. The limits of the continuation paths in θ represent the limits of trim state existence in this locality.

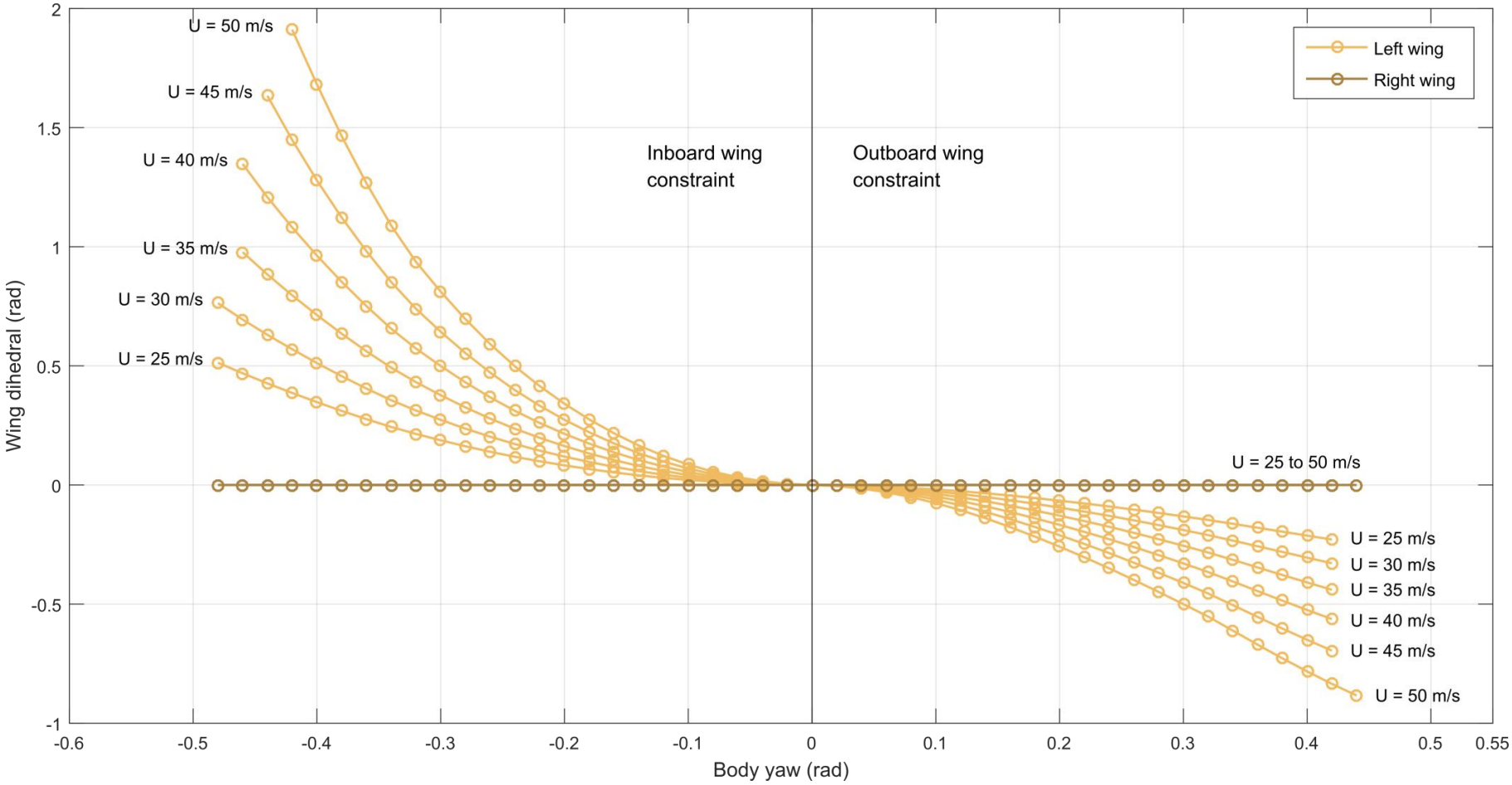

Figure 6.2.9: Trim state wing dihedrals (left and right) as a function of airspeed and body yaw, computed with numerical continuation starting from a solution at $\psi = 0$ rad, $U = 25$ m/s. The limits of the continuation paths in θ represent the limits of trim state existence in this locality. Note the constraint $\theta_{wr} = 0$.

6.2.5. Trim states as a function of pitch and yaw, via dihedral morphing

A wide variety of further trim states are also available. As an immediate extension of the trim states in independent nonzero pitch and yaw, these orientation angles can be varied concurrently, leading to full 3D control of the aircraft fuselage axis orientation. The same degrees of freedom that were used to compute the yaw-only trim states in Section 6.2.4 allow such 3D control, within an appropriate envelope. The size of this envelope and the specification of the trim states within it may be computed by the same two-parameter continuation methods that were used to compute the θ-U and ψ-U envelopes, applied to the orientation angles (θ-ψ).

Figures 6.2.10-6.2.13 show the results of this analysis. Figure 6.2.10 shows the computed trim state points and the interpolated envelope of available states, and Figure 6.2.11 the associated control surface deflections. In Figure 6.2.10, four trim states lying on the envelope are rendered, and for the internal computed points, the fuselage axis unit vector is shown. The right wing zero dihedral constraint from Section 6.2.4 is used; leading to an asymmetric envelope in yaw, corresponding to inboard/outboard wing constraints (indicated for reference in Figure 6.2.10). As can be seen, trim states exist within the bounds -0.49 $< \psi <$ 0.42 rad and 0.41 $< \theta <$ 0.53 rad, and at considerable combined angles – never less than an elliptical interpolation between these limits. As noted earlier, the inboard constraint allows for trim states at slightly larger yaw angles.

The utility of the dihedral variable in constraining trim states resides in its ability to generate additional side force (in y) and yaw moment (in z) – through a sideways component of the lift force, and a vertical component of the aerofoil moment. This can be used to balance an asymmetry in side force and/or yaw moment arising from the yawed fuselage and vertical stabiliser. The distinction between inboard and outboard wing constraints leads thus to left wing dihedral and anhedral, respectively, as yawed trim states in the case study system universally require inboard-directed side force and yaw moment from the dihedral. Figure 6.2.12 indicates this effect. The wing incidence additionally be utilised to control the differential between the lift force (generating a yaw moment and side force) and the aerofoil moment (generating only a yaw moment). This allows independent control of the yaw moment and side force to correct these two asymmetric forces/moments. However,

the choice of inboard / outboard morphing is very significant – not only because the trim state dihedrals are not anti-symmetric (cf. Figure 6.2.10), but because the change between dihedral and anhedral has significant effects on the stability of the aircraft spiral mode. This stability effect is analysed in Section 6.3.

Figure 6.2.11 shows the required control surface deflections over the space of available trim states: this demonstrates again that is the elevator and rudder limits (± 0.87 rad) that are the primary constraints on trim state existence; the elevator in pitch and the rudder in yaw. Indeed, the space of trim states is largely rectangular, with only small edge fillet radii and small curvature in the control surface deflection contours, indicating that the trimmed pitch and yaw degrees of freedom are largely uncoupled, and are limited by their respective control surface limits largely independently. This is however a strongly-system specific result: a greater control surface effectiveness would both increase the size of the trim state envelope and modify its shape (probably to be smoother) as other factors become limiting.

Figures 6.2.10-6.2.11 present results for the case of inboard/outboard constraints at zero dihedral; however these constraints may be fixed to nonzero values, or may be varied continuously throughout a manoeuvre. In the case of the former, such a change effectively creates a new reference state at zero yaw with symmetric dihedral equal to the constraint value; trim states at nonzero yaw are then forced to shift in the same direction as the constraint change (though this shift is not linear). The end result of this is a relatively small shift in the space of trim states – Figure 6.2.13 indicates the effect of a right wing constraint of $\Gamma = 0.3$ rad (c. 17°) – but with the potential for significantly changing the stability properties of the aircraft. Positive dihedral values, such as $\Gamma = 0.3$ rad, would phenomenologically be expected to improve the aircraft spiral mode stability.

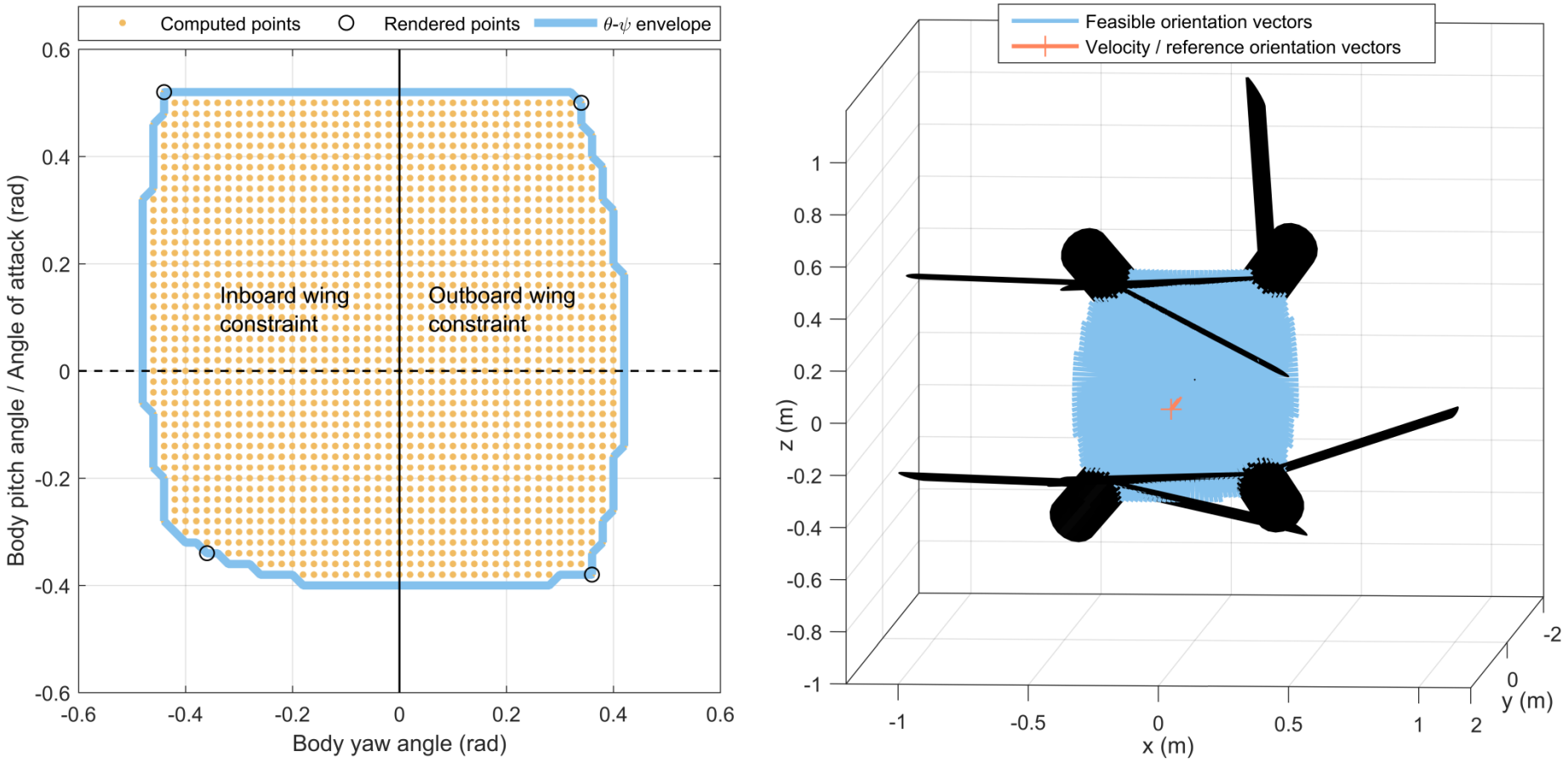

Figure 6.2.10: The space of available trim states in pitch and yaw, for the system with asymmetric incidence and dihedral morphing, under a right wing zero dihedral constraint. Computed trim state points, their corresponding fuselage orientation vectors, four example aircraft renderings, and the interpolated envelope of available states are shown.

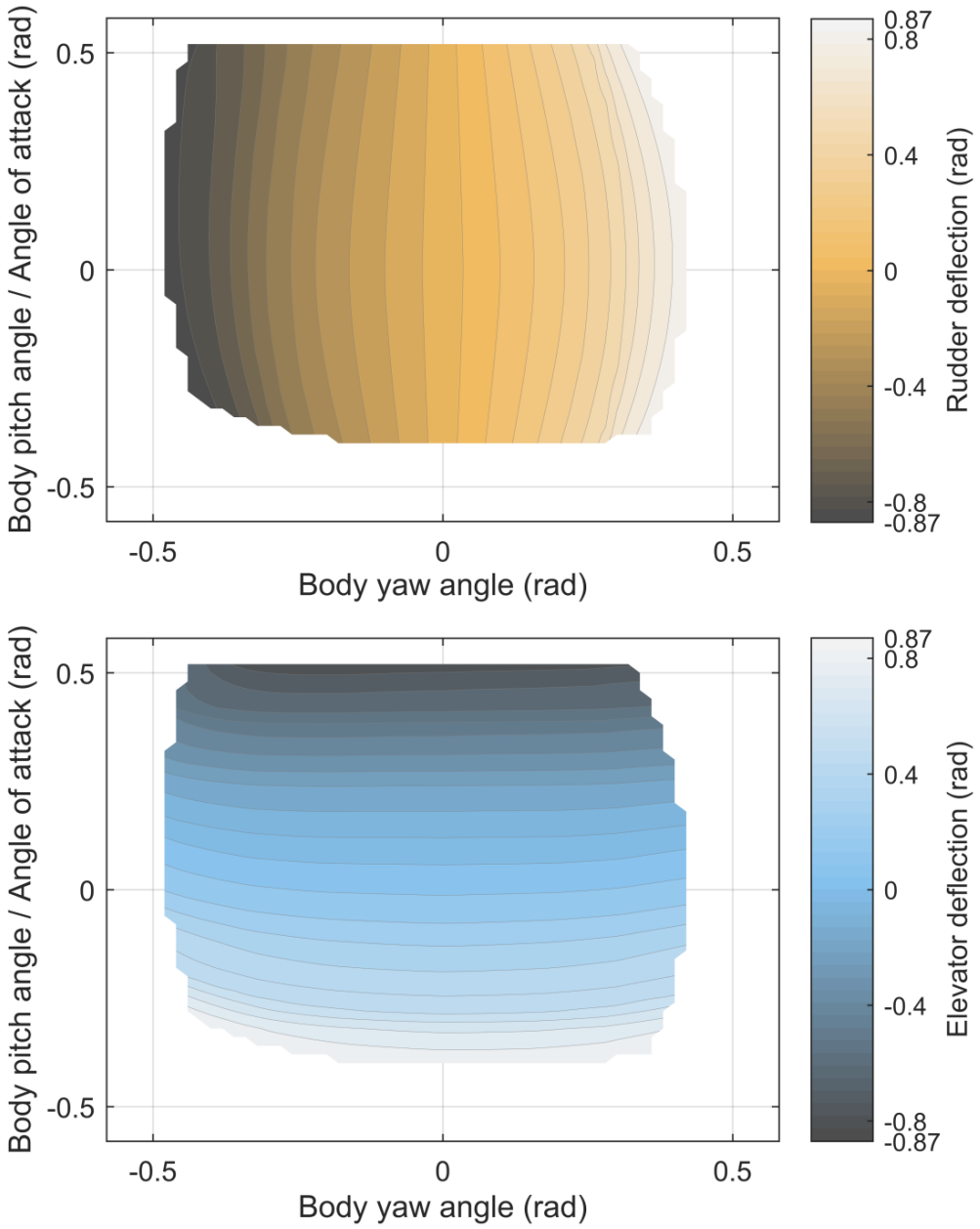

Figure 6.2.11: Trim state control surface deflections over the pitch-yaw trim state envelope, for the system with asymmetric incidence and dihedral morphing, under a right wing zero dihedral constraint.

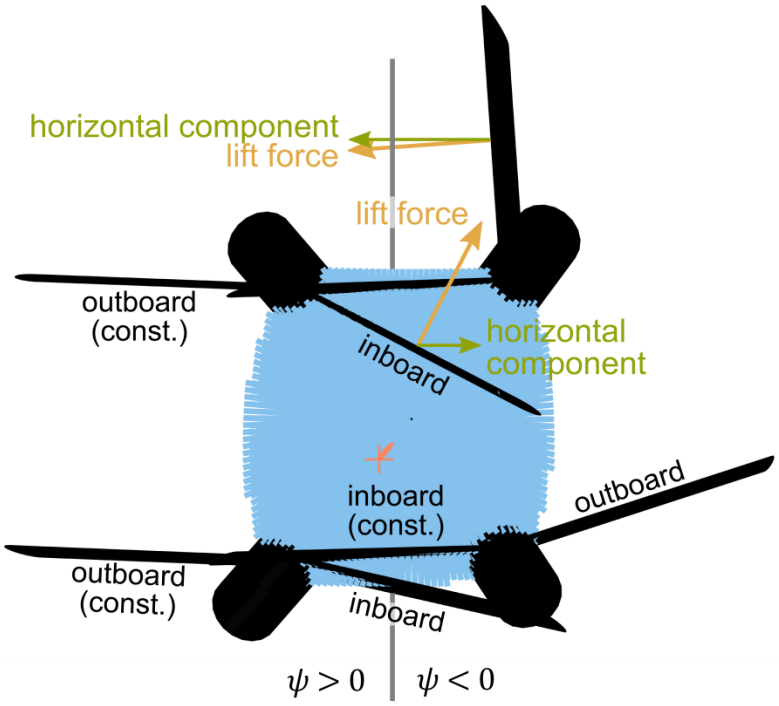

Figure 6.2.12: Schematic of the inboard-oriented forces from the asymmetric wing dihedral.

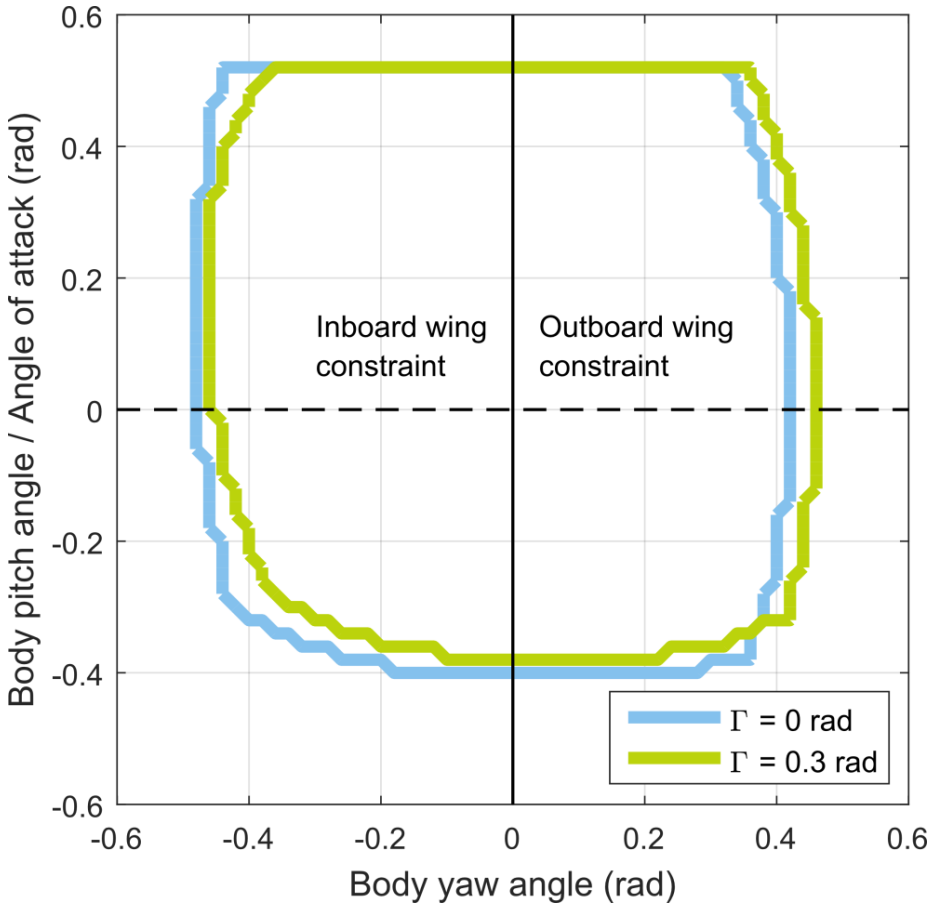

Figure 6.2.13: Overlaid trim spaces for right wing dihedral constraints $\Gamma = 0$ and $\Gamma = 0.3$ rad.

6.2.6. Other trim states

So far, this study has focused on nose-forward trim states with varying pitch and yaw. This is because these states enable a useful form of 3D aircraft orientation control independent of flight state – a form of NPAS or direct force capability, as characterised by Gal-Or [1] and Herbst [2] respectively. This capability is useful for particularly useful for fuselage-mounted equipment with some form of directional action – e.g. weaponry, sensory equipment, or lasers for laser-guidance systems. This form of orientation control is distinct from rapid-nose-pointing-and-shooting (RaNPAS) capability [1], which involves rapid transient changes to the aircraft orientation. More optimal biomimetic morphing controls are available for the latter, and these are studied in Chapter 7. The advantage of trim state orientation control is the capability for precise orientation control over long timescales. In an air-to-air combat environment, this would have utility in situations in which a prolonged lock-on is required – for example, in allowing multiple rounds of ammunition to be dispensed, or maintaining a guidance laser lock. However, the range of orientations in which this form of control is available is more limited (cf. Figure 6.2.10). Further study of this form of direct force capability in this system is presented in Section 6.4.

Other trim states outside this specification are also available, and they also enable forms of orientation control, but these have more limited utility. Nose-backward trim states are available, also with nonzero pitch and yaw, providing that the propulsion system permits the generation of reverse thrust (e.g. a propeller actuated via an electric motor). These states can only be reached from the nose-forward position by transient manoeuvres – not by a continuous trim state path – but such manoeuvres could have situational utility – e.g. in aerial combat, to orient fuselage-mounted weaponry in a rearward direction. Figure 6.2.14 shows an example of a nose-backward trim state, with a comparison between two solutions with the wing leading edge backwards and with it forwards (incidence > 180°), representing the difference between the availability of small-angle and large-angle incidence morphing respectively. The leading-edge-forward solution shows a very significant decrease in the reverse thrust required.

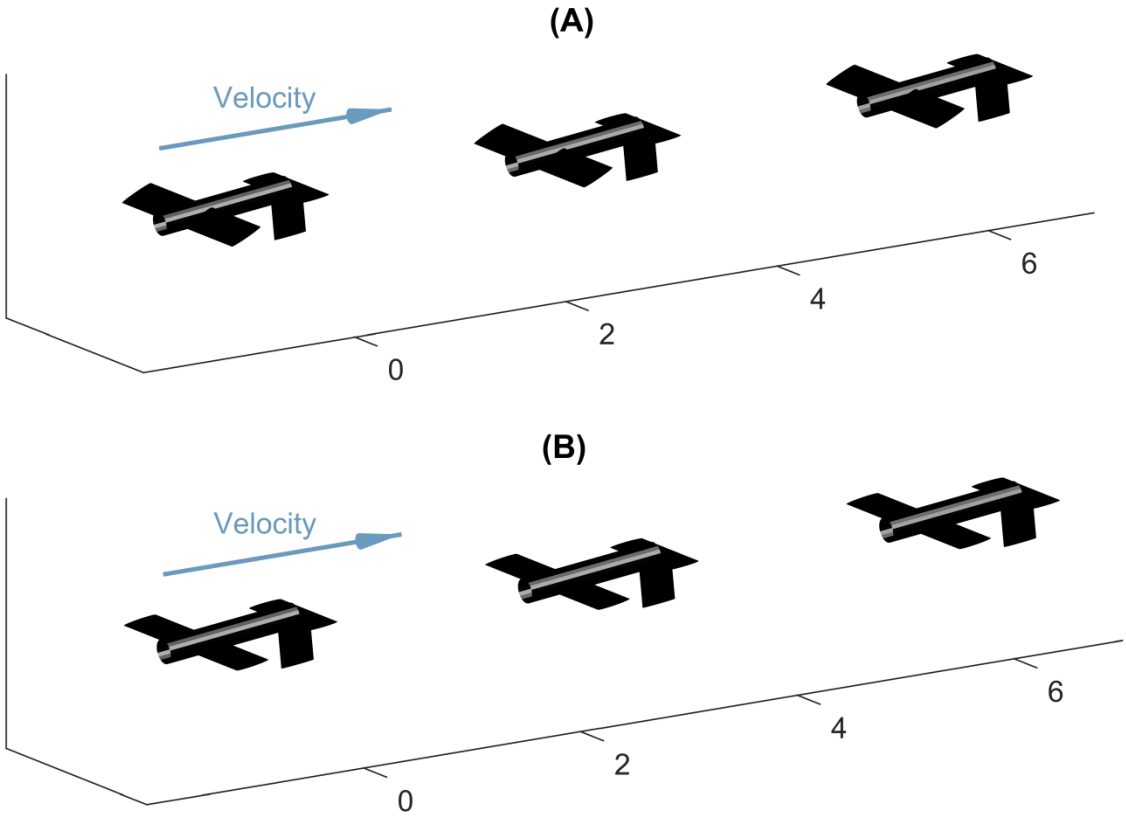

Figure 6.2.14: Flight simulations of two nose-backward, trim states, at $U = 25$ m/s, $\psi = 0$ rad, $\theta = \pi + 0.1$ rad ($= 0.1$ rad in reverse), and utilising reverse thrust. Scale in m.
(A) Elevator deflection -0.0890 rad, Wing incidence 0.324 rad (aerofoil leading edge backward,) Thrust -38.5 N.
(B) Elevator deflection -0.117 rad, Wing incidence $\pi + 0.0471$ rad (aerofoil leading edge forward), Thrust -5.26 N.

Trim states at nonzero roll angle are also available: a simple method of obtaining them is use asymmetric dihedral to set the wings to a conventional orientation (lift collinear with gravity) and then to correct the moment imbalance from the tailplane with asymmetric control surface deflection and / or wing incidence and additional dihedral. However, these trim states have minimal application, apart from rotating equipment that is vertically-oriented on the fuselage in a lateral direction – e.g. side-to-side motion of downwards-facing sensory equipment. However in most conceivable cases, alternative solutions will be preferable, such as use of transient / non-trim states to achieve the same rotation temporarily, or the use of wide-angle lenses for optical equipment. For this reason these trim states are not considered further.

Finally, though this study has demonstrated the existence of pitched, yawed and nose-backward trim states for this aircraft, this analysis has been confined to a relatively restrictive set of morphing and control parameters – the control surfaces, asymmetric incidence, and a restrictive form of asymmetric dihedral. Other parameter selections may have the potential to enlarge the space of available trim states. In particular, the sweep degree of freedom (symmetric or asymmetric) has not yet been considered. Preliminary analyses indicate that the sweep degree of freedom does not significantly enlarge the set of trim states in pitch, but does generate high imbalanced pitching moments – making it more useful as an avenue for a high level of pitch control effectiveness within a trim state, e.g. for transitioning between nose-forward and nose-back states, and for performing other transient manoeuvres. Asymmetric sweep morphing is primarily useful for generating roll moments via the lift deficiency on one swept wing. This can be used to correct the roll moments generated by asymmetric incidence, leading to an isolated yaw moment via the asymmetric drag force – a proxy for rudder control.

Substituting the dihedral degree of freedom in the pitch-yaw continuation analysis (Section 6.2.5) with the sweep degree of freedom, and analogously constraining the right-wing sweep to be zero, a space of trim states in pitch and yaw is again obtained. The results are, however, significantly different to those with dihedral morphing active. Figures 6.2.15-6.2.16 show the results of the continuation analysis for the system with sweep morphing, including the required rudder and elevator deflections. The overall space of trim states forms an hourglass shape: with a general absence of trim states around the origin, particularly at small positive pitch angle. Notably, the non-existence of these states is not a result of the limits of elevator and rudder control effectiveness (as in Figure 6.2.11) but is due to the presence of an uncorrectable roll moment. This is probably connected with the fact that the sweep degree of freedom – whether forwards or backwards – cannot increase the lift of the wing beyond the zero sweep case, and thus cannot correct an excess of lift from the opposing wing; only a deficiency. This effect is also probably the primary reason behind the high degree of lateral asymmetry in the trim state space, e.g. the general nonexistence of states in the $(-\theta,-\psi)$ quadrant.

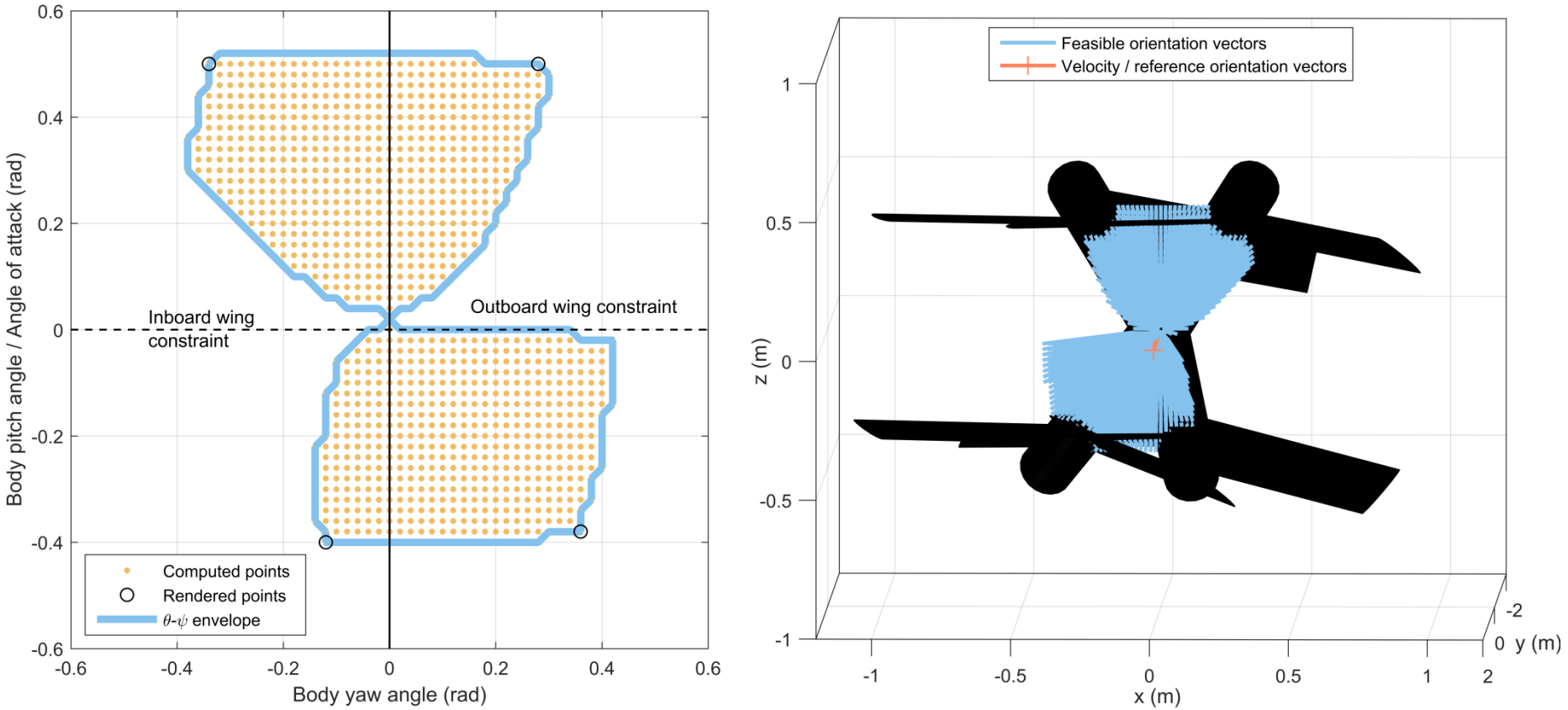

Figure 6.2.15: The space of available trim states in pitch and yaw, for the system with asymmetric incidence and sweep morphing, under a right wing zero sweep constraint. Computed trim state points, their corresponding fuselage orientation vectors, four example aircraft renderings, and the interpolated envelope of available states are shown.

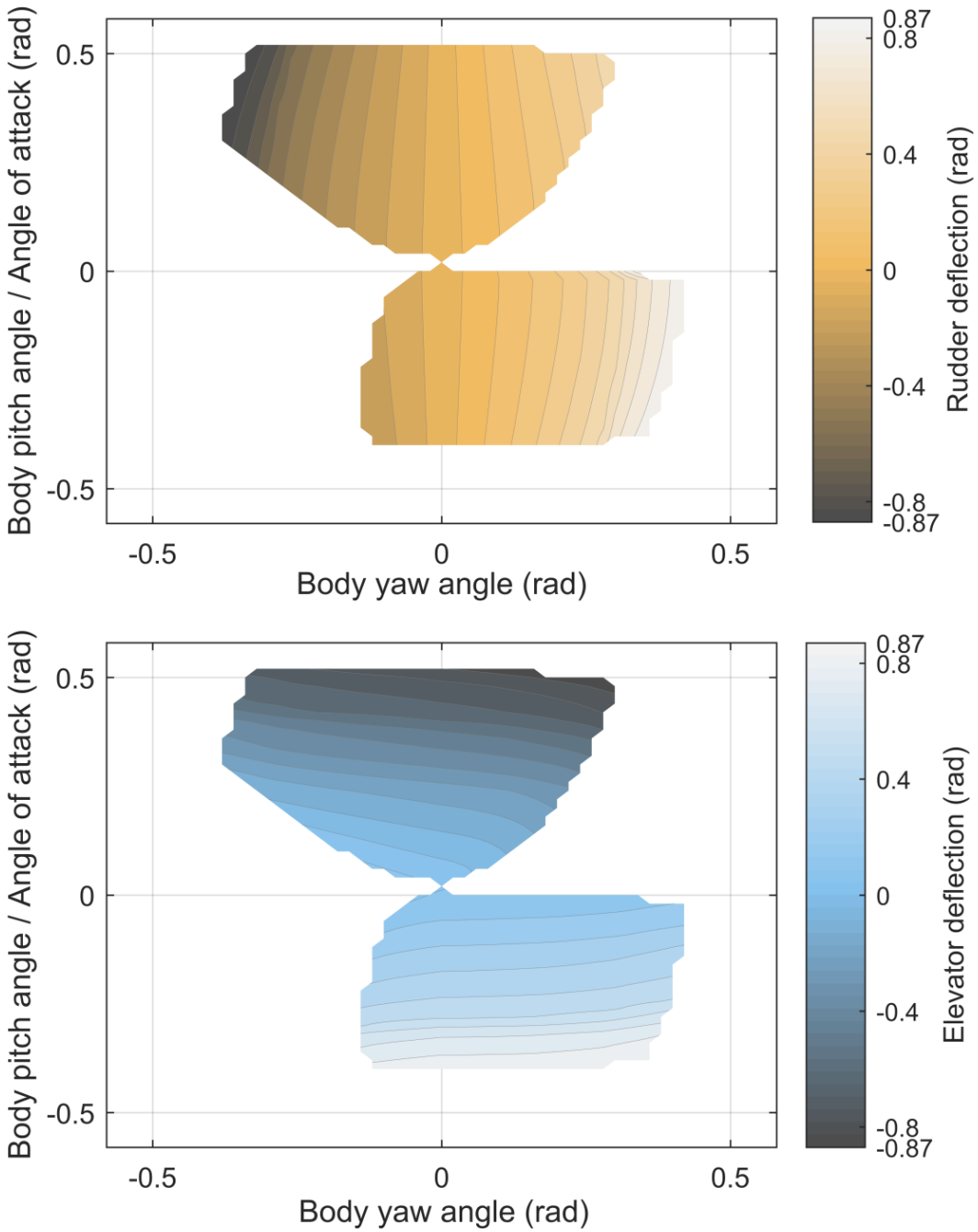

Figure 6.2.16: Trim state control surface deflections over the pitch-yaw trim state envelope, the system with asymmetric incidence and sweep morphing, under a right wing zero sweep constraint.

Approaches for enlarging the trim space could involve activating the opposing wing sweep degree of freedom, or at least constraining it to a nonzero value, as well as the use of differential elevator control to correct roll moments. However, as the hourglass pitch-yaw trim space under asymmetric sweep morphing may be verified to be a pure subset of the pitch-yaw trim space under asymmetric dihedral morphing (with a simple right wing zero dihedral constraint), a switch to dihedral morphing is likely to be preferable.

6.3. TRIM STATE STABILITY

6.3.1. Flight dynamic stability

Trim states may be stable or unstable in their flight dynamic modes. The question of trim state stability is of secondary importance as regards NPAS / direct force capability, as many unstable modes can be stabilised with active control / fly-by-wire systems. Such stabilisation methods are used in a variety of existing aircraft and UAVs which have unstable airframes. For this reason, the stability or otherwise of a trim state has only a secondary effect on its potential for real-world application in the case study system – particularly as such an application is almost certain to require a fly-by-wire system, as the number of morphing degrees of freedom are greater than can be feasibly controlled by manual input. However, the application of these stabilisation methods to the case study system is beyond the scope of this work. For this reason, the direct force capabilities of this aircraft are demonstrated in open-loop flight simulations of trim states that are stable in most or all flight dynamic modes – the exception being the spiral mode, which is permitted to show a degree of instability.

Unstable modes will manifest themselves in flight simulations, and may thereby be identified; they may also be computed via stability analysis. Static longitudinal and lateral stability are addressed via a static stability analysis, and the stability of other modes via parametric flight simulation studies. State-space dynamic stability analysis is a more common alternative to the latter, but is not directly applicable to the case study model, which is strongly nonlinear in the time domain. Deriving and validating a linearised model for state-space analysis would useful but is not otherwise motivated: a nonlinear analysis is more appropriate for the impending NPAS analysis, as nonlinear effects in the system's asymmetric trim states can be very pronounced (see Section 6.3.3).

6.3.2. Static stability

The static longitudinal and lateral stability of the case study aircraft may be characterised by the two classical stability criteria:

$$\begin{aligned} &\frac{\partial \ddot{\theta}}{\partial \theta} < 0, \text{ for longitudinal static stability,} \\ &\frac{\partial \ddot{\psi}}{\partial \psi_S} < 0, \text{ for lateral static stability,} \end{aligned} \tag{6.3.1}$$

where θ is the pitch angle, ψ the yaw angle, and ψ_S the sideslip angle – the yaw angle between the aircraft body-fixed axes, and the aircraft velocity. Note that when $\dot{\mathbf{x}}_S^{(e)} = [U\ 0\ 0]^T$, $\psi = \psi_S$, an assumption used throughout this stability analysis. These criteria are traditionally formulated with an inertia term, leading to the derivative of a moment: $\partial I_\theta \ddot{\theta}/\partial\theta = \partial M_\theta/\partial\theta$, a change which has no effect on the computed stability characteristics. The pitch and yaw accelerations, $\ddot{\theta}$ and $\ddot{\psi}$, may be generated directly from the aircraft constitutive equations, $\dot{\mathbf{z}} = \mathbf{F}_z(t, \mathbf{z}, \mathbf{p})$ (Eq. 6.2.1). Their gradients w.r.t. the appropriate orientation angles (θ, ψ_S or ψ) be approximate by perturbing these angles away from a given trim state condition ($t = 0$, specified $\mathbf{z}, \mathbf{p}$), and computing a finite difference. Second-order differences are used, e.g. in pitch:

$$\frac{\partial \ddot{\theta}}{\partial \theta} \cong \frac{\ddot{\theta}(\theta_{\text{trim}} + \Delta\theta) - \ddot{\theta}(\theta_{\text{trim}} - \Delta\theta)}{2\Delta\theta}. \tag{6.3.2}$$

These stability metrics are then computed across the space of computed trim points (e.g. as per Figure 6.2.10). Figure 6.3.1 shows these metrics across the space of trim points, for two different system configurations with a right wing dihedral constraint; with right wing dihedral constraint $\Gamma = 0$, and with $\Gamma = 0.3$ rad (cf. Section 6.2.5). These systems represent changes to the trim state geometry which are expected to have effects on the aircraft spiral mode stability. Figure 6.3.1 also indicates the stability boundaries (e.g. $\partial\ddot{\theta}/\partial\theta = 0$).

Nearly the entire trim spaces for both $\Gamma = 0$ and $\Gamma = 0.3$ rad are laterally and longitudinally stable, except for a tiny area of lateral instability in the $\Gamma = 0.3$ rad space at c. $0.1 \leq \psi_{\text{tgt}} \leq 0.2$ rad and $\theta_{\text{tgt}} = 0.5$ rad. Around this unstable zone there is a region of borderline stability, larger in the pitch dimension than in yaw. Overall, the difference between $\Gamma = 0$ and $\Gamma = 0.3$ rad is relatively small: the change to $\Gamma = 0.3$ rad leads to a slight increase in longitudinal

stability at positive pitch angles, a slight decrease at negative pitch angles, and a slight decrease in lateral stability across the trim and constraint direction space. The choice between inboard and outboard dihedral constraints has a more significant effect, with the inboard constraint increasing longitudinal stability but decreasing lateral stability across the trim space at both Γ values.

6.3.3. Nonlinear spiral stability

In the open-loop framework of this study, the tendency of the aircraft to spiral away from a level and forward flight path under perturbation is of interest: this will have an effect on the control of the aircraft NPAS / direct force capability, as the controlling trim states are computed under level forward flight (by definition). In the context of a conventional flight stability analysis, this tendency to spiral roughly equates to the stability of the aircraft spiral mode. In precise terms, the spiral mode refers to a static (non-oscillatory) mode in reduced-order models of conventional aircraft with linear stability derivatives. The extent to which spiral-type responses in asymmetric trim states such as those considered in Section 6.2.5 are representations of a traditional spiral mode is thus open to debate. To avoid the potential pitfalls of a conventional spiral-mode stability analysis, and because to perform the latter would require significant state-space model reformulation, we utilise parametric flight simulations in the case study nonlinear time-domain model to assess the extent of spiral-type behaviour in the trim states of the case study system.

This approach has advantages and disadvantages. Disadvantages; in that such simulations conflate two effects within the spiral, the modal mass (as excited by the initial perturbation) and the spiral mode stability (growth rate), as well as the aircraft transient response to perturbation in other modes, e.g. short period or Dutch roll [11]. These effects obscure the stability changes in the individual modes. Advantages; in that the distinction between conventional modes may not be helpful for strongly asymmetric trim states, and that the conflation of modal mass and growth rate via time-domain simulation yields a more accurate assessment of the response of the aircraft to perturbation. The latter is self-evident from the fact that these simulations are direct measurements of the aircraft perturbation response – modal arguments serve only to generalise this behaviour to a wider space of perturbations than those simulated.

Flight simulations are carried out at airspeed $U = 25$ m/s, for a duration of $T = 15$ s, for trim states at target yaw (sideslip) angles $-0.4 \leq \psi_{\mathrm{tgt}} \leq 0.35$ rad and pitch angles $0 \leq \theta_{\mathrm{tgt}} \leq 0.4$ rad, with right dihedral constraints of $\Gamma = 0$ and $\Gamma = 0.3$ rad. Note again that $\psi_{\mathrm{tgt}} < 0$ represents an inboard-wing constraint, and $\psi_{\mathrm{tgt}} > 0$ and outboard-wing constraint, as per Figure 6.2.10. The aircraft is subject to initial yaw perturbations of $\Delta\psi = \pm 0.05$ rad relative to ψ_{tgt}. Yaw rather than roll perturbations are utilised, because the yaw degree of freedom is not dependent on the target trim state orientation, whereas the roll angle is – potentially further obscuring the spiral stability effects due to differences in spiral mode excitation as a function of ψ_{tgt} and θ_{tgt}. For example, in the hypothetical extreme case of a trim state at $\psi_{\mathrm{tgt}} = 90°$, a perturbation in fuselage roll angle would not correspond to a spiral mode excitation at all, but an effective pitch angle perturbation.

To measure the degree of spiral instability in these flight simulations, dimensionless metrics in aircraft lateral (y) position, roll angle and yaw angle are computed (y_{mt}, ϕ_{mt} and ψ_{mt}). These metrics are based on the aircraft lateral position, roll angle and yaw angle at the simulation endpoint, $t = T$.

$$\begin{aligned} y_{\mathrm{mt}} &= y|_{t=T}/(-TU \operatorname{sgn} \Delta\psi) \\ \phi_{\mathrm{mt}} &= \phi|_{t=T}/\Delta\psi \\ \psi_{\mathrm{mt}} &= \left(\psi|_{t=T} - \psi_{\mathrm{tgt}}\right)/\Delta\psi \end{aligned} \tag{6.3.3}$$

The scale factor for the lateral position is the distance travelled by the aircraft under the ideal state of no spiral deflection, i.e. $TU = 375$ m . The scale factor for roll and yaw angles is the yaw perturbation $\Delta\psi$. The metrics are signed, such that the expected spiral response to a positive yaw perturbation ($+\Delta\psi$) are positive lateral deflection, positive yaw, and negative roll metrics ($+y_{\mathrm{mt}}$, $+\psi_{\mathrm{mt}}$, $-\phi_{\mathrm{mt}}$). This is relevant, as some trim states are observed to spiral in the opposite direction to the perturbation. While it is possible to use more sophisticated metrics base on exponential fitting to isolate the spiral mode growth rate, tests with such metrics failed to generate any further fundamental insights due to a strong dependency on the fitted model used. Spectral methods are of no use to isolate the static spiral mode; and while the Hilbert-Huang transform [12] has been previously used to isolate longitudinal modal behaviour from data, a generalisation to lateral behaviour is not yet available.

To aid understanding, Figures 6.3.2-6.3.4 show example dimensional yaw and lateral deflection histories for trim states for $-0.3 \leq \psi_{\mathrm{tgt}} \leq 0$ rad and $\theta_{\mathrm{tgt}} = 0.1, 0, -0.3$ rad. The result from $\theta_{\mathrm{tgt}} = 0.1$ rad is representative of the results from $0.1 \leq \theta_{\mathrm{tgt}} \leq 0.4$ rad. A quasilinear zone is observed from $\psi_{\mathrm{tgt}} = 0$ to c. $\psi_{\mathrm{tgt}} = -0.2$ rad, in which the paths trends are linear. In this zone, $\Gamma = 0.3$ rad yields a stable spiral mode, and $\Gamma = 0$ an unstable spiral mode. However, beyond $\psi_{\mathrm{tgt}} = -0.2$ rad, the lateral and yaw paths diverge erratically from their low-angle equivalents, and in the case of $\Gamma = 0.3$, show a change in spiral direction. Furthermore, in all simulations the spiral direction for $\Gamma = 0$ is opposite to that expected, with negative perturbations in yaw generating a positive spiral in ψ and a negative spiral in y (negative lateral metric and negative yaw metric).

These effects are potentially attributable to two factors: the asymmetry of the trim state, leading to directional spiral tendencies in the aircraft (an effect beyond the capability of the spiral mode to describe), and the ability of the initial aircraft transient response (e.g. in Dutch roll, oscillatory roll and yaw [11]) to provide an excitation of the spiral mode that is different to that of the initial perturbation. The existence of the latter effect exists is confirmed by the simulation at $\psi_{\mathrm{tgt}} = 0$, which spirals in the opposite direction to the perturbation. Thus in the first instance, the tendency of the $\Gamma = 0$ system, in its quasilinear zone, to spiral away from the initial perturbation may be attributed to the transient Dutch roll response, which excites the aircraft spiral mode in the opposite direction to the initial perturbation. While any variation in the aircraft transient response has the potential to introduce uncontrolled variation in the spiral mode results, this response is observed to show relatively minimal variation across ψ_{tgt} and Γ; as may be seen in Figures 6.3.2-6.3.4. On the other hand, while the effect of aircraft asymmetry may be assumed to be qualitatively significant, quantifying this is effect more difficult. This will be done further on in this section.

Figure 6.3.2 shows the raw flight data for $\theta_{\mathrm{tgt}} = 0$, and Figure 6.3.3 that for $\theta_{\mathrm{tgt}} = -0.3$ rad. These results are representative of the zone $-0.3 \leq \theta_{\mathrm{tgt}} \leq 0$ rad, in that they demonstrate the decreasing stability of the Dutch roll mode (oscillatory roll and yaw) with decreasing θ_{tgt} over this zone. For $\Gamma = 0$, this mode remains stable over $-0.3 \leq \theta_{\mathrm{tgt}} \leq 0$ rad despite the

decreasing stability; but for $\Gamma = 0.3$ rad, the mode destabilises rapidly and is highly unstable by $\theta_{\mathrm{tgt}} = -0.3$ rad. This destabilisation represents one disadvantage from the otherwise positive effects of the dihedral increase, and makes the space $\theta_{\mathrm{tgt}} < 0$ with $\Gamma = 0.3$ rad unusable for open-loop orientation control. The prominence of the Dutch roll mode in these subspaces makes the spiral mode difficult to characterise: this is observed when spiral stability metrics are computed over the system trim space.

Figures 6.3.5-6.3.7 show the computed lateral position, roll and yaw metrics fields over the entire trim spaces of the $\Gamma = 0$ and $\Gamma = 0.3$ systems under a right wing dihedral constraint (i.e. inboard at $\psi_{\mathrm{tgt}} < 0$, outboard at $\psi_{\mathrm{tgt}} > 0$), with the fields are capped at maximal values to for clearer presentation. Two notable features of Figures 6.3.5-6.3.7 are the maximal roll and yaw metrics below $\theta_{\mathrm{tgt}} = 0$, often switching erratically in sign. This is due to two factors: the capture of the unstable Dutch roll mode at positive or negative points on its cycle; and nonlinear directional effects, leading to a preferred spiral direction for the aircraft. The former can be observed in Figure 6.3.4 (*in extremis*); and the latter in the same; e.g. in the single erratic path with positive lateral metric. These nonlinear directional effects will be analysed more fully later. Overall, the combination of instabilities below $\theta_{\mathrm{tgt}} = 0$ leads us to restrict further spiral mode analysis to $0 \leq \theta_{\mathrm{tgt}} \leq 0.4$. It is this more usable zone that will be analysed in detail.

Figure 6.3.8-6.3.10 shows lateral position, roll and yaw metric plots for the trim space $0 \leq \theta_{\mathrm{tgt}} \leq 0.4$, $-0.4 \leq \psi_{\mathrm{tgt}} \leq 0.35$ rad, with $\Gamma = 0$ and $\Gamma = 0.3$ rad under a right wing dihedral constraint (inboard $\psi_{\mathrm{tgt}} < 0$, outboard $\psi_{\mathrm{tgt}} > 0$). This represents the trim subspace with stable Dutch roll mode. These plots map the strength of the spiral mode across this space; their purpose is to indicate whether the increase in dihedral to $\Gamma = 0.3$ rad has consistent positive effects for spiral stability, and whether inboard or outboard dihedral constraints are more effective for minimising spiral deflection in this stable zone. As regards the change in dihedral: the lateral and yaw metrics indicate a modest increase (c. 50%) in spiral stability over the quasi-linear zone, $-0.2 \leq \psi_{\mathrm{tgt}} \leq 0.2$, resulting from the increase in dihedral, but significant inconsistency outside this range. In roll metric, however, the results are very clear-cut: the increase in dihedral result in a significant restoring force to $\phi = 0$ for

trim states at nearly all orientations – the primary exceptions being outboard dihedral constraints with $\psi_{\mathrm{tgt}} > 0.2$ rad. Note that, in the roll results, a residual nonzero metric in yaw and lateral is expected even for states with stable spiral modes, as the transient response to the initial perturbation will rotate the flight velocity vector away from $[U\ 0\ 0]^T$ to a new default forward flight state at nonzero yaw. This effect cannot be corrected by passive flight dynamics, but requires active guidance.

As regards the effect of inboard/outboard dihedral constraints: in the case of $\Gamma = 0$, all three metrics indicate that the inboard constraint is yields a significant improvement in spiral stability. In the linear zone, the spiral metrics show an approximately linear dependence on ψ_{tgt}, favouring $\psi_{\mathrm{tgt}} < 0$ for stability, and even the nonlinear zones show a clear improvement in spiral metrics. In the case of $\Gamma = 0.3$ rad, the inboard and outboard quasilinear zones show equally high degrees of stability, but the nonlinear zone shows an erratic trend: the outboard nonlinear zone ($\psi_{\mathrm{tgt}} > 0.2$ rad) shows divergence in roll, a serious effect in an otherwise strongly roll stable system, whereas the inboard nonlinear zone ($\psi_{\mathrm{tgt}} < -0.2$ rad) shows a strong lateral and yaw divergence. Overall, the inboard constraint is preferable in terms of spiral stability, though with diminished benefit at higher dihedral values.

Finally, to investigate the nonlinear zone instability effects in more detail, the effect of positive / negative (inboard / outboard) yaw perturbations on the spiral response of the aircraft is analysed. Asymmetries in the spiral response to $\pm$ perturbations would be directly attributable to nonlinear effects arising from the asymmetry of the trim state – even if the transient Dutch roll response is in fact the prime excitation of the spiral mode, this transient response would be expected to be symmetric in a linear system. In particular, such asymmetries would be indicative of tendencies for the aircraft to spiral in a particular direction (inboard or outboard) even against the direction of perturbation, an effect which would be phenomenologically consistent with the asymmetry of the trim state.

Figures 6.3.11-6.3.13 shows the system lateral position, roll and yaw metrics for positive and negative (outboard and inboard) perturbations to the systems with inboard dihedral

constraint (i.e. right wing constraint, $\psi < 0$), $\Gamma = 0$ and $\Gamma = 0.3$. In the quasilinear zone, no asymmetries are observed between the inboard and outboard perturbations: the trim states perform as a conventional aircraft. The strong spiral effects that mark the end of this zone, on the other hand, show almost perfect antisymmetry, with the extant small differences are attributable to the superposition of linear effects or slight differences in the modal mass of the perturbation response. Antisymmetric peaks which are positive in the inboard perturbation indicate a tendency to spiral inboard; *mutatis mutandis* for antisymmetric outboard positive peaks. These effects may be corroborated with the dimensional flight paths in Figures 6.3.2-6.3.4, which further indicate the unusual nature of these spiral paths, which show an initial exponential growth but then stabilise to an alternate quasi-trim state.

A few effects influencing these spiral paths should be noted. The magnitude of the asymmetric response peaks need not necessarily represent the relative magnitude of the directional effect at the trim state themselves, as the former is also influenced by the state's properties away from the trim state. It is, however, indicative of a directional tendency at least large enough to overcome the initial perturbation direction. An argument for asymmetry of modal mass (i.e. mode excitation) could also be made to account for differences in the magnitude inboard / outboard perturbation response, but would not suffice to explain a reverse in perturbation response direction and the strong antisymmetry observed.

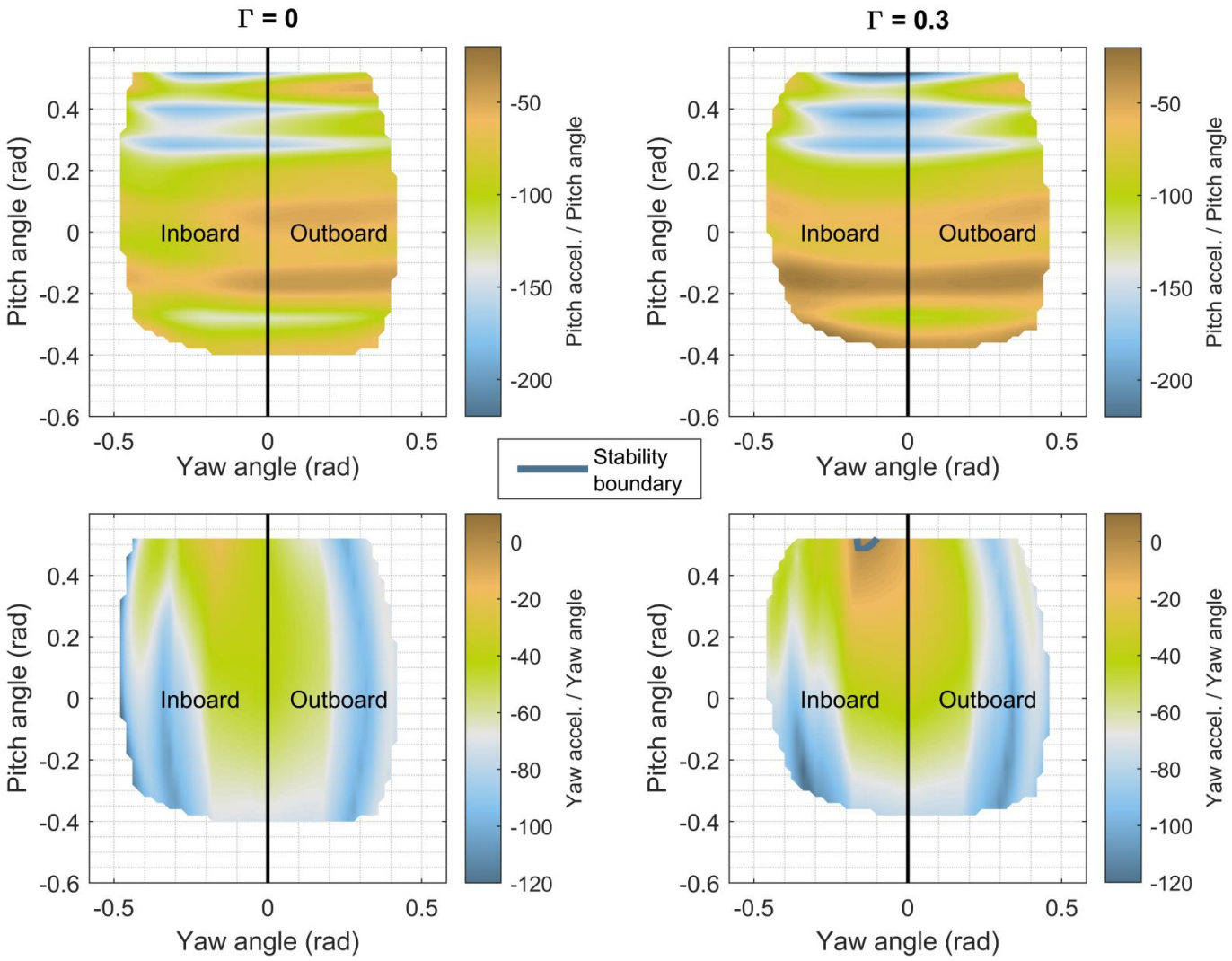

Figure 6.3.1: Longitudinal and lateral static stability metrics across the trim space of the case study system, for zero and positive dihedral states.

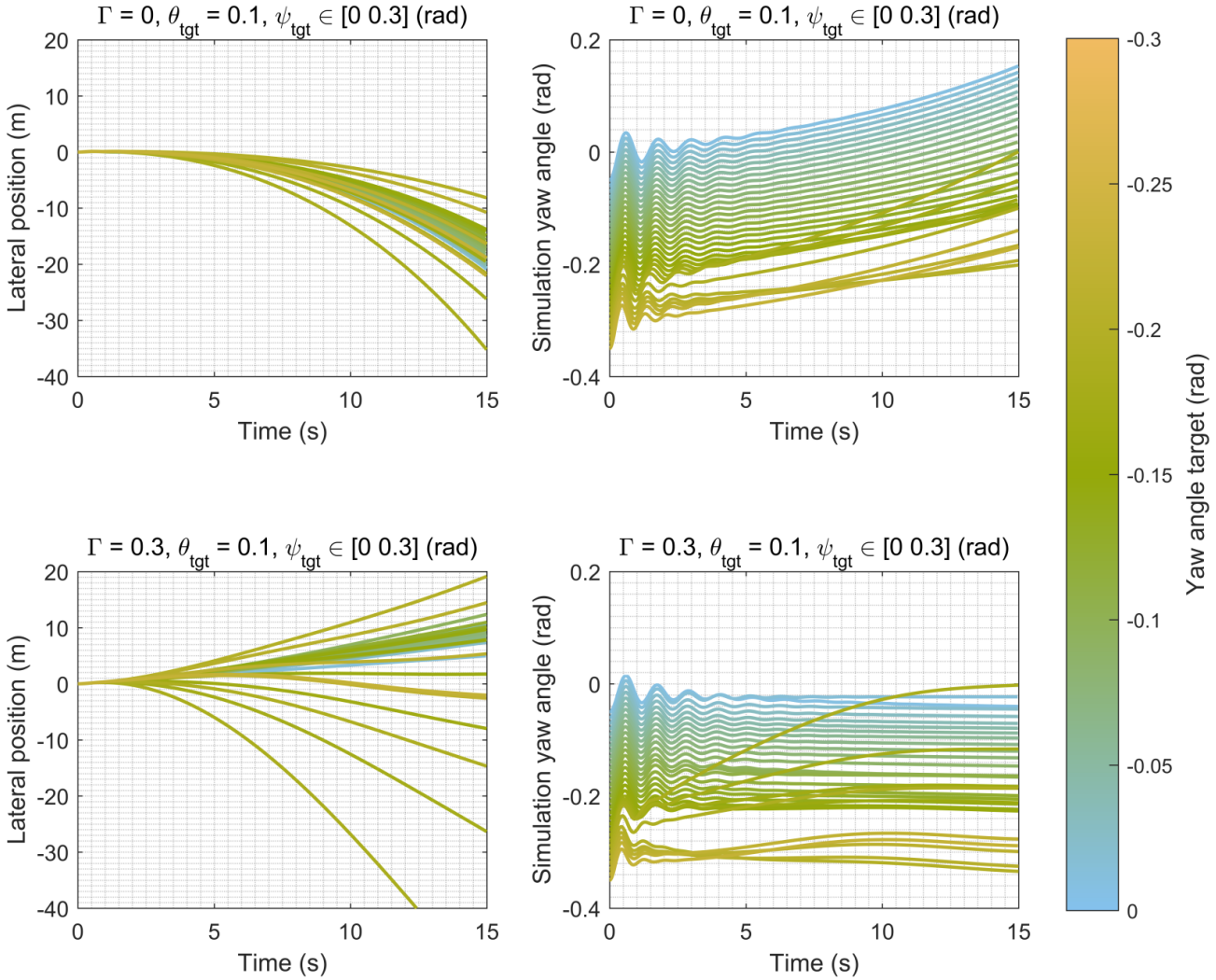

Figure 6.3.2:
Flight simulation results from the spiral mode stability analysis, for trim states at yaw angle target $\psi_{\mathrm{tgt}} \in [0, -0.3]$ rad, and pitch angle target $\boldsymbol{\theta_{\mathrm{tgt}}} =$ **0.1 rad**; for both $\Gamma = 0$ and $\Gamma = 0.3$ rad inboard wing constraints. The yaw perturbation is negative: $\Delta\psi = -0.05$.

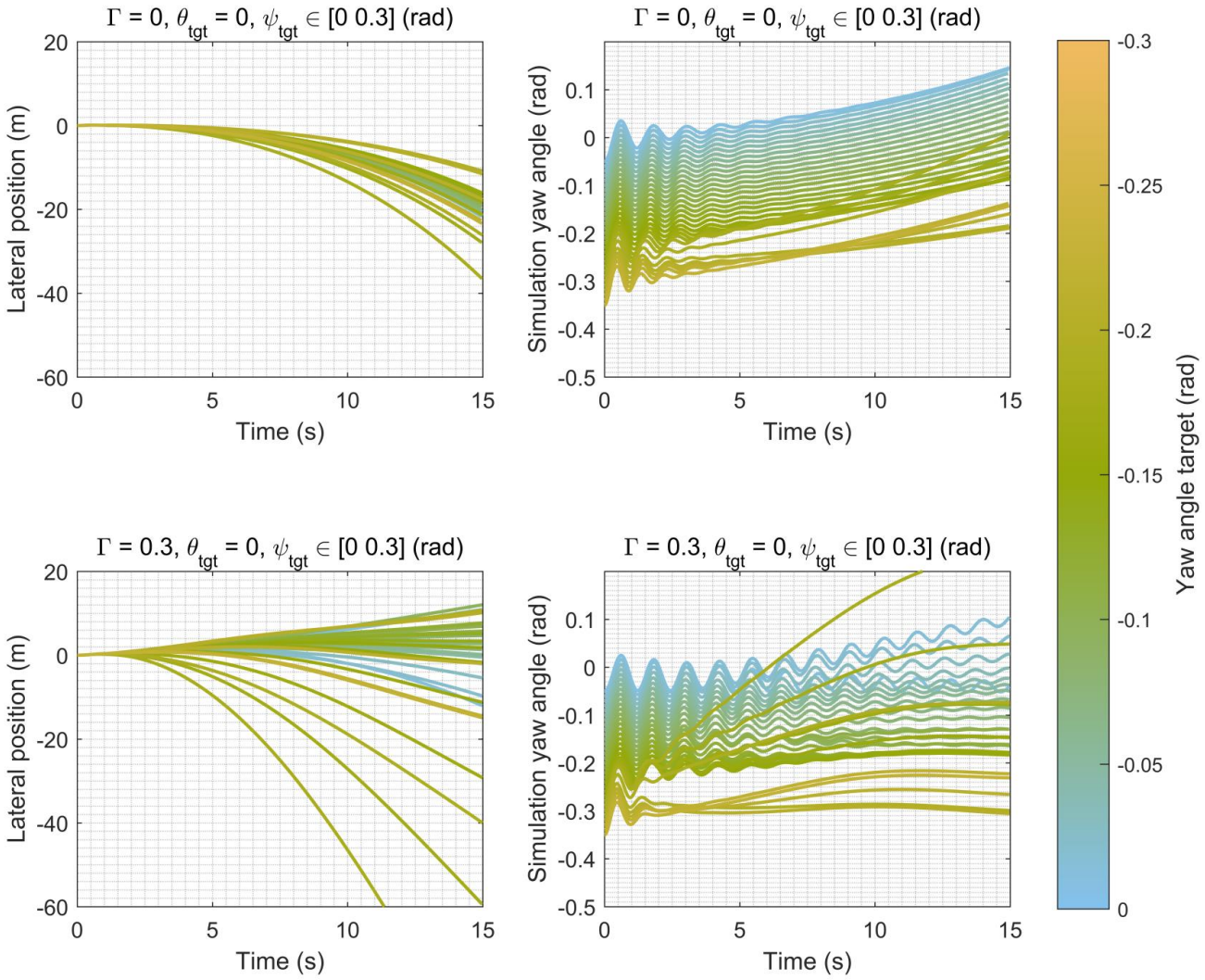

Figure 6.3.3:
Flight simulation results from the spiral mode stability analysis, for trim states at yaw angle target $\psi_{\mathrm{tgt}} \in [0, -0.3]$ rad, and pitch angle target $\boldsymbol{\theta_{\mathrm{tgt}} = 0}$ **rad**; for both $\Gamma = 0$ and $\Gamma = 0.3$ rad inboard wing constraints. The yaw perturbation is negative: $\Delta\psi = -0.05$.

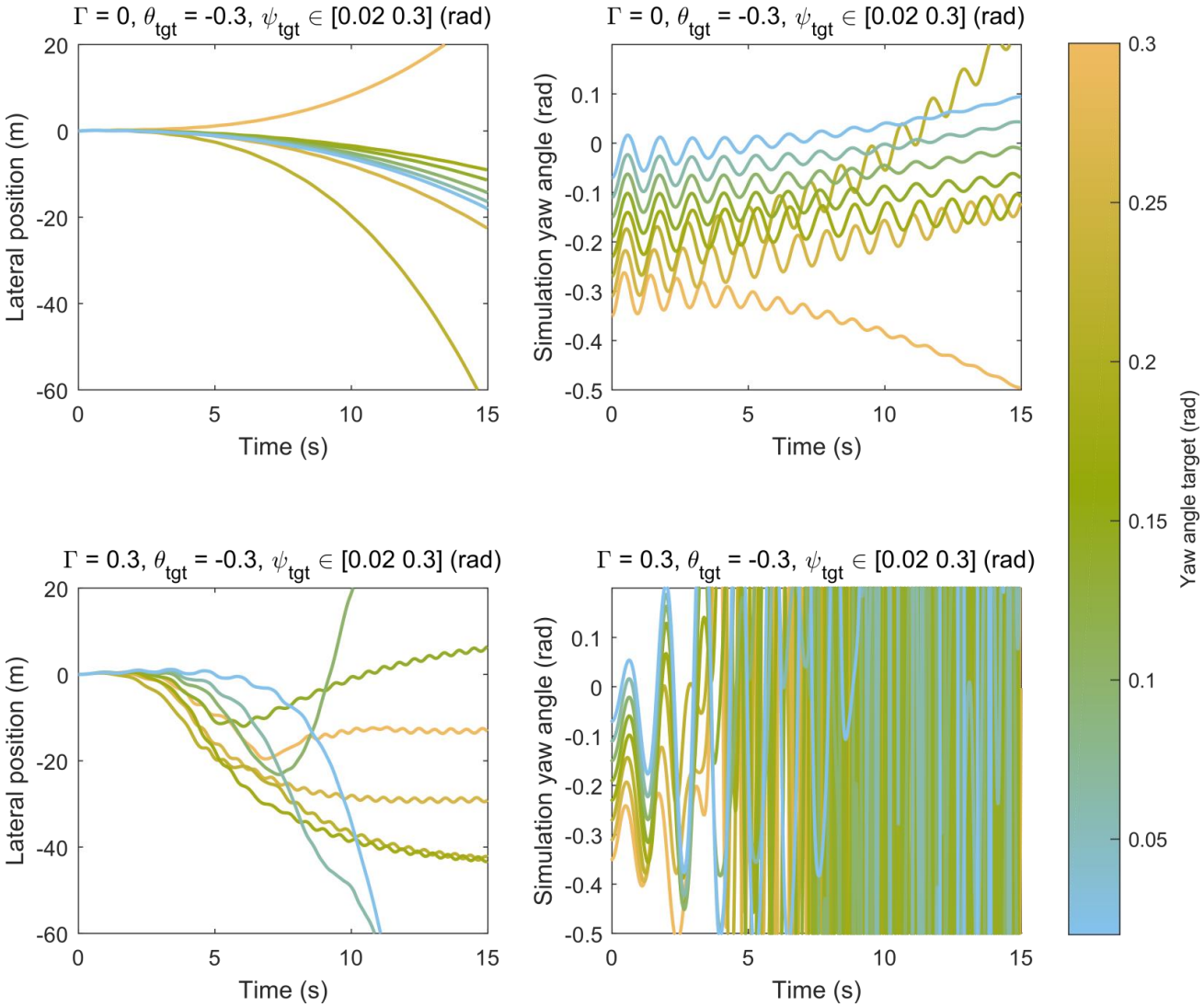

Figure 6.3.4:
Flight simulation results from the spiral mode stability analysis, for trim states at yaw angle target $\psi_{\mathrm{tgt}} \in [0.02, -0.3]$ rad, and pitch angle target $\boldsymbol{\theta_{\mathrm{tgt}} = -0.3}$ **rad**; for both $\Gamma = 0$ and $\Gamma = 0.3$ rad inboard wing constraints. The yaw perturbation is negative: $\Delta\psi = -0.05$.

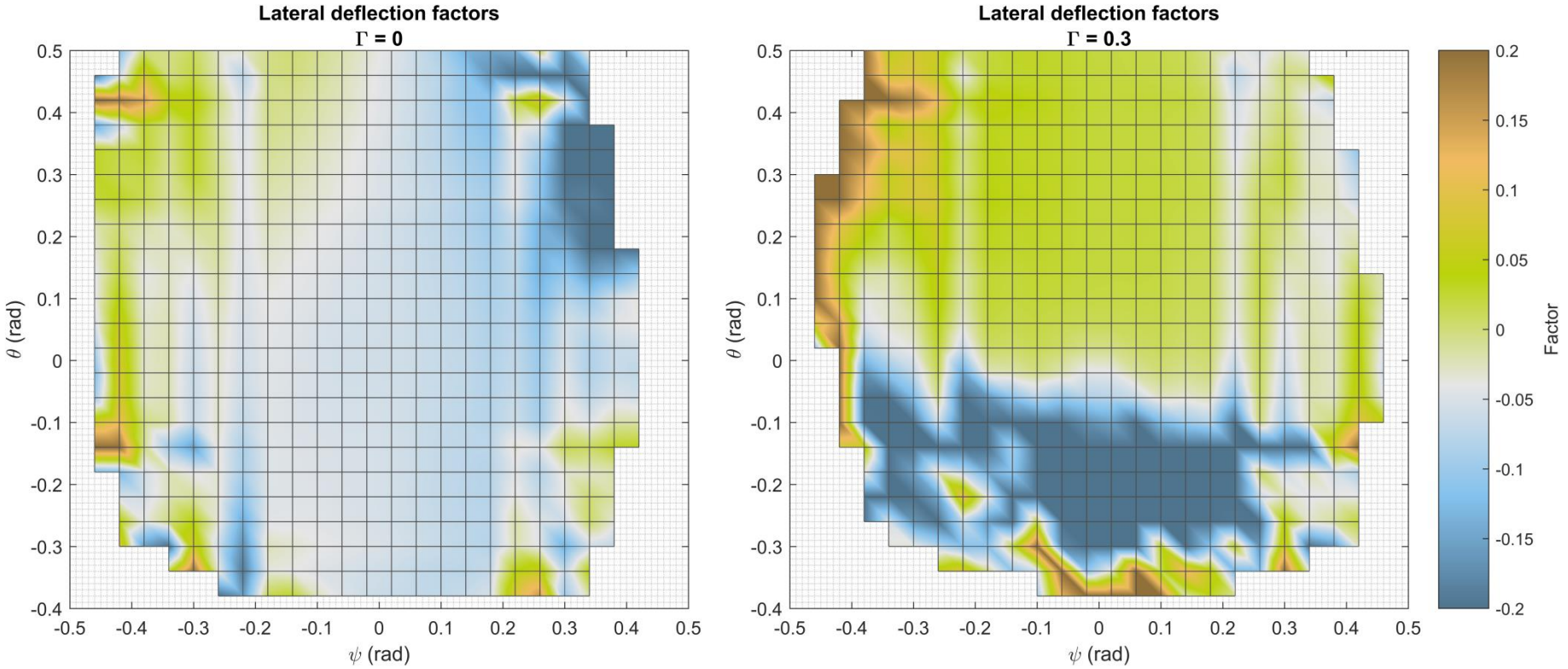

Figure 6.3.5: Lateral deflection factors over the entire $\Gamma = 0$ and $\Gamma = 0.3$ rad trim spaces.

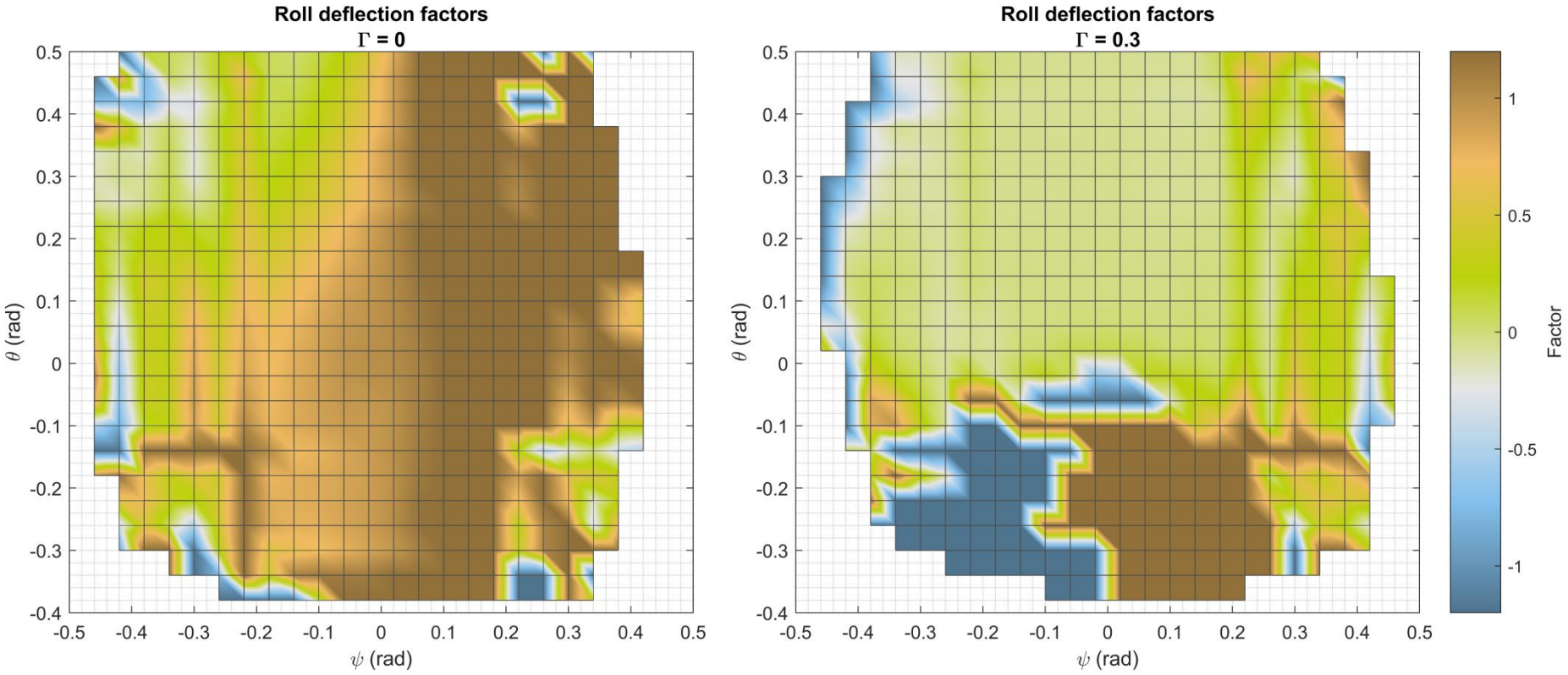

Figure 6.3.6: Roll deflection factors over the entire $\Gamma = 0$ and $\Gamma = 0.3$ rad trim spaces.

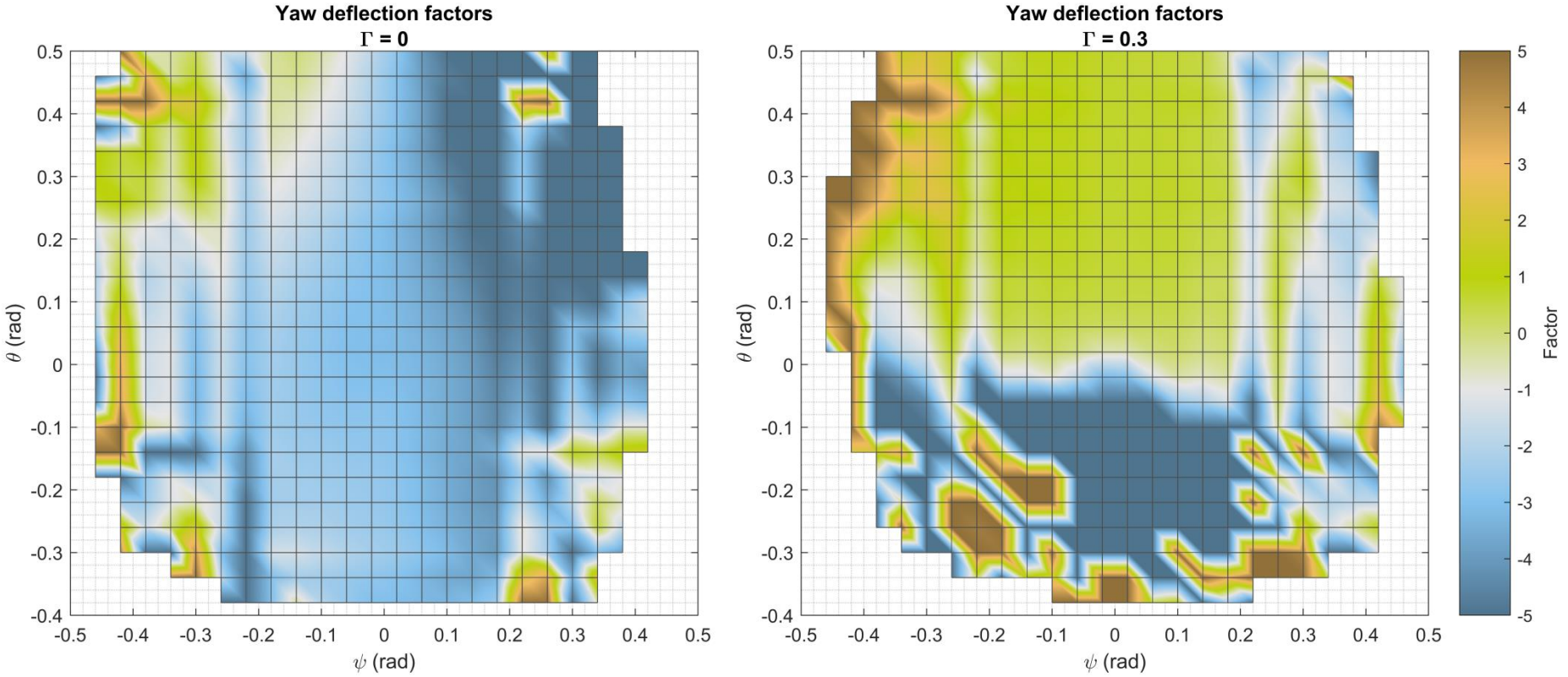

Figure 6.3.7: Yaw deflection factors over the entire $\Gamma = 0$ and $\Gamma = 0.3$ rad trim spaces.

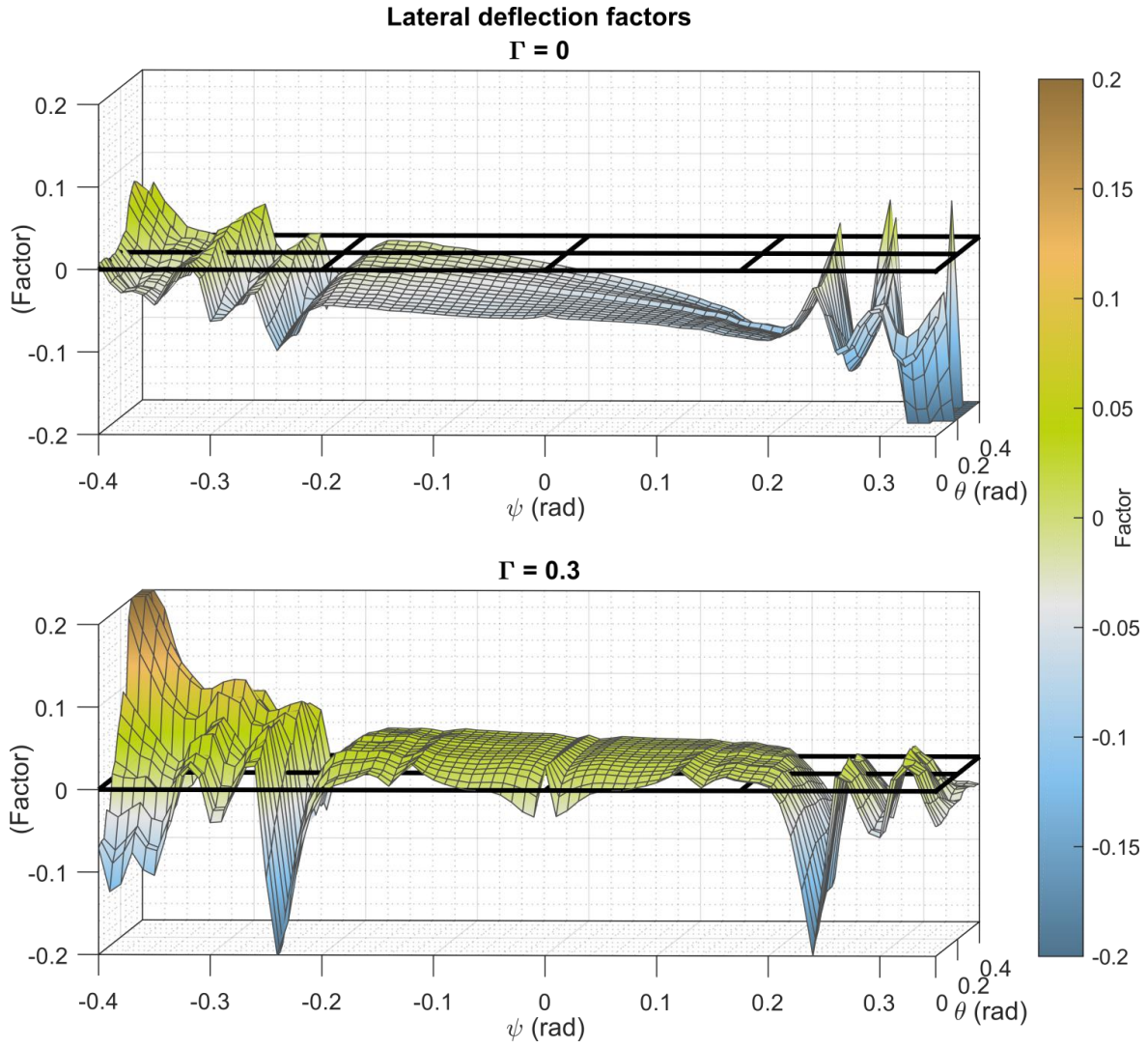

Figure 6.3.8: Lateral deflection factors over the trim space of the case study system, zero and positive dihedral states.

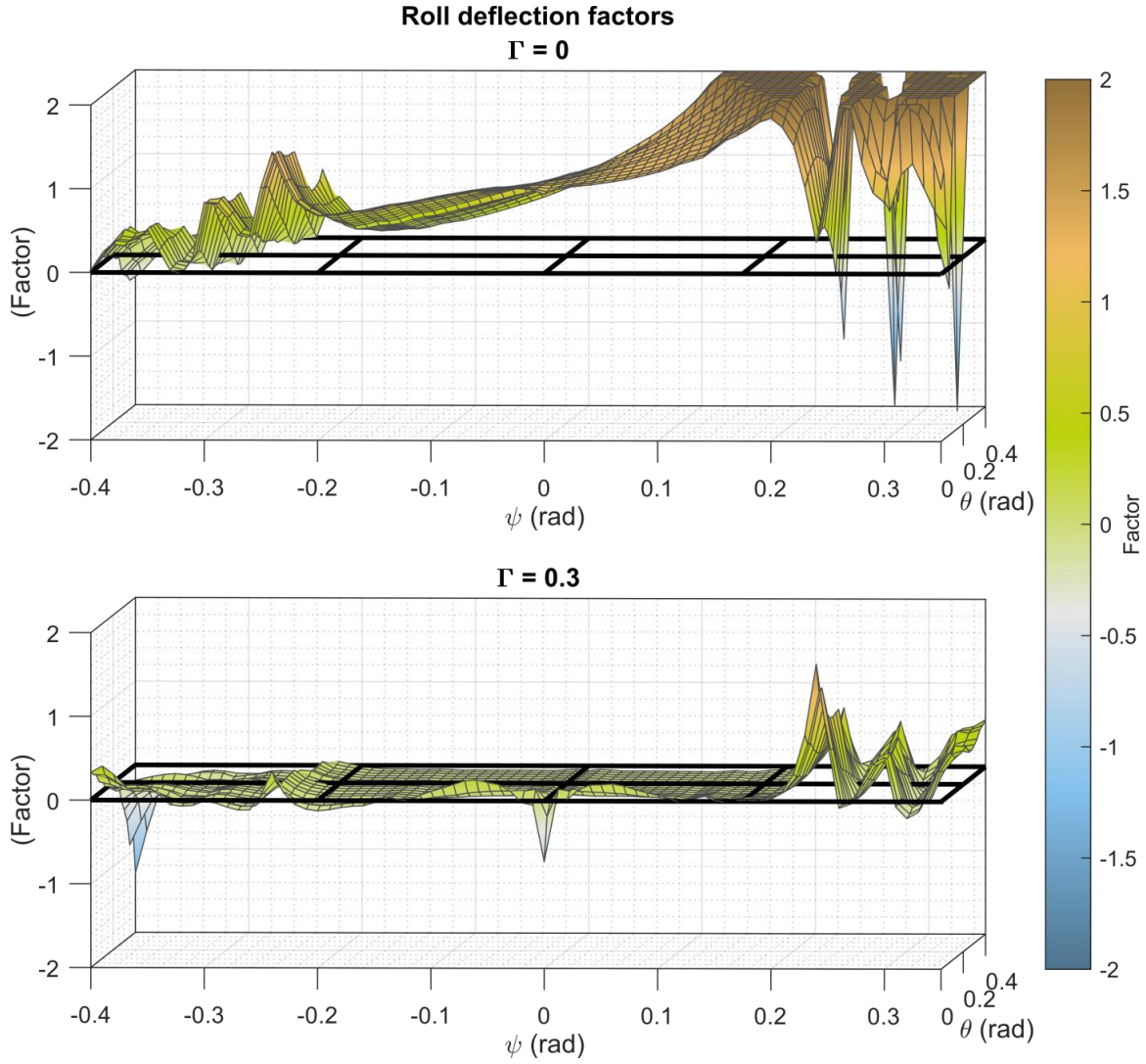

Figure 6.3.9:
Roll deflection factors over the trim space of the case study system, zero and positive dihedral states.

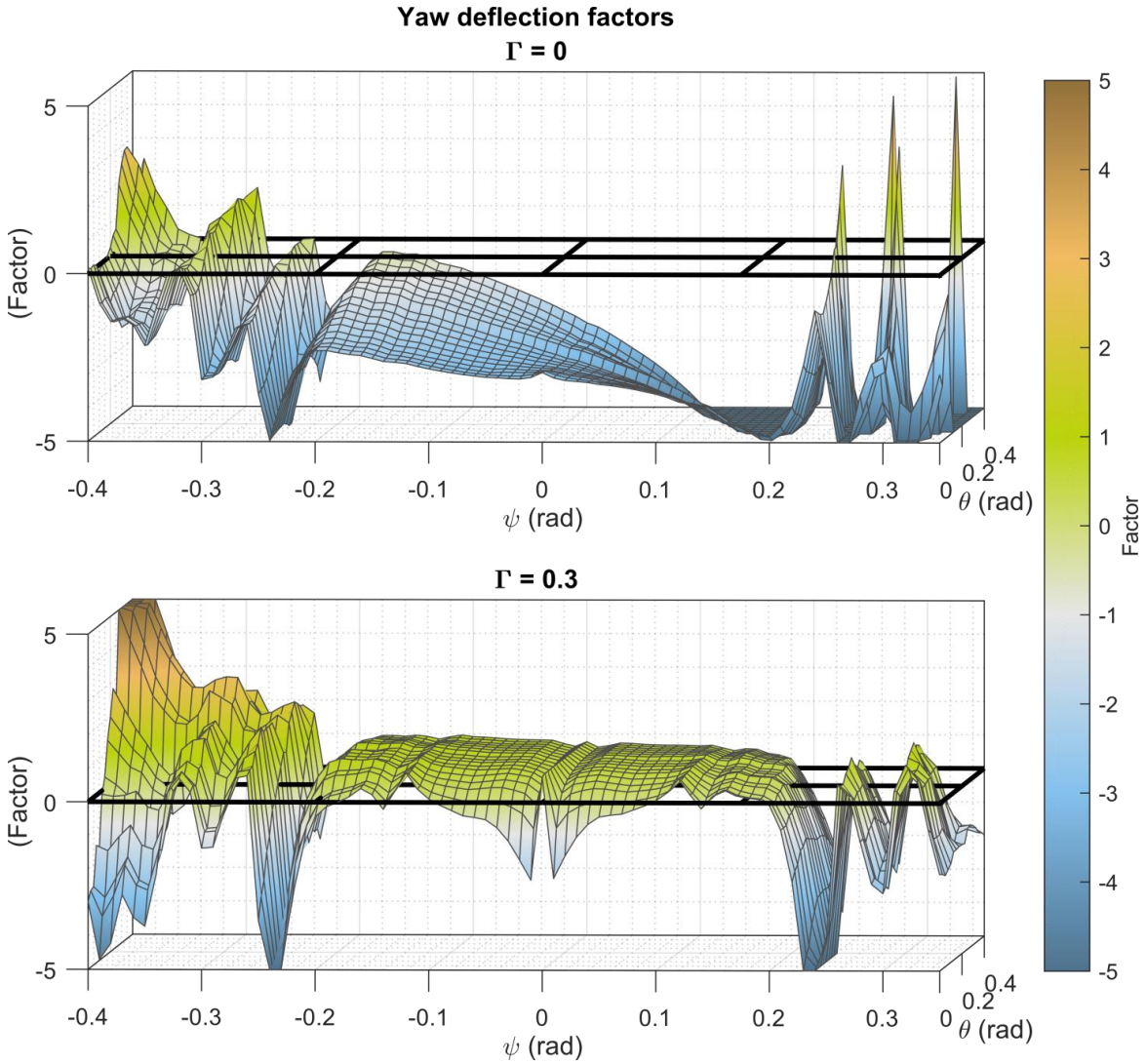

Figure 6.3.10: Yaw deflection factors over the trim space of the case study system, zero and positive dihedral states.

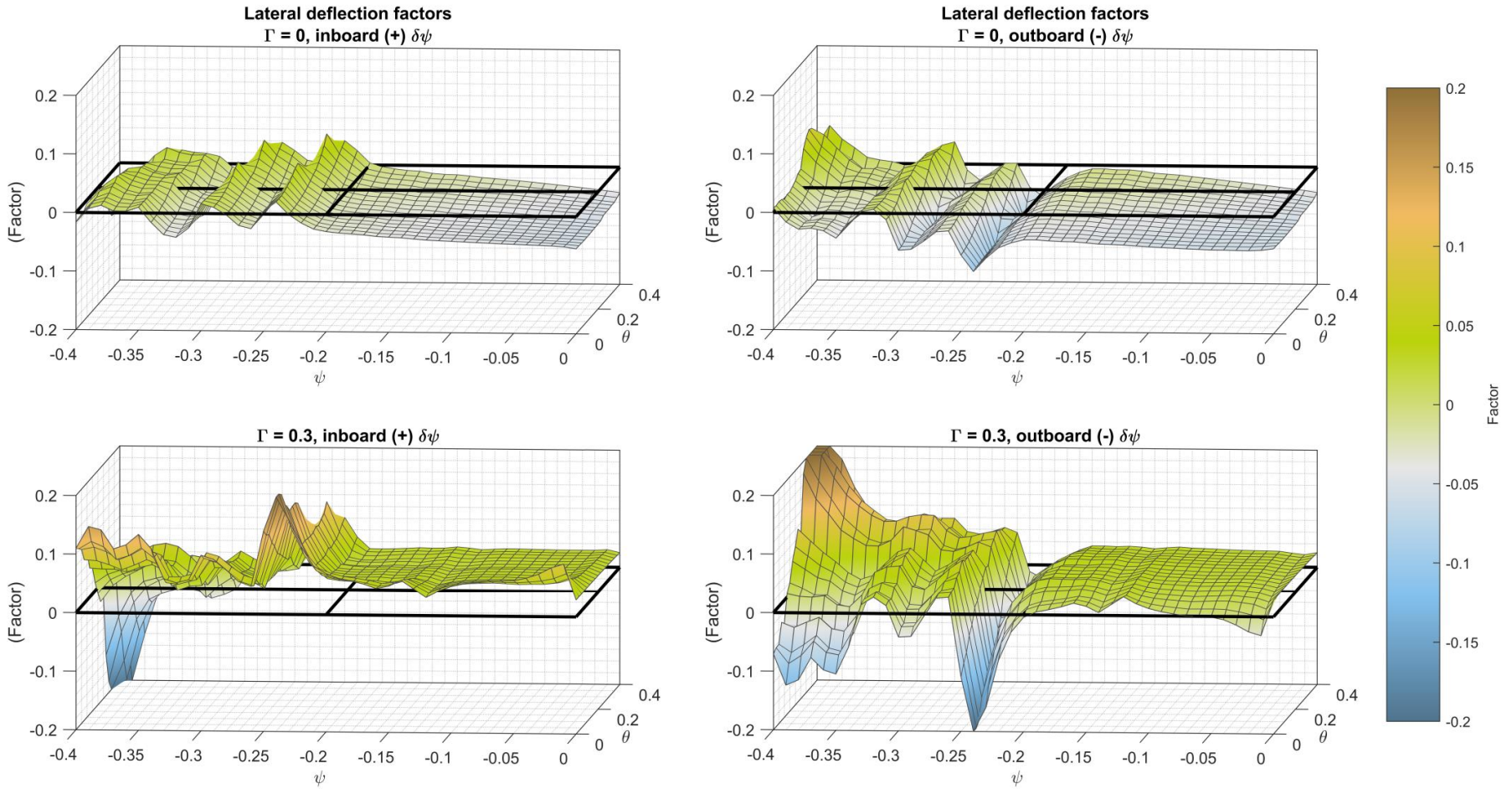

Figure 6.3.11: Symmetry breaking effects in the lateral deflection factors, between inboard- and outboard-directed perturbations to trim states under inboard-wing dihedral constraints (right wing, $\psi < 0$), for dihedral values $\Gamma = 0$ and $\Gamma = 0.3$ rad.

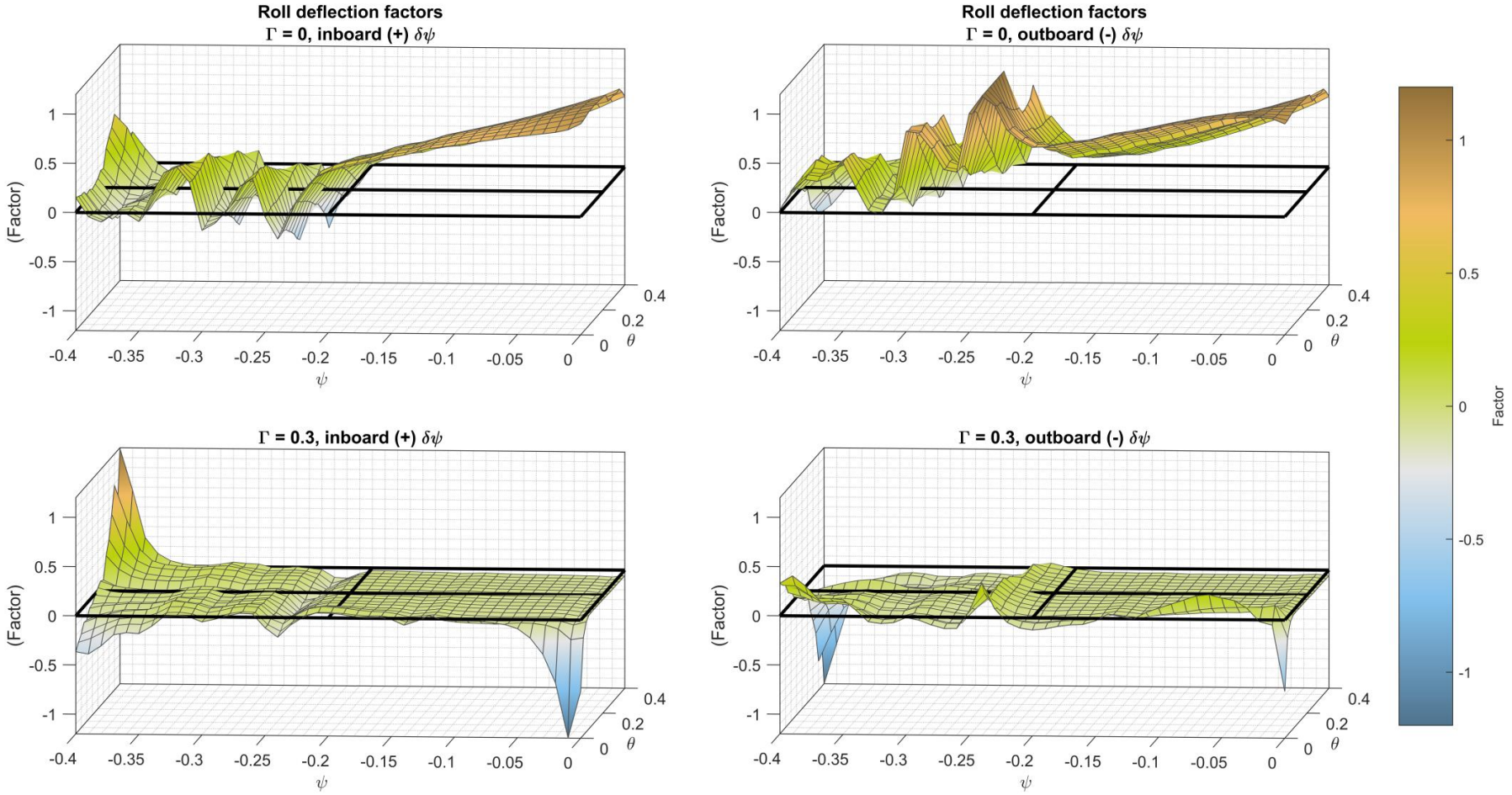

Figure 6.3.12: Symmetry breaking effects in the roll deflection factors, between inboard- and outboard-directed perturbations to trim states under inboard-wing dihedral constraints (right wing, $\psi < 0$), for dihedral values $\Gamma = 0$ and $\Gamma = 0.3$ rad.

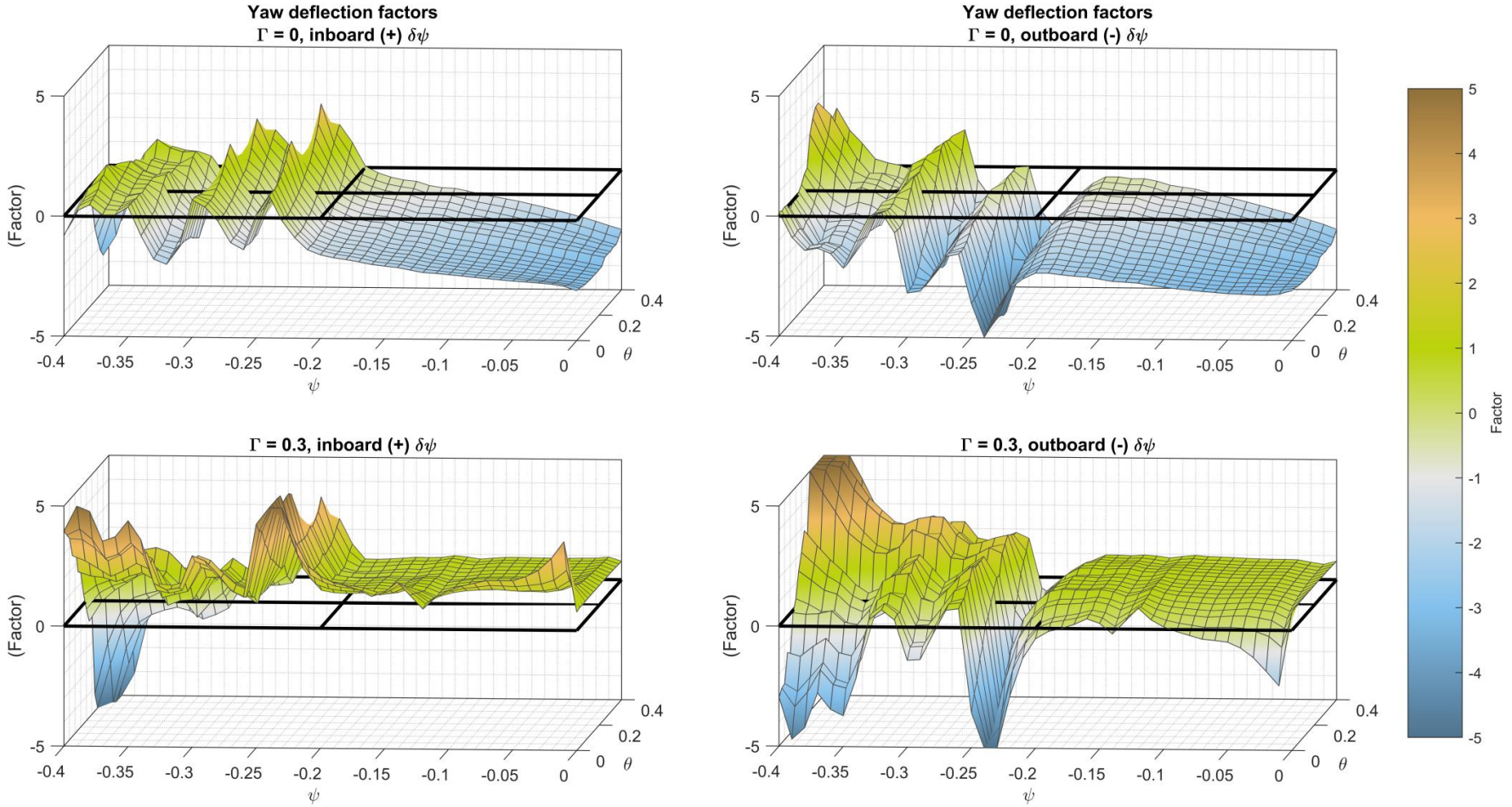

Figure 6.3.13: Symmetry breaking effects in the yaw deflection factors, between inboard- and outboard-directed perturbations to trim states under inboard-wing dihedral constraints (right wing, $\psi < 0$), for dihedral values $\Gamma = 0$ and $\Gamma = 0.3$ rad.

6.4. QUASISTATIC NPAS: DIRECT FORCE CAPABILITY

6.4.1. Introduction

The extended set of trim states in the case study biomimetic aircraft leads immediately to a basic form of supermanoeuvrability. Herbst [2,13] characterised this as direct force capability: the ability to change the orientation of the aircraft independent of the flight state. Moving the aircraft geometry through the space of trim states will lead to aircraft orientation changes that are largely independent of the flight state, providing the trim states are stable (statically, at least), and that the trim state changes are not more rapid than the aircraft can respond to. Herbst characterised this capability as a form of supermanoeuvrability, even though these manoeuvres need be neither post-stall nor strongly transient. This capability intersects the rapid-nose-pointing-and-shooting (RaNPAS) manoeuvres characterised by Gal-Or [1]. Trim state motion can be used to for RaNPAS capability in a limited window of orientation and angular velocity; but it also enables arbitrary forms of nose-pointing-and-shooting (NPAS) within this window, including longer-timescale point-and-hold manoeuvres. Biomimetic wing morphing is a well-suited mechanism for attaining and controlling this quasistatic NPAS capability, which additionally becomes achievable at low or zero thrust. No literature on this subject currently exists: hence the generalisations from non-morphing flight dynamics that have been made over Sections 6.2-6.3.

6.4.2. Response time tests

The response time of the aircraft to changes in trim state configuration is one factor which may cause additional flight path changes alongside intended NPAS orientation changes. In the manner of a first-order system, inducing a change in aircraft trim state during flight – itself a process that is not instantaneous – will yield a transient change in the aircraft orientation towards the target state, if this transition is stable. Again, in the manner of a first-order system, this degree of transience can be characterised with a time constant or response time.

To obtain a quantitative measure of this response time, NPAS capability tests are carried out for basic oscillatory pitch and yaw targets, and the effect of the oscillation period on the

accuracy of the flight simulations w.r.t. to their target is assessed. For oscillatory orientation target paths, a general scroll-shaped oscillatory target formulation is used:

$$\begin{aligned} r &= \begin{cases} 0.5(1-\cos(2\pi t/T)) & 0 \le t \le T/2 \\ 1 & t \ge T/2 \end{cases}, \\ \psi_{\mathrm{tgt}}(t) &= r\big(\psi_{\mathrm{amp}}\cos(2\pi t/T) + \psi_0\big), \\ \theta_{\mathrm{tgt}}(t) &= r\big(\theta_{\mathrm{amp}}\sin(2\pi t/T) + \theta_0\big), \end{aligned} \tag{6.4.1}$$

with parameters $T > 0$, the period of the oscillation; ψ_{amp} and θ_{amp}, the pitch and yaw amplitudes; and ψ_0 and θ_0, the pitch and yaw centre points. Figure 6.4.1 presents the target time histories for two sets of example parameters. For all parameter sets, the orientation targets are continuously differentiable ($\in C^1$) and start from an initial state $\psi_{\mathrm{tgt}} = \theta_{\mathrm{tgt}} = 0$ with zero initial time derivatives for all parameters. This represents a realistic start from a conventional trim state. Trim states are computed along these target paths by a natural parameter continuation method [5,14], in which the solution of the nonlinear trim equations is carried out along a discretisation of the paths, with the solution from the previous step providing the initial guess for the next step. The allows arbitrary target paths to be computed, even for unfamiliar systems.

To estimate the aircraft response times, flight simulations are carried out for isolated pitch and yaw oscillations, with a range of target T values. The simulations are carried out with the $\Gamma = 0.3$ rad inboard-wing constraint, for simulation duration $T_{\mathrm{sim}} = 4T$. To obtain true inboard / outboard constraints for all yaw angles (positive and negative), a constraint switching system is employed in which the inboard wing is constrained based on the aircraft yaw angle. That is, for the trim state variable Γ_{opt}, fed to the trim state optimisation, and dihedral constraint Γ, the left / right wing dihedral values for both constraint chiralities are:

Inboard constraint:

$$[\theta_{wl}, \theta_{wr}] = \begin{cases} [\Gamma_{\mathrm{opt}}, \Gamma] & \psi < 0 \\ [\Gamma, \Gamma] & \psi = 0 \\ [\Gamma, \Gamma_{\mathrm{opt}}] & \psi > 0, \end{cases} \tag{6.4.2}$$

Outboard constraint:

$$[\theta_{wl}, \theta_{wr}] = \begin{cases} [\Gamma, \Gamma_{\mathrm{opt}}] & \psi < 0 \\ [\Gamma, \Gamma] & \psi = 0 \\ [\Gamma_{\mathrm{opt}}, \Gamma] & \psi > 0. \end{cases}$$

Note that this formulation holds providing the target flight path for the trim state analysis is a straight line (axis $[1\ 0\ 0]^T$ with loss of generality). In an open-loop context the actual simulated flight path not relevant, as the trim state control histories are computed based only on the target histories. The use of the absolute yaw angle to govern the inboard / outboard switching is thus appropriate. In a closed loop context, the sideslip angle would be used to switch instead – a trivial modification. The only context in which the computation of the sideslip angle is relevant is in the postprocessing of the yaw response time tests.

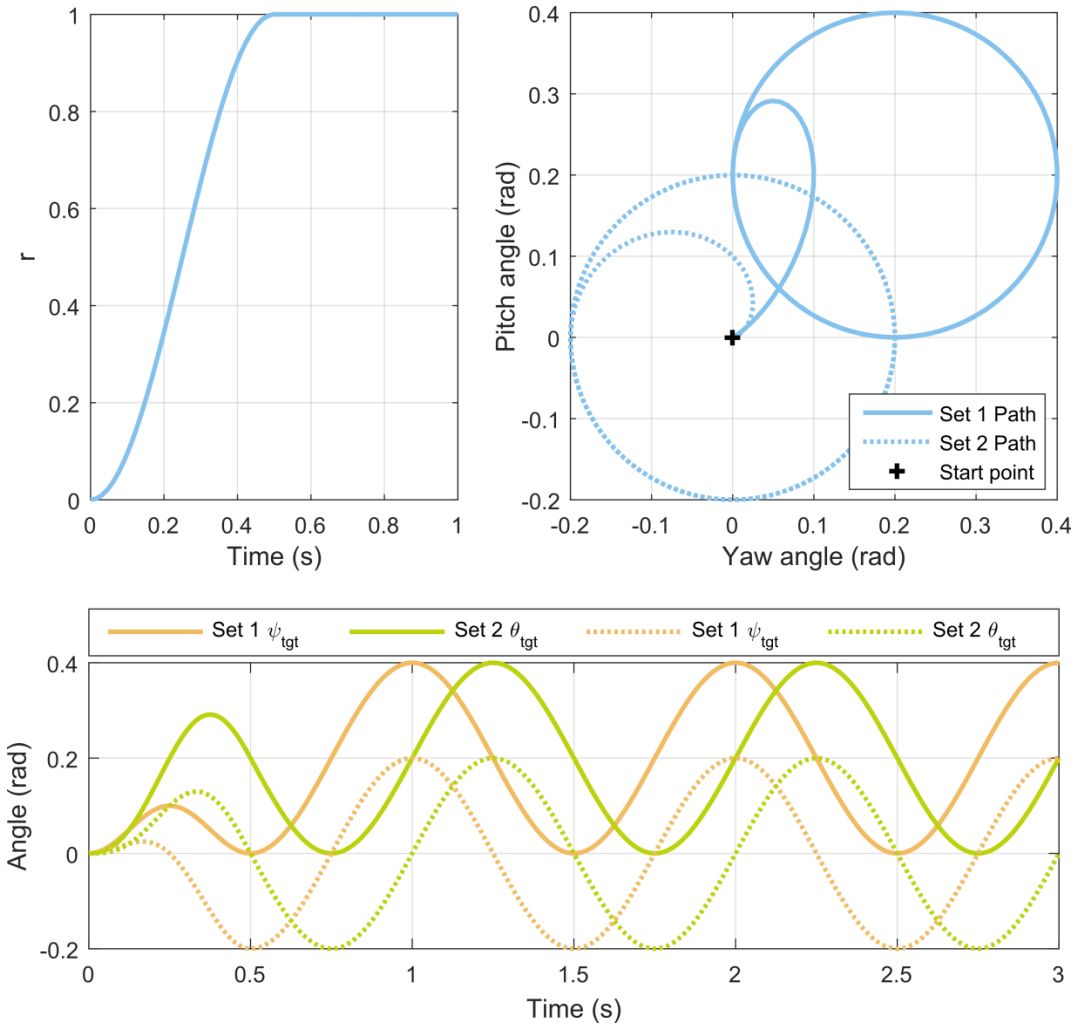

Figure 6.4.1: Example oscillatory orientation target paths, with $T = 1$ s, $\theta_{\text{amp}} = \psi_{\text{amp}} = 0.2$ rad; Set 1: $\theta_0 = \psi_0 = 0.2$ rad, Set 2: $\theta_0 = \psi_0 = 0$.

Figure 6.4.2 shows the results from a pitch response time test, with $\theta_{\text{amp}} = 0.25$ rad and $\theta_0 = 0.15$ rad, $\psi_{\text{amp}} = \psi_0 = 0$, $\Gamma = 0.3$ rad and $T \in [12.5\ 25\ 50\ 100]$ s. This oscillation approximately spans the space of Dutch roll stability in this system; providing a rough

approximation of the largest open-loop manoeuvres that will be studied here. As can be seen, oscillatory periods of $T \leq 25$ s yield a noticeable delay in the system pitch response. Without any initial yaw perturbation, there is no spiral mode excitation and the other orientations remain at negligible levels. Given that this target path represents the near-maximum θ_{amp} to maintain longitudinal static stability in the open loop system, $T = 50$ s serves as a conservative minimum bound of the oscillatory period required for a highly accurate pitch target match.

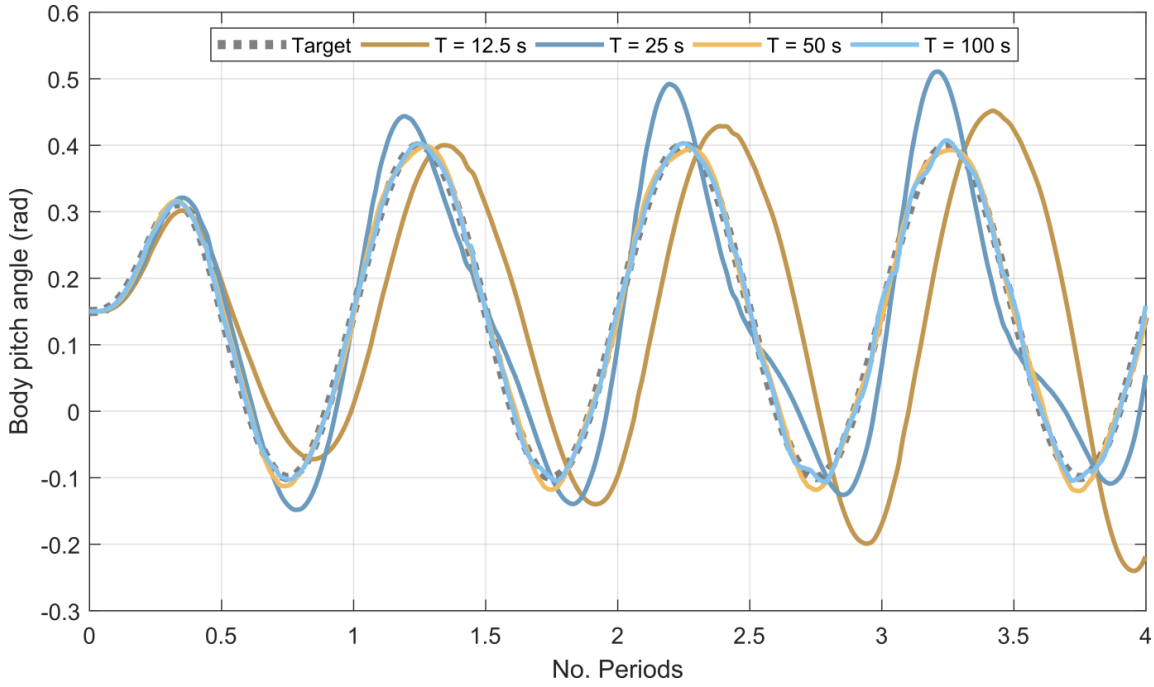

Figure 6.4.2: Pitch histories for the pitch response time tests, with symmetric wing dihedral $\Gamma = 0.3$ rad and pitch amplitude $\theta_{\text{amp}} = 0.4$ rad.

Figures 6.4.3-6.4.5 show the results from a yaw response time test, with $\psi_{\text{amp}} = 0.4$ rad, $\psi_0 = \theta_0 = \theta_{\text{amp}} = 0$ and $T \in [2.5\ 5\ 10\ 20]$ s; significantly larger amplitude and faster oscillations than tested in the pitch response tests. As these yaw tests excite the aircraft spiral mode, leading to a gradual shift in the aircraft yaw angle, an assumption of convenience used frequently in Sections 6.2-6.3 becomes invalid: namely, that the yaw and sideslip angles are identical. This arises because the flight velocity axis is no longer constantly $[1\ 0\ 0]^T$. The distinction between the sideslip angle (the aircraft orientation relative to its velocity vector, controlled by the trim state orientation targets) and the yaw angle (the absolute aircraft orientation) thus arises. This has only a minimal effect on the

effectiveness of NPAS control, except to require the measurement of the capability of the NPAS control in these relative angles – sideslip and relative pitch. The roll degree of freedom is unaffected by this distinction, being already entirely relative.

Figure 6.4.3 shows the yaw response time test results, in sideslip, relative pitch, and roll; and Figures 6.4.4-6.4.5 in flight path. These results are surprising: for both the inboard and outboard constraints, even the highest frequency oscillations ($T = 2.5$ s) show an excellent match in the steady state yaw response, despite large pitch and roll deflections – in roll, up to nearly 250% of the yaw amplitude. That the sideslip NPAS control remains accurate with such large deflections in extremely notable. The degree to which the pitch and roll deflections are acceptable depends on the application, but in general terms $T = 10$ s represents a point beyond which manoeuvre slowdown outweighs the diminishing returns of decreased deflection. However, in the case of a combined pitch and yaw target oscillation, this is likely to be a constraint that is secondary to the primary limitation of the pitch response time of c. 50 s. The only notable difference between the inboard and outboard constraints, in this simulation, is the significant improvement in spiral mode stability offered by the inboard constraint.

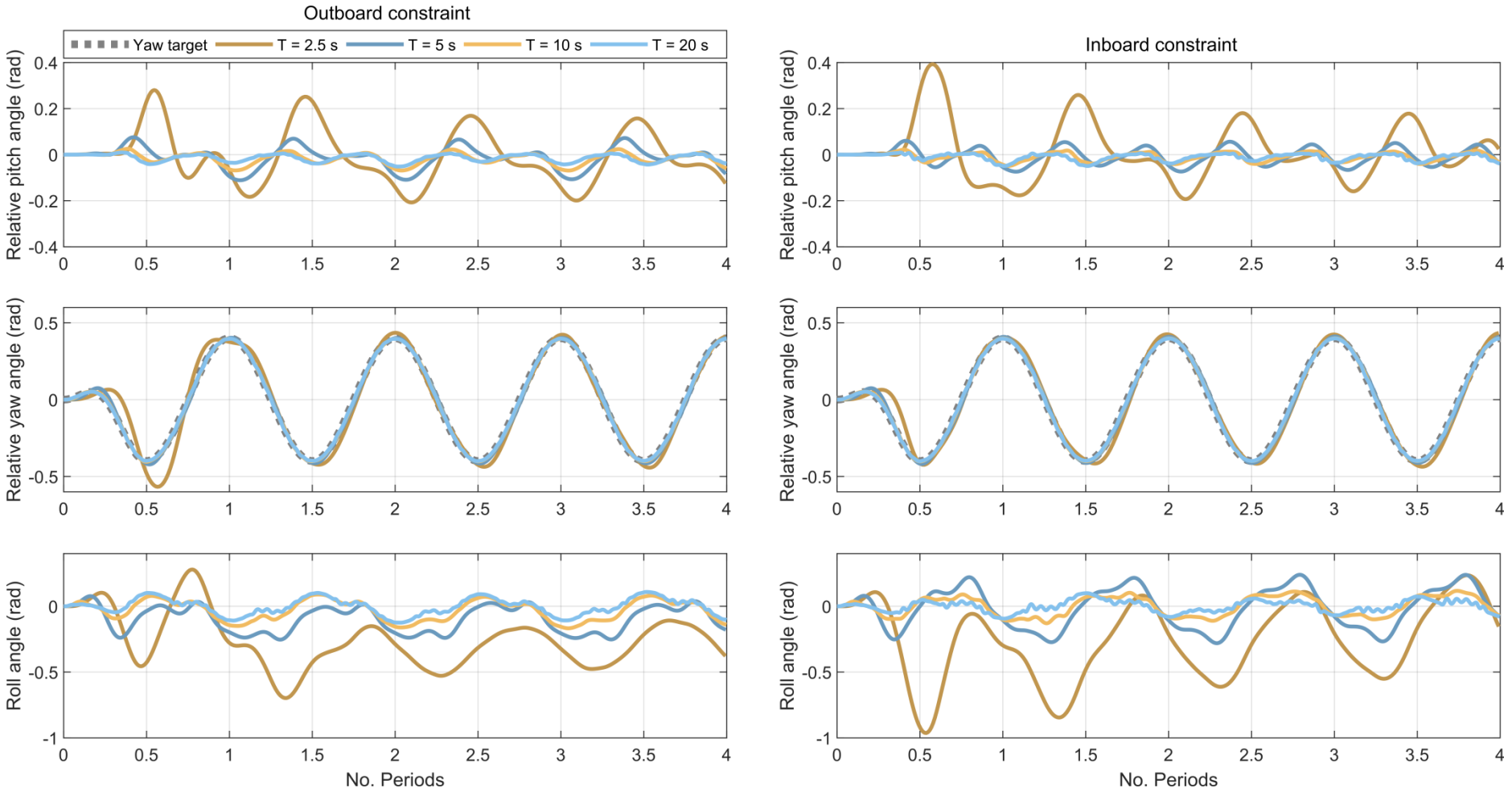

Figure 6.4.3: Orientation histories for the yaw response time tests with inboard/outboard dihedral constraint $\Gamma = 0.3$ rad and yaw amplitude $\psi_{\text{amp}} = 0.4$ rad.

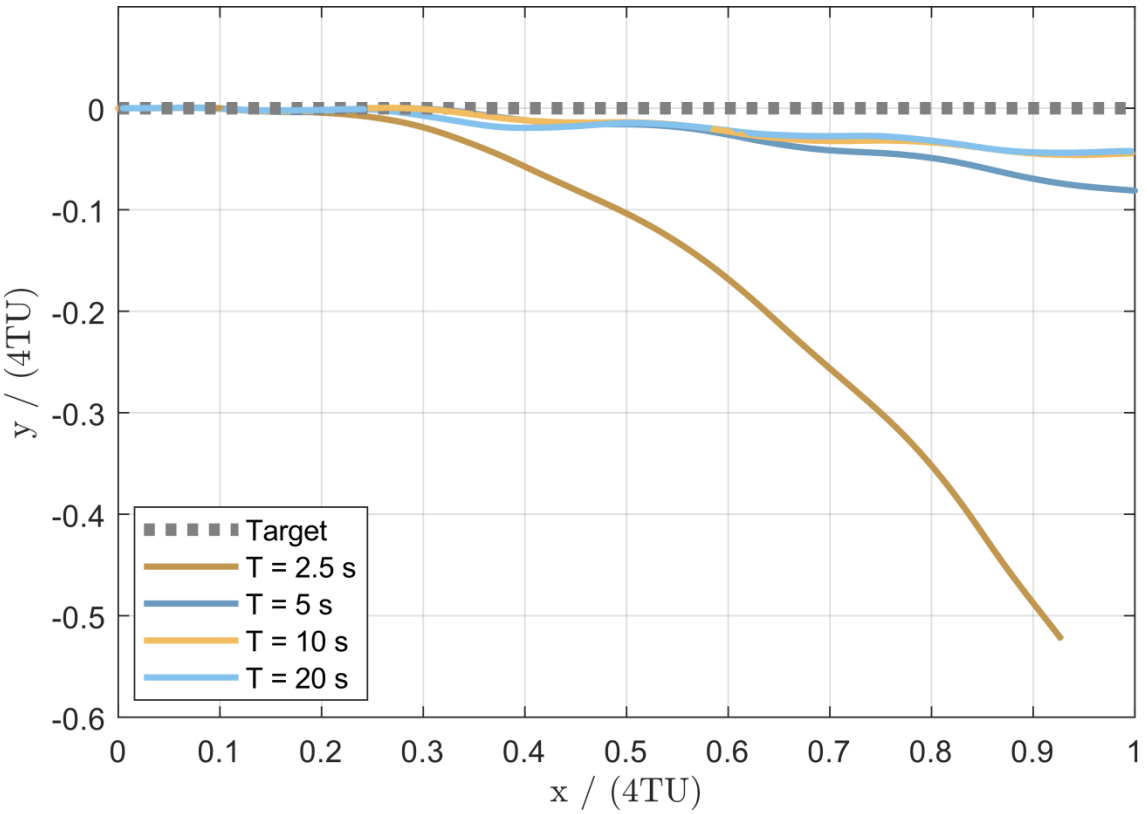

Figure 6.4.4: Flight paths, dimensionless and to scale, for the yaw response time tests with **inboard** dihedral constraint $\Gamma = 0.3$ rad and yaw amplitude $\psi_{\text{amp}} = 0.4$ rad.

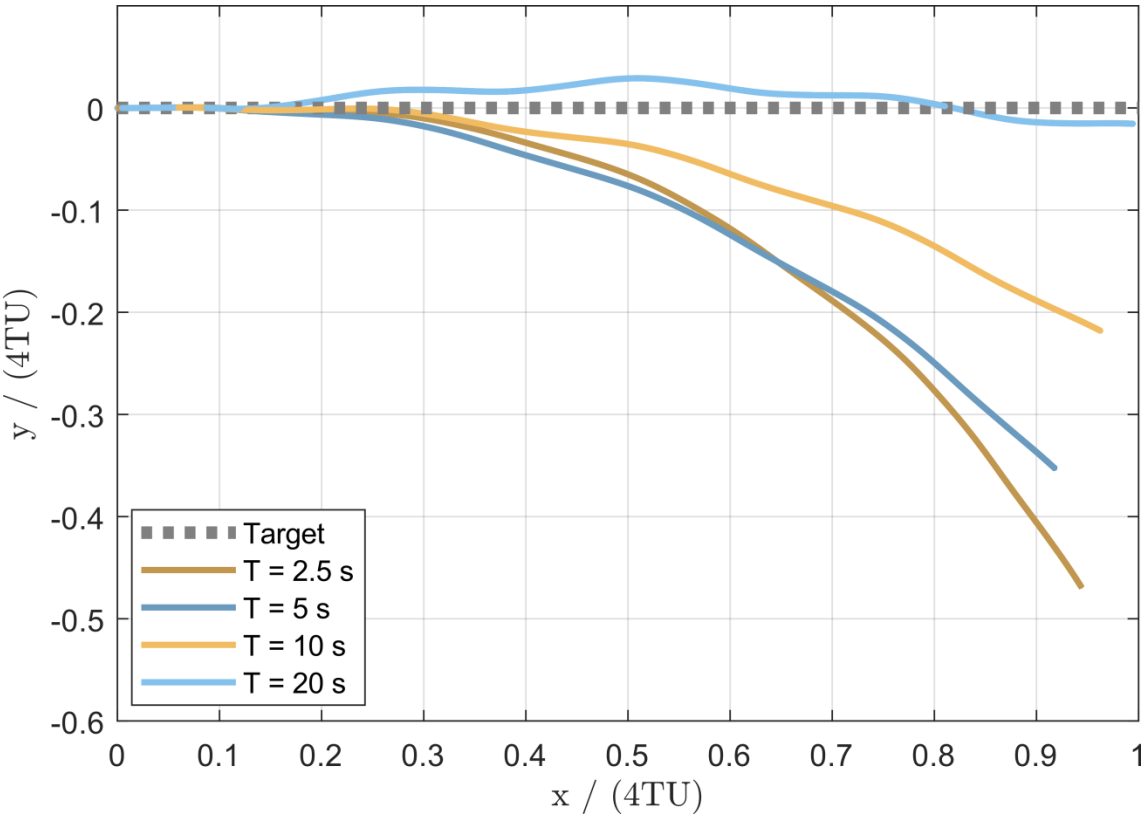

Figure 6.4.5: Flight paths, dimensionless and to scale, for the yaw response time tests with **outboard** dihedral constraint $\Gamma = 0.3$ rad and yaw amplitude $\psi_{\text{amp}} = 0.4$ rad.

6.4.3. Complex quasistatic NPAS capability

Having established the capability of the system for pitch and yaw quasistatic NPAS capability, we attempt more complex quasistatic NPAS manoeuvres – such as those involving concurrently varying pitch and yaw. The process of attaining these manoeuvres is identical to those of the test cases, with the same continuation solution process along the target paths generating the required control histories. As determined in Sections 6.3-6.4, the yaw quasistatic NPAS capability of the aircraft (in an open-loop context) is significantly less restricted in range and faster in response time than the pitch capability; and additionally shows a high degree of resilience to aberrancies in pitch and roll. The pitch capability is thus the determining factor in the performance of coupled quasistatic NPAS motions.

Simulating a small scroll-shaped target path demonstrates the capacity of this system for complex quasistatic NPAS capability. Taking $\psi_{\text{amp}} = 0.2$, $\theta_{\text{amp}} = 0.2$, $\theta_0 = 0.2$, and $\Gamma = 0.3$ rad with an inboard dihedral constraint, the trim state control paths are computed and flight simulations are performed for several oscillatory period values. Figure 6.4.6 shows the result of these simulations, compared with the target paths. An good agreement between the orientation targets and the actual angle-of-attack and sideslip may be observed, and the magnitude of the observed discrepancies is only slightly affected by the period of the target path oscillation. Some aspects of these discrepancies may be attributed to the spiral dynamics of the aircraft, which are coupled to the trim state motion / quasistatic NPAS dynamics – not least because the al trim state motion occurs relative to the local flight velocity. Spiral mode excitation, i.e. transient flight velocity changes, would be expected to induce transient effects in the trim states. Another key factor is the presence of gyroscopic torque effects engendered by the coupled pitch and yaw motion. These effects would be expected to generate further yaw and pitch deflections from the trim state target that cannot be passively stabilised (as can the spiral mode), as they are simple mass effects that are independent of the stability of any of the flight dynamic modes. They can only be eliminated through closed-loop control.

Figure 6.4.7 shows the control histories (for reference) and the flight path of these simulations. As can be seen, the spiral mode undergoes significant excitation, but this is

largely independent of the period – note the nondimensionalisation of the spatial axes. Given that in dimensional terms the flight time of the $T = 25$ s manoeuvre is a third of that of the $T = 75$ s manoeuvre, then if the spiral mode were under a constant (e.g. initial) perturbation then a third of the spiral mode deflection would be expected. As it is, the degree of spiral mode excitation increases inversely proportionately to the quasistatic NPAS control timescale – shorter timescales suffer from increased excitation. This is clearly a result of the roll deflections observed in Figure 6.4.6, engendered by spiral mode coupling and / or gyroscopic torque effects.

As an extension of this manoeuvre, a trim state locus of near-maximum open-loop size may be simulated: $\psi_{\text{amp}} = 0.4$, $\theta_{\text{amp}} = 0.2$, $\theta_0 = 0.2$ rad (and again inboard $\Gamma = 0.3$ rad). Figure 6.4.8 shows simulation results for this locus for several oscillatory period values, and Figure 6.4.9 the system fight path and control histories. An excellent agreement is observed, particularly at $T \geq 50$ s. Similar discrepancies are observed, but at different points on the trim state locus; and again the spiral mode coupling and gyroscopic torque effects are difficult to isolate but are both potentially present. The nondimensional equivalence of the spiral mode paths is even stronger in this simulation; probably indicating that mass-based effects (such as gyroscopic toques) are dominant.

The scroll-shaped trim state target paths shown in Figures 6.4.6-6.4.9 are continuously differentiable. Using nondifferentiable paths is likely to decrease the accuracy of the quasistatic NPAS control, due to the finite system response time. Figure 6.4.10-6.4.11 shows quasistatic NPAS control results for a rectangular trim state path, with leftwards, rightwards, upper and lower bounds l, r, u, b and initialisation path from $(\psi_{\text{tgt}}, \theta_{\text{tgt}}) = (0,0)$ to $(0,u)$. Figure 6.4.10 shows the trim state locus and time histories for this path, and the simulation results for several oscillatory periods, and 6.4.11 the flight path and control histories. As may be observed, the system performance for this nondifferentiable path is significantly worse than for the continuously differentiable scroll-shaped paths, with transient oscillations at the discontinuities; as expected from the continuous aircraft dynamics. Overall, however, the system response for the largest period ($T = 75$ s) is reasonably accurate.

Despite the Dutch roll instability below $\theta_{\mathrm{tgt}} = 0$ in the $\Gamma = 0.3$ rad system, and the low levels of stability in this zone for the $\Gamma = 0$ system, it is nevertheless possible to extend the case-study system open-loop quasistatic NPAS capability down into this zone. To do this a reversed approach is taken: instead of increasing the trim state oscillation period to give the aircraft dynamics longer to respond, the oscillation period is decreased, suppressing the Dutch roll response by passing the system rapidly through borderline stable states. Such circumstances require changes to the dihedral constraint: the inboard $\Gamma = 0.3$ rad constraints is strongly unstable at low pitch values and is unfeasible for open loop quasistatic NPAS control in this area. Two feasible alternatives an outboard $\Gamma = 0.3$ rad or an inboard $\Gamma = 0$ constraint. These both show sufficient Dutch roll stability at low pitch values to allow an open-loop trim locus to pass through this area, but at the cost of stronger spiral instability. Figures 6.4.12-6.4.14 show the simulation results for a scroll shape target path with $\psi_{\mathrm{amp}} = 0.4$, $\theta_{\mathrm{amp}} = 0.3$, $\theta_0 = 0$ rad, $T \in [5,10,15,25,35]$ s, under both these dihedral constraints.

A nonlinear trend in T is identified. Simulations at $T = 5$ s, much faster than the pitch response time of the aircraft, show an unexpectedly high degree of accuracy: it appears that more rapid response time of the yaw degree of freedom has an entraining effect on the slower pitch response. This oscillatory period is also sufficiently small that the spiral mode excitation causes only a limited deflection in the flight path. As the oscillatory period increases, however, and overall decrease in accuracy is observed, with a key exception at $T = 25$ s under the outboard $\Gamma = 0.3$ rad dihedral constraint, a state which shows notably low trim state error and spiral mode excitation. The details behind this are unclear, but resonance or synchronisation effects between the oscillatory effects present in the system are likely to be a factor. Overall, the outboard $\Gamma = 0.3$ rad dihedral constraint is preferable in both key metrics: spiral mode excitation and quasistatic NPAS capability accuracy. The simulations presented in this section give an idea of the range of open-loop quasistatic NPAS capability available through biomimetic wing control. They key morphing degrees of freedom are the wing dihedral and incidence, and the presence of these two allow full 3D orientation control. A variety of dihedral morphing configurations are available, with the optimal choice dependent on the quasistatic NPAS control that is desired. Both rapid and slow trim state motions are available through a wide space of available orientations.

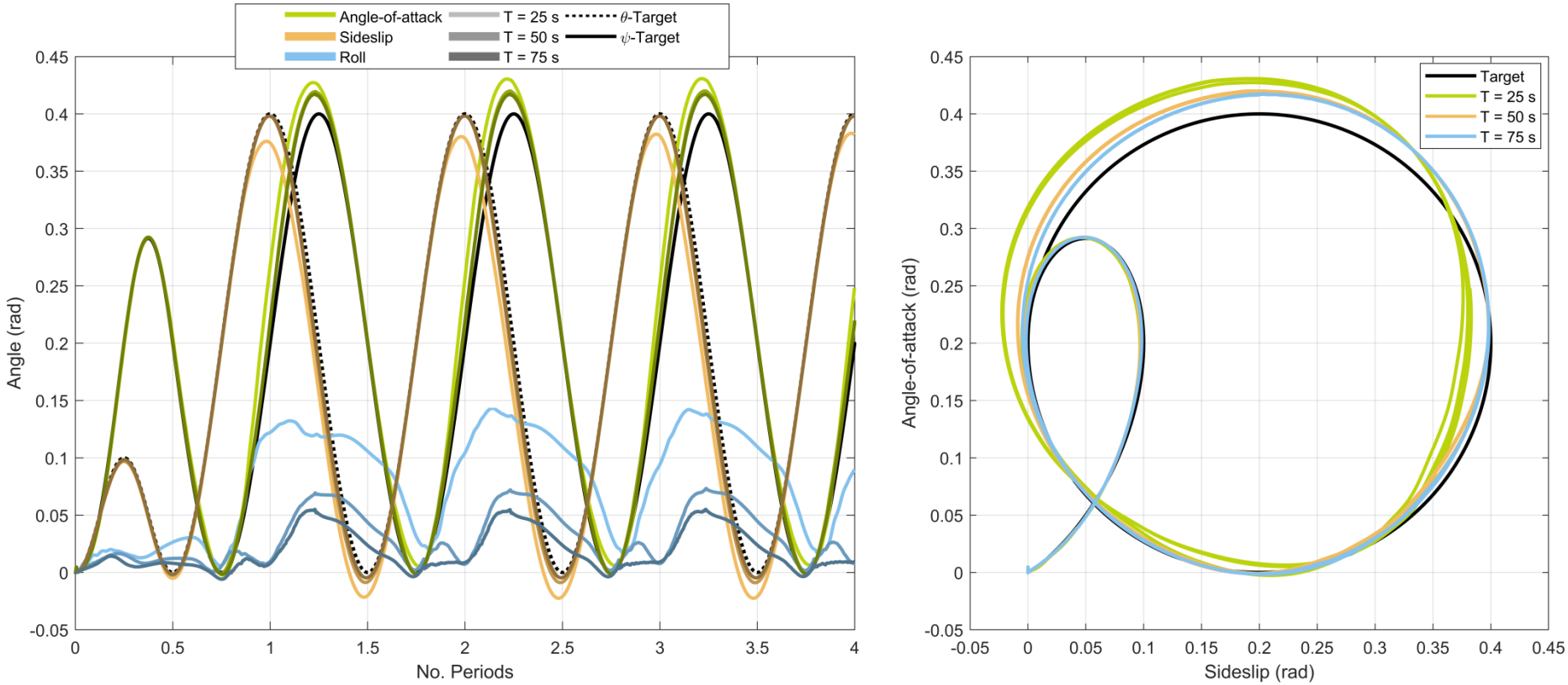

Figure 6.4.6: Flight simulation orientation histories of coupled pitch-yaw quasistatic NPAS capability, utilising an inboard dihedral constraint with $\Gamma = 0.3$ rad for trim state control. A range of oscillatory periods (T) are shown, for a scroll shaped trim state path in the upper right quadrant ($\psi_{\text{amp}} = 0.2$, $\psi_0 = 0$, $\theta_{\text{amp}} = 0.2$, $\theta_0 = 0$ rad).

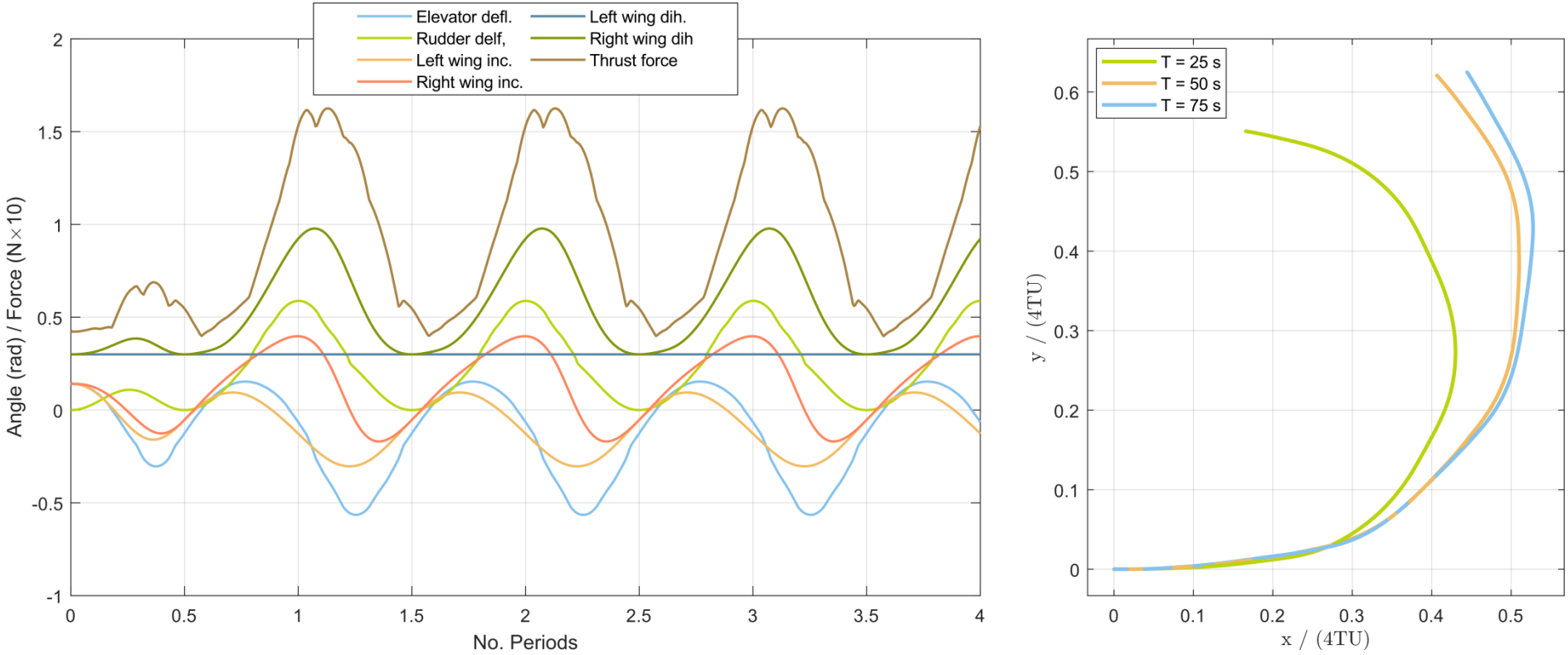

Figure 6.4.7: Flight simulation control histories and flight paths of coupled pitch-yaw quasistatic NPAS capability, utilising an inboard dihedral constraint with $\Gamma = 0.3$ rad for trim state control. A range of oscillatory periods (T) are shown, for a scroll shaped trim state path in the upper right quadrant ($\psi_{\text{amp}} = 0.2$, $\psi_0 = 0$, $\theta_{\text{amp}} = 0.2$, $\theta_0 = 0$ rad).

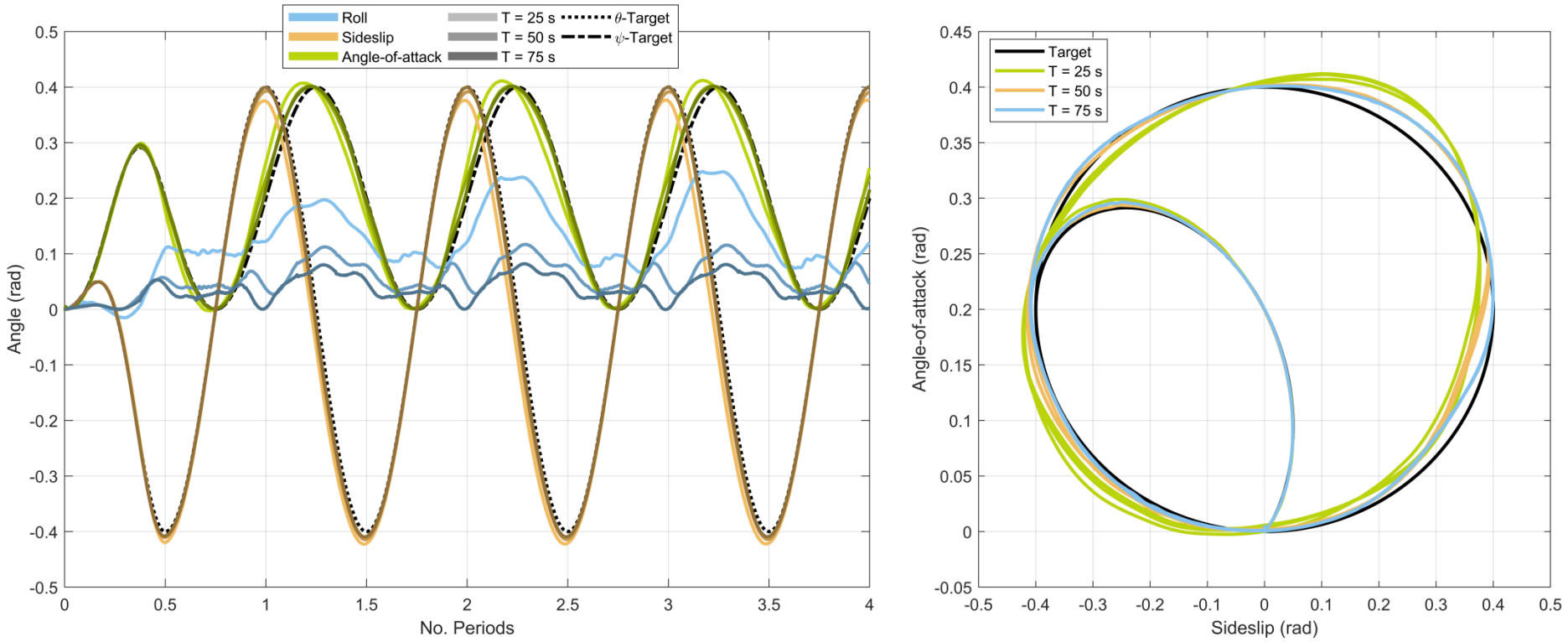

Figure 6.4.8: Flight simulation orientation histories of coupled pitch-yaw quasistatic NPAS capability, utilising an inboard dihedral constraint with $\Gamma = 0.3$ rad for trim state control. A range of oscillatory periods (T) are shown, for a scroll shaped trim state path of near-maximum stable amplitude ($\psi_{\text{amp}} = 0.4$, $\psi_0 = 0$, $\theta_{\text{amp}} = 0.2$, $\theta_0 = 0.2$ rad).

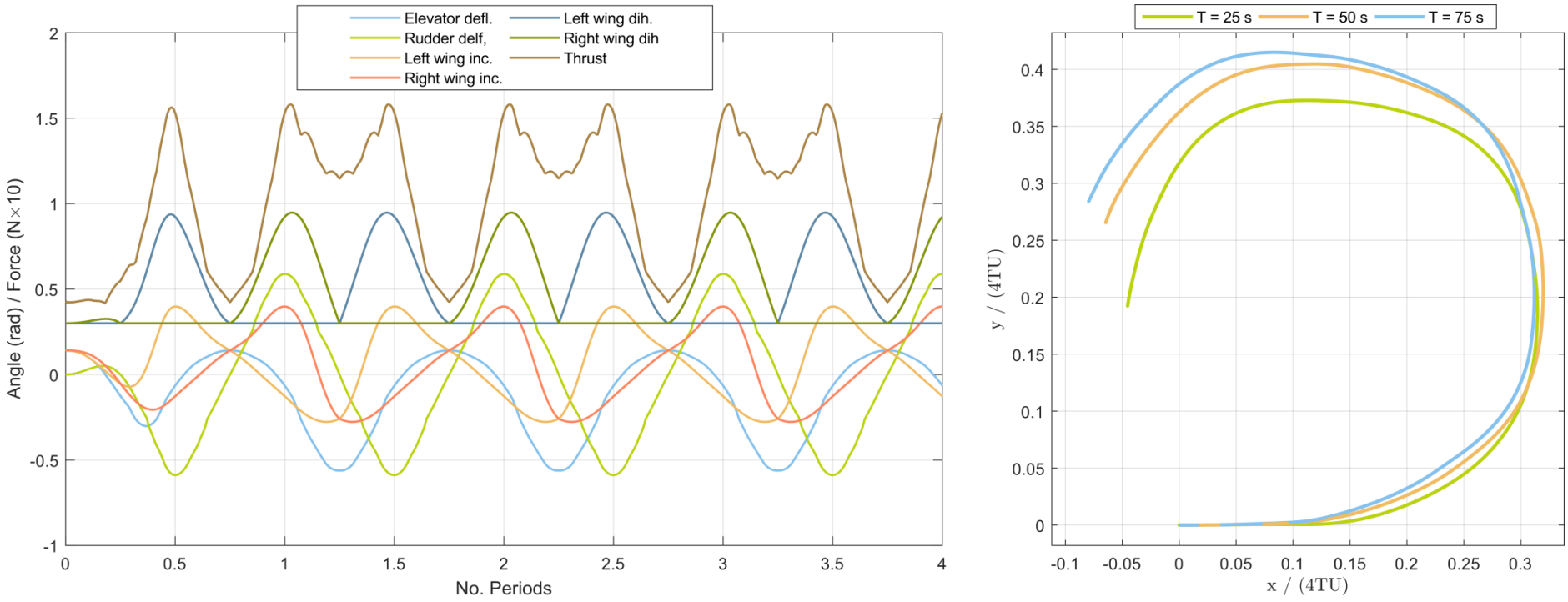

Figure 6.4.9: Flight simulation control histories and flight paths of coupled pitch-yaw quasistatic NPAS capability, utilising an inboard dihedral constraint with $\Gamma = 0.3$ rad for trim state control. A range of oscillatory periods (T) are shown, for a scroll shaped trim state path of near-maximum stable amplitude ($\psi_{\text{amp}} = 0.4$, $\psi_0 = 0$, $\theta_{\text{amp}} = 0.2$, $\theta_0 = 0.2$ rad).

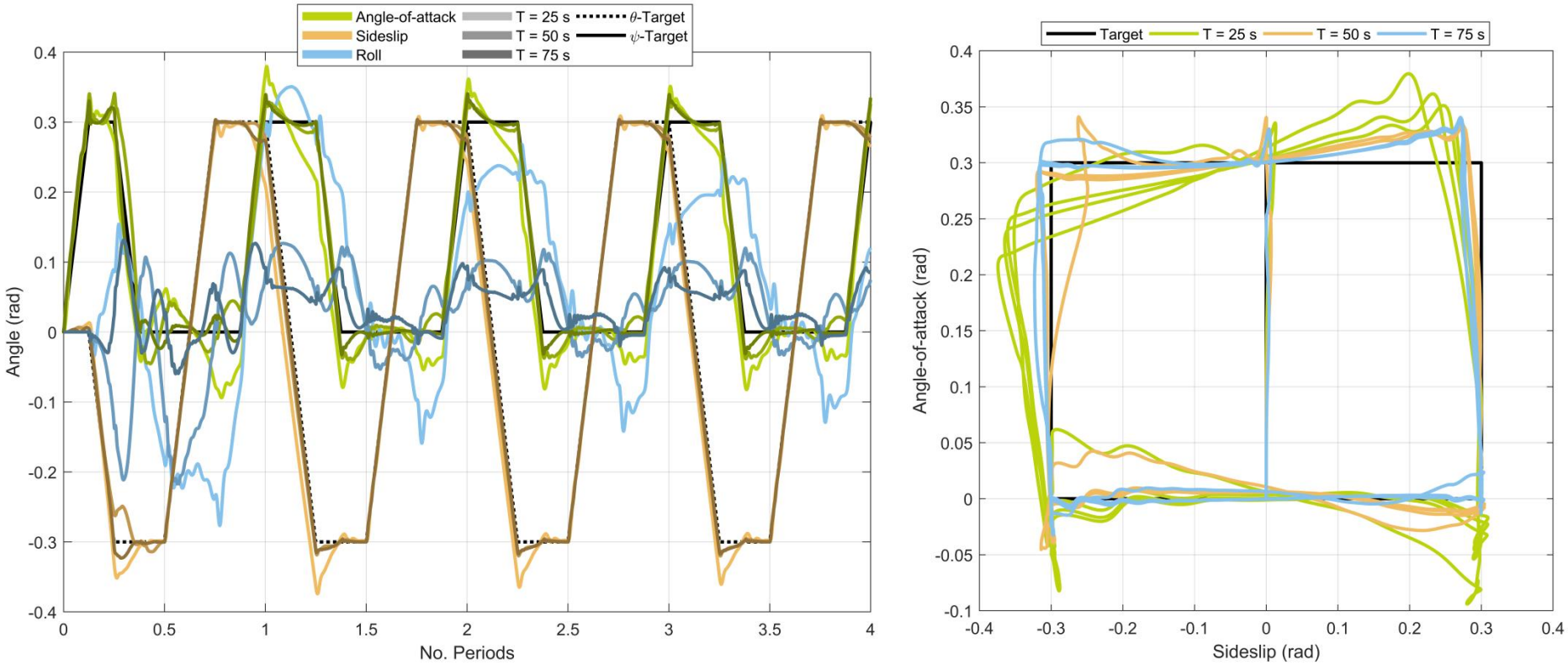

Figure 6.4.10: Flight simulation orientation histories of coupled pitch-yaw quasistatic NPAS capability, utilising an inboard dihedral constraint with $\Gamma = 0.3$ rad for trim state control. A range of oscillatory periods (T) are shown, for a rectangular trim state path of near-maximum stable amplitude ($b = 0, u = 0.4, l = -0.3, r = 0.3$ rad).

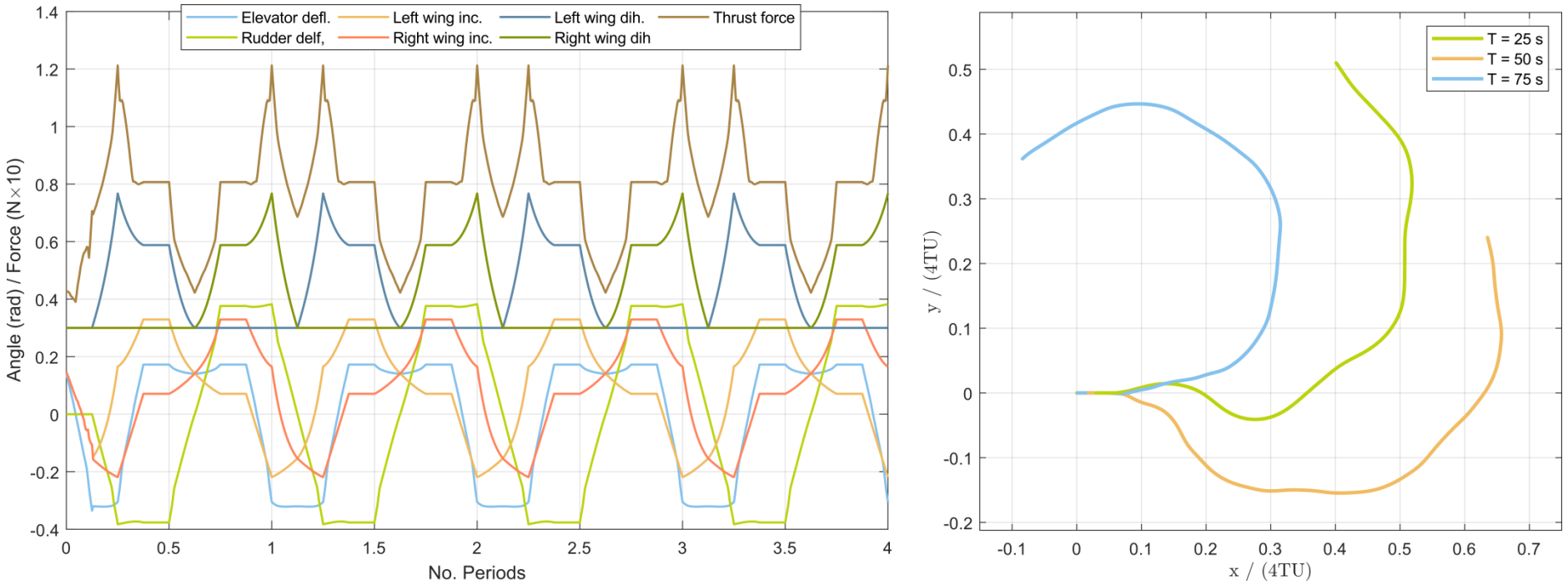

Figure 6.4.11: Flight simulation control histories and flight paths of coupled pitch-yaw quasistatic NPAS capability, utilising an inboard dihedral constraint with $\Gamma = 0.3$ rad for trim state control. A range of oscillatory periods (T) are shown, for a rectangular trim state path of near-maximum stable amplitude ($b = 0$, $u = 0.4$, $l = -0.3$, $r = 0.3$ rad).

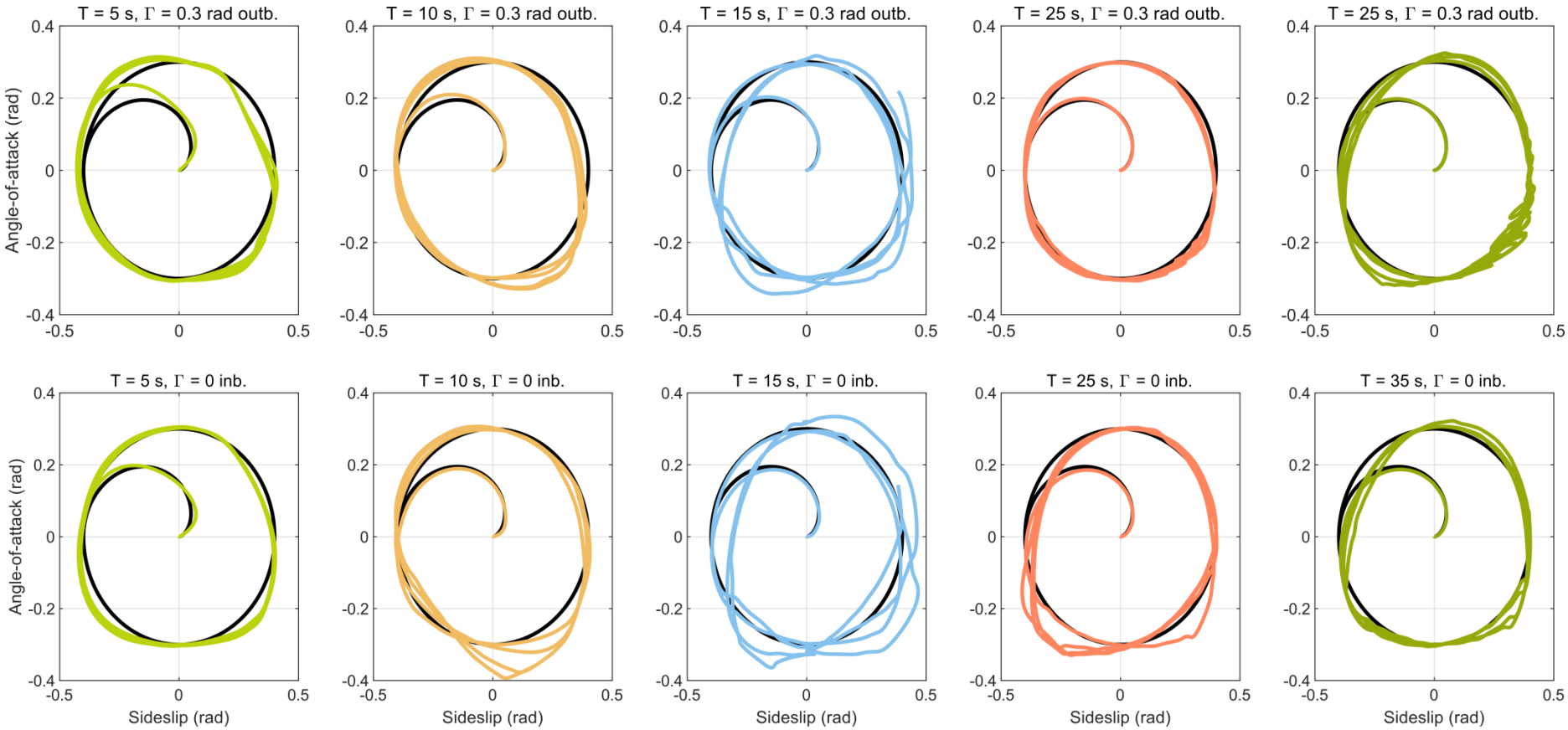

Figure 6.4.12: Flight simulation orientation loci for high-amplitude coupled pitch-yaw quasistatic NPAS capability. A range of oscillatory periods (T) are shown, for outboard $\Gamma = 0.3$ rad and inboard $\Gamma = 0$ dihedral constraints.

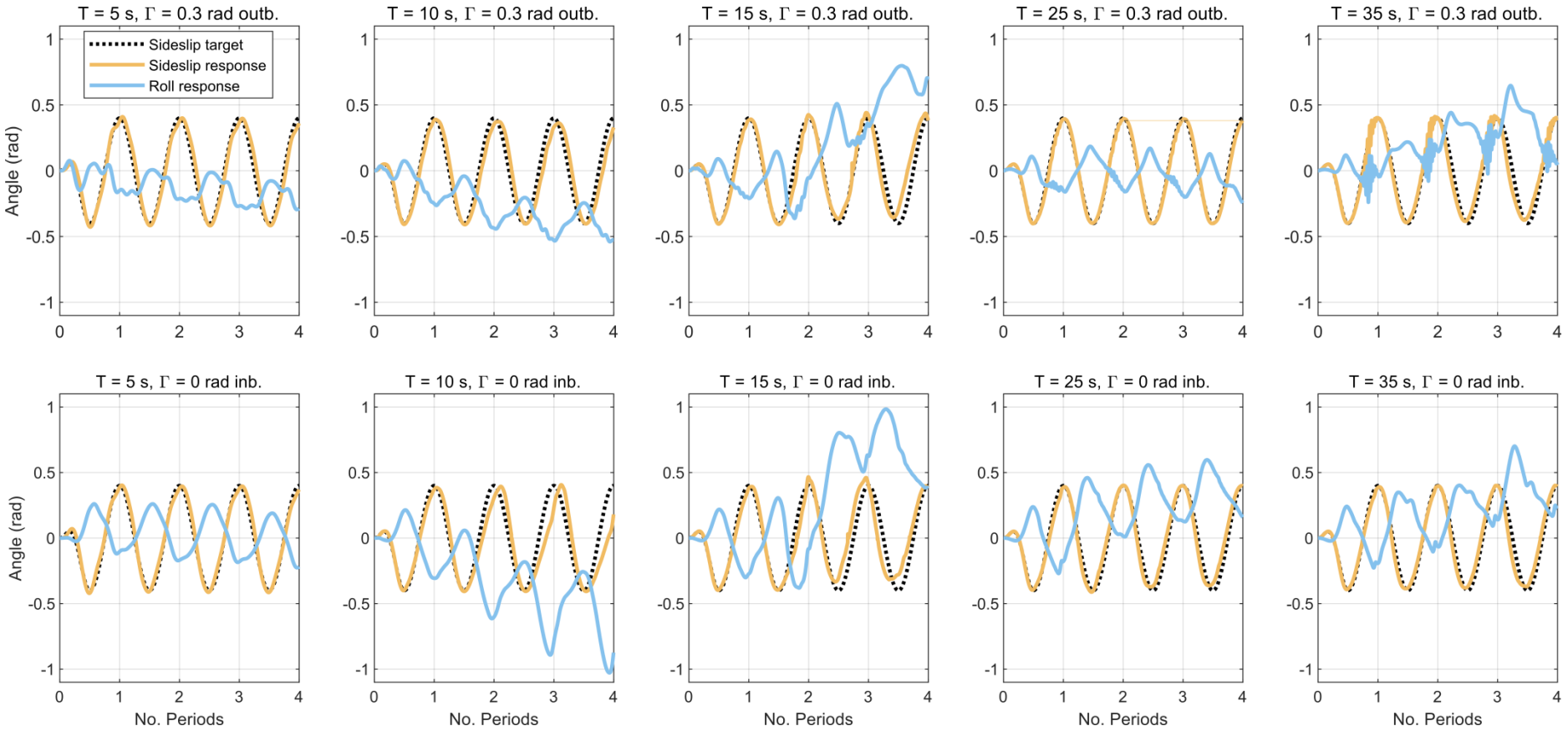

Figure 6.4.13: Flight simulation orientation histories for high-amplitude coupled pitch-yaw quasistatic NPAS capability. A range of oscillatory periods (T) are shown, for outboard $\Gamma = 0.3$ rad and inboard $\Gamma = 0$ dihedral constraints.

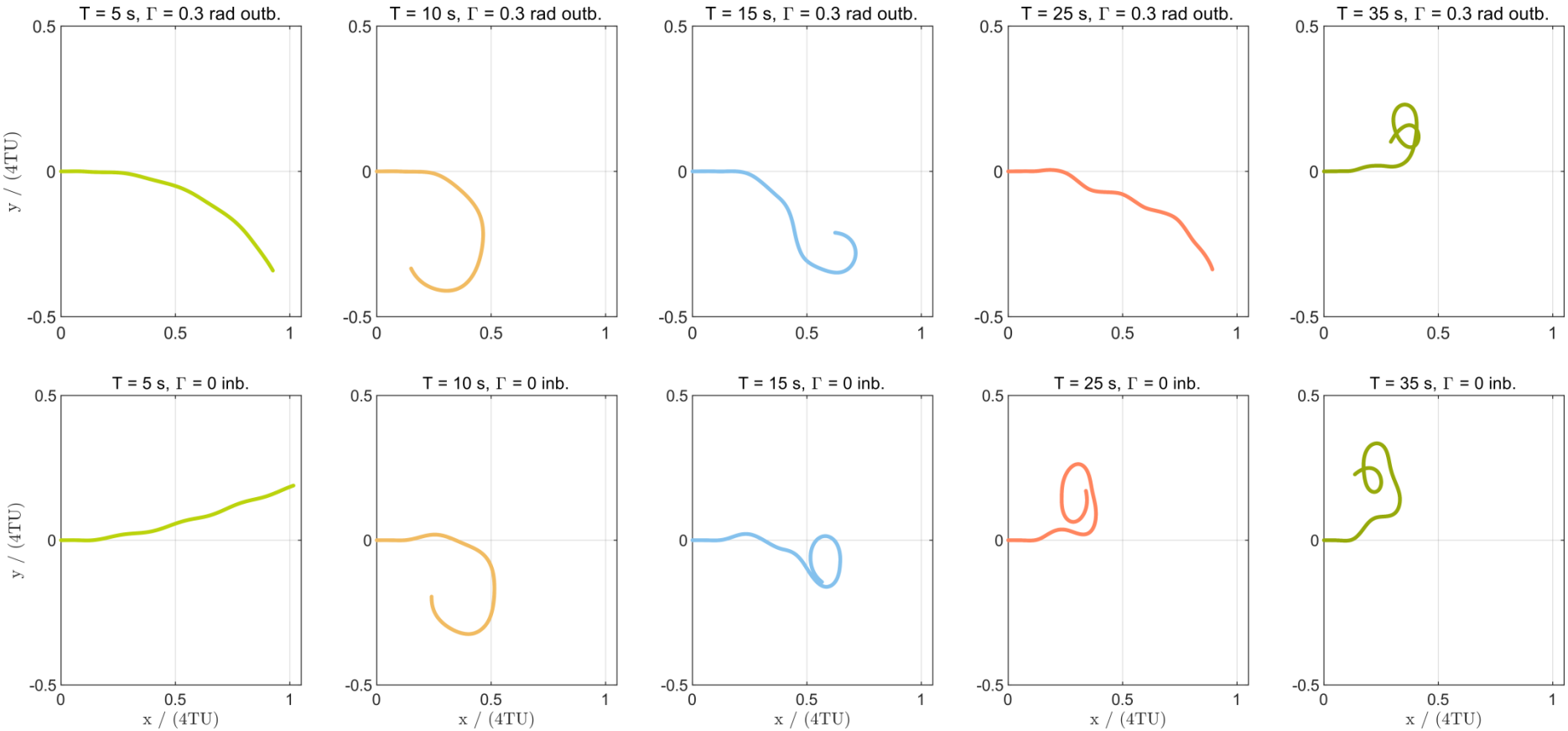

Figure 6.4.14: Simulation flight paths for high-amplitude coupled pitch-yaw quasistatic NPAS capability. A range of oscillatory periods (T) are shown, for outboard $\Gamma = 0.3$ rad and inboard $\Gamma = 0$ dihedral constraints.

6.5. CONCLUDING REMARKS

6.5.1. Results

In this chapter the effect of wing morphing on the space of trim states of the case study system was studied. A continuous space of trim states through pitch angles c. -25° to 30° can be attained thought solely symmetric incidence morphing; and this can be extended to yaw angles through c. ±25° with asymmetric incidence and single-wing dihedral control. The existence of this continuous trim space allows the quasistatic control of the aircraft orientation within this space, corresponding to quasistatic nose-pointing-and-shooting (NPAS) capability, as per Gal-Or [1], or direct force capability as per Herbst [2,13]. These are recognised forms of supermanoeuvrability which are both quasistatic and pre-stall.

A wide range of actuator configurations are available for NPAS control. Pitch NPAS as easily obtainable via symmetric incidence morphing. At minimum actuator complexity, full pitch/yaw NPAS is attainable via the dihedral control on single given wing (left/right), though this leads to asymmetry in the left/right flight dynamics and stability of the aircraft, making guidance and control more complex. A zero dihedral constraint on the non-actuated wing yields the largest controllable trim space; while a positive dihedral constraint (e.g. c. 17°) yields significantly improved spiral stability properties at pitch angles $>0°$, at the expense of Dutch roll instability at pitch angles $<0°$. Alternately, if asymmetric dihedral control is available, then improvements in trim space size and stability can be attained by a switching algorithm in which the wing outboard (or inboard) of the aircraft's yawed orientation is controlled, and the inboard (or outboard) wing is constrained. Outboard control is preferable in terms of spiral mode stability, and the dihedral constraint has a similar effect. If both wings are controlled simultaneously, the trim space is underconstrained, and an optimal method of navigating this space has not yet been developed.

Using these techniques, simulations of quasistatic NPAS control were carried out. Period timescales of c. 25 s yielded reasonably quasistatic profiles; more rapid control was possible, but was more strongly influenced by induced-flow effects. These results demonstrate the capability of the case study system for quasisteady NPAS capability in pitch and yaw; and

the trim state analysis method developed here represents an easily-generalisable approach to quasisteady NPAS design and analysis in other systems.

The trim-state method that was used to design these manoeuvres is novel. It represents an open-loop guidance method only; it cannot be utilised directly for manoeuvre control and is not directly, as the trim states show zero acceleration at the target state by definition, and thus cannot be utilised to effect motion directly. Instead, the manoeuvres rely on the dynamical attractor located at stable trim states to pull the aircraft in a quasistatic motion. Is thus quite distinct from conventional methods of generating such a manoeuvre; for instance, by forms of optimal control (LQR, etc.) [15,16], involving the minimisation of objective functions such as the aircraft state error w.r.t. a path target, acceleration error w.r.t. a derived acceleration target, flight time over a path target constraint, or key performance metric specific to the nature of the manoeuvre [17,18]. The process could be conceived of as a form of optimal control involving (perversely) the minimisation, to zero, of the aircraft acceleration at each point along the target path. As the target state is defined *a priori*, this degenerates into a time-independent optimisation which can be performed *a priori*. In the same way, the trim state method can be seen as entirely distinct from another key paradigm in supermanoeuvre control; that of nonlinear dynamic inversion [19,20]: no feedback linearisation is involved and the computed trim states are exact w.r.t. the model. In Chapter 7 this trim state method will be generalised to more complex time-dependent forms of control, involving states of nonzero acceleration, and in doing so further relationships with existing control strategies will be identified.

6.5.2. Limitations

Given the low levels of transience present in the most of the quasistatic NPAS manoeuvres studied here, the possibility of quasistatic aerodynamic model breakdown does not affect the overall results of this chapter. In some of the more rapid manoeuvres, however, there is the potential for transient aerodynamic effects to have an influence on the results. This possibility is studied in Chapters 8-9. At high angles-of-attack, the possibility of asymmetric forebody flow separation [21] generating nose-slice, coning, and wing rock motion is present. Why this is unlikely, as the angles-of-attack over which quasistatic NPAS is available are not large (max. 30°), the effects are worth attention. In Chapter 7 it is demonstrated

that wing morphing controls are available to counteract the effects of asymmetric forebody separation if required. Overall, the flight conditions of the quasistatic NPAS manoeuvres studied are not qualitatively different to those of the validation simulations in Chapter 5, lending support to the results presented in this chapter.

CHAPTER REFERENCES

[1] Gal-Or, B., *Vectored propulsion, supermaneuverability, and robot aircraft*, Springer-Verlag, New York, 1990.

[2] Herbst, W. B., *Supermaneuverability*, Messerschmidtt-Boelkow-Blohm, Munich, Germany, 1984.

[3] Schmidt, L. V., *Introduction to Aircraft Flight Dynamics*, AIAA, Reston ,VA, 1998.

[4] Lagarias, J. C., Reeds, J. A., Wright, M. H., and Wright, P. E., "Convergence Properties of the Nelder--Mead Simplex Method in Low Dimensions," *SIAM Journal on Optimization*, Vol. 9, No. 1, 1998, pp. 112–147. DOI:10.1137/S1052623496303470.

[5] Krauskopf, B., Osinga, H. M., Galán-Vioque, J., and Doedel, E., eds., *Numerical continuation methods for dynamical systems*, Springer, Dordrecht, The Netherlands, 2007.

[6] Meyer, E. E., "Continuation and Bifurcation in Linear Flutter Equations," *AIAA Journal*, Vol. 53, No. 10, 2015, pp. 3113–3116. DOI:10.2514/1.J053512.

[7] Meyer, E. E., "Unified Approach to Flutter Equations," *AIAA Journal*, Vol. 52, No. 3, 2014, pp. 627–633. DOI:10.2514/1.J052554.

[8] Selig, M., "Modeling Full-Envelope Aerodynamics of Small UAVs in Realtime," AIAA Atmospheric Flight Mechanics Conference, Toronto, ON.

[9] Awange, J. L., ed., *Algebraic geodesy and geoinformatics*, Springer, New York, 2010.

[10] Satran, D. R., *Wind-Tunnel Investigation of the Flight Characteristics of a Canard General Aviation Airplane Configuration*, NASA, Washington, D.C., 1986.

[11] Yechout, T. R., Morris, S. L., Bossert, D. E., Hallgren, W. F., and Hall, J. K., *Introduction to Aircraft Flight Mechanics*, AIAA, Washington, DC, 2014.

[12] Bagherzadeh, S. A., and Sabzehparvar, M., "Estimation of flight modes with Hilbert-Huang transform," *Aircraft Engineering and Aerospace Technology*, Vol. 87, No. 5, 2015, pp. 402–417. DOI:10.1108/AEAT-10-2013-0185.

[13] Herbst, W. B., "Future fighter technologies," *Journal of Aircraft*, Vol. 17, No. 8, 1980, pp. 561–566. DOI:10.2514/3.44674.

[14] Allgower, E. L., and Georg, K., *Introduction to Numerical Continuation Methods*, SIAM, Philadelphia, PA, 2003.

[15] Longuski, J. M., Guzman, J. J., and Prussing, J. E., *Optimal control with aerospace applications*, Springer, New York, 2014.

[16] Levine, W. S., ed., *The Control Handbook*, CRC Press, Boca Raton, FL, 1996.

[17] Miele, A., and Dabney, J. B., "Optimal dive recovery maneuvers of a supermaneuvering jet fighter aircraft," *Journal of the Franklin Institute*, Vol. 338, No. 2–3, 2001, pp. 113–132. DOI:10.1016/S0016-0032(00)00074-0.

[18] Moore, J., Cory, R., and Tedrake, R., "Robust post-stall perching with a simple fixed-wing glider using LQR-Trees," *Bioinspiration & Biomimetics*, Vol. 9, No. 2, 2014, p. 025013. DOI:10.1088/1748-3182/9/2/025013.

[19] Enns, D., Bugajski, D., Hendrick, R., and Stein, G., "Dynamic inversion: an evolving methodology for flight control design," *International Journal of Control*, Vol. 59, No. 1, 1994, pp. 71–91. DOI:10.1080/00207179408923070.

[20] Wu, G., Meng, X., and Wang, F., "Improved nonlinear dynamic inversion control for a flexible air-breathing hypersonic vehicle," *Aerospace Science and Technology*, Vol. 78, 2018, pp. 734–743. DOI:10.1016/j.ast.2018.04.036.

[21] Ericsson, L. E., "Challenges in high-alpha vehicle dynamics," *Progress in Aerospace Sciences*, Vol. 31, No. 4, 1995, pp. 291–334. DOI:10.1016/0376-0421(95)00002-G.

Chapter 7:
Supermanoeuvrability:
RaNPAS and transient manoeuvres

7.1. INTRODUCTION

In Chapter 6, NPAS manoeuvres at relatively low levels of transience were studied. Despite the fact that that the quasistatic aerodynamic submodel will break down at higher levels of transience, an initial analysis of high-transience manoeuvres with this model is required. Such an analysis leads to several key methods for the design of supermanoeuvres and the exploration of supermanoeuvrability, and provides a reference point for the assessment of model breakdown. We study a wide variety of manoeuvres, including traditional thrust-vectoring manoeuvres such as Pugachev's cobra, and more general rapid-nose-pointing-and-shooting (RaNPAS) manoeuvres as per Gal-Or [1]; as well as biomimetic manoeuvres such as ballistic transitions and anchor turns. In further chapters, aerodynamic models will be developed for higher levels of transience; and the utility of the initial quasisteady manoeuvre templates devised here will become apparent.

7.2. LARGE-PERTURBATION STABILITY ANALYSIS

Following Chapter 6, a stability analysis of the system provides an avenue to manoeuvre design. The static lateral and longitudinal trim stability metrics computed in Chapter 6 were linearised metrics, located at the trim point, and only governing the system response to sufficiently small perturbations. Computing identical angular moment/acceleration-gradient metrics at states away from the trim point yields information about the system response to large perturbations, and corresponds to a nonlinear static longitudinal or lateral stability analysis, as per Huenecke [2]. This allows an assessment of the system – or, control configuration – response to large changes in orientation, such as are relevant to RaNPAS and other transient supermanoeuvrability.

Isolating the pitch and yaw degrees of freedom again, the angular acceleration gradients of the aircraft, in a given trim state, as a function of an associated angular perturbation of the trim state, are computed numerically; the expressions:

$$\left.\frac{\partial \ddot{\theta}}{\partial \theta}\right|_{\theta_{\mathrm{tgt}}+\Delta\theta}(\Delta\theta) \tag{7.2.1}$$

$$\left.\frac{\partial\ddot{\psi}}{\partial\psi}\right|_{\psi_{\mathrm{tgt}}+\Delta\psi}(\Delta\psi)$$

The results are conventional static stability analysis plots: for example, Figure 7.2.1 shows the nonlinear longitudinal and lateral static stability profiles for four different trim states: at $\theta_{\mathrm{tgt}} = \psi_{\mathrm{tgt}} = 0$ and $\theta_{\mathrm{tgt}} = \psi_{\mathrm{tgt}} = 0.3$ rad with inboard $\Gamma = 0$ and $\Gamma = 0.3$ rad constraints. The ability of the case study model to accurately predict these pitch and yaw accelerations – relating directly to moments and the aircraft aerodynamic moment coefficients – may be taken from the validation of Chapter 5, which specifically compared these moment coefficients with experimental data. The target trim points are represented by the intersects $\ddot{\theta} = 0$, $\ddot{\psi} = 0$; its linearised static stability by the gradient (e.g. $\partial\ddot{\theta}/\partial\theta$) at the point; and the zone of static stability around the point by the local contiguous space where the gradients are negative (e.g. $\partial\ddot{\theta}/\partial\theta < 0$), i.e. there is attraction to the trim point [2]. As can be seen, all these systems have a reasonably-sized stable zone about their quasi-trim points – the targets θ_{tgt} and ψ_{tgt}, in this case, known to be true trim points. Low pitch angles show the most notable zones of low stability; in particular, the state $\theta_{\mathrm{tgt}} = \psi_{\mathrm{tgt}} = 0.3$ rad and $\Gamma = 0.3$ rad shows marginal longitudinal stability for c. $\theta < 0$.

Note that, in technical terms, a conventional decoupled stability analysis would analyse the effect of sideslip and angle-of-attack perturbations (relative to the flight velocity vector), and not absolute pitch and yaw. This distinction is only relevant at trim states at nonzero target yaw values, and is of minor significance – coupling effects between the absolute angles will only be notable when there are large differences between the system pitch and yaw stability, and such states are of minimal interest here.

Now while a corresponding trim state at some orientation does not necessarily exist for every possible aircraft control configuration, yet in the case study system many non-trim control configurations will have quasi-trim states: points where the acceleration in one or more decoupled variable is zero (here, mathematically, $\ddot{\theta}(\theta) = 0$, or $\ddot{\psi}(\psi) = 0$). These are not trim states, due to the nonzero acceleration in other angular and translational variables, but they serve as instantaneous point attractors in their respective variables. If effect of the accelerations in the other variables is relatively small, or can be controlled to be so – e.g.

because of a faster timescale in the primary variable, a minimal coupling between variables, and/or by further constraining the control configuration space – then the attraction will remain approximately constant for a duration. This leads effectively to a temporary trim state that will remain until the other accelerations shift the location of the point attraction. This temporary trim state / point attractor may then be subject to a nonlinear static stability analysis as per the true trim points, which will give an estimate of its basin of attraction.

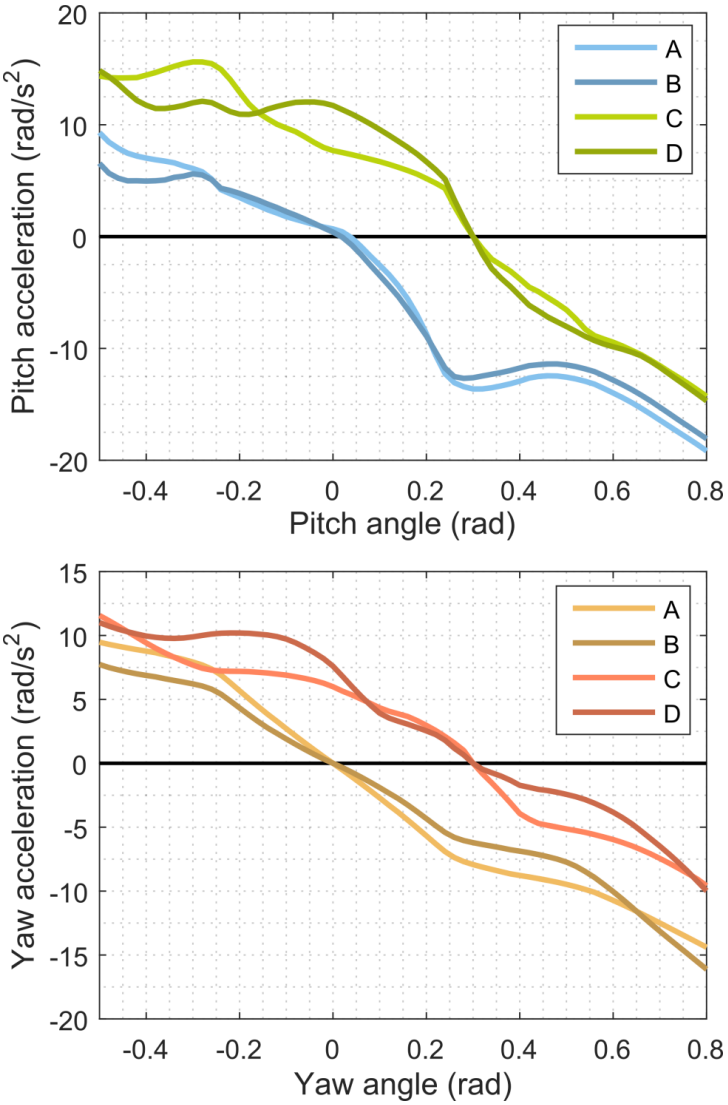

Figure 7.2.1: Pitch and yaw stability plots for four different trim states:
A) $\theta_{\text{tgt}} = \psi_{\text{tgt}} = 0$, inboard $\Gamma = 0$ rad
B) $\theta_{\text{tgt}} = \psi_{\text{tgt}} = 0$, inboard $\Gamma = 0.3$ rad
C) $\theta_{\text{tgt}} = \psi_{\text{tgt}} = 0.3$, inboard $\Gamma = 0$ rad
D) $\theta_{\text{tgt}} = \psi_{\text{tgt}} = 0.3$, inboard $\Gamma = 0.3$ rad.

The application of these methods is in the design of open-loop strongly transient manoeuvres. Strongly transient manoeuvres can be controlled by placing strong quasi-trim attractors along the control configuration histories, each within the basins of attraction of its neighbours, and designed to pull the aircraft rapidly between the quasi-trim point orientations. The key advantage of these quasi-trim states over true trim states for this purpose is that they exist over a far wider orientation field, greatly increasing the range of transient motions available. Their key disadvantage is that they are not attractors in all variables, and thus they offer a significantly less precise form of orientation control due to drift in these other variables. It is only in cases when this drift can be minimised or constrained that quasi-trim orientation control truly becomes useful. As with the trim spaces introduced in Chapter 6, quasi-trim states are a novel concept not previously explored, and arising from the generalisation of trim state analysis to morphing-wing systems.

For example, if the intended transient motion is composed of rotation in a two-dimensional plane – e.g. in yaw (plane x-y) or pitch (plane x-z) – then, with sufficient control effectiveness, the out-of-plane angular variables can be constrained to be at quasi-trim state. In general this can be done by so constraining the space of control configurations used in the manoeuvre, in some cases this constrained set may be a superset of a symmetry-constrained set (e.g. in the case study system, for pitch, configurations with symmetry about the x-z plane.) This leaves the in-planar translational accelerations, and as in general these have a relatively minimal effect on the aircraft trim state (particularly at higher airspeeds), the aircraft can be made to remain approximately in-plane.

A basic example of this principle is shown in Figure 7.2.2. This shows the $\psi_{\mathrm{tgt}} = \theta_{\mathrm{tgt}} = \Gamma = 0$ trim state from Figure 7.2.1, alongside the effect of elevator deflection changes to this state. There are no pitch angles at which these alternate elevator deflection states are trim states – for this to be the case, they require changes in wing incidence and propulsive force as per Chapter 6 – but there are angles at which they are quasi-trim states in pitch. These quasi-trim states function as approximate attractors in pitch, and thus illustrate the phenomenologically obvious transient effect of elevator changes; to cause pitch-up and pitch-down motion.

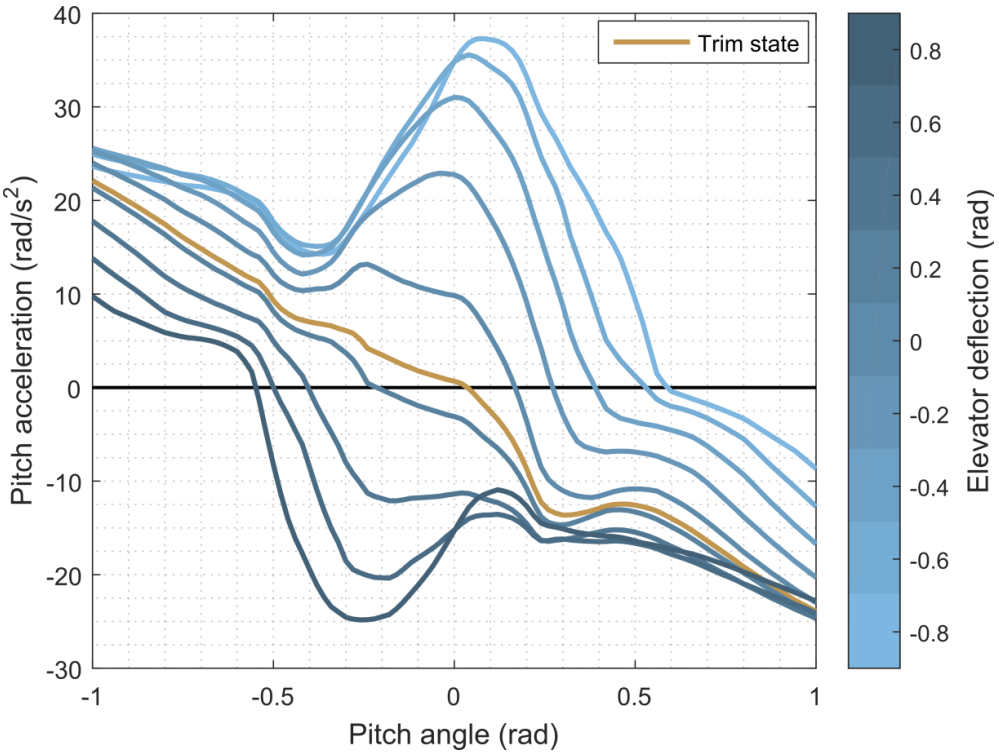

Figure 7.2.2: Effect of elevator deflection on the pitch acceleration profiles of the trim state $\theta_{\text{tgt}} = \psi_{\text{tgt}} = \Gamma = 0$.

7.3. RaNPAS: PUGACHEV'S COBRA

7.3.1. Motivation

The Pugachev cobra is a simple pitch-only supermanoeuvre which involves tilting the aircraft backwards from level flight to beyond $\theta = 90°$, and then forwards to level flight again, while maintaining approximately constant altitude [3]. As such it is a form of RaNPAS capability as per Gal-Or [1]; and although no such RaNPAS capability is observed in biological flyers, the cobra manoeuvre is highly widespread among supermanoeuvrable aircraft. In some cases is achievable without the use of thrust-vectoring; requiring only favourable structural and aerodynamic design [4]. Figure 7.3.1 shows a schematic of the cobra manoeuvre.

In general, RaNPAS capability has the potential to significantly increase the success chance of dogfight engagements [5], but the cobra manoeuvre has the key detrimental effect of draining the aircraft kinetic energy rapidly through the large drag forces generated at high angle-of-attack. Under energy-manoeuvrability theory, and prevailing USAF tactical doctrine, this puts the aircraft at a significant disadvantage should the RaNPAS manoeuver

fail to decisively end combat. The cobra manoeuvre has also been considered as a mechanism to momentarily break the radar lock of air defence systems: this is thought to form part of Russian Aerospace Force (VKS) tactical doctrine, which still places a major emphasis on this form of supermanoeuvrability.

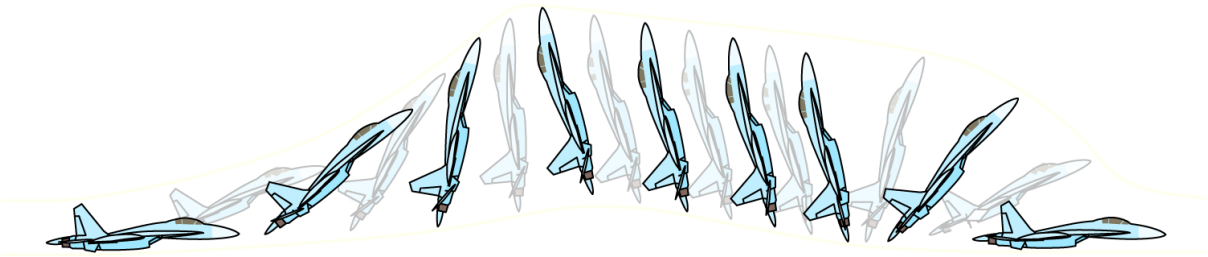

Figure 7.3.1: Schematic of Pugachev's cobra performed by a Sukhoi Su-27. Image from Wikimedia Commons, User:Henrickson, licenced under CC BY-SA 3.0.

Whatever the school of thought regarding the cobra manoeuvre itself, more general pitch-axis supermanoeuvrability nevertheless remains an element of USAF tactical doctrine, and the cobra manoeuvre represents a useful benchmark for such capability. Recent developments have explored a widening spectrum of applications – e.g. for the F-35 Lightning II, short take-off and vertical landing (STOVL) capability [6]. In the context of supermanoeuvrable UAVs, an area of minimal extant literature, there is the potential for even more diverse applications of pitch-axis supermanoeuvrability, as restrictions on pilot g-forces do not apply. Some of these will be studied in this chapter. In the UAV context, the cobra manoeuvre itself may show utility, e.g. as an airbrake mechanism for operations in confined spaces.

7.3.2. Manoeuvre design

The large-perturbation static stability analysis in Section 7.2 provides a basic method of designing such a manoeuvre in the case study system. Other than an initial trim state, in the simplest case at least two control configurations must be identified: a configuration to generate the pitch-up moment required to send the aircraft to the partially inverted position; and a configuration to pitch it forwards and downwards again. The initial trim state is one immediate candidate for the latter – given its wide nonlinear stability profile, cf. Figure 7.2.1 – but to explore and assess other candidates in the morphing configuration

space, a simplex optimisation technique is used in a similar manner to Chapter 6, Section 6.2. The central difference here is the definition of the acceleration-based objective function with respect to which the control configurations will be optimised. As this manoeuvre is constrained to the x-z plane, the control space for manoeuvre design is constrained also by symmetry about this plane. Potential active degrees of freedom are thus the symmetric dihedral Γ ($\theta_{wl} = \theta_{wr} = \Gamma$), the symmetric sweep Λ ($\psi_{wl} = -\pi/2 - \Lambda$, $\psi_{wr} = \pi/2 + \Lambda$), and the symmetric incidence α ($\phi_{wl} = \phi_{wr} = \alpha$) the elevator deflection β_e, and the propulsive force F_{prop}.

For the pitch-up configuration, a variety of objective functions are available. The aircraft point pitch accelerations at low to medium-high angles of attack, $\ddot{\theta}(\theta_i)$ provide simple and physically-relevant metrics to maximise. More complex functions such as the location of the aircraft quasi-trim (pitch-trim) state, $\theta : \ddot{\theta}(\theta) = 0$, and the pitch acceleration integral ($\int \ddot{\theta}(\theta)\, d\theta$) are also available. For physical relevance the point pitch acceleration is used, at a pitch value of 0.8 rad. Constraints on the elevator deflection ($|\beta_e| < 0.87$ rad) and wing sweep ($0.4 \leq |\psi_w| \leq \pi - 0.4$ rad i.e. $|\Lambda| < 1.171$ rad) are enforced. Figure 7.3.2 shows several states generated by pitch-up configuration optimization. Results A-C indicate pitch stability plots for optimal states with (A) all degrees of freedom active, (B) sweep and incidence active and (C) only incidence active. The associated wing configuration is rendered alongside Note that $U = 30$ m/s and $F_{\text{prop}} = 10$ N in all cases; as it is the aerodynamic effects that are of primary interest. In the case of (A), however, significant additional pitch-up moment can be generated by the offset between the propulsive force axis and the centre of mass due to the upwards wing dihedral.

Parameter values for these states are given in Table 7.3.1; values in bold are located on their respective constraint limits, and indicate the effect of these constraints on the state performance. For example, in all states the elevator is at its control limit, and it is self-evident that increased elevator control effectiveness will result in greater pitch control effectiveness. At very high angles of attack (> 1 rad), however, the elevator ceases to have a significant effect on the system pitch dynamics, and morphing controls must take over. In the fully-actuated system (A), the sweep degree of freedom is at its control limit, indicating

that improvements in sweep control effectiveness (e.g. via larger wing chord) would result in greater pitch control effectiveness. However, the Λ-α system, case (B), is not at any control limits, indicating that more complex effects are also at play, for example the balance between the lift- and drag-generated pitch-up moment, and the optimisation trade-off that increased sweep represents for these two moments.

Table 7.3.1: Parameters for optimal pitch-up states

Parameter	**(A)** All DOF	**(B)** Λ-α	**(C)** α
Γ (rad)	0.730	0	0
Λ (rad)	**1.171**	0.699	0
α (rad)	0.247	0.181	0.171
β_e (rad)	**−0.870**	**−0.870**	**−0.870**

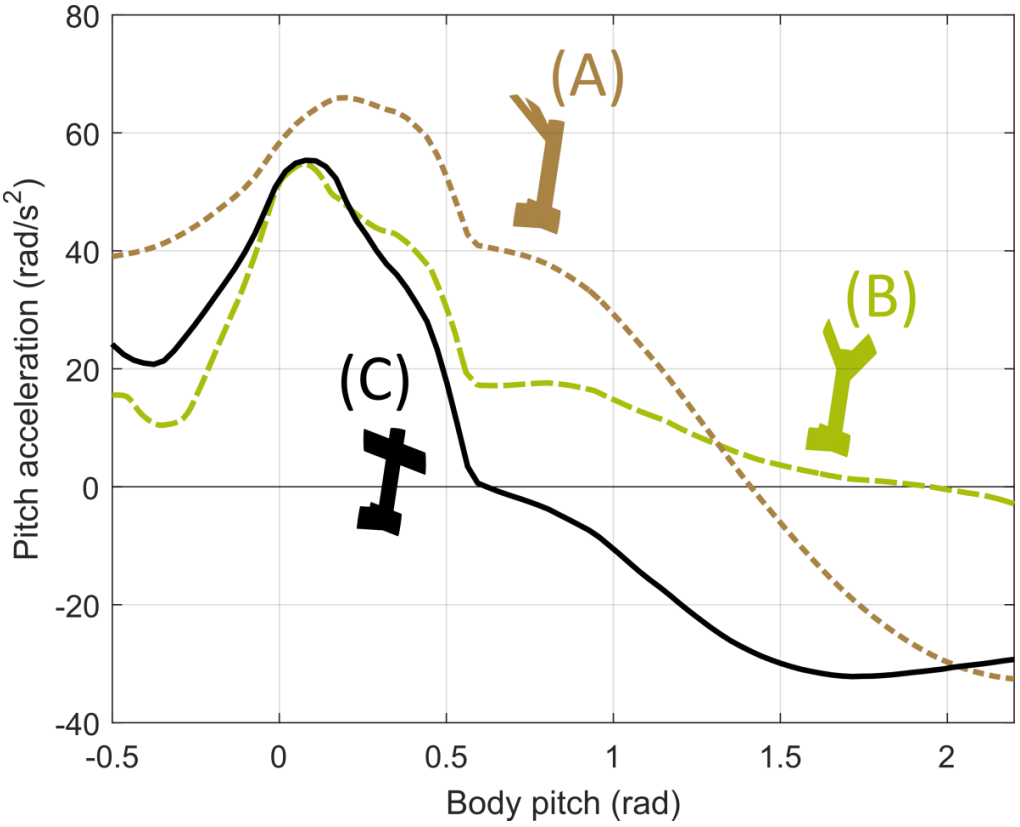

Figure 7.3.2: Static longitudinal stability profile of several candidate pitch-up configurations.

The wing parameters associated a high pitch-up rate are a positive dihedral, forward wing sweep and mild upwards inclination. Upwards inclination increases the wing lift, but too much reduces the drag-induced pitch-back moment at high angles of attack. Positive dihedral, in combination with forward sweep, induces a pitch-back drag moment even at

low angles of attack. The forward sweep is particularly relevant, as this shifts the aerodynamic centre further forward and thus increases its pitching moment about the centre of mass (which is less strongly affected by the sweep motion). The result is that the aircraft's stable pitch quasi-trim state is shifted to a very to a high angle of attack (in result (B), even to the partially-inverted position) thus providing a strong attraction towards that flight state. While result (B) has a quasi-trim state at the highest angle of attack, the strength of its attraction is significantly weaker than that of result (A), as indicated by the pitch acceleration gradient at the quasi-trim state. Result (A) is thus likely to allow the cobra manoeuvre to be carried out more rapidly, and without interference from the non-trimmed variables. In any case, the transient overshoot to the c. $\theta = 1.4$ rad trim state will take the aircraft to higher angles. Note that the use of forward sweep in does have the disadvantage of decreasing the aeroelastic divergence speed of the wings [7], limiting the flight envelope of these forward-swept states.

For the pitch-down configuration similar objective functions are available; though the relevant pitch angles for pitch acceleration minimization are higher (>1 rad). Figure 7.3.3 shows configurations to minimise the point pitch acceleration at 1.4 rad pitch, and Table 7.3.2 shows their parameter values. Results A-C are the optimal configurations for (A) all degrees of freedom active, (B) sweep and incidence active and (C) only incidence active. Result (D) is an example trim state, at $\Gamma = 0$, $\psi_{\mathrm{tgt}} = 0$, and $\theta_{\mathrm{tgt}} = 0.08$ rad – a non-optimal but obvious default candidate, with minimal control deflection. Similar aerodynamic effects to those in Figure 7.3.2 are observed. Backward sweep moves the aerodynamic centre rearwards, and the presence of anhedral allows the maximum wing surface area to be inclined into the flow, for maximum restoring drag moment. In these cases the wing incidence is kept flat to make use of this restoring drag moment; however, when only incidence motion is available, inclining the lifting surface into the local free-stream to reduce its drag is the better option. The tail then provides all the available restoring moment. This configuration has the additional benefit of generating significant lift at high angles of attack; thus reducing the burden on the propulsion during the manoeuvre. The trim state itself, as a result of the airframe stability, generates moderate pitch-up acceleration; but this acceleration can be doubled in the presence of wing morphing.

Table 7.3.2: Parameters for optimal pitch-down states

Parameter	**(A)** All DOF	**(B)** Λ-α	**(C)** α	**(D)** Trim
Γ (rad)	-0.255	0	0	0
Λ (rad)	$\mathbf{-1.171}$	$\mathbf{-1.171}$	0	0
α (rad)	0.168	0.0493	-1.654	0.014
β_e (rad)	0.262	0.262	0.262	0.003

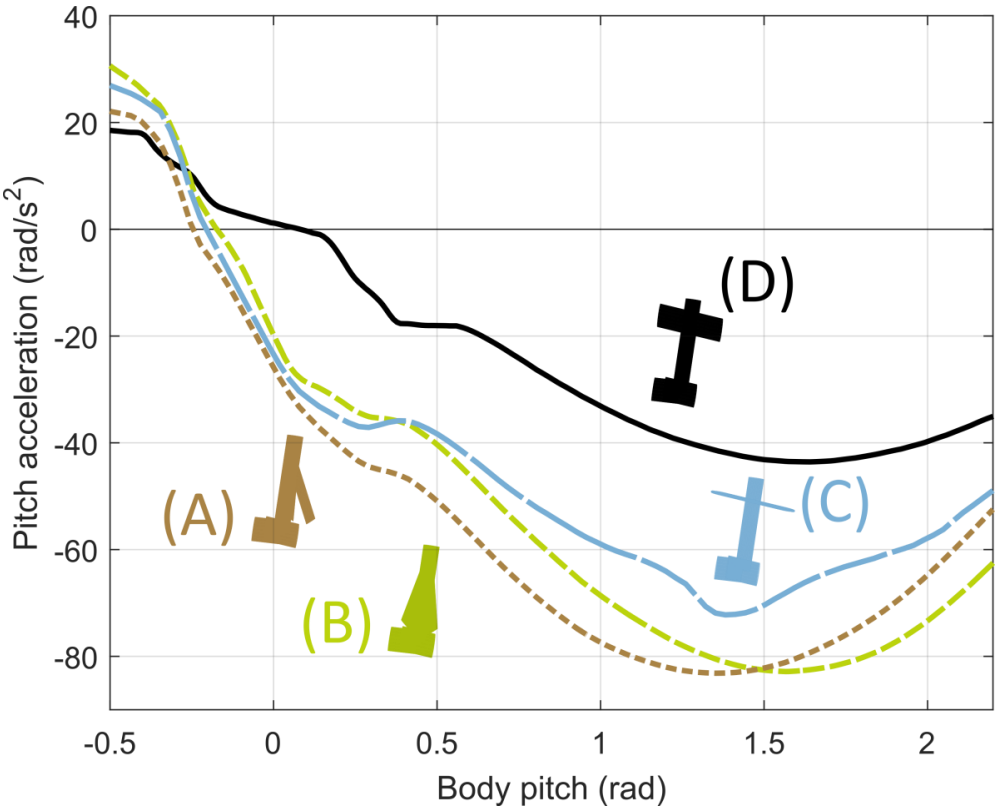

Figure 7.3.3: Static longitudinal stability profile of several candidate pitch-down configurations

7.3.3. Manoeuvre simulation

A simple cobra manoeuvre can be obtained using only the pitch-up states in Section 7.3.2. Transitioning from an initial near-trim state to a pitch-up state and then back again generates a strong transient pitch-up moment which is then stabilised by the near trim-state (cf. Figure 7.3.3). Pitch angles of >90 ° can be obtained. The use of an initial near-trim state rather than a trim state is to generate an upwards flight trajectory and accumulate altitude, both of which serve to mitigate the altitude loss (due to airspeed loss) through the manoeuvre. The degree of aerodynamic transience present in this manoeuvre, and its possible effects, will be assessed in Chapter 9.

Figure 7.3.4 shows the flight simulation results for a simple cobra manoeuvre of this form, including the aircraft flight path, its control and orientation history, and its acceleration history compared with the quasistatic states (Figures 7.3.2-7.3.3). The pitch-up state is the optimised 3DOF pitch-up state in Figure 7.3.2, and the initial and final near-trim state is the trim state at pitch 0.08 rad and airspeed 30 m/s; with the system initialised at pitch 0.08 rad and airspeed 50 m/s. The time-scales of the morphing motion have been adjusted manually, with 500 ms in the near-trim state, 100 ms transition, 50 ms in the trim-up state and then an immediate return to the near-trim state. This discontinuous control path is then smoothed strongly via a Laplacian smoother, leading to the final control commands of Figure 7.3.4.

Several points about Figure 7.3.4 are notable. The cobra manoeuvre is carried out successfully at a constant thrust/weight ratio of T/W = 0.25; this is notably low relative to the capability of supermanoeuvrable thrust-vectoring aircraft, which approach T/W = 1 (cf. [1,4]). Even at this low thrust value, the aircraft reaches a pitch angle of 98°, and stabilises to a low pitch angle without altitude loss and with only c. 6 m transient altitude gain through the manoeuvre. Key factors behind this quite optimistic T/W value is the aircraft lift and drag in the nose-up position; affecting and effecting the altitude and airspeed loss throughout the manoeuvre. Studies of aircraft transient aerodynamics indicate lift peaks at high angles of attack larger than those in quasisteady aerodynamic models (as a result of dynamic stall) [8–10], which would serve to decrease the required T/W value. On the other hand, three-dimensional effects would serve to decrease both the lift and drag coefficient post-stall [11], increasing the T/W required to retain altitude, but decreasing the T/W required to regain airspeed. Overall, these factors would indicate that the current model is unlikely to be overly optimistic, at the very least.

The initial airspeed is also a key parameter for the manoeuvre, as this affects both the magnitude of airspeed loss during the manoeuvre and the effect of this airspeed loss on the aircraft altitude – particularly, the length of time spent below the aircraft stall speed. This effect is linked to that of the aircraft thrust (T/W) which accelerates the aircraft again in the aftermath of the manoeuvre. It is also significant that the manoeuvre is carried out with an airframe which, in the default morphing state and trim states, is strongly stable (cf. Figures 7.2.1-7.2.2, Figure 6.3.1). This is in contrast to thrust vectoring aircraft, which typically show

unstable airframes. Of course, the use of morphing enables the airframe to be destabilised and stabilised at command – cf. Figure 7.3.2, in which the optimised states are typically unstable at zero pitch angle – and this is an alternate what of conceptualising how the cobra manoeuvre is performed; by sequential airframe destabilisation and stabilisation.

Figures 7.3.5-7.3.6 show the effect of the initial airspeed and thrust/weight ratio (T/W = 0.25 and T/W = 0.50) on this manoeuvre. Note that the initial and final near-trim states are unchanged. Figures 7.3.5-7.3.6 also delineate the zone $2.5 < t < 3$ s, during which the transient pitching motion is largely stabilised. The open-loop flight simulation continues through this zone, but in reality some form of closed-loop control / manual guidance would be expected from this area onwards. A notable effect seen in Figures 7.3.5-7.3.6 is that the initial airspeed has only a small effect on the airspeed loss through the manoeuvre: the variation in the airspeed at $t = 2.5$ s is less than 5 m/s, for an initial airspeed range of 25 m/s. This effect is due to the proportional nature of the drag forces ($\propto U$). The primary effect of increased airspeed is to reduce the overall altitude loss over the manoeuvre, by increasing the altitude gain in the initial and pitch-up stages. Similarly, the effect of T/W in accelerating the aircraft after the manoeuvre may be observed – this also leads to reduction in altitude loss, through the more direct method of inclining the aircraft trajectory upwards in the manoeuvre aftermath. Note, of course, that all these effects need a quantitative and qualitative validation with transient aerodynamic modelling; this will be carried out in Chapters 8-9.

Despite the minimal link between the initial and final airspeeds of the cobra manoeuvre so far studied, performing such a manoeuvre at low initial airspeeds (c. 30 m/s) while retaining moderate thrust (c. T/W = 0.5) and altitude loss (< 10 m) is difficult. A key strategy to successfully designing such a high-performance manoeuvre is to ensure the completion the pitch-up pitch-down phase in as short a time as possible, so as to reduce the manoeuvre airspeed loss. This requires the use of the optimal pitch-down states in Figure 7.3.3. While the simplest conceivable arrangement is trim → pitch up → pitch down → trim; we find, for these configurations, that an additional pitch-up state is required before the final trim, to decelerate the extremely strong pitch-down motion of the pitch-down state. Without active deceleration the aircraft immediately transitions into a steep dive.

Figure 7.3.7 shows a low-airspeed cobra manoeuvre performed in this way, with initial airspeed 30 m/s and c. T/W = 0.5. The aircraft flight path, its orientation, control, and velocity history, and its acceleration history compared with the quasistatic states (Figures 7.3.2-7.3.3) are shown. The time-scales of the morphing motion are again set manually, with a transition time of 200 ms between pitch up/down states, 100 ms between trim and pitch up/down states, and Laplacian smoothing. The cobra manoeuvre is successful, reaching a maximum pitch of c. 108°, and carried out in c. 900 ms (between points of pitch 0.08 rad), with minimal undershoot and an altitude loss of less than 4 m between $0 \leq t \leq 2$ s (the timespan of the rendering in Figure 7.3.7). A continuation of the simulation to $t = 2.5$ s is shown in the orientation, control, and velocity histories, and leads to additional altitude loss (c. 6 m total). However, as with Figure 7.3.4, the aircraft is at a stable near-zero pitch angle and it is expected that closed-loop control / manual guidance from $t = 2$ s will be able to return the aircraft to steady level flight or any other specified flight state. But while Figure 7.3.7 represents a high-performance cobra manoeuvre, its control motions are intentionally extreme and entail high actuator efforts and airframe stresses. Indeed, key additional factors in the feasibility of these manoeuvres are the aeroelastic properties of the aircraft; in particular the aeroelastic divergence speed on the forward swept state [7]. In this study structural aspects of the case study system are not modelled; but such modelling is required before the system and its manoeuvres can be said to be truly feasible.

Figure 7.3.8 explores the effect of T/W (0.2-1.0) on the low-airspeed cobra manoeuvre. T/W has relatively small effect on the dynamics of the manoeuvre: it is only required to compensate for the loss of airspeed and return the aircraft to a stable trim state after the manoeuvre. The critical level of thrust for manoeuvres success is thus determined by aircraft stall speed and / or the acceptability of some altitude loss after the manoeuvre – an alternative method of increasing the airspeed above the stall threshold. Returning to gentler variants of the cobra manoeuvre; several alternative forms are available using other control configurations and sequences. One involves shifting from the initial trim state to a high angle-of-attack trim state, then to an optimal pitch-up state as per Table 7.3.1, and then down to the high angle-of-attack trim state and the initial trim state again. The purpose of interspersing the high angle-of-attack trim state within this sequence is to ease the

transition between the pitch-up and trim states by decreasing the distance between the last stable trim state and the nose-back state, thereby decreasing the level of transient overshoot in both directions. Figure 7.3.9-7.3.10 show an example of a cobra manoeuvre of this form, at T/W = 0.5 and using a high angle-of-attack trim state at pitch 0.4 rad. The effect of the initial velocity is shown: note that the parametric nature of this manoeuvre (utilising computed trim states) means that changes in T/W will necessitate small changes in the other control parameters, as shown in Figure 7.3.10.

Even the lowest airspeed, 30 m/s, qualifies as a cobra manoeuvre (maximum pitch c. 100°) and shows a notably favourable stabilisation – to a near-level flight state at c. 6 m altitude gain. Significantly larger maximum pitch angles are obtainable with higher airspeeds; at 60 m/s, c. 117°. This occurs at the cost of less favourable stabilisation; for the latter, near-zero altitude gain and -10° pitch angle at $t = 2$ s. These results are, however, highly favourable relative to those of previous cobra manoeuvres. This is attributable to the use of high angle-of-attack trim states, which generate pitch-up motion (up to pitch 0.4 rad) with significantly reduced drag force. This leads to a significantly reduced airspeed loss through the manoeuvre, as can be observed in Figure 7.3.9. This approach appears to be the most favourable developed so far, and shows parallels with the direct force capability in Chapter 6. These cobra results are significant – pending further validation with transient aerodynamics – in that they demonstrate the possibility of performing cobra manoeuvres in biomimetic systems using only reasonable levels of wing morphing control; and moreover, in a realistic small-scale aircraft with a stable airframe and a thrust-to-weight ratio of 0.5 or less.

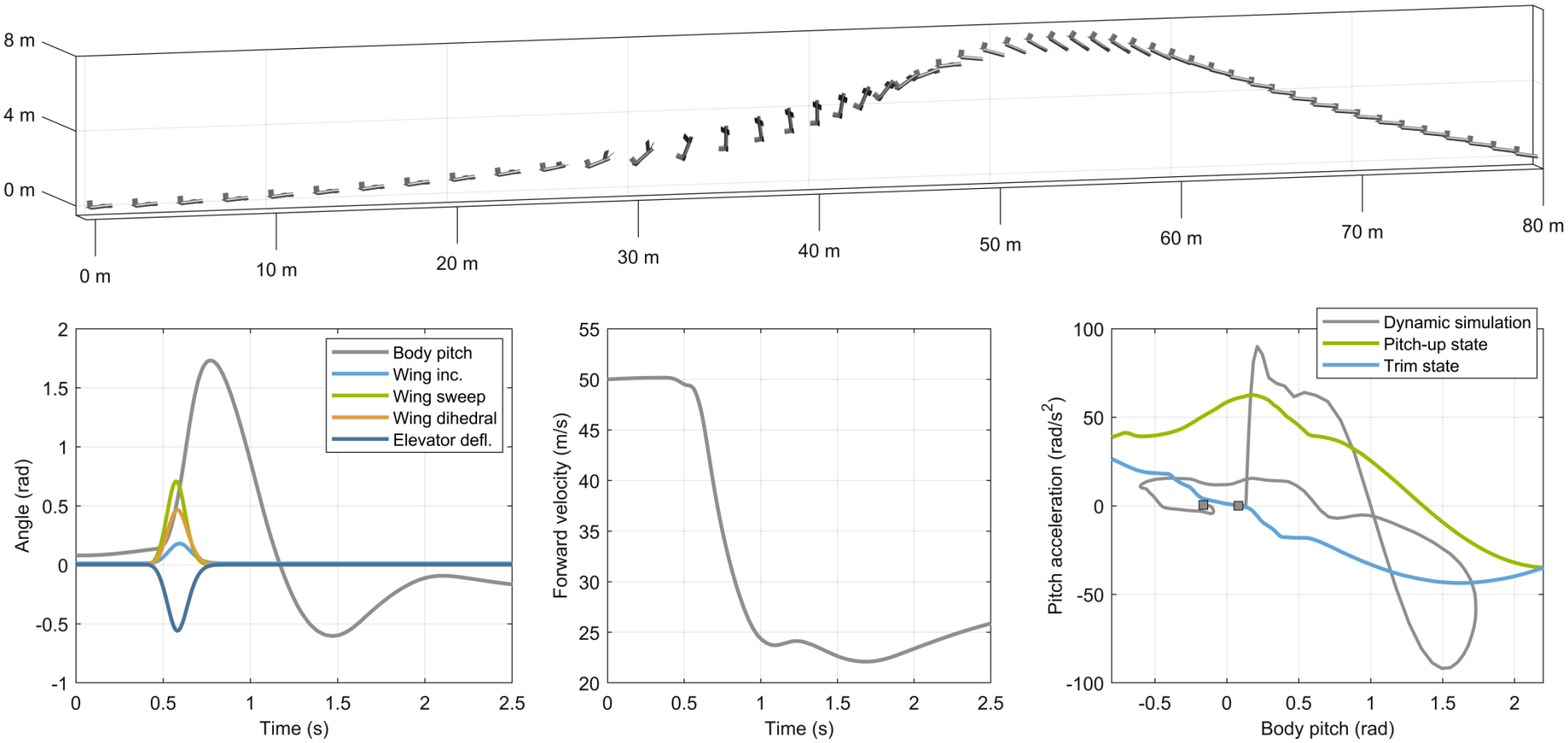

Figure 7.3.4: Flight simulation results for a simple 3DOF-morphing cobra manoeuvre at T/W = 0.25: flight path with aircraft rendered every 50 ms ($0 \leq t \leq 2.5$ s), control and orientation history, forward velocity history, and acceleration history compared with the quasistatic acceleration profiles are shown. The aircraft state sequence is: near-trim → optimal pitchup → near-trim.

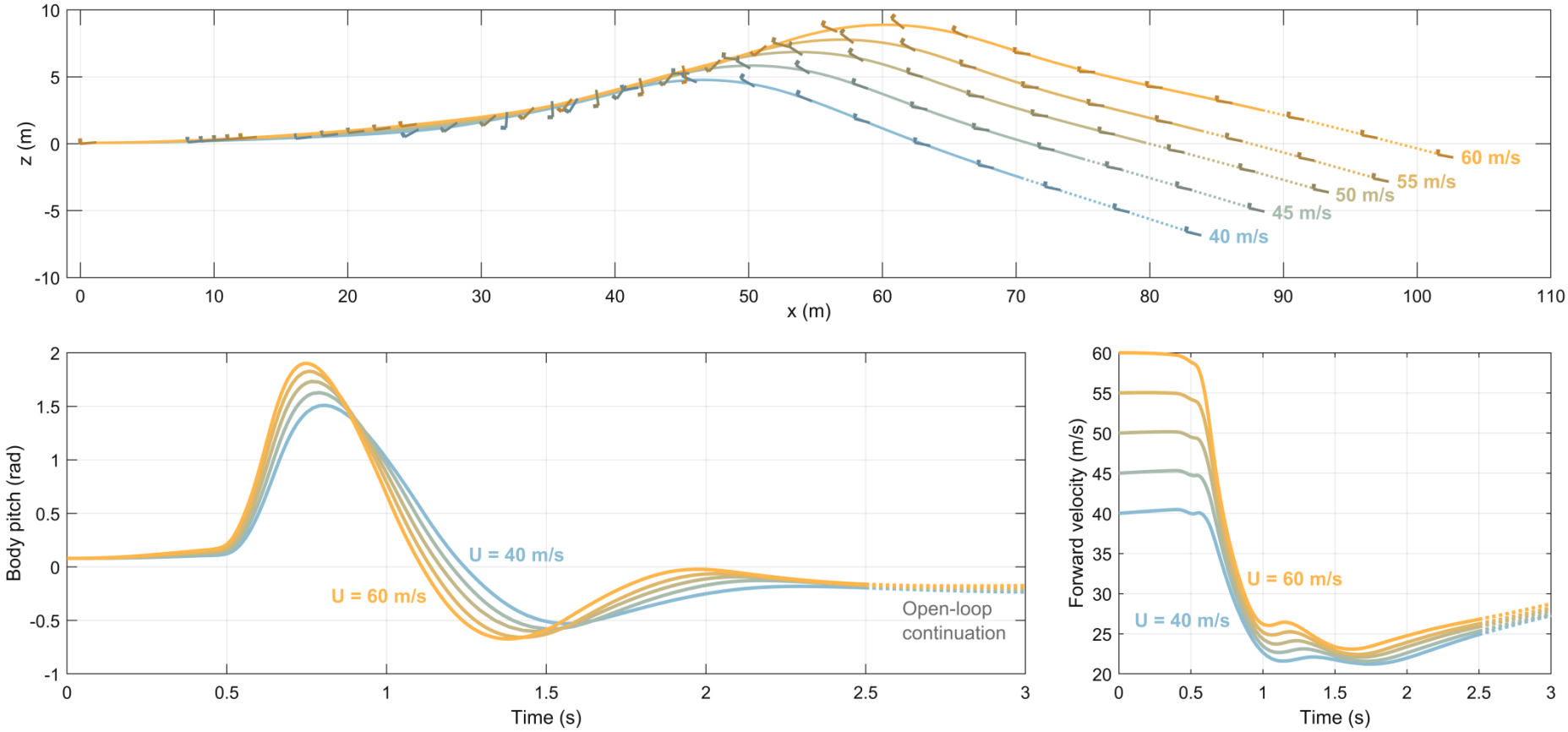

Figure 7.3.5: Flight simulation results for a simple 3DOF cobra manoeuvre at T/W = 0.25, under varying initial airspeed. Aircraft flight paths, body pitch angle histories and forward velocity histories are shown. The aircraft state sequence is: near-trim → optimal pitchup → near-trim.

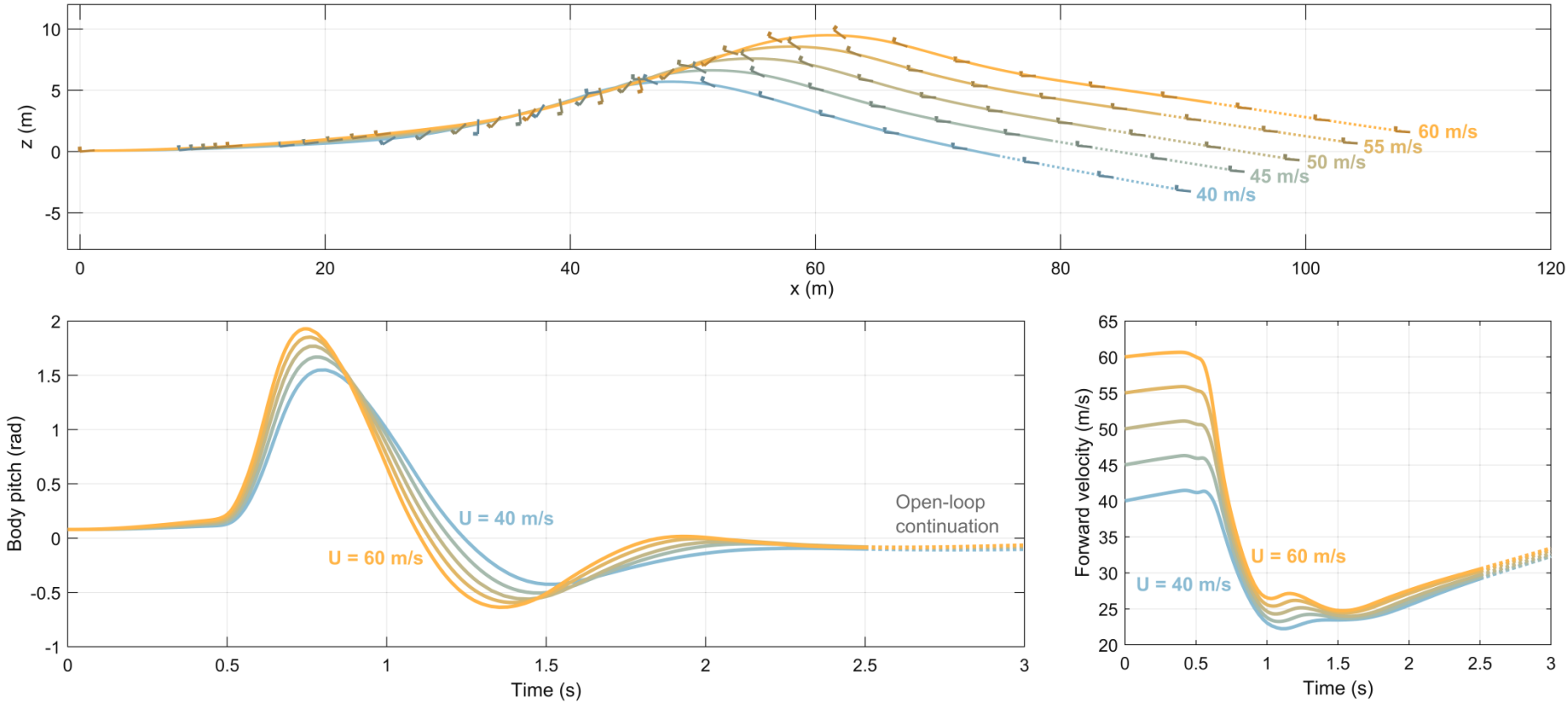

Figure 7.3.6: Flight simulation results for a simple 3DOF cobra manoeuvre at T/W = 0.50, under varying initial airspeed. Aircraft flight paths, body pitch angle histories and forward velocity histories are shown. The aircraft state sequence is: near-trim → optimal pitchup → near-trim.

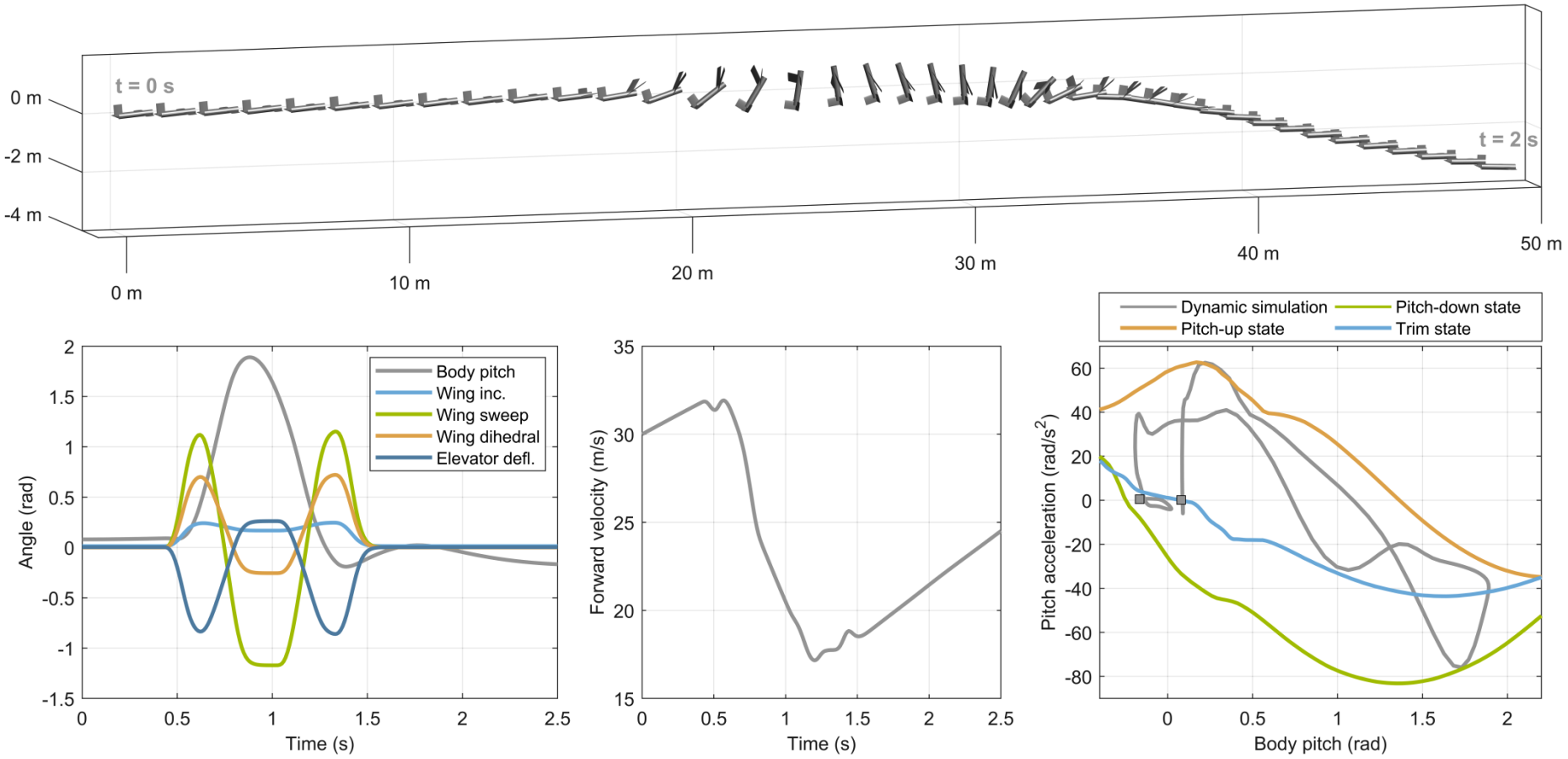

Figure 7.3.7: Flight simulation results for a low-airspeed 3DOF-morphing cobra manoeuvre: flight path with aircraft rendered every 50 ms ($0 \leq t \leq 2$ s), control and orientation history, forward velocity history, and acceleration history compared with the quasistatic acceleration profiles are shown.

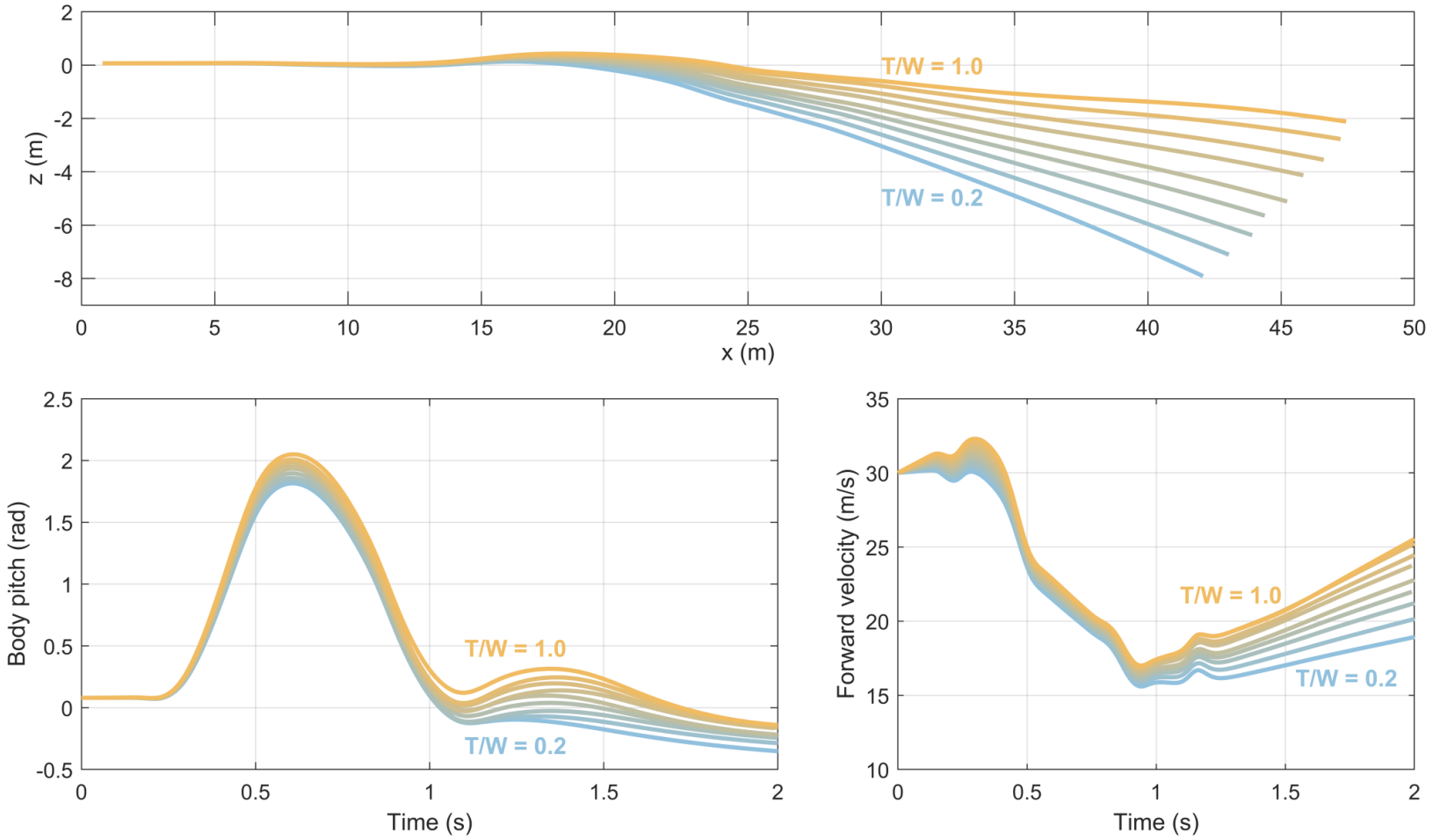

Figure 7.3.8: Flight simulation results for a low-airspeed 3DOF-morphing cobra manoeuvre, under varying constant thrust (T/W). Aircraft flight paths, body pitch angle histories and forward velocity histories are shown.

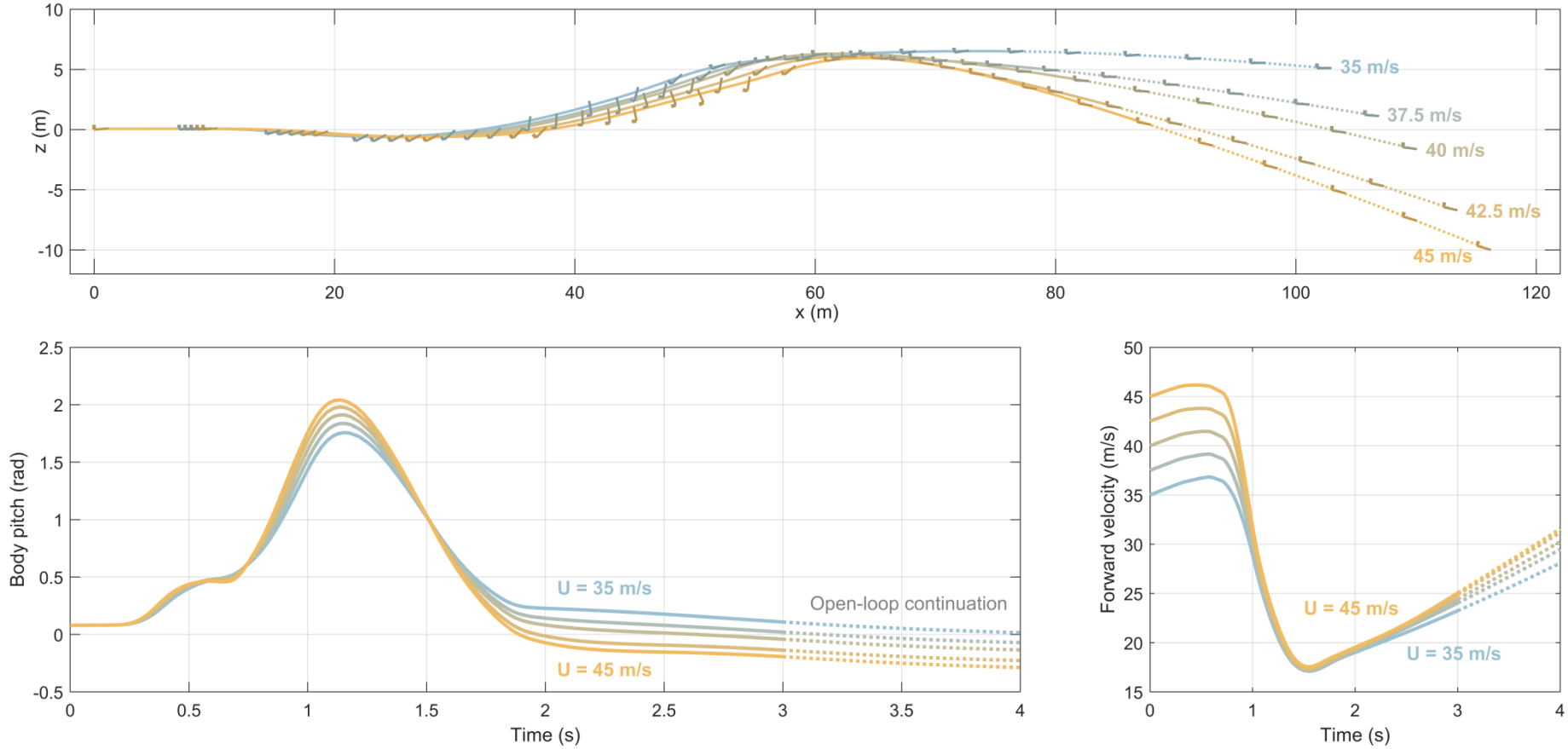

Figure 7.3.9: Flight simulation results for a 2DOF sweep- and incidence-morphing cobra manoeuvre, under varying initial airspeed and corresponding trim state properties. Aircraft flight paths, body pitch angle histories and forward velocity histories are shown. The aircraft state sequence is: trim(@ 0.08 rad) → trim(@ 0.4 rad) → optimal pitchup → trim(@ 0.4 rad) → trim(@ 0.08 rad).

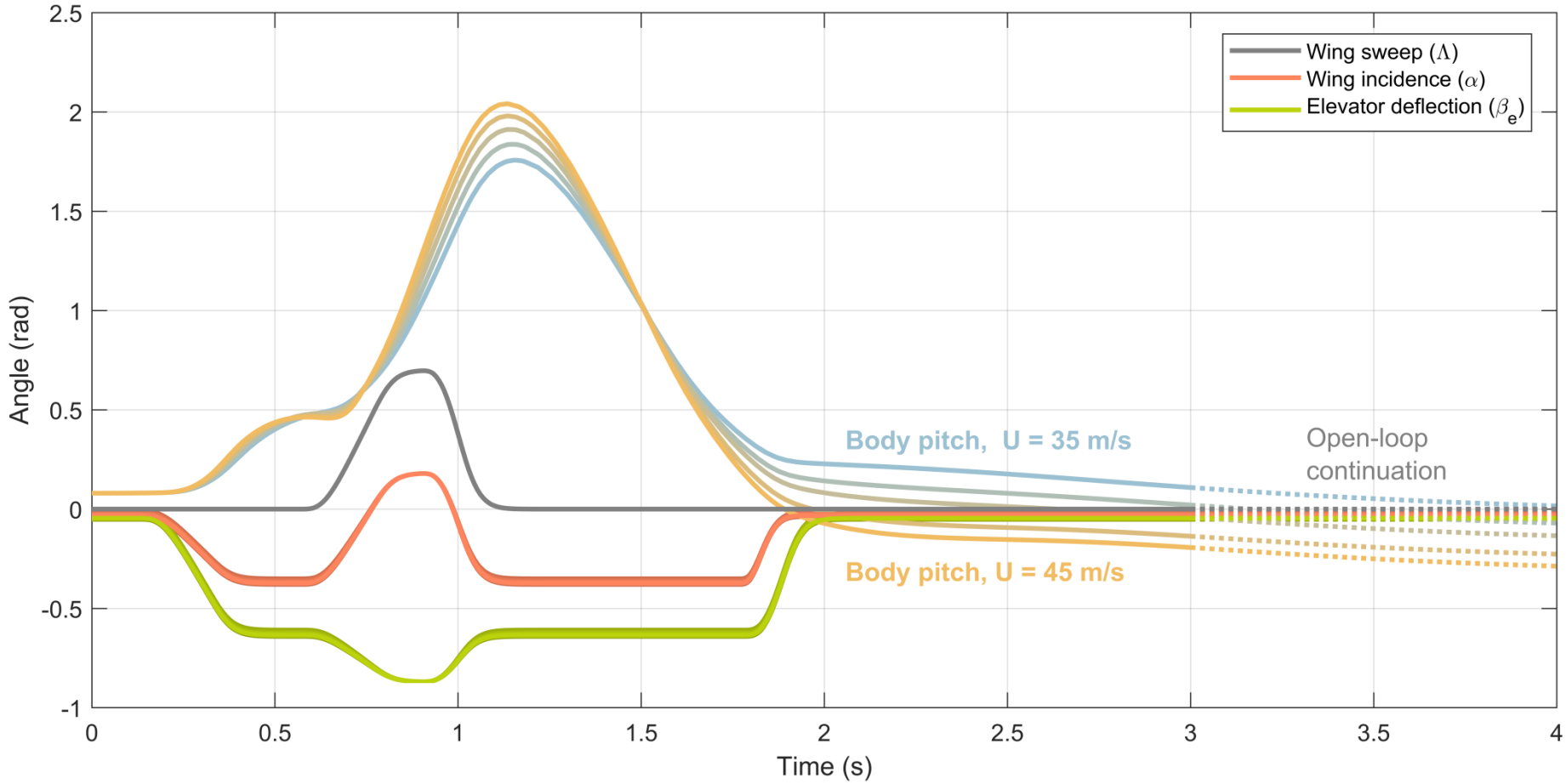

Figure 7.3.10: Flight simulation results for the sweep- and incidence-morphing cobra manoeuvre under varying initial airspeed (U). Body pitch angle and control histories (Λ-α-β_e) are shown, including the very small variation in trim state properties across the simulated airspeed range.

7.4. RaNPAS: PERTURBATIVE MANOEUVRES IN YAW

7.4.1. Motivation

The second orientation in which RaNPAS capability is relevant is the yaw (sideslip) angle. Cobra-type manoeuvres in the yaw DOF are attested in thrust vectoring aircraft [1], though the published literature is relatively minimal. A similar manoeuvre, referred to as the *hook*, is also attested [12–14]: it is often referred to as a horizontal-plane equivalent of the cobra, but in fact refers to a RaNPAS pitching manoeuvre (cobra) performed at 90° roll angle. Gal-Or [1] refers to the true yawed-cobra, at zero roll, simply as yaw RaNPAS capability. Here we suggest the term *rattlesnake* (see Figure 7.4.3) as an analogy of the cobra manoeuvre.

In thrust-vectoring, delta-wing aircraft, RaNPAS motion in yaw is generally expected to lead to less energy dissipation than in pitch, as this is a result of the lower frontal surface area of the aircraft in yaw. For this reason yaw RaNPAS has been considered to be more relevant to air combat manoeuvring, with Gal-Or [1] suggesting a 90° roll, roll stop, and RaNPAS in yaw (rattlesnake), as an energy-efficient method of achieving the same rotation as a cobra manoeuvre. However, in the biomimetic case study system – and in physical implementation of such a system – a significant difference in energy dissipation is less likely to be observed, due to the relative symmetry of the fuselage. The flip side of this is that, in the case study system, the cobra manoeuvre itself is likely to be relatively more useful for air combat manoeuvring RaNPAS than it is in thrust-vectoring delta-wing aircraft, as the pitch RaNPAS drag levels are likely to be similar magnitude to the (small) yaw RaNPAS levels.

7.4.2. Manoeuvre design via constrained quasi-trim state

In the case of RaNPAS pitching motion, the cobras of Section 7.3, manoeuvre design was carried out using quasi-trim states to generate maximal pitch-up and pitch-down moment in specified environments. An analogous process in yaw would be able to compute optimal yaw-left and yaw-right states and would thus enable RaNPAS yawing motion via the same principle. However, in Section 7.3.2 it was easy to constrain the optimal quasi-trim states to the appropriate manoeuvre plane (x-z) via enforcing aircraft symmetry about this plane – leading to an unconstrained optimisation of the pitching moment. RaNPAS yawing motion, on the other hand, is symmetry breaking by necessity. The x-y planar constraint – zero pitching and z-translational acceleration – must thus be enforced as a nonlinear constraint

on the optimisation. This process generates optimal yaw-left or yaw-right states at specified yaw and pitch angles (ψ_s, θ_s). Figure 7.4.1 shows several such states with their lateral stability / yaw acceleration profiles, under the morphing limits of sweep and dihedral $|\Lambda|, |\Gamma| < 0.8$ rad, incidence $|\alpha| < \pi/2$ rad and the elevator and rudder control limits $\pm 50°$. Results A-C indicate pitch stability plots for optimal yaw-left states at $\psi_s, \theta_s = 0$, with (A) all degrees of freedom active, (B) sweep and incidence active and (C) only incidence active. Result D represents the lateral stability profile of the trim state at (ψ_s, θ_s). Tables 7.4.1-7.4.2 shows the control configurations for these states.

Table 7.4.1: Parameters for optimal yaw-left states $\psi_s = 0$

Parameter (rad)	**(A)** All DOF	**(B)** Λ-α	**(C)** α
$\ddot{\psi}$ (rad/s)	-96.4	-80.0	-79.5
Γ_l (rad)	-0.37	0	0
Γ_r (rad)	**0.80**	0	0
Λ_l (rad)	0.099	0.085	0
Λ_r (rad)	**0.80**	0	0
α_l (rad)	1.41	1.45	1.45
α_r (rad)	-0.40	0.065	0.065
β_e (rad)	0.019	0.077	0.075
β_r (rad)	-0.52	$-$**0.87**	$-$**0.87**

Table 7.4.2: Parameters for optimal yaw-left states $\psi_s = -0.7$ rad (40°)

Parameter (rad)	**(A)** All DOF	**(B)** Λ-α	**(C)** α
$\ddot{\psi}$ (rad/s)	-54.1	-38.8	-10.5
Γ_l (rad)	-0.21	0	0
Γ_r (rad)	**0.80**	0	0
Λ_l (rad)	0.70	0.71	0
Λ_r (rad)	0.33	0	0
α_l (rad)	1.34	1.36	1.21
α_r (rad)	-0.60	0.059	0.084
β_e (rad)	0	0.14	0.074
β_r (rad)	$-$**0.87**	$-$**0.87**	$-$**0.87**

Several points should be noted. The dihedral degree of freedom is largely irrelevant; the advantage of using 6DOF morphing over sweep and incidence (4DOF) is minimal. Planar-constrained quasi-trim states do exist at nonzero ψ_s for the system with incidence-only morphing: this is notable because true trim states do not exist in this environment, and opens the possibility of using incidence-only morphing for RaNPAS even though quasisteady NPAS is not available. These incidence-only quasi-trim states are, moreover, competitive

with the sweep and incidence morphing leftwards-yaw states, both in terms of the yaw acceleration objective function, and the range of yaw angles at which leftwards-yaw acceleration is generated. The trim state at $\psi_s, \theta_s = 0$ itself shows a wide zone of stability (Figure 7.2.1); sufficiently so to function as the stabilising state for these RaNPAS manoeuvres. There is thus no need to design specific stabilising (rightwards-yaw) states.

7.4.3. Manoeuvre simulation

In the manner of the simplest cobra manoeuvre in Section 7.3, a simple perturbation of the control configuration to one of the leftwards-yaw states in Figure 7.4.1/Tables 7.4.1-7.4.2 is sufficient to perform a large-yaw angle RaNPAS manoeuvre. Figures 7.4.2-7.4.3 show two such manoeuvres. Figure 7.4.2 utilises a constrained leftwards-yaw state at $\psi_s = -40°$ rad, based only on incidence morphing. In the case study system, with only incidence morphing, it appears impossible to reach a state of $\psi < -90°$. Figure 7.4.3 utilises state at $\psi_s = -40°$ rad based on incidence and sweep morphing, and reaches a state of $\psi = 99°$; analogous to a cobra. The yaw responses are oscillatory, but the stability of the trim state is such that the aircraft stabilises to near zero, with relatively minimal change in flight path.

7.4.4. Generalised RaNPAS

Analogous to the pitch-yaw coupled NPAS capability analysed in Chapter 6, Section 6.4.3, the possibility of coupled pitch-yaw coupled RaNPAS manoeuvres stems immediately from the demonstration of capability in pitch and yaw independently. An easy method for the design of such manoeuvres is also thus apparent; via constrained quasi-trim state analysis in an arbitrary 3D rotation objective direction and constraint plane. If such states exist, then they can be used to design RaNPAS manoeuvres around their associated rotation axes. For reasons of space, such manoeuvres are not simulated in this work; and there are several interesting questions which are left open – particularly regarding the effect of the available active morphing degrees of freedom on the space of available manoeuvres. Analogous to the trim state analyses in Chapter 6, Section 6.2, it should be possibility to compute polar plots of the constrained-state acceleration rates, and another performance metrics, available at different RaNPAS rotation axes, and thereby compare system and morphing DOF RaNPAS effectiveness in general. This is a particularly interesting topic for future research.

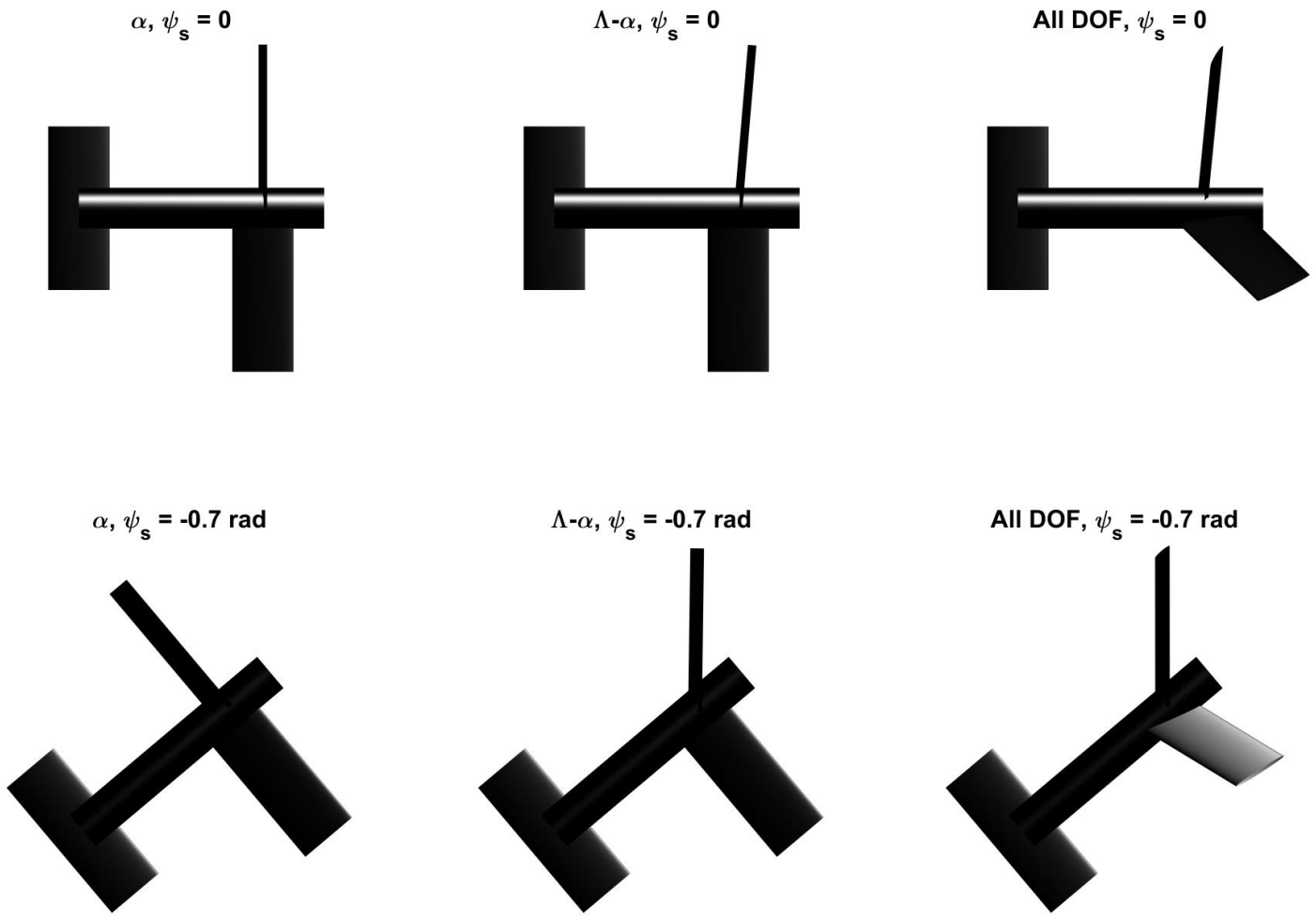

Figure 7.4.1: Six constrained leftwards-yaw quasi-trim states, under variable ψ_s and active morphing DOF combinations.

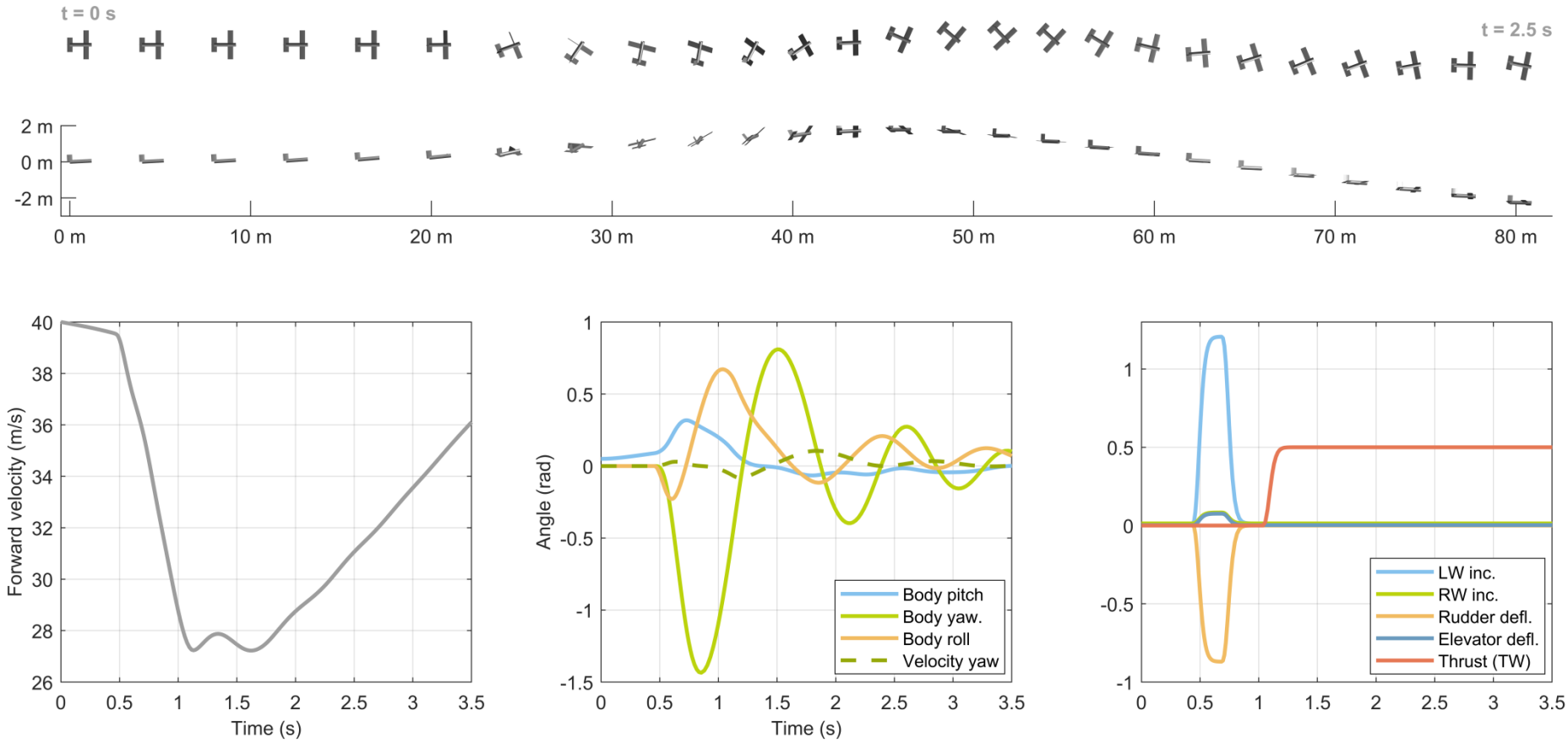

Figure 7.4.2: Flight simulation results for a 2DOF-morphing (LW/RW incidence) yaw RaNPAS manoeuvre, designed via constrained state analysis: flight path with aircraft rendered every 50 ms ($0 \leq t \leq 2.5$ s); forward velocity history, orientation history including the yaw angle of the aircraft velocity; and the aircraft control history.

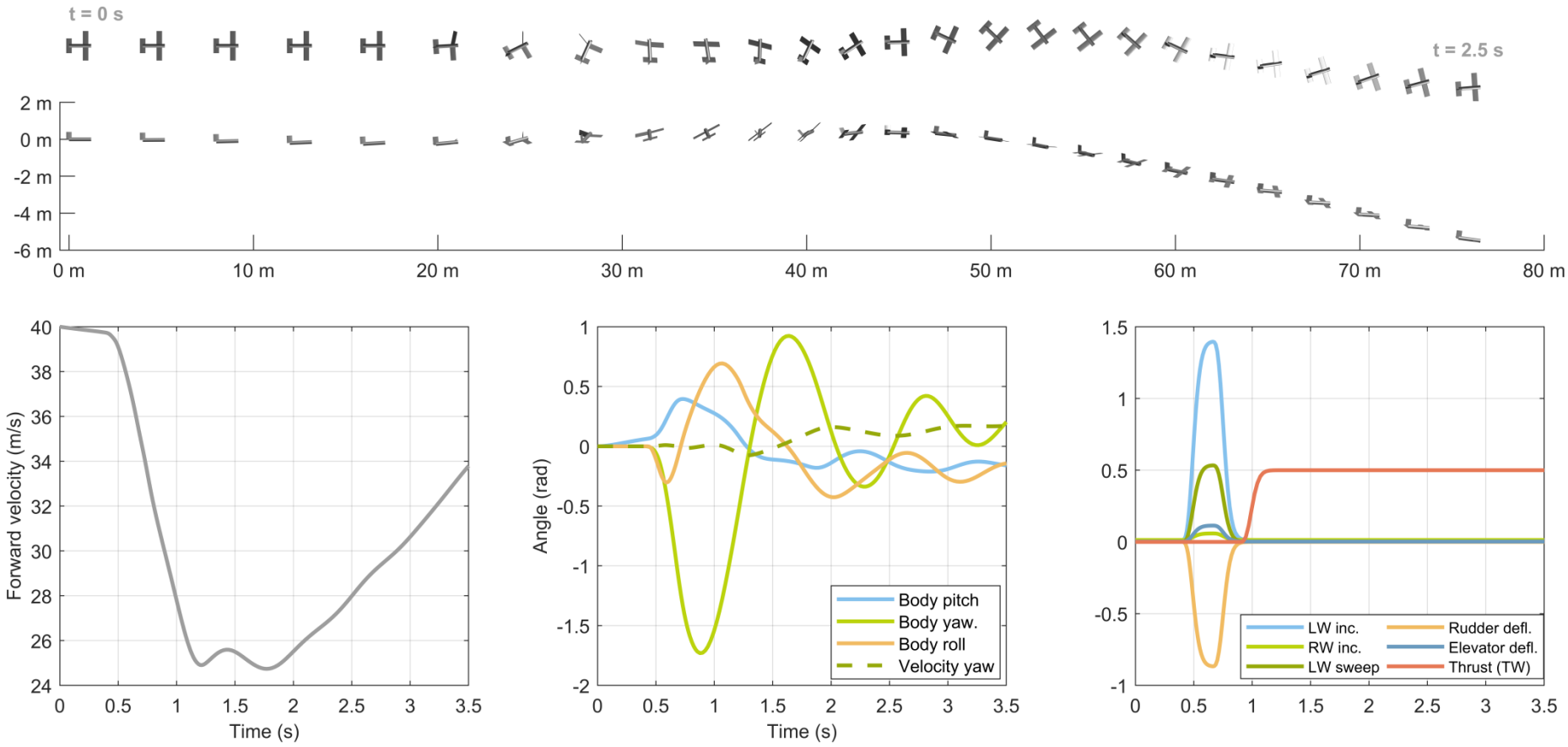

Figure 7.4.3: Flight simulation results for a 4DOF-morphing (LW/RW sweep/incidence) yaw RaNPAS manoeuvre, designed via constrained state analysis: flight path with aircraft rendered every 50 ms ($0 \leq t \leq 2.5$ s); forward velocity history, orientation history including the yaw angle of the aircraft velocity; and the aircraft control history.

7.5. BALLISTIC TRANSITION

7.5.1. Motivation

Even leaving aside the associated use of ranged weapons, RaNPAS manoeuvres have no direct parallels in biological supermanoeuvrability. This may indeed be connection with the close association with such weapons: in their absence, true RaNPAS manoeuvres show minimal utility, and such capability has either not evolved or is not commonly observed. Nevertheless, some biological manoeuvres do show correspondences with more general forms of NPAS capability; though their motivation is not primarily to effect orientation changes, but rather the use of the aerodynamic effects of these changes. One such manoeuvre is the ballistic transition, observed in a variety of gliding mammals [15–17] (See Chapter 1, Section 1.2.5). In the ballistic transition manoeuvre, there is no pitch-down state: the objective is to decrease the airspeed of the aircraft in preparation for an impact landing on a vertical surface.

This corresponds to a form of point-and-hold NPAS, similar to the capability analysed in Chapter 6. However, in this case the objective is not to maintain a constant-airspeed trim state, but to maximise aircraft deceleration. Thus, even within the limited angle-of-attack range available to the trim states of Chapter 6, Section 6.2, the optimal ballistic transition state will be different. However, higher angles of attack would be expected to maximise drag forces further. Thus, in fact, the RaNPAS cobra manoeuvre serves as a useful template for designing a ballistic transition.

7.5.2. Manoeuvre design and simulation

In the case study system, a ballistic transition manoeuvre can be performed with a simple modification of the cobra controls. Generating a pitch-up moment via a 2DOF (Λ-α) morphing pitch-up state (Table 7.3.1/Figure 7.3.2), instead of transitioning subsequently to a pitch-down state, the aircraft transitions to a neutral state which maintains a high pitch angle at decreasing airspeed until the point of impact. A useful example of a conveniently-located near-neutral state is the pitch-up state but with zero incidence and elevator deflection, and only forward sweep. In a manoeuvre of maximum simplicity, this state may be maintained until impact landing.

Figure 7.5.1 shows a simulation of a ballistic transition manoeuvre in the case study system, utilising this sequence of control configurations. The objective is a low-velocity impact landing on a vertical surface 50 m away, starting at forward velocity of 60 m/s. The effect of a varying constant thrust value ($0.2 < T/W < 1$) is shown. The control configurations are completely specified, as per above, and only the state timings are free. For all the simulated thrust values, the ballistic transition manoeuvre is successful: the aircraft lands in an almost exact vertical position, with both the horizontal and vertical velocity < 12 m/s. The use of forward sweep, and the corresponding reduction in wing aeroelastic divergence speed, is likely to limit the initial airspeed of the manoeuvre: a more versatile manoeuvre sequence is to use incidence morphing (and, if available, dihedral) for initial airspeed reduction before a sweep morphing phase. Aeroelastic tailoring is also an option to increase the divergence speed.

Even in the worst case, $T/W = 0.2$, the system kinetic energy is reduced by 94% at the point of impact, with near-zero altitude change. The primary effect of T/W is to increase the altitude gain through the manoeuvre, reducing the system kinetic energy via transfer to gravitational potential. Maximal levels of kinetic energy dissipation (up to 98.6%) are thus associated with maximal available thrust (at least, up to $T/W = 1$). However, the effect of T/W on the aerodynamic energy dissipation is only secondary, as evidenced by the total energy trends: optimal total energy dissipation occurs at $T/W = 0.6$, but the variation is not large. The use of altitude gain for kinetic energy is useful but a) may or may not be permissible in the context of the impact landing, and b) may be achievable through finer morphing control at lower T/W.

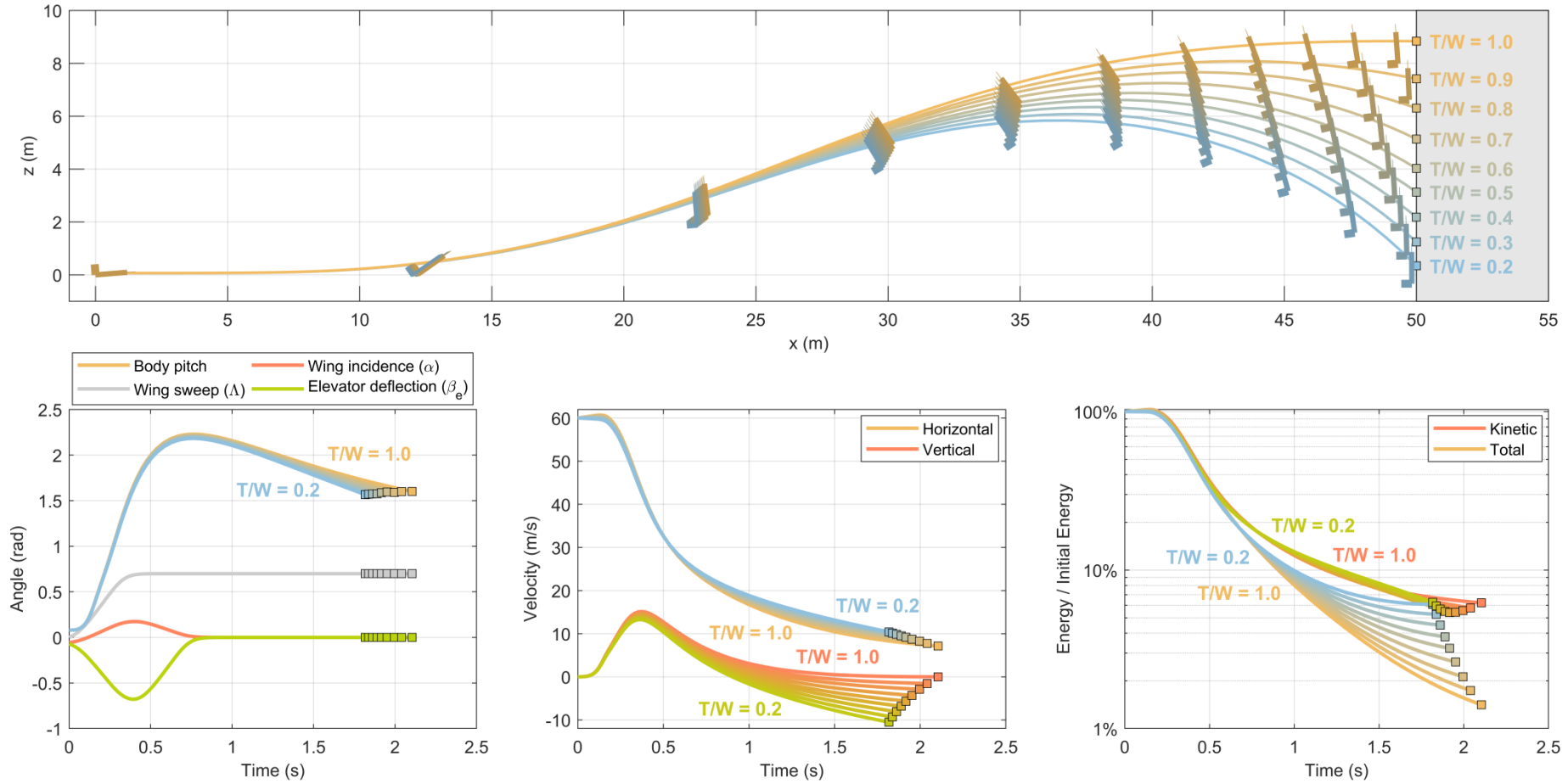

Figure 7.5.1: Flight simulation results for a ballistic transition manoeuvre with initial velocity 60 m/s, under varying initial thrust (T/W). Aircraft flight paths, body pitch angle histories, horizontal and vertical velocity, and relative total and kinetic energy histories. The aircraft state sequence is: trim → pitchup → stabilisation state.

7.6. ANCHOR TURNS

7.6.1. Motivation

Stall or anchor turns represent one of the most interesting, and apparently widespread, of biological supermanoeuvres. However, as alluded to in Chapter 1, Section 1.2 the details of the aerodynamic and morphing-wing dynamic effects associated with this manoeuvre are complex and remain obscure. The presence of a single unified method or characteristic across different flying species or flight regimes has not been demonstrated.

In pigeons (*Columba livia*), studies by Warrick and Dial [18,19] characterised the anchor turn as involving an inclination of the inboard wing to a high angle of attack during low-airspeed flight, causing it to stall and generating a drag-induced turning moment, and lift-induced bank angle. In steppe eagles (*Aquila nipalensis*), high-angle inclination of the hand-wing (outer wing section) is observed to yield similar rapid turns [20], and in flying squirrels [21] both drag and lift-based turns controlled by lifting surface inclination have been observed. The latter suggests the existence of multiple anchor turning mechanisms even in the absence of flapping-wing propulsion; and indeed, Warrick and Dial [18] also found evidence that supination (negative incidence) on the inboard wing can be used to generate similar turning motion solely through the drag-induced moment. There are, of course, further mechanisms utilising continual flapping propulsion: the use of asymmetries in wing downstroke velocity, or asymmetries in wing flex (adduction/extension); both to generate asymmetries in lift, with a corresponding bank angle and rotation in yaw [19]; and the use of anterior (forward) sweep and extreme pronation motions [22]. This study, however, concentrates on the most widely attested mode of anchor turning; via inboard wing inclination.

7.6.2. Heuristic design and simulation

On the basis of this biological literature, an analogous turn in the case study system can be designed through heuristic methods. The manoeuvre designed and studied here consists of four components. The aircraft enters the turn during an unpowered climb; the purpose of which is to bleed off speed before the turn. The simulation is started part way up this climb, with the aircraft at a high pitch and flight path angle (40°) and at a low airspeed (18 m/s). Initially, a slight rudder deflection is used to prepare the aircraft for the turn, which is then

initiated by inclining up the inboard wing to a very high drag state (75°). Simultaneously, the outboard wing is inclined down (to $-23°$) to reduce its drag, and the rudder takes a hard leftward state ($-50°$). Both operations contribute to a strong coupled pitch-yaw-roll motion in the aircraft, rotating it first to a nose-left position and then to a nose-down position, and rapidly decreasing its forward airspeed.

As the aircraft turns the throttle is increased (up to T/W $= 1$) to pre-emptively gain airspeed for the turn recovery. Before the nose-down position is reached, the aircraft transitions to a corrective state in which the control inputs are reversed: the outboard wing is inclined upwards (75°), the inboard returns to level (0°), and the rudder to a moderate rightward yaw position (29°). This slows the rotation of the aircraft and causes it to the turn at a c. 90° roll angle. The aircraft is restored to level by a corrective state with moderate left wing incidence, at which point at which point a near-trim state can be resumed while the aircraft loses altitude and regains airspeed in its new orientation (c. 90° to the original).

Figures 7.6.1-7.6.3 shows the results of a flight simulation of this anchor turn manoeuvre. The entire set of manoeuvre parameters have been tuned manually to provide appropriate levels of rotation and correction, but only left and right wing (LW/RW) incidence morphing and the tailplane control surfaces are utilised, and the thrust is limited to T/W $= 1$. As can be seen, the turning manoeuvre is successful, with the aircraft transitioning in 4 s to a flight path rotated by 90° at level pitch and yaw, with near-collinear velocity and orientation, and undergoing a stable altitude loss / airspeed acceleration. However the turning performance is not spectacular: the turn radius is c. 15 m (c. 9 wingspans); significantly larger than has been observed in biological flight. However, under a heuristic approach it is difficult to find avenues to increase this performance. It is clear a more formal method of manoeuvre design is required

7.6.3. Constrained quasi-trim space design and simulation

A more general method for the design of anchor turns involves the constrained quasi-trim state analysis developed in Section 7.4.2. We seek a small set of such states, optimised at a particular quasisteady environment under appropriate constraints, which can be interpolated through to yield a manoeuvre. Based on the heuristic anchor turn performance

in Section 7.6.2, the aircraft enters the turn at a near-trim state during an unpowered climb (30°, 20 m/s), and the turn is initiated by a strong leftward yaw rotation (as per Figures 7.6.1-7.6.3).

Generating this yaw moment can be achieved by exactly the same constrained quasi-trim states that were computed in Section 7.4.2. The aircraft configuration (all morphing and control DOFs) is optimised to generate maximal leftward yaw acceleration / moment at specified airspeed U_s and yaw angle ψ_s, subject to the constraints of zero pitching and z-translational acceleration, and specified control limits (sweep and dihedral $|\Lambda|, |\Gamma| < 0.8$ rad, incidence $|\alpha| < \pi/2$ rad, elevator and rudder $\pm 50°$). The effects of the choice of U_s and ψ_s on the optimal state may then be noted. U_s has a relatively minimal effect, with the caveat that it must be above a critical value (the local stall speed, dependent on ψ_s) for the pitch and z-translational acceleration constraints to be satisfied. As in this manoeuvre the initial velocity is below this value, the optimisation airspeed is increased (to 30 m/s) to ensure these constraints are properly taken into account.

The effect of ψ_s, on the other hand, is both significant and discontinuous. Figures 7.6.4-7.6.5 show the effect of ψ_s on a system with all-DOF morphing, and one with only sweep and incidence (Λ-α) morphing. In the Λ-α system, quasi-trim states only exist up to c. $|\psi_s| = 1$ rad, and these are indeed largely based on wing incidence, consistent with the biological literature. The left wing is inclined to high angle, swept forward ($\Lambda_l \approx -\psi_s$), and at near-zero dihedral; the right wing incidence takes a small corrective value, with sweep and dihedral near-zero; and the elevator and rudder deflection take appropriate extreme values. However, beyond c. $|\psi_s| = 1$ rad these type of states are unable to satisfy the planar quasi-trim constraints; and moreover, generate instantaneous stabilising yaw moments.

An extension to all-DOF morphing enables constrained quasi-trim states to exist at all yaw angles. At small yaw angles, the optimal constrained yaw-left states show a qualitative similarity to the Λ-α case, with high left wing incidence, but also with stronger forward sweep and asymmetric wing dihedral. However, beyond c. $|\psi_s| = 0.6$ rad – a value which may be associated with the limit of yawed trim state existence under dihedral morphing, cf. Chapter 6, Section 6.2.4 – the optimal state changes to be radically different, with a step

change in right wing sweep and incidence, and a continual reduction in left wing incidence. Further step changes in the optimal elevator deflection are observed, and the results are complex, but leftwards yaw states can be generated for all ψ_s. The most problematic area is the dead zone at c. $|\psi_s| = 1.7$ rad, in which only minimal leftwards-yaw moments can be generated: the aircraft must rely on momentum to pass though this zone.

These optimal states allow the aircraft to be rotated to nose-backward positions. At the most complex, a model-based control procedure could be devised in which optimal constrained states are computed as the manoeuvre progresses, potentially taking into account other current aircraft state information (e.g. angular velocities). However, a simpler alternative method is to take two states at discrete points, and transition between the two when required. In this manoeuvre, states are taken at $\psi_s = -0.6$ rad, $U_s = 23$ m/s under Λ-α morphing (to minimise the initial forward sweep); and at $\psi_s = -1.6$ rad, $U_s = 33$ m/s under all-DOF morphing (as the Λ-α morphing is insufficient at these angles). The transition between must be tuned, manually or automatically, to ensure that the aircraft transitions to the sweep/dihedral regime state before stabilising yaw accelerations are generated.

Flight simulations up to and beyond these two states are shown in Figures 7.6.6-7.6.8: there, State 1 represents the initial near-trim state, and States 2 and 3 the optimised leftwards-yaw states in the two respective regimes. After transitioning through these three states, the aircraft is in a free-fall environment, with low horizontal airspeed; at a high negative yaw angle (below $-90°$), rapidly decreasing; and at a negative pitch angle, also rapidly decreasing. The latter is the highest priority for control action: strong pitch-up acceleration is required to minimise altitude loss; by increasing the aircraft free-fall drag, eliminating the downward vertical thrust component of aircraft thrust, and accelerating the aircraft in its new yaw direction through the horizontal thrust component. Anticipating the motion of the aircraft, a loose description of the optimisation environment is taken: airspeed vector $\mathbf{u}_s = [-10, 0, -10]^T$ m/s, representing reversed and falling flight; pitch $\theta_s = -0.6$ rad; and roll $\phi_s = 0.4$ rad. In this environment the aircraft configuration (all DOFs) is optimised to generate maximal upwards pitch yaw acceleration / moment, subject to the constraints of zero yaw acceleration and horizontal (x,y) translational acceleration and the same control limits. The resulting optimal state is designated as State 4 in Figures 7.6.6-7.6.8. It shows

simple dependencies on the environment variables, with the wings at maximum sweep, and anti-symmetric dihedral such that the wings are horizontal in the earth frame of reference ($|\Gamma| = \phi_s$).

This combination of optimised states, timed appropriately, reorients the aircraft to a stable dive at a new yaw angle of $-135°$. The final control action required is a transition to near-trim state to pull the aircraft up from a dive. A state of maximal sweep is taken, with small symmetric incidence and elevator deflection. This is not an optimal state, but the requirement for lateral symmetry restricts the morphing space significantly, and so a heuristic approach is feasible. Finally, an increase in propulsion from zero initially (to maximise the loss of airspeed) to T/W = 1 when the aircraft is reorientates (to maximise the regain of airspeed) is overlaid on the manoeuvre.

This completes an anchor turn manoeuvre through 135°: Figures 7.6.6-7.6.8 show the full finalised turn. The transitions between states require tuning, but the key working states (2-4) are generated via constrained optimisation, with a relatively small set of free parameters (e.g. ψ_s for 2-3). The turn performance is good, with a turn radius (in the x-y plane) of c. 4 m or c. 2.5 wingspans – approaching biological capability. The quasisteady acceleration predictions from optimisation (Figure 7.6.5 and other data) match reasonably well with the observed dynamic accelerations of the aircraft. The key difficulty in performing the manoeuvre is the large altitude cost: c. 35 m loss from the apex to a point of zero pitch, with the flight path still not yet stabilised. Even with further optimisation, it is unlikely that the case study system will be able to approach the minimal levels of altitude loss observed biologically (cf. Chapter 1, Section 1.2.2), as biomimetic propulsion systems allow a degree of hovering capability via thrust / wing force vectoring that cannot be replicated. Such hovering-based turning manoeuvres probably cannot be categorised as anchor turns in the way that this term has been characterised here. The manoeuvres studied here bear significantly more affinity to the Herbst manoeuvre in thrust-vectoring aircraft, which is also associated with large altitude losses (Chapter 1, Section 1.2.2).

7.6.4. Concluding remarks

This section considered only two specific anchor turn manoeuvres (90°, incidence-only and 135°, all DOFs). While this forms only a basic study, the flexibility in aircraft states and state timings indicates that a wider spectrum of turns are available. In particular, there is no immediate reason to believe that incidence-only anchor turns are restricted to rotations of 90° of less. However, it is also the case that turns at the extreme end of the spectrum (135°-180°) are probably outperformed by an equivalent flight manoeuvre involving direction reversal via pitch, with a roll transition out of the resulting inverted flight state, and a slight further turn if required; an extension of the cobra and ballistic transition manoeuvres in Sections 7.3 and 7.5. Such a manoeuvre has not been studied in this work, but the system capability demonstrated thus far renders it highly likely to be feasible; and as the control configuration will be symmetric, manoeuvre control and design will be significantly easier. The primary application for anchor turns appears to be turning angles between c. 45° and 135°.

A few further points should be noted. The reliance of forward sweep in the 135° manoeuvre will significantly decrease the aeroelastic divergence speed of the wings [7]. For this reason, a low-sweep state is chosen to initiate the turn. However, during most of the manoeuvre, the aircraft velocity is very low and so this is unlikely to be a major problem; but divergence may make the use of the forward swept state during the final dive and pull-up phase unfeasible. For this reason, and for the reduction of aircraft morphing complexity, the design of high-performance incidence-only anchor turns is an area of particular interest and relevance. A key possibility that was omitted in this analysis, but which shows potential for this purpose, is the use of reverse thrust – in propulsion systems that can conveniently generate it – to decrease the manoeuvre altitude loss, and increase its turning performance.

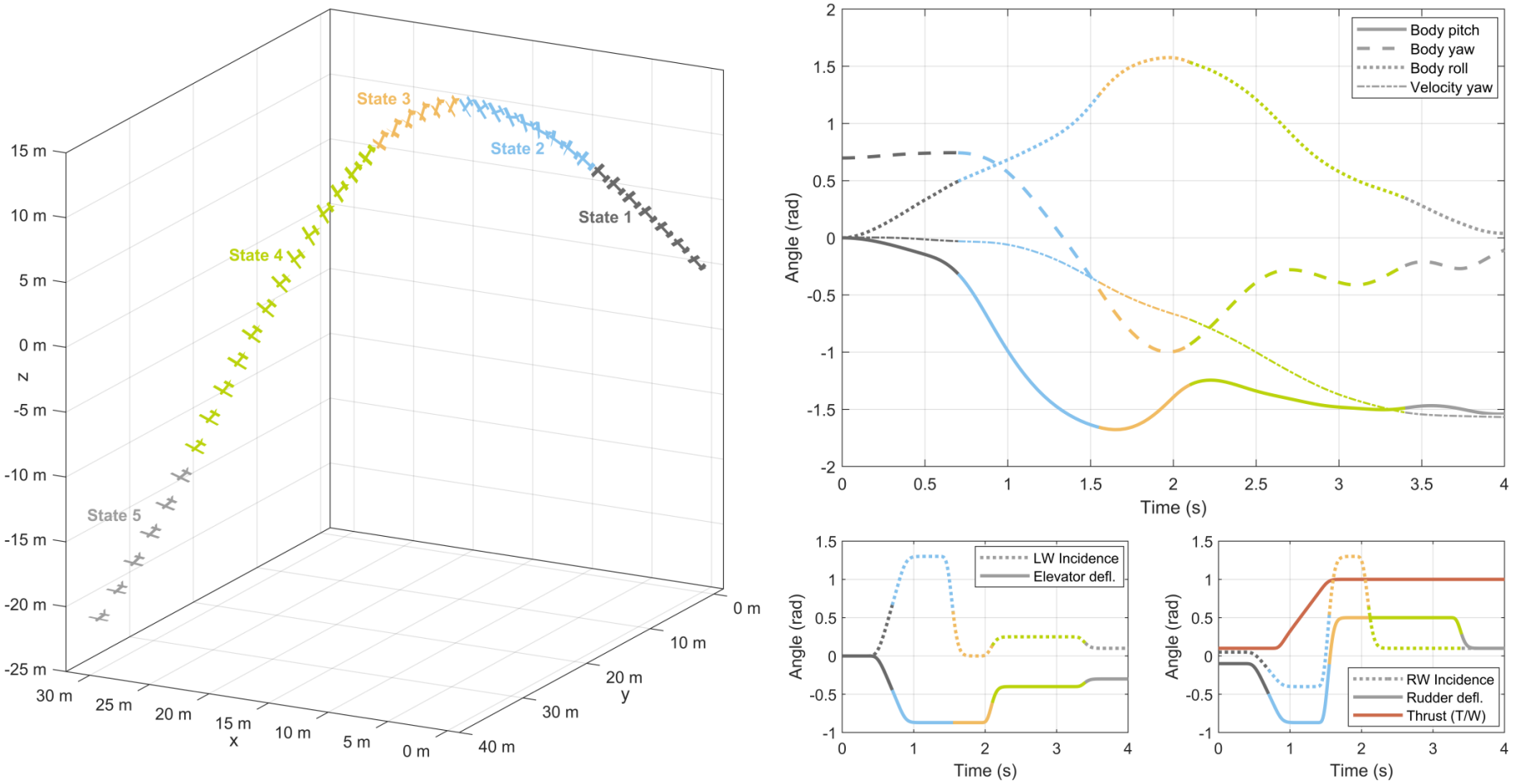

Figure 7.6.1: Flight simulation results for a 90° 2DOF-morphing (LW/RW incidence) anchor turn designed heuristically: flight path with aircraft rendered every 50 ms ($0 \leq t \leq 4$ s) and distinct morphing states indicated; orientation history including the yaw angle of the aircraft velocity; and the aircraft control history.

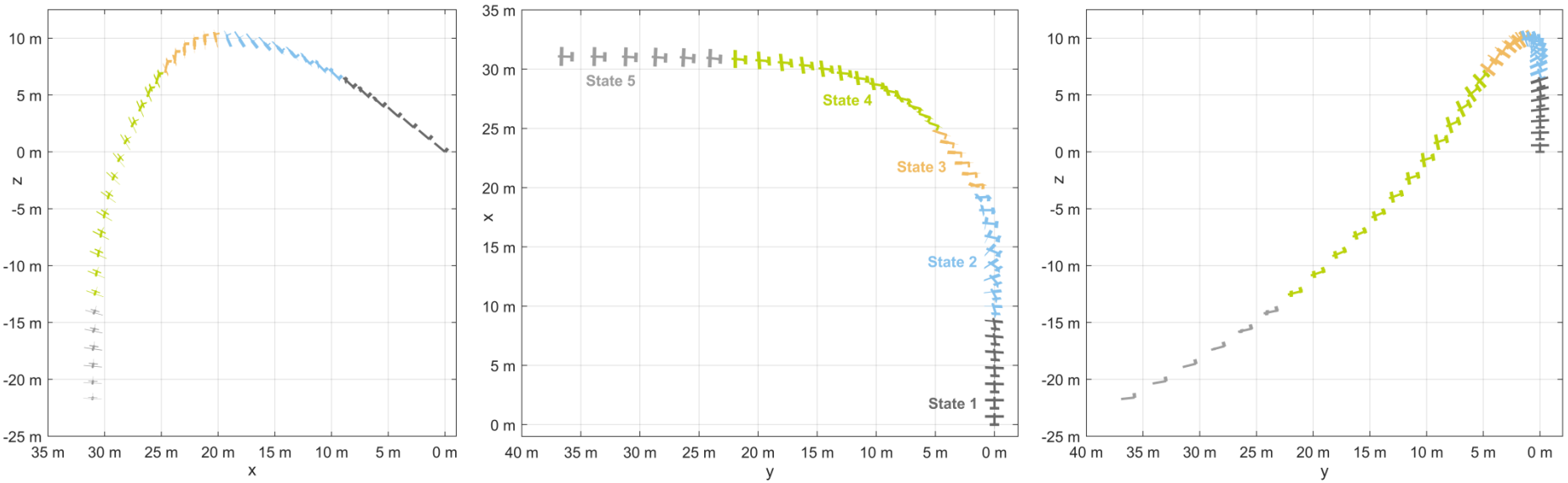

Figure 7.6.2: Flight simulation results for a 90° 2DOF-morphing (LW/RW incidence) anchor turn: orthographic views of the aircraft flight path with aircraft rendered every 50 ms ($0 \leq t \leq 4$ s) and distinct morphing states indicated.

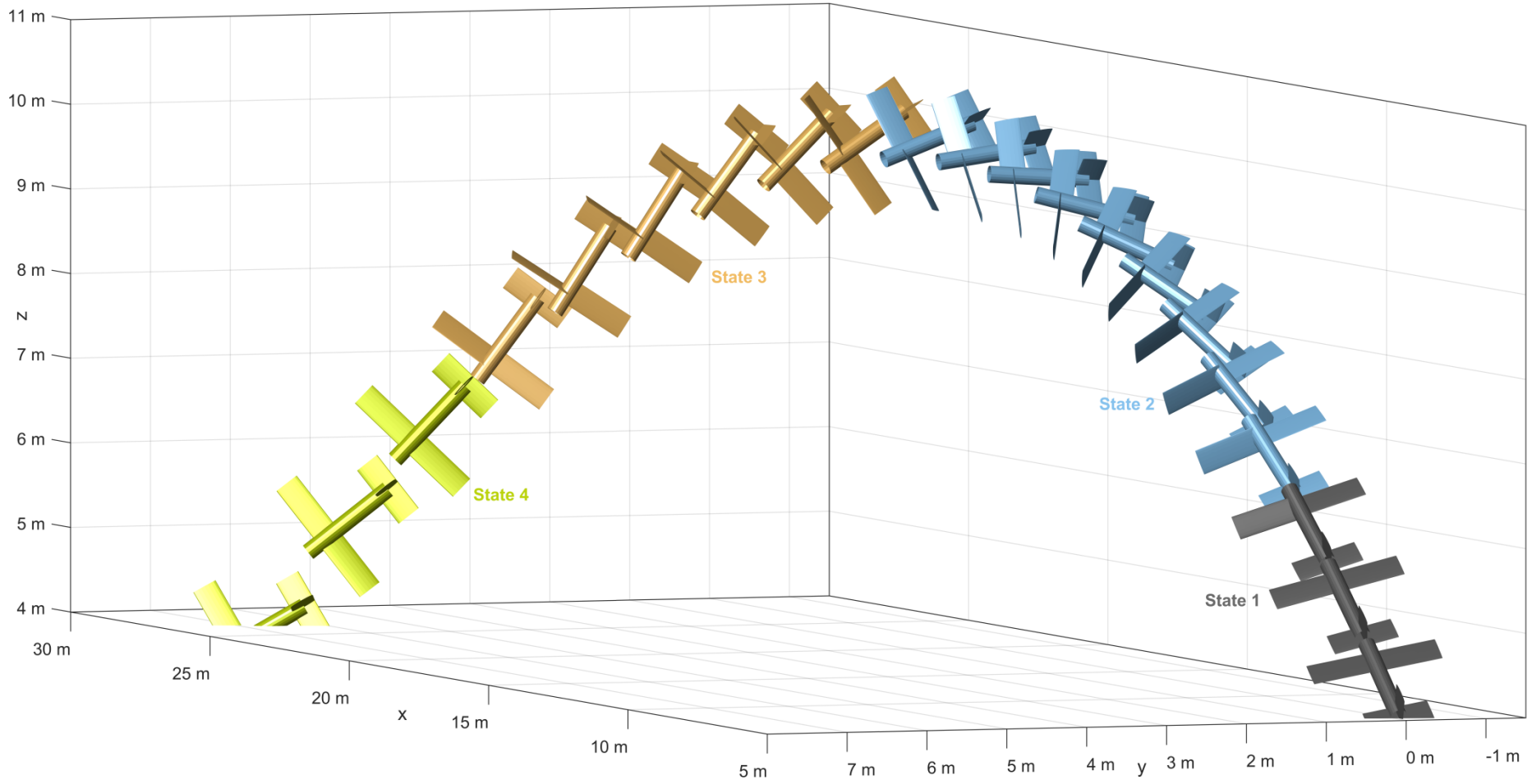

Figure 7.6.3: Flight simulation results for a 90° 2DOF-morphing (LW/RW incidence) anchor turn: close-up of flight path in the vicinity of maximum angular acceleration, with aircraft rendered every 50 ms and distinct morphing states indicated.

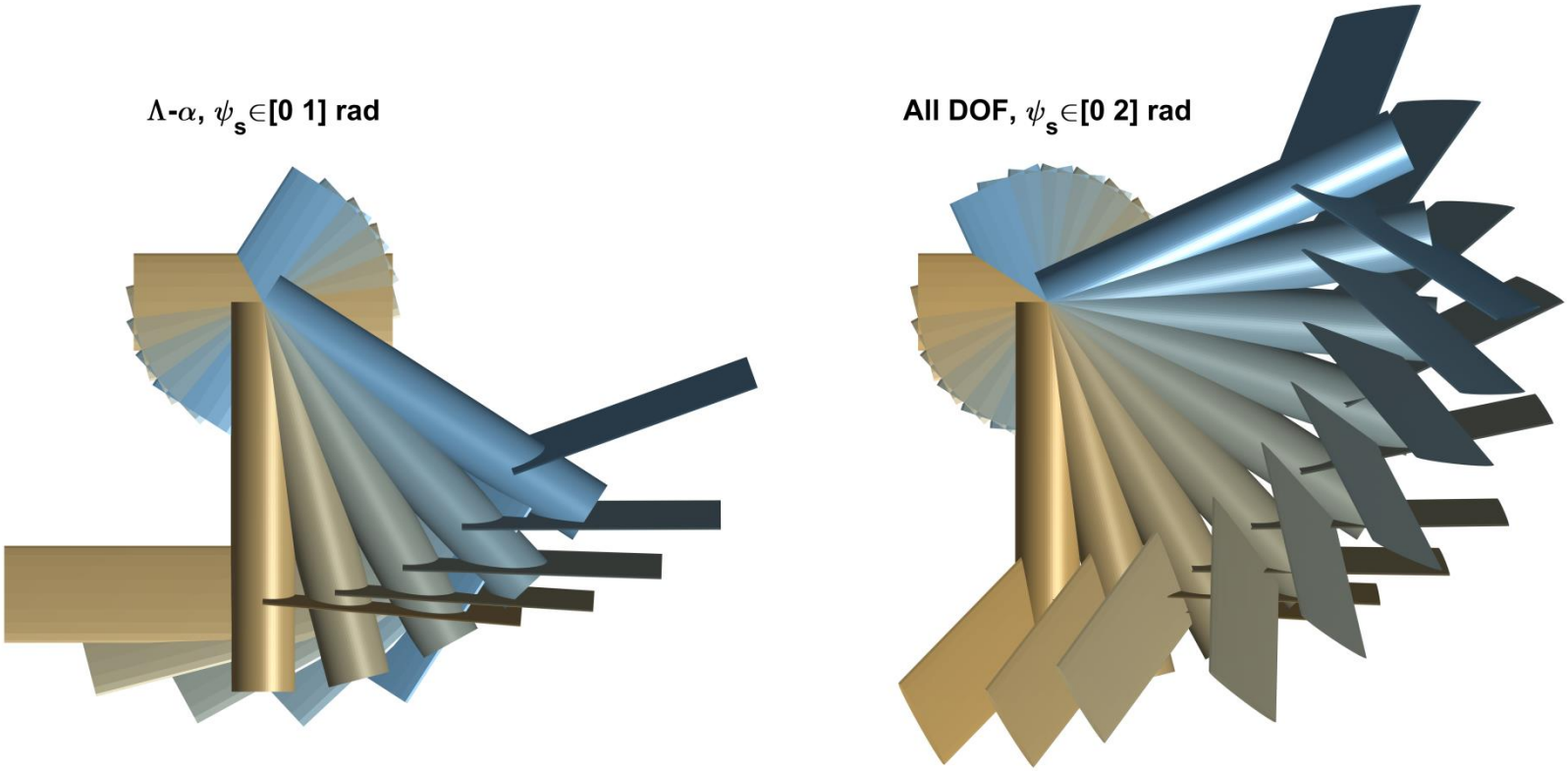

Figure 7.6.4: Visualisation of the constrained leftwards-yaw quasi-trim states, as a function of ψ_s, for Λ-α and all-DOF morphing. The former only exists for c. $|\psi_s| < 1$; the latter exists for all ψ.

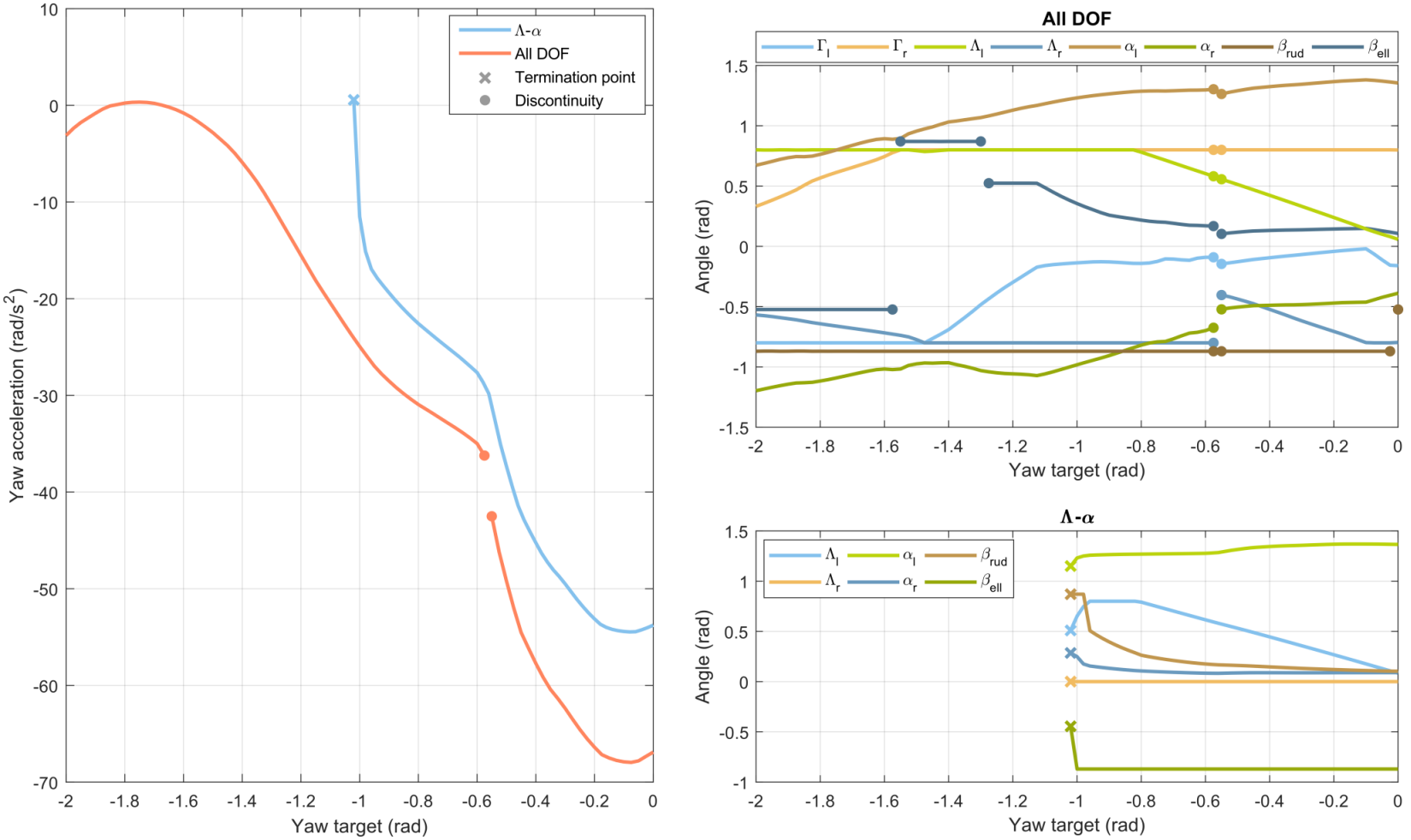

Figure 7.6.5: Control and yaw acceleration profiles for constrained leftwards-yaw quasi-trim states, as a function of ψ_s, for Λ-α and all-DOF morphing. Note the termination of the Λ-α states at c. $|\psi_s| = 1$, and the discontinuities in the all-DOF control and acceleration profiles.

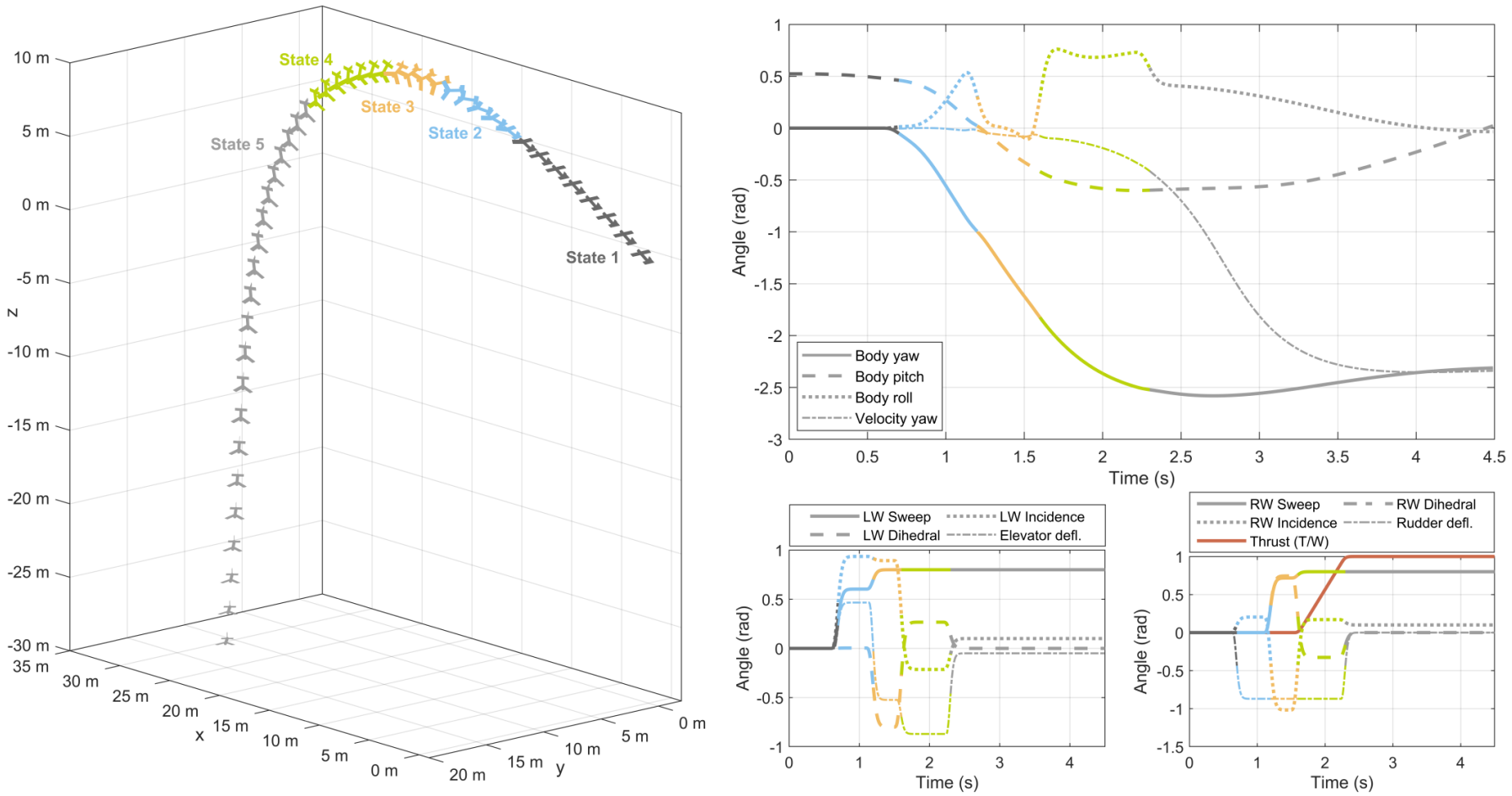

Figure 7.6.6: Flight simulation results for a 135° 6DOF-morphing anchor turn designed via constrained state analysis: flight path with aircraft rendered every 50 ms ($0 \leq t \leq 4.5$ s) and distinct morphing states indicated; orientation history including the yaw angle of the aircraft velocity; and the aircraft control history.

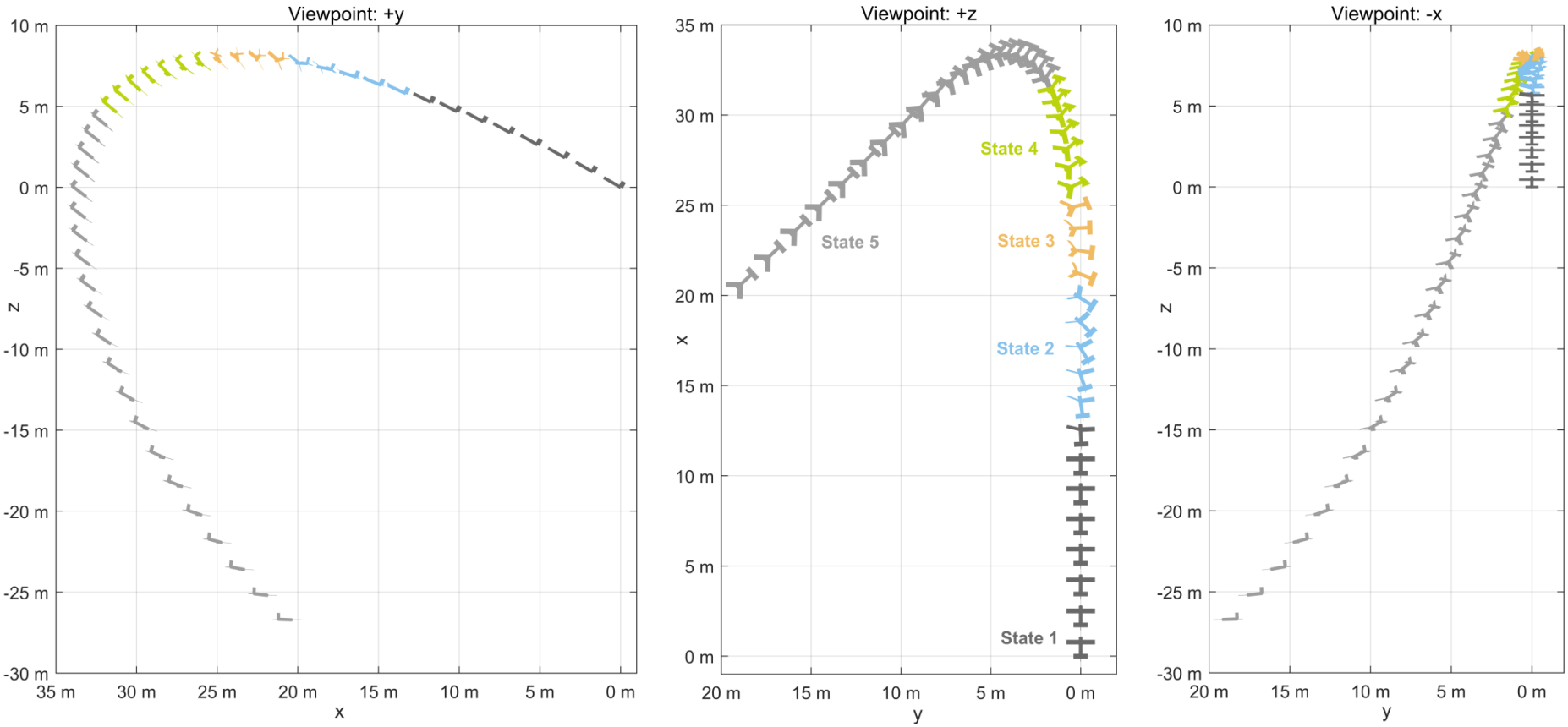

Figure 7.6.7: Flight simulation results for a 135° 6DOF-morphing anchor turn: orthographic views of the aircraft flight path with aircraft rendered every 50 ms ($0 \leq t \leq 4.5$ s) and distinct morphing states indicated.

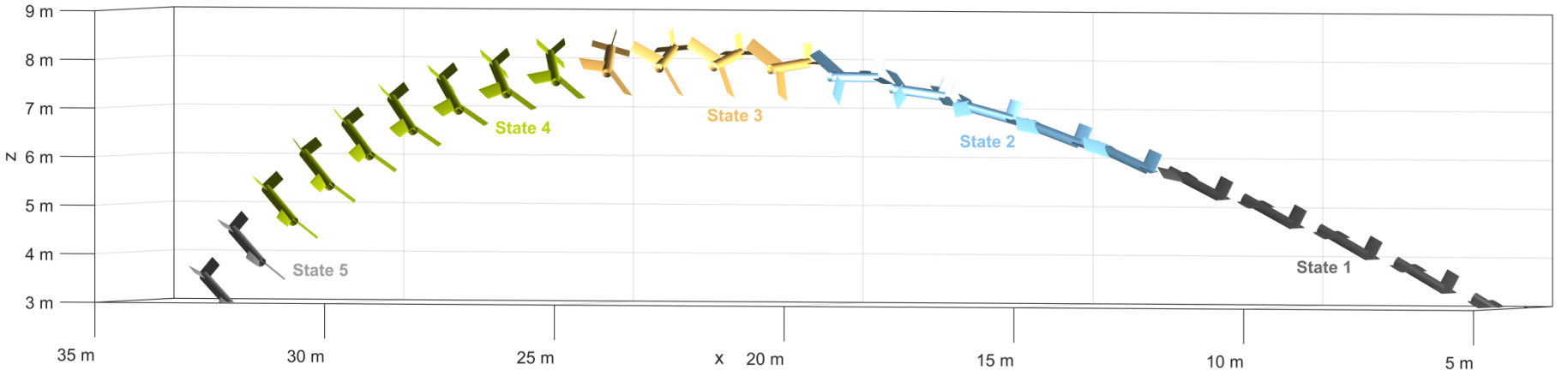

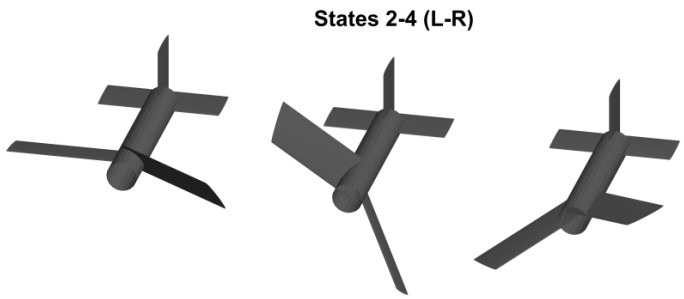

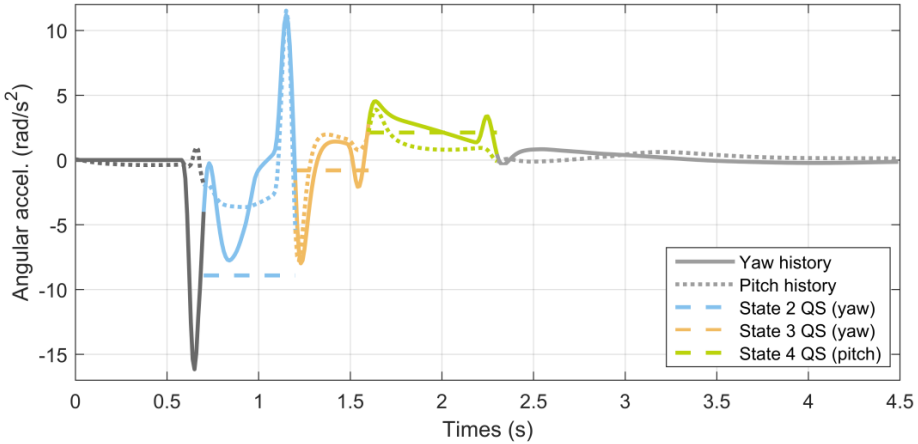

Figure 7.6.8: Flight simulation results for a 135° 6DOF-morphing anchor turn: close-up of flight path in the vicinity of maximum angular acceleration, with aircraft rendered every 50 ms and distinct morphing states indicated; close-up of the optimised morphing states; and angular acceleration histories of the aircraft compared to the quasistatic predictions for the optimised states.

7.7. SYNTHESISED CONTROL SURFACE ACTIONS

7.7.1. Motivation

In Chapter 6 the possibility of high angle-of-attack asymmetric forebody separation was identified as a possible source of simulation error and/or manoeuvre failure for the quasistatic NPAS manoeuvres. This asymmetric separation – one manifestation of which is lateral vortex shedding off the fuselage – may lead to three distinct effects in the aircraft flight dynamics [23]:

- Nose-slicing; in which the aerodynamic yaw moments exceed the rudder control authority, leading to departure from controlled flight via (inertial-frame) yaw.
- Wing rock; an oscillatory instability in roll.
- Coning; a rolling rotation around the aircraft velocity vector axis, when distinct from the reference roll axis. This may be visualised as a rotation of the nose around the velocity vector axis.

The suppression of these effects via passive control surfaces, such as nose strakes, is an area of post-stall aerodynamics research [23,24]; as is the more ambitious goal of controlling them via active control methods [25]. The biomimetic case study system provides an immediate additional mechanism for the latter via the existing biomimetic wing control.

7.7.2. Qualitative arguments for synthesised control

Geometrical arguments indicate that asymmetric yaw and roll moments can be generated independently at high angles of attack by biomimetic morphing. Moment control of this form would correspond to synthesised (morphing-engendered) analogues of the rudder and aileron control surfaces. Asymmetric incidence control can be used to generate coupled inertial-frame yaw and roll moments via asymmetric lift and drag forces. These forces can be decoupled via anti-symmetric morphing from a wing angle-of-attack of zero (leading to drag symmetry); or near-anti-symmetric morphing from a wing angle-of-attack of c. 40° (a lift maxima, leading to lift symmetry). The effects of aerodynamic moment and the location of the aerofoil quarter-chord points are secondary factors. Asymmetric sweep and dihedral control can be used to generate similar yaw-roll coupling via lift/drag deficiency, with the restriction that the direction of motion has little effect; a deficiency will always be

generated. Note that the inertial-frame angles refer to the angular directions of their associated earth-frame angles ($\boldsymbol{\theta}$), with the fuselage as a reference point, as if the aircraft was located at the state $\boldsymbol{\theta} = \mathbf{0}$. This avoids the difficulties with terminology engendered by gimbal lock in the nose-up position.

The presence of these effects will, at least conceptually, allow the generation of uncoupled yaw/roll moments, or moments of the appropriate direction for asymmetric separation control. Practically, however, the effects of the morphing changes on the other system accelerations (e.g. pitching and translational) may not be correctable, and whether the available range of moment directions and magnitudes is actually sufficiently large has not been established. To understand these factors a quantitative test analysis is carried out.

7.7.3. Cobra manoeuvre test case

As a representative context for asymmetric forebody separation, and the associated possibility for control via synthesised control surface action, the cobra manoeuvre studied in Section 7.3 is taken. It is conceptually clear that a degree of synthesised control surface action is possible; and that this could be used to control against the effects of asymmetric forebody separation control: it is a question of whether the magnitudes of the synthesised surface effects are sufficient. The question of whether the actuator response is fast enough requires a more detailed system specification; beyond the scope of this current study.

Analysing the point of maximum pitch angle in the simple cobra simulation (Figure 7.3.4, $t = 0.77$ s), the inertial-frame pitch, yaw, and roll accelerations are computed over the space of left- and right-wing incidence control. The results are surprising. Figure 7.7.1 shows the state of interest in its manoeuvre context, and the inertial-frame pitch, yaw, and roll acceleration fields as a function of the wing incidences. Changes in wing incidence do not significantly alter the pitching dynamics of the aircraft (acceleration changes are $<$30%), and almost always improve the system pitch-down acceleration – in this regard the original state is of near-minimal optimality. Incidence-based asymmetric separation control is thus unlikely to alter the overall behaviour of the cobra manoeuvre. Incidence control does, however, yield a wide spectrum of yaw and roll accelerations. Tracking the contours of zero yaw acceleration within the field of roll acceleration (and vice versa) yields pathways

through the 2D incidence space which represent decoupled yaw and roll control. These decoupled paths represent synthesised (morphing-engendered) analogues to the aileron and rudder; but at much greater control effectiveness.

Figure 7.7.1 shows these decoupled paths/synthesised control surface actions expressed as effective inertial-frame aerodynamic yaw (ψ) and roll (ϕ) coefficients, given as:

$$C_\psi = \frac{I_\psi \ddot{\psi}}{\frac{1}{2}\rho U^2 A_{\mathrm{ref}} L_{\mathrm{ref}}}, \qquad C_\phi = \frac{I_\phi \ddot{\phi}}{\frac{1}{2}\rho U^2 A_{\mathrm{ref}} L_{\mathrm{ref}}}, \tag{7.7.1}$$

where I_i are the appropriate moments of inertia around the c.o.m, U is the state airspeed (33.7 m/s), and ρ is the air density (1.2 kg/m^3). A_{ref} and L_{ref} are reference lengths and areas; the wing planform area and the wingspan, respectively. These effective coefficient control paths are compared with estimates of the expected maximum yaw and roll coefficients generated by asymmetric forebody separation, as per the literature. These are, in yaw, a maximum of $C_\psi =$ c. 0.1 for the Rockwell-MBB X-31 and a generic swept-wing aircraft [23,24]; and in roll, a maximum of $C_\phi =$ c. 0.1 for a generic delta wing aircraft [26]. Note that these maximum values occur at states different to the one considered in this analysis – in yaw, at angle-of-attack c. 60°; and in roll, at angle-of-attack c. 60° and roll angle c. 40°. In the latter case, this large roll angle makes this assessment highly conservative; this comparison serves only to demonstrate that the forces exerted by asymmetric separation are likely to be within the capability of incidence-morphing to control. This does not address the potential for yaw-roll coupled moments induced by asymmetric separation; a decoupled preserves the phenomenological distinction between wing rock (roll), nose-slicing (yaw) and coning (coupled) effects. Not all of these are likely to be a problem simultaneously; and some may be amenable to passive suppression.

There are a wide range of topics for future research in this area, particularly with regard to control design (model-based and non-model-based), transient turbulent effects such as vortex shedding, and the nature and significance of all asymmetric separation effects in a non-delta-wing supermanoeuvrable aircraft. This section demonstrated, in a basic way, that asymmetric incidence morphing offers a range of yaw/roll moment control at high angles-of-attack – including fully-decoupled moments of a magnitude sufficient to control

asymmetric separation effects. The ramifications of this extend beyond asymmetric separation control, to the capability for more general yaw/roll control at high angles-of-attack. This opens up the possibility of the design of more complex variants of the cobra manoeuvre, involving yaw and roll motions; and possibly provides a genesis point for a different form supermanoeuvre control – one based on synthesised control surfaces of high effectiveness, and not on *a priori* manoeuvre design.

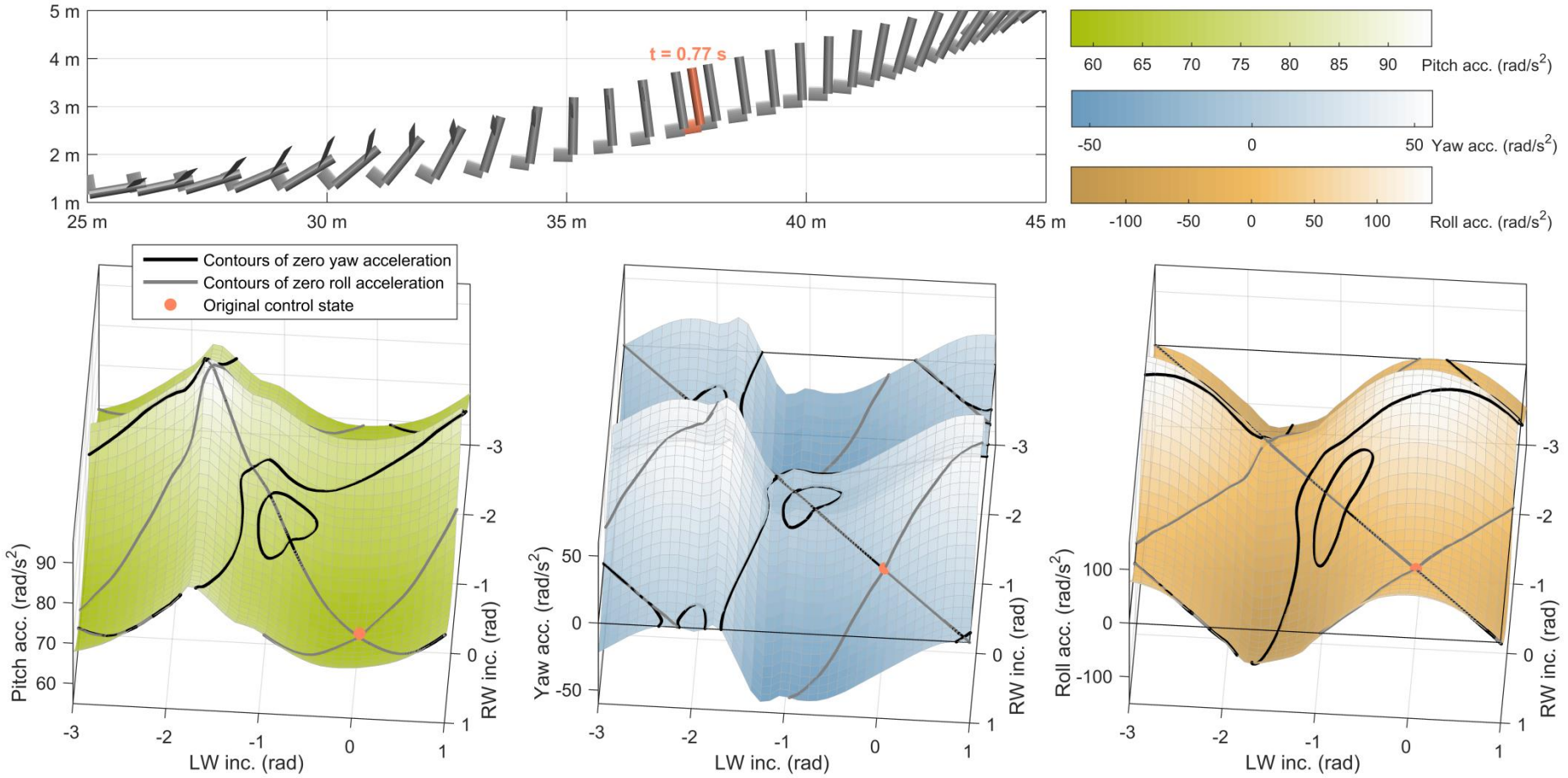

Figure 7.7.1: Inertial-frame pitch, yaw and roll accelerations as a function of left (LW) and right (RW) wing incidence at the point of maximum pitch ($t = 0.77$ s) in the simple cobra (Figure 7.3.4). The associated control paths/contours for decoupled orientation control (roll at zero yaw, yaw at zero roll) are also shown.

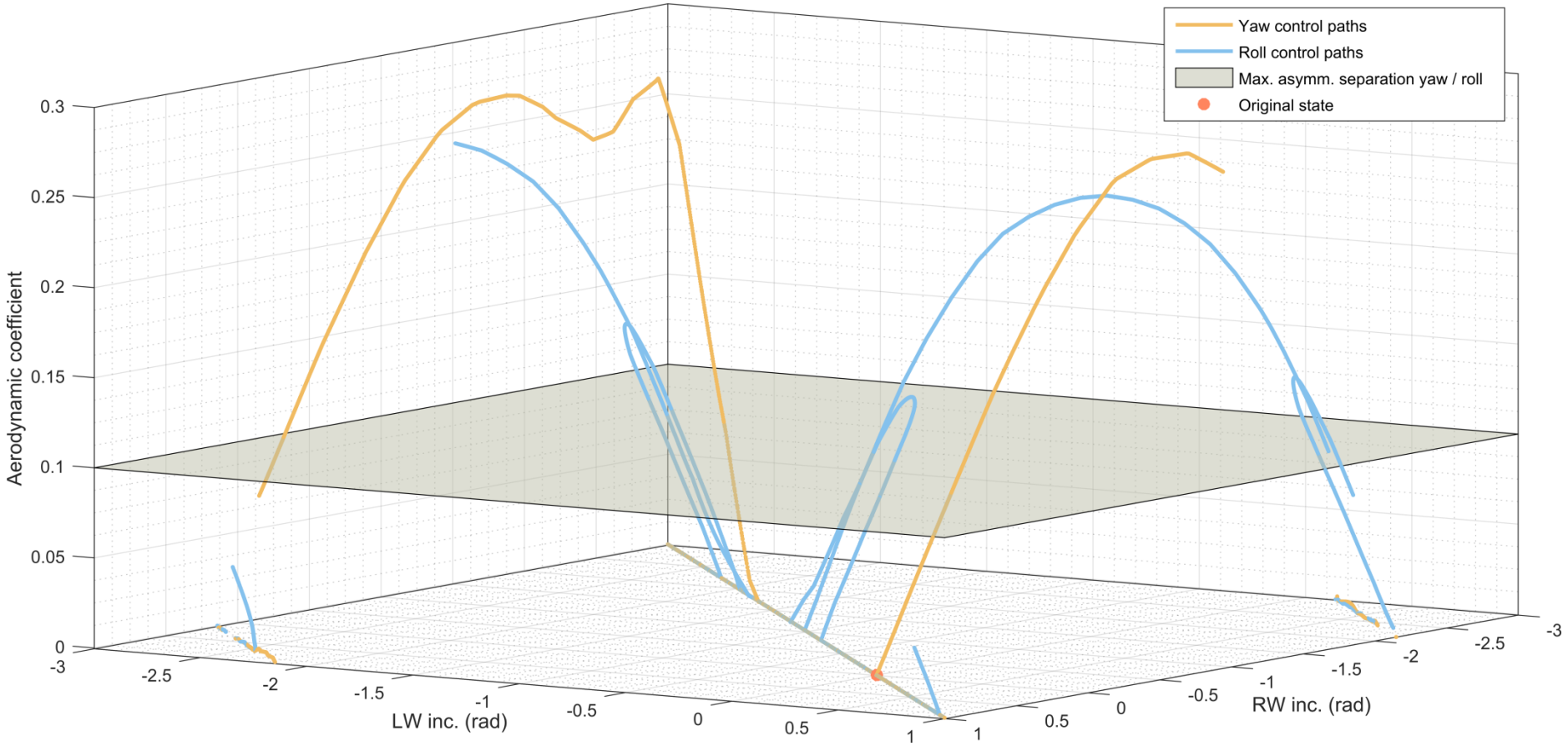

Figure 7.7.2: Control paths/contours for decoupled orientation control (roll at zero yaw, yaw at zero roll) expressed as effective full-system inertial-frame aerodynamic coefficients (C_ψ, C_ϕ). Estimated maximum levels of C_ψ, C_ϕ under asymmetric forebody separation are given: for the X-31 and generic swept wing aircraft, $C_\psi = 0.1$ [23,24]; and for a generic delta wing aircraft, $C_\phi = 0.1$ [26]. Symmetry about the x-y plane is observed.

7.8. CONCLUDING REMARKS

7.8.1. Results

In this chapter a wide range of transient supermanoeuvres were studied, motivated both by biological analogy and by manoeuvres in thrust-vectoring aircraft. The capability of the case study system is significant: rapid nose-pointing-and-shooting (RaNPAS) in both pitch and yaw, including Pugachev's cobra, through a variety of mechanisms; ballistic transition manoeuvres for impact landing on a vertical surface; and anchor turns up to 135° were all demonstrably possible at actuator complexities lower than maximum ($<$6DOF). Based on this performance, extensions to flight reversal manoeuvres, perching manoeuvres, and more complex cobra-type manoeuvres are thought possible.

Immediate applications of this hybrid aircraft are likely to show minimal actuator complexities: in this study, asymmetric incidence morphing was found to be a highly effective 2DOF morphing strategy, allowing quasistatic pitch NPAS between $-25°$ and 30° and an undetermined range of pitch RaNPAS; yaw RaNPAS up to 90°; anchor turning up to at least 90°; and a degree of asymmetric forebody separation control. If symmetric sweep control is additionally available, then pitch RaNPAS is possible to beyond 90° (Pugachev's cobra), as is ballistic transition capability. Or instead, if single-wing dihedral control is available, then quasistatic yaw NPAS is available up to $\pm 25°$, and performance improvements in yaw RaNPAS, anchor turning, and asymmetric forebody separation control are expected. These three morphing configurations represent the most promising industrially-relevant configurations that were found in this study.

7.8.2. Methodology

Finally, the constrained quasi-trim space methodology used in this study represents an efficient and flexible approach to manoeuvre design and exploration in the presence of multiple morphing degrees of freedom. It represents an extension of the trim space method developed in Chapter 6 to the case of states of nonzero acceleration; and is a key methodological development which allows the space of morphing configurations to be explored efficiently in a way that is not possible with purely heuristic or purely numerical methods. The concept of a quasi-trim space – in the sense of pseudo-trim space; a space of states nearby to trim states – is itself a useful and novel concept, allowing morphing aircraft

control configurations to be characterised not by their control state, but by their effect on the aircraft acceleration profile to a reference wind. This allows a conceptual understanding of complex supermanoeuvres (e.g. anchor turns) to be built up.

The development of quasi-trim manoeuvre design methods represents a formalisation of this principle, only partially attained in this thesis: the capability was demonstrated for the simple system yaw NPAS (rattlesnake) manoeuvre (Section 7.4), with a simple perturbative control; and for the complex anchor turn manoeuvre (Section 7.6) in combination with heuristic methods. Given these results, there is reason to believe that further formalisation, such as a refinement of the mesh of pointer states in alongside an implementation in an optimal control context, would yield finer (if less flexible) manoeuvre design capability. Furthermore, quasi-trim states could be used to provide perturbation control, through the defined acceleration of quasi-trim states, in addition to manoeuvre guidance. The analysis of synthesised control surface actions (Section 7.7) represents the zenith of this train of thought in this work: there, a quasi-trim analysis, in its broadest conception, is used to demonstrate how morphing actions can be used to generate uniaxial control moments (analogous to the low-angle of attack effect of aileron and rudder), or indeed, polyaxial ones; suitable for use in a control loop.

As with the trim space analysis (Chapter 6), the quasi-trim space analysis remains distinct from traditional methods of optimal control and nonlinear dynamic inversion. In reference to optimal control [27,28]; it represents a possible approach to formulating the objective function; that being, the aircraft acceleration or acceleration components along a target path. In this context, quasi-trim analysis can be done in-loop, w.r.t. a candidate or current path, or out-of-loop (*a priori*), w.r.t. the target path; a distinction represented by the methodology for the rattlesnake manoeuvre (Section 7.4) and the anchor turn (Section 7.6) respectively. In reference to nonlinear dynamic inversion, the quasi-trim space analysis involves a numerical inversion process – computing the control configurations associated with a specified acceleration state – but this inversion is not used to define a linearising control law. Rather, in a feedback control context, the quasi-trim space analysis provides a method for obtaining control configurations that can be used by multiple controllers (e.g. even simple PID), enabling a wide range of different forms of biomimetic supermanoeuvre

control. Further development and extension of this methodology is closely allied with further exploration of supermanoeuvrability in biomimetic morphing-wing aircraft.

7.8.3. Limitations

The analysis and conclusions presented here are subject to several limitations. A key limitation is that transient aerodynamic effects, including dynamic stall, are not included in the quasistatic aerodynamic submodel used for flight simulation in this chapter. It is **not** expected that the quasistatic model has remained fully accurate for the manoeuvres studied here. This may appear to obviate all the results of this chapter; but Chapters 8-9 will demonstrate that many of the manoeuvres studied here can be recovered under a transient aerodynamic model through changes in the control histories. Ultimately, this will allow quasistatic methods of manoeuvre design to be used to study supermanoeuvrability under transient aerodynamics. The effects of asymmetric forebody flow separation [23] were also not included in the analysis, and the possibility of controlling these effects via wing morphing were only demonstrated in basic way. A more detailed assessment of these effects would be useful.

The actuator or aerostructural feasibility of these manoeuvres has not been studied. In the case e.g. of asymmetric incidence morphing, neither of these effects are likely to be greatly significant, as the required actuator efforts are small, and the structural stresses involved are no larger than those present in non-morphing flight within an 360° angle-of-attack envelope. Actuator effort is likely to be a limiting factor in rapid dihedral morphing, and when the number of morphing controls is larger (up to 6DOF). Structural integrity is likely to be a limiting factor on the use forward sweep, as aeroelastic divergence effects will become significant. This is a subjective assessment, and much depends on the required actuator effort and aircraft payload/application. A quantitative assessment of these effects would form a useful avenue for further research; as would a more dedicated assessment of a detailed biomimetic concept design (e.g. including actuator specifications). Finally, in this assessment of supermanoeuvrability in this chapter has focused on *a priori* manoeuvre design: a focus which allows us to demonstrate the case-study system capability for a wide range of manoeuvres, but not address problems with their guidance and control.

CHAPTER REFERENCES

[1] Gal-Or, B., *Vectored propulsion, supermaneuverability, and robot aircraft*, Springer-Verlag, New York, 1990.

[2] Huenecke, K., *Modern Combat Aircraft Design*, Airlife, Shrewsbury, UK, 1994.

[3] Ericsson, L. E., "Cobra maneuver unsteady aerodynamic considerations," *Journal of Aircraft*, Vol. 32, No. 1, 1995, pp. 214–216. DOI:10.2514/3.46706.

[4] Erickson, G. E., "High Angle-of-Attack Aerodynamics," *Annual Review of Fluid Mechanics*, Vol. 27, No. 1, 1995, pp. 45–88. DOI:10.1146/annurev.fl.27.010195.000401.

[5] Joyce, D. A., *Flying beyond the stall: the X-31 and the advent of supermaneuverability*, NASA, Washington, DC, 2014.

[6] Wiegand, C., "F-35 Air Vehicle Technology Overview," *2018 Aviation Technology, Integration, and Operations Conference*, 2018 Aviation Technology, Integration, and Operations Conference, Atlanta, GA.

[7] Bisplinghoff, R. L., Ashley, H., and Halfman, R. L., *Aeroelasticity*, Addison-Wesley, Reading, MA, 1957.

[8] Gharali, K., and Johnson, D. A., "Dynamic stall simulation of a pitching airfoil under unsteady freestream velocity," *Journal of Fluids and Structures*, Vol. 42, 2013, pp. 228–244. DOI:10.1016/j.jfluidstructs.2013.05.005.

[9] Reich, G. W., Eastep, F. E., Altman, A., and Albertani, R., "Transient Poststall Aerodynamic Modeling for Extreme Maneuvers in Micro Air Vehicles," *Journal of Aircraft*, Vol. 48, No. 2, 2011, pp. 403–411. DOI:10.2514/1.C000278.

[10] Lego, Z. M., "Analysis of High Angle of Attack Maneuvers to Enhance Understanding of the Aerodynamics of Perching," Master's Thesis, University of Dayton, 2012.

[11] Selig, M., "Modeling Full-Envelope Aerodynamics of Small UAVs in Realtime," AIAA Atmospheric Flight Mechanics Conference, Toronto, ON.

[12] Rajiv, N., Savita, D., and Udai Bhanu, S., "Defence and Disarmament Review," *Strategic Digest*, Vol. 23, 1993, p. 1269 ff.

[13] Gal-Or, B., "Thrust Vectoring For Flight Control & Safety: A Review," *International Journal of Turbo and Jet Engines*, Vol. 11, No. 2–3, 1994. DOI:10.1515/TJJ.1994.11.2-3.119.

[14] Lyons, T. J., *Human Consequences of Agile Aircraft*, NATO RTO HFM, Neuilly-sur-Seine, France, 2001.

[15] Jackson, S. M., "Glide angle in the genus Petaurus and a review of gliding in mammals," *Mammal Review*, Vol. 30, No. 1, 2000, pp. 9–30. DOI:10.1046/j.1365-2907.2000.00056.x.

[16] Ando, M., and Shiraishi, S., "Gliding flight in the Japanese giant flying squirrel Petaurista leucogenys," *Journal of the Mammalogical Society of Japan*, Vol. 18, No. 1, 1993, pp. 19–32.

[17] Stafford, B. J., Thorington, R. W., and Kawamichi, T., "Gliding behaviour of Japanese giant flying squirrels (Petaurista Leucogenys)," *Journal of Mammalogy*, Vol. 83, No. 2, 2002, pp. 553–562.

[18] Warrick, D. R., "Bird Maneuvering Flight: Blurred Bodies, Clear Heads," *Integrative and Comparative Biology*, Vol. 42, No. 1, 2002, pp. 141–148. DOI:10.1093/icb/42.1.141.

[19] Warrick, D. R., and Dial, K. P., "Kinematic, aerodynamic and anatomical mechanisms in the slow, maneuvering flight of pigeons," *Journal of Experimental Biology*, Vol. 201, No. 12, 1998, pp. 655–672.

[20] Gillies, J. A., Thomas, A. L. R., and Taylor, G. K., "Soaring and manoeuvring flight of a steppe eagle Aquila nipalensis," *Journal of Avian Biology*, Vol. 42, No. 5, 2011, pp. 377–386. DOI:10.1111/j.1600-048X.2011.05105.x.

[21] Bishop, K. L., "The relationship between 3-D kinematics and gliding performance in the southern flying squirrel, Glaucomys volans," *Journal of Experimental Biology*, Vol. 209, No. 4, 2006, pp. 689–701. DOI:10.1242/jeb.02062.

[22] Ros, I. G., Badger, M. A., Pierson, A. N., Bassman, L. C., and Biewener, A. A., "Pigeons produce aerodynamic torques through changes in wing trajectory during low speed aerial turns," *Journal of Experimental Biology*, Vol. 218, No. 3, 2015, pp. 480–490. DOI:10.1242/jeb.104141.

[23] Ericsson, L. E., "Challenges in high-alpha vehicle dynamics," *Progress in Aerospace Sciences*, Vol. 31, No. 4, 1995, pp. 291–334. DOI:10.1016/0376-0421(95)00002-G.

[24] Cobleigh, B. R., *High-Angle-of-Attack Yawing Moment Asymmetry of the X-31 Aircraft from Flight Test*, NASA, Washington, DC, 1994.

[25] Wong, G. S., Rock, S. M., Wood, N. J., and Roberts, L., "Active control of wing rock using tangential leading-edge blowing," *Journal of Aircraft*, Vol. 31, No. 3, 1994, pp. 659–665. DOI:10.2514/3.46545.

[26] de Oliveira Neto, P. J., “An Investigation of Unsteady Aerodynamic Multi-axis State-Space Formulations as a Tool for Wing Rock Representation,” Doctoral Dissertation, Virginia Polytechnic Institute and State University, 2007.

[27] Longuski, J. M., Guzman, J. J., and Prussing, J. E., *Optimal control with aerospace applications*, Springer, New York, 2014.

[28] Levine, W. S., ed., *The Control Handbook*, CRC Press, Boca Raton, FL, 1996.

THIS PAGE LEFT BLANK

Chapter 8:
Transient aerodynamic modelling

8.1. INTRODUCTION

A transient aerodynamic submodel for the case study system is required in order to accurately assess the system's capability for highly transient manoeuvres. A wide range of transient model fidelities are available. At the highest level, 2D or 3D turbulent computational fluid dynamics (CFD) simulations via large-eddy simulation (LES) or Reynolds-averaging are extremely expensive to apply to a morphing aircraft – whether in a full-system context, or only a single lifting surface – but are still sometimes utilised [1,2]. The one-parameter Spalart-Allmaras turbulence model is commonly utilised for reasons of computational efficiency [3–6]; higher-fidelity approaches such as LES are feasible only for insect-scale simulations [25]. CFD approaches are in general too computationally costly to be coupled directly to flight simulation systems: in the case study system, doing so would significantly limit the manoeuvre timescale and the possibility for exploration of the manoeuvre / control configuration space. A more efficient approach is to use a data-driven or phenomenological lower-order model. Data-driven model-reduction techniques – e.g. eigensystem realisation [7], Volterra theory [8] and support vector machines [9] – are capable of reducing a large CFD or experimental dataset to a lower-order model.

Alternatively, a phenomenological model of particular transient flow effects can be utilised: of particular relevance are dynamic stall and lift hysteresis models, including the ONERA [10] and Goman-Khrabrov (GK) [11] models, among others [12]. These models focus largely on the dynamic effects of pitching (and to some extent, dihedral motion) of the aerofoil, with particular reference to delay flow attachment/separation. The effect of dynamic sweep motion, apart from the obvious induced flow, is very rarely studied [13], though results from the study of unsteady freestream flows indicate that it may have more significance than previously thought [14–16]. Phenomenological models are less general in the range of effects that they model; but they do not require a large source dataset, and by their nature allow a better phenomenological characterisation of the model limitations. Even simpler model-reduction and phenomenological models are available: Theodorsen's aerodynamic theory [17,18] provides a method by which the dynamic effects of low-amplitude pitching and dihedral motion may be modelled [17,18]. Wagner's indicial response function [19] and the finite-state theory of Peters et al. [20] provide similar modelling capability. However, the

limitations of these models to low amplitude, pre-stall behaviour [19] makes them poorly suited to modelling transient supermanoeuvrability.

In this chapter, a Goman-Khrabrov (GK) aerodynamic model for the case study system is developed and identified. Quasistatic model data is identified from existing quasistatic data for the ST50W/H aerofoils; transient model parameters are identified from CFD simulations. This yields an aerodynamic model that accounts for the dynamic effects of aerofoil angle-of-attack changes, and yields accurate aerodynamic force predictions over a much wider range of flow transience level.

8.2. GOMAN-KHRABROV AERODYNAMIC MODELLING

8.2.1. Formulation

To include dynamic stall effects into the case study model, a modified GK model is implemented in the surface-element framework; extending upon the work of Goman and Khrabrov [11], Reich et al. [21] and Wickenheiser and Garcia [22]. Under the modified GK model, for each lifting surface station i across the system, the aerodynamic coefficients for force F as a function of effective angle-of-attack, $C_{i,F}(\alpha_i)$, are given by:

$$C_{i,F}(\alpha_i) = p_i C_{i,F,\text{att}}(\alpha_i) + (1 - p_i) C_{i,F,\text{sep}}(\alpha_i), \tag{8.2.1}$$

where $C_{i,F,\text{att}}(\alpha_i)$ and $C_{i,F,\text{sep}}(\alpha_i)$ are the aerodynamic coefficient functions for the hypothetical cases of local attached and separated flow respectively. p_i are local dynamic mixing parameters [22], loosely connected to the location of the separation point along the airfoil chord [11,23], and governed by the first-order differential equation:

$$\tau_{1,i} \dot{p}_i(\alpha_i) = p_{0,i}\left(\alpha_i - \tau_{2,i}\dot{\alpha}_i\right) - p_i(\alpha_i), \tag{8.2.2}$$

where α_i and $\dot{\alpha}_i$ are the local angle of attack and corresponding rate, $\tau_{1,i}$ and $\tau_{2,i}$ are situation- and station-specific delay parameters and $p_{0,i}(\alpha)$ are mixings function representing the transition between attached and unattached flow. It is the identification of the functions $C_{i,F,\text{att}}(\alpha_i)$, $C_{i,F,\text{sep}}(\alpha_i)$ and $p_{0,i}(\alpha_i)$; and the delays $\tau_{1,i}$ and $\tau_{2,i}$ which are crucial in determining the accuracy of the model. Notably, the former three functions are identifiable based only on static aerodynamic coefficient data, when $p_i = p_{0,i}$. A traditional

procedure [21,22] has been to assume simple linear attached flow and flat plate separated flow behaviour, leading to the widely-used relations:

$$\begin{aligned} C_{i,L,\,\text{att}}(\alpha) &= C_{i,L\alpha}\alpha_i \\ C_{i,D,\,\text{att}}(\alpha) &= C_{i,D\alpha}\alpha_i \\ C_{i,L,\,\text{sep}}(\alpha) &= 1.1\sin 2\alpha_i. \\ C_{i,D,\,\text{sep}}(\alpha) &= 0.95(1-\cos 2\alpha_i), \end{aligned} \tag{8.2.3}$$

For airfoil-specific $C_{i,L\alpha}$ and $C_{i,D\alpha}$. Note that aerofoil moment coefficients have not previously been considered. Wickenheiser and Garcia [22] and Reich et al. [21] provide a trigonometric expression for $p_{0,i}$ based on the arctangent sigmoid curve, approximately equivalent to:

$$p_{0,i}(\alpha_i) = \begin{cases} 1 & |\alpha_i| < 4° \\ -0.0058\tan^{-1}(|\alpha_i| + 16) & 4° \leq |\alpha_i| \leq 32° \\ 0 & |\alpha_i| > 32°. \end{cases} \tag{8.2.4}$$

Note that the expression in [21,22] confuses radians and degrees; here the input, α_i ranges and and $\tan^{-1}$ output are all in degrees. In addition, the α_i ranges are modified slightly to remove an area of nonphysical $p_0 < 0$ present in the original function. Together with the aerodynamic models, this provides a complete set of functions for the GK model.

8.2.2. Static parameter identification: ST50W

Unfortunately, the simple relations in Eq. 8.2.3-8.2.4 are not a good approximation to the case study system aerofoils. A more recent and more versatile application of the GK model, following from [23–25], involves the identification of the separated and attached models from the aerodynamic coefficient data from CFD or experiment. There are several lifting surfaces to model in this way: the wing surfaces and the horizontal and vertical stabilisers; the latter additionally modified by the elevator and rudder deflections. The two aerofoils in the system, the ST50W and ST50H, are modelled using the wing and stabiliser datasets from Selig [26] (cf. Chapter 3). Starting with the wing data; curve fitting indicates that it is approximated well (see Figure 8.2.2) by the relations:

$$\begin{aligned} C_{i,L,\,\text{sep}}(\alpha_i) &= a_{i,L}\,\text{sgn}\,\alpha_i \sin\left(b_{i,L}\left|\alpha_i + c_{i,L}\right| + d_{i,L}\right) + e_{i,L}, \\ C_{i,D,\,\text{sep}}(\alpha_i) &= a_{i,D}\sin\left(b_{i,D}|\alpha_i| + c_{i,D}\right) + d_{i,D}, \\ C_{i,M,\,\text{sep}}(\alpha_i) &= a_{i,M}\,\text{sgn}\,\alpha_i \sin\left(b_{i,M}\left|\alpha_i + c_{i,M}\right| + d_{i,M}\right) + e_{i,M}, \end{aligned} \tag{8.2.5}$$

for all α_i, with model parameters $a_{i,j}$, $b_{i,j}$, $c_{i,j}$, $d_{i,j}$ and $e_{i,j}$; and for the leading and trailing edge considered separately:

$$\begin{aligned} C_{i,L,\,\text{att}}(\alpha_{l,i}) &= C_{i,L\alpha,l}\alpha_{l,i}, & C_{i,L,\,\text{att}}(\alpha_{t,i}) &= C_{i,L\alpha,t}\alpha_{t,i}, \\ C_{i,M,\,\text{att}}(\alpha_{l,i}) &= 0, & C_{i,M,\,\text{att}}(\alpha_{t,i}) &= C_{i,M\alpha,t}\alpha_{t,i}, \\ C_{i,D,\,\text{att}}(\alpha_{l,i}) &= 0, & C_{i,D,\,\text{att}}(\alpha_{t,i}) &= 0, \end{aligned} \tag{8.2.6}$$

where $\operatorname{sgn}\alpha_i$ is the sign function, and $\alpha_{l,i}$ and $\alpha_{t,i}$ are the leading and trailing edge angles of attack (representing a partition of the full domain, $|\alpha_i| < 180°$, into $|\alpha_i| \leq 90°$ and $\big||\alpha_i| - 180°\big| \leq 90°$, the latter of which is mapped back to $|\alpha_i| \leq 90°$ again.) Three of the attached flow models ($C_{i,M,\,\text{att}}(\alpha_{l,i})$ and both $C_{i,D,\,\text{att}}(\alpha_{i,i})$) are observably zero. Note that the separated flow function are still symmetric (odd or even) about $\alpha_i = 0$, as is expected for the symmetric aerofoil. The effect of aileron deflection is not considered, as this control function can be achieved by incidence morphing.

The parameters for these expressions model are identified via nonlinear least-squares regression applied to selections of obviously attached and separated flow. $p_{0,i}$ can then also be estimated by solving $p_i = p_{0,i}$ in Eq. 8.2.1 using the empirical source data. Figure 8.2.1 shows the results of this process, compared to the arctangent $p_{0,i}$ expression (Eq. 8.2.4). For the trailing edge this is modified to account for the earlier and faster separation:

$$p_{0,i}(\alpha_{t,i}) = \begin{cases} 1 & |\alpha_{t,i}| < 4° \\ -0.0058\tan^{-1}\big(1.6|\alpha_{t,i}| + 16\big) & 4° \leq |\alpha_{t,i}| \leq 21° \\ 0 & |\alpha_{t,i}| > 21°. \end{cases} \tag{8.2.7}$$

The results indicate that the arctangent $p_{0,i}$ is a reasonably accurate approximation for the ST50W. The quasistatic source coefficient data for the ST50W wing may then be reconstructed for comparison. Figure 8.2.2 shows this data alongside the GK reconstruction using the arctangent p_0 (Eq. 8.2.4 and 8.2.7). The result is overall very good: the separated and attached flow regimes are modelled well. The most notable discrepancies are around the trailing edge transition in the drag and moment coefficients – as can be seen also in Figure 8.2.1, the trailing edge drag and moment data appear to be requiring different $p_{0,i}$ functions. Such an approach however would destroy much of the remaining physical realism of the GK model – already only loosely connected to Goman and Khrabrov's separation-point formulation [11,23] – and the potential increase in modelling accuracy is not great.

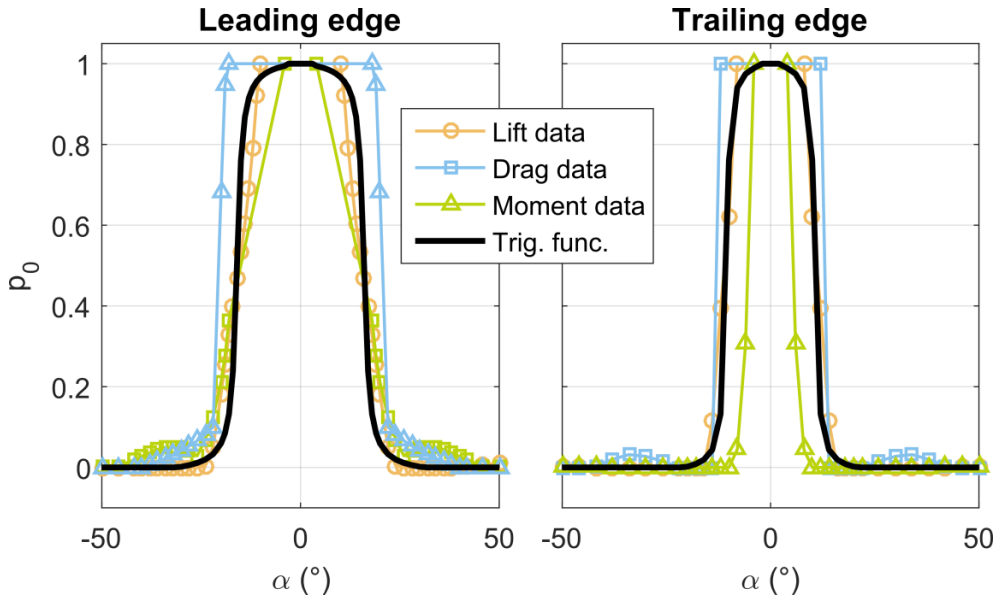

Figure 8.2.1: Filtered approximations to $p_{0,i}$ derived from ST50W leading and trailing edge experimental data, compared to the approximate trigonometric function.

8.2.3. Static parameter identification: ST50H

The stabiliser data presents the additional difficulty of the dependence of all aerodynamic coefficients on the stabiliser aerofoil shape, and thus on the stabiliser control surface deflection. To begin, quasistatic behaviour for the control-surface motion is assumed (that the control-surface motion itself induces no flow). Although the dataset from Selig [26] contains aerodynamic coefficient data at seven different elevator deflections (−50°, −30°, −15°, 0°, 15°, 30°, 50°); only four of these are unique (e.g. $\beta_e \in [-50, 0]°$ or $\beta_e \in [0, 50]°$). This is due to the symmetric aerofoil profile: downwards aerofoil motion at downwards control surface deflection is equivalent to upwards motion at upwards deflection.

Selecting the unique set $\beta_e \in [-50, 0]°$; for each control surface deflection data entry therein the attached and separated flow relations are identified according to a slightly modified model definition:

$$C_{i,L,\,\mathrm{sep}}(\alpha_i) = a_{i,L}\,\mathrm{sgn}\big(\alpha_i + c_{i,L}\big)\sin\big(b_{i,L}\big|\alpha_i + c_{i,L}\big| + d_{i,L}\big) + e_{i,L},$$

$$C_{i,D,\,\mathrm{sep}}(\alpha_i) = \begin{cases} a_{i,D}\cos\big(b_{i,D}\big|\alpha_i + c_{i,D}\big| + e_{i,D}\big) + e_{i,D}, & \beta_e = 0 \\ a_{i,D}\sin\big(b_{i,D}\alpha_i + c_{i,D}\big) + d_{i,D} & \text{o.w.,} \end{cases} \tag{8.2.8}$$

$$C_{i,M,\,\mathrm{sep}}(\alpha_i) = a_{i,M}\,\mathrm{sgn}\big(\alpha_i + c_{i,M}\big)\sin\big(b_{i,M}\big|\alpha_i + c_{i,M}\big| + d_{i,M}\big) + e_{i,M}.$$

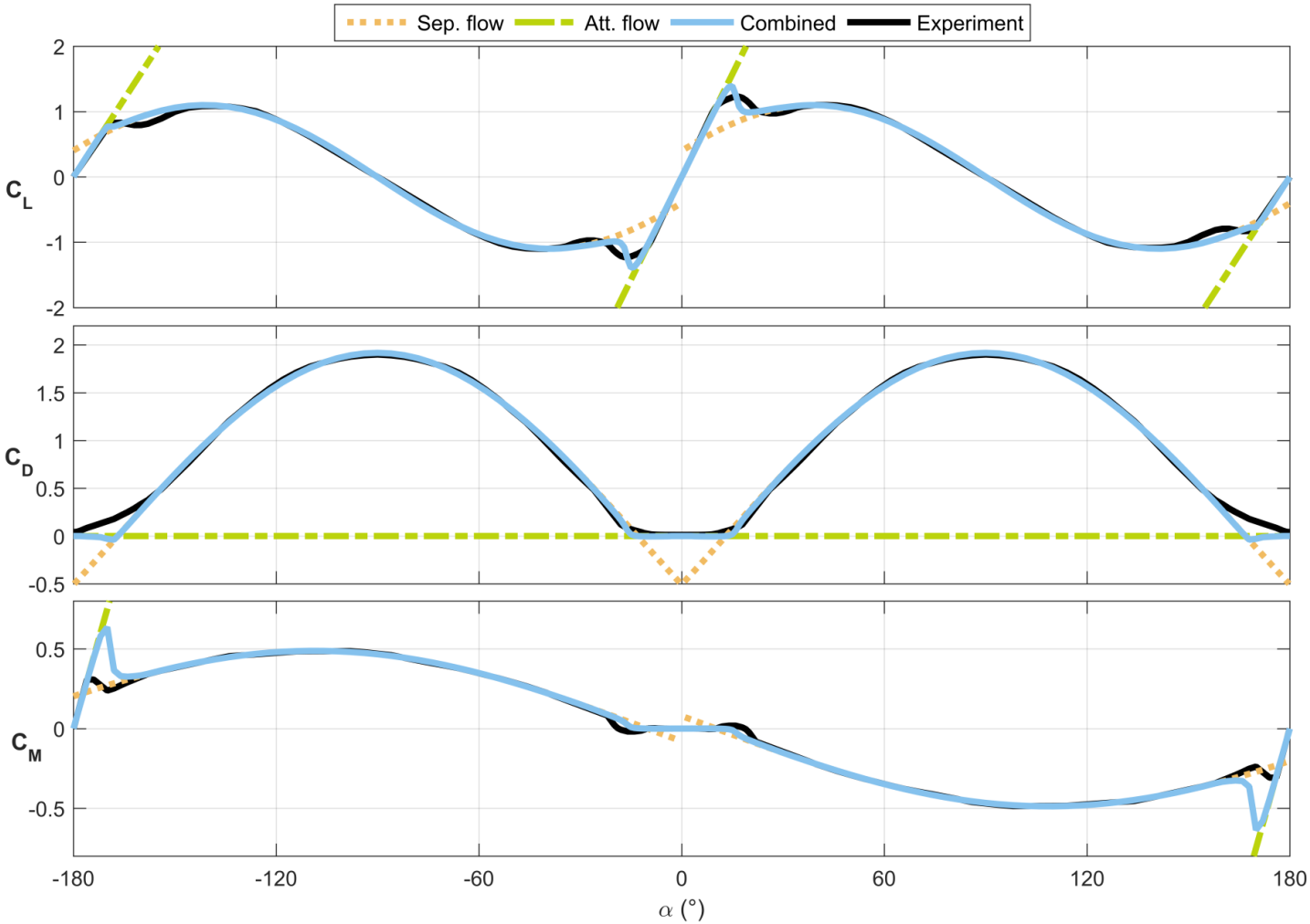

Figure 8.2.2: Aerodynamic coefficient data reconstructed from the GK model data, compared to the original data.

with attached models exactly as per Eq. 8.2.6. The key difference is the sinusoid drag model at nonzero β_e: the simpler model allows for an increased robustness in identification; the complexity of the coefficient data does not permit an easy identification of the more complex models of Eq. 8.2.5.

The identification is automatic except for a manual indication of where to find the attached and separated flow area. The separated flow models are then smoothed with a Laplacian smoother to ease the interpolation across β_e. Figures 8.2.3-8.2.5 show the four unique identified models in each aerodynamic coefficient. To reconstruct a quasistatic aerodynamic profile, and utilise these models in a GK framework, an estimate of $p_{0,i}$ is required. Figure 8.2.6 shows the estimates obtained, as per Section 8.2.2, by solving Eq. 8.2.1 for $p = p_0$ in the vicinity of the transition region. Figure 8.2.6 shows the raw unfiltered results for p_0, given by C_L and C_M where possible, at the leading and trailing edge, and with respect to the reference angles-of-attack, $\alpha_{l,i,\mathrm{ref}}$ / $\alpha_{t,i,\mathrm{ref}}$. These values are the centre-points of the attached flow regions, specified manually, and nonzero for nonzero β_e.

A particularly notable feature of these results is their asymmetry, with long tails at negative α (for $\beta_e < 0$). The assertion that this is a physical effect, and not a result of inaccuracy in the attached/separated flow models, may be supported by the empirical lift coefficient histories. At positive α values (for $\beta_e < 0$), large stall peaks are observed; whereas at negative α there is a flat plateau. Phenomenologically, this is thought to arise from flow reattachment effects when both the control surface and the aerofoil are inclined e.g. upwards ($\beta_e < 0$, $\alpha > 0$), leading to a state in which the control surface itself is effectively at low angle-of-attack. Conversely, for $\beta_e < 0$, $\alpha < 0$, more rapid flow separation is expected. The arctangent sigmoid of Reich [21] is not capable of capturing these asymmetric effects, and suffers from the further difficulty that the model parameters are not easily interpretable. To model both symmetric and asymmetric effects better, we propose a new GK sigmoid function, based on the logistic function. Its symmetric form, for the leading edge, is:

$$p_{0,l,i,\mathrm{sym}}(\alpha_{l,i}) = S\left(\frac{1}{m_{l,i}}\left(\left|\alpha_{l,i} - \alpha_{l,i,\mathrm{ref}}\right| - \psi_{l,i}\right)\right), \qquad S(x) = \frac{1}{1+\exp(x)}, \tag{8.2.9}$$

where $S(x)$ is the logistic function, $\alpha_{l,i,\mathrm{ref}}$ is the centre point of the attached flow region (specified manually, and nonzero for nonzero β_e), and ($m_{l,i}$, $\psi_{l,i}$) are model parameters. The shift parameter $\psi_{l,i}$ is the α-value (w.r.t $\alpha_{l,i,\mathrm{ref}}$) of the inflection or 50% point; that is $p_{0,l,i,\mathrm{sym}}(\psi_{l,i} + \alpha_{l,i,\mathrm{ref}}) = 0.5$. The width parameter $m_{l,i}$ governs the gradient at this point. The interpretable nature of these parameters is an aid to identification.

To account for the asymmetric nature of the empirical profiles, a one-sided Gaussian function is added to the symmetric sigmoid, to yield the completed $p_{0,l,i}$:

$$\begin{aligned} p_{0,l,i}(\alpha_{l,i}) &= \left(1 - p_{0,i,\mathrm{sym}}(\alpha_{l,i})\right) G(\alpha_{l,i}) + p_{0,i,\mathrm{sym}}(\alpha_{l,i}), \\ G(\alpha_{l,i}) &= M_{l,i} \exp\left(-\left(\frac{\alpha_{l,i} - \alpha_{l,i,\mathrm{ref}} + \psi_{l,i}}{w_{l,i}}\right)^2\right) \left[\alpha_{l,i} - \alpha_{l,i,\mathrm{ref}} < 0\right]_{\mathrm{IV}}, \end{aligned} \tag{8.2.10}$$

where $w_{l,i}$ and $M_{l,i}$ are model parameters, $\psi_{l,i}$ is the parameter identified in Eq. 8.2.9, and $[\cdot]_{\mathrm{IV}}$ is the Iverson bracket [27], such that $[s]_{\mathrm{IV}} = 1$ if s is true, and $[s]_{\mathrm{IV}} = 0$ if s is false. The nature of this addition ensures that the resulting profile is smooth (C^∞) over the halfspaces $\alpha_{l,i} > \alpha_{l,i,\mathrm{ref}}$ and $\alpha_{l,i} < \alpha_{l,i,\mathrm{ref}}$. The parameter $w_{l,i}$ governs the width of the Gaussian function, and the parameter $M_{l,i}$ its height.

In the case of the trailing edge, the discrepancy between the empirical p_0 estimates computed from C_L and C_M makes an asymmetric $p_{0,t,i}$ too difficult to identify. For this reason, the simple symmetric form is used:

$$p_{0,t,i,\mathrm{sym}}(\alpha_{t,i}) = S\left(\frac{1}{m_{t,i}}\left(\left|\alpha_{t,i} - \alpha_{t,i,\mathrm{ref}}\right| - \psi_{t,i}\right)\right), \qquad S(x) = \frac{1}{1 + \exp(x)}, \tag{8.2.11}$$

with model parameters ($m_{t,i}$, $\psi_{t,i}$) distinct from ($m_{l,i}$, $\psi_{l,i}$). Four the four dataset points considered, leading- and trailing-edge p_0 parameters are estimated for $\beta_e = -50°$ and $\beta_e = 0°$; and then models at the internal surface-deflection points are generated by linearly interpolating model parameters. Table 8.2.1 shows the identified model parameters, including the associated interpolation index ($k \in [0, 1]$ for $\beta_e \in [-50, 0]°$), and Figure 8.2.6 the identified p_0 functions. The parameter interpolation is two-point ($k \in \{0, 1\}$), with the exception of $M_{l,i}$, which shows a rising trend with k but must necessarily be zero at $k = 1$ to

preserve symmetry. For this reason, a non-monotonic piecewise-linear profile with the additional data-point $M_{l,i}(k = 0.75) = 0.6$ is used. These parameter variations are modelled at minimal complexity to maintain a reasonable level of model robustness and simplicity, consistent with the phenomenological nature of the model.

The resulting identified models can be extended extended to $\beta_e > 0$ by symmetry – pitch-up motion at positive deflection corresponding to pitch-down motion at negative deflection. The estimated quasistatic coefficient profiles can then be reconstructed using the relevant sigmoid $p_{0,i}$ expressions and the separated- and attached-flow models. Figure 8.2.7 shows the GK reconstruction of the ST50H quasistatic aerodynamic coefficients as a function of elevator deflection and α_i, compared with the original results of Selig [26]. Figure 8.2.7 shows this comparison a function of elevator deflection and α_i, in contour format; at intermediate control surface deflections, the model functions (not their generative parameters) are interpolated. As can be seen, a generally good agreement is observed, despite the some variation in the laminar-turbulent transition zones. The primary limitations of the identification are the discrepancy in identified separation point between the lift and moment coefficient data.

Table 8.2.1: Model parameters for the logistic p_0 functions

Parameter	$\boldsymbol{\beta_e = -50°}$	$\boldsymbol{\beta_e = -30°}$	$\boldsymbol{\beta_e = -15°}$	$\boldsymbol{\beta_e = 0°}$
k	0	0.4	0.7	1
$\alpha_{l,i,\mathrm{ref}}$	30.5°	19°	8°	0°
$\alpha_{t,i,\mathrm{ref}}$	−148°	−162°	−172°	−180°
$m_{l,i}$	0.8	lin. interp.		3
$\psi_{l,i}$	4.4	lin. interp.		20
$M_{l,i}$	0.4	lin. interp. via 0.6@0.75k		0
$w_{l,i}$	18	lin. interp.		14
$m_{t,i}$	1.5	constant		1.5
$\psi_{t,i}$	11	lin. interp.		9

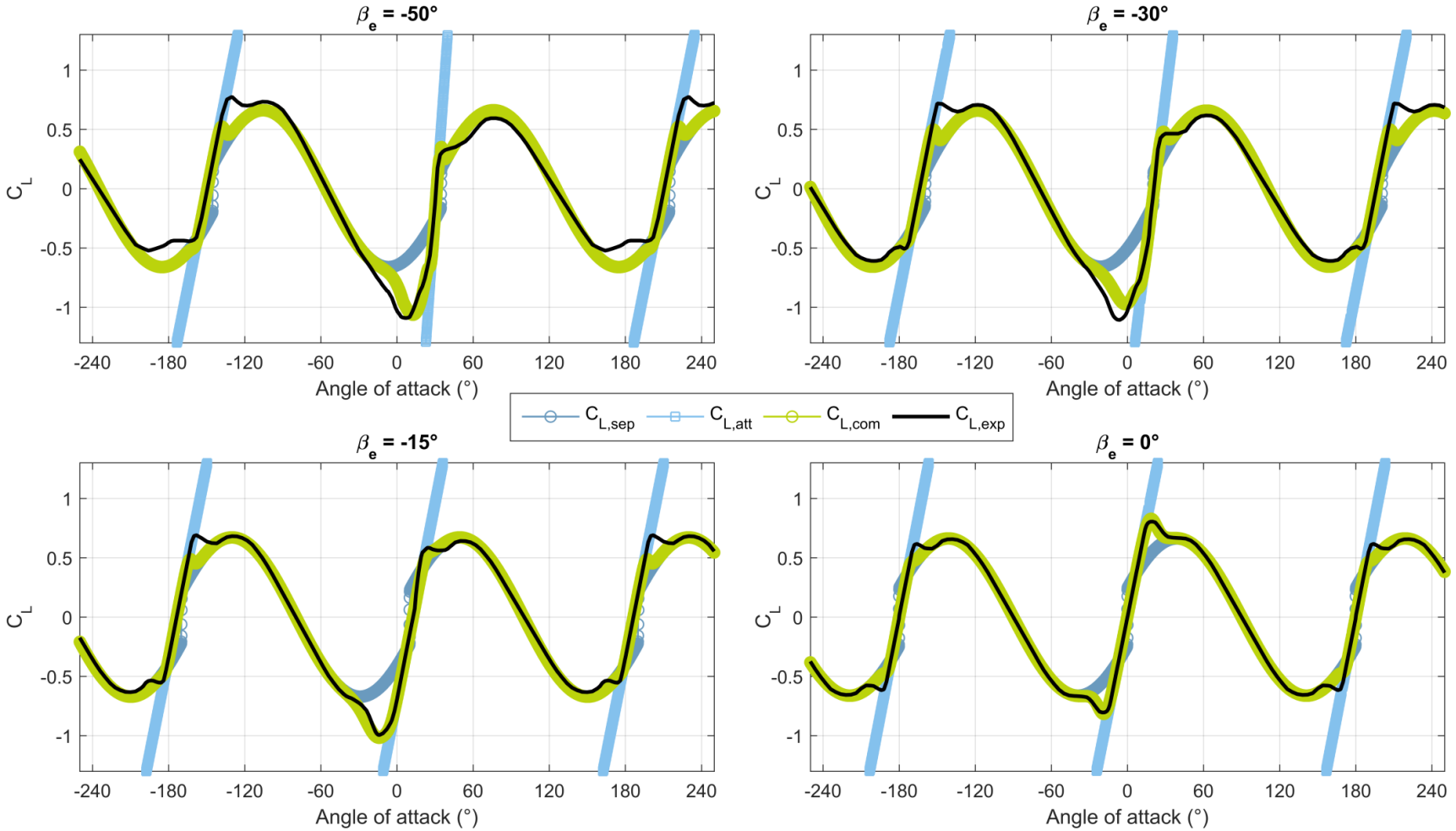

Figure 8.2.3: Empirical quasistatic lift coefficient results ($C_{L,exp}$) compared with the identified GK attached-flow ($C_{L,att}$), separated-flow ($C_{L,sep}$) and reconstructed ($C_{L,com}$) quasistatic lift coefficient functions, under elevator deflections (β_e) of −50°, −30°, −15° and 0°.

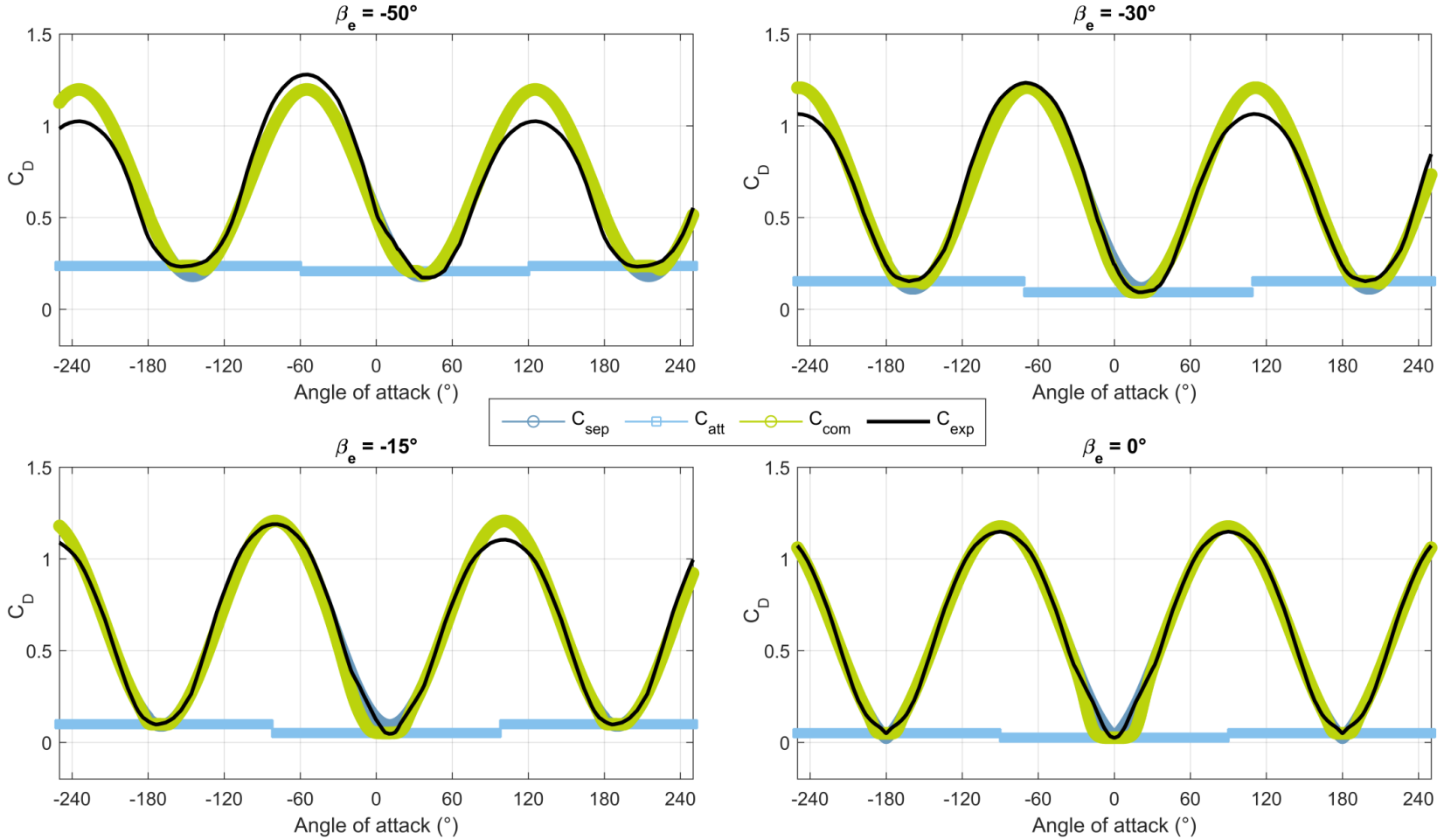

Figure 8.2.4: Empirical quasistatic drag coefficient results (C_{exp}) compared with the identified GK attached-flow (C_{att}), separated-flow (C_{sep}) and reconstructed (C_{com}) quasistatic drag coefficient functions, under elevator deflections (β_e) of −50°, −30°, −15° and 0°.

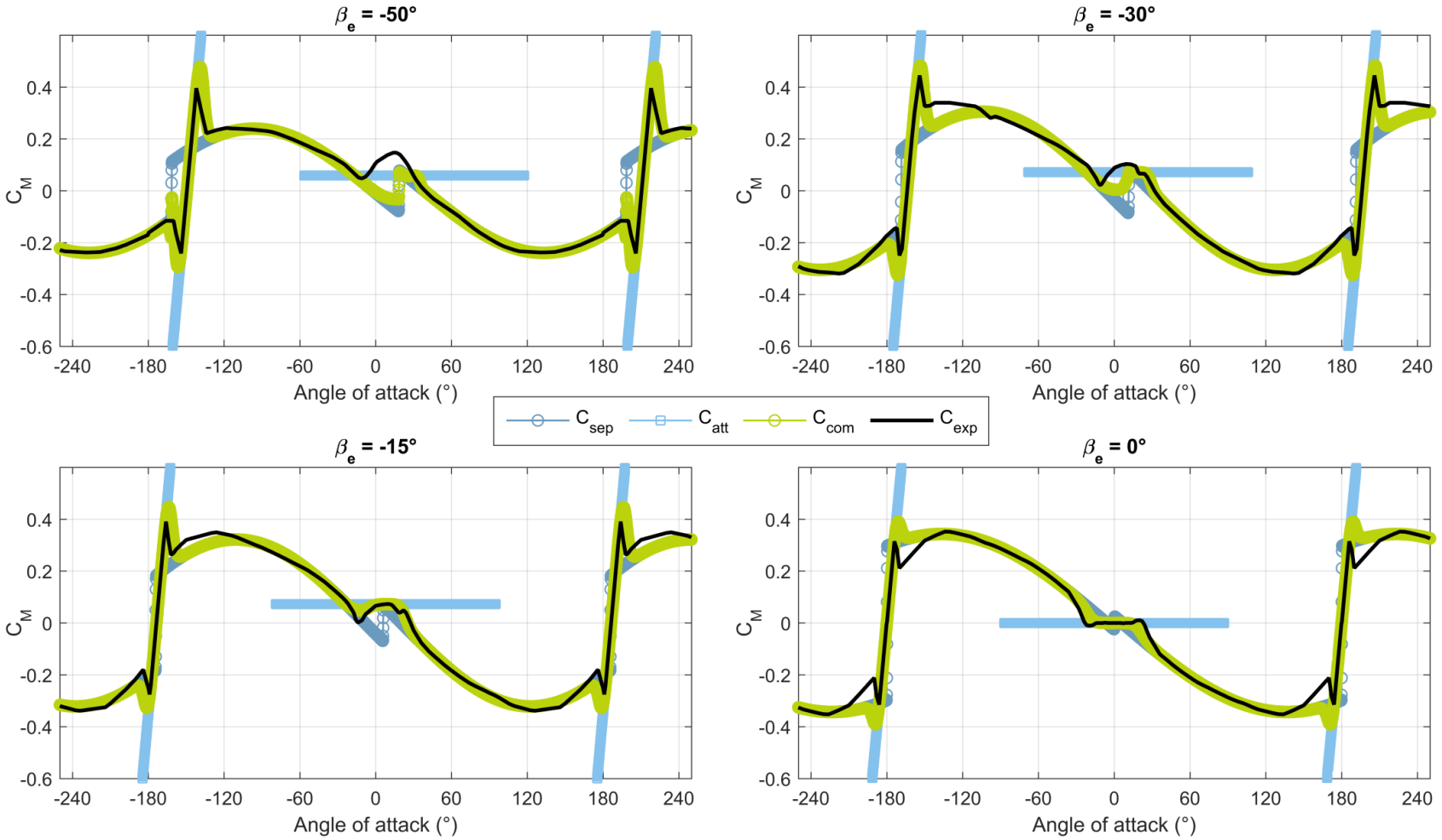

Figure 8.2.5: Empirical quasistatic moment coefficient results (C_{exp}) compared with the identified GK attached-flow (C_{att}), separated-flow (C_{sep}) and reconstructed (C_{com}) quasistatic coefficient functions, under elevator deflections (β_e) of −50°, −30°, −15° and 0°.

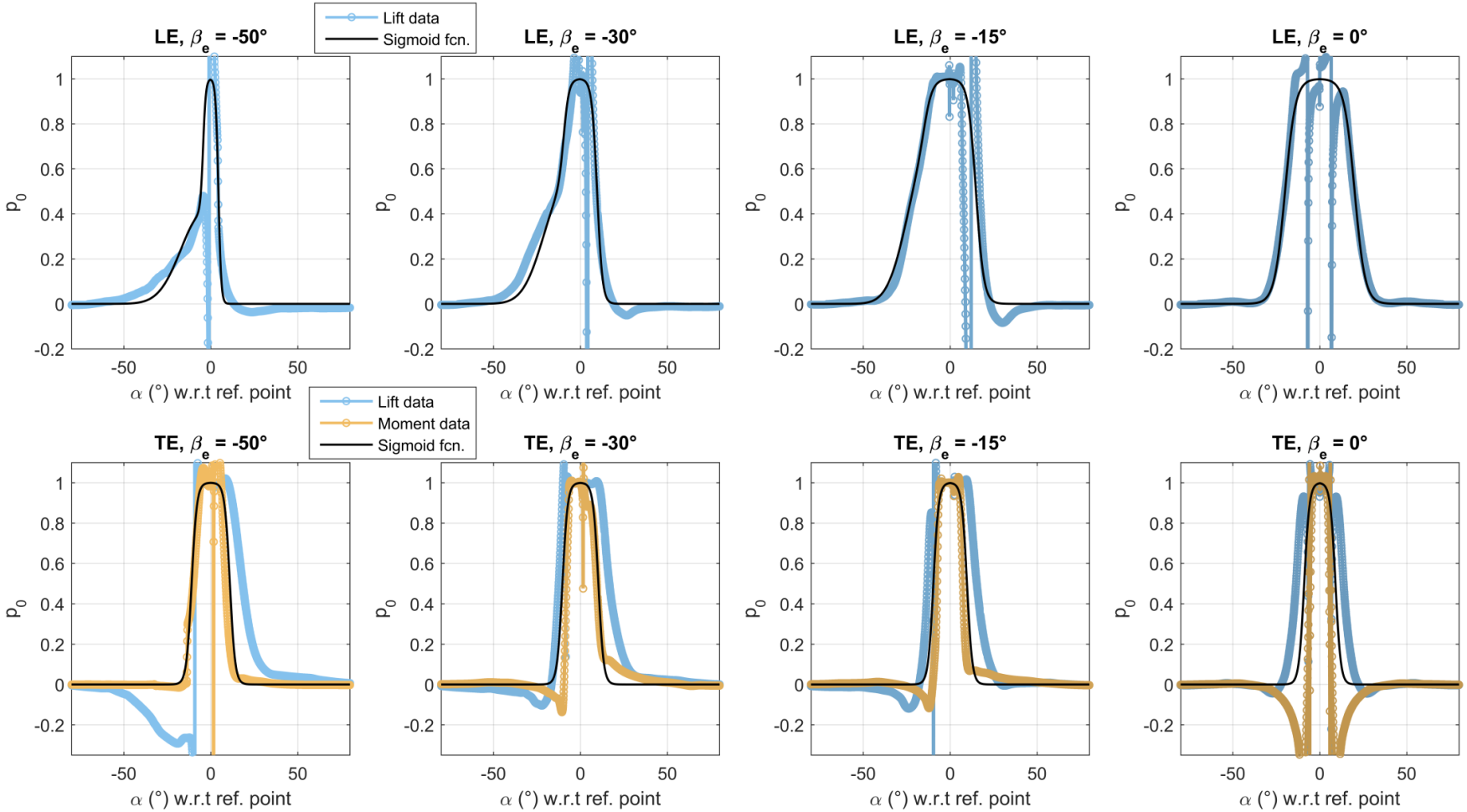

Figure 8.2.6: Empirical estimates of the leading edge (LE) and trailing edge (TE) p_0 functions, centred with respect to the reference angles-of-attack $\alpha_{l,i,\mathrm{ref}}$ / $\alpha_{t,i,\mathrm{ref}}$, compared with the identified approximations based on the logistic sigmoid function.

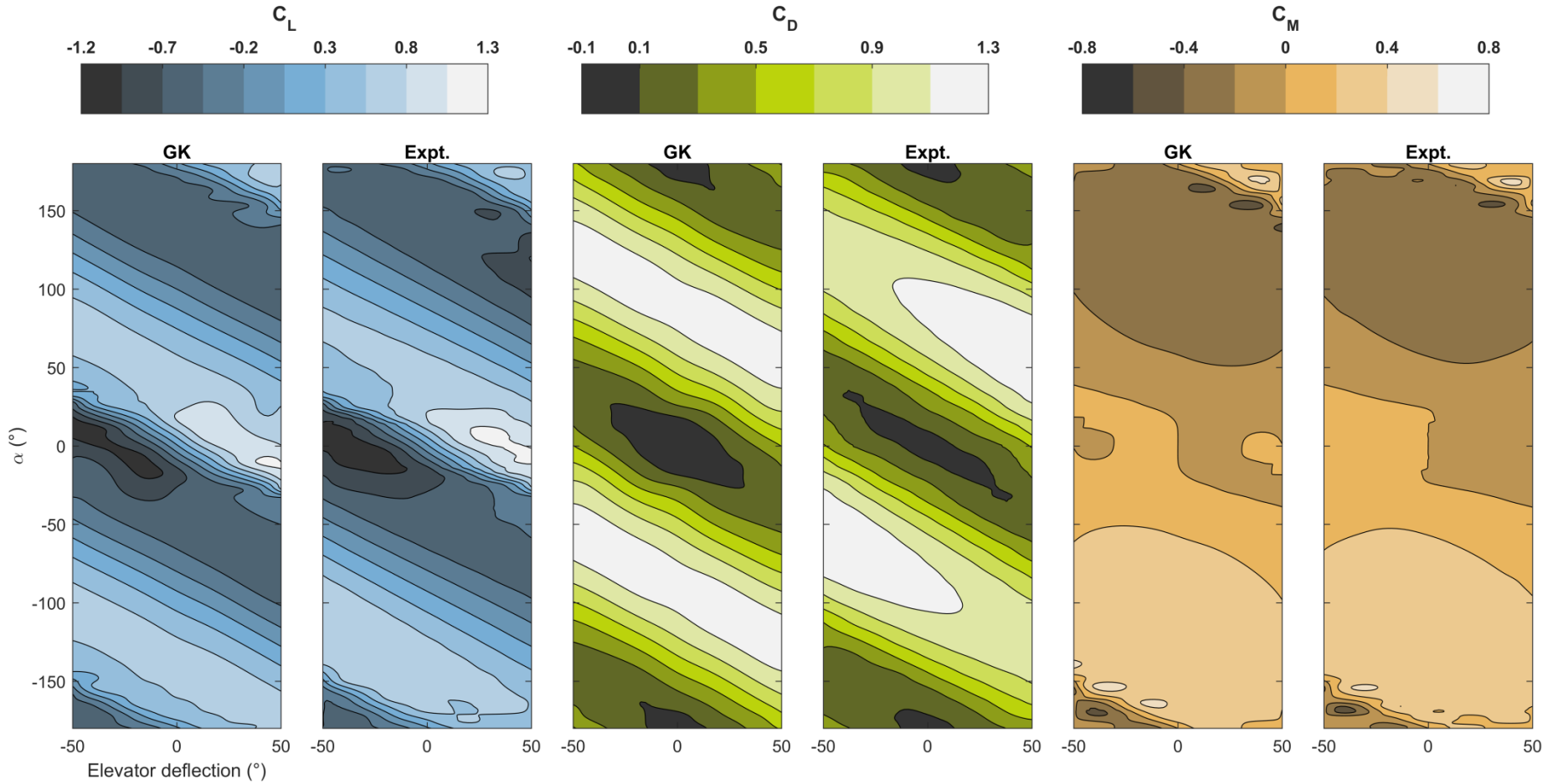

Figure 8.2.7: Aerodynamic coefficient data reconstructed from the GK separated and attached flow data, combined using $p_{0,i}$ and compared to the original results.

8.2.4. Dynamic parameter identification

This nearly completes the GK model formulation for all lifting surfaces. However, two key parameter sets are yet to be identified; the delays $\tau_{1,i}$ and $\tau_{2,i}$. Transient aerodynamic data is required for their identification. In the current literature, experimental data is available for a variety of oscillating airfoils – particularly with regard to wind turbines [12,14,28], which can show significant dynamic stall effects – but not for the proprietary case study aerofoils (ST50W/H). The choice of these aerofoils was motivated both by their use in existing highly-manoeuvrable aircraft, and, more importantly, by the availability of aerodynamic data for all angles of attack and with control surface deflections. No aerofoils were found for which an existing complete dataset of transient and quasistatic aerodynamic data was available. Existing GK model identifications are also available for a few aerofoils, but the variation in identified delay parameters across similar or even identical aerofoils indicates that the GK-delays are strongly dependent on the GK-decomposed quasistatic model. Table 8.2.2 presents a range of delay parameters identified in the literature for three different aerofoils.

Table 8.2.2: GK delay parameters reported in the literature

Aerofoil	$\tau_1\ (c/U)$	$\tau_2\ (c/U)$	Source	Reynolds No.
NACA0009	2.5	2.0	An et al. [29]	4.9×10^4
	2.28	3.41	Reich et al. [21]	not stated
	2.6	2.8	Williams et al. [23]	5×10^4
	3.6	4.3	Williams et al. [24]	5.7×10^4
NACA0015	0.52	4.5	Goman [11]	c. 2×10^5
	2.14	13.56	Fan [30]	not stated
NACA0018	0.25	3.6	Williams et al. [23]	2.5×10^5
	1.57	1.52	Greenblatt et al. [31]	3×10^5
	1.73	4.83	Niel [32]	1.9×10^5

The variation across the reported values – with minimal change in Reynolds number – is large: for the NACA0009 factor of 2 variation (in τ_2) is observed across the reported values; for the NACA0012 a factor of 4 (in τ_1); and for the NACA0018 a factor of 7 (in τ_1). These results indicate that the identification of the delay parameters is highly sensitive to the dataset – potential factors include wind-tunnel/wall effects, surface roughness, and CFD

modelling inaccuracies. This is consistent with the observation that the identification of the delay parameters is dependent on the aerofoil behaviour in the laminar-turbulent transition, and the projection to the hypothetical attached flow model at angles-of-attack below quasistatic stall – both of are strongly dependent on modelling / dataset specifics. It is thus not possible to obtain delay parameter values from the literature in a manner that is robust and justifiable.

A similar difficulty is observed when attempting to use transient aerodynamic data from other similar aerofoils to compute delay parameters for the ST50W/H: this was attempted, but even minor inconsistencies between the quasistatic and transient data sources prevent the delay parameters from being accurately identified. For this reason, CFD is used to generate situationally-specific transient aerodynamic data, which is used to identify the GK delay parameters for the ST50W/H aerofoils, consistent with their CFD quasistatic data. This adds robustness and situational appropriateness to the GK model, and provides some justification for the modelling parameters taken.

8.3. TRANSIENT COMPUTATIONAL FLUID DYNAMICS

8.3.1. Model formulation

To gather higher-fidelity data on the effect of the system parameters on the GK dynamic stall delays, this study turns to computational fluid dynamics (CFD). A two-dimensional transient flow simulation of the aerofoil is created in OpenFOAM, equipped with a moving-mesh solver to allow arbitrary specified in-plane wing motion. Figure 8.3.1 shows the simulation geometry, along with the standard simulation mesh shown (see Section 8.3.2) and the boundary conditions noted below. A moving-mesh approach (with a grid fixed to surfaces, but flexible in the flow) is chosen over an immersed boundary method (with the moving aerofoil immersed in a rigid grid) or a chimera approach (with overlapping rigid grids) as the former allows better resolution of boundary layer separation at low model complexity. This comes at the cost of a somewhat restricted mesh displacement (e.g. in the case study system, rotation angles $<40°$).

Turbulence in the flow domain is modelled using the Menter shear-stress-transport (SST) turbulence model [33], and wall functions are used to resolve boundary layer effects. The domain geometry and boundary conditions are specified in Figure 8.3.1. The freestream condition on the turbulent kinetic energy (k) and specific rate of dissipation (ω) boundary conditions is a switching condition which imposes a fixed freestream value on cells with flow into the domain, and zero gradient on cells with outward flow. The flow initial conditions are supplied via a steady state solution to system at the initial aerofoil orientation, obtained via the SIMPLE algorithm [34]. The transient flow equations are solved using the PIMPLE algorithm, an OpenFOAM -specific combination of the SIMPLE and PISO algorithms [35,36]. The aerofoil profile is extracted from the ST50W aerofoil with the permission of Horizon Hobby LTD, utilising the data provided by Selig [26]. The aerofoil is smoothed at the trailing edge to enable continuous meshing. The smoothed aerofoil chord is normalised; the length different is <5% of the extracted profile.

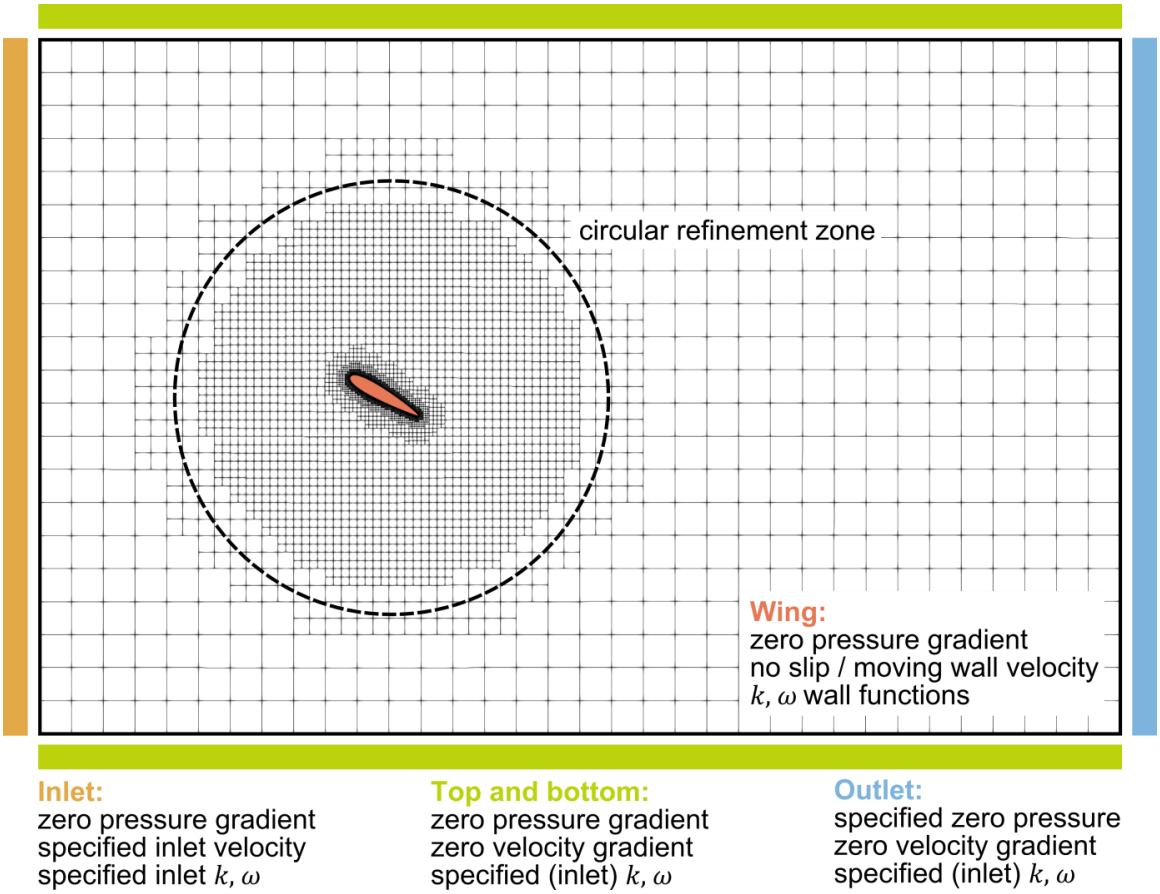

Figure 8.3.1: Schematic of CFD model geometry, mesh and boundary conditions at static angle-of-attack 30°.

8.3.2. Meshing and mesh independence

The flow domain mesh is generated from an initial uniform hex mesh, which is refined in a circular area around the aerofoil profile. Boundary-layer cells are extruded from the aerofoil surface. The result is a mesh composed primarily of hex elements, with a minority of polyhedral elements. Figure 8.3.1 shows an example mesh for the domain. The key parameters controlling the mesh generation are the initial hex mesh size, the degrees of refinement, and the number of boundary cell layers. A mesh independence study is carried out to determine the appropriate mesh resolution. The benchmark test is the aerofoil lift at Reynolds number 3.08×10^5, a dynamically-equivalent state to forward flight at airspeed 30 m/s in the biomimetic case study system, and at a static angle-of-attack of 30°. This point is directly within the laminar-turbulent transition of the aerofoil. The lift, drag and moment coefficients, along with the aerofoil surface pressure distributions at specified times, are compared for logarithmically spaced mesh sizes. Note that the initialisation of the simulation at a constant airspeed at all flow points generates spurious lift peaks at $t < 0.1$ s: timesteps below this value are not used in the calculation of the results in Tables 8.3.1-8.3.2. This effect can be avoided by simulating dynamic aerofoil motion from attached flow-states; which is what is used for the delay parameter identification simulations.

Table 8.3.1 shows the statistics for the studied meshes; Table 8.3.2 the quantified results of the mesh independence study; Figures 8.3.2-8.3.4 the mesh independence study time- and mesh size-dependent results. The primary metrics of mesh independence are the aerodynamic coefficient profiles (Figures 8.3.2), with the aerofoil pressure distributions at specified time values (Figures 8.3.3) as corroborating evidence. The latter are not good primary metrics as they are sensitive to time and hydrodynamic instability – that is, small shifts in e.g. the vortex shed time lead to significant pressure distribution changes; a fact reflected in the high coefficient derivatives observed in Figure 8.3.2. The mean cell size h is calculated from the number of cells N, domain area A, and aerofoil chord c, as $h = \sqrt{A/N}/c$ (in %), and represents the mean lengthscale of the cells relative to aerofoil chord. The lift, drag, moment and pressure errors are computed relative to the reference mesh (no. 6). This reference mesh is consistent with the benchmark results of [37], which attain mesh independence within the aerofoil laminar-turbulent transition, at $Re > 10^6$, with c.

700 nodes on the aerofoil surface. These benchmark results, however, also indicate the presence of a systematic overestimation of lift coefficient by RANS results for two-dimensional aerofoil flow; attributable either to the importance of three-dimensional effects in the generation of this lift coefficient; or to some systematic flaw common to a range of turbulence models (SST [33], Spalart-Allmaras [38], DRSM [39], WJ-BSL-EARSM [40], and others) [37]. The ramifications for this are that the aerodynamic coefficients computed by our CFD model will be approximate; and will require a dedicated GK quasistatic parameter identification in the likely event of any discrepancy between the experimental and computational results. However, one saving grace in this context is that the only output for the model is the time delay parameters (τ_i), which will be applied to the experimental GK quasistatic aerodynamic profiles, without any reference to the CFD profiles. In this way, providing that the timescale of the lift hysteresis effects are modelled accurately, the delay parameters will be identified accurately. Or put another way; the identification of delay parameters occurs in an internally-consistent system that is analogous to the empirical quasistatic system (i.e. the CFD system), and even if the lift coefficient is overestimated, there is more reason to believe that the lift hysteresis timescale will remain analogous. Of course, effects behind the lift coefficient overestimation may also affect the lift hysteresis timescale: to what extent this is the case is an open question. In the case of three-dimensional effects, there may be physical reason to suppose an analogous timescale. If so, then the identified time delay parameters may be less inaccurate that the lift coefficient results themselves.

As can be seen, an approximately mesh-independent solution is reached by mesh nos. 4-5: the aerodynamic coefficient profiles up to $t = 2.5$ s ($= 0.56\ c/U$) are converging observably to a mesh-independent state with errors of c. 10% or less relative to the reference mesh. The pressure distributions show similar good convergence, with an anomaly in the minimum pressure at $t = 2$ s for mesh no. 5, attributable to time- and instability-sensitivity, and a coincidently accurate value at the coarsest mesh for the maximum pressure also at $t = 2$ s. Mesh no. 5 is utilised for further simulations: Figures 8.3.5-8.3.6 show snapshots of the flow properties (flow velocity magnitude and total pressure) at times $t = 1.5$ s and $t = 2$ s. for interpretation. One further point may be made: the only difference between meshes no. 3 and 3b is the number of aerofoil boundary layer; the purpose of this univariate change is to

demonstrate the negligible difference in solution between simulations at maximum y^+ of ≅ 10 and ≅ 1 (see Figures 8.3.2-8.3.3). This indicates the that the k-ω wall-functions are appropriately accurate at the larger y^+ values, and that there is no need to attempt to resolve the viscous sublayer.

Table 8.3.1: Mesh specifications for mesh independence study

Mesh no.	Total no. nodes	Mean cell size	Refinement	Layers	Aerofoil nodes.	Max. y^+
1	9183	12.0% c	6L / 4C	13	279	0.82
2	14129	9.7% c	6L / 4C	13	410	0.60
3	18411	8.5% c	6L / 4C	6	573	6.93
3b	21276	7.9% c	6L / 4C	11	573	1.03
4	29413	6.7% c	6L / 4C	4	818	8.81
5	47159	5.2% c	5L / 2C	6	577	7.31
6	89933	3.8% c	5L / 2C	5	818	7.16

Table 8.3.2: Mesh independence study results

Mesh no.	Mean cell size	Lift error	Drag error	Moment error
1	12.0% c	54.6%	50.4%	101.2%
2	9.7% c	34.8%	34.1%	61.9%
3	8.5% c	21.8%	20.2%	36.3%
3b	7.9% c	21.0%	19.4%	34.4%
4	6.7% c	7.1%	6.7%	10.7%
5	5.2% c	6.0%	5.3%	9.2%
6	Reference			

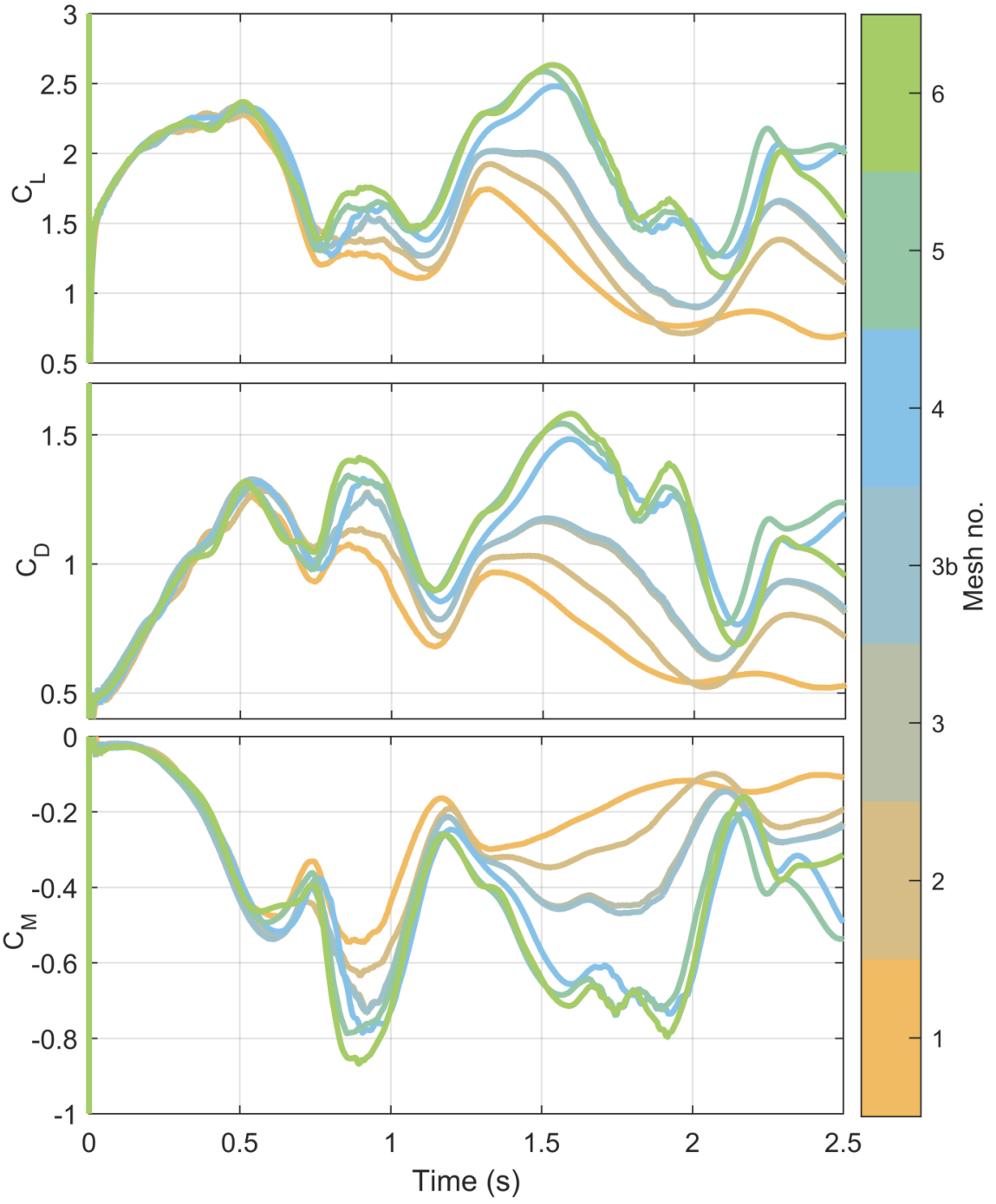

Figure 8.3.2: Aerodynamic coefficient histories for the mesh independence study meshes.

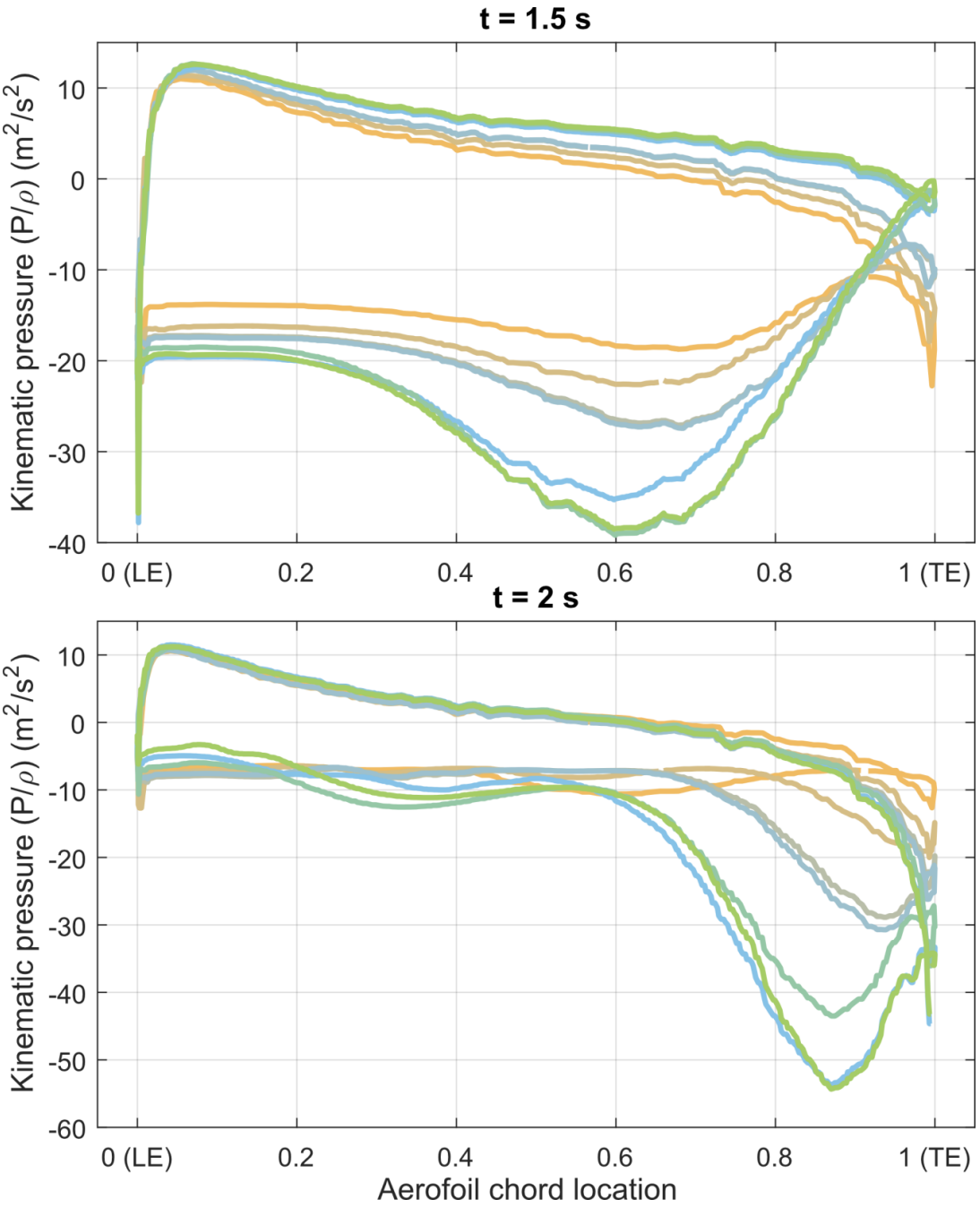

Figure 8.3.3: Aerofoil pressure distributions at $t = 1.5$ s and $t = 2$ s for the mesh independence study meshes.

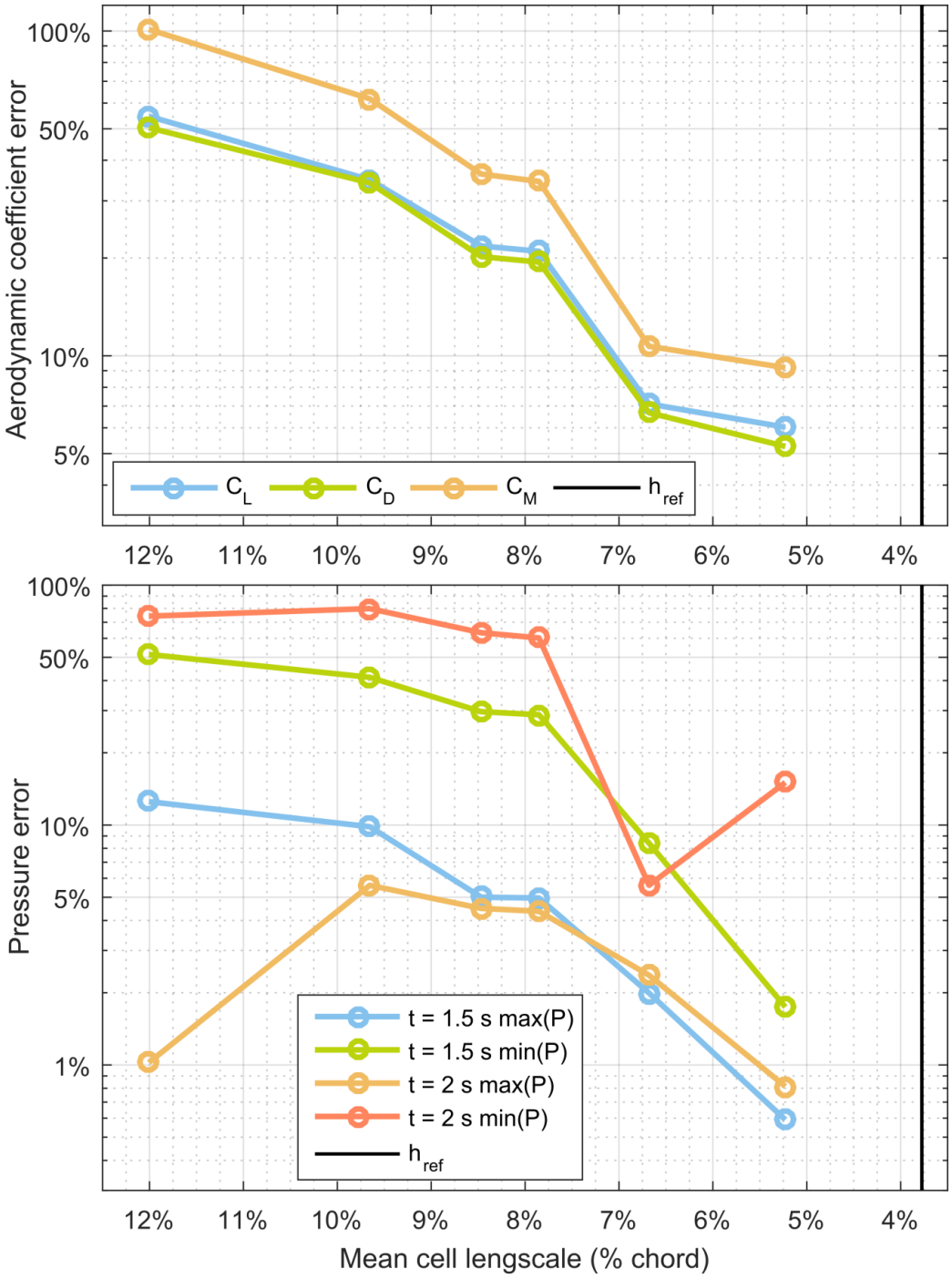

Figure 8.3.4: Aerodynamic coefficient and pressure distribution errors for the mesh independence study.

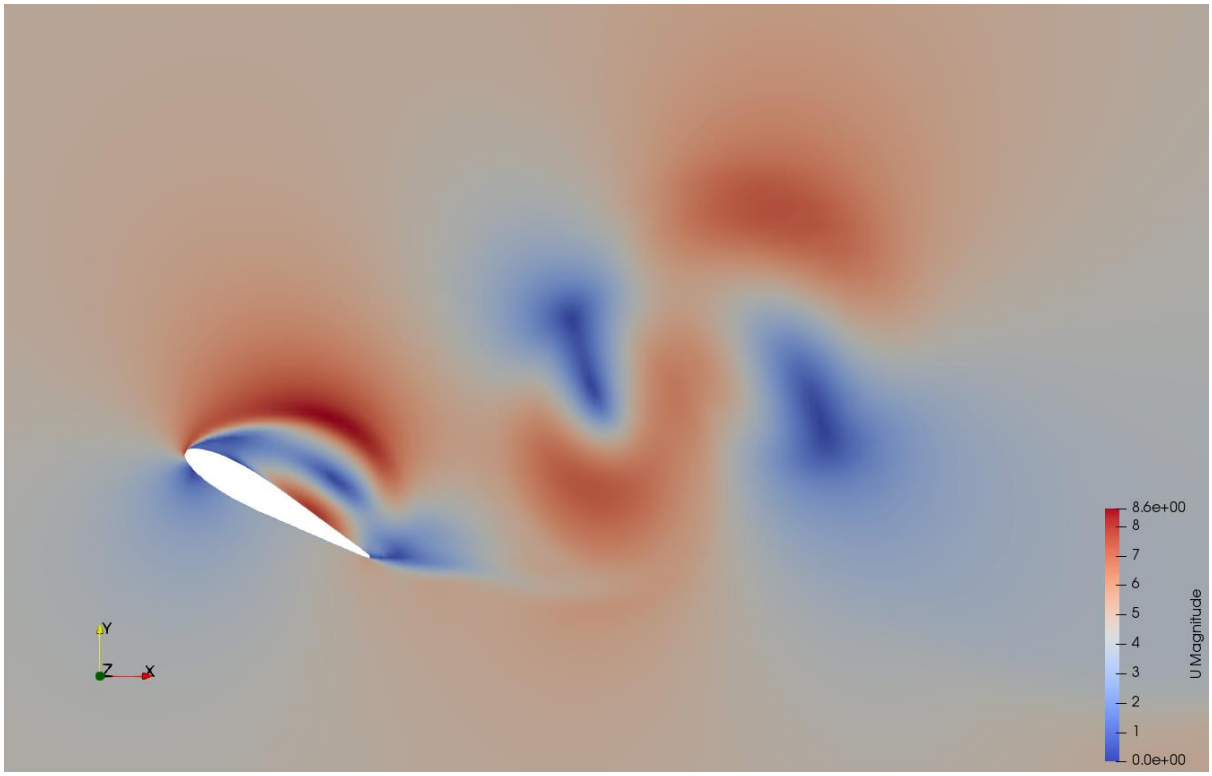

Flow velocity magnitude at t = 1.5 s (zoomed)

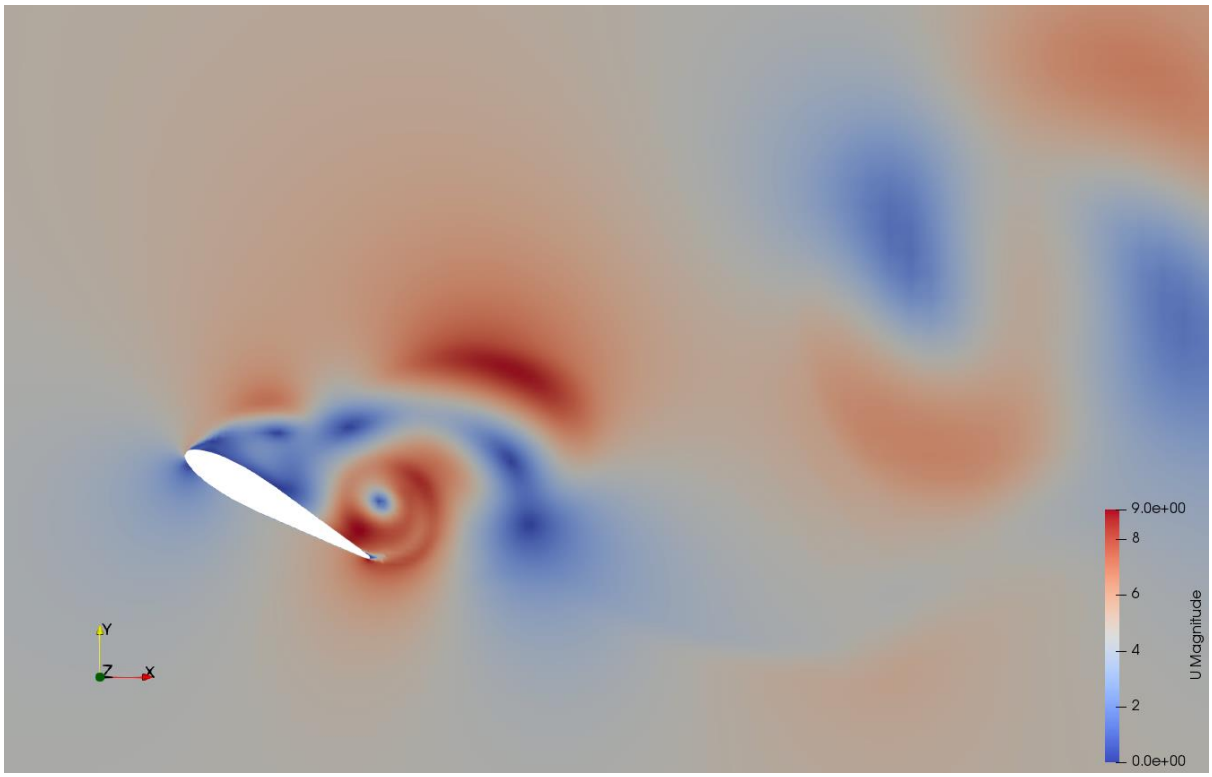

Flow velocity magnitude at t = 2 s (zoomed)

Figure 8.3.5: Rendering of the flow velocity magnitude at $t = 1.5$ s and $t = 2$ s for the converged mesh.

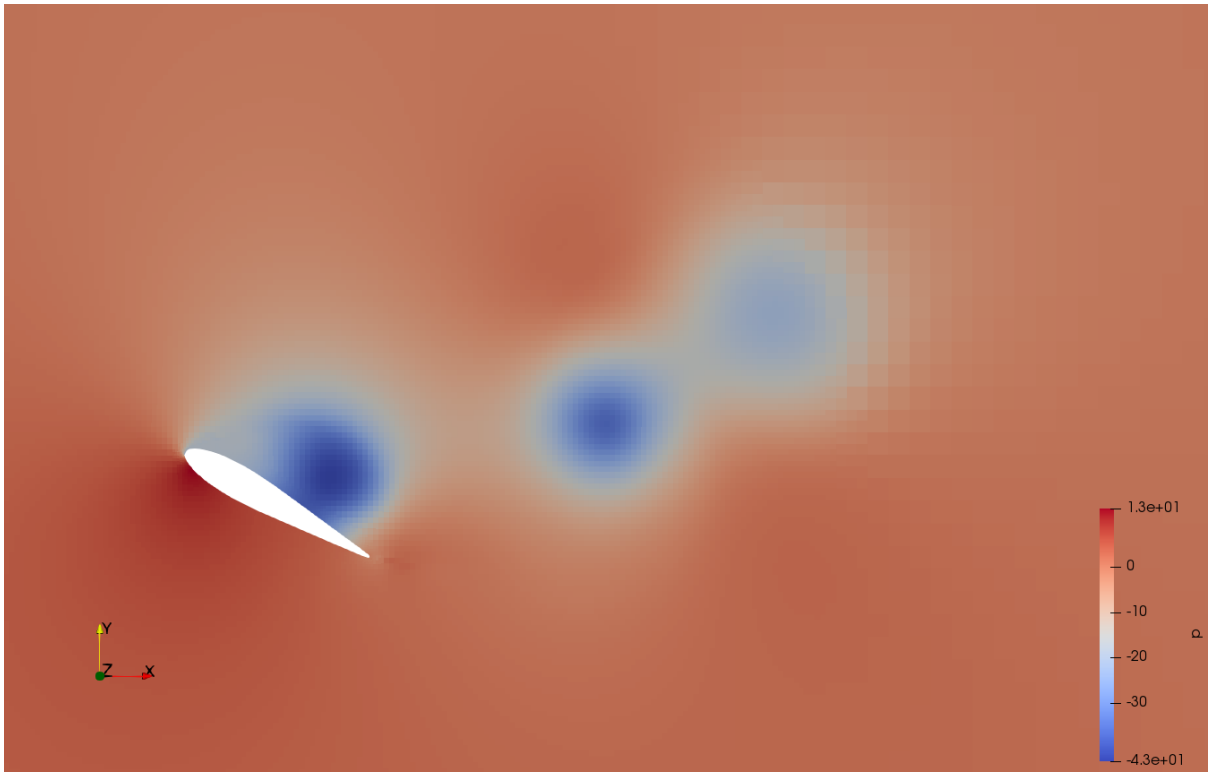

Flow total pressure distribution at t = 1.5 s (zoomed)

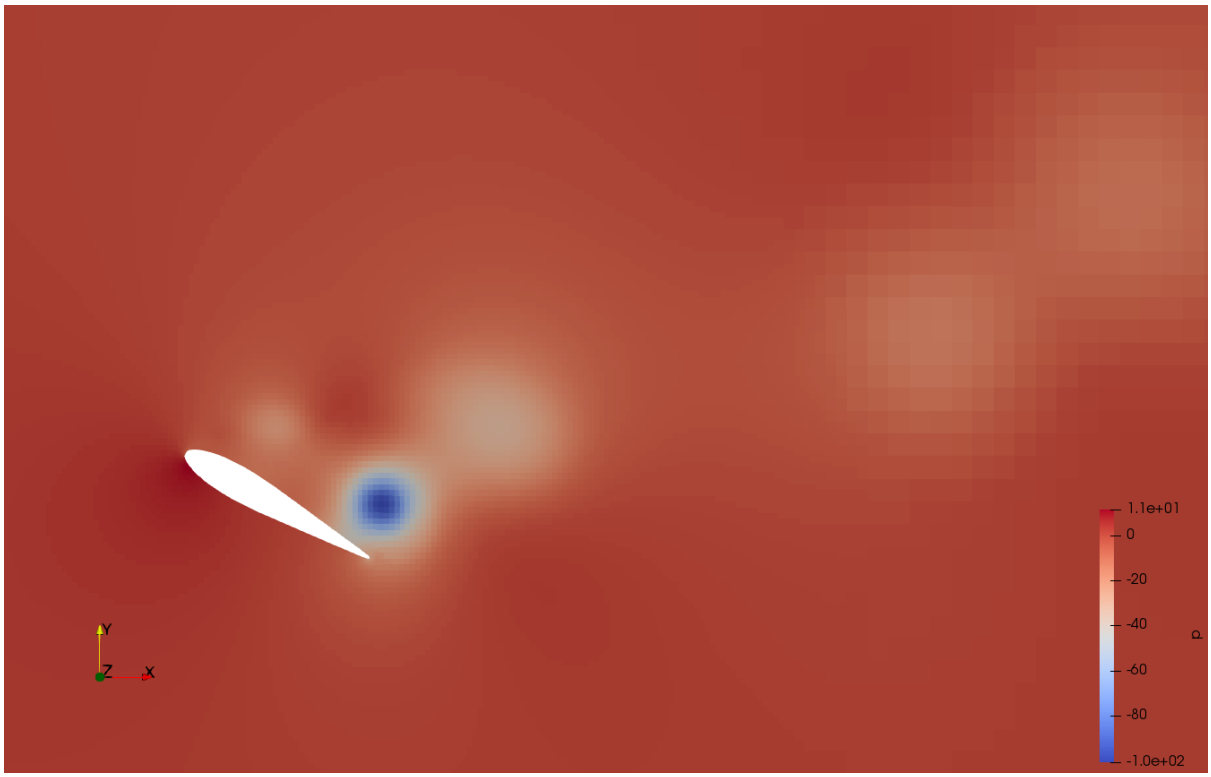

Flow total pressure distribution at t = 2 s (zoomed)

Figure 8.3.6: Rendering of the flow total pressure distribution at $t = 1.5$ s and $t = 2$ s for the converged mesh.

8.3.3. Quasistatic coefficient functions

To enable an identification of the dynamic GK parameters from the CFD data, a re-identification of the static properties of the CFD model is first required – the appropriate quasistatic GK functions may differ from those of the empirical data. This data is generated via steady-state and transient simulations at fixed angles-of-attack – steady-state for solutions without vortex shedding; and transient for those with vortex shedding. These simulations are carried out at a dynamically-equivalent state to forward flight at airspeed 30 m/s in the biomimetic case study system – representative of the transient manoeuvres studied in Chapters 6-7. For the wings and stabilisers this corresponds to Reynolds number 3.08×10^5 (airspeed 4.5 m/s for reference chord 1 m). Mesh no. 5 from the mesh independence study, which was established as showing acceptably mesh-independent behaviour, is utilised. As per the mesh independence study, Figure 8.3.7 shows the mesh properties and format. Figure 8.3.7 shows the mesh no. 5, generated for an ST50W aerofoil at zero angle-of-attack.

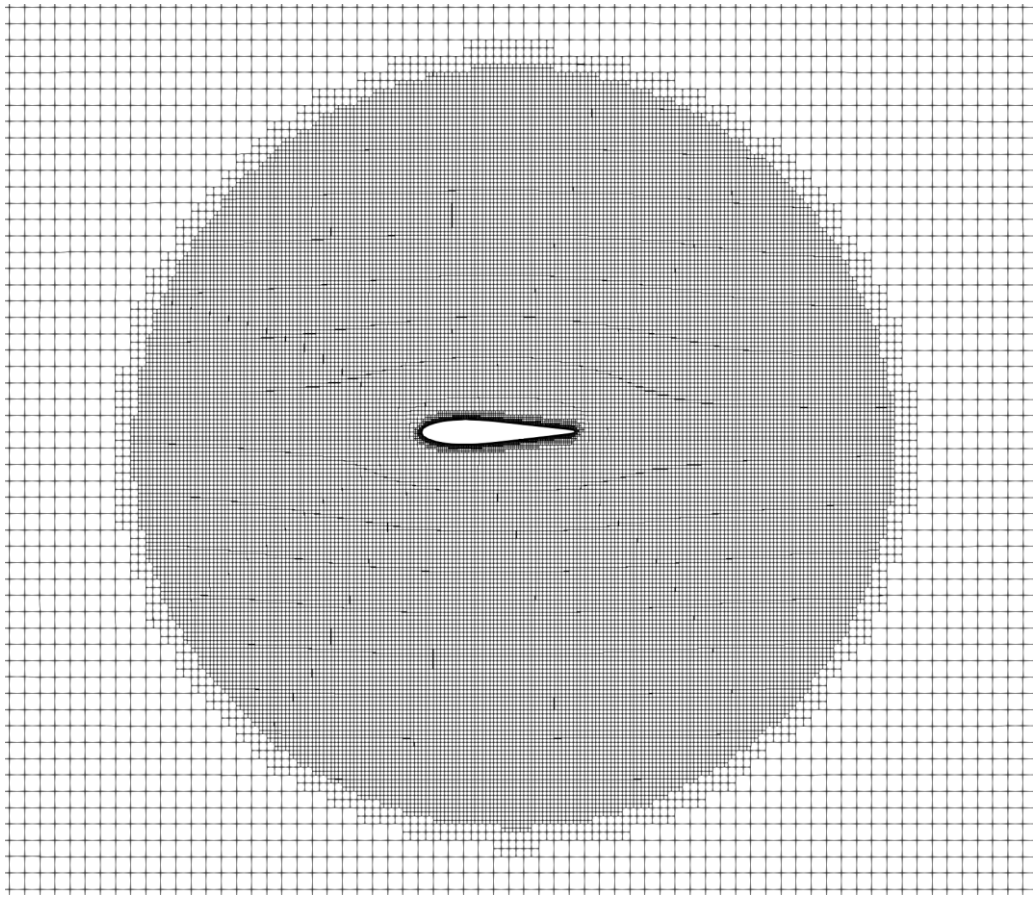

Figure 8.3.7: Dynamic stall simulation mesh in the vicinity of the aerofoil.

Figure 8.3.8 shows these quasistatic results for the ST50W aerofoil, and the results of GK static parameter identification in the lift coefficient, computed as per the ST50W identification in Section 8.2.2, and using the arctangent p_0 function modified from Reich et al. [21] (Eq. 8.2.4) with $w = 1.45$. Additional to the fixed-angle simulations; the aerofoil is subjected to a low-frequency sinusoidal oscillating motions of the form:

$$\alpha = \frac{1}{2}\hat{\alpha}(1 - \cos(\Omega t)), \tag{8.3.1}$$

with amplitude $\hat{\alpha}$ and frequency Ω determined by the reduced frequency $\kappa = b\Omega/U$. Simulations of this format will form the basis of the dynamic stall analysis in this work, but at low frequencies the results tend towards their quasistatic counterparts. At $\kappa = 0.05$ ($\hat{\alpha} = 20^{\circ}$), taken by several authors as a threshold value for quasistatic/transient behaviour [41,42], the error between the peak lift values is c. 30%.

Some discrepancy is observed between the CFD results and the original data. The details behind this are unclear: in addition to the expected inaccuracy in CFD results, as per [37], lift hysteresis, dynamic or static, may also have an effect – the slower continuous pitch-up results show significant affinity with the original results of Selig [26]. This possibility is given further weight by the identification in Section 8.2.2 that the lift and moment separation points for this dataset were inconsistent – as per Figure 8.3.8, hysteresis delay effects are much more visible in lift coefficient than they are in moment coefficient. A further factor in the CFD/original dataset discrepancy is the presence of tunnel-like flow conditions in the CFD simulation, which may accentuate the aerofoil lift under separated flow [43], among other possible effects. The domain, being a width of $9c$ and length of $14c$ with open boundary conditions, may not be completely large enough to eliminate wall effects from the local aerofoil flow. However, these effects are consistently replicated in the dynamic stall data; and, at low magnitude, they are not expected to significantly alter the identified flow time delays. The effect of wall conditions on the GK time delays would be a useful topic for further research and validation; as it might enable CFD simulations for GK identification to be carried out in small domain sizes, reducing the computational effort required.

A further notable aspect of these results is the failure of the GK model to predict the transient drag and moment behaviour of the aircraft. Drag and moment peaks are observed

in the aerofoil pitch-up phase, associated with shed vortices, and directly contradicting the GK predictions of a longer attached-flow (low drag/moment) region. This is the primary transient effect associated with drag and moment coefficients – corroborating evidence for this, across of a range of reduced frequencies, is presented in Section 8.3.4 – but it is not capturable by the GK model. For this reason, drag and moment coefficients are omitted in further GK modelling, with the original quasistatic data being used instead.

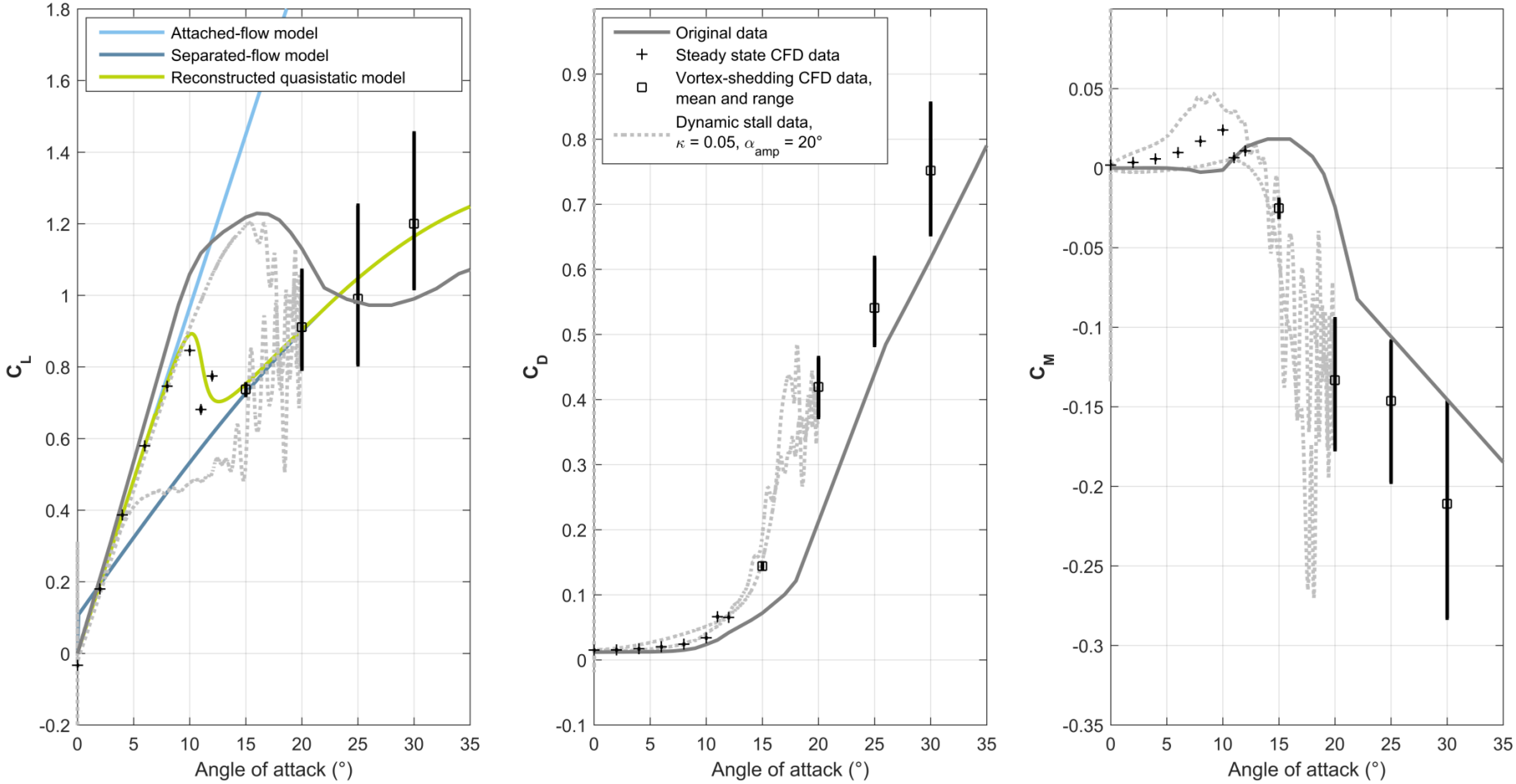

Figure 8.3.8: Quasistatic aerodynamic coefficients for the ST50W aerofoil computed via CFD, and the associated GK static parameter identification results. $\hat{\alpha}$ is denoted α_{amp} due to notation limitations.

8.3.4. Delay parameter identification

Dynamic stall simulations are carried out as per Section 8.3.3, with $\kappa \in [0.05\ 1]$ and $\hat{\alpha} \in [20\ 30]°$. Figures 8.3.9-8.3.10 show the angle-of-attack-domain and time-domain lift coefficient data for the simulated scenarios. Figure 8.3.11 shows the field of identification errors for those datasets identified qualitatively to be within the range of GK model validity; these are computed as:

$$E = \frac{1}{T}\int_{t=0}^{t=T} \left| C_{L,\mathrm{GK}} - C_{L,\mathrm{CFD}} \right| dt. \tag{8.3.2}$$

Figure 8.3.12 shows the mean identification error across these datasets; Figure 8.3.13 the GK identification errors as a function of κ and the maximum reduced pitch rate $\max(r)$. The reduced pitch rate analogously to κ as $r(t) = \dot{\alpha}(t)b/U$, with $\dot{\alpha}(t)$ in rad/s; for oscillations according to Eq. 8.3.1, $\max(r) = \hat{\alpha}\Omega b/2U = \hat{\alpha}\kappa/2$ for $\hat{\alpha}$ in rad. Figure 8.3.12 shows the CFD drag and moment coefficient results.

Figures 8.3.9-8.3.10 show several significant flow effects. Delayed-separation and delayed-attachment are observed, particularly for $\kappa \leq 0.25$, and are consistent with the expected nature of dynamic stall. Vortex shedding effects are significant: at $\kappa = 0.05$ these are generated freely in the separated-flow region; but for $\kappa \geq 0.25$, these vortex effects are also observably entrained by the aerofoil oscillation. This leads to consistent vortex shedding peaks at the maximum angle of attack, and consistent shedding profiles in the delayed-separation region ($\dot{\alpha} < 0$). At $\kappa = 0.4$ there is what may be a resonance effect; with entrained vortices in the delayed-separation region leading to an otherwise inexplicably narrow profile.

Added mass effects begin to become significant for $\kappa \geq 0.5$; these are manifested in the form of ellipsoid curvature in the lift coefficient profiles, and increasing lift values across the initial attached flow region even before the peak angle-of-attack. This phenomena may be compounded by other unsteadiness in the circulatory lift; and indeed these effects may be amendable to modelling as a linear function of $\dot{\alpha}(t)$, as per Theodorsen's theory [44]. However, they are uncapturable by the GK model, which can only ever operate in the space between $C_{L,\mathrm{att}}(\alpha)$ and $C_{L,\mathrm{sep}}(\alpha)$. The increasing dominance of added-mass effects must thus be regarded as the limiting factor on the accuracy of the GK model at high κ. In this

system, a qualitative assessment yields $\kappa = 0.5$ as the threshold for GK model breakdown due to added mass effects.

In Figures 8.3.11, note the variation in the local optimal τ_1,τ_2 over κ, with a trend of $\tau_1 \propto 1/\kappa$. The mean error profile indicates an identification error minimum at $\tau_1 =$ c. $4c/U$, $\tau_2 =$ c. $2.5c/U$; but several qualitative considerations are also present. Increasing τ_2 serves to increase the length of the initial delayed-separation region, while maintaining a sharp cut-off in separation at the peak (the original p_0 scale), as is observed in the CFD data. However, values of τ_2 that are too large ($>3c/U$) will lead to separation at very low angles-of-attack via the negative ($\alpha < 0$) branch of p_0. This effect may be observed in the second- and third-period branches of the identified model at $\kappa =$ 0.5 and 1. Increasing τ_1 also increases the length of the delayed-separation region, but leads to more gradual separation, as the effect of p_0 is scaled proportional to τ_1. This is not observed in the CFD data. Moreover, values of τ_1 that are too large ($>2.5c/U$) lead to delay effects that are active across aerofoil oscillation periods at high κ – an effect which can be observed for $\kappa \geq 0.25$ in the identified model. In the CFD data, however, cross-period delay effects only manifest themselves at $\kappa \geq 0.5$.

The balance of these considerations leads to an identified result at $\tau_1 = \tau_2 = 2.3c/U$: while the identification errors can be improved by an increase in τ_1, this leads to an increasing degree of phenomenological inaccuracy. Figures 8.3.9-8.3.10 show the resulting identified model. Figure 8.3.13 presents a characterisation of the identified GK model accuracy: in terms of the absolute C_L error; and the improvement of the GK model over the quasistatic model. Within the bounds of validity, the GK model yields a reduction in the quasistatic error by a consistent factor of 0.5. This is a significant improvement, and the qualitative improvement in modelling fidelity may be observed clearly in Figures 8.3.9-8.3.10.

The same improvement in modelling fidelity is not possible in the drag and moment coefficients: Figure 8.3.14 presents further evidence to the conclusion of Section 8.3.3; that the GK model is not capable of capturing the transient effects associated with these coefficients. For this reason these coefficients are modelled via a quasistatic approach.

Further research into transient drag and moment reduced-order modelling is important if model-based control of biomimetic supermanoeuvrability is to be countenanced.

The upper bound of model validity is taken as $\kappa = 0.5$ and $r = 0.13$. Characterising the lower bound is more difficult. At $\kappa = 0.05$, taken by some authors [41,42] as the threshold of quasistatic behaviour, dynamic stall effects are still observed, with the quasistatic model showing an error in error in peak lift of c. 25%. Results from the literature are consistent the conclusion that dynamic stall effects are non-negligible at this reduced frequency [45–47]. Other authors locate the quasistatic/transient threshold at $\kappa = 0.03$ [48], $\kappa = \mathcal{O}(0.01)$ [49], and other values. CFD simulations of the ST0W at lower κ were not carried out due to the computational expensive involved in simulating long-period oscillations; but on the basis of further evidence from the literature, only the $\kappa = 0.01$ can be taken as a reliable threshold for quasistatic model validity. From the literature; at $\kappa = 0.025$;

- results by Ahaus [45] for the VR-12 aerofoil at oscillatory amplitudes (= ranges, as per Eq. 8.3.1) up to 20° indicate dynamic stall effects gradually becoming less significant (error in peak lift c. 10%, maximum hysteresis loop width c. 45% of peak lift);
- results by Coder [46] for the VR-7 aerofoil at oscillatory amplitudes up to 20° indicate slightly more significant effects (error in peak lift c. 25%, maximum hysteresis loop width c. 45% of peak lift);
- and results by Gerontakos [47] for the NACA0012 aerofoil at amplitudes up to 30° indicate highly significant dynamic stall effects (error in peak lift c. 67%, maximum hysteresis loop width c. 130% of peak lift).

Reynolds number and aerofoil profile differences are likely to be a factor in this discrepancy; but also, the neglect of the oscillatory amplitude – directly affecting the reduced pitch rate (r) – is also a significant oversight. At $\kappa = 0.01$; results by both Ramasamy et al. [50] and Guntur et al. [28] affirm the relatively minimal (though not vanishing) significance of dynamic stall effects. We take $\kappa = 0.01$ as the critical value for quasistatic model validity. For reference, as a lower bound for r, we take the maximum value for oscillations of amplitude 20° at $\kappa = 0.01$; $r = 0.0017$.

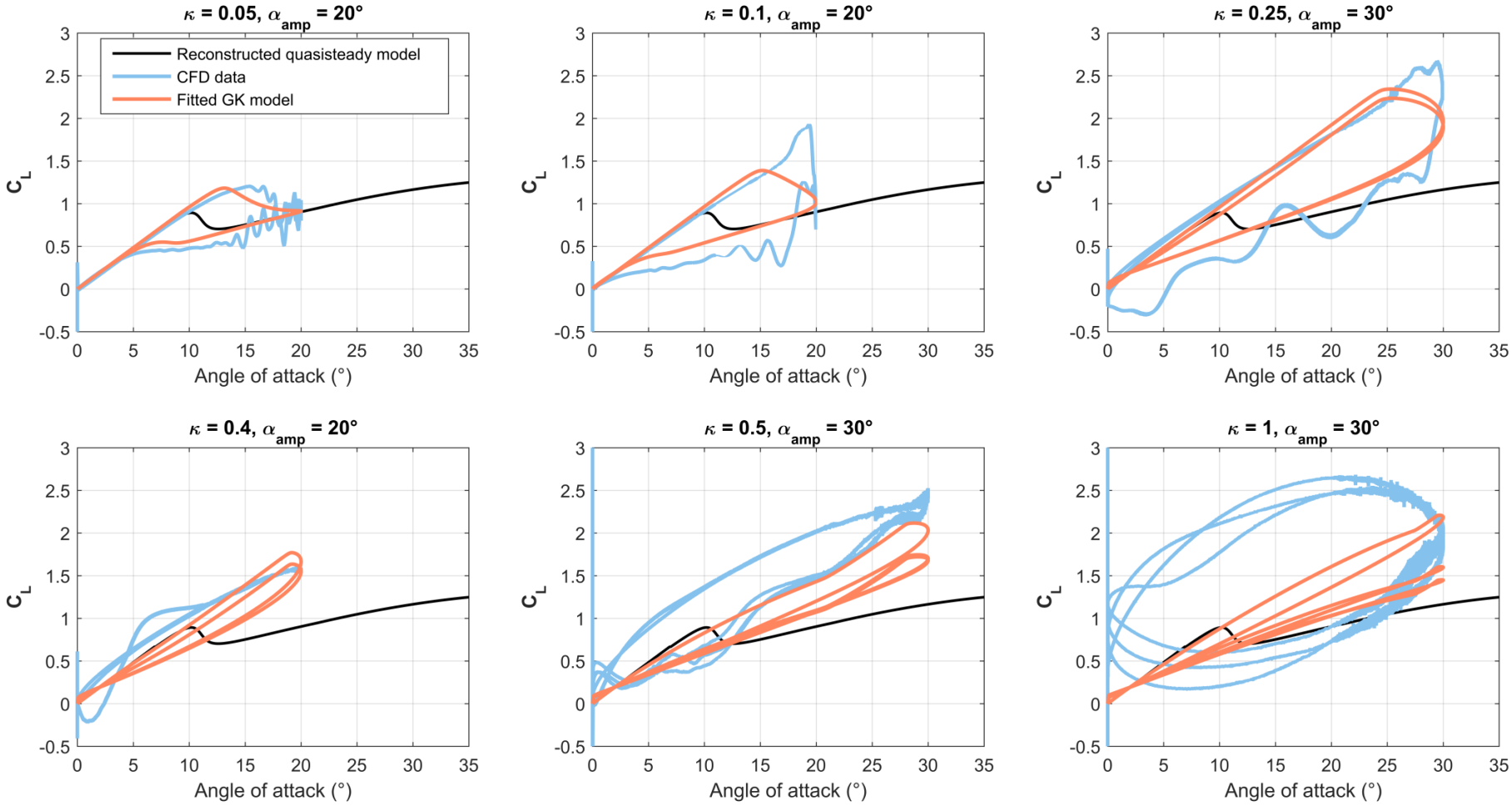

Figure 8.3.9: Dynamic stall results: CFD lift coefficient results in the angle-of-attack domain, with the identified GK model ($\tau_1 = \tau_2 = 2.3c/U$). $\hat{\alpha}$ is denoted α_{amp} due to notation limitations.

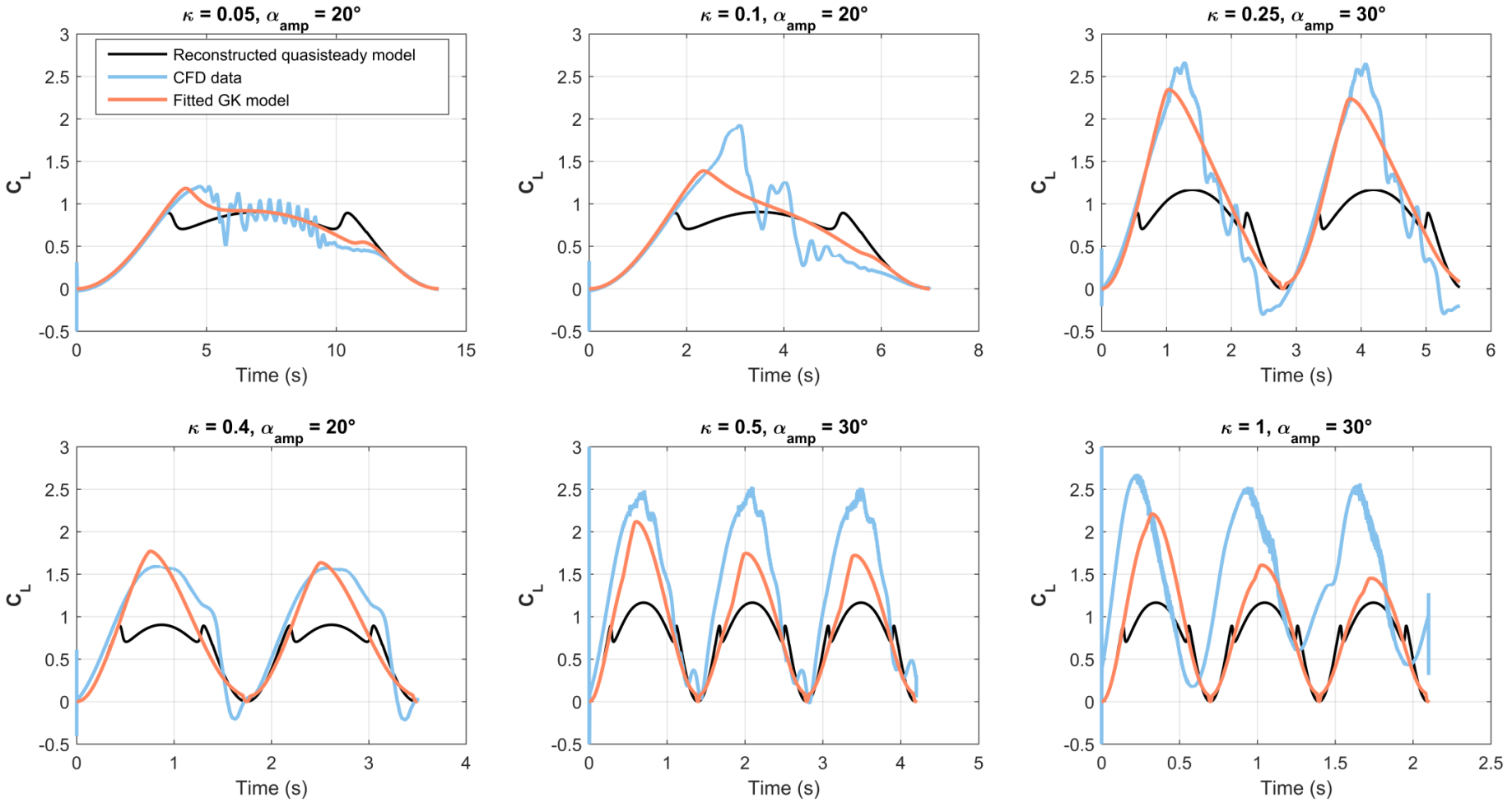

Figure 8.3.10: Dynamic stall results: CFD lift coefficient results in the time domain, with the identified GK model ($\tau_1 = \tau_2 = 2.3c/U$). $\hat{\alpha}$ is denoted α_{amp} due to notation limitations.

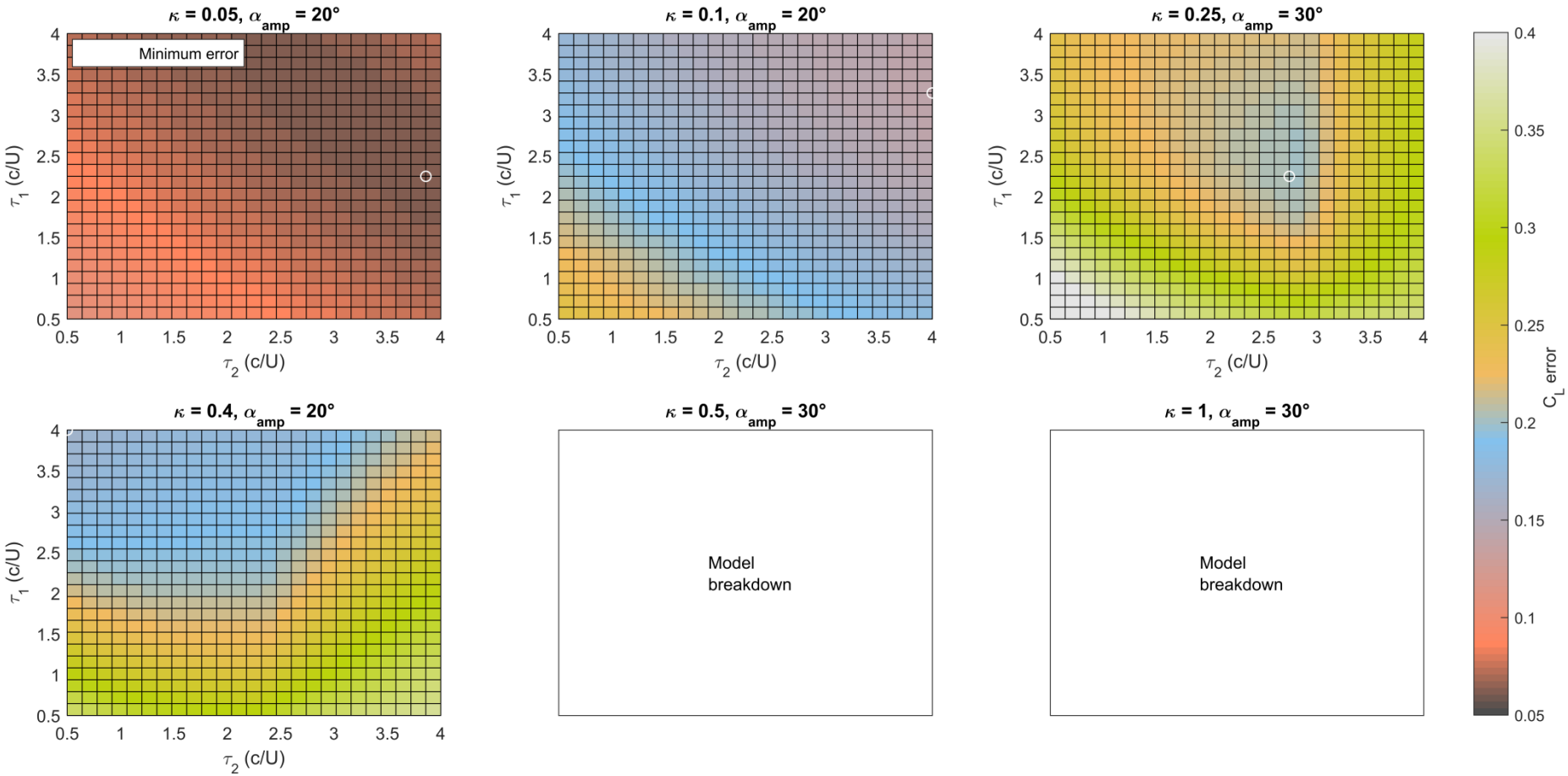

Figure 8.3.11: GK identification error (1-period C_L error integral, normalised by T) over the space of τ_1,τ_2, for reduced frequencies identified to be within the range of GK model validity. $\hat{\alpha}$ is denoted α_{amp} due to notation limitations.

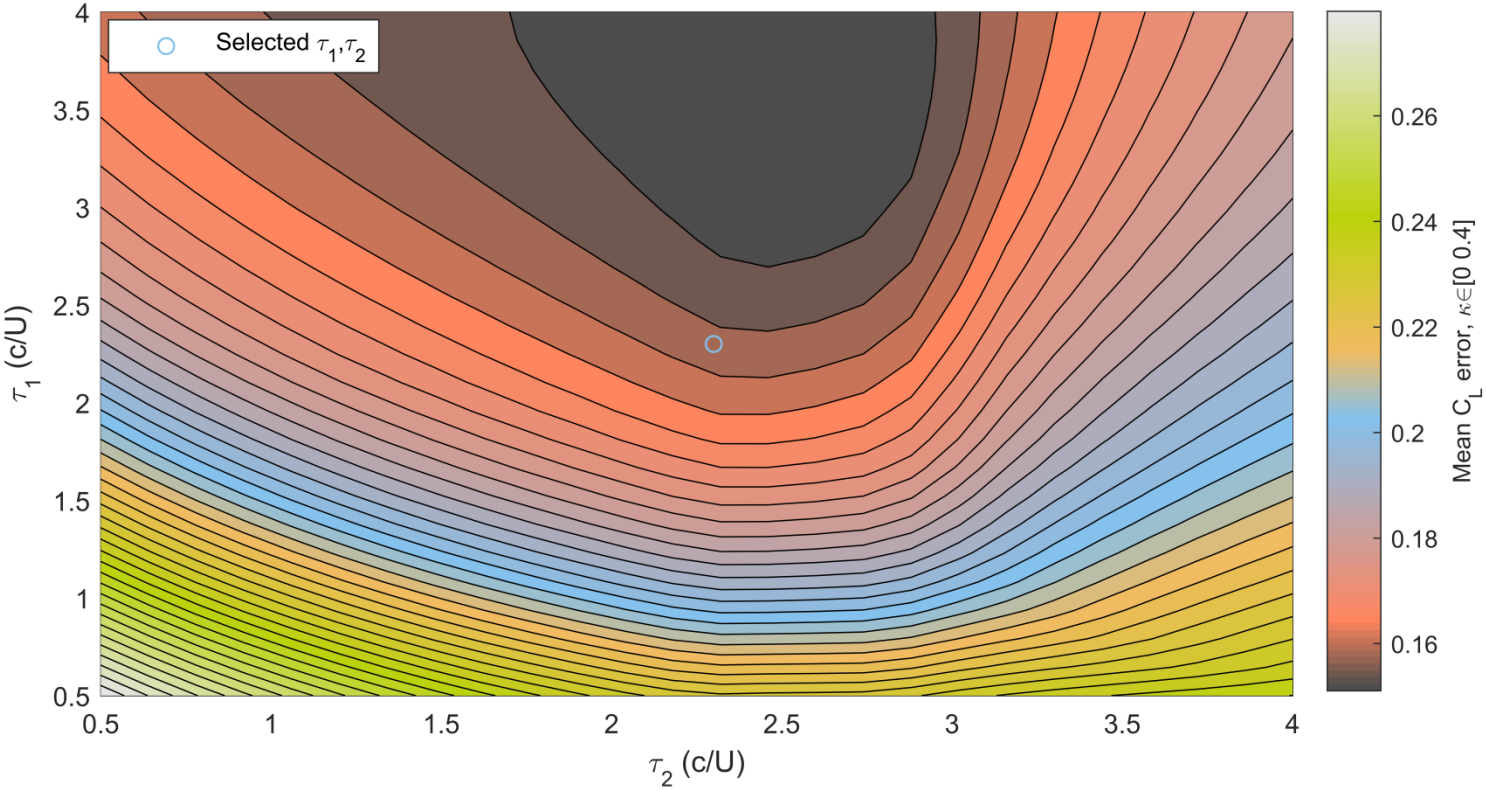

Figure 8.3.12: Mean GK identification error (mean 1-period C_L error integral, normalised by T) over the space of τ_1,τ_2, for reduced frequencies identified to be within the range of GK model validity. The selected point ($\tau_1 = \tau_2 = 2.3c/U$) is shown – note that considerations other than this error profile are present.

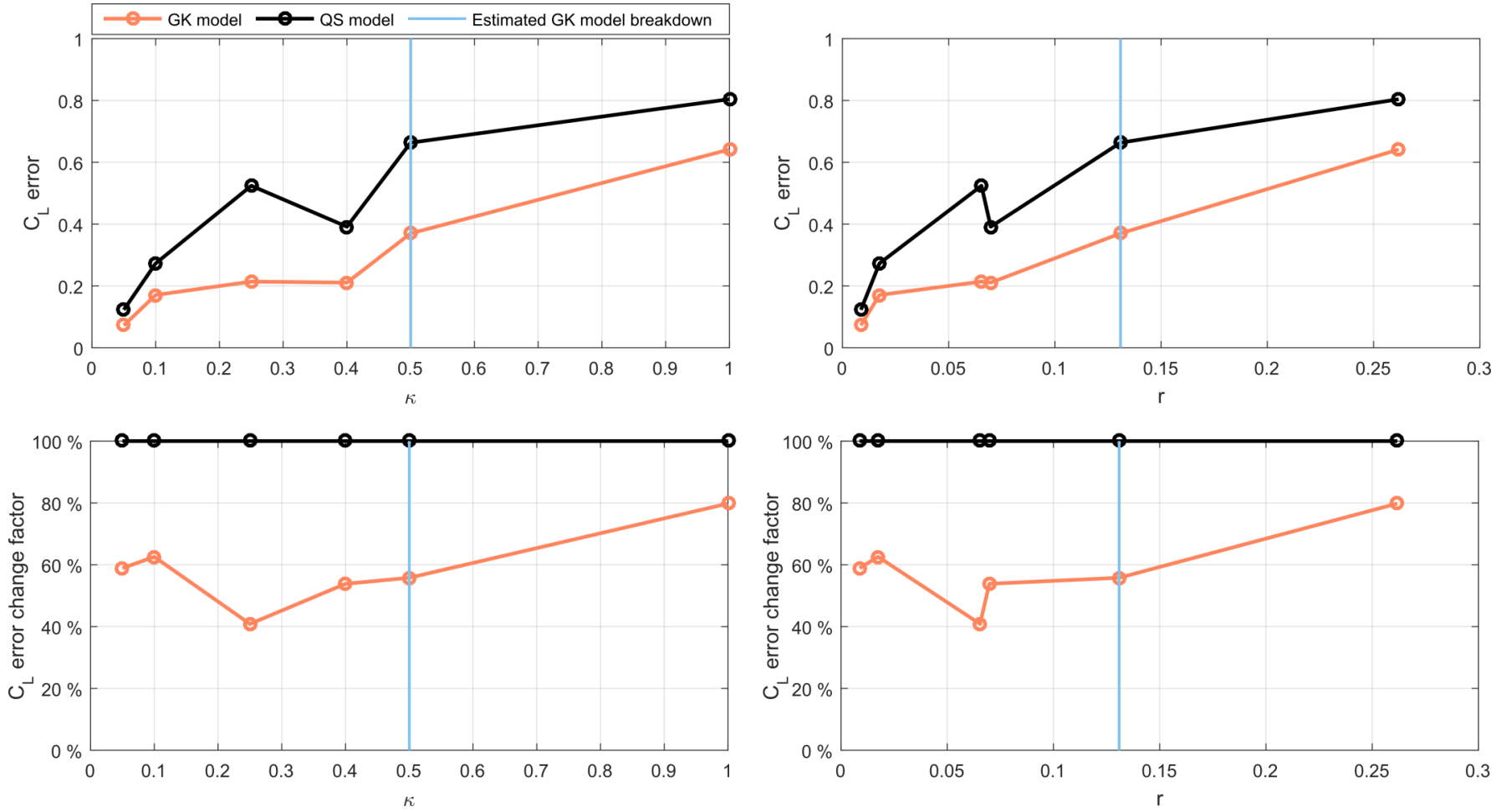

Figure 8.3.13: GK identification error (mean 1-period C_L error integral, normalised by T), and GK model improvement over the quasistatic (QS) model (GK error as a % of QS model error).

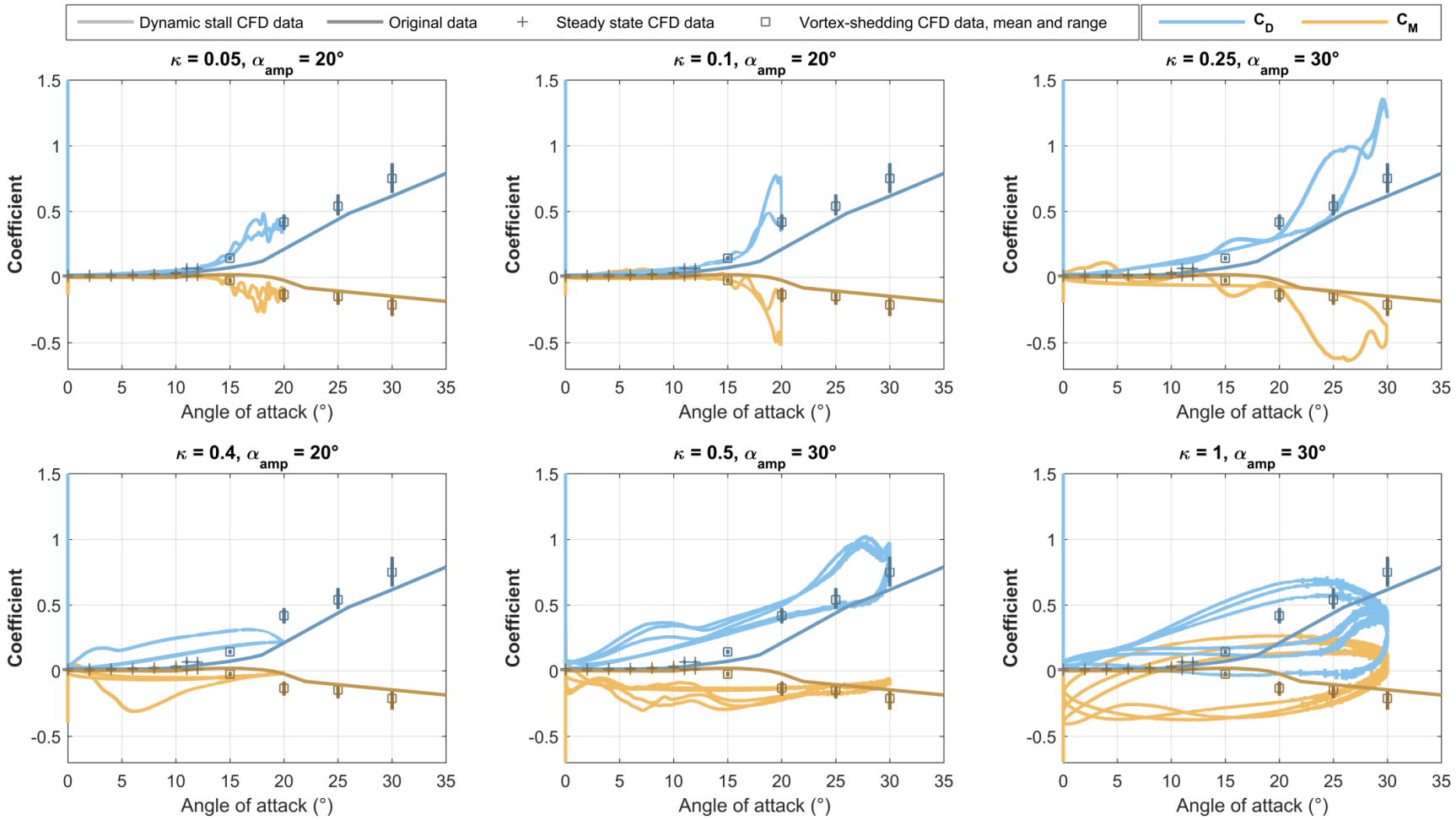

Figure 8.3.14: Dynamic stall results: CFD drag and moment coefficient results in the angle-of-attack domain, with the quasistatic data from Section 8.3.3. $\hat{\alpha}$ is denoted α_{amp} due to notation limitations.

8.3.5. Approaches to model validity

In Section 8.3.4, the model validity boundaries were expressed in terms of both the reduced frequency κ and reduced pitch rate r. The choice between the two, as a general metric of model validity in flight simulation, is an open question. In the absence of any conclusive studies in this regard, we utilise a dual criterion of both κ and r. As a lower bound, below which the quasistatic model is valid; $\kappa = 0.01$, $r = 0.0017$; and as an upper bound; $\kappa = 0.5$; $r = 0.13$.

Computing $r(t)$ for a general flight simulation is easy, but κ is a frequency-domain parameter, and an open question is immediately raised as to how to best generalise the κ-criteria to manoeuvres with complex angle-of-attack histories. One possible solution may be found in spectral analysis. For a manoeuvre with arbitrary $\alpha(t)$, the angle-of-attack frequency spectrum, $\hat{\alpha}(\Omega)$, may be computed. The frequency space of this spectrum is analogous to Ω in $\kappa = b\Omega/U$. This space may then be transformed into the κ-domain via $\kappa = b\Omega/U$, with a caveat: like $\alpha(t)$, $U(t)$ is time-varying. An exact transformation to the κ-domain may be possible via the spectrum $U(\Omega)$; but in the case of manoeuvres with $|\min U| \gg 0$, a simple approximation is to compute maximum κ ($b\Omega/\min U$) and minimum κ ($b\Omega/\max U$) profiles based on the manoeuvre minimum and maximum airspeed. These profiles must bound the exact spectrum. When $\min U \to 0$, this approach breaks down; though in this case broader questions regarding the validity of using κ as a metric must be raised.

Providing it may be computed, the spectrum $\hat{\alpha}(\kappa)$ or power spectrum $\hat{\alpha}(\kappa)^2$ may then be assessed with respect to the validity threshold reduced frequencies. Purely objective methods of doing so have not yet been developed. In the ideal case, validity is assured if the spectrum is contained within the model's window of validity. If spectral content outside this window is observed, then the ratio of maximum amplitude or power of such content w.r.t to that at the frequency peak frequency will give the ratio of significance associated with such content. If the point of maximum spectral power is located at the critical κ, this is indicative of the decreasing significance of supercritical effects; if the point of maximum power is located elsewhere, then there may be a phenomenological effect (significant or insignificant) that is not captured by the model. This approach represents a convenient

generalisation of the κ-criteria, but further work is needed to validate it with respect to empirical data. While the tools used in the CFD analysis presented here are sufficient to model arbitrary aerofoil motions, allowing the spectral analysis predictions to be tested; this analysis beyond the scope of this work, and is left to future research.

8.3.6. Delay parameter functional dependencies

An open question in GK modelling, and one which has not been adequately acknowledged, is the dependency of the GK delay parameters on the airspeed U. This dependency is particularly acute in applications of GK modelling to flight simulation, in which the local section model airspeeds may take a wide range of values. Existing flight simulator implementations do not appear to countenance anything other than constant dimensional delays (τ_1, τ_2), despite the established effect of the convection timescale ($t_{\mathrm{conv}} = c/U$), with respect to which these delays are traditionally nondimensionalised.

An immediate improvement is naturally suggested by the traditional dimensional analysis: to take the nondimensional values $T_i : \tau_i = T_i c/U$ as constants, leading to an inverse proportionality in U. As with κ, this has the practical problem of a singularity at $U = 0$; a minimum value of U must be specified. Phenomenologically, this dependency is partly justified: in a timescale study, Dunne et al. [51] found that the leading-edge vortex development and shedding that leads to dynamic stall are dominated by the effect of c/U. However, the fact remains that the (inverse) linear relation $\tau_i = T_i c/U$ is the most basic form of approximation to these effects. For example, the inclusion of zeroth-order or higher polynomial terms in c/U is an immediate avenue for model generalisation. Phenomenological inspiration for such procedures may come from more detailed analyses of the flow timescales around pitching aerofoils – these indicate the presence of at least three timescales, of which c/U is only one [51]. The use of CFD for delay parameter identification provides an easy avenue though which generalised models of these forms may be explored. However, such exploration is beyond the scope of this work, for reasons of time and space.

8.3.7. Stabiliser surfaces

So far this study has focused on the identification of GK delay parameters for the wing aerofoil (the ST50W). It would be trivial, but computationally intensive, to repeat this process for the horizontal and vertical stabiliser aerofoil (the ST50H). However, without modelling the control surface deflection, the results would only be valid for the case of zero control deflection. The control surfaces for the ST50H are relatively large, and the effects of control deflection on the GK delays are a significant unknown factor. However, in terms of overall modelling fidelity, these effects may hold less significance: the control range and effectiveness of wing incidence-morphing is large, and such morphing provides an avenue through which a wide range of changes in stabiliser forces and moments can be corrected. The effect of inaccuracies in the stabiliser GK delays on the space (or, flight envelope) of feasible supermanoeuvres for the case study system would thus be expected to be small; but this requires quantification. GK modelling for systems with control surfaces is not a topic that has seen any previous research, but is an area of importance for future developments in biomimetic post-stall control.

In the case study model, the same GK delay values (and airspeed dependency) are taken for the ST50H as for the ST50W, that is $\tau_1 = \tau_2 = 2.3c/U$. An alternative would be to take delay coefficient values from the literature (as per Table 8.2.2), but the variation in reported GK delays across the literature is not well understood, and again the selection of a particular value would not be well justified. In taking the ST50W values, at least a consistent modelling approach is guaranteed.

8.4. CONCLUDING REMARKS

This chapter has presented the development and identification of a reduced-order transient aerodynamic model, based on the approach pioneered by Goman and Khrabrov [11] and extended by other authors [21,23]. This model offers demonstrably significant improvements over a quasistatic model in the fidelity of aerodynamic modelling in the case-study system. This model – and by association, the aerodynamic modelling of the case-study system – has been validated via CFD simulation. CFD data is used to identify key model parameters, establish the limits of model validity and the factors affecting model accuracy

and breakdown, and explore phenomenological effects associated with dynamic stall. To devise this reduced-order model, significant novel methodological contributions have been made, in the form of extensions to the GK modelling framework: to a 3D blade element context; a 360° angle of attack range (via leading-edge/trailing-edge models); a generalised transition-region sigmoid function; and in a limited manner, to aerofoils with control surfaces. GK modelling has never previously been used in 3D flight simulation.

Associated with this development, several important open questions have been raised:

- regarding the nature and cause of the wide variation of GK delay parameters reported in literature for the same aerofoils;
- regarding the dependency of the GK delay parameters on the system airspeed (and/or chord); a topic not addressed in existing GK-based 2D flight simulators;
- regarding the modelling of the GK delays in systems with control surfaces and how this can be accurately and cost-effectively carried out.
- regarding appropriate methods for the characterisation of GK and quasistatic model validity (reduced frequency, angle-of-attack rate, or other metrics); a topic which existing literature treats inconsistently.

For some of these questions, novel working solutions are offered: a basic form of airspeed dependency, based on dimensional analysis; a dual-metric approach to model validity, based on both reduced frequency and angle-of-attack rate. For others, further research would both elucidate the mechanisms at work in transient aerofoil motion; and would improvement the fidelity at which biomimetic supermanoeuvrability, and other applications, can be modelled.

CHAPTER REFERENCES

[1] Culbreth, M., Allaneau, Y., and Jameson, A., “High-Fidelity Optimization of Flapping Airfoils and Wings,” 29th AIAA Applied Aerodynamics Conference.

[2] De Gaspari, A., and Ricci, S., “Knowledge-Based Shape Optimization of Morphing Wing for More Efficient Aircraft,” *International Journal of Aerospace Engineering*, Vol. 2015, 2015, pp. 1–19. DOI:10.1155/2015/325724.

[3] Lankford, J., Mayo, D., and Chopra, I., "Computational investigation of insect-based flapping wings for micro air vehicle applications," *International Journal of Micro Air Vehicles*, Vol. 8, No. 2, 2016, pp. 64–78. DOI:10.1177/1756829316646640.

[4] Dwivedi, V., and Damodaran, M., "Computational Aeromechanics of a Manuevering Unmanned Aerial Vehicle with Variable-Incidence Wings," *Journal of Aircraft*, Vol. 52, No. 6, 2015, pp. 1914–1926. DOI:10.2514/1.C033102.

[5] Fincham, J. H., Ajaj, R. M., and Friswell, M. I., "Aerodynamic Performance of Corrugated Skins for Spanwise Wing Morphing," 14th AIAA Aviation Technology, Integration, and Operations Conference, Atlanta, GA.

[6] Jones, M. A., "CFD Analysis and Design Optimization of Flapping Wing Flows," Doctoral Thesis, North Carolina Agricultural and Technical State University, 2013.

[7] Brunton, S., and Rowley, C., "Unsteady Aerodynamic Models for Agile Flight at Low Reynolds Number," 48th AIAA Aerospace Sciences Meeting, Orlando, FL.

[8] Balajewicz, M., Nitzsche, F., and Feszty, D., "Application of Multi-Input Volterra Theory to Nonlinear Multi-Degree-of-Freedom Aerodynamic Systems," *AIAA Journal*, Vol. 48, No. 1, 2010, pp. 56–62. DOI:10.2514/1.38964.

[9] Wang, Q., Qian, W., and He, K., "Unsteady aerodynamic modeling at high angles of attack using support vector machines," *Chinese Journal of Aeronautics*, Vol. 28, No. 3, 2015, pp. 659–668. DOI:10.1016/j.cja.2015.03.010.

[10] McAlister, K. W., Lambert, O., and Petot, D., *Application of the ONERA Model of Dynamic Stall*, NASA, Washington, D.C., 1984.

[11] Goman, M., and Khrabrov, A., "State-space representation of aerodynamic characteristics of an aircraft at high angles of attack," *Journal of Aircraft*, Vol. 31, No. 5, 1994, pp. 1109–1115. DOI:10.2514/3.46618.

[12] Holierhoek, J. G., de Vaal, J. B., van Zuijlen, A. H., and Bijl, H., "Comparing different dynamic stall models: Comparing different dynamic stall models," *Wind Energy*, Vol. 16, No. 1, 2013, pp. 139–158. DOI:10.1002/we.548.

[13] An, J., Yan, M., Zhou, W., Sun, X., and Yan, Z., "Aircraft dynamic response to variable wing sweep geometry," *Journal of Aircraft*, Vol. 25, No. 3, 1988, pp. 216–221. DOI:10.2514/3.45580.

[14] Karbasian, H. R., Esfahani, J. A., and Barati, E., "Effect of acceleration on dynamic stall of airfoil in unsteady operating conditions: Effect of acceleration on dynamic stall of airfoil," *Wind Energy*, Vol. 19, No. 1, 2016, pp. 17–33. DOI:10.1002/we.1818.

[15] Gharali, K., and Johnson, D. A., "Dynamic stall simulation of a pitching airfoil under unsteady freestream velocity," *Journal of Fluids and Structures*, Vol. 42, 2013, pp. 228–244. DOI:10.1016/j.jfluidstructs.2013.05.005.

[16] Shi, Z.-W., and Ming, X., "Effects of Unsteady Freestream on Aerodynamic Characteristics of a Pitching Delta Wing," *Journal of Aircraft*, Vol. 45, No. 6, 2008, pp. 2182–2185. DOI:10.2514/1.38925.

[17] Liska, S., and Dowell, E. H., "Continuum Aeroelastic Model for a Folding-Wing Configuration," *AIAA Journal*, Vol. 47, No. 10, 2009, pp. 2350–2358. DOI:10.2514/1.40475.

[18] Wang, I., "Aeroelastic and Flight Dynamics Analysis of Folding Wing Systems," Doctoral Dissertation, Duke University, 2013.

[19] Brunton, S., and Rowley, C., "Modeling the Unsteady Aerodynamic Forces on Small-Scale Wings," 47th AIAA Aerospace Sciences Meeting, Orlando, FL.

[20] Peters, D. A., Karunamoorthy, S., and Cao, W.-M., "Finite state induced flow models. I - Two-dimensional thin airfoil," *Journal of Aircraft*, Vol. 32, No. 2, 1995, pp. 313–322. DOI:10.2514/3.46718.

[21] Reich, G. W., Eastep, F. E., Altman, A., and Albertani, R., "Transient Poststall Aerodynamic Modeling for Extreme Maneuvers in Micro Air Vehicles," *Journal of Aircraft*, Vol. 48, No. 2, 2011, pp. 403–411. DOI:10.2514/1.C000278.

[22] Wickenheiser, A. M., and Garcia, E., "Optimization of Perching Maneuvers Through Vehicle Morphing," *Journal of Guidance, Control, and Dynamics*, Vol. 31, No. 4, 2008, pp. 815–823. DOI:10.2514/1.33819.

[23] Williams, D. R., Reißner, F., Greenblatt, D., Müller-Vahl, H., and Strangfeld, C., "Modeling Lift Hysteresis on Pitching Airfoils with a Modified Goman–Khrabrov Model," *AIAA Journal*, Vol. 55, No. 2, 2017, pp. 403–409. DOI:10.2514/1.J054937.

[24] Williams, D. R., An, X., Iliev, S., King, R., and Reißner, F., "Dynamic hysteresis control of lift on a pitching wing," *Experiments in Fluids*, Vol. 56, No. 112, 2015. DOI:10.1007/s00348-015-1982-y.

[25] Luchtenburg, D. M., Rowley, C. W., Lohry, M. W., Martinelli, L., and Stengel, R. F., "Unsteady High-Angle-of-Attack Aerodynamic Models of a Generic Jet Transport," *Journal of Aircraft*, Vol. 52, No. 3, 2015, pp. 890–895. DOI:10.2514/1.C032976.

[26] Selig, M., "Modeling Full-Envelope Aerodynamics of Small UAVs in Realtime," AIAA Atmospheric Flight Mechanics Conference, Toronto, ON.

[27] Graham, R. L., Knuth, D. E., and Patashnik, O., *Concrete mathematics: a foundation for computer science*, Addison-Wesley, Reading, MA, 1994.

[28] Guntur, S. K., and Sørensen, N. N., "A Detailed Study of the Rotational Augmentation and Dynamic Stall Phenomena for Wind Turbines," Doctoral Dissertation, Technical University of Denmark, 2013.

[29] An, X., Williams, D. R., Eldredge, J., and Colonius, T., "Modeling Dynamic Lift Response to Actuation," 54th AIAA Aerospace Sciences Meeting, San Diego, CA.

[30] Fan, Y., "Identification of an Unsteady Aerodynamic Model up to High Angle of Attack Regime," Doctoral Dissertation, Virginia Polytechnic Institute and State University, 1997.

[31] Greenblatt, D., Mueller-Vahl, H., Williams, D. R., and Reissner, F., "Goman-Khrabrov Model on a Pitching Airfoil with Flow Control," 8th AIAA Flow Control Conference, Washington, DC.

[32] Niel, F., "Modeling and control of a wing at low Reynolds number with high amplitude aeroelastic oscillations," Doctoral Dissertation, University of Toulouse, 2018.

[33] Menter, F. R., "Two-equation eddy-viscosity turbulence models for engineering applications," *AIAA Journal*, Vol. 32, No. 8, 1994, pp. 1598–1605. DOI:10.2514/3.12149.

[34] Ferziger, J. H., and Perić, M., *Computational methods for fluid dynamics*, Springer, New York, 2002.

[35] Robertson, E., Choudhury, V., Bhushan, S., and Walters, D. K., "Validation of OpenFOAM numerical methods and turbulence models for incompressible bluff body flows," *Computers & Fluids*, Vol. 123, 2015, pp. 122–145. DOI:10.1016/j.compfluid.2015.09.010.

[36] Robertson, E. D., "Verification, validation, and implementation of numerical methods and models for OpenFOAM 2.0 for incompressible flow," Master's Thesis, Mississippi State University, 2015.

[37] Matyushenko, A. A., Kotov, E. V., and Garbaruk, A. V., "Calculations of flow around airfoils using two-dimensional RANS: an analysis of the reduction in accuracy," *St. Petersburg Polytechnical University Journal: Physics and Mathematics*, Vol. 3, No. 1, 2017, pp. 15–21. DOI:10.1016/j.spjpm.2017.03.004.

[38] Spalart, P., and Allmaras, S., "A one-equation turbulence model for aerodynamic flows," *30th Aerospace Sciences Meeting and Exhibit*, 30th Aerospace Sciences Meeting and Exhibit, Reno, NV.

[39] Wilcox, D. C., *Turbulence modeling for CFD*, DCW Industries, La Cãnada, CA, 2006.

[40] Menter, F. R., Garbaruk, A. V., and Egorov, Y., "Explicit algebraic reynolds stress models for anisotropic wall-bounded flows," *Progress in Flight Physics*, Progress in Flight Physics, Versailles, France, pp. 89–104.

[41] Leishman, J. G., *Principles of helicopter aerodynamics*, Cambridge University Press, Cambridge, UK, 2002.

[42] Yu, J. M., Leu, T. S., and Miau, J. J., "Investigation of reduced frequency and freestream turbulence effects on dynamic stall of a pitching airfoil," *Journal of Visualization*, Vol. 20, No. 1, 2017, pp. 31–44. DOI:10.1007/s12650-016-0366-6.

[43] Du, L., Berson, A., and Dominy, R. G., "Aerofoil behaviour at high angles of attack and at Reynolds numbers appropriate for small wind turbines," *Proceedings of the Institution of Mechanical Engineers, Part C: Journal of Mechanical Engineering Science*, Vol. 229, No. 11, 2015, pp. 2007–2022. DOI:10.1177/0954406214550016.

[44] Bisplinghoff, R. L., Ashley, H., and Halfman, R. L., *Aeroelasticity*, Addison-Wesley, Reading, MA, 1957.

[45] Ahaus, L., "An Airloads Theory for Morphing Airfoils in Dynamic Stall with Experimental Correlation," Washington University in St. Louis, 2010.

[46] Coder, J. G., "CFD investigation of unsteady rotocraft airfoil aerodynamics," Master's Thesis, Pennsylvania State University, 2010.

[47] Gerontakos, P., "An Experimental Investigation of Flow Over an Oscillating Airfoil," Master's Thesis, McGill University, 2004.

[48] Mueller, T. J., ed., *Fixed and Flapping Wing Aerodynamics for Micro Air Vehicle Applications*, AIAA, Reston, VA, 2001.

[49] Leishman, J. G., "Challenges in modelling the unsteady aerodynamics of wind turbines," *Wind Energy*, Vol. 5, No. 2–3, 2002, pp. 85–132. DOI:10.1002/we.62.

[50] Ramasamy, M., Wilson, J. S., McCroskey, W. J., and Martin, P. B., "Characterizing Cycle-to-Cycle Variations in Dynamic Stall Measurements," *Journal of the American Helicopter Society*, Vol. 63, No. 2, 2018, pp. 1–24. DOI:10.4050/JAHS.63.022002.

[51] Dunne, R., Schmid, P. J., and McKeon, B. J., "Analysis of Flow Timescales on a Periodically Pitching/Surging Airfoil," *AIAA Journal*, Vol. 54, No. 11, 2016, pp. 3421–3433. DOI:10.2514/1.J054784.

Chapter 9:
Biomimetic supermanoeuvrability under transient aerodynamics

9.1. INTRODUCTION

In Chapter 8 an aerodynamic submodel was developed that captured transient delayed separation/attachment effects in the system aerofoils. The model retained validity up to a reduced frequency $k \approx 0.5$ and reduced pitch rate $r \approx 0.13$, at which point added mass effects began to show significance. The objective of this chapter is to utilise this transient model to simulate some of the manoeuvres in Chapters 6-7, and in doing so, to explore the significance of transient effects to these manoeuvres, the capability of the GK model to model them, and the relevance of quasistatic manoeuvre design procedures to transient flight dynamics.

9.2. QUASISATIC NPAS CAPABILITY

Heuristic arguments would lead us to expect that the quasistatic NPAS capability demonstrated in Chapter 6, Section 6.4 would be relatively unaffected by transient aerodynamic effects. As per Chapter 8, Section 8.3.5, the approximate critical reduced frequency for quasistatic model breakdown (κ^*) is 0.01, and the critical reduced pitch rate (r^*) 0.0017. In the quasistatic NPAS manoeuvres of the case study system, carried out at reference velocity $U = 25$ m/s, this leads to a critical timescale $t^* = 1.9$ s, computed as $t^* = 2\pi/\Omega^*$, $\Omega^* = \kappa^* U/b$. The minimum NPAS oscillation period studied in Chapter 6 was $T = 5$ s.

For these manoeuvres, reference angle-of-attack histories are computed at the outer tips of each lifting surface – the tip points may be confirmed to have the greatest angle-of-attack variation within their respective surfaces. The horizontal stabilisers show identical tip histories, which are also identical to the aircraft yaw history; and the vertical stabiliser shows a tip history which if effectively equivalent to the aircraft pitch history. Four reference points are thus sufficient to characterise the level of lifting-surface transience: the left-wing (LW) tip, right-wing (RW) tip, a horizontal stabiliser (HS) tip, and the vertical stabiliser (VS) tip. An analysis of these angle-of-attack histories indicates that the wings remained in pre-stall conditions for all of the manoeuvres studied – though the stabiliser surfaces did reach post-stall conditions. As oscillatory overshoot effects were observed in some manoeuvres, and these may be exacerbated by transient aerodynamic effects, it

would be prudent to quantify the degree of unsteadiness involved. For this purpose we use the spectral analysis of Chapter 8, Section 8.3.5.

Figure 9.2.1 shows the angle-of-attack and reduced-pitch-rate time histories, and angle-of-attack power spectra, for the $T = 25$ s NPAS oscillation with $\psi_{\text{amp}} = 0.2$, $\theta_{\text{amp}} = 0.2$, $\theta_0 = 0.2$ rad, and an inboard dihedral constraint of $\Gamma = 0.3$ rad. The critical reduced frequency for quasistatic model breakdown (κ^* = 0.05) is indicated, as well as the reduced frequency associated with the NPAS forcing / target oscillation path, which is computed from T as $\kappa_{\text{T}} = 2\pi b/TU_{\text{ref}}$. Unless strong higher-frequency effects are at work, κ_{T} will correspond to the peak spectral power – as is the case in Figure 9.2.1. The angle-of-attack time histories are relatively smooth and simple, and no strong high-frequency effects are observed: the reduction in spectral power between κ_{T} and κ^* is a factor of 4000, corresponding to an amplitude reduction of factor c. 60. Transient effects are not likely to be significant in this manoeuvre.

Figures 9.2.2-9.2.4 show the angle-of-attack and reduced-pitch-rate time histories, and angle-of-attack power spectra, for a set of wider-amplitude NPAS manoeuvres; those with $\psi_{\text{amp}} = 0.4$, $\theta_{\text{amp}} = 0.3$, $\theta_0 = 0$ rad, at $T \in [5,10]$ s, and for outboard $\Gamma = 0.3$ rad or an inboard $\Gamma = 0$ constraints (as per Chapter 6, Section 6.4). The stabiliser angle-of-attack time histories are smooth in the manner of Figure 9.2.1 and are not shown. These manoeuvres are the most rapid quasistatic NPAS manoeuvres studied, and angle-of-attack oscillations are observed on the timescale of t^*. The amplitude of these oscillations are small: in reduced frequency, Figure 9.2.3, the κ_{T}-κ^* spectral power reduction factor takes a maximum value of c. 40 ($T = 5$ s, outboard $\Gamma = 0.3$ rad constraint); an amplitude reduction of factor c. 6; with non-negligible spectral peaks beyond κ^*. In reduced pitch rate, the maximal r is approximately equal to r^*. Both these metrics indicate that GK dynamic stall effects could have minor significance. This is notable and anticipated, as these manoeuvres (at $T = 5$ s) are well faster than the pitch/yaw response times of the aircraft, i.e. the timescales at which induced-flow effects become significant.

Figure 9.2.5 shows a GK model simulation of the quasistatic NPAS oscillation with $T = 5$ s and for an outboard $\Gamma = 0.3$ rad constraint; under $\psi_{\text{amp}} = 0.4$, $\theta_{\text{amp}} = 0.3$, and $\theta_0 = 0$ rad, as per Figure 6.4.12-6.4.14. Dynamic stall events are observed to be insignificant; demonstrating the conservative nature of the threshold values chosen, and indicating that, even in the presence of induced-flow effects, the quasistatic aerodynamic model is sufficient for modelling these manoeuvres. However, this assessment is exacerbated by the fact that the estimated validity thresholds are based on CFD data, and not the behaviour of the model: the model delay parameters were identified based on data with mid-range angle-of-attack rates; and so for quasistatic threshold-level angle-of-attack rates, it is expected that the identified GK model will underestimate dynamic stall effects. In reality, transient effects may be more observable than in Figure 9.2.5; and may be a further motivation for the development of closed-loop NPAS control.

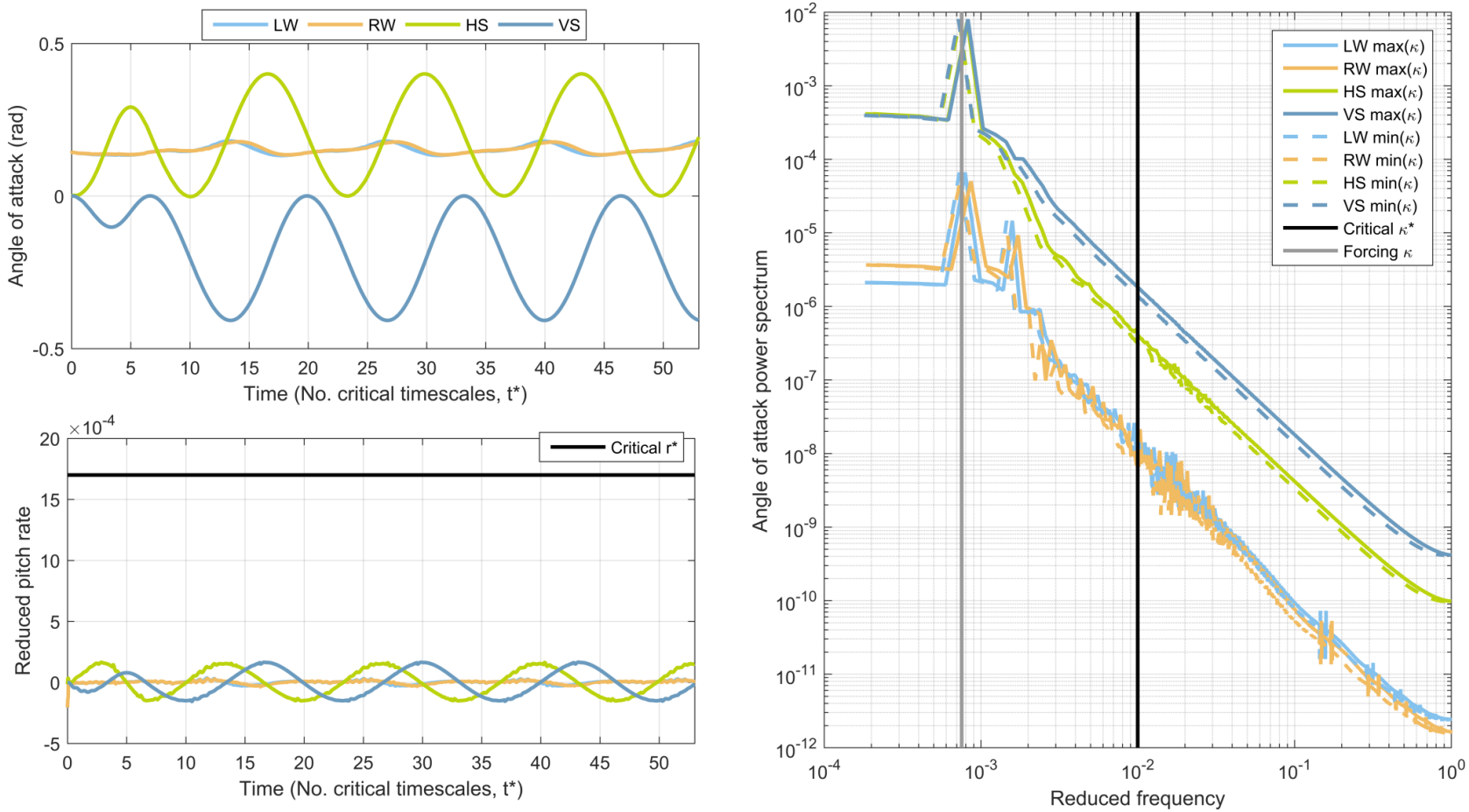

Figure 9.2.1: Angle-of-attack time histories and power spectra for the circle-profile quasistatic NPAS oscillation with $T = 25$ s, $\psi_{\text{amp}} = 0.2$, $\theta_{\text{amp}} = 0.2$, $\theta_0 = 0.2$ rad, and an inboard dihedral constraint of $\Gamma = 0.3$ rad. Reference points are the left-wing (LW), right-wing (RW), a horizontal stabiliser (HS), and the vertical stabiliser (VS) tips.

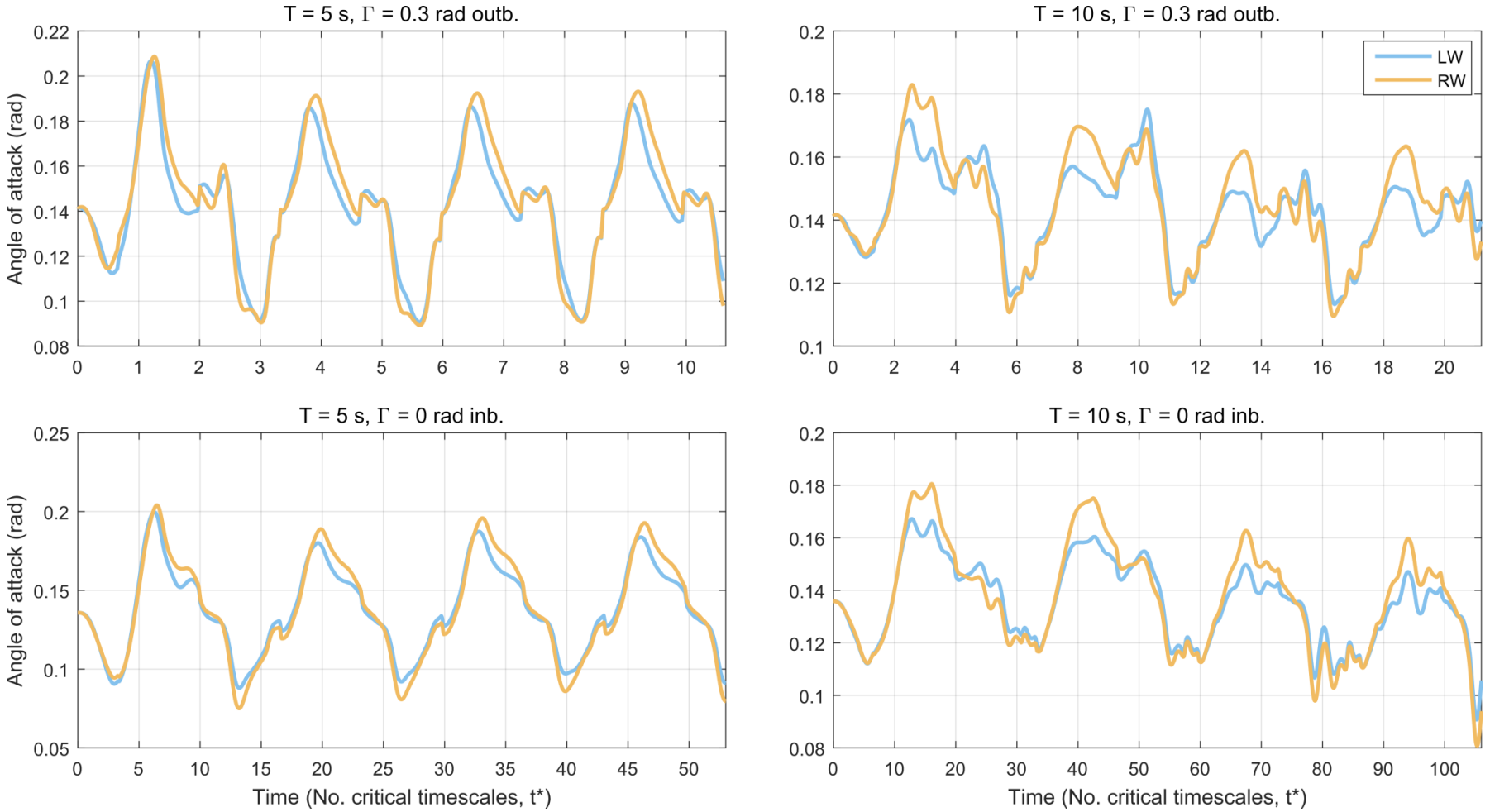

Figure 9.2.2: Left-wing (LW) and right-wing (RW) angle-of-attack time histories for the circle-profile quasistatic NPAS oscillation with $T \in [5,10]$ s, $\psi_{\text{amp}} = 0.4$, $\theta_{\text{amp}} = 0.3$, $\theta_0 = 0$ rad, and under two different dihedral constraints.

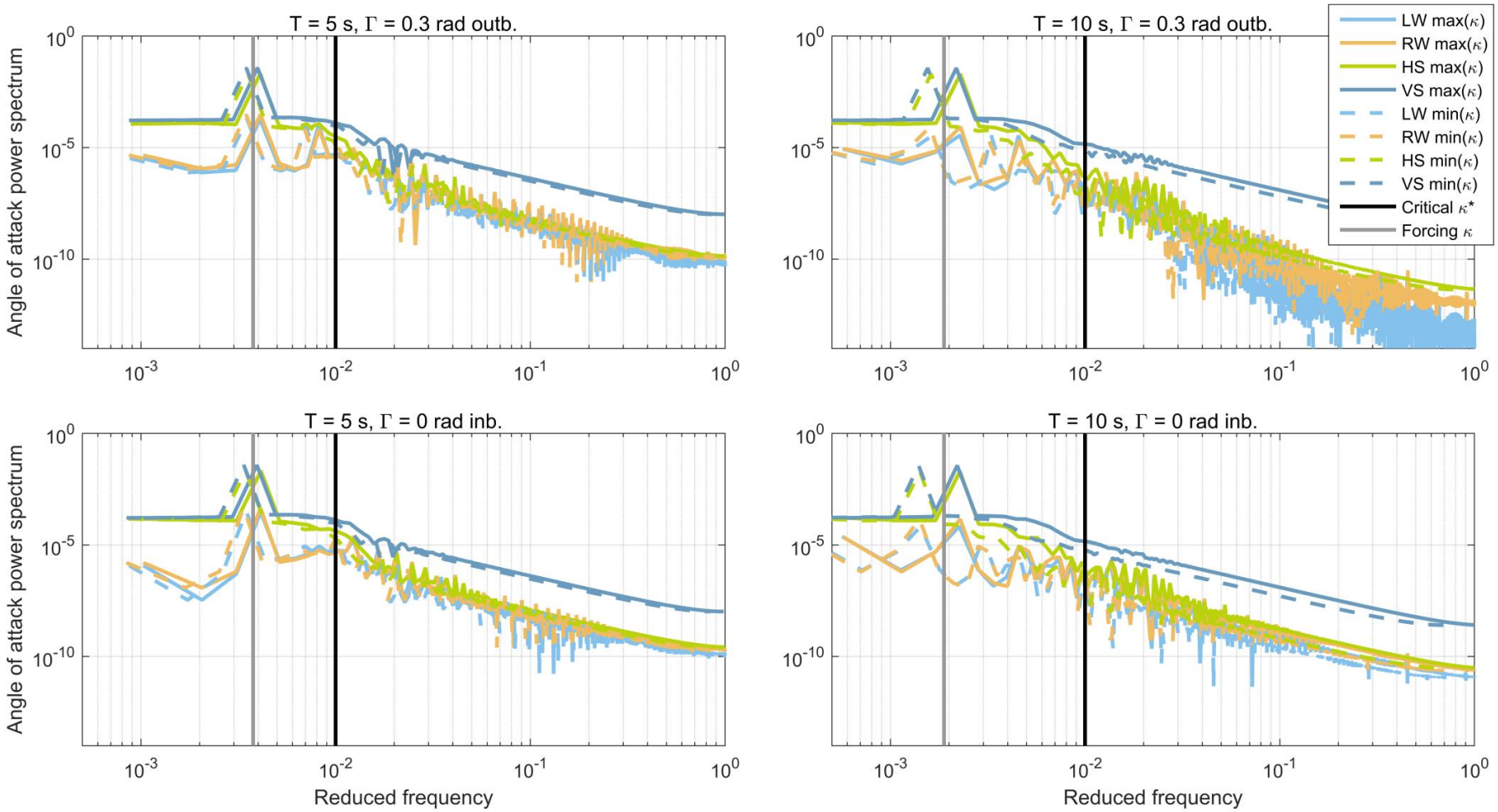

Figure 9.2.3: Left-wing (LW) and right-wing (RW) reduced frequency spectra for the circle-profile quasistatic NPAS oscillation with $T \in [5,10]$ s, $\psi_{\text{amp}} = 0.4$, $\theta_{\text{amp}} = 0.3$, $\theta_0 = 0$ rad, and under two different dihedral constraints.

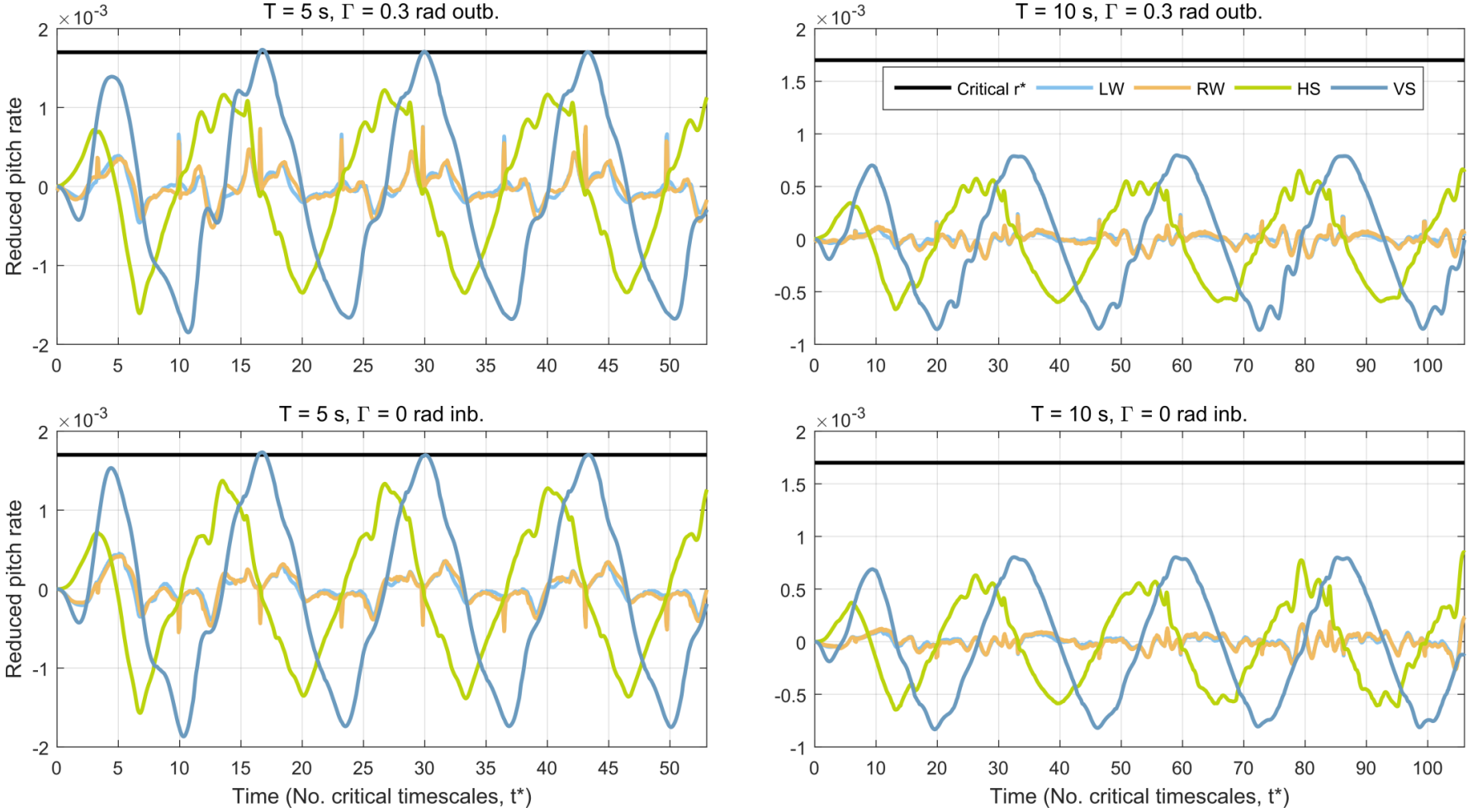

Figure 9.2.4: Left-wing (LW) and right-wing (RW) reduced pitch rate time histories for the circle-profile quasistatic NPAS oscillation with $T \in$ [5,10] s, $\psi_{\text{amp}} = 0.4$, $\theta_{\text{amp}} = 0.3$, $\theta_0 = 0$ rad, and under two different dihedral constraints.

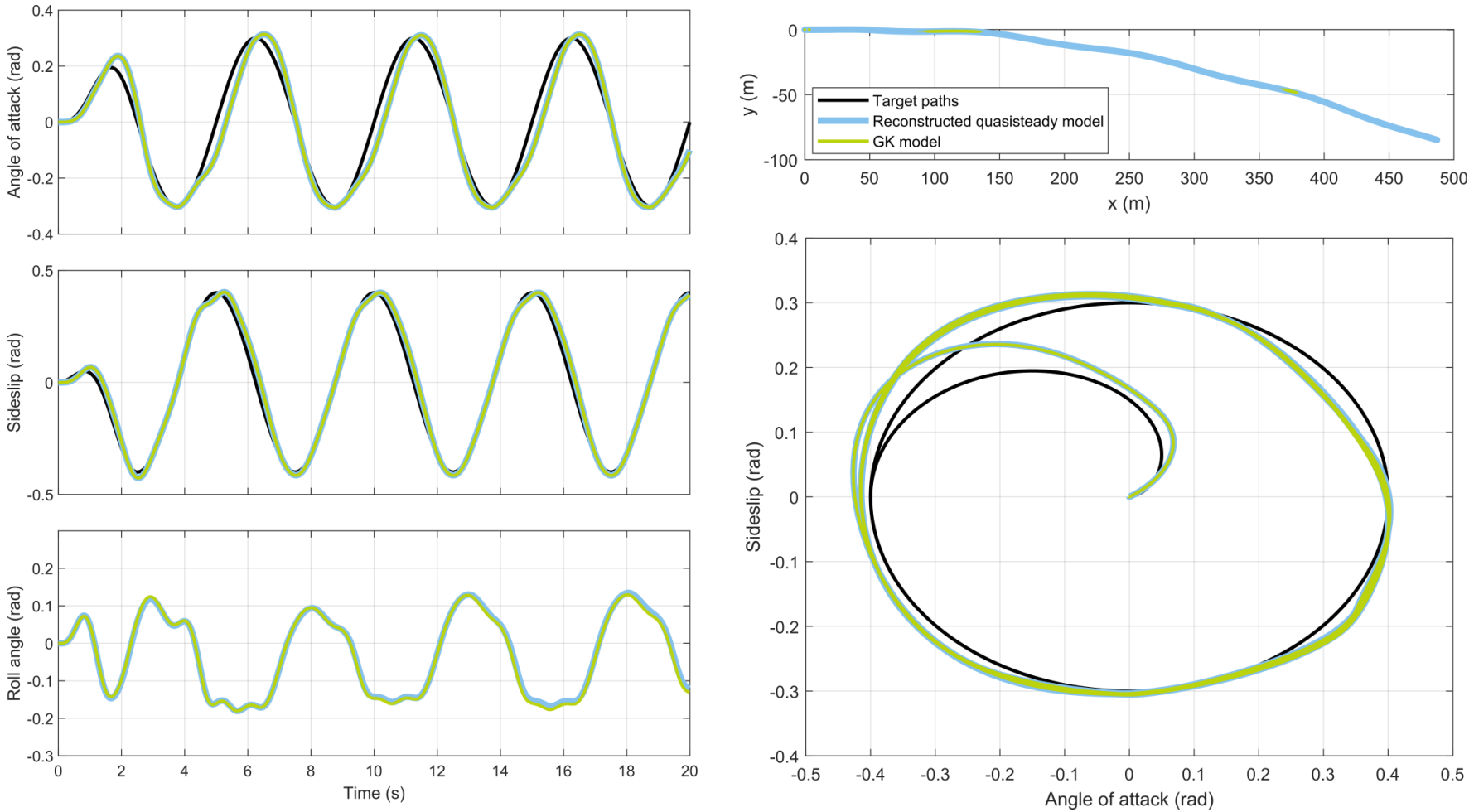

Figure 9.2.5: The effects of GK dynamic stall on the circle-profile quasistatic NPAS oscillation with $T = 5$ s, and for an outboard $\Gamma = 0.3$ rad constraint; under $\psi_{\text{amp}} = 0.4$, $\theta_{\text{amp}} = 0.3$, and $\theta_0 = 0$ rad.

9.3. PUGACHEV'S COBRA

Figure 9.3.1 show the effects of dynamic stall on the simple cobra manoeuvre studied in Chapter 7, Section 7.3.3. This manoeuvre is representative of the pitch-axis RaNPAS capability studied in Chapter 7, Section 7.3. Figure 9.3.1 shows flight simulation results (pitch angle and flight path) for the control paths of Chapter 7, Section 7.3.3, under the original quasistatic, GK-reconstructed quasistatic, and transient GK models. Also shown are the wing- and stabiliser-tip lift coefficient histories for the three simulations. Figure 9.3.1 shows an assessment of the GK simulation in terms of reduced frequency and reduced pitch rate. The thresholds for GK and quasistatic model validity are noted.

Unexpectedly, the transient effects modelled in the GK model are remarkably insignificant, despite the manoeuvre lying well within the range of GK model effects. Dynamic stall lift coefficient peaks are observed but do not significantly alter the aircraft behaviour – and thus, do not destabilise the manoeuvre. Furthermore, a part of the small discrepancy observed is attributable to the difference between the GK-reconstructed quasistatic model; and would be present even in the absence of the delay effects. Several explanations for this behaviour are available. The GK model does not model pre-stall transient effects (e.g. Wagner / Theodorsen effects) and in this situation these may be a more significant factor than dynamic stall effects; which require a stall transition. The cobra manoeuvre may show intrinsic high levels of stability in simulation, arising from the planar nature of the manoeuvre – eliminating the possibility of roll drift. This may explain why the large but short-timescale lift peaks arising from delayed separation do not significantly perturb the manoeuvre. In addition, the symmetric nature of the hysteresis loop (with delayed stall and delayed reattachment) may serve to self-cancel in a sufficiently stable system. The planar assumption obviously neglects more complex transient effects arising from asymmetric forebody separation (as per Chapter 7, Section 7.7); if uncontrolled, these could initiate a GK-based destabilisation. Furthermore, the cobra manoeuvre is generated partially by strong drag effects – which remain unaffected by dynamic stall, according to the GK model, if not in reality! (see Chapter 8, Section 8.3.4). The uncertain nature of these effects implies that, in a real system, they may be more significant, and may require a control response. However, in the current system, the quasistatic cobra simulations in Chapter 7, Section 7.3, may be regarded as validated with respect to the dynamic stall lift hysteresis effects.

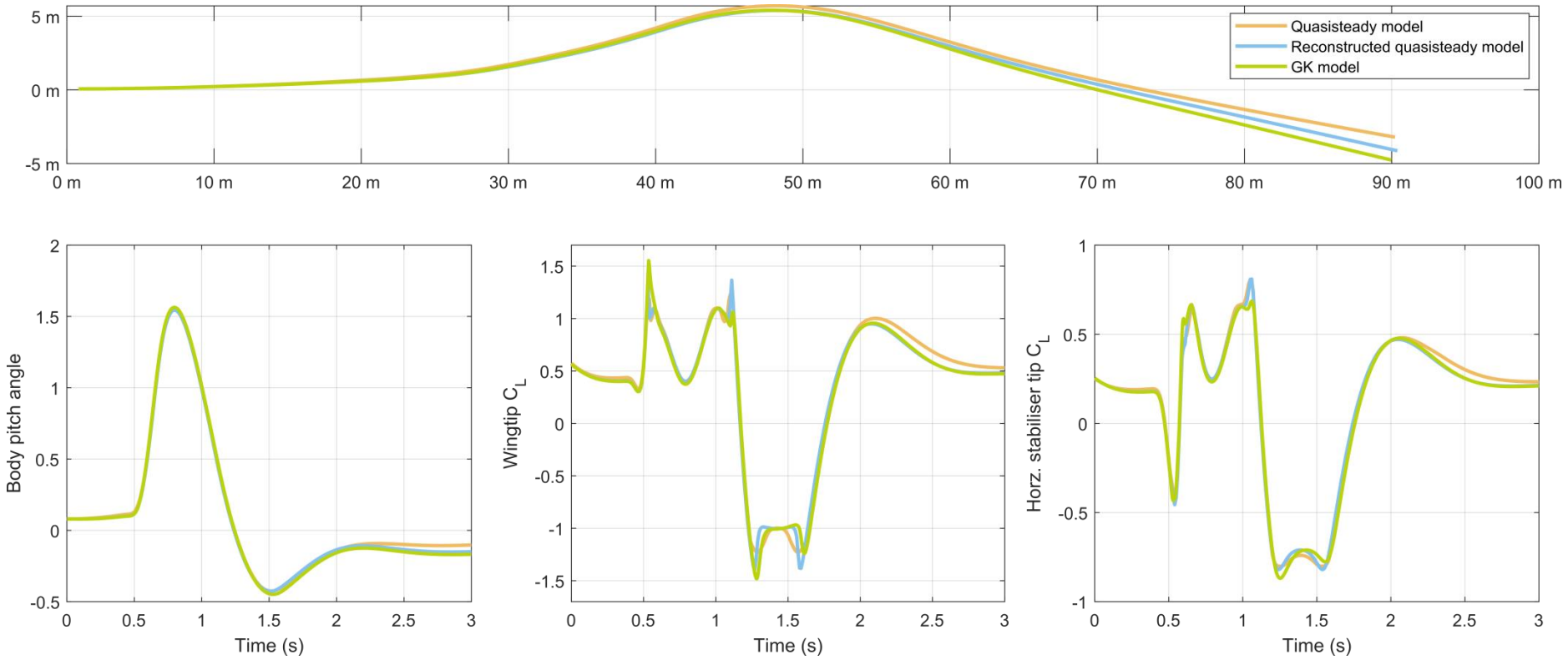

Figure 9.3.1: Effects of dynamic stall on a simple Cobra manoeuvre: flight path, pitch angle history, and wing/stabiliser tip lift coefficients.

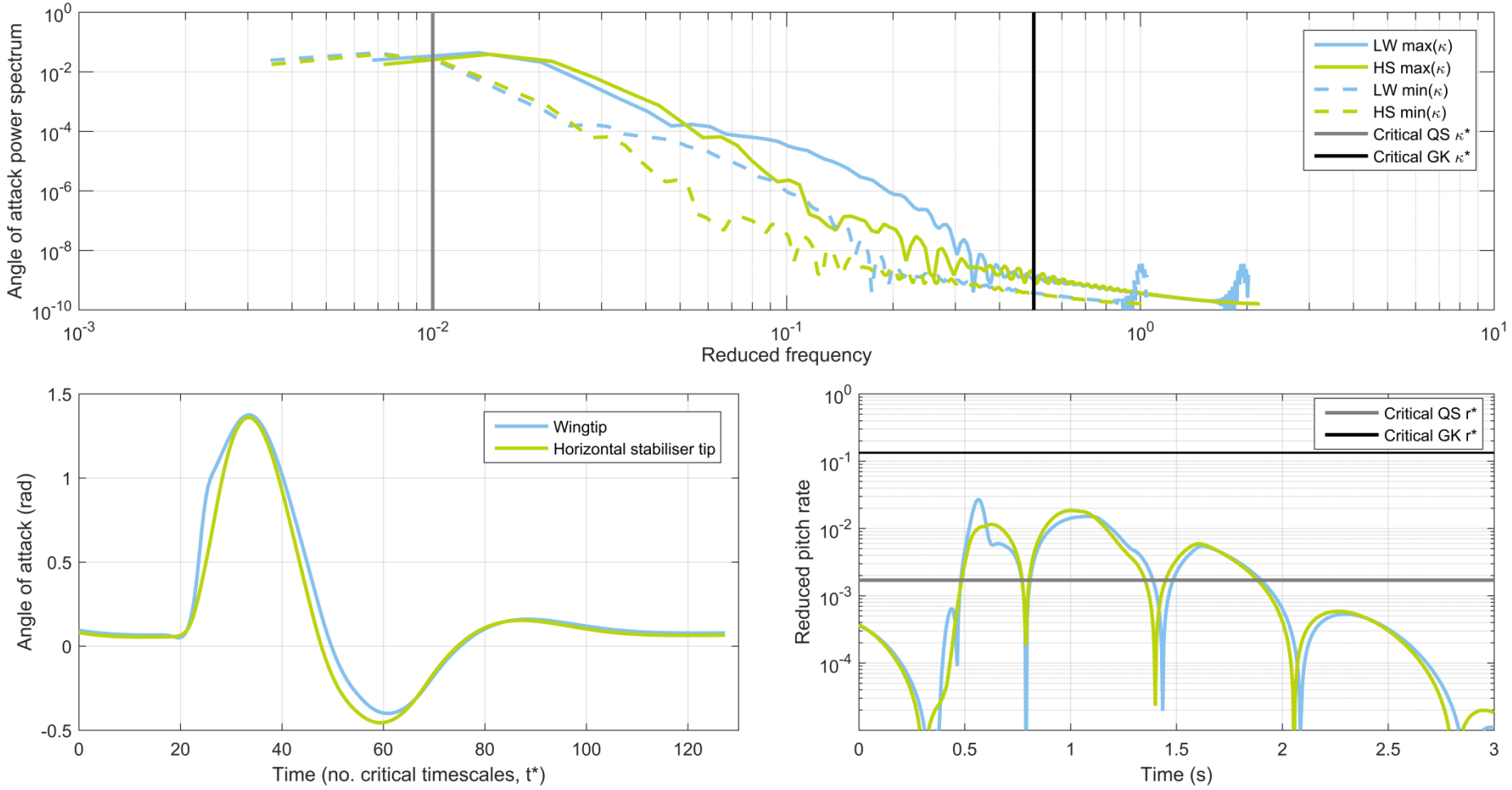

Figure 9.3.2: Assessment of GK model validity in reduced frequency and reduced pitch rate, for the simple cobra manoeuvre.

9.4. ANCHOR TURNS

9.4.1. Effects of the quasistatic reconstructed model

In conclusion, the complex 6-DOF morphing anchor turn manoeuvre of Chapter 7, Section 7.6.3 is studied. A confounding factor in the study of this manoeuvre is the difference between the quasistatic GK-reconstructed model and the original reference quasistatic model: this has a significant effect on the manoeuvre, which is strongly sensitive to changes in the aircraft flight dynamics or controls. The error induced by this change in aerodynamic submodel is shown as part of Figure 9.4.1.

To separate the effect of dynamic stall on the anchor turn manoeuvre from the effects of quasistatic model change, the aircraft morphing and surface controls are optimised to generate the reference anchor turn manoeuvre under GK-reconstructed quasistatic aerodynamics. The optimisation objective function is formulated as the error in translational and rotational acceleration ($[\ddot{\mathbf{x}}_S;\ \ddot{\boldsymbol{\theta}}_S]$) between the reference simulation (on its reference flight path), and the prediction of the GK-reconstructed quasistatic model when evaluated over the reference flight path. If the of the acceleration predictions and the reference acceleration converge, then the assumed reference flight path will be recovered.

This objective function can be optimised pointwise over time; a property which significantly decreases the computational cost of optimisation relative to an objective function based on direct flight simulation. As optimisation variables there are the morphing state of the aircraft and the control surface deflections, including differential elevator. However, at this point a further difficulty arises: attempting to optimise this problem point-wise over time with the full (underconstrained) complement of variables leads to a strongly discontinuous solution which is not suitable for flight simulation. However, simple reducing the variable space down to a more strongly constrained set (e.g. 2-3 DOF) leads to suboptimal solutions which do not recover the reference flight path.

A novel solution to this difficulty can be found in an iterative univariate optimisation. The acceleration objective function is optimised, point-wise across the full manoeuvre time, with respect to a single control DOF. This leads to a low-optimality solution with an improvement in continuity. This univariate optimisation is then repeated in sequence for different (and/or

the same) variables, gradually resulting in a high-optimality solution. The resulting control paths still have some continuity issues, but the results are sufficient to recover the reference flight path. Figure 9.4.2 shows the optimised control histories and the improvement in the acceleration objective function metric for a successful optimisation of this form, operating on the aircraft L/R wing incidence, L/R sweep and L/R elevator deflection. Figure 9.4.1 shows the anchor turn manoeuvre recovered from this control history, compared with the reference and pre-optimisation results. The optimised manoeuvre even represents an improvement in anchor turn performance over the reference manoeuvre; stabilising at a more acute angle of c. 160°.

9.4.2. GK model validity

This optimised manoeuvre can then be subjected to a GK model analysis. To do this in an intelligible way, the lifting surface tip angle of attack histories are computed, and subjected to a local GK analysis – coupled with their local control surface deflections. Figures 9.4.3-9.4.4 show these results for all the lifting surfaces; Figure 9.4.5 the reduced pitch rates associated with these motions; and Figure 9.4.6 a detailed analysis of the vertical stabiliser motion, as a case study. Note that the rudder control was not optimised in Section 9.4.1 (Figure 9.4.2), and so the vertical stabiliser is not affected by any control discontinuities introduced by optimisation.

The results are problematic. In the case of the wing, the simulations show expected GK behaviour, and the wing reduced pitch rates approach but do not exceed the critical threshold for GK model validity. However, the stabiliser surfaces show extreme model breakdown, with peaks (not shown) reaching $r > 12$; two orders of magnitude greater than the GK model breakdown threshold. This breakdown arises from two integral aspects of anchor turning: simultaneous rapid high-amplitude rotation, and low airspeed, at the apex of the turn.

The high-amplitude rotation generates large delays associated with τ_2, via $p_0(\alpha - \tau_2\dot{\alpha})$. This leads to some lifting surfaces, e.g. the vertical stabiliser in Figure 9.4.6, passing through multiple attachment/separation cycles in a short time period. The prospect of GK delays being carried across attachment/separation cycles – e.g. from the leading edge to the

trailing edge; a non-physical notion. The effect of the low airspeed exacerbates this: as per Chapter 8, Section 8.3.6, these delays are dependent on the local airspeed via the factor c/U; and thus a decrease to near-zero airspeed leads to a large increase in the delay times, exacerbating the cross-cycle effects. Additionally, this leads to a breakdown in the spectral reduced frequency method for assessing GK model validity, rendering it invalid for this manoeuvre. The problems generated by the near-zero airspeed can be supressed, if not solved, by capping the minimum airspeed used in GK delay calculations. In Figure 9.4.6 this cap is taken as 5 m/s: yet even this value, well above the minimum, still yields reduced pitch rates that greatly exceed the model validity boundary.

While the large errors in modelling the apex of the manoeuvre are offset somewhat by the low airspeed – generating lower aerodynamic forces overall – these errors still have a significant effect on the manoeuvre performance, and obscure real physical effects which are of unknown magnitude. It is probable that the turn apex would be modelled best with a low-airspeed unidirectional-rotation model; but it is at least clear that a comprehensive GK model, as devised, is not appropriate. For this reason we cannot validly simulate this anchor turn manoeuvre with the GK model flight simulator – nor, incidentally, does attempting to do so yield a functional anchor turn, but only a destabilising manoeuvre. The modelling of anchor turn manoeuvres is a fundamental limitation of the GK model; and further research is required in order to accurately capture the transient effects associated with the anchor turn apex.

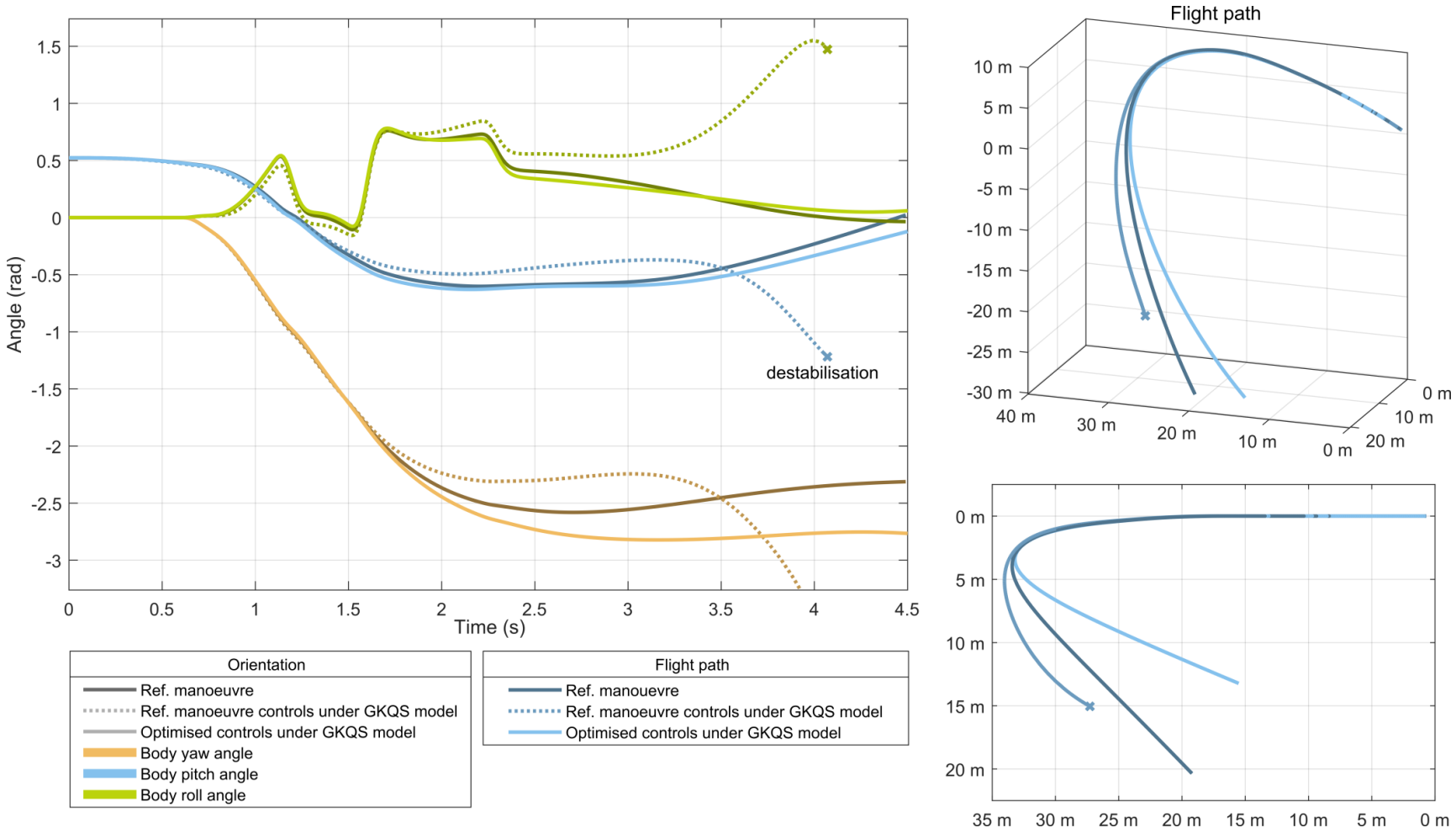

Figure 9.4.1: Flight simulation results (orientation and flight path) for the optimised control histories under the quasistatic GK-reconstructed model, compared with the pre-optimisation results.

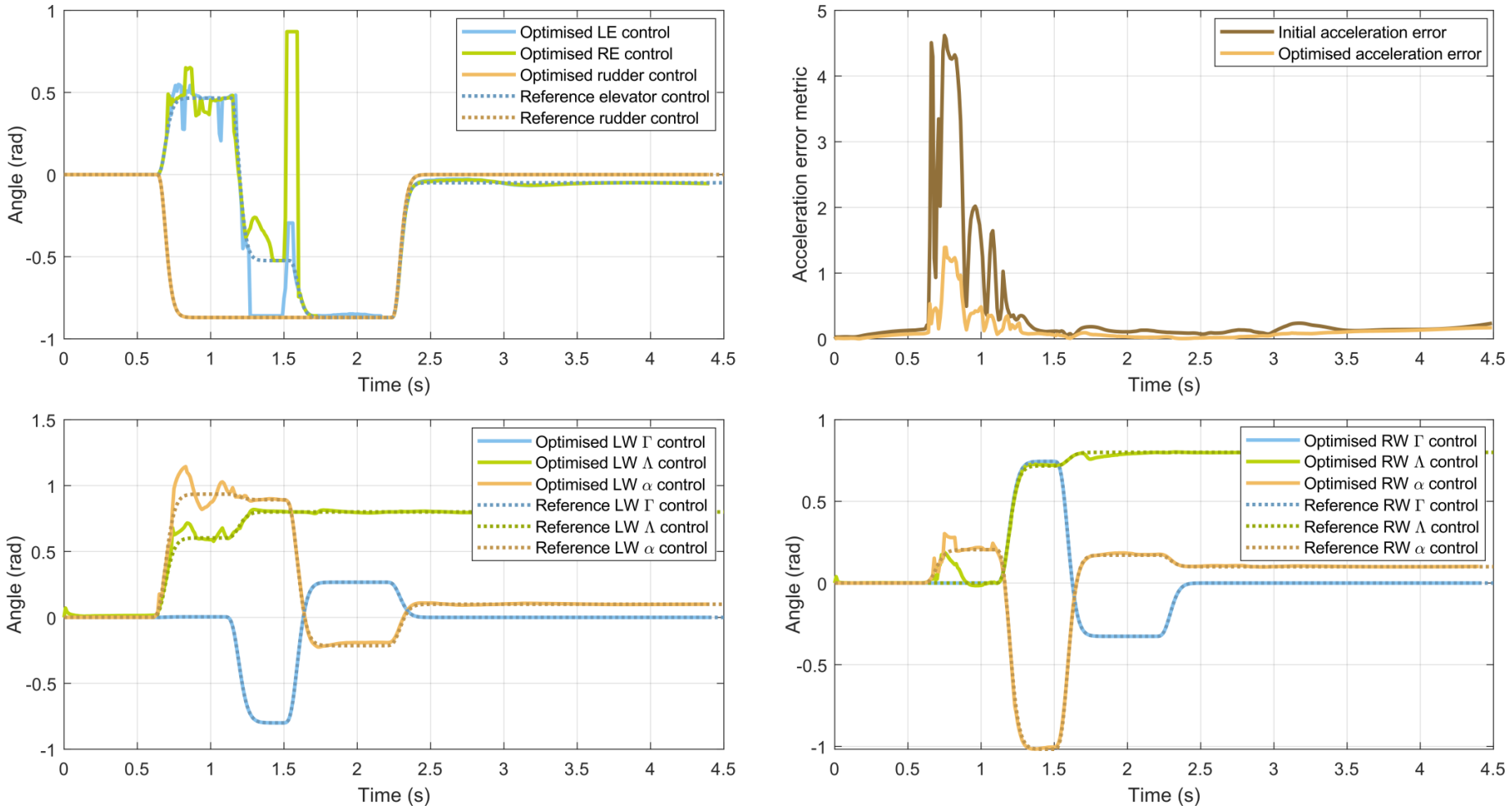

Figure 9.4.2: Control paths under the quasistatic GK-reconstructed model, optimised via a cyclic approach to match an anchor turn manoeuvre under the reference quasistatic model. The improvement in acceleration error (combined rotational/translational) is shown.

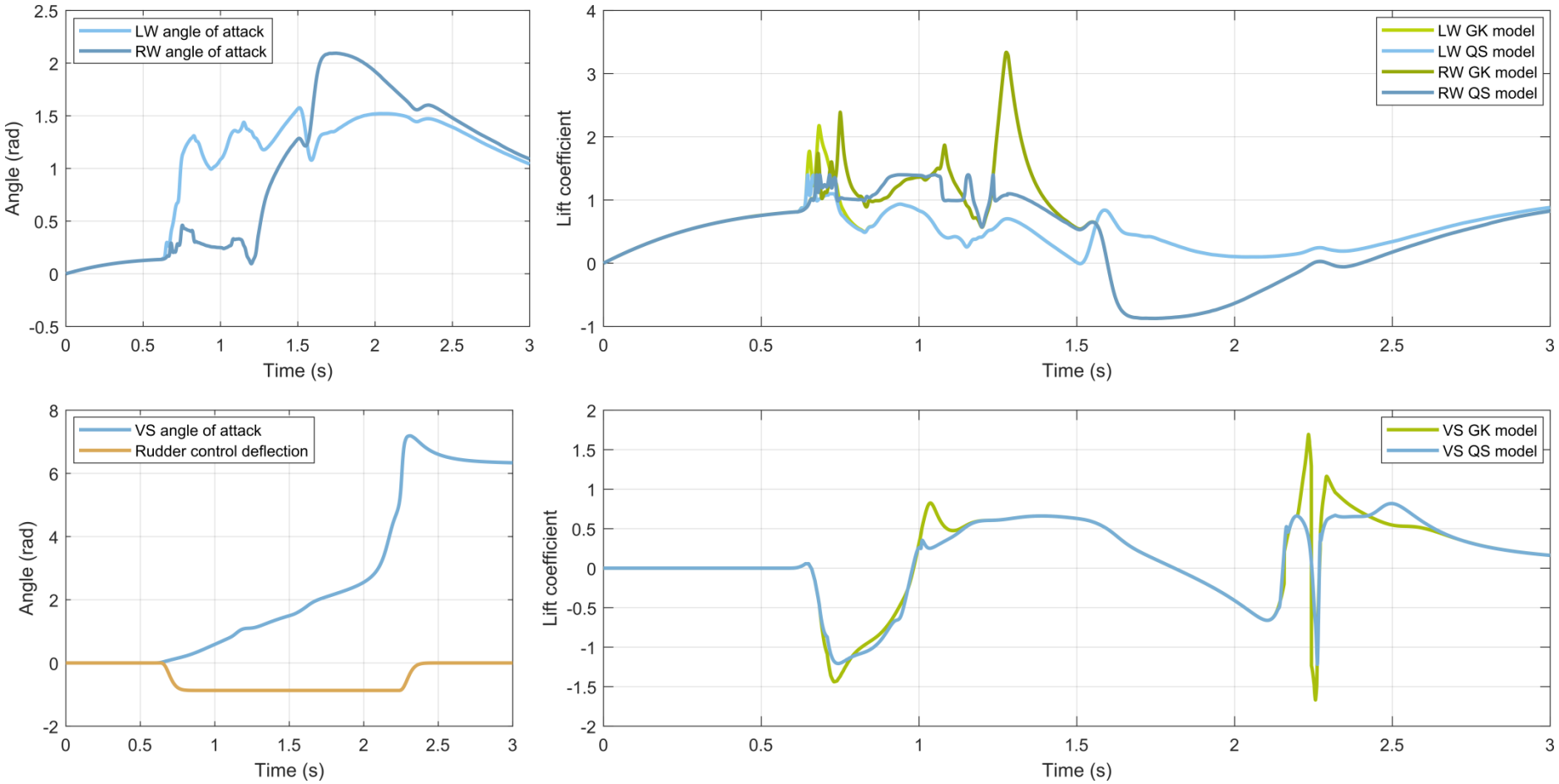

Figure 9.4.3: GK lift coefficient results for assumed lifting-surface-tip angle-of-attack histories given by the optimised anchor turn manoeuvre under the quasistatic GK-reconstructed model: left and right wings (LW/RW) and vertical stabiliser (VS).

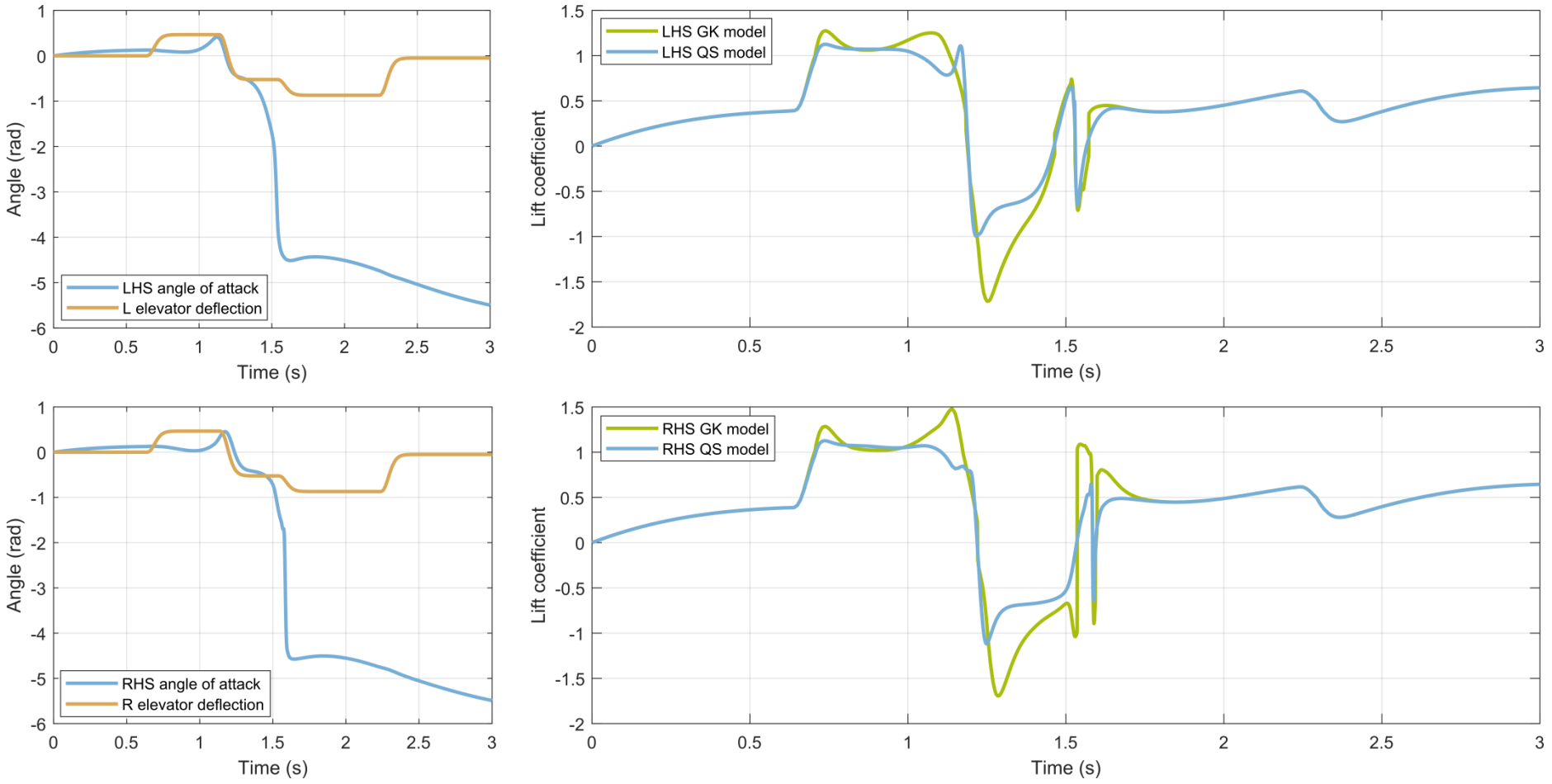

Figure 9.4.4: GK lift coefficient results for assumed lifting-surface-tip angle-of-attack histories given by the optimised anchor turn manoeuvre under the quasistatic GK-reconstructed model: left and right horizontal stabiliser (LHS/RHS).

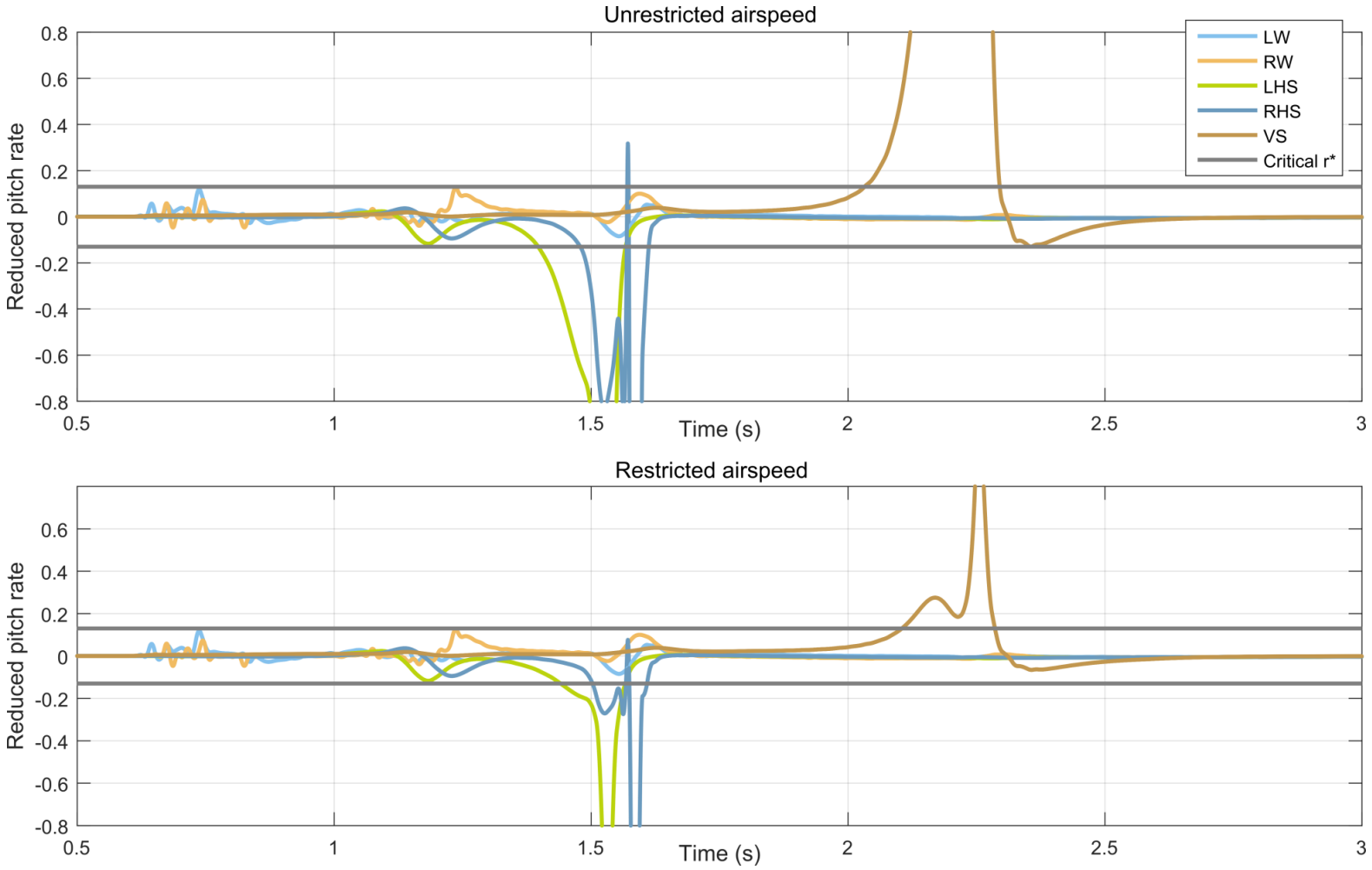

Figure 9.4.5: Reduced pitch rate histories for the GK simulations of the aircraft lifting-surface tips under the optimised anchor turn manoeuvre.

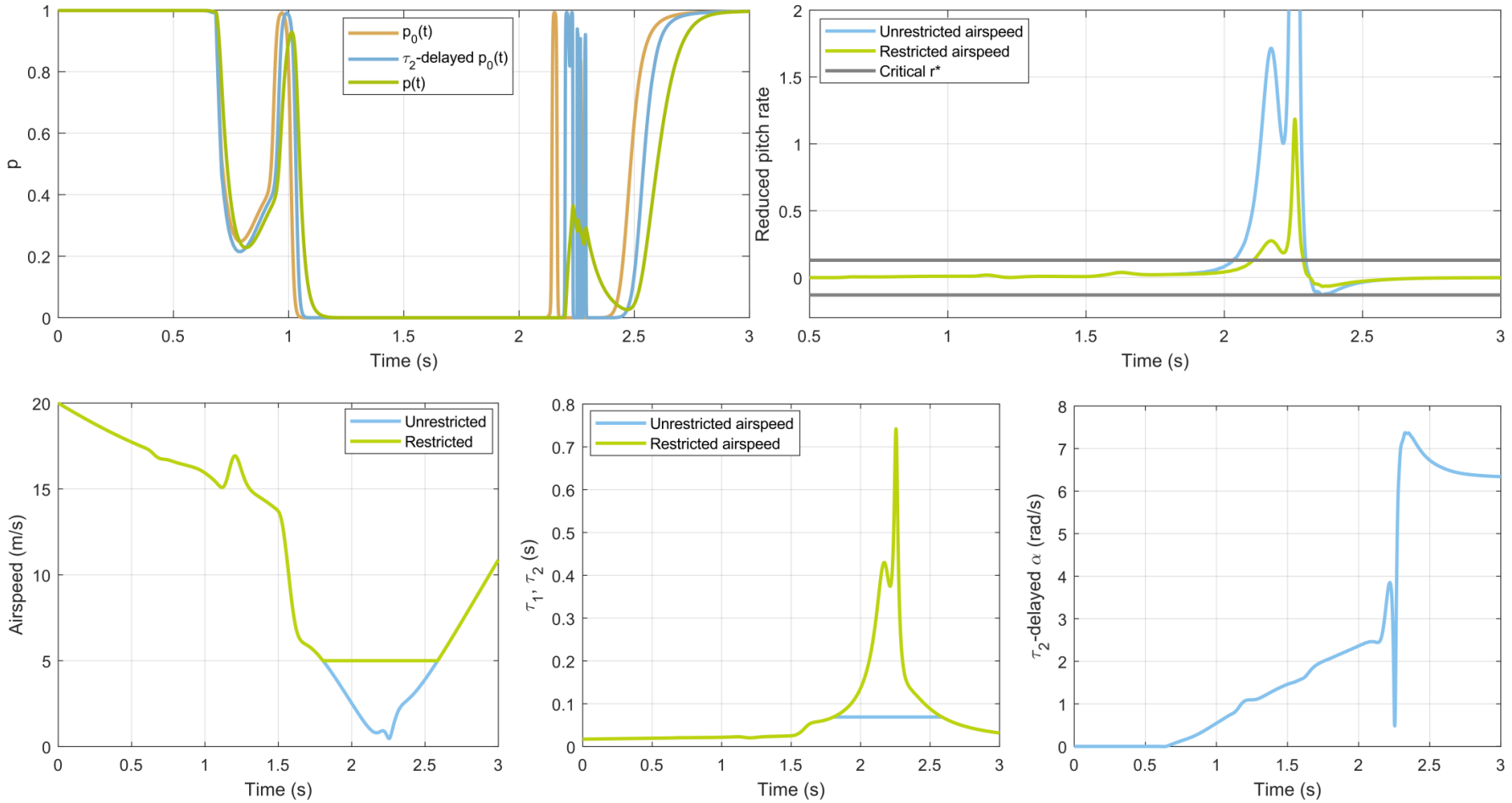

Figure 9.4.6: Case study of the vertical stabiliser tip, GK model, assuming the optimised anchor turn manoeuvre motion: GK attachment parameters $(p_0(\alpha(t)),\ p_0(\alpha(t)-\tau_2\dot{\alpha}(t)),\ p(t))$; reduced pitch rate; local airspeed; delay parameter values; and the delayed angle $\alpha(t)-\tau_2\dot{\alpha}(t)$. The effect of restricting the local airspeed to a minimum of 5 m/s is shown.

9.5. CONCLUSIONS

In this chapter we have studied the influence of GK dynamic stall effects on a three supermanoeuvres in the case study system: a fast quasistatic NPAS manoeuvre; Pugachev's cobra; and an anchor turn manoeuvre. In the case of the quasistatic NPAS manoeuvre and Pugachev's cobra, dynamic stall effects had relatively little influence on the manoeuvre performance – either because of a sufficiently slow timescale (quasistatic NPAS) or because such effects as were present did not fundamentally alter the manoeuvre behaviour (the cobra). Model validity tests found that the fast quasistatic NPAS manoeuvre lay just within the range of quasistatic model validity; and that the cobra manoeuvre lay within the range of GK model validity. In both cases, the relative insignificance of dynamic stall effects demonstrated the capability of the quasistatic manoeuvre design tools devised in Chapters 6-7 to provide useful templates for manoeuvres under transient aerodynamic models.

The anchor turn manoeuvre, on the other hand, retained GK model validity over the lifting surfaces, but suffered from severe model breakdown on the stabiliser surfaces at the apex of the turn. This breakdown was caused by simultaneous high angle-of-attack rate and low airspeed, generating rapid attachment/reattachment cycles and peaks in the delay times. Ultimately, a full-system GK model is not appropriate for modelling the anchor turn manoeuvre, and more tailored modelling approaches are required. To compare the GK model with its quasistatic counterpart (the GK-reconstructed model), however, a novel cyclic-univariate optimisation technique was devised for matching manoeuvre acceleration profiles. This technique was able to successfully match the GK-reconstructed model manoeuvre with the manoeuvre under the reference quasistatic model, and may be seen as an alternative to the quasi-trim state manoeuvre design method used in Chapter 7. Overall, the results and methods obtained and devised in this Chapter provide a starting ground for future studies in the transient modelling of biomimetic supermanoeuvrability; in particular, the use of low-order modelling and manoeuvre design techniques for the exploration of the space of supermanoeuvres.

Chapter 10:
Concluding overview

10.1. NOVEL CONTRIBUTIONS

10.1.1. Biomimetic supermanoeuvrability

In this work we undertook a broad-spectrum study into the supermanoeuvrability capability of a case-study biomimetic morphing-wing aircraft. This case study system was designed to replicate theorized biological mechanisms for supermanoeuvrability without necessitating flapping-wing propulsion capability: pronation/supination/incidence control, sweep and dihedral control were utilised, alongside an unspecified conventional propulsion system. The system scaling, geometry and mass were fixed for the case study; but were derived from representative biological flying creatures and small UAV aircraft. A validated flight dynamic model based on quasisteady aerodynamics was developed for the case-study system, and through computational fluid dynamics a model capturing some transient aerodynamic effects was also developed and validated.

Existing capability in both biological flight manoeuvrability and thrust-vectoring supermanoeuvrability provided avenues for the exploration. Of the latter, nose-pointing-and-shooting (NPAS) manoeuvres formed the basis of a study into analogous quasistatic orientation control, independent of flight path, in biomimetic systems. Such control is widely available in the case study system, constrained only by (1) the available morphing and stabiliser and range, affecting the available orientation control range; and (2) the flight dynamic stability and orientation response time constant of the aircraft in its quasistatic morphing conditions, generating areas of instability under open-loop control and affecting the fidelity of the response to the control input.

Symmetric incidence morphing was sufficient to control pitch angles within c. $-25°$ to $30°$; asymmetric incidence and single-wing dihedral control were sufficient to control pitch and yaw angles up to c. $\pm 25°$. In these cases, the control effectiveness of the stabiliser control surfaces (elevator and rudder) was found to be the primary limiting factor of the available orientation control range, indicating that immediate improvements in this metric could be achieved with stabiliser augmentation. Symmetric incidence and single-wing sweep control also enabled pitch and yaw control in an irregular zone, with morphing-based limits on the available orientation control range. An easy method of generating open-loop morphing control paths corresponding to arbitrary specified orientation paths was devised. Higher

degree-of-freedom morphing increased the available orientation control range at the cost of underconstrainedness at lower angles, leading to discontinuity in the computed control paths. The effect of the target NPAS timescale on the manoeuvre performance is complex: apart from the expected trend of higher fidelity with slower timescale, there is some evidence that performing manoeuvres faster than any anticipated instability timescales yields fidelity improvements. Overall, the biomimetic morphing present in the case study system allows a high level of quasistatic NPAS capability. Dynamic stall effects, as per the GK model, had no impact on this capability.

This capability leads immediately to the possibility of rapid nose-pointing-and-shooting (RaNPAS) manoeuvres – in this work, Pugachev's cobra, and an analogous manoeuvre in yaw were studied. In the design of these manoeuvres, continuous control paths are replaced by indicative pointer states, leading to a guidance process that is much more heuristic: thus, more flexible but coarser. This allows the exploration of several formats of successful cobra manoeuvre: utilising a simple morphing perturbation, or a high-angle trim state prior to a perturbation, or a pitch-up→pitch-down→pitch-up sequence; and in varying morphing degrees of freedom. Symmetric sweep morphing is of key importance in these manoeuvres as it is able to generate large pitching moments by shifting the aircraft aerodynamic centre fore and aft. Dynamic stall effects, as per the Goman-Khrabrov (GK) model, were found to have a relatively minimal effect on the cobra manoeuvre dynamics, validating the use of the quasistatic model and the quasistatic pointer state design method. Asymmetric forebody separation effects were not modelled directly, but a preliminary study indicates that such effects, even at expected maximal levels, are within the space of acceleration vectors that are controllable by asymmetric incidence morphing. This implies that such effects should be fully correctable with sufficiently rapid actuation. The design of yaw RaNPAS manoeuvres is more complex, as the control design can no longer rely on symmetry to enforce planar motion. This requires a more advanced pointer state method, in which these states are constrained to in-plane accelerations. This approach yields successful RaNPAS manoeuvres to yaw angles of beyond 80° with only asymmetric incidence morphing, and beyond 90° with all-DOF morphing.

From existing studies into biological manoeuvrability, two directions for study were selected: ballistic transition manoeuvres and anchor turns. These function as connecting points between biological and mechanical supermanoeuvrability. In the case study system, a ballistic transition manoeuvre can be performed with a simple modification of the RaNPAS cobra controls. Utilising the same pitch-up state sequences as in Chapter 7, Section 7.3, instead of transitioning subsequently to a pitch-down state, the aircraft transitions to a neutral state which maintains a high pitch angle at decreasing airspeed until the point of impact. This leads to successful impact landing with large reductions in kinetic energy (>98%). The validation of the cobra manoeuvre with respect to the transient Goman-Khrabrov aerodynamic model is taken to extend to the studied ballistic transition manoeuvre, as the aircraft and morphing control rotation rates are not significantly different.

In a similar manner, anchor turn manoeuvres can be generated by destabilising the yaw RaNPAS manoeuvres at low airspeed to yield a permanent orientation shift, followed by a recovery of airspeed in the shifted direction. This is possible, for turns up to at least 90°, with only asymmetric incidence morphing, or up to at least 160° with additional asymmetric sweep morphing. These manoeuvres were validated with respect to changes in the quasistatic model, indicating that this capability is not confined to this specific planform or aerodynamic model. They were not, however, validated with respect to the transient Goman-Khrabrov aerodynamic model, as this model breaks down under the high rotation rates present in this system. A higher-fidelity model is likely to be required to accurately assess the effectiveness of the quasistatic design process used to generate the manoeuvre. Unmodelled transient effects are not expected to significantly alter the aerodynamic mechanisms utilised in the manoeuvre; but may significantly impede real-time manoeuvre control.

This work demonstrates, in broad and general terms, that biomimetic morphing-wing systems are capable of an advanced level of supermanoeuvrability, rivalling that of thrust-vectored aircraft, and analogous to that found in biological flying creatures. This capability has not previously been recognised. The analysis of this study suggests a UAV/MAV equipped with asymmetric incidence morphing as the best option for further more detailed

research and experimental validation. According to our modelling, such a craft is capable of quasistatic NPAS manoeuvres in pitch, RaNPAS manoeuvres in yaw, and anchor turning. The addition of single-wing dihedral control leads to simultaneous pitch-yaw quasistatic NPAS; or the addition of symmetric sweep morphing to RaNPAS manoeuvres in pitch (and possibly simultaneous pitch-yaw) and ballistic transition manoeuvres. The possible actualisation of an operational aircraft of this form has ramifications for several areas of combat aircraft and missile weapons design.

10.1.2. Methodological contributions

The process of exploring biomimetic supermanoeuvrability, as per Section 10.1.1, led to the development of novel analysis methods and methodologies in several areas of flight dynamics and simulation. The flight simulator presented in this work represents an improvement in modelling fidelity over most existing flight simulators based on reduced-order models; with a multibody dynamic analysis of all lifting surfaces, quasistatic and transient (GK) aerodynamic models, and under quaternion variational integration or pole-switching Euler angle RK45 integration.

The requirement for singularity-free integration over all possible orientations led to the development of a novel quaternion variational integrator (QVI) for complex systems, with improvements in stability over existing QVIs. Notably, however, pole-switching Euler angle RK45 integration, representing a relatively simple extension to existing simulators based on single-format Euler angle integration, was found to be more computationally efficient. The implementation of the GK dynamic stall model in a three-dimensional context led to several key model developments: split leading/trailing edge models; the parametric effects of aircraft control surfaces; the development of improved separated model fits and an improved GK sigmoid function; and the assessment of model validity via time-domain and spectral methods. These developments led to an array of open questions, discussed in Section 10.1.3.

The existence of a continuous space of trim states in the case study system led to a wide-ranging manoeuvre design methodology based on the computation of trim or quasi-trim states. The analysis of quasistatic NPAS capability was enabled by a parametric trim state

manoeuvre design method, which tracked an orientation target function though the system's space of trim states. This method generalised to quasi-trim state approach, involving the computation or optimisation of quasi-trim states with specified acceleration vectors, enabling the design of pointer states for RaNPAS or more complex manoeuvres (e.g. Pugachev's cobra, anchor turns). This manoeuvre design methodology is necessarily restricted to the quasistatic aerodynamic model: but studies with transient models indicate that its predictions remain accurate for the manoeuvres studied, with the exception of the anchor turn, which shows transient aerodynamic model breakdown. The supermanoeuvres considered here would be significantly more difficult to design and study without this manoeuvre design methodology.

The introduction and study of trim and quasi-trim spaces, and the development of trim and quasi-trim state-based design methods (rigorous and heuristic) are two key contributions of this thesis. The study of trim and quasi-trim spaces in biomimetic and / or morphing aircraft has the potential to open up a wide range of manoeuvre capability in these aircraft. As demonstrated, trim space analysis offers a rigorous and immediate avenue into NPAS capability (even if, at a minimum, only quasistatically). Quasi-trim space analysis is a tool for the generation of more complex NPAS manoeuvres; it shows particular value in constraining motion to a plane, via the use of planar acceleration constraints. This allows relatively complex supermanoeuvres (e.g. the NPAS manoeuvre in yaw; the rattlesnake) to be achieved in open-loop with a simple definition of the control input.

Quasi-trim states / control inputs are remarkably versatile: they can be used as an open-loop platform for manoeuvres, on which closed-loop control is superimposed (as in many of the studies in this work); but they can also be used to generate states to use in closed-loop control. The latter capability was reference in the analysis of synthesised control actions (Chapter 7, Section 7.7), which demonstrated that rudder and aileron-type control could be synthesised at high angles of attack by morphing actions, via a quasi-trim analysis. More generally, defining a desired aircraft moment or acceleration output (e.g. an enhanced rudder moment, manoeuvre trajectory acceleration, or any instantaneous closed-loop control moment), a quasi-trim analysis, with the desired acceleration as the quasi-trim objective, will yield control configurations, or perturbations to the existing control

configurations, that will generate that desired moment / acceleration. This is a powerful tool for the exploration, analysis and control of morphing-wing supermanoeuvrability. The approach is not restricted to NPAS capability: Chapter 7, Section 7.6 presented approaches to the generation of anchor turn manoeuvres through quasi-trim analysis of this form.

10.1.3. Open questions raised

A range of open questions were raised in the process of this work's analysis, particularly with regard to the GK aerodynamic model. The GK model is formulated in a wind tunnel-type context with single flow-direction, no control surfaces, and at constant airspeed. Extending this to a three-dimensional flight dynamic model with multiple aerofoils raises several open questions, as in Chapter 8, Section 8.4:

- regarding the nature and cause of the wide variation of GK delay parameters reported in literature for the same aerofoils;
- regarding the dependency of the GK delay parameters on the system airspeed (and/or chord); a topic not addressed in existing GK-based 2D flight simulators;
- regarding the modelling of the GK delays in systems with control surfaces and how this can be accurately and cost-effectively carried out.
- regarding appropriate methods for the characterisation of GK and quasistatic model validity (reduced frequency, angle-of-attack rate, or other metrics); a topic which existing literature treats inconsistently.

GK model breakdown due to added mass / unsteady circulatory lift effects was observed for sufficiently rapid manoeuvres, and there is also the open question of how to model these effects in combination with the GK model. Further computational and experimental study is required to resolve these questions; leading potentially to improvements in the accuracy and flexibility of the model. Such study was not carried out in this work for reasons of time and space: the primary intent was to design and explore biomimetic supermanoeuvres holistically; rather than derive new transient aerodynamic models.

10.2. LIMITATIONS

10.2.1. Model limitations

In this study we attempted the development and implementation of reduced-order aerodynamic and flight dynamic models of maximum available fidelity. However, this was not sufficient to model all the aerodynamic and structural effects that are relevant to the system. Among the aerodynamic phenomena not modelled are flow shadowing, spanwise lifting surface flow, vortex shedding, aerodynamic added mass at high rotation rates, propulsion-induced flower, and the effect of transient airspeed changes. Dynamic stall is modelled at moderate fidelity via the GK model, and asymmetric forebody separation is studied in magnitude, for a basic assessment of controllability, but not in its time-dependent dynamics.

Structurally, the system is modelled via multibody dynamics; an exact formulation for a rigid-body system. Structural deformation is not modelled: the aircraft is conceived as a rigid, not flexible, aircraft, for which any significant deformation would represent an unacceptable risk of structural failure. In this context, an analysis of deformation may be replaced with analysis of stresses, with reference to a structural failure criterion. This is entirely possible in the case study model, but is not implemented: the purpose of this work has been to design and define manoeuvres and explore their aerodynamic and flight dynamic feasibility; a necessary prerequisite to an analysis of structural feasibility. To characterise the system's aerostructural stresses and stability adequately, a system specification more detailed than the current case study (with material and actuator specifications) is required. The restriction to a simplistic actuator was not a limitation on this study's conclusions *per se*: within the manoeuvre design framework in which this study operated, all actuators are identical, as all control inputs are specified *a priori*. However, complex actuator models are required for further studies into the feasibility of open- and closed-loop manoeuvre control.

The system was validated with respect to an experimentally-derived nonlinear stability derivatives model. This validation does not directly cover strongly transient flight regimes; and while the local transient aerodynamic models are validated with respect to computational fluid dynamics, their synthesis is not validated with respect to experimental

flight data at high levels of transience. This is an important, though difficult, area for future research; as this form of validation data is largely non-existent in the literature. Flight or wind tunnel tests focusing on specific supermanoeuvres would lead to an increased understanding of the limits of validity of our flight dynamic model, and may indicate avenues for further improvements in model fidelity.

10.2.2. Case study limitations

The nature of this work, as a case study, leads to results that are broad in terms of the manoeuvres studied, but limited in terms of the effect of system changes on these manoeuvres. Parametric studies are carried out with respect to manoeuvre parameters, but not the case study system parameters. For this reason, the results of this study shed light only on a limited space of system capability, and avoid its limit zones. This avoidance is intentional: the limited fidelity of the aircraft flight dynamic model, as per Section 10.2.1, significantly restricts the accuracy with which the location of these zones can be predicted. In the limit zones, where the control effort required is some critical metric, complex flow effects are likely to degrade system performance, whereas in areas well within system capability there is at least a wider spectrum of available control effort. A significantly more detailed study, with a significantly more detailed model, is required to fully assess the limits of system capability, even for a given system performing a given manoeuvre.

10.3. FUTURE DIRECTIONS

The limitations discussed in Sections 10.2.1-10.2.2 lead on to several directions for further research and development. More specialised study is a key theme: that of a specified morphing configuration performing a single manoeuvre, and of areas such as the manoeuvre flight envelope under aerostructural, actuator, aerodynamic and other constraints; closed-loop control; feasibility for target applications; and the impact of complex aerodynamic effects (asymmetric forebody separation/flow shadowing/etc.). Such studies require model expansion, and experimental validation, in all these areas. We recommend initial research into a system with asymmetric incidence morphing: such a system shows low actuator complexity, is amenable to simple flight dynamic models due to the small lifting motion, and has the capability for a range of supermanoeuvres as discussed

in Section 10.1.1. In addition, at a methodological level, the techniques of quasi-trim analysis show the potential for significant further application to the analysis and control of supermanoeuvrability. In particular, the use of quasi-trim analysis to generate states for use in closed-loop control is an immediate application of significant impact. Prior to this work, the study of biomimetic supermanoeuvrability was restricted to simple perching manoeuvres. With the results now gathered here, there is motivation to broaden this study to a range of biomimetic supermanoeuvres that is many times greater, opening up opportunities for the design of new forms of high-performance unmanned aircraft.

END OF BODY

Appendix 1:
Case study system specification

A1.1. PARAMETER SPECIFICATION

We select case study system parameters to match the scale of a number of source aircraft and biological creatures – including the NextGen MFX-1 morphing-wing aircraft [1], the remote-control ShowTime 50 [2,3], greylag geese (*Anser anser*) [4–8], and steppe eagles (*Aquila nipalensis*, previously *A. rapax*) [9,10]. Relative to these biological creatures, we accentuate the case study system mass to account for operational payloads – though, at 8 kg, our default mass is not as large as could be desired for some applications. We perform parametric studies in mass further on in this thesis. Relative to all sources, we decrease the wing and stabiliser chords; to allow a wider range of morphing before collision between the wings and stabilisers; to minimise the actuator effort required for morphing; and to represent an aerodynamically suboptimal system – so that the conclusions we draw from the case study need not be restricted only to highly optimised systems.

Figure A1.1.1 shows the definition of some key geometric parameters, and Table A1.1.1 the complete set of parameters for the system with relevant comparisons. Several disparate points should be noted regarding the specification of these parameters:

- The case study system aerofoils chosen are taken from the ShowTime 50, an existing highly manoeuvrable remote control aircraft. The ShowTime 50 wing aerofoil (ST50W) is a symmetric aerofoil similar to a NACA0015, and is used for the case study system wings. The ShowTime 50 horizontal stabiliser aerofoil (ST50H) is a symmetric aerofoil similar to a NACA0009 and is used for the horizontal and vertical stabilisers.

- Alongside the masses of the lifting surfaces and cylindrical fuselage, a point mass is included in the model to allow a finer specification of the aircraft centre of mass location. We will demonstrate after the kinematic and dynamic analysis has been carried out that this system has appropriate stability properties and trim properties. Stability and trim analysis will be carried out in Chapter 6.

- The aircraft propulsion system is not specified in detail: only a thrust force is utilised in the model description, and no further propulsion dynamics are modelled. Depending on application and manoeuvrability requirements several options are

available, including propeller, jet and rocket systems. Approximate maximum propulsive forces for such systems implemented in an aircraft of this scale are 60N for a propeller, based on a thrust-weight ratio of 2:1 for the ShowTime 50 [2]; and 100 N for a jet, based on the NextGen MFX-1 [1] at 50% capacity. Rocket propulsion is likely to be relevant only in applications involved in the delivery of ordinance, and is given no detailed consideration in this study. Biomimetic propulsion via wing flapping is relevant in the application of our findings on manoeuvrability to aircraft utilising such modes of propulsion; but the scope of this study is concerned solely with biomimetic manoeuvrability independent of biomimetic propulsion.

The specific aircraft geometry of our case study system is of minor relevance overall: key questions we are interested in are whether in general a biomimetic aircraft of this type is capable of supermanoeuvrability, and the extent to which its wing morphing is useful in post-stall manoeuvring.

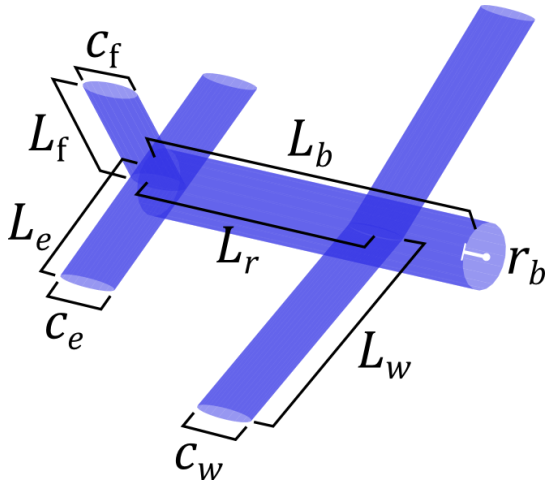

Figure A1.1.1: Aircraft with geometric parameters

Appendix 1: Case study system specification

Table A1.1.1: Case study system properties with relevant comparisons: *n/a*, *n/av* and *n/spec* denote data not applicable, not available, and not specified in this study; *mean* and *sample* denote mean and single-individual values; circa (c.) denotes approximate values, including approximate means from small sample sizes.

	This study	**NextGen MFX-1** [1]	**ShowTime 50** [2,3]	**Greylag Goose (*A. Anser*)** [4–8]	**Steppe Eagle (*A. nipalensis*)** [9,10]
Properties:	**Values:**				
Fuselage length – L_b	1.20 m	2.1 m	1.51 m	mean c. 0.82 m	mean c. 0.71 m
Wing root length – L_r	0.80 m	c. 1.17 m	c. 0.94 m	n/a	n/a
Wing semispan – L_w	0.80 m	1.4 m	0.73 m	mean c. 0.81 m	mean c. 0.95 m
Wing chord – c_w	0.15 m	mean c. 0.23	mean 0.32 m	mean c. 0.26 m	sample c. 0.3 m
Elevator semispan – L_e	0.40 m	n/a	c. 0.31 m	n/a	n/a
Elevator chord – c_e	0.15 m	n/a	mean c. 0.22 m	n/a	n/a
Fin height – L_f	0.40 m	n/a	c. 0.17 m	n/a	n/a
Fin chord – c_f	0.15 m	n/a	c. 0.09 m	n/a	n/a
Body radius – r_b	0.10 m	mean c. 0.15 m	mean c. 0.088 m	n/a	n/a
Aerofoils	ST50 W/H	n/av	ST50 W/H/V	complex	complex
Total mass – m_{tot}	8 kg	45 kg	2.9 kg	mean c. 3.3 kg	mean c. 3.5 kg
Single wing mass – m_w	1 kg	n/av	n/av	n/av	n/av
Single elevator mass – m_e	0.15 kg	n/av	n/av	n/a	n/a
Fin mass – m_f	0.20 kg	n/av	n/av	n/a	n/a
Max propulsive force	n/spec	c. 200 N	c. 60N	n/av	n/av
Propulsive mechanism	n/spec	jet	propeller	flapping-wing	flapping-wing
Non-comparable properties:					
Point mass length – L_{pm}	1.1 m				
ST50W max. thickness – $h_{\mathrm{W,max}}$	0.0216 m				
ST50W mean thickness – $h_{\mathrm{W,av}}$	0.0148 m				
ST50H max. thickness – $h_{\mathrm{H,max}}$	0.0216 m			n/a	
ST50H mean thickness – $h_{\mathrm{H,av}}$	0.0148 m				
Fuselage mass – m_b	3.0 kg				
Point mass – m_{pm}	2.5 kg				

APPENDIX 1 REFERENCES

[1] Flanagan, J., Strutzenberg, R., Myers, R., and Rodrian, J., "Development and Flight Testing of a Morphing Aircraft, the NextGen MFX-1," 48th AIAA/ASME/ASCE/AHS/ASC Structures, Structural Dynamics, and Materials Conference, Honolulu, HI.

[2] Selig, M., "Modeling Full-Envelope Aerodynamics of Small UAVs in Realtime," AIAA Atmospheric Flight Mechanics Conference, Toronto, ON.

[3] Horizon Hobby Ltd., *HAN4275 ShowTime 50 Manual*, 2006.

[4] Dunning, J. B., ed., *CRC handbook of avian body masses*, CRC Press, Boca Raton, 2008.

[5] Matthews, G. V. T., and Campbell, C. R. G., "Weights and measurements of Greylag Geese in Scotland," *Wildfowl*, Vol. 20, 1969, pp. 86–93.

[6] Royal Society for the Protection of Birds, *RSPB Wildlife Guide: Greylag goose*.

[7] Vargas, S., *Animal Diversity Web: Anser anser (Online)*, 2002.

[8] Speakman, J. R., and Banks, D., "The function of flight formations in Greylag Geese Anser anser; energy saving or orientation?," *Ibis*, Vol. 140, No. 2, 2008, pp. 280–287. DOI:10.1111/j.1474-919X.1998.tb04390.x.

[9] Meyburg, B. U., Boesman, P., Marks, J. S., and Sharpe, C. J., "Steppe Eagle (Aquila nipalensis)," *Handbook of the Birds of the World (Alive)*, J. del Hoyo, A. Elliott, J. Sargatal, D.A. Christie, and E. de Juana, eds., Lynx Edicions, Barcelona, Spain, 2018.

[10] Westphal, J., *Animal Diversity Web: Aquila rapax (Online)*, 2007.

END OF THESIS

THIS PAGE LEFT BLANK

THIS PAGE LEFT BLANK